A Large Hadron Electron Collider at CERN - the LHeC

Conceptual Design Report

LHeC Study Group

March 25, 2011

Draft 0.1

Abstract

The physics programme and the design are described of a new $e^{\pm}p/A$ collider based on the LHC. The Large Hadron Electron Collider extends the kinematic range of HERA by two orders of magnitude in four-momentum square Q^2 and Bjorken x, and its design achieves a factor of hundred higher luminosity, of $\mathrm{O}(10^{33})\,\mathrm{cm}^{-2}\mathrm{s}^{-1}$. The LHeC thus becomes the world's cleanest high resolution microscope and a crucial instrument to resolve the expected new physics at the TeV scale of mass and to also continue the path of deep inelastic lepton-hadron scattering into unknown areas of physics and kinematics. The LHeC may be realised as a ring-ring or linac-ring collider, and thorough design considerations are presented for both options in terms of their physics reach and technical realisation. Corresponding designs of interaction regions are presented as is a complete study of a suitable detector including tagging devices in forward and backward directions. The LHeC may be built, installed and operated while the LHC is still in operation. It thus represents a major opportunity for particle physics to progress and for the LHC to be further exploited.

Contents

Part I

Introduction

Chapter 1

General Introduction

Chapter 2

DIS and Theory

Chapter 3

Design Considerations

Chapter 4

Executive Summary

Part II

Physics

Chapter 5

Precision QCD and Electroweak Physics

5.1 Inclusive ep Cross sections and structure functions

Editors: Max Klein, Enrico Tassi, 10 pages

5.2 QCD fits (PDFs and α_s)

Editors: Claire Gwenlan, Alberto Guffanti, Max Klein, Voica Radescu 11 pages

5.3 Electroweak physics

Editors: Paolo Gambino, Claire Gwenlan, Nandi Soumitra, Precision electroweak measurements at low energy have played a central role in establishing the Standard Model (SM) as the theory of fundamental interactions. More recently, measurements at LEP, SLD, and the Tevatron have confirmed the SM at the quantum level, verifying the existence of its higher-order loop contributions. The sensitivity of these contributions to virtual heavy particles has allowed for an estimate of the mass of the top quark prior to its actual discovery in 1995 by the CDF and DØ Collaborations. Now that the determination of the top mass at the Tevatron has become quite accurate, reaching the 1% level, electroweak precision measurements imply significant constraints on the mass of the last missing piece of the SM, the Higgs boson. The current situation is illustrated in fig.5.3, where the Higgs mass sensitivity of a global fit to electroweak precision observables in the SM is shown [1] (a similar analysis has been performed in [2]). The left panel shows the $\Delta\chi^2$ of a fit to all relevant electroweak observables, while the right panel also include information from direct searches for the Higgs boson at LEP-2 and the Tevatron. Indeed, direct searches exclude a Higgs boson with mass lower than 114GeV or in a narrow window around 160GeV. An important implication (at 95% CL) is that if the SM is correct, the Higgs boson must soon be found with mass below 155GeV either at the Tevatron or at LHC.

Electroweak precision measurements are also very effective in constraining the possible extensions of the SM. In general, the observed good quality of the SM fit disfavors new physics

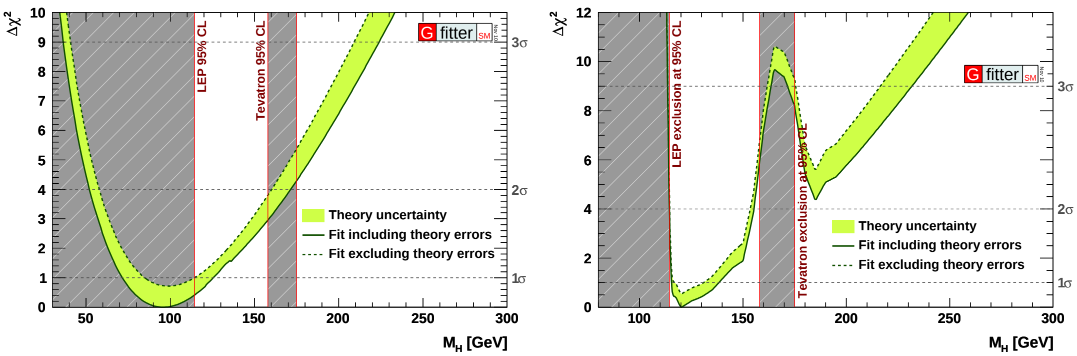

Figure 5.1: Higgs mass sensitivity of a current fit to precision electroweak observables [1]. The right panel includes the information from direct searches.

at an energy scale of $O(100\text{GeV})$ that modifies the Higgs mechanism in a drastic way. On the other hand, the fit does present a few interesting deviations at the level of 2-3σ. An important one is related to the tension between the FB asymmetry of $Z \to b\bar{b}$ measured at LEP, which favors a heavy Higgs, and the LR asymmetry in $Z \to \ell\bar{\ell}$ and the W mass, which both favors a very light Higgs. Unfortunately, the present determination of M_H depends largely on these conflicting information, whose origin could be either statistical or rooted in new physics around the corner [3]. Another plausible $\sim 3\sigma$ hint of physics beyond the SM, without Higgs implications, is the discrepancy between the measured magnetic anomalous moment of the muon and its SM prediction [4].

It is unlikely that operating experiments will change significantly the above picture of electroweak precision measurements. The Tevatron and LHC will marginally improve the current precision on the top mass and reach a combined 15 MeV uncertainty on M_W, while LHCb might be able to achieve an interesting accuracy in the measurement of $\sin^2\theta_W$, perhaps at the level of LEP [5, 6]. Two experiments at Jefferson Lab, Q-weak [7] and (later) MOLLER [8], will measure the weak mixing angle from parity violation in $e - p$ and $e^- - e^-$ scattering at low energy: these are interesting measurements complementary to the existing ones; MOLLER, in particular, will reach an accuracy similar to that of LEP. On the other hand, it is widely expected that either the Higgs boson or new physics will be discovered at the LHC, if not both. This is the context in which precision electroweak measurements at LHeC have to be set: rather than improving bounds on the SM parameters they might help understand new physics, if that is discovered at LHC.

The electroweak measurements possible at LHeC are in essence the same that have already been performed at HERA (see [9, 10] for an overview), but they will greatly benefit from the higher energy and larger luminosity. A first class of measurements involves polarized charged currents (CC) only.

They include a verification of the left-handedness of CC from the polarization dependence of the CC cross-section. At HERA this has led to a bound on possible right-handed currents, expressed in terms of the mass of a right-handed W_R boson that couples to quarks with the same strength as the SM one. While HERA-I result, $M_{W_R} > 210\text{GeV}$ at 95% CL, can be significantly improved at the LHeC, low-energy flavour bounds are much stronger. It is otherwise difficult to

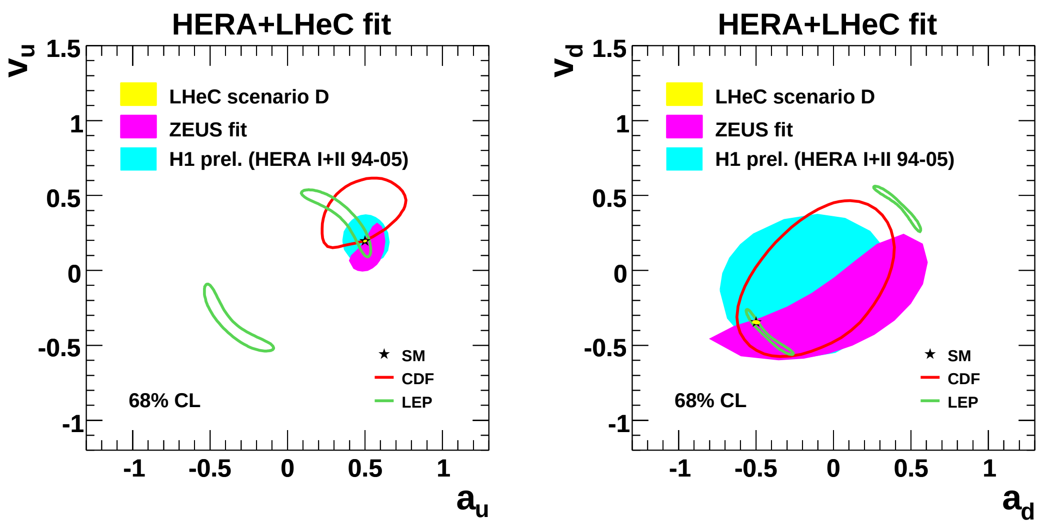

Figure 5.2: Determination of the vector and axial NC couplings of the light quarks at LEP, CDF, HERA and LHeC.

learn from CC alone. For instance, the Q^2-dependence of the CC cross sections, proportional to $G_F^2(M_W^2/(M_W^2+Q^2))^2\phi(x,Q^2)$, allows in principle to extract the propagator mass M_W, but the residual dependence on the structure of the nucleon requires a simultaneous fit to the pdfs, which necessarily includes NC cross sections as well. In fact, the sensitivity to M_W that can be achieved in this way is rather low: at LHeC, assuming SM NC couplings, the experimental error is about 150MeV (scenario D), far from being competitive. Higher sensitivity to M_W can in principle be obtained by trading G_F for the appropriate combination of $\alpha(M_Z), M_W, M_Z$ but then the precision in luminosity and other systematics become a bottleneck and one cannot achieve an M_W determination much better than above.

Paolo: this statement has to be checked. Using only HERA-I data H1 find an experimental uncertainty of about 200MeV if data are analyzed in this way. How much can this be improved at LHeC? I see a clear bottleneck: the precision in luminosity (most of the M_W sensitivity comes from the overall normalization) and the model error which in H1 paper is 40MeV. All other theoretical uncertainties can be brought significantly down.

On the other hand, LHeC will be able to measure at the percent level the neutral current couplings of the light quarks. As can be seen in Fig. 5.2, LEP has been able to constrain well only a combination of them. On the other hand, DIS experiments with polarized electron and positron beams can completely disentangle the vector and axial couplings of up and down type light quarks. Of course this requires a simultaneous fit to pdfs and electroweak couplings, keeping fixed the leptonic couplings, which have been very precisely measured at LEP and SLD. As illustrated in Fig.5.2, the preliminary results by ZEUS and H1 have improved on the LEP determination in the case of the up quarks [10–12]. The expected resolution for scenario D of LHeC is hardly visible on the scale of Fig. 5.2: the results for the various LHeC scenarios (and combination thereof) are shown in Table **??** *(still to be made, see later. It should be something*

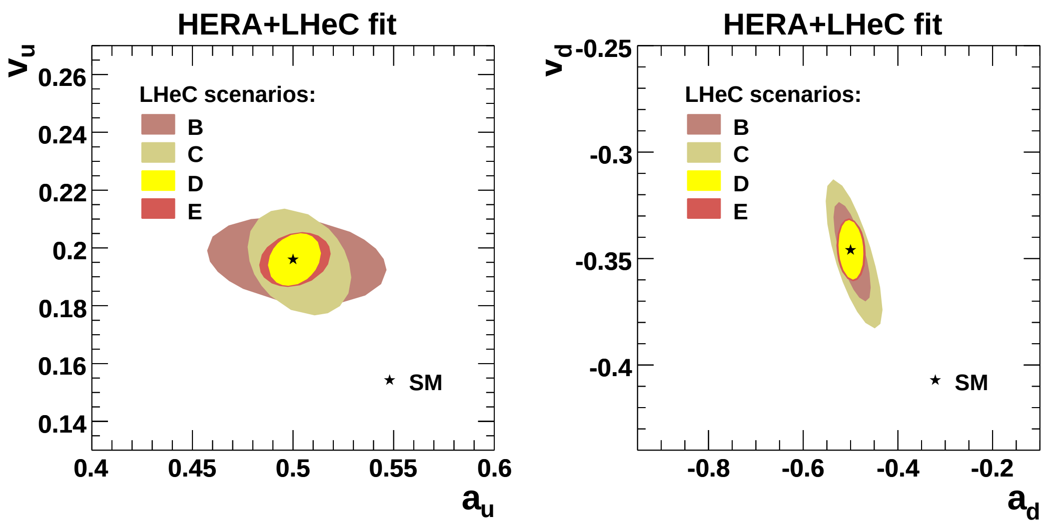

Figure 5.3: Determination of the vector and axial NC couplings of the light quarks at LHeC, comparison different scenarios. (TO BE UPDATED??)

like slide 43 of Claire's LHeC talk). The accuracy on the vector and axial vector couplings of the $u, d = s$ quarks ranges, in the best possible scenario, ranges between 1 and 4%, with an improvement wrt HERA by a factor 10 to 40. A comparison among the various LHeC scenarios can be found in Fig. 5.3: the most interesting scenarios are B and D. *(Assuming Voica's results for scenario B)* A high degree of polarization (scenario D) can be compensated by much higher luminosity (scenario B).

A better determination of the light quark NC couplings will particularly constrain New Physics models that modify significantly the light quark NC couplings, without affecting the well-measured lepton and heavy quark couplings. It is not easy to realize such an exotic scenario in a natural way, although family non-universal (leptophobic) Z' models (see for instance [13,14] and refs. therein), R-parity violating supersymmetry (see [15] for a review) and leptoquarks [16] can in principle succeed. LHeC could therefore accurately test a spectrum of interesting new physics models. A specific linear combination of the light quark NC vector couplings (v_u and v_d) will be soon be measured at the % level by the QWeak Collaboration [7]. Their results, combined with existing precise measurement of Atomic Parity Violation and DIS, will provide a percent determination of v_u and v_d [17] and test the same kind of models, but it will not probe the axial couplings.

Additional issues concerning this fit:

- *Voica has shown that high precision can be obtained also in scenario B. Claire's results for B are less precise, likely because of lower angular coverage (down to 10 degrees, only for B). However, there are a few strange features in Voica's numbers (see my dec 10 email)*
- *what is the effect of combining scenarios B+H and other similar combinations of scenarios?*

- *what is the effect on electroweak couplings of relaxing the assumptions on the sea quarks (as Voica discusses on p.13 of her Chavannes slides)?*

- *I think somebody in Chavannes asked a question on the importance of polarized positrons for electroweak physics. Can we answer?*

If there is time, two easy, complementary analyses that might give a feeling of the constraining power in more general new physics models are the following

1. *we express all the NC quark and lepton couplings in terms of* $\sin^2\theta_W$*, and fit for it. NC and CC couplings are all normalized to* G_F*.*

2. *we express the lepton and quark couplings in terms of* $G_F, sin^2\theta_W$ *and* ρ *(a renormalization factor in front of the NC coupling), and fit for them, see PDG.*

A fit to oblique parameters S, T, U *is also possible but requires more work. Not important.*

5.4 Charm and Beauty production

Editors: Gustav Kramer, Hubert Spiesberger, Gokhan Unel, Olaf Behnke 12 pages

5.4.1 Introduction

The understanding of the dynamics of charm and beauty heavy quark production has been improved considerably over the last years, in particular by the large amount of precise data from the experiments at HERA and the TEVATRON. At HERA, heavy quarks are produced in leading order via the Boson Gluon Fusion (BGF) process shown in Figure 5.4. This process provides direct access to the gluon density in the proton. On the theoretical side, the description of heavy quark production in the framework of perturbative QCD is complicated due to the presence of several large scales like the heavy quark masses, the transverse momentum p_T of the produced quarks and the momentum transfer Q^2. Depending on the kinematic range considered, the mass m of the heavy quark may have to be taken into account. Different calculation schemes have been developed to obtain predictions from perturbative QCD, depending on the specific kinematical region and the relative importance of the relevant scales. At HERA, it was observed that the charm and beauty production data are described reasonably well over the whole accessible phase space by Next-to-Leading Order (NLO) fixed flavour number scheme (FFNS) calculations, where the quark masses are fully accounted for. An LHeC collider with a factor ~ 20 higher squared centre-of-mass energy s would allow to extend the studies to a much larger kinematical phase space. The applicability of the different schemes could be tested up to very high Q^2 and P_T scales. Here the NLO FFNS scheme predictions might start to break down since large logarithms $\ln(p_T^2/m^2)$ are neglected which can be resummed to all orders in the alternative zero-mass schemes (for details see next section). The much higher centre-of-mass energy compared to HERA also allows the gluon density involved in the BGF process to be probed at smallest proton momentum fractions down to $x_g \leq 10^{-5}$, where it is currently not well known.

The remainder of this article is organised as follows. First the different calculation schemes are introduced. Then phase space extensions, expected cross sections and implications for QCD tests are discussed for various processes: charm meson photoproduction, charm and beauty production at a photon proton collider option of the LHeC, charm and beauty quark production in neutral current DIS and finally total cross sections for various processes involving charm, beauty and also top quarks in the final state. The article concludes with a brief summary.

5.4.2 Calculation schemes for heavy quark productions

In the case of relatively small transverse momentum, $p_T \lesssim m$, the fixed-flavour number scheme (FFNS) is usually applied [?]. Here one assumes that the light quarks and the gluon are the only active flavours within the colliding hadrons (and the photon in the case of photoproduction). In the FFNS the charm quark appears only in the final state. The charm quark mass m can explicitly be taken into account together with the transverse momentum of the produced heavy meson; this approach is therefore expected to be reliable when p_T and m are of the same order of magnitude.

In the complementary kinematical region where $p_T \gg m$, calculations are usually based on the zero-mass variable-flavour-number scheme (ZM-VFNS). This is the conventional parton model approach where the zero-mass parton approximation is applied also to the charm quark, although its mass is not small compared with Λ_{QCD}. In the ZM-VFNS, the charm quark acts also as an incoming parton with its own parton distribution function (PDF) leading to additional direct and resolved contributions. Usually, charm quark PDFs and also the fragmentation functions (FFs), describing the transition of the charm quark to the charmed meson, are defined at an initial scale μ_0 chosen equal to the charm mass m. Then this is the only place, where the charm mass enters in this scheme. The heavy meson is produced not only by fragmentation from the charm quark created in the hard scattering process; but also fragmentation from the light quarks and the gluon has to be taken into account. The well-known factorization theorem provides a unique procedure for incorporating the FFs into the perturbative calculations. The predictions obtained in this scheme are expected to be reliable only in the region of large p_T since all terms of the order m^2/p_T^2 are neglected in the hard scattering cross section. For photoproduction, calculations for charm-production in the ZM-VFNS have been performed in Ref. [?].

A unified scheme that combines the virtues of the FFNS and the ZM-VFNS is the so-called general-mass variable-flavour-number scheme (GM-VFNS) [?]. In this approach the large logarithms $\ln(p_T^2/m^2)$, which appear due to the collinear mass singularities in the initial and final state, are factorized into the PDFs and FFs and summed by the well known DGLAP evolution equations. The factorization is performed following the usual $\overline{\mathrm{MS}}$ prescription which guarantees the universality of both PDFs and FFs. At the same time, mass-dependent power corrections are retained in the hard-scattering cross sections, as in the FFNS. In order to conform with the $\overline{\mathrm{MS}}$ factorization, finite subtraction terms must be supplemented to the results of the FFNS. As in the ZM-VFNS, one has to take into account processes with incoming charm quarks, as well as light quarks and gluons in the final state which fragment into the heavy meson. It is expected that this scheme is valid not only in the region $p_T^2 \gg m^2$, but also in the kinematic region where p_T is larger than only a few times the charm mass m. The basic features of the GM-VFNS are described in Ref. [?]. Analytic results for the required hard scattering cross sections can be found in Refs. [?].

5.4.3 D^* meson photoproduction at LHeC compared to HERA

It is the purpose of this work to present theoretical predictions for the production of D^*-meson production in electron proton scattering at the LHeC. We assume an experimental analysis with data taken in the photoproduction regime, i.e. with an upper limit of $Q^2 \leq 1$ GeV^2. Since the cross section is dominated by low Q^2, our results should not depend too strongly on the precise value of this cutoff and our conclusions still be valid. Details of the calculation can be found in Ref. [?].

The D^*-production cross section $\sigma_{ep}(\sqrt{s})$ at the ep centre-of-mass energy $\sqrt{s}$ is related to the photoproduction cross section at centre-of-mass energy $W_{\gamma p}$, $\sigma_{\gamma p}(W_{\gamma p})$, through

$$\sigma_{ep}(\sqrt{s}) = \int_{y_{\min}}^{y_{\max}} dy f_{e\gamma}(y) \sigma_{\gamma p}(y\sqrt{s})\,. \tag{5.1}$$

Here, $f_{e\gamma}$ is the energy spectrum of the exchanged virtual photon which in the Weizsäcker-Williams approximation is given by

$$f_{e\gamma}(y) = \frac{\alpha}{2\pi}\left[\frac{1+(1-y)^2}{y}\ln\frac{(1-y)Q^2_{\max}}{y^2 m_e^2} + 2(1-y)\left(\frac{y m_e^2}{(1-y)Q^2_{\max}} - \frac{1}{y}\right)\right]\,.$$

The photon flux $f_{e\gamma}$ depends on $Q^2_{\max}$ and on $y = E_\gamma/E_e$, the ratio of the energies of the incoming photon and electron, which is determined by the inelasticity $y = Q^2/(2P\cdot q)$ where P and q are the 4-momenta of the incoming proton and the photon. The range of y, $y_{\min} \leq y \leq y_{\max}$ are determined by the cuts in the experimental analysis. For simplicity we have chosen $y_{\min} = 0.1$, $y_{\max} = 0.9$, but these limits can easily be adjusted as soon as more details about the detector layout are known. α is the electromagnetic fine structure constant.

The cross section for direct photoproduction in Eq. (5.1) is a convolution of the proton PDF, the FF for the transition of a parton to the observed heavy meson, and the cross section for the hard scattering process. For the resolved contribution, an additional convolution with the photon PDFs has to be performed. The hard scattering cross sections are calculated including next-to-leading order corrections. The PDFs and FFs are evolved at NLO. For the photon PDF we use the parametrization of Ref. [**?**] with the standard set of parameter values and for the proton PDF we have chosen the parametrization CTEQ6.5 [**?**] of the CTEQ group.

For the FFs we use the set Belle/CLEO-GM of Ref. [**?**] based on a fit of the combined Belle [**?**] and CLEO [**?**] data at $\sqrt{s} = 10.52$ GeV. For similar calculations at HERA we had observed that the photoproduction cross section $d\sigma/dp_T$ are larger by $25-30\%$ in average when using the Belle/CLEO-GM parametrization, as compared to the set Global-GM of Ref. [?]. The strong coupling constant $\alpha_s^{(n_f)}(\mu_R)$ is evaluated with the two-loop formula [**?**] with $n_f = 4$ active quark flavours and the asymptotic scale parameter $\Lambda^{(4)}_{\overline{\rm MS}} = 328$ MeV, corresponding to $\alpha_s^{(5)}(m_Z) = 0.118$. The charm quark mass is fixed to $m = 1.5$ GeV. We choose the renormalization scale μ_R and the factorization scales μ_F related to initial- and final-state singularities to be $\mu_R = \xi_R m_T$ and $\mu_F = \xi_F m_T$, where $m_T = \sqrt{m^2 + p_T^2}$ is the transverse mass. Variations of the parameters ξ_R and ξ_F can be used to study theoretical scale uncertainties; but in the present work we fix them to the default values $\xi_R = \xi_F = 1$. In Ref. [?], we had studied these scale uncertainties for photoproduction at HERA, as well as uncertainties due to various possible choices for input variables, as for example, the proton and photon PDFs and the D^* FFs and the influence of the charm quark mass.

In our calculation we study various combinations of beam energies. To compare with the situation at HERA, we include, as a reference, the values $E^p = 920$ GeV and $E^e = 27.5$ GeV for proton and electron energies, respectively. For the LHeC we take for the proton energy always $E^p = 7$ TeV and consider the options $E^e = 50$, 100 and 150 GeV. The transverse momentum p_T and the rapidity η of the D^*-meson are varied in the kinematic ranges $5 < p_T < 20$ GeV or $20 < p_T < 100$ and $|\eta| < 2.5$.

Numerical results are shown in Fig. 5.5 for the differential cross section $d\sigma/dp_T$ integrated over the rapidity $|\eta| \leq 2.5$ and in Fig. 5.6 for $d\sigma/d\eta$, integrated over the p_T-ranges $5 \leq p_T \leq 20$ GeV and $20 \leq p_T \leq 100$ GeV. The higher centre-of-mass energies available at the LHeC lead to a considerable increase of the cross sections as compared to the situation at HERA. Obviously one can expect an increase in the precision of corresponding measurements and much higher values of p_T, as well as higher values of the rapidity η, will be accessible. Since theoretical predictions also become more reliable at higher p_T, measurements of heavy quark production constitute a promising testing ground for perturbative QCD. One may expect that the experimental information will contribute to an improved determination of the (extrinsic and intrinsic) charm content of the proton and the charm fragmentation functions.

5.4.4 Charm and Beauty production at a photon proton collider

Introduction and Available beams The problem of precise measurement of parton distribution functions (PDF) is yet to be solved for the energy scales relevant for LHC results. One of the needed measurements is the gluon PDF for low momentum fraction: small $x(g)$. The last machine which has probed x(g) was HERA which had a reach of about $x(g) > 10^{-3}$.

The proton beam from LHC can be hit with a high energy electron or photon beam. The photons may be virtual ones from the electron beam resulting in a typical DIS event or they can be real photons originating from the compton back scattering process. In the latter case, the photon spectrum consists of the high energy photons peaking at about 80% of the electron beam energy on the continum of Weizsacker-Williams photons. The type (Linear or Circular) and the energy of the electron machine are yet to be determined. The following study aims to investigate the feasibility of a $x(g)$ measurement with such a machine. The generator level results are obtained using CompHEP and CalcHEP [**?**] software packages.

Final states interesting for $x(g)$ The final states that can be easily distinguished from the background events and that would give a good measure of the $x(g)$ are $\gamma g \rightarrow q\bar{q}$ where the gluon (g) is from the LHC protons, the photons are from a new accelerator to be build and the q stands for a heavy quark flavour, such as c quark and possibly b as well. The b quark final states are easier to identify due to b-tagging possibility using a silicon detector. The differential cross sections and the lowest x(g) reach for two electron beam energies (50 and 150 GeV) are shown in Figure 5.7 in the top row, on the left side for c quarks and on the right side for b quarks. The proton PDF is selected as CTEQ 6L1 and the masses of the c- and $b$quarks are taken as 1.65 GeV and 4.85 GeV, respectively. For comparison the HERA reach is also presented on the same plots. In all cases, higher electron beam energy results in reach to smaller $x(g)$: almost an order of magnitude by going from 50 to 150 GeV. For comparison also cross sections have been simulated for $eg \rightarrow eq\bar{q}$ in the DIS kinematic regime at the standard ep collider scenario for LHeC. The observed kinematical reaches are similar to those at a γp collider. However, the charm (beauty) cross sections at a γp collider are a factor 700 (200) larger than those at a ep collider in DIS.

Detector effects The angular dependency of the relevant processes is important to estimate the necessary η coverage of the detector and also to estimate the eventual electron machine selection. This dependency is shown in Figure 5.7 in the bottom row for $c\bar{c}$ (left) and $b\bar{b}$ (right) final states. One can notice that even for an angular loss of only about 5 degrees, there is considerable drop in both the cross section and in the $x(g)$ reach. This effect can be understood by considering the η dependence of the heavy quark pair production cross section in γp collisions which is shown in Figure **??**. The vertical solid line is representative for a 1 degree, the dashed line for a 5 degree and the dot-dashed line is for 10 degree detector. Therefore in order to have the best experimental reach the tracking should have an η coverage up to 5.

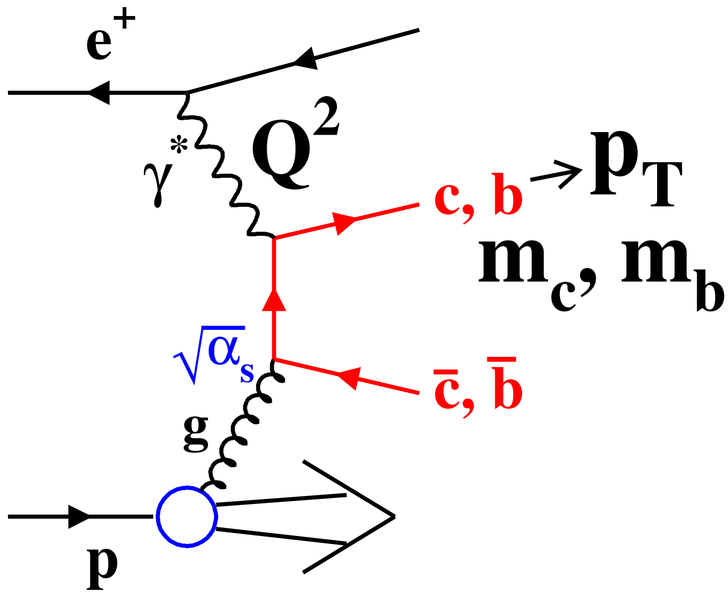

Figure 5.4: Leading order Boson Gluon Fusion (BGF) diagram for charm and beauty production in *ep*-collisions.

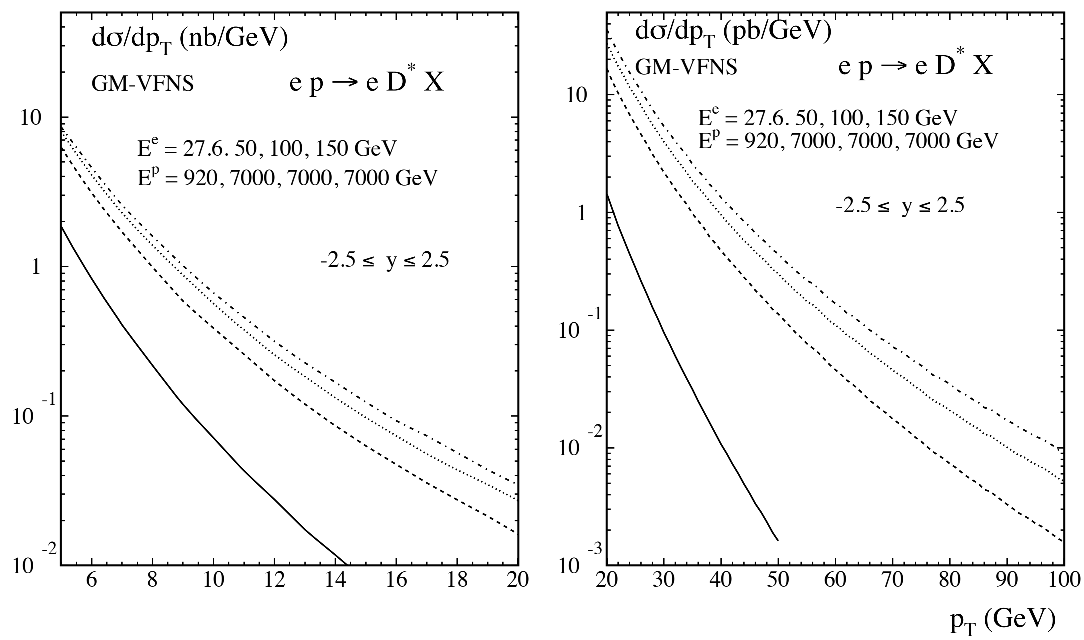

Figure 5.5: The p_T-differential cross section for the production of D^* mesons at LHeC for different beam energies integrated over rapidities $|\eta| \leq 2.5$. The curves from bottom to top correspond to the combinations of beam energies as indicated in the figure.

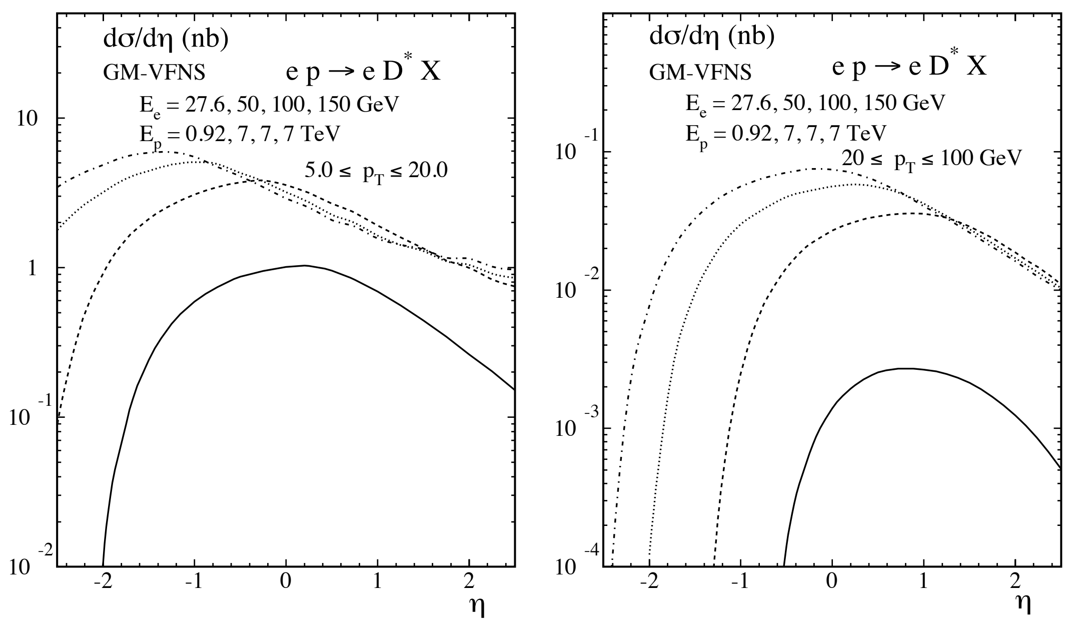

Figure 5.6: Rapidity distribution of the cross section for the production of D^* mesons at LHeC for different beam energies integrated over the low-p_T range 5 GeV$\leq p_T \leq$ 20 GeV. The curves from bottom to top correspond to the combinations of beam energies as indicated in the figure.

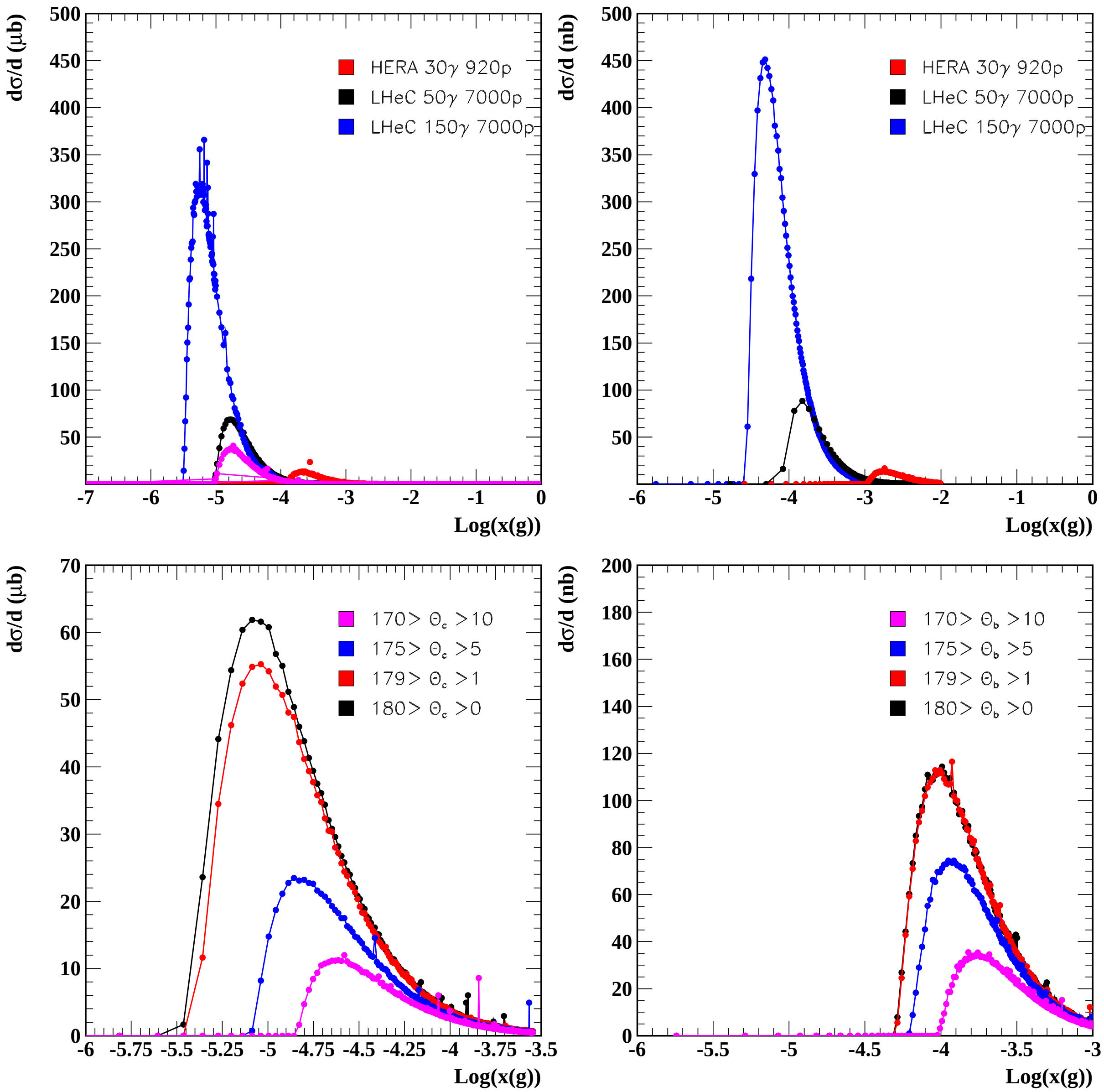

Figure 5.7: The x(g) reach and differential cross sections at a γp collider for $c\bar{c}$ (left) and $b\bar{b}$ (right) final states, in the top for different photon beam energies and in the bottom for fixed (which????) photon beam energy but various detector polar angle acceptance cuts for the produced heavy quarks.

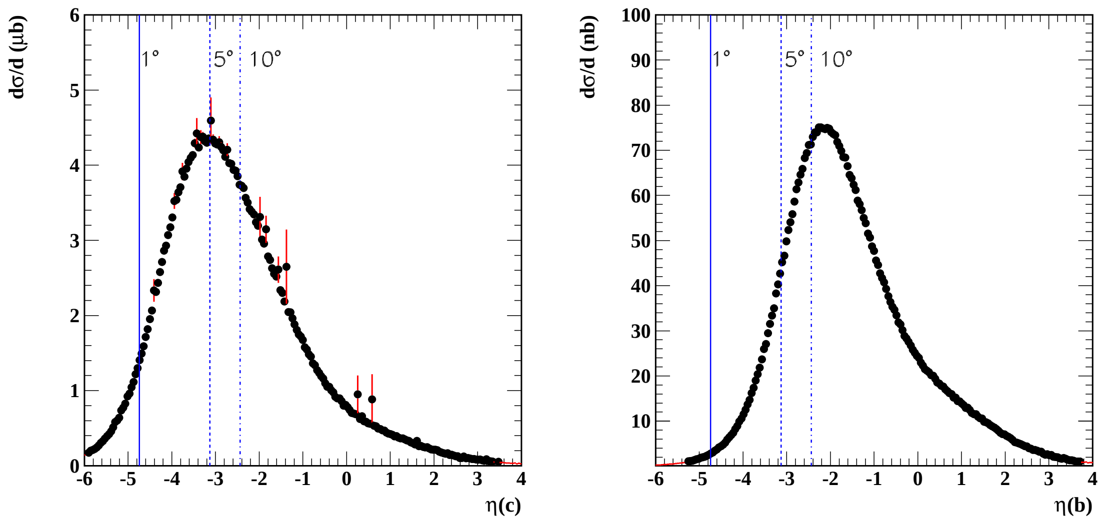

Figure 5.8: The η dependency of the $c\bar{c}$ (left) and $b\bar{b}$ (right) production cross section in γp collisions.

5.4.5 Charm and Beauty production in DIS

This section presents predictions for charm and beauty production in neutral current DIS, for Q^2 values of at least a few GeV^2. The predictions are given for the structure functions $F_2^{c\bar{c}}$ and $F_2^{b\bar{b}}$, which are defined as the parts of F_2 from events with charm and beauty quarks in the final state. These two structure functions are of large interest for the understanding of proton structure. Experimentally they are obtained by determining the total charm and beauty cross sections in (two-dimensional) bins of x and Q^2. The LHeC projections shown here were obtained with the Monte Carlo programme RAPGAP [18] using the version 3.1. RAPGAP generates charm and beauty production with massive leading order matrix elements supplemented by parton showers. The proton Parton Distribution Function set CTEQ5L [19] were used and the heavy-quark masses were set to $m_c = 1.5$ GeV and $m_b = 4.75$ GeV. In general at HERA the RAPGAP predictions are known to provide a reasonable description of the measured charm and beauty DIS production data.

The RAPGAP data presented in the following have been generated for an LHeC collider scenario with 100 GeV electrons colliding with 7 TeV protons. The statistical uncertainties have been evaluated such that they correspond to an integrated data luminosity of 10 fb^{-1}. All studies were done at the parton level, hadronisation effects were not taken into account. Tagging efficiencies of 10% have been assumed for both charm and beauty quarks and no background dilution was taken into account. The detector geometric acceptance was assumed to cover the full polar angle range. Figures 5.9 and 5.10 show the resulting RAPGAP predictions at LHeC for the structure functions F_2^{cc} and F_2^{bb}, respectively. The data are shown as a function of Q^2 for various x values. For illustration purposes the data for different x values are offset by constant factors. The projected data are presented as points with error bars which indicate the estimated statistical uncertainties. Measurements with expected uncertainty larger than 100% are shown as open points. For comparison, the kinematic regions covered by HERA (as taken from the published data) are also shown. It can be immediately seen that at LHeC a tremendous increase of phase space is possible. For fixed x much larger Q^2 values are accessible and for fixed Q^2 much lower values of x. The limitations from polar angle detector acceptance cuts for the outgoing heavy quarks are also indicated in the two Figures by thin lines. For a given line representing an acceptance cut only the data above that line will be accessible. From this it is clear that charm and beauty tagging in the forward (proton) region down to smallest polar angles is crucial to enable the desired wide kinematic coverage, in particular for accessing large x values. **Discuss intrinsic charm here?**

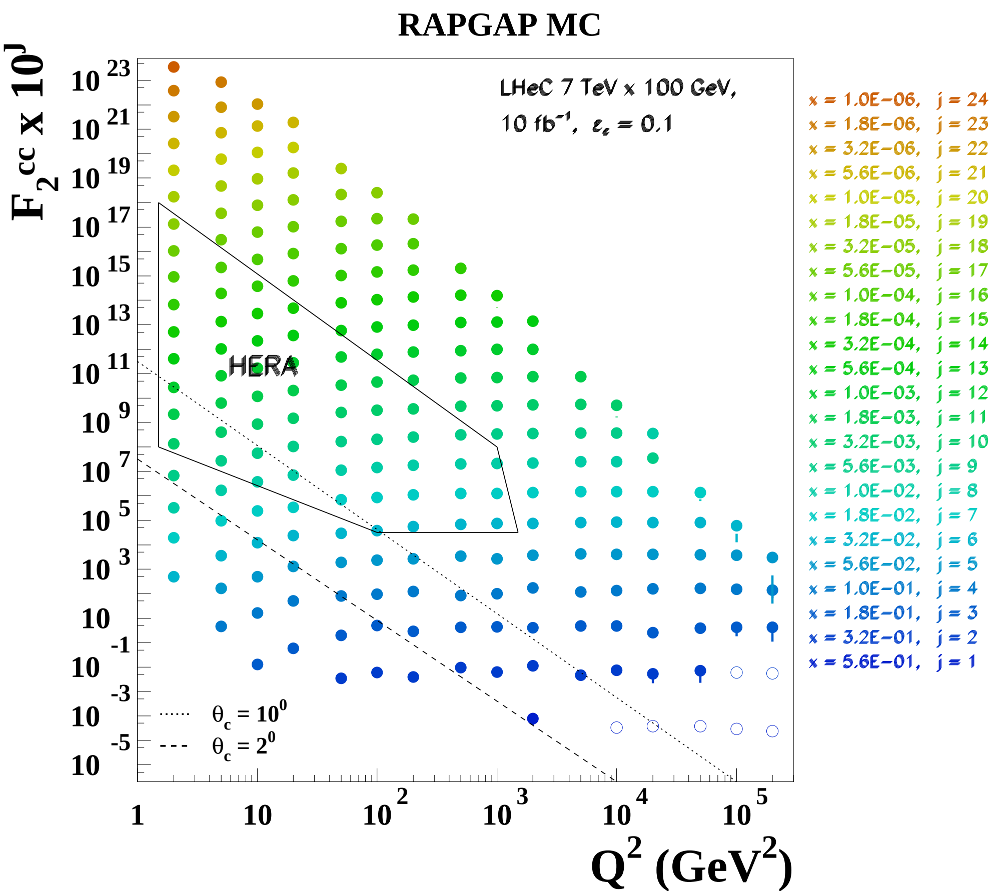

Figure 5.9: RAPGAP MC predictions for the measurements of the structure functions F_2^{cc} at LHeC. The simulated scenario is with electrons of 100 GeV energy colliding with 7 TeV protons, an integrated data luminosity of 10 fb^{-}1 and a charm quark tagging efficiency of 10%. The data are shown as points with error bars, representing the expected statistical uncertainties. The data points with expected uncertainty larger than 100% are shown as open points. The dashed and dotted lines represent the curves of fixed polar angles 2^0 and 10^0 for the scattered outgoing charm quark and thus indicate the restrictions from detector polar angle acceptance cuts. Also presented in the plot is the kinematic region which was covered at HERA. For further details see the main text.

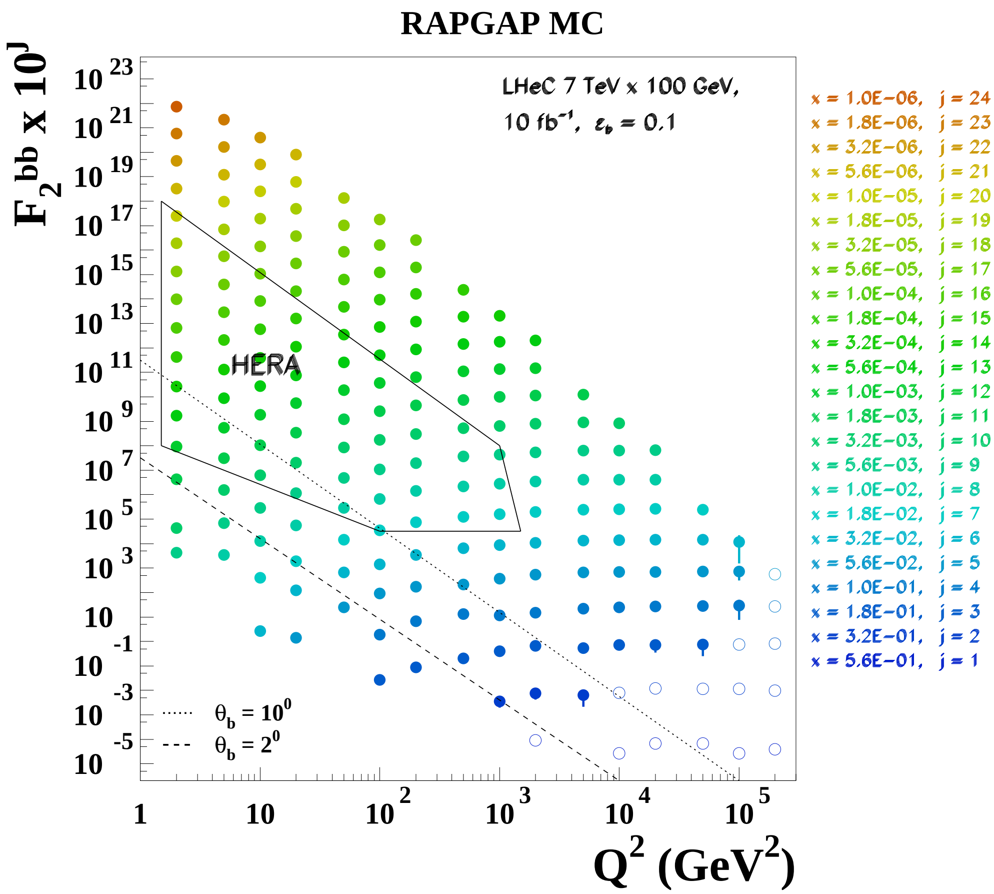

Figure 5.10: RAPGAP MC predictions for the structure functions F_2^{bb}, for further details see the caption of Fig. 5.10.

5.4.6 Total production cross sections for charm, beauty and top quarks

This section presents total cross sections for various heavy quark processes at LHeC as a function of the lepton beam energy. Predictions are obtained for: charm and beauty production in photoproduction and DIS, the charged current processes $sW \to c$ and $bW \to t$ and top pair production in photoproduction and DIS. For comparison the flavour inclusive charged current total cross section is also shown. Table 5.1 lists the generated processes, the used Monte Carlo generators, the selected parton distribution functions for the proton and some other relevant information. The resulting cross sections are shown in Figure 5.11. For comparison also the predicted cross sections for the HERA collider are presented (open symbols). The cross sections at LHeC are typically about one order of magnitude larger compared to HERA. This demonstrates that LHeC will be the first ep collider which provides access to all quark flavours and with high statistics.

Process	Monte Carlo	PDF	Remarks
Charm γp	PYTHIA6.4 [20]	CTEQ6L [21]	Proc. ID 84
Beauty γp			
tt γp			m(top) = 170 GeV
Charm DIS	RAPGAP3.1 [18]	CTEQ5L [19]	IPRO 12
Beauty DIS			
tt DIS			m(top) = 170 GeV
CC e^+p	LEPTO6.5 [22]	CTEQ5L	
CC e^-p			
$sW \to c$			
$sW \to \bar{c}$			
$bW \to t$			m(top) = 170 GeV
$\bar{b}W \to \bar{t}$			
tt DIS	RAPGAP 3.1	CTEQ5L	

Table 5.1: Used generator programmes for the predictions of total cross sections at LHeC, shown in Figure 5.11. For further details see the main text.

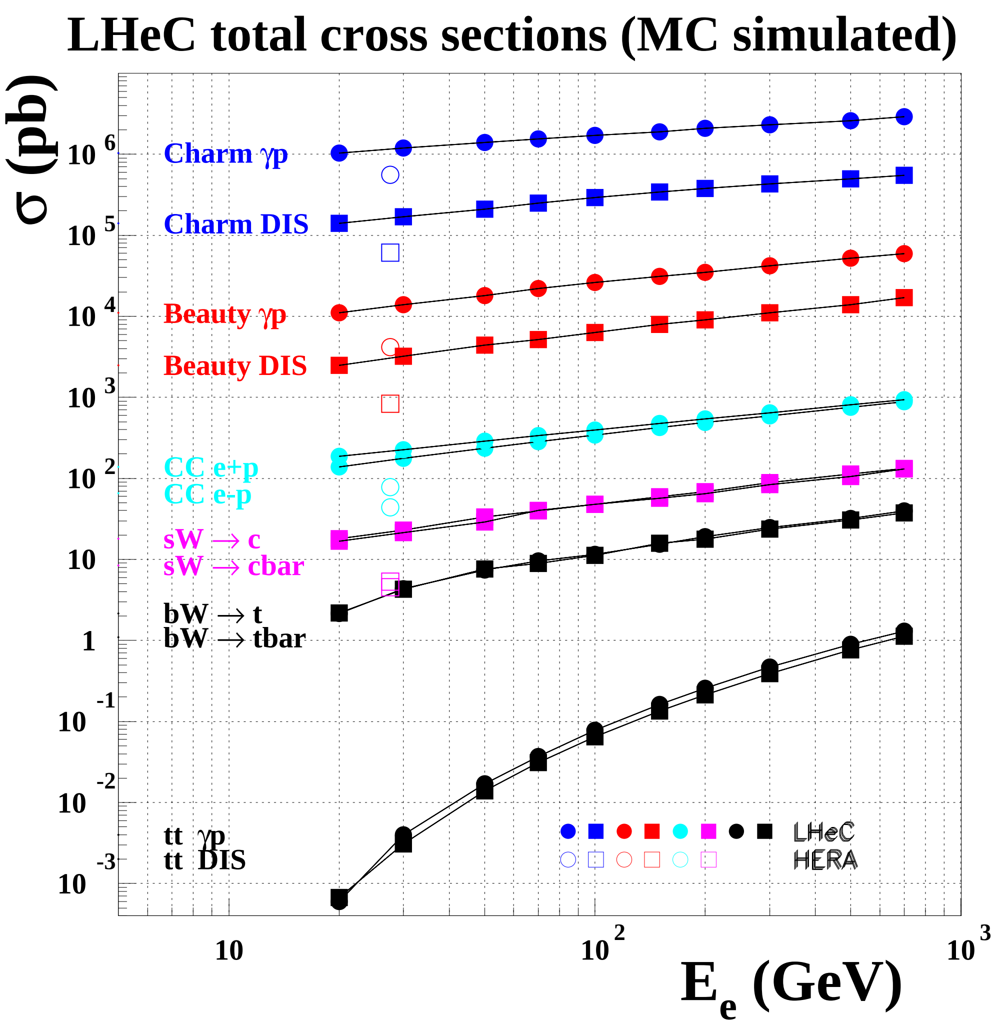

Figure 5.11: Total production cross section predictions for various heavy quark processes at the LHeC, as a function of the lepton beam energy. The following processes are covered: charm and beauty production in photoproduction and DIS, the charged current processes $sW \rightarrow c$ and $bW \rightarrow t$ and top pair production in photoproduction and DIS. The flavour inclusive charged current total cross section is also shown. All predictions are taken from Monte Carlo simulations, the details can be found in Table 5.1. For comparison also the predicted cross sections at HERA are shown (open symbols).

5.4.7 Summary

A consistent description of heavy quark production in ep collisions is a challenging problem for perturbative QCD, due to the presence of several hard scales (heavy quark masses, transverse momenta and momentum transfer Q^2). With an expected increase of the squared centre-of-mass energy s by a factor ~ 20, the LHeC will enable to study this multi-scale problem in a much wider phase space compared to HERA. This has been demonstrated in this article for various processes with charm and beauty quarks in the final state. The presented studies of D^* meson photoproduction show the increased reach to much higher p_T values. This will allow to map the expected transition from the "massive charm" to the "massless charm" regime much better than at HERA. Charm and beauty quarks are produced in ep collisions in leading order via the BGF process $g\gamma \rightarrow c\bar{c}, b\bar{b}$ which provides direct access to the gluon density in the proton. The study of charm and beauty quark production at a photon proton collider variant of the LHeC show the extended sensitivity to probe gluons in the proton with momentum fractions as small as $\sim 10^{-5}$, where their density is so far largely unknown. This reach can be only obtained if the LHeC detector is capable of tagging charm and beauty quarks in the very backward region. In DIS (at the standard ep collider option for LHeC) the contributions from events with charm and beauty quarks to F_2, the structure functions F_2^{cc} and F_2^{bb} have been investigated. Much lower x and higher Q^2 values will be accessible compared to HERA. Again, this will allow to probe the gluon density in the proton at smallest momentum fractions and also to test the validity of the different calculation schemes over a large range of Q^2 scales, from $Q^2 \sim m_{c.b}^2$ to $Q^2 \gg m_{c,b}^2$. Finally the total cross sections for various processes, involving charm, beauty and also top quarks have been studied and found to be typically one order of magnitude (or more) larger than at HERA, making LHeC a genuine multiflavour factory.

5.5 High p_t jets

Editors: Claudia Glasman, Thomas Gehrmann, Juan Terron 8 pages

5.5.1 Jets in photoproduction and deep inelastic scattering

Contributors: J. Behr, T. Gehrmann, C. Glasman, T. Schörner-Sadenius, J. Terron

The study of the jet final states in lepton-proton collisions allows the determination of aspects of the nucleon structure which are not accessible in inclusive scattering. Moreover, jet production allows for probing predictions of QCD to a high accuracy. Depending on the virtuality of the exchanged photon, one distinguishes processes in photoproduction (quasi-real photon) and deep inelastic scattering.

The photoproduction cross section for di-jet final states can be studied in different kinematical regions, thereby covering a wide spectrum of physical phenomena, and probing the structure of the proton and the photon. Two-jet production in deep inelastic scattering is a particularly sensitive probe of the gluon distribution in the proton and of the strong coupling constant α_s. Both processes allow the study of potentially large enhancement effects in di-jet and multi-jet production.

Jet production in photoproduction proceeds via the direct processes, in which the quasi-real photon interacts as a point-like particle with the partons from the proton, and the resolved processes, in which the quasi-real photon interacts with the partons from the proton via its partonic constituents. The parton distributions in the quasi-real photon are constrained mostly from the study of processes at e^+e^- colliders, and are less well-determined than their counterparts in the proton. In both the direct and the resolved processs, there are two jets in the final state at lowest-order QCD. The jet production cross section is given in QCD by the convolution of the flux of photons in the electron (usually estimated via the Weizacker-Williama approximation), the parton densities in the photon, the parton densities in the proton and the partonic cross section (calculable in pQCD). Therefore, the measurements of jet cross sections in photoproduction provide tests of perturbative QCD and the structure of the photon and the proton.

Owing to the large size of the cross section, photoproduction of di-jets can be used for precision physics in QCD. A measurement at LHeC could improve upon previous HERA results and enter into a much larger kinematical region. In measurements made by the ZEUS collaboration, the available photon-proton centre-of-mass energy ranged from 142 to 293 GeV, and jets of a transverse energy of up to 90 GeV could be observed. By comparing the measured cross section with the theoretical prediction in NLO pQCD, a value of $\alpha_s(M_Z)$ was extracted with a total uncertainty of $\pm 3\%$and the running of α_s was tested over a wide range of E_t^{jet} in a single measurement. The limiting factors in this measurement were the theoretical uncertainty inherent to the NLO prediction (which could be improved by computing NNLO corrections to jet photoproduction) and the experimental systematic uncertainty in the detector energy calibration.

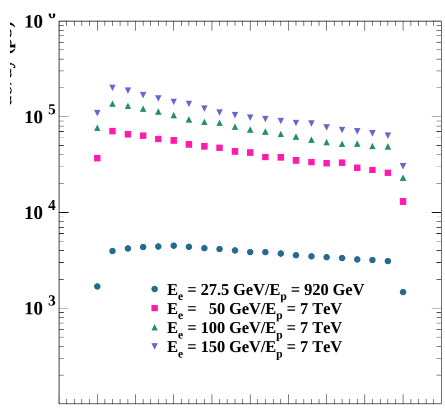

Figure 5.12: PYTHIA predictions for photoproduction cross section at HERA and for three LHeC scenarios.

Another motivation for making new photoproduction experiments is to improve the knowledge of the parton content of the photon. At present, most information on the photon structure is inferred from the colliison of quasi-real photons with electrons at e^+e^- colliders, resulting in a decent determination of the total (charge weighted) quark content of the quasi-real photon. Its gluonic content, and the quark flavour decomposition are on the other hand only loosely constrained. Improvements to the photon structure are of crucial importance to physics studies at a future linear e^+e^- collider like the ILC or CLIC. Such a collider, operating far above the Z-boson resonance, will face a huge background from photon-photon collisions. This background can be suppressed only to a certain extent by kinematical cuts. Consequently, accurate predictions of it (which require an improved knowledge of the photon's parton content) are mandatory

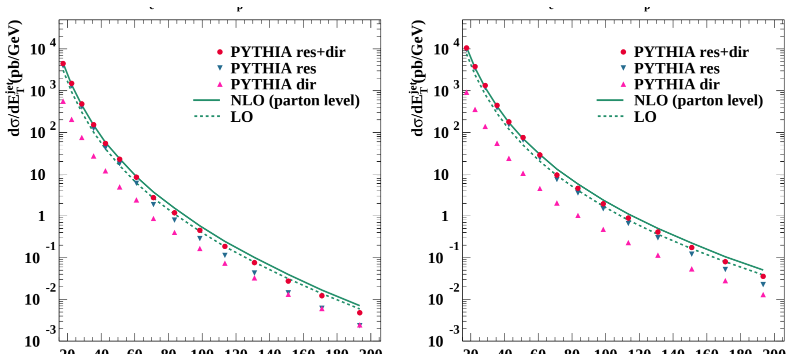

Figure 5.13: Parton level predictions for the inclusive transverse energy distribution in photoproduction.

for the reliable interpretation of hadronic final states at the ILC or CLIC. Several parametrizations of the parton distributions in the photon are available. They differ especially in the gluon content of the photon. For the studies presented here, the GRV-HO parametrization [23] is used as default.

The photoproduction studies performed at LHeC were done for three different electron energy scenarios: E_e=50, 100 and 150 GeV. In all cases, the proton energy was set to 7 TeV. PYTHIA MC samples of resolved and direct processes were generated for these three scenarios. Jets were searched using the k_t-cluster algorithm in the kinematic region of $0.1 < y < 0.9$ and $Q^2 < 1$ GeV^2. Inclusive jet cross sections were done for jets of $E_t^{\rm jet} > 15$ GeV and $3 < \eta^{\rm jet} < 3$. Figure 5.12 shows the PYTHIA MC cross sections as functions of y for the three scenarios plus the corresponding cross section for the HERA regime. It can be seen that the LHeC cross sections are one to two orders of magnitude larger than the cross section at HERA.

The full study was complemented with fixed-order QCD calculations at order α_s and α_s^2 using the program by Klasen et al. [24] with the CTEQ6.1 sets for the proton PDFs, GRV-HO sets for the photon PDFs, $\alpha_s(M_Z) = 0.119$ and the renormalisation and factorisation scales were set to the transverse energy of each jet.

Figure 5.13 shows the inclusive jet cross sections at parton level as functions of $E_t^{\rm jet}$ for the three energy scenarios for the PYTHIA res+dir (red dots), PYTHIA resolved (blue triangles) and PYTHIA direct (pink triangles) together with the predictions from the NLO (solid curves) and LO (dashed curves) QCD calculations. The calculations predict a sizeable rate for Etjet of at least up to 200 GeV. Resolved processes dominate at low $E_t^{\rm jet}$, but the direct processes become increasingly more important as $E_t^{\rm jet}$ increases. The PYTHIA cross sections (which have been normalised to the NLO integrated cross section) agree well in shape with the NLO calculations. Investigating the $\eta^{\rm jet}$ distribution, we find that resolved processes dominate in the forward region, while direct processes produce more central jets.

Figure 5.14 show the inclusive jet cross sections at parton level as functions of $E_t^{\rm jet}$ (on the left) and $\eta^{\rm jet}$ (on the right) for the PYTHIA resolved+direct (symbols) and the predictions from the NLO (solid curves) and LO (dashed curves) QCD calculations together for the three energy scenarios. For comparison, the calculations for the HERA regime are also included. It is seen that the cross sections at fixed $E_t^{\rm jet}$ increase and that the jets tend to go more backward

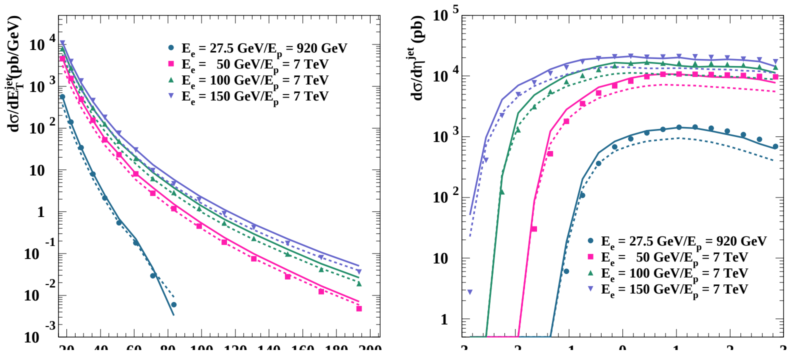

Figure 5.14: Dijet distributions in photoproduction as function of the jet transverse energy (left) and of the jet rapidity (right) for different LHeC energies compared to the HERA kinematic range.

as the collision energy increases. The much larger photon-proton centre-of-mass energies that could be available at LHeC provide a much wider reach in $E_t^{\rm jet}$ and $\eta^{\rm jet}$ compared to HERA.

Hadronisation corrections for the cross sections shown were investigated. The corrections are predicted to be quite small, below +5% for the chosen scenarios. Since the hadronisation corrections are very small, the features observed at parton level remain unchanged.

Inclusive-jet and dijet measurements in deep-inelastic scattering (DIS) have since long been a tool to test concepts and predictions of perturbative QCD. Especially at HERA, jets in DIS have been thoroughly studied, and the results have provided deep insights, giving for example precise values for the strong coupling constant, α_s and providing constraints for the proton PDFs.

An especially interesting region for such studies has been the regime of large (for HERA) Q^2 values of, for example, $Q^2 > 125$ GeV^2. In this regime, the theoretical uncertainties, especially those due to the unknown effects of missing higher orders in the perturbative expansion, are found to be small. Recently, both the H1 and ZEUS collaborations have published measurements of inclusive-jet and dijet events in this kinematic regime.

An extension of such measurements to the LHeC is interesting for two reasons: First, the provided high luminosity will allow measurements in already explored kinematic regions with still increased experimental precision. Second, the extension in centre-of-mass energy, $\sqrt{s}$, and thus in boson virtuality, Q^2, and in jet transverse energy, $E_{T,jet}$, will potentially allow to study pQCD at even higher scales, extending the scale reach for measurements of the strong coupling or the precision of the proton PDFs at large values of x.

To explore the potential of such a measurement, we investigated DIS jet production for the following LHeC scenario: proton beam energy 7 TeV, electron beam energy 70 GeV and integrated luminosity 10 fb^{-1}. The study concentrates on the phase space of high boson virtualities Q^2, with event selection cuts $100 < Q^2 < 500\ 000$ GeV^2 and $0.1 < y < 0.7$, where y is the inelasticity of the event. Jets are reconstructed using the k_T clustering algorithm in the longitudinally invariant inclusive mode in the Breit reference frame. Jets were selected by requiring: a jet pseudorapidity in the laboratory of $-2 < \eta_{lab} < 3$, a jet transverse energy in the Breit frame of $E_{T,jet}^{Breit} > 20$ GeV for the inclusive-jet measurement and jet transverse energies in the Breit frame of 25(20) GeV for the leading and the second-hardest jet in the case of the dijet selection.

For inclusive-jet production we study cross sections in the indicated kinematic regime as functions of Q^2, x_{Bj}, $E_{T,jet}^{Breit}$ and η_{jet}^{lab}, the jet pseudorapidity in the laboratory frame. For dijet production, studies are presented as functions of Q^2, the logarithm of the proton momentum fraction ξ, $\log_{10}\xi$, the invariant dijet mass M_{jj}, the average transverse energy of the two jets in the Breit frame, $\overline{E_{T,jet}^{Breit}}$, and of half of the absolute difference of the two jet pseudorapidities in the laboratory frame, η'.

For the binning of the observables shown here, the statistical uncertainties for the indicated LHeC integrated luminosity can mostly be neglected, even at the highest scales. The systematic uncertainties were assumed to be dominated by the uncertainty on the jet energy scale which was assumed to be known to 1% or 3% (both scenarios are indicated with different colours in the following plots), leading to typical effects on the jet cross sections between 1 and 15%. A further relevant uncertainty is the acceptance correction that is applied to the data which was assumed to be 3% for all observables.

The theoretical calculations where performed with the DISENT program [25] using the CTEQ6.1 proton PDFs [21, 26]. The central default squared renormalisation and factorisation scales were set to Q^2. The theory calculations for the LHeC scenario were corrected for the effects of hadronisation and Z^0 exchange using Monte Carlo data samples simulated with the LEPTO program [22].

Theoretical uncertainties were assessed by varying the renormalization scale up and down by a factor 2 (to estimate the potential effect of contributions beyond NLO QCD), by using the 40 error sets of the CTEQ6.1 parton distribution functions, and by varying α_s using the CTEQ6AB PDF [27]. The dominant theory uncertainty turned out to be due to the scale variations, resulting in effects of a few to up to 20% or more, for example for low values of Q^2 or, for the case of the dijet measurement, for low values of the invariant dijet mass, M_{jj}, or the logarithm of momentum fraction carried into the hard scattering, $\log_{10}\xi$.

Note that for the inclusive-jet results also the predictions for a HERA scenario with almost the same selection are shown in order to indicate the increased reach of the LHeC with respect to HERA. The only change is a reduction in centre-of-mass energy to 318 GeV and a reduced Q^2 reach, $125 < Q^2 < 45\ 000$ GeV^2. The HERA predictions shown were also corrected for hadronisation effects and the effects of Z^0 exchange.

Figure 5.15 shows the inclusive jet cross section as function of Q^2 and of the jet transverse energy in the Breit frame, while Figure 5.16 shows the dijet cross section as funtion of Q^2 and of $\xi = x_{Bj}(1+M_{jj}^2/Q^2)$. The top parts of the figures show the predicted cross sections together with the expected statistical and (uncorrelated) experimental systematic uncertainties as errors bars. The correlated jet energy scale uncertainty is indicated as a coloured band; the inner, yellow band assumes an uncertainty of 1%, the outer, blue band one of 3%. Also shown as a thin hashed area are the theoretical uncertainties; the width of the band indicates the size of the combined theoretical uncertainty. In case of inclusive-jet production, also the predictions for HERA are indicated as a thin line.

The bottom parts of the figures show the relative uncertainties due to the jet energy scale (yellow band for 1%, blue band for 3%), the statistical and uncorrelated experimental systematic uncertainties as inner / outer error bars, and the combined theoretical uncertainties as hashed band. The inner part of this band indicates the uncertainty due to the variation of the renormalisation scale.

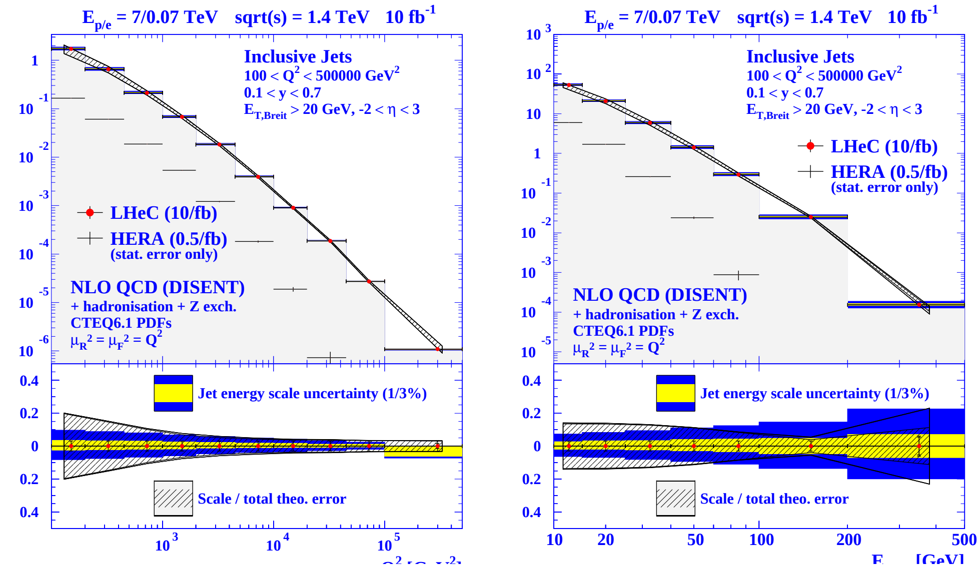

Figure 5.15: Predicted LHeC results for inclusive jet production as function of Q^2 and of E_T in the Breit frame. Predictions for HERA results are also shown.

The inclusive-jet cross section as function of Q^2 shows a typical picture: In most region of the phase space, the uncertainties are dominated by the theory uncertainties, and here mainly by the renormalisation scale uncertainty. The typical size of experimental uncertainties is of the order of 10%, with larger values in regions with low relevant scales — i.e. low invariant dijet masses, low jet transverse energies or low Q^2 values. The theoretical uncertainties are typically between 5 and 20%, with partially strong variations over the typical range of the observable in question.

A comparison with the HERA predictions for inclusive-jet production shows that the LHeC cross sections is typically larger by 1 to 3 orders of magnitude. The dijet final state allows for a full reconstruction of the partonic kinematics, and can thus be used to probe the parton distribution functions in Q^2 and ξ. It can be seen that a measurement at LHeC covers a large kinematical range ranging down to $\xi \approx 10^{-3}$ and up to $Q^2 = 10^5$ GeV^2. Potentially limiting factors in an extraction of parton distribution functions are especially the jet energy scale uncertainty on the experimental side and missing higher order (NNLO) corrections on the theory side. The jet energy scale uncertainty can be addressed by the detector design and by the experimental setup of the measurement. NNLO corrections to dijet production in deep inelastic scattering are already very much demanded by the precision of the HERA data, their calculation is currently in progress [28, 29].

In summary, jet final states in photoproduction and deep inelastic scattering at the LHeC promise a wide spectrum of new results on the partonic structure of the photon and the proton. They allow for precision tests of QCD by independent determinations of the strong coupling constant over a kinematical range typically one to two orders of magnitude larger than what was accessible at HERA. The resulting parton distributions will have a direct impact for precision

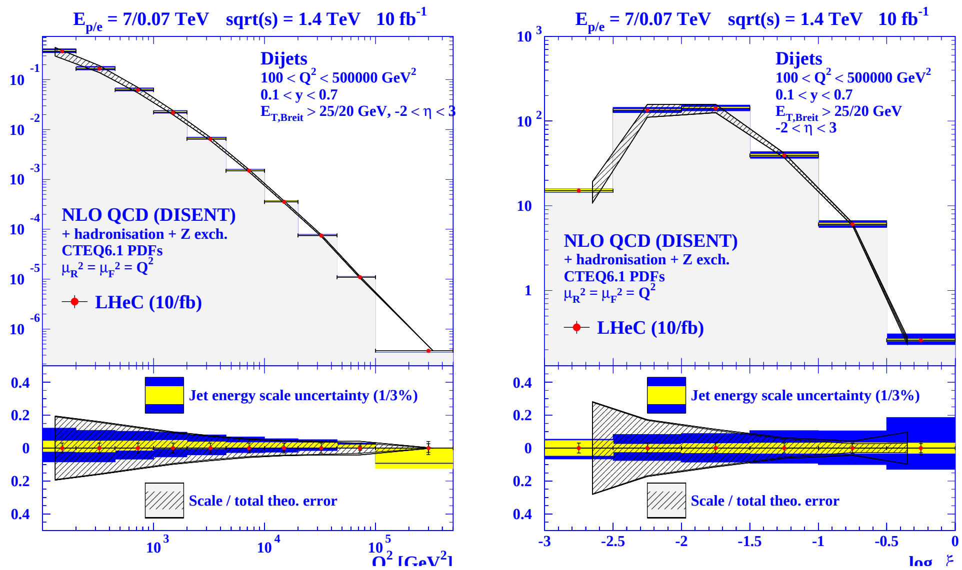

Figure 5.16: Predicted LHeC results for dijet production as function of Q^2 and of ξ.

predictions at the LHC and a future linear collider.

Chapter 6

New Physics at Large Scales

Although the LHC is expected to be the discovery machine for physics beyond the Standard Model at the TeV scale, it will not always be possible to measure with precision the parameters of the new physics. In this section, it is shown that in many cases the LHeC can probe in detail deviations from the expected electroweak interactions shared by leptons and quarks, thus adding essential information on the new physics. Previous studies [30–33] of the potential of high-energy $e-p$ colliders for the discovery of exotic phenomena have considered a number of processes, most of which are reviewed here.

In some cases, Standard Model processes can also be better measured at the LHeC. Here, the charged and neutral current processes of SM Higgs production by vector boson fusion are investigated with the goal of measuring the $H-b-b$ coupling.

6.1 New Physics in inclusive DIS at high Q^2

The LHeC collider would enable the study of deep inelastic neutral current scattering at very high squared momentum transfers Q^2, thus probing the structure of eq interactions at very short distances. At large scales new phenomena not directly detectable may become observable as deviations from the Standard Model predictions. A convenient tool to assess the experimental sensitivity beyond the maximal available center of mass energy and to parameterise indirect signatures of new physics is the concept of an effective four-fermion contact interaction. If the contact terms originate from a model where fermions have a substructure, a compositeness scale can be related to the size of the composite object. If they are due to the exchange of a new heavy particle, such as a leptoquark, the effective scale is related to the mass and coupling of the exchanged boson. Contact interaction phenomena are best observed as a modification of the expected Q^2 dependence and all information is essentially contained in the differential cross section $\mathrm{d}\sigma/\mathrm{d}Q^2$. An alternative way to parameterize the effects of fermion substructure makes use of form factors, which would also lead to deviations of $\mathrm{d}\sigma/\mathrm{d}Q^2$ with respect to the SM prediction. As a last example, low scale quantum gravity effects, which may be mediated via gravitons coupling to SM particles and propagating into large extra spatial dimensions, could also be observed as a modification of $\mathrm{d}\sigma/\mathrm{d}Q^2$ at highest Q^2. These possible manifestations of new physics in inclusive DIS are addressed in this section.

6.1.1 Quark substructure

The remarkable similarities in the electromagnetic and weak interactions of leptons and quarks in the Standard Model, and their anomaly cancellations in the family structure, strongly suggest a fundamental connection. It would therefore be natural to conjecture that they could be composed of more fundamental constituents, or that they form a representation of a larger gauge symmetry group than that of the Standard Model, in a Grand Unified Theory.

A possible method to investigate fermion substructures is to assign a finite size of radius R to the electroweak charges of leptons and/or quarks while treating the gauge bosons γ and Z still as pointlike particles [34]. A convenient parametrisation is to introduce 'classical' form factors $f(Q^2)$ at the gauge boson–fermion vertices, which are expected to diminish the Standard Model cross section at high momentum transfer

$$f(Q^2) = 1 - \frac{1}{6} \langle r^2 \rangle Q^2 \ , \tag{6.1}$$

$$\frac{d\sigma}{dQ^2} = \frac{d\sigma^{SM}}{dQ^2} f_e^2(Q^2) \, f_q^2(Q^2) \ . \tag{6.2}$$

The square root of the mean-square radius of the electroweak charge distribution, $R = \sqrt{\langle r^2 \rangle}$, is taken as a measure of the particle size. Since the pointlike nature of the electron/positron is already established down to extremely low distances in $e^+ e^-$ and $(g-2)_e$ experiments, only the quarks are allowed to be extended objects i.e. the form factor f_e can be set to unity in the above equation.

Figure.6.1 shows the sensitivity that an LHeC collider could reach on the "quark radius" [35]. Two configurations have been studied ($E_e = 70$ GeV and $E_e = 140$ GeV), and two values of the integrated luminosity, per charge, have been assumed in each case. A sensitivity to quark radius below 10^{-19} m could be reached, which is one order of magnitude better than the current constraints, and comparable to the sensitivity that the LHC is expected to reach.

6.1.2 Contact Interactions

New currents or heavy bosons may produce indirect effects through the exchange of a virtual particle interfering with the γ and Z fields of the Standard Model. For particle masses and scales well above the available energy, $\Lambda \gg \sqrt{s}$, such indirect signatures may be investigated by searching for a four-fermion pointlike $(\bar{e}\, e)(\bar{q}\, q)$ contact interaction. The most general chiral invariant Lagrangian for neutral current vector-like contact interactions can be written in the form [36–38]

$$\begin{aligned} \mathcal{L}_V = \sum_{q\,=\,u,\,d} \{ & \eta^q_{LL} \, (\bar{e}_L \gamma_\mu e_L)(\bar{q}_L \gamma^\mu q_L) + \eta^q_{LR} \, (\bar{e}_L \gamma_\mu e_L)(\bar{q}_R \gamma^\mu q_R) \\ & + \eta^q_{RL} \, (\bar{e}_R \gamma_\mu e_R)(\bar{q}_L \gamma^\mu q_L) + \eta^q_{RR} \, (\bar{e}_R \gamma_\mu e_R)(\bar{q}_R \gamma^\mu q_R) \} \ , \end{aligned} \tag{6.3}$$

where the indices L and R denote the left-handed and right-handed fermion helicities and the sum extends over *up*-type and *down-type* quarks and antiquarks q. In deep inelastic scattering at high Q^2 the contributions from the first generation u and d quarks completely dominate and contact terms arising from sea quarks s, c and b are strongly suppressed. Thus, there are eight independent effective coupling coefficients, four for each quark flavour

$$\eta^q_{ab} \equiv \epsilon \frac{g^2}{\Lambda^{q\ 2}_{ab}} \ , \tag{6.4}$$

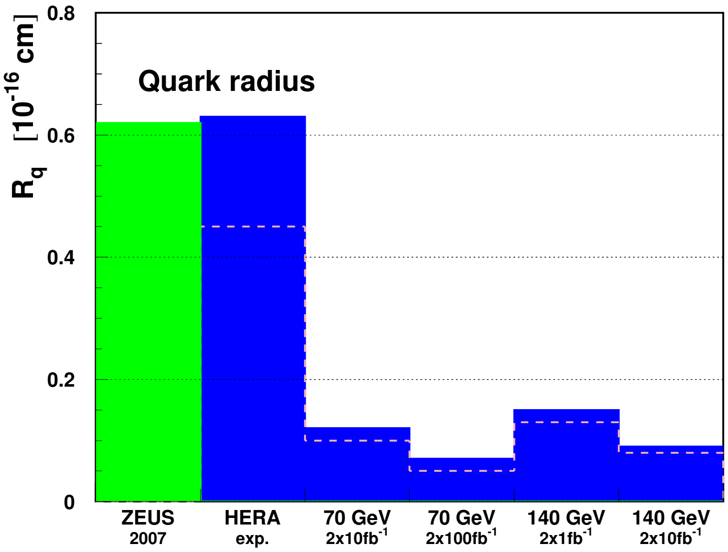

Figure 6.1: Sensitivity (95% confidence level limits) of an LHeC collider to the effective quark radius.

where a and b indicate the L, R helicities, g is the overall coupling strength, Λ^q_{ab} is a scale parameter and ϵ is a prefactor, often set to $\epsilon = \pm 1$, which determines the interference sign with the Standard Model currents. The ansatz eq. (6.3) can be easily applied to any new phenomenon, *e.g.* (eq) compositeness, leptoquarks or new gauge bosons, by an appropriate choice of the coefficients η_{ab}. Scalar and tensor interactions of dimension 6 operators involving helicity flip couplings are strongly suppressed at HERA [38] and therefore not considered.

Figure 6.2 shows the sensitivity that an LHeC could reach on the scale Λ, for two example cases of contact interactions [35]. In general, with 10 fb^{-1} of data, LHeC would probe scales between 25 TeV and 45 TeV, depending on the model. The sensitivity of LHC to such $eeqq$ interactions, which would affect the di-electron Drell-Yan (DY) spectrum at high masses, is similar.

Figure 6.3 shows how the DY cross-section at LHC would deviate from the SM value, for three examples of $eeqq$ contact interactions. In the "LL" model considered here, the sum in eq. (6.3) only involves left-handed fermions and all amplitudes have the same phase ϵ. With only pp data, it will be difficult to determine simultaneously the size of the contact interaction scale Λ and the sign of the interference of the new amplitudes with respect to the SM ones: for example, for $\Lambda = 20$ TeV and $\epsilon = -1$, the decrease of the cross-section with respect to the SM prediction for di-electron masses below ~ 3 TeV, which is characteristic of a negative interference, is too small to be firmly established when uncertainties due to parton distribution functions are taken into account.

For the same "LL" model, the sign of this interference can be unambiguously determined at LHeC from the asymmetry of σ/σ_{SM} in e^+p and e^-p data, as shown in Fig. 6.4.

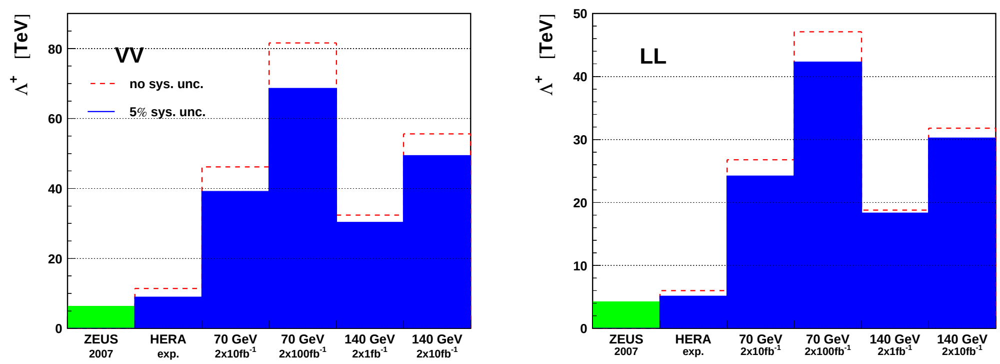

Figure 6.2: Sensitivity (95% confidence level limits) on the scale Λ for two example contact interactions.

Moreover, with a polarised lepton beam, ep collisions would help determine the chiral structure of the new interaction. More generally, it is very likely that both pp and ep data would be necessary to underpin the structure of new physics which would manifest itself as an $eeqq$ contact interaction. Such a complementarity of pp, ep (and also ee) data was studied in [39] in the context of the Tevatron, HERA and LEP colliders.

6.1.3 Kaluza-Klein gravitons in extra-dimensions

In some models with n large extra dimensions, the SM particles reside on a four-dimensional "brane", while the spin 2 graviton propagates into the extra spatial dimensions and appears in the four-dimensional world as a tower of massive Kaluza-Klein (KK) states. The summation over the enormous number of Kaluza-Klein states up to the ultraviolet cut-off scale, taken as the Planck scale M_S in the $4+n$ space, leads to effective contact-type interactions $fff'f'$ between two fermion lines, with a coupling $\eta = O(1)/M_S^4$. In ep scattering, the exchange of such a tower of Kaluza-Klein gravitons would affect the Q^2 dependence of the DIS cross-section $\mathrm{d}\sigma/\mathrm{d}Q^2$. At LHeC, such effects could be observed as long as the scale M_S is below $4-5$ TeV. While at the LHC, virtual graviton exchange may be observed for scales up to ~ 10 TeV, and the direct production of KK gravitons, for scales up to $5-7$ TeV depending on n, would allow this phenomenom to be studied further, LHeC data may determine that the new interaction is universal by establishing that the effect in the $eq \to eq$ cross-section is independent of the lepton charge and polarization, and, to some extent, of the quark flavor.

6.2 Leptoquarks and leptogluons

The high energy of the LHeC extends the kinematic range of DIS physics to much higher values of electron-quark mass $M = \sqrt{sx}$, beyond those of present ep colliders. By providing both baryonic and leptonic quantum numbers in the initial state, it is ideally suited to a study of the properties of new bosons possessing couplings to an electron-quark pair in this new mass range. Such particles can be squarks in supersymmetric models with R-parity violation ($\not{R}_p$), or first-generation leptoquark (LQ) bosons which appear naturally in various unifying theories

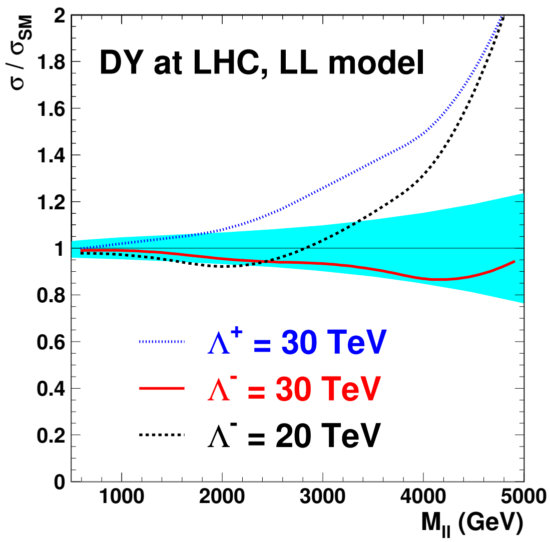

Figure 6.3: Example deviations, from its SM value, of the Drell-Yan cross-section at LHC as a function of the dilepton mass, in the presence of an $eeqq$ contact interaction. The blue band shows the relative uncertainty of the predicted SM cross-sections due to the current uncertainties of the parton distribution functions, as obtained from the CTEQ 6.1 sets.

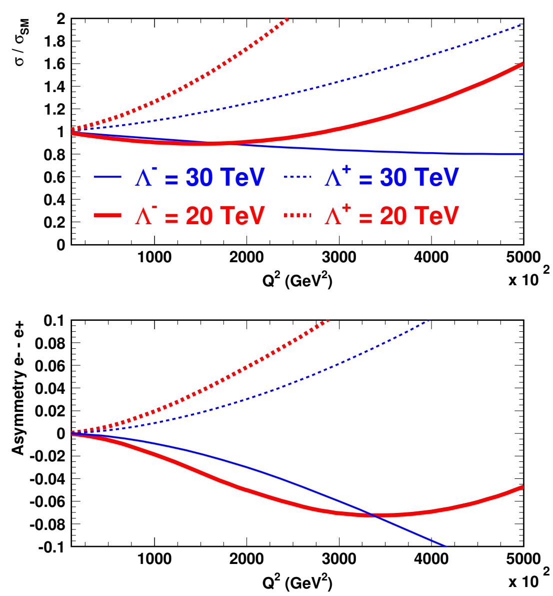

Figure 6.4: (top) Example deviations of the e^-p DIS cross-section at LHeC, in the presence of an $eeqq$ CI. The ratio of the "measured" to the SM cross-sections, $r = \sigma/\sigma_{SM}$, is shown. (bottom) Asymmetry $\frac{r(e^+)-r(e^-)}{r(e^+)+r(e^-)}$ between e^+p and e^-p measurements of σ/σ_{SM}.

beyond the Standard Model (SM) such as: E_6 [40], where new fields can mediate interactions between leptons and quarks; extended technicolor [41,42], where lwptoquarks (LQ) result from bound states of technifermions; the Pati-Salam model [43], where the leptonic quantum number is a fourth color of the quarks or in lepton-quark compositeness models. They are produced as single $s-$channel resonances via the fusion of incoming electrons with quarks in the proton. They are generically referred to as "leptoquarks" in what follows. The case of "leptogluons", which could be produced in ep collisions as a fusion between the electron and a gluon, is also addressed at the end of this section.

6.2.1 Phenomenology of leptoquarks in ep collisions

In ep collisions, LQs may be produced resonantly up to the kinematic limit of $\sqrt{s_{ep}}$ via the fusion of the incident lepton with a quark or antiquark coming from the proton, or exchanged in the u-channel, as illustrated in Fig. 6.5. The coupling λ at the $LQ-e-q$ vertex is an unknown

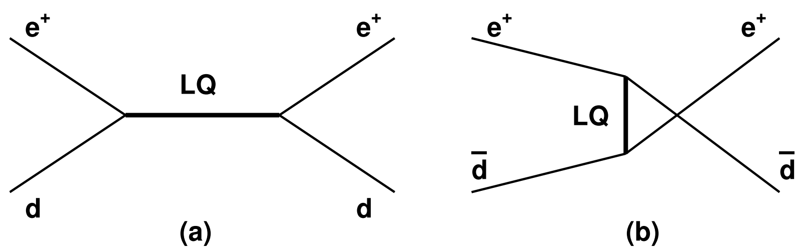

Figure 6.5: Example diagrams for resonant production in the s-channel (a) and exchange in the u-channel (b) of a LQ with fermion number $F = 0$. The corresponding diagrams for $|F| = 2$ LQs are obtained from those depicted by exchanging the quark and antiquark.

parameter of the model.

In the narrow-width approximation, the resonant production cross-section is proportional to $\lambda^2 q(x)$ where $q(x)$ is the density of the struck parton in the incoming proton.

The resonant production or t-channel exchange of a leptoquark gives $e + q$ or $\nu + q'$ final states leading to individual events indistinguishable from SM NC and CC DIS respectively. For the process $eq \to LQ \to eq$, the distribution of the transverse energy $E_{T,e}$ of the final state lepton shows a Jacobian peak at $M_{LQ}/2$, M_{LQ} being the LQ mass. Hence the strategy to search for a LQ signal in ep collisions is to look, among high Q^2 (i.e. high $E_{T,e}$) DIS event candidates, for a peak in the invariant mass M of the final $e-q$ pair. Moreover, the significance of the LQ signal over the SM DIS background can be enhanced by exploiting the specific angular distribution of the LQ decay products (see spin determination, below).

6.2.2 The Buchmüller-Rückl-Wyler Model

A reasonable phenomenological framework to study first generation LQs is provided by the BRW model [44]. This model is based on the most general Lagrangian that is invariant under $SU(3) \times SU(2) \times U(1)$, respects lepton and baryon number conservation, and incorporates dimensionless family diagonal couplings of LQs to left- and/or right-handed fermions. Under these assumptions LQs can be classified according to their quantum numbers into 10 different LQ isospin multiplets (5 scalar and 5 vector), half of which carry a vanishing fermion number $F = 3B + L$ (B and L denoting the baryon and lepton number respectively) and couple to $e^+ + q$ while the other half carry $|F| = 2$ and couple to $e^+ + \bar{q}$. These are listed in Table 6.1.

$F=-2$	Prod./Decay	β_e	$F=0$	Prod./Decay	β_e
		Scalar Leptoquarks			
${}^{1/3}S_0$	$e_R^+\bar{u}_R \to e^+\bar{u}$	1/2	${}^{5/3}S_{1/2}$	$e_R^+ u_R \to e^+ u$	1
	$e_L^+\bar{u}_L \to e^+\bar{u}$	1		$e_L^+ u_L \to e^+ u$	1
${}^{4/3}\tilde{S}_0$	$e_L^+\bar{d}_L \to e^+\bar{d}$	1	${}^{2/3}S_{1/2}$	$e_L^+ d_L \to e^+ d$	1
${}^{4/3}S_1$	$e_R^+\bar{d}_R \to e^+\bar{d}$	1	${}^{2/3}\tilde{S}_{1/2}$	$e_R^+ d_R \to e^+ d$	1
${}^{1/3}S_1$	$e_R^+\bar{u}_R \to e^+\bar{u}$	1/2			
		Vector Leptoquarks			
${}^{4/3}V_{1/2}$	$e_L^+\bar{d}_R \to e^+\bar{d}$	1	${}^{2/3}V_0$	$e_L^+ d_R \to e^+ d$	1
	$e_R^+\bar{d}_L \to e^+\bar{d}$	1		$e_R^+ d_L \to e^+ d$	1/2
${}^{1/3}V_{1/2}$	$e_L^+\bar{u}_R \to e^+\bar{u}$	1	${}^{5/3}\tilde{V}_0$	$e_L^+ u_R \to e^+ u$	1
${}^{1/3}\tilde{V}_{1/2}$	$e_R^+\bar{u}_L \to e^+\bar{u}$	1	${}^{5/3}V_1$	$e_R^+ u_L \to e^+ u$	1
			${}^{2/3}V_1$	$e_R^+ d_L \to e^+ d$	1/2

Table 6.1: Leptoquark isospin families in the Buchmüller-Rückl-Wyler model. For each leptoquark, the superscript corresponds to its electric charge, while the subscript denotes its weak isospin. β_e denotes the branching ratio of the LQ into $e + q$.

We use the nomenclature of [45] to label the different LQ states. In addition to the underlying hypotheses of BRW, we restrict LQs couplings to only one chirality state of the lepton, given that deviations from lepton universality in helicity suppressed pseudoscalar meson decays have not been observed [46,47].

In the BRW model, LQs decay exclusively into eq and/or νq and the branching ratio $\beta_e = \beta(LQ \to eq)$ is fixed by gauge invariance to 0.5 or 1 depending on the LQ type.

6.2.3 Phenomenology of leptoquarks in pp collisions

Pair production In pp collisions leptoquarks would be mainly pair-produced via gg or qq interactions. As long as the coupling λ is not too strong (e.g. $\lambda \sim 0.3$ or below, corresponding to a strength similar to or lower than that of the electromagnetic coupling, $\sqrt{4\pi\alpha_{em}}$), the production cross-section is essentially independent of λ. At the LHC, LQ masses up to about 1.5 to 2 TeV will be probed [48], independently of the coupling λ. However, the determination of the quantum numbers of a first generation LQ in the pair-production mode is not possible (e.g. for the fermion number) or ambiguous and model-dependent (e.g. for the spin). Single LQ production is much better suited for such studies.

Single production Single LQ production at the LHC is also possible. So far, only the production mode $gq \to e + LQ$ (see example diagrams in Fig. 6.6a and b) has been considered

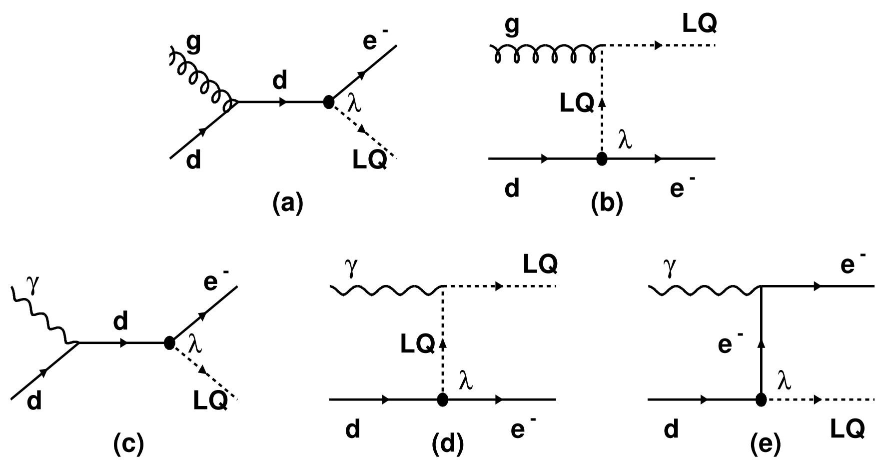

Figure 6.6: Diagrams for single LQ production in pp collisions, shown for the example case of the $\tilde{S}^L_{1/2}$ scalar leptoquark. The production may occur via qg interactions (a and b), or via $q\gamma$ interactions (c, d and e). In the latter case, the photon can be emitted by the proton (elastic regime) or by a quark coming from the proton (inelastic regime).

in the literature (see e.g. [48]). In the context of this study, the additional production mode $\gamma q \to e + LQ$ has been considered as well (see example diagrams in Fig. 6.6c, d and e). This cross-section has been calculated by taking into account:

- the inelastic regime, where the photon virtuality q^2 is large enough and the proton breaks up in a hadronic system with a mass well above the proton mass. In that case, the photon is emitted by a parton in the proton, and the process $qq' \to q + e + LQ$ is calculated.

- the elastic regime, in which the proton emitting the photon remains intact. This calculation involves the elastic form factors of the proton.

As the resonant LQ production in ep collisions, the cross-section of single LQ production in pp collisions approximately scales with the square of the coupling, $\sigma \propto \lambda^2$. Figure 6.7 (left) shows the cross-section for single LQ production at the LHC as a function of the LQ mass, assuming a coupling $\lambda = 0.1$. While the inelastic part of the γq cross-section can be neglected, the elastic production plays an important role at high masses; its cross-section is larger than that of LQ production via gq interactions for masses above ~ 1 TeV. However, the cross-section for single LQ production at LHC is much lower than that at LHeC, in e^+p or e^-p collisions, as shown in Fig.6.7 (right).

The Contact Term Approach For LQ masses far above the kinematic limit, the contraction of the propagator in the $eq \to eq$ and $qq \to ee$ amplitudes leads to a four-fermion interaction. This is depicted in Fig. 6.8 for the case of eq scattering. Such interactions are studied in the context of general contact terms, which can be used to parameterize any new physics process with a characteristic energy scale far above the kinematic limit.

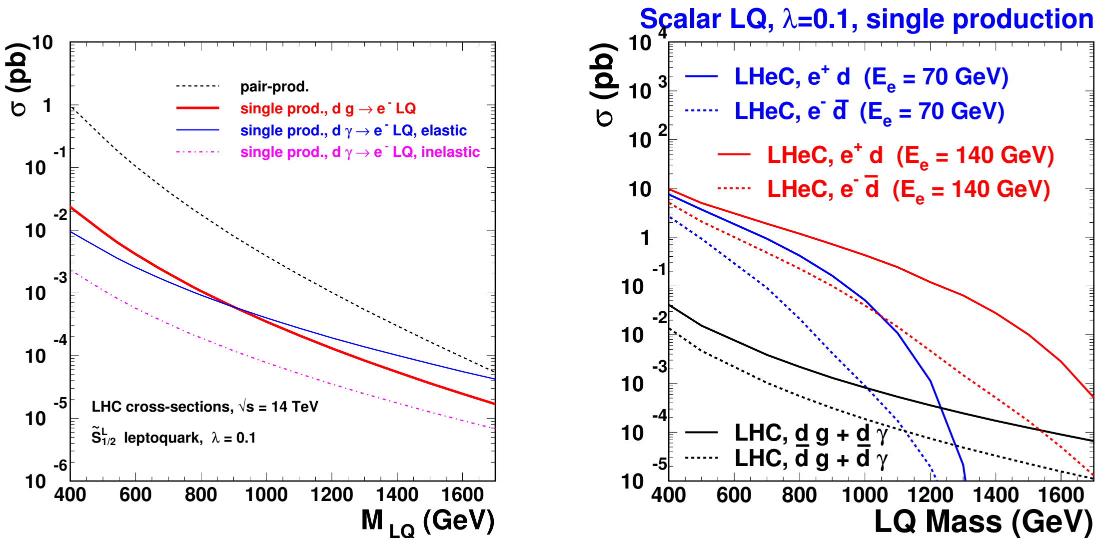

Figure 6.7: left: Single LQ production cross-section at the LHC. right: comparison of the cross-section for single LQ production, at LHC and at LHeC.

In ep collisions, Contact Interactions (CI) would interfere with NC DIS processes and lead to a distorsion of the Q^2 spectrum of NC DIS candidate events. The results presented in section 6.1 can be re-interpreted into expected sensitivities on high mass leptoquarks.

6.2.4 Current status of leptoquark searches

The H1 and ZEUS experiments at the HERA ep collider have constrained the coupling λ to be smaller than the electromagnetic coupling ($\lambda < \sqrt{4\pi\alpha_{em}} \sim 0.3$) for first generation LQs lighter than 300 GeV. The D0 and CDF experiments at the Tevatron pp collider set constraints on first-generation LQs that are independent of the coupling λ, by looking for pair-produced LQs that decay into eq (νq) with a branching ratio β ($1-\beta$). For a branching fraction $\beta = 1$, masses below 299 GeV are excluded by the D0 experiment [49]. The CMS and ATLAS experiments have recently set tighter constraints. Fig.XXX show the bounds obtained by the XXX experiment, in the β versus M_{LQ} plane. For $\beta = 1$, masses below xxx are ruled out.

6.2.5 Sensitivity on leptoquarks at LHC and at LHeC

Mass - coupling reach Fig. 6.9 shows the expected sensitivity [35] of the LHC and LHeC colliders for scalar leptoquark production. The single LQ production cross section depends on the unknown coupling λ of the LQ to the electron-quark pair. For a coupling λ of $\mathcal{O}(0.1)$, that LQ masses up to about 1 TeV could be probed at the LHeC, where such leptoquarks would be mainly produced via pair production or singly with a much reduced cross section.

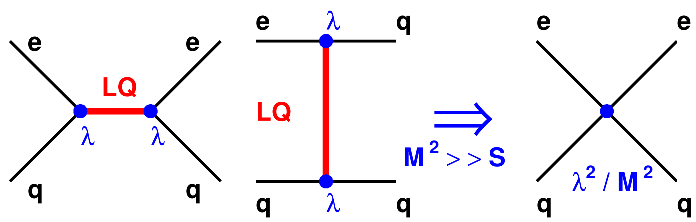

Figure 6.8: Contraction of the LQ propagator in the s- and u-channel exchanges, leading to a four-fermion interaction.

6.2.6 Determination of LQ properties

In ep collisions LQ production can be probed in detail, taking advantage of the formation and decay of systems which can be observed directly as a combination of jet and lepton invariant mass in the final state. It will thereby be possible at the LHeC to probe directly and with high precision the perhaps complex structures which will result in the lepton-jet system and to determine the quantum numbers of new states. Examples of the sensitivity of high energy ep collisions to the properties of LQ production follow. In particular, a quantitative comparison of the potential of LHC and LHeC to measure the fermion number of a LQ is given.

Fermion number (F) Since the parton densities for u and d at high x are much larger than those for $\bar{u}$ and $\bar{d}$, the production cross section at LHeC of an $F = 0$ ($F = 2$) LQ is much larger in e^+p (e^-p) than in e^-p (e^+p) collisions. A measurement of the asymmetry between the e^+p and e^-p LQ cross sections thus determines the fermion number of the produced leptoquark. Pair production of first generation LQs at the LHC will not allow this determination. Single LQ production at the LHC, followed by the LQ decay into $e^\pm$ and q or $\bar{q}$, could determine F by comparing the signal cross sections with an e^+ and an e^- coming from the resonant state. However, the single LQ production cross section at the LHC is two orders of magnitude lower than at the LHeC (Fig. 6.7), so that the asymmetry measured at the LHC may suffer from statistics in a large part of the parameter space. For a coupling $\lambda = 0.1$, no information on F can be extracted from the LHC data for a LQ mass above ~ 1 TeV, while the LHeC can determine F for LQ masses up to 1.4 TeV (Fig. 6.10 and Fig. 6.11). Details of this determination at the LHC are given in the next paragraph.

An estimate of the precision with which the fermion number determination of a leptoquark can be determined at the LHC was obtained from a Monte Carlo simulation. First, using the model [50] implemented in CalcHep [51], samples were generated for the processes $g\, u \rightarrow e^+e^-u$ and $g\, \bar{u} \rightarrow e^+e^-\bar{u}$, keeping only diagrams involving the exchange of a scalar LQ exchange of charge 1/3, isospin 0 and fermion number 2. This leptoquark (${}^{1/3}S_0$ in the notation of Table 6.1) couples to $e^-_R u_R$. Assuming that it is chiral, only right-handed coupling was allowed. The ${}^{1/3}S_0$ leptoquark was also assumed to couple only to the first generation. Masses of 500 GeV, 750 GeV and 1 TeV were considered. The renormalization and factorization scales were set at $Q^2 = m^2_{LQ}$

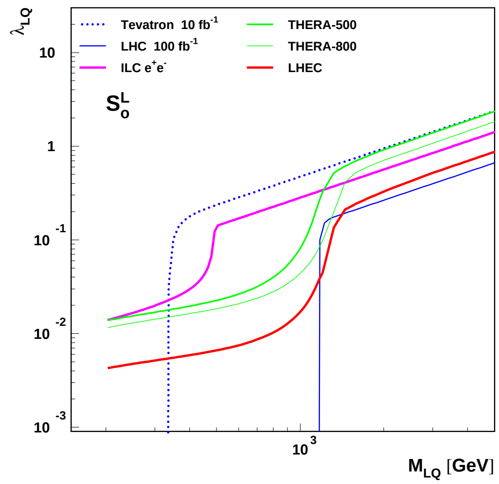

Figure 6.9: *Mass-dependent upper bounds on the LQ coupling λ as expected at LHeC for a luminosity of* 10 fb^{-1} *(full red curve) and at the LHC for* 100 fb^{-1} *(full blue curve). These are shown for an example scalar LQ coupling to e^-u.*

and the coupling parameter $\lambda = 0.1$. A center of mass energy of 14 TeV was assumed at the LHC.

High statistics background samples, corresponding to 150 fb^{-1} were also produced by generating the same processes $pp \to e^+e^- + \text{jet}$, including all diagrams except those involving the exchange of leptoquarks. Kinematic preconditions were applied at the generation level to both signals and background: (i)$p_T(jet) > 50$ GeV, (ii) $p_T(e^\pm) > 20$ GeV, (iii) invariant mass of jet-$e^+ - e^-$ system > 200 GeV. The cross sections for the signals and backgrounds under these conditions are: 19.7 fb, 3.4 fb and 0.87 fb for LQ's of mass 500 GeV, 750 GeV and 1 TeV respectively, and 1780 fb for the background. These events were subsequently passed to Pythia [20] to perform parton showering and hadronization, then processed through Delphes [52] for a fast simulation of the ATLAS detector. Finally, considering events with two reconstructed electrons of opposite sign and, assuming that the leptoquark has already been discovered (at the LHC), the combination of the highest p_T jet with the reconstructed e^- or e^+ with a mass closest to the known leptoquark mass is chosen as the LQ candidate. The following cuts for $m_{LQ} = 500$, 750 and 1000 GeV, respectively, are applied:

- dilepton invariant mass $m_{ll} > 150, 200, 250$ GeV. This cut rejects very efficiently the $Z+$ jets background.

- $p_T(e_1) > 150, 200, 250$ GeV and $p_T(e_2) > 75, 100, 100$ GeV, where e_1 is the reconstructed $e^\pm$ with higher p_T and e_2 the lower p_T electron.

- $p_T(j_1) > 100, 250, 400$ GeV, where j_1 is the reconstructed jet with highest p_T, used for the reconstruction of the LQ.

Table 6.2 summarizes the results of the simulation for an integrated luminosity of 300 fb^{-1}. The expected number of signal events shown in the table is then simply the number of events due to the leptoquark production and decay, falling in the resonance peak within a mass window of width (60, 100, 160 GeV) for the three cases studied, respectively. Although this simple analysis can be improved by considering other less dominant backgrounds and by using optimized selection criteria, it should give a good estimate of the precision with which the asymmetry can be measured. This precision falls rapidly with increasing mass and, above ~ 1 TeV, it becomes impossible to observe simultaneously single production of both ${}^{1/3}S_0$ and ${}^{1/3}\bar{S}_0$. It must be noted that the asymmetry at the LHC will be further diluted by the abundant leptoquark pair production, not taken into account here.

LQ mass	${}^{1/3}S_1 \to e^+\bar{u}$		${}^{1/3}\bar{S}_1 \to e^- u$		Charge Asymmetry
(GeV)	Signal	Background	Signal	Background	
500	121	431	771	478	0.73 ± 0.05
750	18.3	137	132	102	$0.76^{+0.16}_{-0.14}$
1000	4.9	57	44	42	$0.77^{+0.23}_{0.24}$

Table 6.2: Estimated number of events of signal and background, and the charge aymmetry measurement with 300 fb^{-1} at the LHC, for $\lambda = 0.1$.

Flavour structure of the LQ coupling More generally, using the same charge asymmetry observable, the LHeC will be sensitive to the flavour structure of the leptoquark, through the dependence on the parton distribution functions of the interacting quark in the proton. Fig. 6.12 shows the calculated asymmetry for scalar quarks.

Spin At the LHeC, the angular distribution of the LQ decay products is unambiguously related to its spin. Indeed, scalar LQs produced in the s-channel decay isotropically in their rest frame leading to a flat $d\sigma / dy$ spectrum where $y = \frac{1}{2}(1 + \cos\theta^*)$ is the Bjorken scattering variable in DIS and θ^* is the decay polar angle of the lepton relative to the incident proton in the LQ centre of mass frame. In contrast, events resulting from the production and decay of vector LQs would be distributed according to $d\sigma / dy \propto (1-y)^2$. These y spectra from scalar or vector LQ production are markedly different from the $d\sigma / dy \propto y^{-2}$ distribution expected at fixed M for the dominant t-channel photon exchange in neutral current DIS events [1]. Hence, a LQ signal in the NC-like channel will be statistically most prominent at high y.

The spin determination will be much more complicated, even possibly ambiguous, if only the LHC leptoquark pair production data are available. Angular distributions for vector LQs depend strongly on the structure of the $g\, LQ\, \overline{LQ}$ coupling, i.e. on possible anomalous couplings. For a structure similar to that of the γWW vertex, vector LQs produced via $q\bar{q}$ fusion are unpolarised and, because both LQs are produced with the same helicity, the distribution of the LQ production angle will be similar to that of a scalar LQ. The study of LQ spin via single LQ production at the LHC will suffer from the relatively low rates and more complicated backgrounds.

[1] At high momentum transfer, Z^0 exchange is no longer negligible and contributes to less pronounced differences in the y spectra between LQ signal and DIS background.

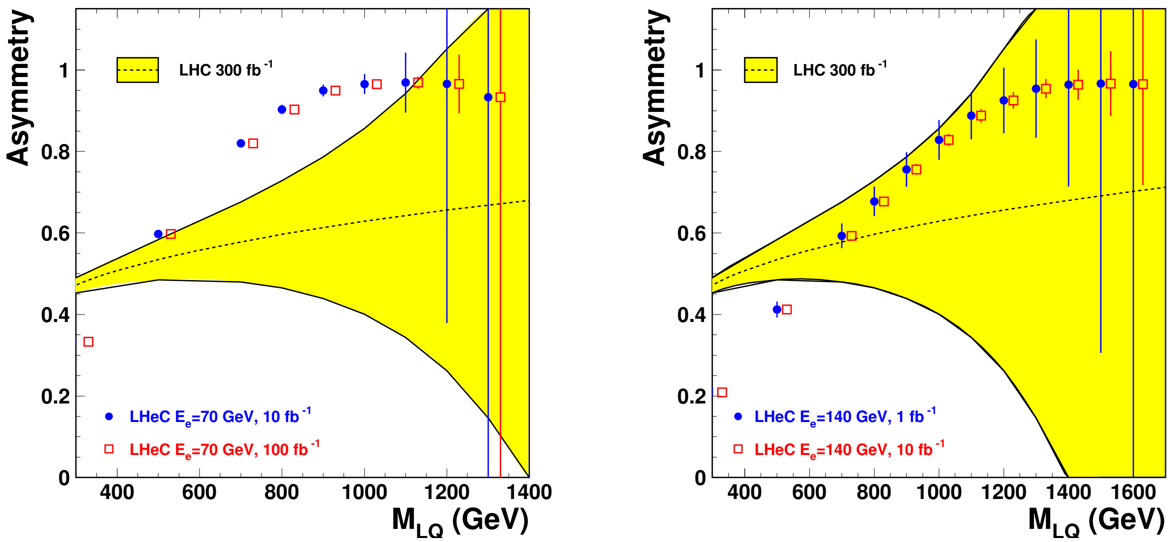

Figure 6.10: *Asymmetries which would determine the fermion number of a LQ, the sign of the asymmetry being the relevant quantity. The dashed curve shows the asymmetry that could be measured at the LHC; the yellow band shows the statistical uncertainty of this quantity, assuming an integrated luminosity of* 300 fb^{-1}. *The red and blue symbols, together with their error bars, show the asymmetry that would be measured at LHeC, assuming* $E_e = 70$ GeV *(left) or* $E_e = 140$ GeV *(right). Two values of the integrated luminosity have been assumed. These determinations correspond to the* $\tilde{S}^L_{1/2}$ *(scalar LQ coupling to* $e^+ + d$*), with a coupling of* $\lambda = 0.1$.

Neutrino decay modes At the LHeC, there is similar sensitivity for LQ decay into both eq and νq. At the LHC, in pp collisions, LQ decay into neutrino-quark final states is plagued by huge QCD background. At the LHeC, production through eq fusion with subsequent νq decay is thus very important if the complete pattern of LQ decay couplings is to be determined.

Coupling λ At the LHeC there is large sensitivity down to small values of the coupling λ. With less sensitivity, in pp interactions at the LHC, information can be obtained from single LQ production and also from dilepton production via the t-channel LQ exchange. Since the single LQ production cross sections depend on both λ and the flavour of the quark to which the LQ couples, determining λ and this flavour requires pp and ep data.

Chiral structure of the LQ coupling Chirality is central to the SM Lagrangian. Polarised electron and positron beams[2] at the LHeC will shed light on the chiral structure of the LQ-e-q couplings. Measurements of a similar nature at LHC are impossible.

[2]Whether it is possible to achieve longitudinal polarisation in a 70 GeV $e^{\pm}$ beam in the LHC tunnel remains to be clarified.

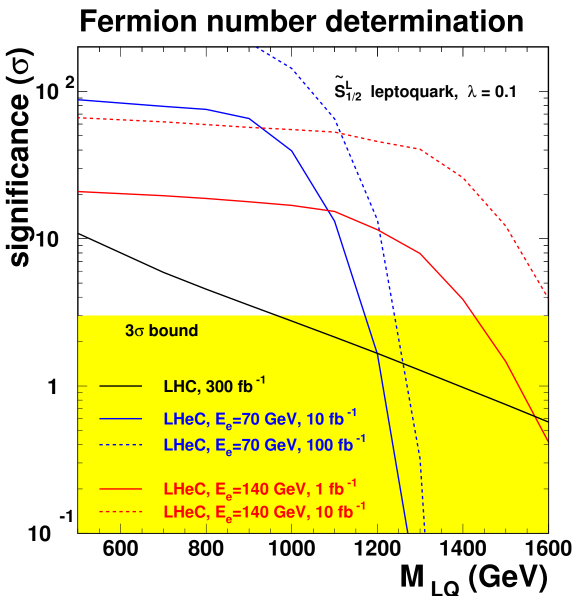

Figure 6.11: Significance of the determination of the fermion number of a LQ, at the LHC (black curve) and at the LHeC (blue and red curves). This corresponds to a $\tilde{S}^L_{1/2}$ leptoquark, assuming a coupling of $\lambda = 0.1$.

6.2.7 Leptogluons

While leptoquarks and excited fermions are widely discussed in the literature, leptogluons have not received the same attention. However, they are predicted in all models with colored preons [53–58]. For example, in the framework of fermion-scalar models, leptons would be bound states of a fermionic preon and a scalar anti-preon $l = (F\bar{S}) = 1 \oplus 8$ (both F and S are color triplets), and each SM lepton would have its own colour octet partner [58].

A study of leptogluons production at LHeC is presented in [59]. It is based on the following Lagrangian:

$$L = \frac{1}{2\Lambda} \sum_l \left\{ \bar{l}_8^\alpha g_s G^\alpha_{\mu\nu} \sigma^{\mu\nu} (\eta_L l_L + \eta_R l_R) + h.c. \right\} \tag{6.5}$$

where $G^\alpha_{\mu\nu}$ is the field strength tensor for gluon, index $\alpha = 1, 2, ..., 8$ denotes the color, g_s is gauge coupling, η_L and η_R are the chirality factors, l_L and l_R denote left and right spinor components of lepton, $\sigma^{\mu\nu}$ is the anti-symmetric tensor and Λ is the compositeness scale. The leptonic chiral invariance implies $\eta_L \eta_R = 0$.

The phenomenology of leptogluons at LHC and LHeC is very similar to that of leptoquarks, despite their different spin (leptogluons are fermions while leptoquarks are bosons) and their different interactions. Figure 6.13 shows typical cross-sections for single leptogluon production at the LHeC, assuming Λ is equal to the leptogluon mass. It is estimated that, for example, a sensitivity of to a compositeness scale of 200 TeV, at 3σ level can be achieved with LHeC having $E_e = 70$ GeV and with 1 fb^{-1}. The mass reach for M_{e8} is 1.1 TeV for $\Lambda = 10$ TeV.

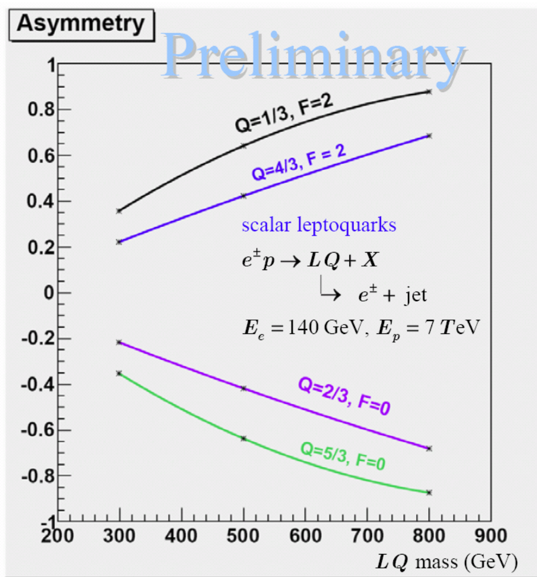

Figure 6.12: Charge asymmetry vs LQ mass for different types of scalar LQ's.

As for leptoquarks, would leptogluons be discovered at the LHC, LHeC data would be of highest value for the determination of the properties of this new particle.

6.3 Excited leptons and other new heavy leptons

The three-family structure and mass hierarchy of the known fermions is one of the most puzzling characteristics of the Standard Model (SM) of particle physics. Attractive explanations are provided by models assuming composite quarks and leptons [60]. The existence of excited states of fermions (F^*) is a natural consequence of compositeness models. More generally, various models predict the existence of fundamental new heavy leptons, which can have similar experimental characteristics as excited leptons. They could, for example, be part of a fourth Standard model family. They arise also in Grand Unified Theories, and appear as colorless fermions in technicolor models.

New heavy leptons could be pair-produced at the LHC up to masses of $\mathcal{O}(300)$ GeV. As for the case of leptoquarks, pp data from pair-production of new leptons may not allow for a detailed study of their properties and couplings. Single production of new leptons is also possible at the LHC, but is expected to have a larger cross-section at LHeC, via $e\gamma$ or eW interactions. The case of excited electrons is considered in the following, with more details being given in [61].

Single production of excited leptons at the LHC ($\sqrt{s}$ up to 14 TeV) may happen via the reactions $pp \to e^{\pm}e^{*} \to e^{+}e^{-}V$ and $pp \to \nu e^{*} + \nu^{*}e^{\pm} \to e^{\pm}\nu V$. The LHC should be able to tighten considerably the current constraints on these possible new states and to probe excited lepton masses of up to 1 TeV [62]. A sensitivity similar to the LHC could be reached at the ILC [63], with different $e^{+}e^{-}$, $e\gamma$ and $\gamma\gamma$ collisions modes and a centre of mass energy of $\sqrt{s} \geq 500$ GeV.

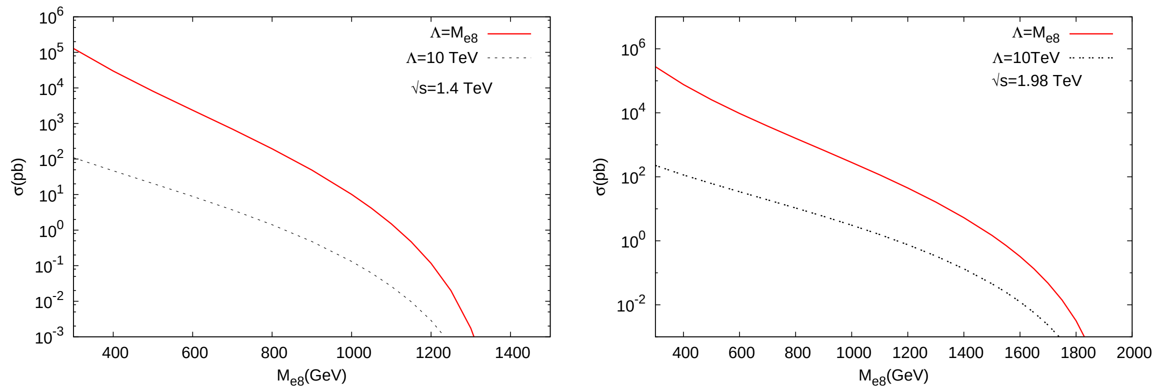

Figure 6.13: Resonant e_8 production at the LHeC, for two values of the center-of-mass energy.

Recent results of searches for excited fermions [64–66] at HERA using all data collected by the H1 detector have demonstrated that ep colliders are very competitive to pp or e^+e^- colliders. Indeed limits set by HERA extend at high mass beyond the kinematic reach of LEP searches [67, 68] and to higher compositeness scales than those obtained at the Tevatron [69] using 1 fb^{-1} of data. Therefore a future LHeC machine, with a centre of mass energy of $1-2$ TeV, much higher than at the HERA ep collider, would be ideal to search for and study excited fermions. This has motivated us to examine excited electron production at a future LHeC collider and compare it to the potential of other types of colliders at the TeV scale, the LHC and the ILC.

6.3.1 Excited Fermion Models

Compositeness models attempt to explain the hierarchy of masses in the SM by the existence of a substructure within the fermions. Several of these models [70–72] predict excited states of the known fermions, in which excited fermions are assumed to have spin 1/2 and isospin 1/2 in order to limit the number of parameters of the phenomenological study. They are expected to be grouped into both left- and right-handed weak isodoublets with vector couplings. The existence of the right-handed doublets is required to protect the ordinary light fermions from radiatively acquiring a large anomalous magnetic moment via F^*FV interaction (where V is a γ, Z or W).

Interactions between excited and ordinary fermions may be mediated by gauge bosons, as described by the effective Lagrangian:

$$\mathcal{L}_{GM} = \frac{1}{2\Lambda}\bar{F}^{*}_{R}\,\sigma^{\mu\nu}\left[g\,f\frac{\tau}{2}\,\mathbf{W}_{\mu\nu} + g'\,f'\,\frac{Y}{2}\,B_{\mu\nu} + g_s\,f_s\,\frac{\lambda}{2}\,\mathbf{G}_{\mu\nu}\right]F_L \;+\; h.c., \tag{6.6}$$

where Y is the weak hypercharge, $g_s,\ g = \frac{e}{\sin\theta_W}$ and $g' = \frac{e}{\cos\theta_W}$ are the strong and electroweak gauge couplings, where e is the electric charge and θ_W is the weak mixing angle; λ and τ are the Gell-Mann matrices and the Pauli matrices, respectively. $G_{\mu\nu}$, $W_{\mu\nu}$ and $B_{\mu\nu}$ are the field strengh tensors describing the gluon, the $SU(2)$, and the $U(1)$ gauge fields. $f_s,\ f$ and f' are the coupling constants associated to each gauge field. They depend on the composite dynamics. The parameter Λ has units of energy and can be regarded as the compositeness scale which reflects the range of the new confinement force.

In addition to gauge mediated (GM) interactions, novel composite dynamics may be visible as contact interactions (CI) between excited fermions and ordinary fermions. Such interactions can be described by an effective four-fermion Lagrangian [72]:

$$\mathcal{L}_{CI} = \frac{4\,\pi}{2\Lambda^2} j^\mu j_\mu \,, \tag{6.7}$$

where Λ is here assumed to be the same parameter as in the gauge interaction Lagrangian (6.6) and j_μ is the fermion current

$$j_\mu = \eta_L \bar{F}_L \gamma_\mu F_L + \eta'_L \bar{F^*}_L \gamma_\mu F^*_L + \eta"_L \bar{F^*}_L \gamma_\mu F_L + h.c. + (L \rightarrow R). \tag{6.8}$$

By convention, the η factors of left-handed currents are set to ± 1, while the factors of right-handed currents are considered to be zero.

6.3.2 Simulation and Results

In the following study, excited electron (e^*) production and decays via both GM and CI are considered. For GM interactions, the e^* production cross section under the assumption $f = -f'$ becomes much smaller than for $f = +f'$ and therefore only the case $f = +f'$ is studied.

Considering pure gauge interactions, excited electrons could be produced in ep collisions at the LHeC via a t-channel γ or Z bosons exchange. The Monte Carlo (MC) event generator COMPOS [73] is used for the calculation of the e^* production cross section and the simulation of signal events. The production cross sections of excited neutrinos at the LHeC is also shown in figure 6.14. These results are obtained with the assumption $f = +f'$ and $M_{e^*} = \Lambda$ and are compared to production cross section at HERA and also at the LHC [62]. In the mass range accessible by the LHeC, the e^* production cross section is clearly much higher than at the LHC.

Considering gauge and contact interactions together, formulae for the e^* production cross section via CI and of the interference term between contact and gauge interactions have been incorporated into COMPOS [64, 74]. For simplicity, the relative strength of gauge and contact interactions are fixed by setting the parameters f and f' of the gauge interaction to one. Comparisons of the e^* production cross section via only gauge interactions and via GM and CI together, as a function of the e^* mass, are presented in figure 6.15(a) for $M_{e^*} = \Lambda$ and figure 6.15(b) for $\Lambda = 10$ TeV, respectively. These results for the LHeC at $\sqrt{s} = 1.4$ TeV are compared to the cross section at an LHC operating at $\sqrt{s} = 14$ TeV. These plots demonstrate that at the LHeC the ratio of the contact and gauge cross sections (proportional to $\hat{s}/\Lambda^4$ and $1/\Lambda^2$ respectively) decreases as Λ and M_{e^*} increase differently than for the LHC where contact interactions may be an important source of production of excited electrons. In the mass range accessed at the LHeC, e^* decays are dominated by gauge decays, provided that Λ is large enough. Therefore, only gauge decays are looked for in the present study.

In order to estimate the sensitivity of excited electron searches at the LHeC, the e^* production followed by its decay in the channel $e^* \rightarrow e\gamma$ is considered. This is the key channel for excited electron searches in ep collisions as it provides a very clear signature and has a large branching ratio. Only the main sources of backgrounds from SM processes are considered

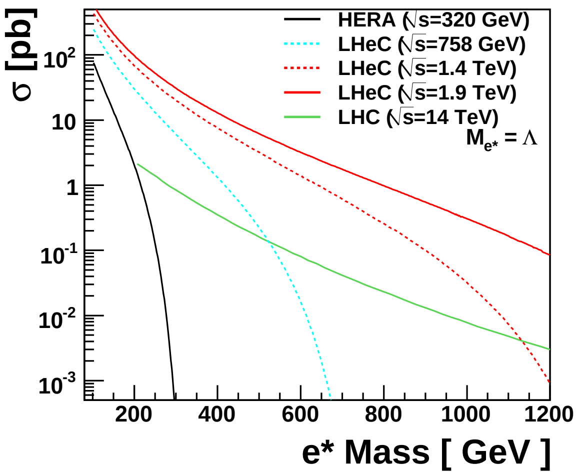

Figure 6.14: The e^* production cross section for different design scenarios of the LHeC electron-proton collider, compared to the cross sections at HERA and at the LHC.

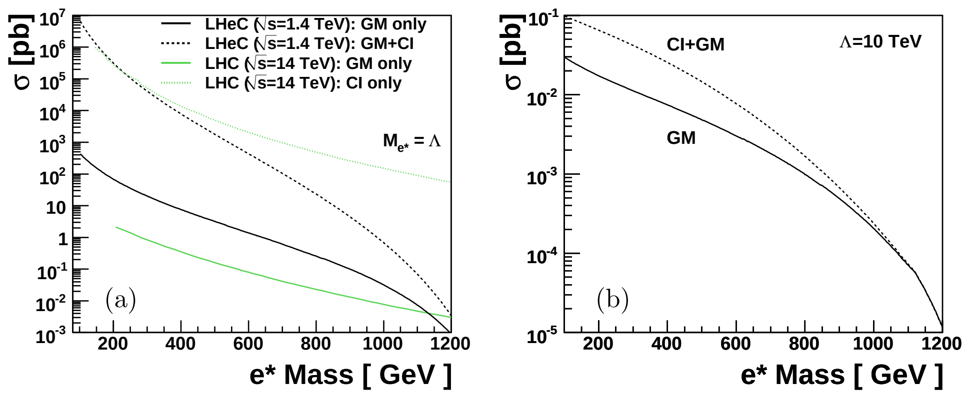

Figure 6.15: Comparison of the e^* production cross section via gauge and contact interactions. In figure (a), the results for the LHeC ($\sqrt{s} = 1.4$ TeV) and for the LHC ($\sqrt{s} = 14$ TeV) are compared. Production cross sections for a fixed Λ value of 10 TeV are shown in figure (b) for the LHeC.

here, namely neutral currents (NC DIS) and QED-Compton ($e\gamma$) events. Other possible SM backgrounds are negligible. The MC event generator WABGEN [75] is used to generate these background events. Figure 6.16 compares the e^* production cross section to the total cross section of SM backgrounds. Background events dominate in the low e^* mass region. Hence to enhance the signal, candidate events are selected with two isolated electromagnetic clusters with a polar angle between 5° and 145° and transverse energies greater than 15 GeV and 10 GeV, respectively.

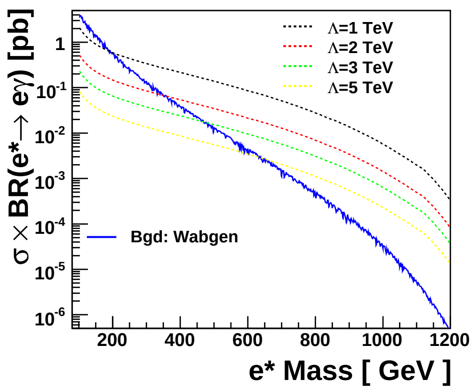

Figure 6.16: Electromagnetic production cross section for e^* ($e^* \to e\gamma$) for different values of Λ.

To translate the results into exclusion limits, expected upper limits on the coupling f/Λ are derived at 95% Confidence Level (CL) as a function of excited electron masses.

In case of gauge interaction, the attainable limits at the LHeC on the ratio f/Λ are shown in figure 6.17 for excited electrons, for the hypothesis $f = +f'$ and different integrated luminosities $L = 10$ fb^{-1} for $\sqrt{s}$ up to 1.4 TeV and $L = 1$ fb^{-1} for $\sqrt{s}$ up to 2 TeV. They are compared to the upper limits obtained at LEP [67,68], HERA [64] and also to the expected sensitivity of the LHC [62]. Considering the assumption $f/\Lambda = 1/M_{e^*}$ and $f = +f'$, excited electrons with masses up to 1.2(1.5) TeV, corresponding to centre of mass energies of $\sqrt{s} = 1.4(1.9)$ TeV of the LHeC, are excluded. Under the same assumptions, LHC ($\sqrt{s} = 14$ TeV) could exclude e^* masses up to 1.2 TeV for an integrated luminosity of 100 fb^{-1}. In the accessible mass range of LHeC, the LHeC would be able to probe smaller values of the coupling f/Λ than the LHC. Similarly to leptoquarks (see section 6.2), if an excited electron is observed at the LHC with a mass of $\mathcal{O}(1$ TeV$)$, the LHeC would be better suited to study the properties of this particle, thanks to the larger single production cross-section (see Fig. 6.14).

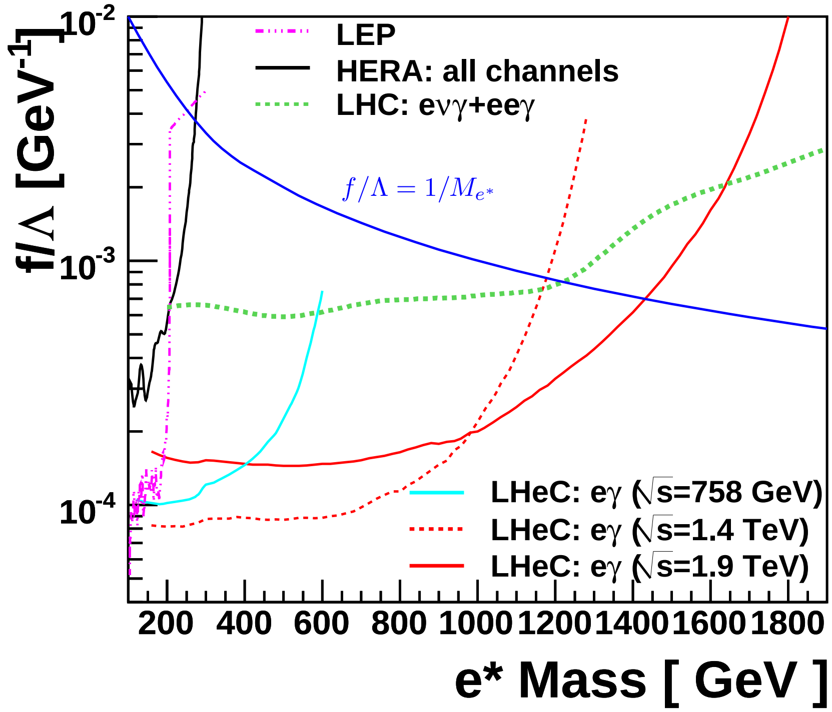

Figure 6.17: Sensitivity to excited electron searches for different design scenarios of the LHeC electron-proton collider, compared to the expected sensitivity of the LHC ($\sqrt{s}$ = 14 TeV, L = 100 fb^{-1}). Different integrated luminosities at the LHeC (L = 10 fb^{-1} for $\sqrt{s}$ up to 1.4 TeV and $L = 1$ fb^{-1} for $\sqrt{s}$ up to 2 TeV) are assummed. The curves present the expected exclusion limits on the coupling f/Λ at 95% CL as a function of the mass of the excited electron with the assumption $f = +f'$. Areas above the curves are excluded. Present experimental limits obtained at LEP and HERA are also represented.

6.3.3 New leptons from a fourth generation

New leptons from a fourth generation (l_4, ν_4) may have anomalous couplings to the standard leptons, as given by the following effective Lagrangian:

$$\begin{aligned}
\mathcal{L}_{nc} &= \left(\frac{\kappa_\gamma^{\ell_4 \ell_i}}{\Lambda}\right) e_\ell g_e \overline{\ell_4} \sigma_{\mu\nu} \ell_i F^{\mu\nu} \\
&+ \left(\frac{\kappa_Z^{\ell_4 \ell_i}}{2\Lambda}\right) g_Z \overline{\ell_4} \sigma_{\mu\nu} \ell_i Z^{\mu\nu} + \left(\frac{g_Z}{2}\right) \overline{\nu_i} \frac{i}{2\Lambda} \kappa_Z^{\nu_4 \nu_i} \sigma_{\mu\nu} q^\nu P_L \nu_4 Z^\mu + h.c. \\
\mathcal{L}_{cc} &= \left(\frac{g_W}{\sqrt{2}}\right) \overline{l_i} \left[\frac{i}{2\Lambda} \kappa_W^{\nu_4 l_i} \sigma_{\mu\nu} q^\nu\right] P_L \nu_4 W^\mu + h.c.
\end{aligned}$$

In that case, the single production of l_4 and ν_4 would be similar to that of excited electrons and neutrinos. For a study of the properties and couplings of such a new lepton, an *ep* machine would offer the same advantages as presented above in the case of excited electrons. A study of the processes $ep \to l_4 X \to Ze(\gamma\mu)X$ and $ep \to \nu_4 X \to W(e,\mu)X$ at the LHeC is presented in [76]. For example, for an anomalous coupling $\kappa/\Lambda = 1$ TeV^{-1}, LHeC would be able to cover l_4 masses up to ~ 900 GeV.

6.4 New physics in boson-quark interactions

Several extensions of the Standard Model predict new phenomena that would be directly observable in boson-quark interactions. For example, the top quark may have anomalous couplings to gauge bosons, leading to Flavour Changing Neutral Current (FCNC) vertices $tq\gamma$, where q is a light quark. Similarly, excited quarks (q^*) or quarks from a fourth generation (Q) could be produced via $\gamma q \to q*$ or $\gamma q \to Q$. The transitions $\gamma q \to t, q^*, Q$ can be studied in *ep* collisions at the LHeC, but a much larger cross-section would be achieved at a γp collider, due to the much larger γp centre-of-mass energy. The single production of q^*, Q or of a top quark via anomalous couplings is also possible at the LHC, but it involves an anomalous coupling together with an electroweak coupling and the main background processes involve the strong interaction. The signal to background ratio will thus be much more challenging at the LHC, and any constraints on anomalous couplings would therefore be obtained from the decay channels of these quarks. The example of anomalous single top production is detailed in the following.

6.4.1 An LHeC-based γp collider

- refer to the appropriate section in the machine part.
- short summary here

6.4.2 Anomalous Single Top Production at the LHeC Based γp Collider

The top quark is expected to be most sensitive to physics beyond the Standard Model (BSM) because it is the heaviest available particle of the Standard Model (SM). A precise measurement of the couplings between SM bosons and fermions provides a powerful tool for the search of

BSM physics allowing a possible detection of deviations from SM predictions [77]. Anomalous tqV ($V = g, \gamma, Z$ and $q = u, c$) couplings can be generated through dynamical mass generation [78],sensitive to the mechanism of dynamical symmetry breaking. They have a similar chiral structure as the mass terms, and the presence of these couplings would be interpreted as signals of new interactions. This motivates the study of top quark flavour changing neutral current (FCNC) couplings at present and future colliders.

Current experimental constraints at 95% C.L. on the anomalous top quark couplings are [79]: $BR(t \to \gamma u) < 0.0132$ and $BR(t \to \gamma u) < 0.0059$ from HERA; $BR(t \to \gamma q) < 0.041$ from LEP and $BR(t \to \gamma q) < 0.032$ from CDF. The HERA has much higher sensitivity to $u\gamma t$ than $c\gamma t$ due to more favorable parton density: the best limit is obtained from the ZEUS experiment.

The top quarks will be produced in large numbers at the Large Hadron Collider (LHC), allowing great precision measurement of the coupling. For a luminosity of 1 fb^{-1} (100 fb^{-1}) the expected ATLAS sensitivity to the top quark FCNC decay is $BR(t \to q\gamma) \sim 10^{-3}(10^{-4})$ [80, 81]. The production of top quarks by FCNC interactions at hadron colliders has been studied in [82–94], e^+e^-colliders in [78,95–98] and lepton-hadron collider in [78,99–101]. LHC will give an opportunity to probe $BR(t \to ug)$ down to 5×10^{-3} [102]; ILC/CLIC has the potential to probe $BR(t \to q\gamma)$ down to 10^{-5} [103].

A linac-ring type collider presents the sole realistic way to TeV scale in γp collisions [104–109]. Recently this opportunity has been widely discussed in the framework of the LHeC project [110]. Two stages of the LHeC were considered: QCD Explorer ($E_e = 50 - 100$ GeV) and Energy Frontier ($E_e > 250$ GeV). The potential of the LHeC as a γp collider to search for anomalous top quark interactions has been investigated [111]. The effective Lagrangian involving anomalous $t\gamma q$ ($q = u, c$) interactions is given by [102].

$$L = -g_e \sum_{q=u,c} Q_q \frac{\kappa_q}{\Lambda} \bar{t} \sigma^{\mu\nu}(f_q + h_q \gamma_5) q A_{\mu\nu} + h.c. \tag{6.9}$$

where $A_{\mu\nu}$ is the usual photon field tensor, $\sigma_{\mu\nu} = \frac{i}{2}(\gamma_\mu\gamma_\nu - \gamma_\nu\gamma_\mu)$, Q_q is the quark charge, in general f_q and h_q are complex numbers, g_e is the electromagnetic coupling constant, κ_q is a real and positive anomalous FCNC coupling constant and Λ is the new physics scale. The neutral current magnitudes in the Lagrangian satisfy $|(f_q)^2 + (h_q)^2| = 1$ for each term. The anomalous decay width can be calculated as

$$\Gamma(t \to q\gamma) = (\frac{\kappa_q}{\Lambda})^2 \frac{2}{9} \alpha_{em} m_t^3 \tag{6.10}$$

Taking $m_t = 173$ GeV and $\alpha_{em} = 0.0079$, the anomalous decay width ≈ 9 MeV for $\kappa_q/\Lambda = 1$ TeV^{-1} while the SM decay width is about 1.5 GeV.

For numerical calculations anomalous interaction vertices are implemented into the CalcHEP package [51] using the CTEQ6M [21] parton distribution functions. The Feynman diagrams for the subprocess $\gamma q \to W^+ b$, where $q = u, c$ are shown in Fig. 6.18. The first three diagrams correspond to irreducible backgrounds and the last one to the signal. The main background comes from associated production of W boson and the light jets.

The differential cross sections for the final state jets are given in Fig. 6.19 ($\kappa/\Lambda = 0.04$ TeV^{-1}) for $E_e = 70$ GeV and $E_p = 7000$ GeV assuming $\kappa_u = \kappa_c = \kappa$. It is seen that the transverse momentum distribution of the signal has a peak around 70 GeV.

Here, b-tagging efficiency is assumed to be 60% and the mistagging factors for light (u, d, s) and c quarks are taken as 0.01 and 0.1, respectively. A p_T cut reducese the signal (by $\sim 30\%$

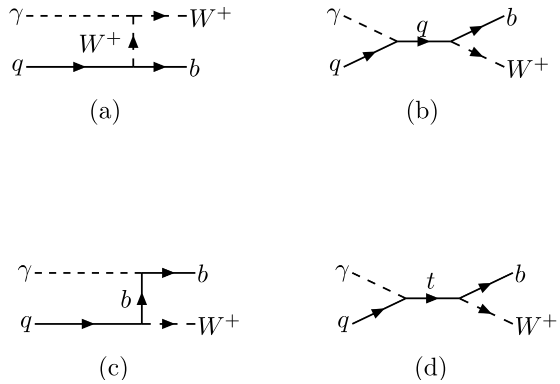

Figure 6.18: Feynman diagrams for $\gamma q \to W^+ b$, where $q = u, c$.

for $p_T > 50$ GeV), whereas the background is essentially suppressed (by a factor 4-6) . In order to improve the signal to background ratio further, one can apply a cut on the invariant mass of $W + jet$ around top mass. In Table 6.3, the cross sections for signal and background processes are given after having applied both a p_T and an invariant mass cuts ($M_{Wb} = 150 - 200$ GeV).

Table 6.3: The cross sections (in pb) according to the p_T cut and invariant mass interval ($M_{Wb} = 150 - 200$ GeV) for the signal and background at γp collider based on the LHeC with $E_e = 70$ GeV and E_p =7000 GeV.

$\kappa/\Lambda = 0.01$ TeV^{-1}	$p_T > 20$ GeV	$p_T > 40$ GeV	$p_T > 50$ GeV
Signal	8.86×10^{-3}	7.54×10^{-3}	6.39×10^{-3}
Background: W^+b	1.73×10^{-3}	1.12×10^{-3}	7.69×10^{-4}
Background: W^+c	3.48×10^{-1}	2.30×10^{-1}	1.63×10^{-1}
Background: W^+jet	1.39×10^{-1}	9.11×10^{-2}	6.38×10^{-2}

In order to calculate the statistical significance (SS) we use following formula [112] :

$$SS = \sqrt{2\left[(S+B)\ln(1+\frac{S}{B}) - S\right]} \tag{6.11}$$

where S and B are the numbers of signal and background events, respectively. Results are presented in Table 6.4 for different κ/Λ and luminosity values. It is seen that even with 2 fb^{-1} the LHeC based γp collider will provide 5σ discovery for $\kappa/\Lambda = 0.02$ TeV^{-1}.

Table 6.4: The signal significance (SS) for different values of κ/Λ and integral luminosity for $E_e = 70$ GeV and E_p =7000 GeV (the numbers in parenthesis correspond to $E_e = 140$ GeV).

SS	$L = 2$ fb^{-1}	$L = 10$ fb^{-1}
$\kappa/\Lambda = 0.01$ TeV^{-1}	2.58 (2.88)	5.79 (6.47)
$\kappa/\Lambda = 0.02$ TeV^{-1}	5.26 (5.92)	11.78 (13.25)

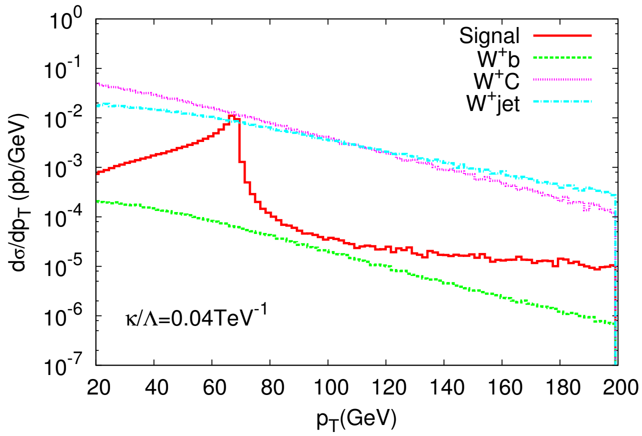

Figure 6.19: The transverse momentum distribution of the final state jet for the signal and background processes. The differential cross section includes the b-tagging efficiency and the rejection factors for the light jets. The center of mass energy $\sqrt{s_{ep}} = 1.4$ TeV and κ/Λ =0.04 TeV $^{-1}$.

Up to now, we have assumed $\kappa_u = \kappa_c = \kappa$. However, it would be interesting to analyze the case $\kappa_u \neq \kappa_c$. Indeed, at HERA, valence u-quarks dominate whereas at LHeC energies the c-quark and u-quark contributions become comparable. Therefore, the sensitivity to κ_c will be enhanced at LHeC comparing to HERA. In Fig. 6.20 contour plots for anomalous couplings in $\kappa_u - \kappa_c$ plane are presented. For this purpose, a χ^2 analysis was performed with

$$\chi^2 = \sum_{i=1}^{N} \left(\frac{\sigma^i_{S+B} - \sigma^i_B}{\Delta \sigma^i_B} \right)^2 \tag{6.12}$$

where σ^i_B is the cross-section for the SM background in the i^{th} bin, including both b-jet and light-jet contributions with their corresponding efficiency factors. In the σ_{S+B} calculations, we take into account the different values for κ_u and κ_c as well as the signal-background interference. Figs. 6.19-6.20 show that the sensitivity is enhanced by a factor of 1.5 when the luminosity changes from 2 fb^{-1} to 10 fb^{-1}. Concerning the energy upgrade, increasing electron energy from 70 GeV to 140 GeV results in 20% improvement for κ_c [111]. Increasing the electron energy further (energy frontier ep collider) does not give an essential improvement in the sensitivity to anomalous couplings [113].

Table 6.4 shows that a sensitivity to anomalous coupling κ/Λ down to 0.01 TeV^{-1} could be reached. Noting that the value of $\kappa/\Lambda = 0.01$ TeV^{-1} corresponds to $BR(t \to \gamma u) \approx 2 \times 10^{-6}$ which is two orders smaller than the LHC reach with 100 fb^{-1}, it is obvious that even an upgraded LHC will not be competitive with LHeC based γp collider in the search for anomalous $t\gamma q$ interactions. Different extensions of the SM (SUSY, technicolor, little Higgs, extra dimensions etc.) predict branching ratio $BR(t \to \gamma q)$=$O(10^{-5})$, hence the LHeC will provide an opportunity to probe these models. The top quark could provide very important information for the Standard Model extentions due to its large mass close to the electroweak symmetry breaking scale.

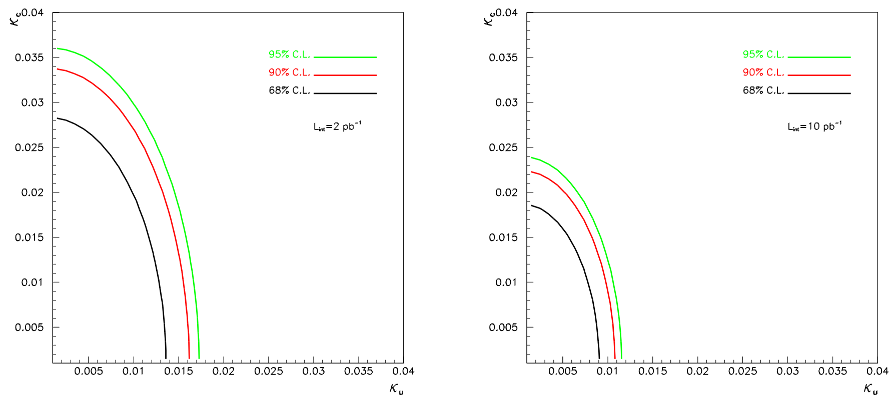

Figure 6.20: Contour plot for the anomalous couplings reachable at the LHeC based γp collider with the ep center of mass energy $\sqrt{s_{ep}} = 1.4$ TeV and integrated luminosity of $L_{int} = 2$ fb^{-1} (left) or $L_{int} = 10$ fb^{-1} (right)

6.4.3 Excited quarks in γp collisions at LHeC

Excited quarks will have vertices with SM quark and gauge bosons (photon, gluon, Z or W bosons). They can be produced at ep and γp colliders via quark photon fusion. Interactions involving excited quark are described by the Lagrangian of eq. 6.6 (where F is now a quark q)

A sizeable f_s coupling would allow for resonant q^* production at the LHC via quark-gluon fusion. In that case, the LHC would offer a large discovery potential for excited quarks and would be well suited to study the properties and couplings of these new quarks. However, if the coupling of excited quarks to gq happens to be suppressed, the LHC would mainly produce q^* via pair-production and would have little sensitivity to couplings f/Λ or f'/Λ. Such couplings would be better studied, or probed down to much lower values, via single-production of q^* at the LHeC. A study of the LHeC potential for excited quarks is presented in [114]. An example of the 3σ discovery reach, assuming $f = f' = f_s$ and setting Λ to be equal to the q^* mass, is given in Fig. 6.21. Both decays $q^* \to q\gamma$ and $q^* \to qg$ have been considered here.

6.4.4 Quarks from a fourth generation at LHeC

The case of fourth generation quarks with magnetic FCNC interactions to gauge bosons and standard quarks,

$$\mathcal{L} = \left(\frac{\kappa_\gamma^{q_4 q_i}}{\Lambda}\right) e_q g_e \bar{q}_4 \sigma_{\mu\nu} q_i F^{\mu\nu} + \left(\frac{\kappa_Z^{q_4 q_i}}{2\Lambda}\right) g_Z \bar{q}_4 \sigma_{\mu\nu} q_i Z^{\mu\nu} + \left(\frac{\kappa_g^{q_4 q_i}}{\Lambda}\right) g_s \bar{q}_4 \sigma_{\mu\nu} T^a q_i G_a^{\mu\nu} + h.c. \tag{6.13}$$

is very similar to that of excited quarks. A γp collider based on LHeC would have a better sensitivity than LHC to anomalous couplings κ_γ and κ_Z. A detailed study is presented in [76] and example results are shown in Fig. 6.22. These figures also show the clear advantage of a γp collider compared to an ep collider, for the study of new physics in γq interactions.

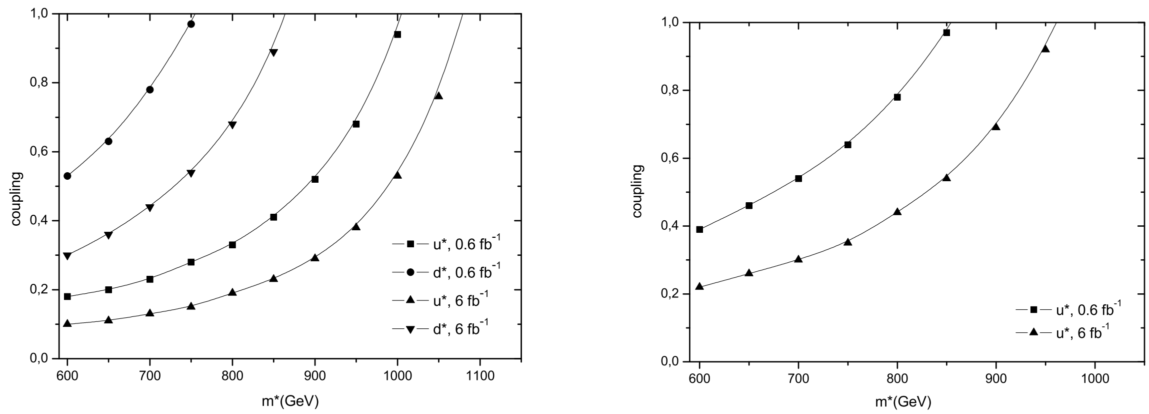

Figure 6.21: Observation reach at 3σ for coupling and excited quark mass at a γp collider with $\sqrt{s} = 1.27$ TeV from an analysis of (left) the jj channel and (right) the γj channel.

6.4.5 Diquarks at LHeC

The case of diquark production at LHeC has been studied in [115]. The production cross-section can be sizeable at n high energy ep machine, especially when operated as a γp collider. The measurement of the $\gamma p \to DQ + X$ cross-section, for a diquark DQ of known mass and known coupling to the diquark pair[3] would provide a measurement of the electric charge of the diquark. It would thus be complementary to the pp data, which offer no simple way to access the DQ electric charge. However, the diquark masses and couplings that could be accessible at LHeC appear to be already excluded by the recent search for dijet resonances at the LHC [116].

6.4.6 Quarks from a fourth generation in Wq interactions

In case fourth generation quarks do not have anomalous interactions as in Eq. 6.13, they (or vector-like quarks coupling to light generations [117]) could be produced in ep collisions by Wq interactions provided that the V_{Qq} elements of the extended CKM matrix are not too small, via the usual vector WqQ interactions. An example of the sensitivity that could be reached at LHeC is presented in [118], assuming some values for the V_{Qq} parameters. Measurements of single Q production at LHeC would provide complementary information to the LHC data, that could help in determining the extended CKM matrix.

6.4.7 Sensitivity to a light Higgs boson

Understanding the mechanism of electroweak symmetry breaking is a key goal of the LHC physics programme. In the SM, the symmetry breaking is realized via a scalar field (the Higgs field) which, at the minimum of the potential, develops a non-zero vacuum expectation value.

[3]The LHC would observe diquark as di-jet resonances, and could easily determine its mass, width and coupling to the quark pair.

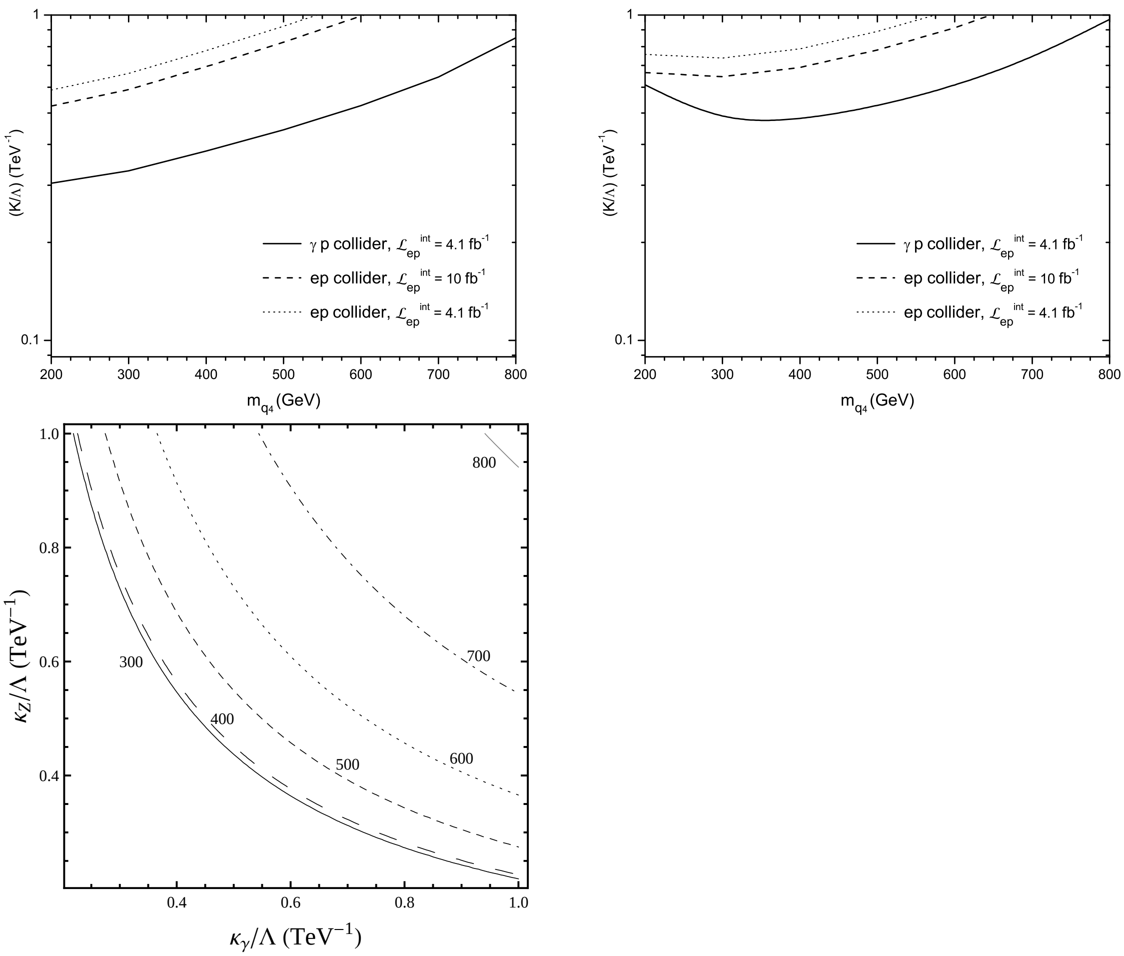

Figure 6.22: The achievable values of the anomalous coupling strength at ep and γp colliders for a) $q_4 \to \gamma q$ anomalous process and (b) $q_4 \to Zq$ anomalous process as a function of the q_4 mass; (c) the reachable values of anomalous photon and Z couplings with $L_{int} = 4.1$ fb^{-1}.

The broken $SU(2)_L \times U(1)_Y$ symmetry gives mass to the electroweak gauge bosons and the interaction of the Higgs field with the SM fermions leads to mass terms for them. The LHC experiments should be able to discover a Higgs boson within the full allowable mass range, with an integrated luminosity of less than 10 fb^{-1}. Following its discovery, it will be crucial to measure the couplings of this Higgs boson to the SM particles, in particular to the fermions, in order to:

- establish that the Higgs field is indeed accounting for the fermion masses, via Yukawa couplings $y_f H\bar{f}f$;
- disentangle between the SM and (some of) its extensions. For example, despite the richer content of the Higgs sector in the Minimal Supersymmetric Standard Model, only the light SUSY Higgs boson h would be observable at the LHC in certain regions of

parameter space. Its properties are very similar to those of the SM Higgs H, and precise measurements of ratios $BR(\Phi \to VV)/BR(\Phi \to f\bar{f})$ will be essential in determining whether or not the observed boson, Φ, is the SM higgs scalar.

Electroweak precision measurements strongly suggest that the SM Higgs boson should be light, in which case it would decay into a $b\bar{b}$ pair with a branching ratio of $\sim 70\%$, but a measurement of the $Hb\bar{b}$ coupling will be very challenging at the LHC [80,112,119]. Indeed, the observation of $H \to b\bar{b}$ in the inclusive production mode is made very difficult by the huge QCD background. The observability of the signal in the $t\bar{t}H$ production mode also suffers from a large background, including background of combinatorics origin, and from experimental systematic uncertainties. The signal $H \to b\bar{b}$ may be observed in the exclusive production mode, thanks to the much cleaner environment in a diffractive process. However, the production cross-section in this mode suffers from large theoretical uncertainties, such that this measurement, if feasible at all, would not translate into a precise measurement of the $Hb\bar{b}$ coupling.

At LHeC, a light Higgs boson could be produced via WW or ZZ fusion with a sizeable cross-section. This section focusses on the observability of the signal $ep \to H + X \to b\bar{b} + X$ at LHeC, which may be the first observation of the $H \to b\bar{b}$ decay.

Higgs production at LHeC

In ep collisions, the Higgs boson could be produced in neutral current (NC) interactions via the ZZH coupling, and in charged current (CC) interactions via the WWH coupling. The corresponding diagrams are shown in Fig. 6.23, and the production cross-sections, as a function of the Higgs mass, can be seen in Fig. 6.24. The WWH production largely dominates the total cross-section. As is the case for the inclusive CC DIS interactions, the cross-section is much larger in e^-p collisions than in e^+p collisions, due to the more favorable density of the valence quark that is involved (u in e^-p, d in e^+p), and to the more favorable helicity factors. Table 6.5 shows the Higgs production cross-section (at leading order) via CC interactions in e^-p collisions, for various values of the Higgs mass and three example values of the electron beam energy. The scale dependency of these leading order estimate is of $\mathcal{O}(10\%)$. Next-to-leading order corrections were calculated in [**?**]. The NLO QCD corrections are small, but can affect within $\mathcal{O}(20\%)$ the shape of some kinematic distributions.

M_H in GeV :	100	120	160	200	240	280
$E_e = 50$ GeV	102	81	50	32	20	12
$E_e = 100$ GeV	201	165	113	79	55	39
$E_e = 150$ GeV	286	239	170	123	90	67

Table 6.5: Production cross-section in fb of a SM Higgs boson via charged current interactions in e^-p collisions, for three example values of the electron beam energy.

Signal and background Monte-Carlo samples

The dominating source of background at large missing transverse energy is coming from multi-jet production in CC DIS interactions. In particular, a good rejection of the background

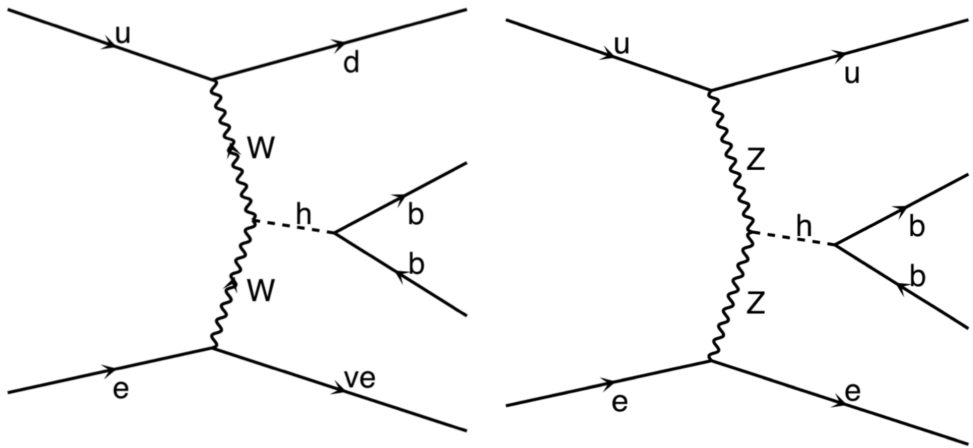

Figure 6.23: Feynman diagrams for CC(left) and NC(right) Higgs production at the LHeC.

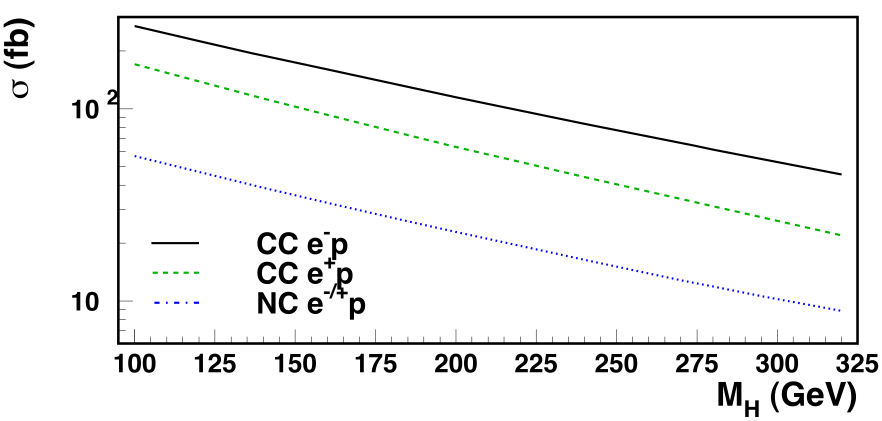

Figure 6.24: Production cross-section of a SM Higgs boson in *ep* collision with E_e=150 GeV and E_p=7 TeV, as a function of the Higgs mass.

coming from single top production ($e^- b \to \nu t$), where the top decays hadronically, puts severe constraints on the acceptance and the resolution of the detector, as will be seen below. The background due to multijet production in NC interactions is also considered.

MadGraph [120] has been used to generate SM Higgs production, CC and NC DIS background events. Calculations of cross-section and final states of outgoing particles are produced by MadGraph with given beam parameters, considering all possible tree-level Feynman diagrams in the SM. For the CC and NC DIS background, processes producing three outgoing partons were simulated. In the case of NC, since the cross section is very high, diverging at low scattering angle, only processes producing two or more b quarks were generated in order to have sufficient MC statistics. Fragmentation and hadronization processes were simulated by PYTHIA [20] with custom modifications to apply for ep collisions. Finally, particles were passed through a generic detector using the PGS [121] fast detector simulation tool. We assumed tracking coverage of $|\eta| < 3$ and calorimeter coverage of $|\eta| < 5$ with electromagnetic calorimeter resolution of $5\,\%/\sqrt{E(\mathrm{GeV})}$ (plus 1% of constant term) and hadronic calorimeter resolution of $60\,\%/\sqrt{E(\mathrm{GeV})}$. Jets were reconstructed by a cone algorithm with a cone size of $\Delta R = 0.7$. The efficiency of b-flavor tagging was assumed to be 60 % and flat within the calorimeter coverage, whereas mistagging probabilities of 10 % and 1 % for charm-quark jets and for light-quark jets, respectively, were taken into account.

We set 150 GeV of electron beam energy with 7 TeV of proton beam energy as the reference beam configuration and assumed 120 GeV of SM Higgs boson mass in the MC simulation study. The results were compared with those with a different beam energy and Higgs mass.

Observability of the signal

The following selection criteria were applied, based on observable variables generated by the PGS detector simulation, to distinguish $H \to b\bar{b}$ from the CC and NC DIS backgrounds.

- **cut (1): Primary cuts**
  - Exclude electron-tagged events
  - $E_{T,miss} > 20\,\mathrm{GeV}$
  - $N_{jet}(P_{T,jet} > 20\,\mathrm{GeV}) \geq 3$
  - $E_{T,total} > 100\,\mathrm{GeV}$
  - $y_{JB} < 0.9$, where $y_{JB} = \Sigma(E - p_z)/2E_e$
  - $Q^2_{JB} > 400\,\mathrm{GeV}$, where $Q^2_{JB} = E^2_{T,miss}/(1 - y_{JB})$
- **cut (2): b-tag requirement**
  - $N_{b\text{-}jet}(P_{T,jet} > 20\,\mathrm{GeV}) \geq 2$, where b-jet means a b-tagged jet
- **cut (3): Higgs invariant mass cut**
  - $90 < M_H < 120\,\mathrm{GeV}$; due to the energy carried by the neutrino from b decays, the mass peaks are slightly lower than the true Higgs mass

Fig. 6.25 shows the missing E_T and number of b-tagged jets for $H \to b\bar{b}$ events together with the CC and NC DIS background. The NC background is strongly suppressed by the missing E_T cut and electron-tag requirement. We required at least two b-tagged jets, and reconstructed

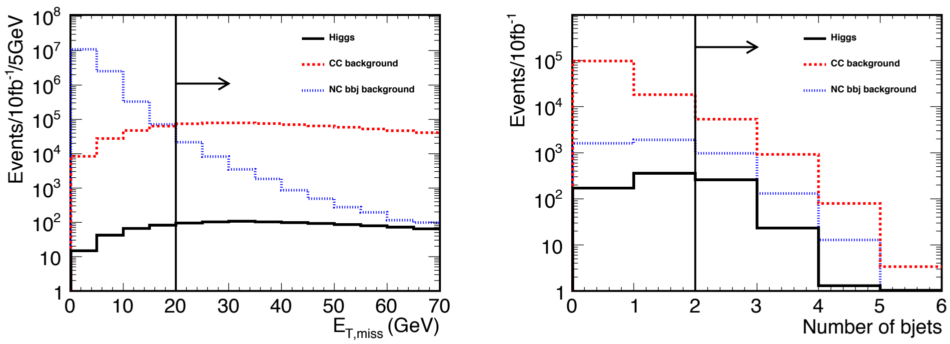

Figure 6.25: Missing E_T (left) and number of b-tagged jets (right). Solid (black), dashed (red) and dotted (blue) histograms show $H \rightarrow b\bar{b}$, CC and NC DIS background, respectively. The right plot is for events passing cut (1) in the text.

the Higgs invariant mass using the two b-tagged jets with lowest and second lowest η. After cuts (1) + (2) + (3) were applied, 44.4 % of the remaining CC background was due to single top production. The following cuts were further applied.

- **cut (4): rejection of single top production**
  - $M_{jjj,top} > 250\,\mathrm{GeV}$, where the three-jet invariant mass ($M_{jjj,top}$) was reconstructed from two b-jets with the lowest η and any third jet with the lowest η regardless of b-tag
  - $M_{jj,W} > 130\,\mathrm{GeV}$, where di-jet invariant mass ($M_{jj,W}$) was reconstructed from one b-jet with the lowest η and any second jet with the lowest η regardless of b-tag but excluding the second lowest η b-jet
- **cut (5): forward jet tagging**
  - $\eta_{jet} > 2$ for the lowest-η jet excluding the two b-jets

Fig. 6.26 shows the reconstructed three-jet ($M_{jjj,top}$) and di-jet ($M_{jj,W}$) invariant masses after cuts (1) and (2) are applied. It is seen that, for CC background, the former peaks at the top mass and the latter peaks at the W mass. The last cut is motivated by the fact that the jet from light quark participating in the CC reaction for the signal is kinematically boosted to forward rapidity (in the proton beam direction), as shown in Fig. 6.27.

Fig. 6.28 shows the reconstructed Higgs mass distribution for an integrated luminosity of $10\,\mathrm{fb}^{-1}$, after all selection criteria except for the Higgs mass cut have been applied. The results are summarized in Table 6.6. After the selection, 85 $H \rightarrow b\bar{b}$ events are expected for $10\,\mathrm{fb}^{-1}$ luminosity with a 150 GeV electron beam. The signal to background ratio is 1.79 and the significance of the signal $S/\sqrt{N} = 12.3$. For a higher Higgs mass, m_H=150 GeV, the production cross section decreases and the $b\bar{b}$ branching ratio also decreases. The expected number of signal events becomes 25 and S/N and $S/\sqrt{N}$ are 0.52 and 3.60, respectively. On the other hand, with 60 GeV electron beam and five times larger luminosity ($50\,\mathrm{fb}^{-1}$), for 120 GeV Higgs, 124

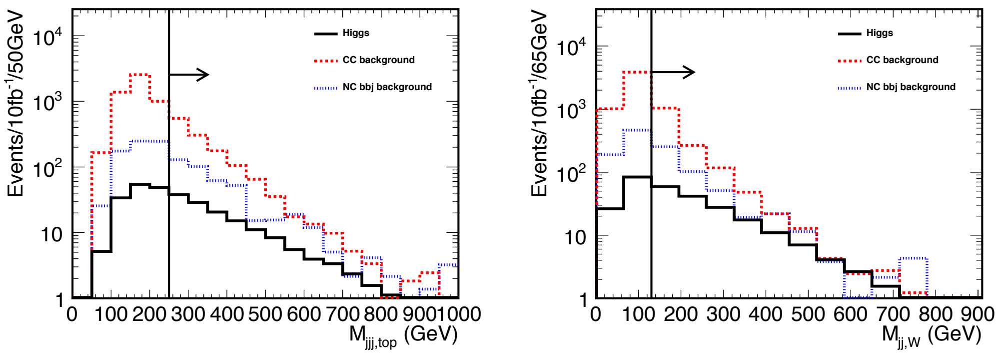

Figure 6.26: Three-jet (left) and di-jet (right) invariant masses. Solid (black), dashed (red) and dotted (blue) histograms show $H \to b\bar{b}$, CC and NC DIS background, respectively.

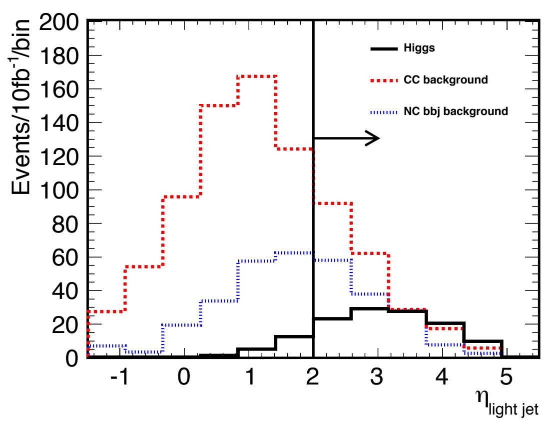

Figure 6.27: η_{jet} distribution for the lowest-η jet excluding the two b-tagged jets. Solid (black), dashed (red) and dotted (blue) histograms show $H \to b\bar{b}$, CC and NC DIS background, respectively.

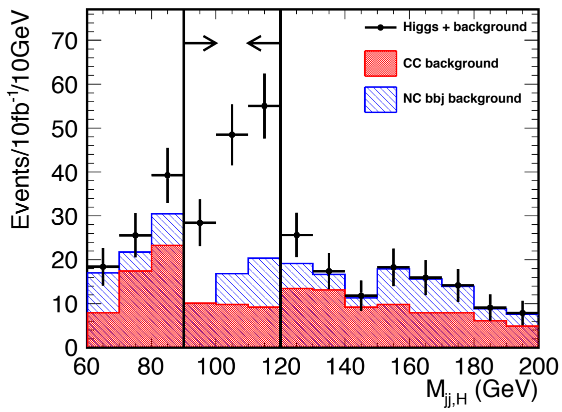

Figure 6.28: Reconstructed invariant Higgs mass after all selection criteria, except for the Higgs mass cut, have been applied. Points with error bars (black) show the $H \to b\bar{b}$ signal added to the CC (red histogram) and NC (hatched blue histogram) DIS background for an integrated luminosity of $10\,\mathrm{fb}^{-1}$.

$H \to b\bar{b}$ events are expected after the same cuts have been applied. Considering the CC and NC DIS background, S/N and $S/\sqrt{N}$ are 1.05 and 11.4, respectively.

	Higgs production	CC DIS	NC bbj	S/N	$S/\sqrt{N}$
cut (1)	816	123000	4630	6.38×10^{-3}	2.28
cut (1) + (2) + (3)	178	1620	179	9.92×10^{-2}	4.21
All cuts	84.6	29.1	18.3	1.79	12.3

Table 6.6: Expected $H \to b\bar{b}$ signal and background events with 150 GeV electron beam for an integrated luminosity of $10\,\mathrm{fb}^{-1}$. Contents of the cuts are listed in text.

Chapter 7

Physics at High Parton Densities

7.1 Physics at small x

7.1.1 Unitarity and QCD

Introduction

QCD [122] is the fundamental theory of the strong interaction that has been extensively tested in the last 37 years. Still, many open questions remain to be solved. One of them, which can be addressed at high energies, is the transition between the regimes in which the strong coupling constant is either large or small - the so-called *strong and weak coupling* regimes. In the former the standard perturbation theory techniques are not applicable and exact analytical results are not yet within the reach of current knowledge. Therefore various models, *effective* theories, whose parameters cannot yet be derived from QCD, or numerical lattice computations, have to be used. One example of such an effective theory which has been used through the years and actually predates QCD, is the Regge-Gribov [123–125] theory.

The weak coupling regime has been well tested in high-energy experiments through a selected class of measurements - often referred to as *hard processes* - where weak and strong coupling effects can be cleanly separated. There exists a well-defined theoretical concept which has been derived from first principles and probed in the weak coupling regime, namely the collinear factorization theorem (for a comprehensive review see [126] and references therein). It allows a separation of the cross sections involving hadrons into: (i) parts that can be computed within perturbation theory, corresponding to the cross section for parton scattering, and (ii) pieces which cannot be calculated using weak coupling techniques but its evolution is still perturbative. The latter are universal, process-independent distributions that either characterize the partonic content of the hadron - *parton densities* on which we will focus the discussion -, or the eventual projection of partons onto hadrons. Together with their corresponding linear evolution equations [127–129], they have been used to describe experimental data to high accuracy. Examples include the production of jets with large transverse momenta or final states with heavy quarks.

However, in recent years high-energy experiments have started measuring kinematical regions in which the coupling is small but the factorizaton assumption may no longer be valid. As an example, several HERA DIS measurements at small longitudinal momentum fractions

x where parton densities are large, indicate deviations from the behavior expected within the standard collinear factorization. Similarly, hadronic or nuclear collisions involving partons with small x may also show such deviations. At the same time, in these small-x regions the cross sections grow rapidly. Experiments sensitive to this kinematical region thus provide a way to test QCD in the new regime where the parton densities become very large. We will refer to this region as a high parton density domain.

From a theoretical viewpoint, this situation bears chances and challenges. The fact that, at small-x, there is no abrupt transition between the dilute and dense regimes, allows the use of techniques which, while still being weak coupling, go beyond those used in the dilute limit. The usual parton multiplication processes have to be supplemented by processes in which partons recombine - thus adding non-linear terms to the evolution equations [130]. There are deep theoretical arguments for this new dense partonic regime in QCD to become important as at high energies the scattering amplitudes are close to the unitarity limit, and therefore one expects that the growth of parton densities should be tamed by recombination effects - this phenomenon is generically referred to as *saturation*. Thus, in the weak coupling limit the physics responsible for the unitarity in QCD is expected to be describable in partonic language. Theoretical calculations [131–134] in high-energy QCD justify these generic expectations. Furthermore, the experimental exploration of this transition region where the standard perturbative description requires large corrections, provides new possibilities of further understanding the strong coupling regime where the cross sections are very large.

Deep inelastic lepton-hadron scattering has proven to address this question in the most efficient manner. It provides the cleanest way of measuring the parton densities, including the small-x region in which, as indicated above, the border between the dilute and dense regimes of QCD should occur within the weak coupling region where calculations can be done at present. Approaching this transition region from the dilute side by decreasing x or by increasing the target size, one should observe features which cannot be understood within the framework of linear QCD evolution equations but, using more elaborate tools (non-linear evolution equations) can still be analyzed in terms of weak coupling techniques. In fact, within the standard framework of the leading-twist linear QCD evolution equations (DGLAP) the parton densities are predicted to rise at small x, and this rise has been seen in HERA experiments. But unitarity prevents such a rise from continuing beyond any limits, leading to saturation of gluon densities. In hadron-hadron scattering it is unitarity which limits the growth of the total cross sections as a function of energy: according to Froissart and Martin [135, 136]

$$\sigma_{\rm tot} \leq {\rm const.} \ln^2 s/s_0 \; . \tag{7.1}$$

This bound comes from two fundamental assumptions. One is that the amplitude for the scattering at fixed value of the impact parameter is bounded by unity and the second assumption is about the finite range of the strong interactions. The bound on the amplitude has a simple physical interpretation that the probability of the interaction becomes very high, so the target (or more precisely the interaction region) is completely absorptive. This situation is usually referred to as a *black disk* regime. The description of this regime is very challenging theoretically and it is expected that new phenomena will occur which are direct manifestations of a new state in QCD which is characterized by a high parton density. The black disk regime can be achieved by two ways: either by increasing the energy of the collision, or by selecting heavier colliding particles. The LHeC will offer a unique possibility of exploring the new state of dense QCD matter as it can pursue a two-pronged approach: high center-of-mass energy and the possibility of deep inelastic scattering off heavy nuclei.

In the rest of this section we will present the different approaches that are currently under discussion to describe the high-energy regime of QCD. We will recall the ideas that lead from linear evolution equations to non-linear ones. On the former, we will discuss both cases in which the evolution equations are computed within fixed-order perturbation theory (the DGLAP evolution equations) and when they include some kind of resummation - thus going beyond any fixed order in the perturbative expansion in the QCD coupling constant - whose most famous example is the Balitsky-Fadin-Kuraev-Lipatov (BFKL) equation [137, 138]. Concerning the latter, non-linear evolution leads to the phenomenon of saturation of partonic densities in the hadron or nucleus. We will briefly review the realizations of saturation of partonic densities both at strong coupling and, mainly, at weak coupling. We will end by discussing the importance of diffractive observables and of the use of nuclear targets for the investigation of the small-x behavior of the hadron or nucleus wave function.

From DGLAP to non-linear evolution equations in QCD: saturation

In DIS the structure function $F_2(x, Q^2)$ is proportional to the total cross section $\sigma_{\rm tot}$ for the scattering of a virtual photon on a proton, $\gamma^* p \to X$. The growth of F_2 at small x translates into the rise of $\sigma_{\rm tot}$ as a function of the energy of the virtual photon-proton system. Although the Froissart-Martin bound, derived for hadron-hadron scattering, cannot be applied literally to the interaction involving a virtual photon, direct calculations based on the evaluation of the QCD diagrams demonstrate unambiguously that, at small x, large corrections exist and need to be resummed. These corrections suppress the leading-twist results and there is no doubt that, for F_2, the rise with $1/x$ predicted by DGLAP is modified by contributions which are not included in the framework of leading-twist linear evolution equations. As a complementary point of view, the linear evolution equations satisfy the set of unitarity conditions in an approximate way only. The corrections which become numerically important in the small-x limit are also important for the restoration of the unitarity bound. As a result of these modifications parton saturation is reached for sufficiently large energies or small values of Bjorken-x.

In deep inelastic electron-proton scattering, the virtual photon emitted by the incoming electron interacts with partons inside the proton whose properties are specified by the kinematics of the photon. In particular, the transverse size of the partons is (roughly) inversely proportional to the square root of the virtuality of the photon, $\langle r_T^2 \rangle \sim 1/Q^2$. The deep inelastic cross section, parametrized through parton densities (quarks and gluons) thus *counts* the number of partons per rapidity interval. For sufficiently large photon virtualities Q and not too small x, the improved QCD parton model works well because the partons forming the hadron, on the distance scale defined by the small photon, are in a dilute regime, and they interact only weakly. This is a direct consequence of the property of the asymptotic freedom which makes the strong coupling constant small. This diluteness condition is not satisfied if the density of partons increases. This happens if either the number of partons increases (large structure function) or the interaction between the partons becomes strong (large α_s). The former situation is realized at small x since the parton densities grow for small x, the latter for smaller photon virtuality Q^2 which sets the scale of the strong coupling $\alpha_s(Q^2)$. This simple qualitative argument shows that corrections to the standard QCD parton picture can be described in terms of quarks and gluons and their interactions as long as Q^2 is not too small ($\alpha_s(Q^2) \ll 1$) and the gluon density is large (small x). Combining these two conditions one arrives at the picture shown in Fig. 7.1: there is a line in the $\ln Q^2 - \ln 1/x$ plane below which the parton distributions are dilute, and the standard QCD parton picture applies. In this regime linear evolution equations

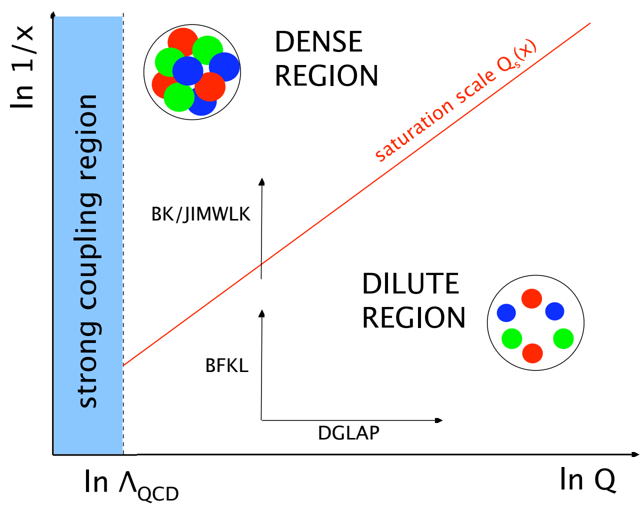

Figure 7.1: Schematic view of the different regions for the parton densities in the $\ln Q^2 - \ln 1/x$ plane. See the text for comments.

provide the correct description of parton dynamics. In the vicinity of the line, non-linear QCD corrections become important, and above the line partons are in a high-density state. Further away above the line, interactions become strong, and standard perturbation theory is not valid. The line which divides the two regimes is the saturation line which is specified by a dynamically generated saturation scale which grows with decreasing x. Within this picture one easily understands which type of corrections can be expected. Once the density of gluons increases, it becomes probable that, prior to their interaction with the photon, gluons undergo recombination processes.

Saturation in perturbative QCD

While unitarity is an unavoidable feature of any quantum field theory, the microscopic dynamics which leads to it in QCD is not very well understood, and it may be realized in different ways. There are several proposals to implement unitarity in strong interactions, which can be roughly classified into those which use non-perturbative models and those based on perturbative QCD calculations.

The usual non-perturbative framework to implement unitarity are Regge-Gribov based models [124, 139, 140]. Though they are quite successful in describing existing data on inclusive and diffractive ep and eA scattering (see e.g. [141, 142] and references therein), they lack theoretical foundations within QCD.

On the other hand, many attempts have been going on for the last 30 years to implement parton rescattering or recombination in perturbative QCD in order to describe its high-energy behavior - note that both concepts correspond to the same physical mechanism viewed in different frames, the rest frame and the infinite momentum frame of the hadron respectively. In the pioneering works in [130, 143], a non-linear evolution equation in $\ln Q^2$ was proposed to provide the first correction to the linear equations. A non-linear term appeared, which was proportional to the local density of color charges seen by the probe.

An alternative, independent approach was developed in [144], where the amplitudes for diffractive processes in the triple Regge limit were calculated. This resulted in the extraction of the triple Pomeron vertex in QCD at small x which is responsible for the nonlinear term in the evolution equations.

Later on these ideas were developed to include all corrections enhanced by the local density, to constitute what is called the Color Glass Condensate (CGC) [131–134, 145–152], see the most recent developments in [153–156]. The linear limit of the basic CGC equation is the BFKL equation, which is the linear evolution equation in the high-energy limit. As illustrated in Fig. 7.1, the evolution in the $\ln Q^2 - \ln 1/x$ plane driven by both linear equations, DGLAP and BFKL, is complementary: along $\ln Q^2$ for DGLAP and along $\ln 1/x$ for BFKL.

The basic framework in which saturation ideas are discussed is illustrated in Fig. 7.2. The CGC provides a non-perturbative, but weak-coupling, realization of the parton saturation ideas within QCD. One is considering the hadron wave function at high energy. Its partonic components can be separated into those with a large momentum fraction x (fast) and those with small x (slow). The fast components are dilute and provide color sources for the corresponding small-x components. Due to multiple splittings of the small-x gluons, a dense system is eventually formed. One can then construct within this formalism an evolution equation for the gluon correlators in the hadron wave function which is a renormalization group equation with respect to the rapidity separating fast and slow partons. This renormalization procedure assumes perturbative gluon emissions from the fast partons which imply a redefinition of the source at each step in rapidity.

Its mean field version, the Balitsky-Kovchegov (BK) equation [133, 134], provides a non-linear evolution equation for unintegrated gluon densities. It turns out that such approach results in a gluon density which, for a fixed resolution of the probe, is saturated for small longitudinal momentum fractions x. At large values of x, the non-linear term is a negligible contribution and partons are in a dilute regime. The separation is given by a dynamically generated saturation momentum $Q_s(x)$ which increases with decreasing x, and therefore saturation is determined by the condition $Q_s(x) > Q$. Then, for large energies or small x, the system is in a dense regime of high gluon fields (thus non-perturbative) but the typical gluon momentum, $\sim Q_s$, is large (thus the coupling constant which determines gluon interactions is weak). The qualitative behavior of the saturation scale with energy and nuclear size can be argued as follows: The transition from a dilute to a dense regime is marked by the packing factor (in this case, the product of the density of gluons per unit transverse area times the gluon-gluon cross section) becoming of the order unity i.e.

$$\frac{A \times xg(x, Q_s^2)}{\pi A^{2/3}} \times \frac{\alpha_s(Q_s^2)}{Q_s^2} \sim 1 \implies Q_s^2 \sim A^{1/3} Q_0^2 \left(\frac{1}{x}\right)^{\lambda}, \tag{7.2}$$

where the growth of the gluon density at small x has been approximated by a power law, $xg(x, Q^2) \sim x^{-\lambda}$, logarithms are neglected and the nucleus is simply considered a mere superposition of nucleons. The exponent $\lambda \simeq 0.3$ can be derived from QCD, whereas the scale Q_0^2 has to be taken from experiment.

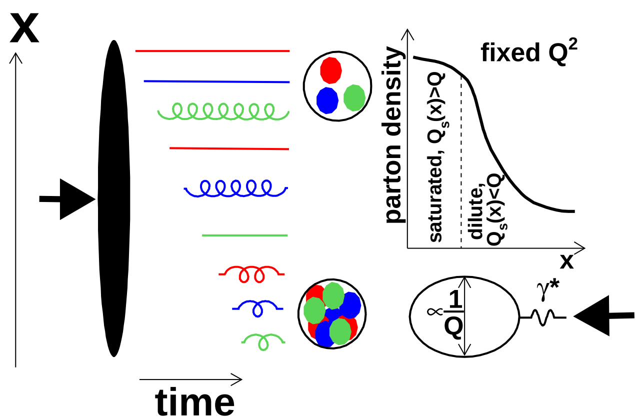

Figure 7.2: Illustration of the saturation ideas. The hadron is moving very fast to the right, and its wave function contains many partonic components. Apart from fast moving components it includes also slow moving partons which are characterized by the small fraction of its longitudinal momentum x. The photon with virtuality Q^2 is moving to the left and it constitutes a probe of the hadron wave function.

The BK equation was derived under several simplifying assumptions like scattering of a dilute projectile on a dense target, large number of colors and lack of correlations in the target. At present, the discussion is concentrated on how to overcome these difficulties [153,157,158]. Possible, yet unclear, phenomenological implications [159–161], are considered. Also, the proposed relation between high-energy QCD and Statistical Mechanics [157, 162] is investigated.

All approaches to saturation, point unambiguously to the effect of the high density of partons. For example, in the CGC formalism, the resummed terms are those enhanced by the energy and by the local density of partons, and the saturation scale depends on the matter (color charge) density at the impact parameter probed by the virtual photon. For a nucleus, the nuclear size plays the role of an enhancement factor, see Eq. (7.2), exactly in an analogous way. Therefore, it is expected that when scanning the impact parameter from the center to the periphery of the hadron, one should go from a nonlinear to a linear regime. Analogously, nonlinear effects will become more important for large nuclei than for smaller ones or for nucleons. Thus, a study of the variation of parton densities with impact parameter and with the nuclear size, will be a strong test of our ideas on parton saturation.

Resummation at low x

The generic challenges that the small-x region bears in QCD are inherently related to the divergence of the gluon number density with decreasing values of x. As is well known, deep-inelastic partonic cross sections and parton splitting functions receive large corrections in the small-x limit due to the presence of powers of $[\alpha_s \log x]$ to all orders in the perturbative expansion [127, 137, 138, 163, 164]. It thus suggests dramatic effects from logarithmically enhanced corrections, so the success of fixed order NLO perturbation theory at HERA has been for a long time very hard to explain. Only recently, it has been shown that indeed the DGLAP fits tend to deteriorate systematically in the region of small x and Q^2, [165]. Direct calculations at next-to-leading logarithmic accuracy in the BFKL framework were performed [166, 167], and showed a slow convergence of the perturbative series in the high-energy, or small-x regime. Therefore, generically one expects deviations from fixed-order DGLAP evolution in the small-x and small-Q regime which call for resummation of higher orders in perturbation theory.

Extensive analyses have been performed in the last several years [168–173], which indeed point to the importance of resummation to all orders. Resummation should embody important constraints like kinematic effects, momentum sum rules and running coupling effects.

Several important questions arise here such as the relation and interplay of the resummation and the non-linear effects, and possibly the role of resummation in the transition between the perturbative and non-perturbative regimes in QCD. Precise experimental measurements in extended kinematic regions are needed to explore the deviations from the standard DGLAP evolution and to quantify the role of resummation at small x.

The importance of diffraction

It was observed at HERA that a substantial fraction, about 10%, of the deep inelastic interactions are diffractive events i.e. events in which the interacting proton stays intact, despite the inelasticity of the interaction. Moreover, the proton appears well separated from the rest of the system observed in the detector by a large rapidity gap. The rest of the system looks similar to normal deep inelastic events. Therefore, the measurement of a large rapidity gap is the characteristic feature of diffractive DIS.

Diffraction has been extensively analyzed at HERA, with a variety of measurements in bins of x and Q^2, as well as more differential analyses which include the dependence on the momentum transfer t. Physically, for the diffractive event to occur, there must be an exchange of a coherent, color neutral cluster of partons (a quasiparticle) which leaves the interacting proton intact. This color neutral cluster is often called the *pomeron*, and it can be characterized [174] by a set of partonic densities analogous to those for the proton or nucleus.

There are strong theoretical indications that diffraction is closely linked with the phenomena of partonic saturation. From a wide range of calculations, mostly based on the so-called dipole model, see for example [175, 176], it is known that the diffractive DIS events involve softer scales than the non-diffractive events. Thus, the exploration of diffractive phenomena offers a unique window to analyze the transition between perturbative and non-perturbative dynamics in QCD.

LHeC will provide a widely extended kinematic coverage for diffractive events. By their study one could extract diffractive parton densities for a larger range in Q^2 than at HERA, and thus provide crucial tests of parton dynamics in diffraction as well as of the factorization theorems. The high energy involved also enables the production of diffractive states with large masses which could include W and Z bosons as well as states with heavy flavors or even exotic states with quantum numbers 1^-.

Of particular importance are the processes of exclusive diffractive production of vector mesons for which the differential measurement in momentum transfer is performed. It has been demonstrated that in this case the information about the momentum transfer of the cross section can be translated into the dependence of the scattering amplitude on impact parameter. As a result, a profile in impact parameter of the interaction region can be extracted. The precise determination of the dynamics of governing the high parton density regime requires a detailed picture of the spatial distribution of partons in the interaction region in impact parameter space. As mentioned previously, by selecting small impact parameter values one is probing the regions of higher parton density where the saturation phenomenon is more likely to occur. One can then extract the value of the saturation scale as a function of energy and impact parameter.

But even more inclusive measurements of diffractive production of vector mesons can provide valuable information about parton dynamics. For example, the measurement of the energy dependence of the diffractive cross section for the production of J/ψ at the LHeC can distinguish between different scenarios for parton evolution and thus explore parton saturation to a greater accuracy than ever before.

The importance of nuclei

In the context of small-x physics, studying lepton-nucleus collisions has a twofold importance:

- On the one hand and as discussed in Subsecs. 7.1.4 and 7.2.2, the nuclear structure functions and partons densities are basically unknown at small x. The main reason for this lack of knowledge comes from the rather small area in the $\ln Q^2 - \ln 1/x$ plane covered by presently available experimental data, see Fig. 7.3. Current theoretical and phenomenological analyses [177] point to the importance of the nonlinear dynamics in DIS off nuclei at small and moderate Q^2 and small x which needs to be tested experimentally. In this respect, a relation exists, as reviewed in Sec. 7.2.4, between diffraction in lepton-proton collisions and the small-x behavior of nuclear structure functions. Such relation relies on basic properties of Quantum Field Theory and its verification provides stringent tests of our understanding of these phenomena.

- Non-linear effects in the parton evolution are enhanced by increasing the density of partons. Such increase can be achieved in two different ways (see Fig. 7.4): either by increasing the energy of the collision (or equivalently decreasing the fractional momenta x of the explored partons), or by increasing the effective mass number A. The latter can be accomplished by either using very large nuclei or selecting subsets of nuclear collisions with more nucleons involved (i.e. more central collisions) through a decrease of the impact parameter between the nucleus and the virtual photon. This can be alternatively expressed through the dependence on x and A of the saturation scale which indicates the transition between the linear and nonlinear regimes, see Eq. (7.2). This is a key prediction of the formulations which resum multiple interactions and result in parton saturation. As such it must be checked in experiment in order to clearly settle the mechanism underlying non-linear parton dynamics.

Also, the study of lepton-nucleus collisions has strong implications on the understanding of the experimental data from ultrarelativistic nucleus-nucleus collisions, as discussed later in Subsec. 7.1.4.

7.1.2 Status following HERA data

As discussed in previous section, in the low-x region, a high parton density can be achieved in DIS and various novel phenomena are predicted. Ultimately, unitarity constraints become important and a 'black body' limit is approached [139], in which the cross section reaches the geometrical bound given by the transverse proton size. When α_s is small enough for

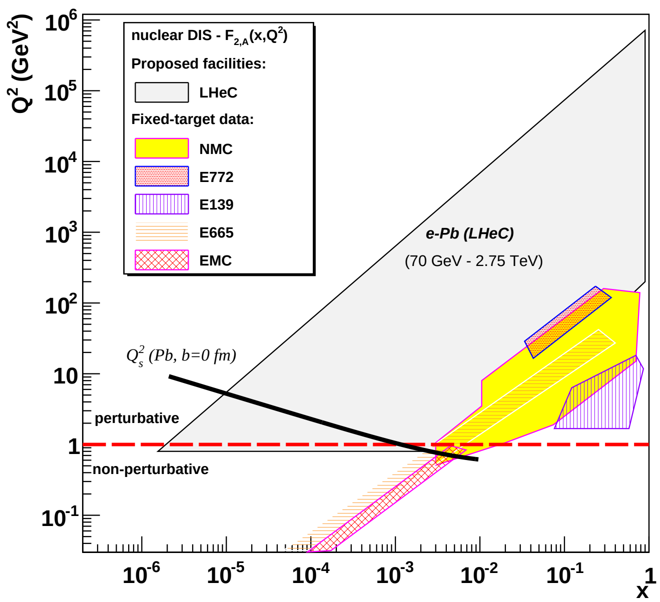

Figure 7.3: Kinematical coverage of the LHeC in the $\ln Q^2 - \ln 1/x$ plane for nuclear beams, compared to existing nuclear DIS and Drell-Yan experiments.

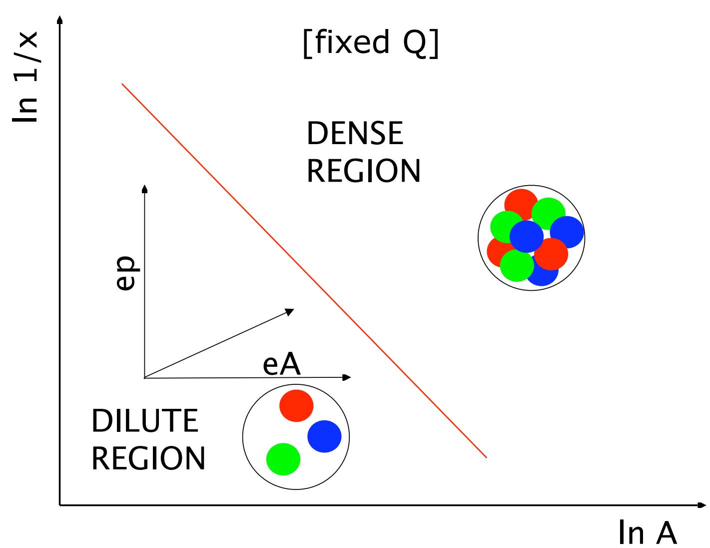

Figure 7.4: Schematic view of the different regions for the parton densities in the $\ln 1/x - \ln A$ plane, for fixed Q^2. See the text for comments.

quarks and gluons to be the right degrees of freedom, parton saturation effects are therefore expected to occur. In this small-x limit, many striking observable effects are predicted, such as Q^2 dependences of the cross sections which differ fundamentally from the usual logarithmic variations, and diffractive cross sections approaching 50% of the total [178]. This fairly good phenomenological understanding of the onset of unitarity effects is, unfortunately, not very quantitative. In particular, the precise location of the saturation scale line in the DIS kinematic plane (see Fig. 7.1) is to be determined experimentally. The search for parton saturation effects has been therefore a major issue throughout the lifetime of the HERA project.

Although no conclusive saturation signals have been observed in parton density fits to existing HERA data, various hints have been obtained. For example by studying the change in fit quality in the NNPDF framework as low-x and Q^2 data are progressively omitted [165] (see Subsec. 7.1.2).

A more common approach is to fit the data to dipole models [175, 176, 179, 180], which are applicable at very low Q^2 values, beyond the range in which quarks and gluons can be considered to be good degrees of freedom. The typical conclusion [180] is that HERA data in the perturbative regime exhibit at best weak evidence for saturation. However, when data in the $Q^2 < 1$ GeV^2 region are included, models which include saturation effects are quite successful in the description of the wide variety of experimental data.

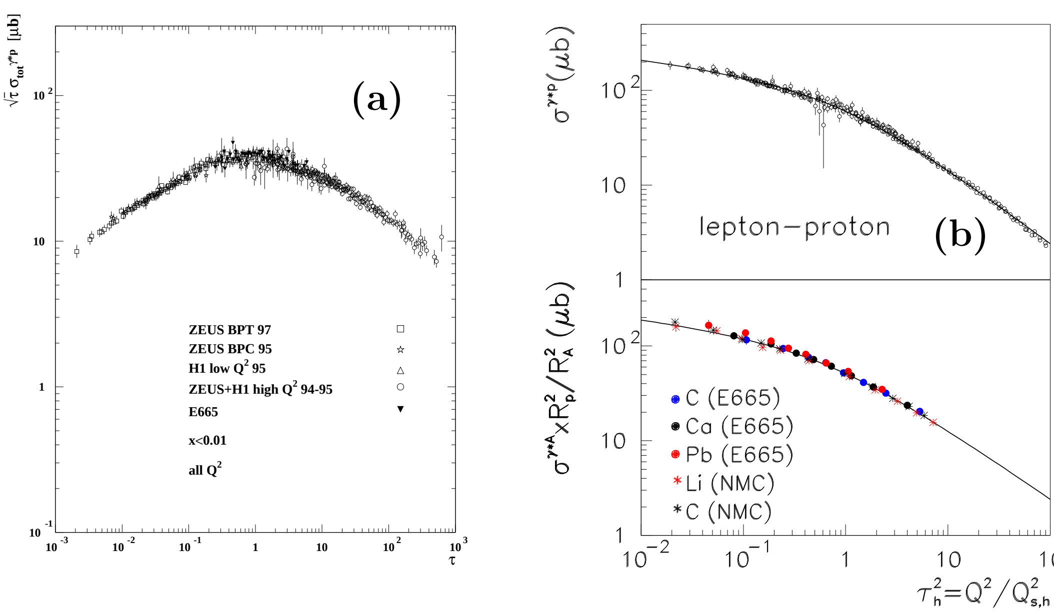

Figure 7.5: (a) Geometric scaling plot [181], in which low x data on $\gamma^* p$ cross section from HERA and E665 are plotted as a function of the dimensionless variable τ (see text). The cross sections are scaled by $\sqrt{\tau}$ for visibility. (b) Geometric scaling plot showing cross sections for electron scattering off nuclei as well as off protons [182].

The ‘geometric scaling’ [181] feature of the HERA data (Fig. 7.5a) reveals that, to a good approximation, the low-x cross section is a function of a single combined variable $\tau = Q^2/Q_s^2(x)$, where $Q_s^2 = Q_0^2\ x^{-\lambda}$ is the saturation scale, see Eq. (7.2). This parameterisation works well for scattering off both protons and ions, as shown in Fig. 7.5 [181, 182]. Geometric scaling is observed not only for the total $\gamma^* p$ cross section, but also for other, more exclusive observables in $\gamma^* p$ collisions [183] or even in hadron production in proton-proton collisions at the LHC [184] or nucleus-nucleus collisions at RHIC [182]. This feature supports the view (Sec. 7.1.1) of the cross section as being invariant along lines of constant 'gluon occupancy'. When viewed in detail (Fig. 7.5), there is a change in behaviour in the geometric scaling plot near $\tau = 1$, which has been interpreted as a transition to the saturation region shown in Fig. 7.1. However, data with $\tau < 1$ exist only at very low, non-perturbative, Q^2 values to date, precluding a partonic interpretation. Also, the fact that the scaling extends to large values of τ which is the dilute regime, prompted theoretical explanations of this phenomenon which do not invoke physics of saturation [185].

Dipole models

As mentioned previously, one of the interesting observations at HERA is the success of the description of many aspects of the experimental data within the framework of the so-called dipole picture [131, 186, 187] with models that include unitarization or saturation effects [188, 189]. These models are suited for the description of high-energy phenomena and they are based on the assumption that the relevant degrees of freedom at high energy are colour dipoles. The dipole models in DIS can be thought to be equivalent to the Good-Walker picture [190] previously developed for soft processes in hadron-hadron collisions. In high-energy DIS dipoles are shown to be the eigenstates of high-energy scattering in QCD, and the photon wave function can be expanded onto the dipole basis.

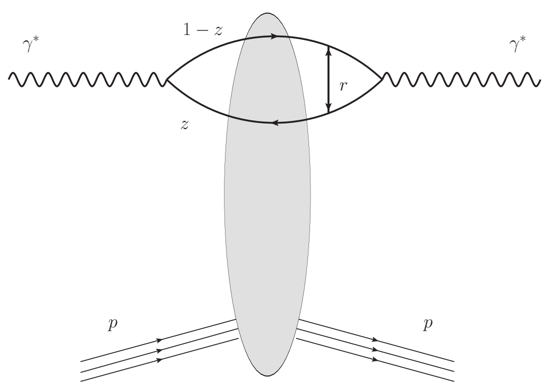

Figure 7.6: Schematic representation of the dipole factorization at small x in DIS. The virtual photon fluctuates into a quark-antiquark pair and subsequently interacts with the target. All the details of the dynamics of the interaction are encoded in the dipole scattering amplitude.

The dipole factorization for the inclusive cross section in DIS is illustrated in Fig. 7.6. It differs from the usual picture of the virtual photon probing the parton density of the target in a sense that the very partonic structure of the probed hadron here is not evident. Instead, one chooses a particular Lorentz frame where the photon fluctuates into a quark-antiquark pair with a transverse separation r and at impact parameter b with respect to the target. For sufficiently small $x \ll (2m_N R_h)^{-1}$, with m_N the nucleon mass and R_h the hadron or nuclear radius) the lifetime of the $q\bar{q}$ fluctuation is much longer than the typical time for interaction with the target. The interaction of the $q\bar{q}$ dipole with the hadron or nucleus is then described by the scattering matrix $S(r,b;x)$ such that $|S(r,b;x)| < 1$. The unitarity constraints can be incorporated naturally in this picture [191] by the requirement that $|S(r,b;x)| \geq 0$, with $S(r,b;x) = 0$ corresponding to the black disk limit. Integrating $1 - S(r,b;x)$ over the impact parameter b one obtains the dipole cross section $\sigma^{q\bar{q}}(r,x)$ which depends on the dipole size and the energy (through the dependence on $x = x_{\rm Bj}$ variable). The transverse size of the partons probed in this process is roughly proportional to the inverse of the virtuality of the photon Q^2. This statement is more accurate in the case of the longitudinally polarized photon, while in the case of the transversely polarized one, the distribution of the probed transverse sizes of dipoles is broadened due to the so-called aligned jet configurations.

At small values of the dipole size, such that $r \ll 1/Q$, the dipole cross section can be shown to be related to the integrated gluon distribution function

$$\sigma^{q\bar{q}}(r,x) \sim r^2 \, \alpha_s(C/r^2) \, xg(x, C/r^2) \;, \tag{7.3}$$

where C is a constant. In this regime, where r is small, the dipole cross section is small and consequently the amplitude is far away from the unitarity limits. With increasing energy the dipole cross section grows and saturation corrections must be taken into account in order to guarantee the unitarity bound on $S(r,b;x)$. The transition region between the two limits is characterized by the saturation scale $Q_s(x)$. Several models [175,179,192] were proposed up to date which successfully described the HERA data on the structure function F_2.

Once the dipole cross section has been constrained by the data on the inclusive structure functions, it can be used to predict, without almost any other additional parameters, the cross sections for diffractive production at small x. The inclusive diffraction has been computed within the dipole picture in [176], and the exclusive diffraction of the vector mesons in [193,194]. One of the interesting aspects of these models is that they automatically lead to the constant ratio of the diffractive to total cross sections as a function of the energy [176]. In the models with saturation it is related to the fact that the saturation scale provides a natural x-dependent cutoff and gives the same leading-twist behavior for inclusive and diffractive cross sections. As a result the ratio of inclusive to diffractive cross sections is almost constant as a function of the energy.

In spite of the fact that this approach has been able to successfully describe the inclusive data and predict the diffraction at small values of x, there are still important conceptual progresses to be made. Certainly there are important hints from dipole models about the nature of the perturbative–non-perturbative transition in QCD. Nevertheless, dipole models should be rather regarded as effective phenomenological approaches. As such they only parametrize the essential dynamics at small x. For instance, the transverse impact parameter dependence of the dipole scattering amplitude $S(r,b;x)$ is very poorly constrained. Indeed, one has been able to describe F_2 and correctly predict F_2^D with two rather different impact parameter dependences. On the theoretical side, it has not been possible so far to successfully predict the realistic profile of the interaction region in the transverse size. It is therefore of vital importance to measure accurately the t-dependencies of the diffractive cross sections in an extended kinematics to pin down the impact parameter distribution of the proton at high energies.

Deviations from fixed order linear DGLAP evolution in inclusive HERA data

HERA provided extremely valuable information about the proton structure functions based on the measurement of the virtual photon-proton cross section. As discussed in previous sections, the experimental data on the inclusive structure function F_2 have been successfully described by the fits which use the linear fixed order DGLAP evolution, see [19,21,195–200]. The current status of the calculations is fixed order at next-to-next-to-leading accuracy.

There are several theoretical indications that at small x and/or at small Q^2 the NLO DGLAP framework needs to be extended, since in these regimes perturbative QCD predicts other relevant effects: linear small-x resummation, non-linear evolution and parton saturation or other higher-twist effects. Even if it is unclear in which kinematical regime these effects should become relevant, it is evident that at some point they will lead to deviations from fixed-order DGLAP evolution. Therefore, the important question which needs to be answered from the phenomenological point of view is whether need of these deviations is already present in HERA data or not. Several analyses have been performed which aimed to address the question of the evidence of the saturation effects in the inclusive observables at HERA.

In one analysis [180], the inclusive structure function $F_2(x, Q^2)$ is subjected to fits in which the dipole cross section either does not exhibit saturation properties, or saturates as expected in two rather different models [179,180]. All three dipole fits are able to describe the HERA data adequately in the perturbative region $Q^2 \geq 2$ GeV^2, whereas a clear preference for the models containing saturation effects becomes evident when data in the range $0.045 < Q^2 < 1$ GeV^2 are added [180]. Due to the nonperturbative nature of this kinematic region, there is no clear interpretation in terms of parton recombination effects. Similar conclusions are drawn when the same dipole cross sections are applied to various less inclusive observables at HERA [201].

In another analysis, Ref. [165], possible indications of the deviation from the linear DGLAP evolution were discussed. It was based on an unbiased PDF analysis of the inclusive HERA data. Below, we discuss briefly the updated version of this study which uses the most precise experimental inclusive DIS data up-to-date, the combined HERA–I dataset [202].

Deviations from DGLAP evolution can be investigated exploiting the more discriminating and sensitive framework of global PDF fits. The key idea in this kind of analysis is to perform global fits only in the large-x, large-Q^2 region, where NLO DGLAP is expected to be reliable. This way one can determine *safe* parton distributions which are not contaminated by possible non-DGLAP effects. These PDFs are then evolved backwards into the potentially *unsafe* low-x and low-Q^2 kinematic region, and used to compute physical observables, which are compared with data. A deviation between the predicted and observed behavior in this region can then provide a signal for effects beyond NLO DGLAP.

The analysis of Ref. [165] was based on the NNPDF1.2 analysis [203] and later on it was extended to the global NNPDF2.0 set, which includes the very precise combined HERA dataset as well as all relevant hadronic data. The crucial point was to define a *safe* region, where non-DGLAP effects are expected to be negligible. In this analysis, PDFs were determined within the *safe* kinematic region in which

$$Q^2 \geq A_{\mathrm{cut}} \cdot x^{-\lambda}, \tag{7.4}$$

with $\lambda = 0.3$ and varying A_{cut}. To be precise, only data were fitted which passed the cut Eq. (7.4) (see the left plot in Fig. 7.7). The above definition is theoretically appealing, since it has the same effective form of a saturation scale, and it is also very practical, since it does not remove moderate-Q^2, large-x data which are expected to be fully consistent with DGLAP and which are very important to constrain PDFs.

The NNPDF2.0 analysis [204] was repeated for different choices of the kinematical cuts, one for each A_{cut}, and compared the results obtained from them with experimental data. If one computes the proton structure function F_2 and compared them with data, both at a higher

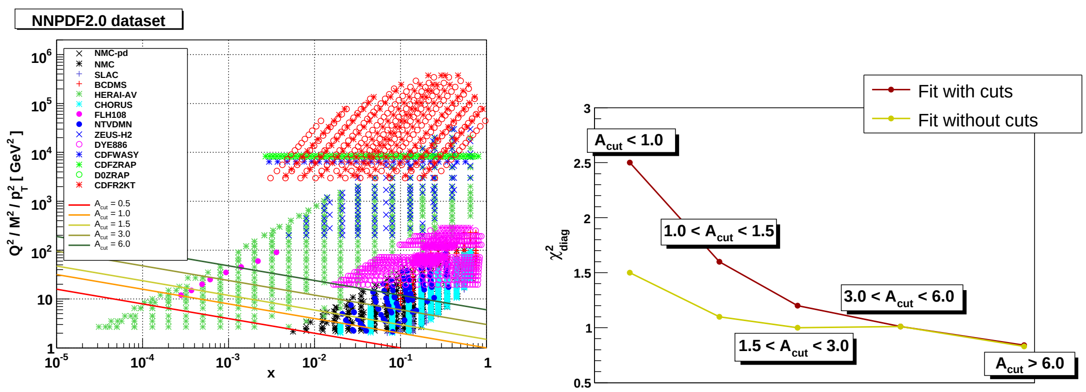

Figure 7.7: Left plot: the kinematical coverage of the data used in the NNPDF2.0 analysis with the different regions in $A_{\rm cut}$ used to probe deviations from DGLAP. Right plot: the diagonal $\chi^2_{\rm diag}$ computed in the different kinematic slices in $A_{\rm cut}$, where $\chi^2_{\rm diag}$ has been computed using both the reference NNPDF2.0 fit without kinematical cuts (yellow line) and the NNPDF2.0 with the maximum $A_{\rm cut} = 1.5$ cut (red line).

$Q^2 = 15$ GeV^2 and at a lower $Q^2 = 3.5$ GeV^2 scale (Fig. 7.8), it is clear that at a higher $Q^2 = 15$ GeV^2 scale one does not see any significant deviation from NLO DGLAP. In this region all PDF sets agree with data, and among each other. The only difference between different sets is that as $A_{\rm cut}$ increases the PDFs errors grow larger, as it is statistically expected due to the missing experimental information removed by the cuts. Situation is different at low $Q^2 = 3.5$ GeV^2 scale: the prediction obtained from the back-evolution of the data above the cut exhibits a systematic downward trend. This trend, becomes more and more evident as we raise $A_{\rm cut}$. It is thus apparent that, at low-x, low-Q^2, NLO DGLAP evolution fails to provide an accurate description of the data. More precisely, one observes that NLO DGLAP evolves faster with Q^2 than actual data.

To be sure that what one is observing is a genuine small-x effect, one needs to check that it becomes less and less relevant as x and Q^2 increase. To this aim the diagonal χ^2 was computed in different kinematic slices, both from the fit without cuts and from the one with the maximum cut $A_{\rm cut} = 1.5$. The expectation is that at larger x and Q^2 the difference between the two fits becomes smaller, as deviations from NLO DGLAP should become irrelevant. This is exactly what happens, as one can see from the right plot in Fig. 7.7: starting from $A_{\rm cut} \gtrsim 4$ the statistical features of the two fits are comparable.

In summary, there is at present rather strong evidence that the low-Q^2–low-x region covered by HERA is incompatible with fixed-order linear evolution. In particular, deviations from fixed order NLO DGLAP have been found in the combined HERA–I dataset from an unbiased global PDF analysis [205]. Similar conclusions have been reached in other independent studies like, for example, the HERAPDF analysis [202] which confirms that the fit quality in the low Q^2 region gets systematically worse when these data are not included in the fit. Also, the fit quality to the small-Q^2 data at NNLO is actually worse than at NLO [199] in agreement with the claims in Ref. [165] that these deviations are consistent with either expectations from small-x resummations or saturation models, though not from NNLO. Still, it should be noted that there is no general consensus [206]. It is clear that this method should be used to analyze LHeC

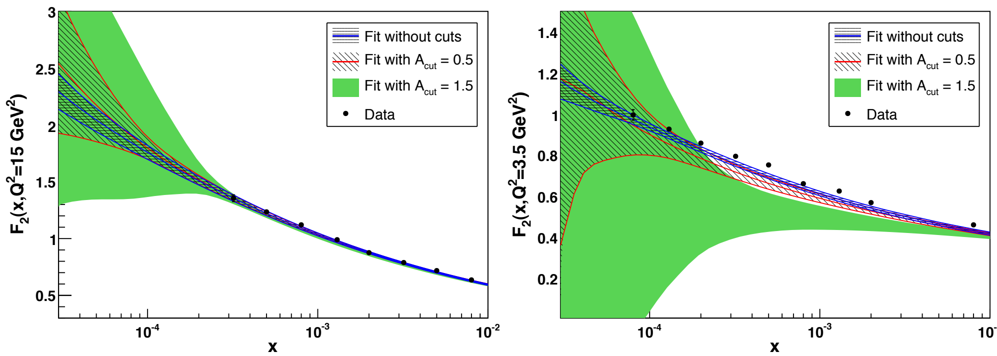

Figure 7.8: Left: the proton structure function $F_2(x, Q^2 = 15\ \mathrm{GeV}^2)$ at small-x, computed from PDFs obtained from the NNPDF2.0 fits with different values of A_{cut}. Right: the same but at a lower $Q^2 = 3.5\ \mathrm{GeV}^2$ scale.

inclusive structure function data, and would allow a detailed characterization of the new high-energy QCD dynamics unveiled by the LHeC. The novel phenomenon should be established cleanly in the high Q^2 perturbative region where it can be understood in terms of parton degrees of freedom. This can be only achieved by analyzing DIS at lower x values than are accessible at HERA i.e. at higher center-of-mass energy $\sqrt{s}$.

Linear resummation schemes

The deviations from DGLAP evolution could be caused by higher order effects at small x and small Q which need to be resummed to all orders of perturbation theory. As mentioned previously, the problem of resummation at small x has been extensively studied in the last years, see for example [168–173]. It has been demonstrated that the small-x resummation framework accounts for running coupling effects, kinematic constraints, gluon exchange symmetry and other physical constraints. The results were shown to be very robust with respect to scale changes and different resummation schemes. As a result, the effect of the resummation of terms which are enhanced at small x is perceptible but moderate - comparable in size to typical NNLO fixed order corrections in the HERA region.

A major development for high–energy resummation was presented in Ref. [170] where the full small-x resummation of deep-inelastic scattering (DIS) anomalous dimensions and coefficient functions was obtained including quark contribution. This allowed for the first time a consistent small-x resummation of DIS structure functions. These results are summarized in Fig. 7.9, taken from Ref. [170], where the K-factors for F_2 and F_L for the resummed results as compared. As is evident from this figure, the resummation is quite important in the region of low x and for a wide range of Q^2 values. One observes, for example, that the fixed order NNLO contribution leads to an enhancement of F_2 with respect to the NLO, whereas the resummed calculation leads to a suppression. This means that a truncation at any fixed order is very likely to be insufficient for the description of the LHeC data and therefore fixed order perturbative expansion becomes unreliable in the low x region, which calls for the resummation. Furthermore, the resummation of hard partonic cross sections has been performed for several LHC processes such as heavy quark production [207], Higgs production [208, 209], Drell-Yan [210, 211] and prompt photon production [212, 213].

We refer to the recent review in Ref. [214] as well as to the HERA-LHC workshop proceedings [215] for a more detailed summary of recent theoretical developments in high–energy resummation.

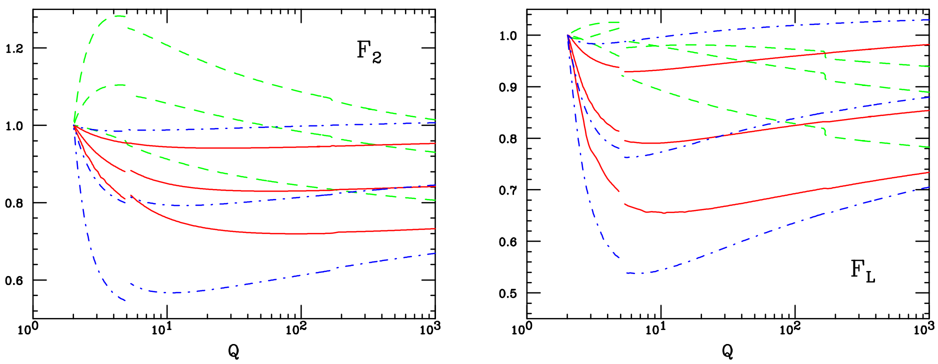

Figure 7.9: The K-factors, defined as the ratio of the fixed order NNLO or resummed to the NLO fixed order results for the singlet F_2 and F_L structure functions, with F_2 and F_L kept fixed for all x at $Q_0 = 2$ GeV. Results are shown at fixed $x = 10^{-2}$, 10^{-4} or 10^{-6} as function of Q in the range $Q = 2 - 1000$ GeV with α_s running and n_f varied in a zero–mass variable flavour number scheme. The breaks in the curves correspond to the b and t quark thresholds. The curves are: fixed order perturbation theory NNLO (green, dashed); resummed NLO in $\mathrm{Q_0\overline{MS}}$ scheme (red, solid), resummed NLO in the $\overline{\mathrm{MS}}$ scheme (blue, dot-dashed). Curves with decreasing x correspond to those going from bottom to top for NNLO and from top to bottom in the resummed cases.

To summarize, small-x resummation is becoming a very important component for precision LHC physics, and will become a crucial ingredient of the LHeC small-x physics program [216, 217]. The LHeC extended kinematical range will allow to enhance the differences between the resummed predictions with respect to the fixed order DGLAP calculation.

7.1.3 Low-x physics perspectives at the LHC

The low-x regime of QCD can be also analyzed in hadron and nucleus collisions at the LHC. The experimentally accessible values of x range from about $x \sim 10^{-3}$ to about $x \sim 10^{-6}$ for central and forward rapidities respectively. The estimates for the corresponding saturation scale, based on Eq. (7.2), result in $Q_s^2 \approx 1$ GeV^2 for proton and $Q_s^2 \approx 5$ GeV^2 lead collisions.

The significant increase in the center-of-mass energy and the excellent rapidity coverage of the LHC detectors will allow one to extend the kinematical reach in the x–Q^2 plane by orders of magnitude compared to previous measurements at fixed-target and collider energies (see Fig. 7.10). Such measurements are particularly important in the nuclear case since, due to the scarcity of nuclear DIS data, the gluon PDF in the nucleus is virtually unknown at fractional momenta below $x \approx 10^{-2}$ [218]. In addition, due to the dependence of the saturation scale on the hadron transverse size, nonlinear QCD phenomena are expected to play a central role in the phenomenology of collisions involving nuclei. We succinctly review here the experimental possibilities to study saturation physics in p-p, p-A and A-A collisions at the LHC.

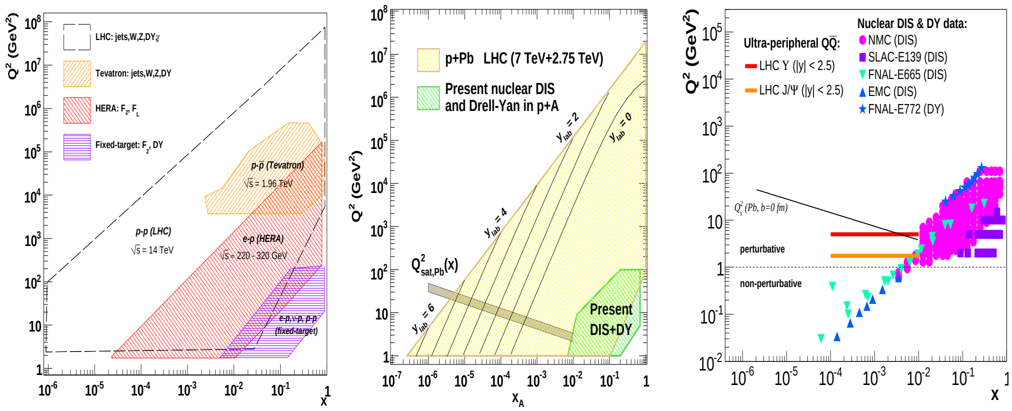

Figure 7.10: Kinematical reaches in the (x, Q^2) plane covered in proton-proton (left), proton-nucleus (center) [219] and ultraperipheral nucleus-nucleus (right) [220] collisions at the LHC. Also shown are the regions studied so far in deep-inelastic (nuclear) collisions, and in hadronic (nuclear) collisions at collider and fixed-target energies included in global fits of (nuclear) PDFs. Estimates of the saturation scale for lead are also shown.

Low-x studies in proton-proton collisions

The LHC experiments feature unique detection capabilities at forward rapidities ($|\eta| \gtrsim 3$), which will allow to measure various perturbative processes sensitive to the underlying parton structure and its dynamical evolution in the proton. The *minimum* parton momentum fractions probed in a $2 \to 2$ process with a particle of momentum p_T produced at pseudo-rapidity η is

$$x_{min} = \frac{x_T\, e^{-\eta}}{2 - x_T\, e^{\eta}} \quad , \quad \text{where} \quad x_T = 2p_T/\sqrt{s}\,, \tag{7.5}$$

i.e. x_{min} decreases by a factor of $\sim$10 every 2 units of rapidity. The extra e^{η} lever-arm motivates the interest of *forward* particle production measurements to study the PDFs at small values of x. From Eq. (7.5) it follows that, the measurement at the LHC of particles with transverse momentum $p_T = 10$ GeV/c at rapidities $\eta \approx 5$ allows to probe x values as low as $x \approx 10^{-5}$ (Fig. 7.10, left). Various experimental measurements have been proposed at forward rapidities at the LHC to constrain the low-x PDFs in the proton and to look for possible evidences of non-linear QCD effects such as: forward jets and Mueller-Navelet dijets in ATLAS and CMS [221]; and forward isolated photons [222] and Drell-Yan (DY) [223] in LHCb.

Low-x studies in proton-nucleus collisions

Proton-nucleus collisions will be, before an electron-ion collider, the best available tool at hand to study small-x physics in a nuclear environment without the complications from a strongly-interacting final-state medium as in the A-A case. Though proton-nucleus collisions are not yet scheduled at the LHC, detailed feasibility studies exist [224] and strategies to define the accessible physics programme are being developed [219]. The p-A programme at the LHC serves a dual purpose [219]: to provide "cold QCD matter" benchmark measurements for the physics measurements of the A-A programme without significant final-state effects, and to study the nuclear wavefunction in the small-x region. In Fig. 7.10 (center) we show how dramatically the LHC will extend the region of phase space in (x, Q^2) plane[1] by orders of magnitude compared to those studied at present. The same figure also shows the scarcity of nuclear DIS and DY measurements and, correspondingly, the lack of knowledge of nuclear PDFs in regions needed to perform calculations for the A-A programme – there is almost no information at present in the region $x \lesssim 10^{-2}$ [218].

Nuclear PDF constraints, checks of factorization (universality of PDFs) and searches for saturation of partonic densities will be performed in p-A collisions at the LHC by studying different production cross sections for e.g. inclusive light hadrons [225], heavy-flavor [226], isolated photons [227], electroweak bosons [228] and jets. Additional opportunities also appear in the so-called ultra-peripheral collisions in which the coherent electromagnetic field created by the proton or the large nuclei effectively acts as one of the colliding particles with γ-induced collisions at c.m. energies higher than those reached at the HERA collider [229] (see next).

At this point it is worth mentioning that particle production in the forward (proton) rapidity region in dAu collisions at RHIC shows features suggestive of saturation effects, although no consensus has been reached so far, see [230–234] and references therein. The measurements at RHIC suffer from the limitation of working at the edge of available phase space in order to study the small-x region in the nuclear wave function. This limitation will be overcome by the much larger available phase space at the LHC.

Low-x studies in nucleus-nucleus collisions

Heavy-ion (A-A) collisions at the LHC aim at exploration of collective partonic behaviour both in the initial wavefunction of the nuclei as well as in the final produced matter. The latter one is eventually forming a hot and dense QCD medium (see the discussions in Subsection 7.1.4). The nuclear PDFs at small x define the number of parton scattering centers and thus the initial conditions of the system which then thermalizes. Global properties of the collision such as the total multiplicities or the existence of long-range rapidity structures (seen in AuAu collisions at RHIC [235] and in pp collisions at the LHC [236]) are sensitive to the saturation momentum which at the LHC is expected to be well in the weak-coupling regime [237], $Q^2_{\mathrm{sat,Pb}} \approx 5 - 10$ GeV^2. CGC predictions for charged hadron multiplicities in central Pb-Pb at 5.5 TeV per nucleon are $dN_{ch}/d\eta|_{\eta=0} \approx$ 1500–2000 [238]. (Note that the predictions done before the start of RHIC in 2000 were 3 times higher). Recent data from ALICE [239] give $dN_{ch}/d\eta|_{\eta=0} \approx 1600$ in central Pb-Pb at 2.76 TeV per nucleon, in rough agreement with CGC expectations. In addition, particles which do not interact strongly with the surrounding medium such as photons [240] or electroweak bosons [228] provide direct information on the nuclear parton distribution functions.

Arguably, one of the cleanest ways to study the low-x structure of the Pb nucleus at the LHC is via ultra-peripheral collisions (UPCs) [229] in which the strong electromagnetic fields (the equivalent flux of quasi-real photons) generated by the colliding nuclei can be used for photoproduction studies at maximum energies $\sqrt{s_{\gamma N}} \approx 1$ TeV, that is 3–4 times larger than at HERA. In particular, exclusive quarkonia photoproduction offers an attractive opportunity

[1] Asymmetric colliding systems imply a rapidity shift in the two-in-one magnet design of the LHC. This shift has been taken into account in the figure: the quoted y values are those in the laboratory frame.

to constrain the low-x gluon density at moderate virtualities, since in such processes the gluon couples *directly* to the c or b quarks and the cross section is proportional to the gluon density *squared*. The mass of the $Q\bar{Q}$ vector meson introduces a relatively large scale, amenable to a perturbative QCD treatment. In $\gamma\mathrm{A} \rightarrow J/\psi\,(\Upsilon)\,\mathrm{A}^{(*)}$ processes at the LHC, the gluon distribution can be probed at values as low as $x = M_V^2/W_{\gamma\mathrm{A}}^2 e^y \approx 10^{-4}$ (Fig. 7.10 right). Full simulation studies [220, 241] of quarkonia photoproduction tagged with very-forward neutrons, show that ALICE and CMS can carry out detailed p_T,η measurements in the dielectron and dimuon decay channels.

7.1.4 Nuclear targets

As discussed in Subsection 7.1.1, the use of nuclei offers an additional possibility for modifying the partonic density through colliding different nuclear species or varying the impact parameter of the collision. Therefore, the study of DIS on nuclear targets is of uttermost importance for our understanding of the dynamics which controls the behaviour of hadron and nuclear wave functions at small x. On the other hand, the characterization of partonic densities inside nuclei and the study of other aspects of lepton-nucleus collisions like particle production, are of strong interest both fundamentally and because they are crucial for a correct interpretation of the experimental results from ultrarelativistic ion-ion collisions. In the rest of this section we focus on these last two aspects.

Comparing nuclear parton density functions

The nuclear modification of structure functions has been extensively studied since the early 70's [242, 243]. Such modification is usually characterized through the so-called nuclear modification factor which, for a given structure function or parton density f, reads

$$R_f^A(x, Q^2) = \frac{f^A(x, Q^2)}{A \times f^N(x, Q^2)} \, . \tag{7.6}$$

In this equation, the superscript A refers to a nucleus of mass number A, while N denotes the nucleon (either a proton or a neutron, or deuterium as their average). The absence of nuclear effects would result in $R = 1$.

Apart from possible isospin effects, the nuclear modification factor for F_2 shows a rich structure: an enhancement ($R > 1$) at large $x > 0.8$, a suppression ($R < 1$) for $0.3 < x < 0.8$, an enhancement for $0.1 < x < 0.3$, and a suppression for $x < 0.1$ where isospin effects can be neglected. The latter effect is called shadowing [177], and is the dominant phenomenon at high energies (the kinematical region $x < 0.1$ will determine particle production at the LHC, see Sec. 7.1.3 and [244]).

The modifications in each region are believed to be of different dynamical origin. In the case of shadowing, the explanation is usually given in terms of a coherent interaction involving several nucleons which reduces the nuclear cross section from the totally incoherent situation, $R = 1$, towards a region of total coherence. In the region of very small x, small-to-moderate Q^2 and for large nuclei, the unitarity limit of the nuclear scattering amplitudes is expected to be approached and some mechanism of unitarization like multiple scattering should come into work. Therefore, in this region nuclear shadowing is closely related to the onset of the unitarity limit in QCD and the transition from coherent scattering of the probe off a single parton to coherent scattering off many partons. The different dynamical mechanisms proposed to deal with this problem should offer a quantitative explanation for shadowing, with the nuclear size playing the role of a density parameter in the way discussed in Subsection 7.1.1.

At large enough Q^2 the generic expectation is that the parton system becomes dilute and the usual leading-twist linear DGLAP evolution equations should be applicable. In this framework, global analyses of nuclear parton densities (in exact analogy to those of proton and neutron parton densities) have been developed up to NLO accuracy [218, 245, 246]. In these global analyses, the initial conditions for DGLAP evolution are parametrized by flexible functional forms but they lack theoretical motivation. These should include the dynamical mechanisms for unitarization mentioned above. All these analyses [218,245,246] include data from NC DIS and DY experiments, and [218] also from particle production at mid-rapidity in deuterium-nucleus collisions at RHIC. Error sets obtained through the Hessian method are provided in [218]. CC DIS data have been considered only recently [247, 248][2] in this context.

On the other hand, the relation between diffraction and nuclear shadowing [139, 140] has been employed to provide initial conditions for the DGLAP evolution which is performed at LO [142] and NLO [249][3] accuracy.

Results of the different analyses performed at NLO accuracy are shown in Fig. 7.11, with the band indicating the uncertainty obtained using the error sets in [218]. Apart from the discrepancies concerning the existence of an enhancement/suppression at large x, at small x the different approaches show clear differences both in magnitude and in shape, even if they could be considered as marginally compatible one each other within the large uncertainty band shown. With nuclear effects dying logarithmically in the DGLAP analysis, the corresponding differences and uncertainties diminish, although they remain sizable until rather large Q^2.

Note that, such uncertainties are due to the lack of experimental data on nuclear structure functions for $Q^2 > 2$ GeV^2 and x smaller than a few times 10^{-2}, and - in common with the case of the proton - due to the lack of constraints on the gluon, particularly at small x. Particle production data at mid-rapidity coming from deuterium-nucleus collisions at RHIC offer an indirect constraint on the small-x sea and glue [218], but these data are bound to contain sizable uncertainties intrinsic to particle production in hadronic collisions. Therefore, only high-accuracy data on nuclear structure functions at smaller x and with a large lever arm in Q^2, as those achievable at the LHeC, will be able to substantially reduce the uncertainties and clearly distinguish between the different approaches.

Importance of LHeC measurements to ultra-relativistic heavy ion programs at RHIC and the LHC

The LHeC will offer most valuable information on several aspects of high-energy hadronic and nuclear collisions. On the one hand, it will characterize hard scattering processes in nuclei through a precise determination of initial parton kinematics. On the other hand, it will provide quantitative constraints on theoretical descriptions of initial particle production in ultra-relativistic nucleus-nucleus collisions and the subsequent evolution into the quark-gluon plasma, the deconfined partonic state of matter whose production and study offers key information about confinement. Such knowledge will complement that coming from pA collisions and self-calibrating hard probes in nucleus-nucleus collisions (see [219, 240, 244, 251, 252]) re-

[2]The analysis in [248] shows the compatibility of the nuclear corrections as extracted in [218] with CC DIS data on nuclear targets, while in [247] some tension is found between NC and CC DIS data.

[3]In the approach in [249] predictions are provided only for sea quarks and gluons, with the valence taken from the analysis in [250].

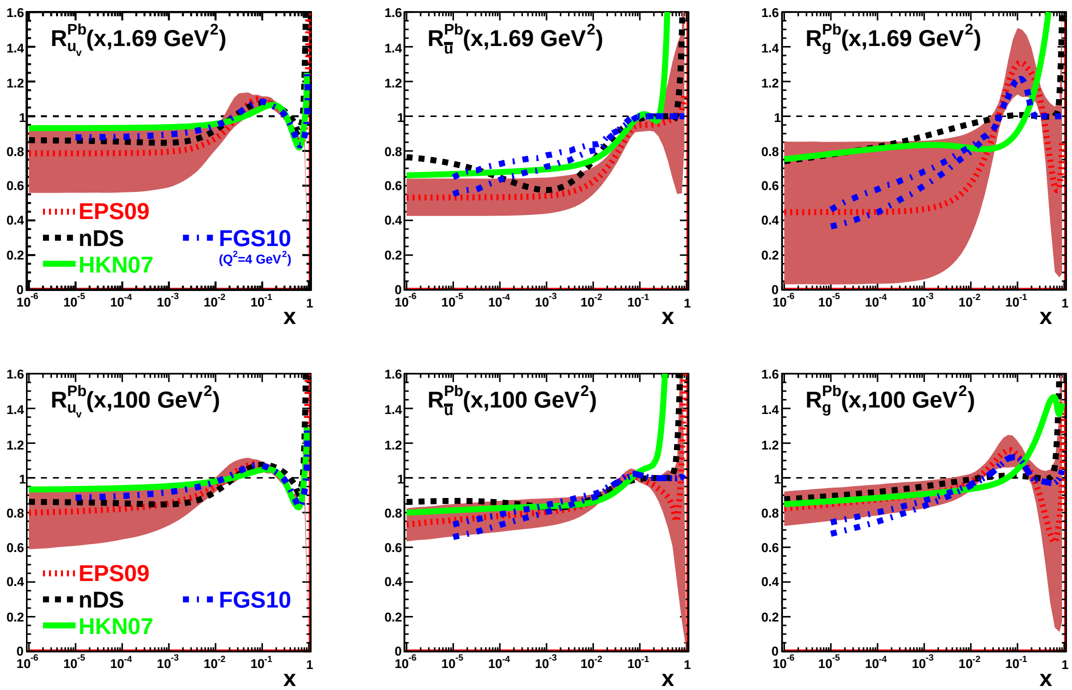

Figure 7.11: Ratio of parton densities in a bound proton in Pb over those in a free proton, for valence u (left), $\bar{u}$ (middle) and g (right), at $Q^2 = 1.69$ (top) and 100 (bottom) GeV^2. Results from [245] (nDS, black dashed), [246] (HKN07, green solid), [218] (EPS09, red dotted) and [249] (FGS10, blue dashed-dotted; in this case the lowest Q^2 is 4 GeV^2 and two lines are drawn reflecting the uncertainty in the predictions) are shown. The red band indicates in each case the uncertainties in the EPS09 analysis [218].

garding the correct interpretation of the findings of the heavy-ion programme at RHIC (see e.g. [253, 254] and refs. therein) and at the LHC. Beyond the qualitative interpretation of such findings, the LHeC will greatly improve the quantitative characterization of the properties of QCD extracted from such studies. The relevant information can be classified into three items:

a. Parton densities inside nuclei:

The knowledge of parton densities inside nuclei is an essential piece of information for the analysis of the medium created in ultra-relativistic heavy-ion collisions using hard probes i.e. those observables whose yield in nucleon-nucleon collisions can be predicted in pQCD (see [240, 244, 251, 252]). The comparison between the expectation from a incoherent superposition of nucleon-nucleon collisions and the measurement in nucleus-nucleus characterizes the nuclear effects. But we need to disentangle those effects which originate from the creation of a hot medium in nucleus-nucleus collisions, from effects arising only from differences in the partonic content between nucleons and nuclei.

Our present knowledge of parton densities inside nuclei is clearly insufficient in the kinematical regions of interest for RHIC and, above all, for the LHC (see [244] and Subsection 7.1.3). Such ignorance reflects in uncertainties larger than a factor $3-4$ for the calculation of different cross sections in nucleus-nucleus collisions at the LHC (see Fig. 7.11 and [225]), thus weakening strongly the possibility of extracting quantitative characteristics of the produced hot medium. While the pA program at the LHC will offer new constraints on the nuclear parton densities (e.g. [219, 225]), the measurements at the LHeC would be far more constraining and reduce the uncertainties in nucleus-nucleus cross sections to less than a factor two.

b. Parton production and initial conditions for a heavy-ion collision:

The medium produced in ultra-relativistic heavy-ion collisions develops very early a collective behavior, usually considered as that of a thermalized medium and describable by relativistic hydrodynamics. The initial state of a heavy-ion collision for times prior to its eventual thermalization, and the thermalization or isotropization mechanism, play a key role in the description of the collective behavior. Such initial condition for hydrodynamics or transport is presently modeled and fitted to data. But it should eventually be determined by a theoretical formalism of particle production within a saturation framework.

The CGC offers a well-defined framework in which such initial condition and thermalization mechanism can be computed from QCD, see Subsection 7.1.1 and e.g. [255] and refs. therein. Although our theoretical knowledge is still incomplete, electron-nucleus is a simpler system than nucleus-nucleus collisions, in which these calculations within the CGC framework already exist and can be checked. In this way, electron-ion collisions offer a testing ground of our ideas on parton production in a dense environment which is required for a first principle calculation of the initial conditions for the collective behavior in ultra-relativistic heavy-ion collisions. The LHeC offers the possibility of studying particle production in the kinematic region relevant for experiments at RHIC and the LHC.

c. Parton fragmentation and hadronization inside the nuclear medium:

The mechanism through which a highly virtual parton evolves from a highly off-shell colored state to final state hadrons, is still subject to great uncertainties. Electron-ion experiments offer a testing ground of our ideas and understanding of such phenomena, see [256] and refs. therein, with the nucleus being a medium of controllable extent and density which modifies the radiation and hadronization process.

The LHeC will have capabilities for particle identification and jet reconstruction for both nucleon and nuclear targets. Its kinematical reach will allow the study of partons traveling through the nucleus from low energies, for which hadronization is expected to occur inside the nucleus, to high energies with hadronization outside the nucleus. Therefore the modification of the yields of energetic hadrons, observed at RHIC[4] and usually attributed to energy loss - the so-called jet quenching phenomenon -, will be investigated. With jet quenching playing a key role in the present discussions on the production and characterization of the hot medium produced in ultra-relativistic heavy-ion collisions, the LHeC will offer most valuable information on effects in cold nuclear matter of great importance for clarifying and reducing the existing uncertainties.

7.2 Prospects at the LHeC

7.2.1 Strategy: decreasing x and increasing A

As discussed previously, in order to analyze the regime of high parton densities at small x, we will follow a two-pronged approach which is illustrated in Fig. 7.4. To reach an interesting novel regime of QCD one can either decrease x by increasing the center-of-mass energy or increase the matter density by increasing the mass number A. In addition, we will see that diffraction, and especially exclusive diffraction will play a special role in unravelling the new dense, parton regime of QCD. This is due to the fact that in diffractive events the impact parameter of the interaction can be controlled.

The LHeC will offer a huge lever arm in x and also a possibility of changing the matter density at fixed value of x. This will allow to pin down and compare the small x and saturation phenomena both in protons and nuclei and offer an excellent testing ground for theoretical predictions. Thus, in the following the simulations in electron-proton collisions will be paralleled by those in electron-lead when possible.

7.2.2 Inclusive measurements

Predictions for the proton

LHeC is expected to provide measurements of structure functions with unprecedented accuracy which will allow the detailed studies of small-x QCD dynamics. In particular, it will allow to pin down departures of the inclusive observables like F_2, F_L from the fixed-order DGLAP framework, in the region of small x and Q^2. These deviations are expected by several theoretical arguments, as discussed in detail previously.

In Fig. 7.12 we show several predictions for the proton structure functions, F_2 and F_L, in ep collisions at $Q^2 = 10$ GeV^2 and for $10^{-6} \le x \le 0.01$ i.e. $F_{2(L)}(x, Q^2 = 10\,\mathrm{GeV}^2)$. The different curves correspond to the extrapolation of models that reproduce correctly the available HERA data for the same observables in the small-x region. They are classified into two

[4] LHC experiments have already observed the jet quenching phenomenon both at the level of single-particle spectra [257] and through the study of jets [258, 259] which will play a central role in heavy-ion physics at these energies.

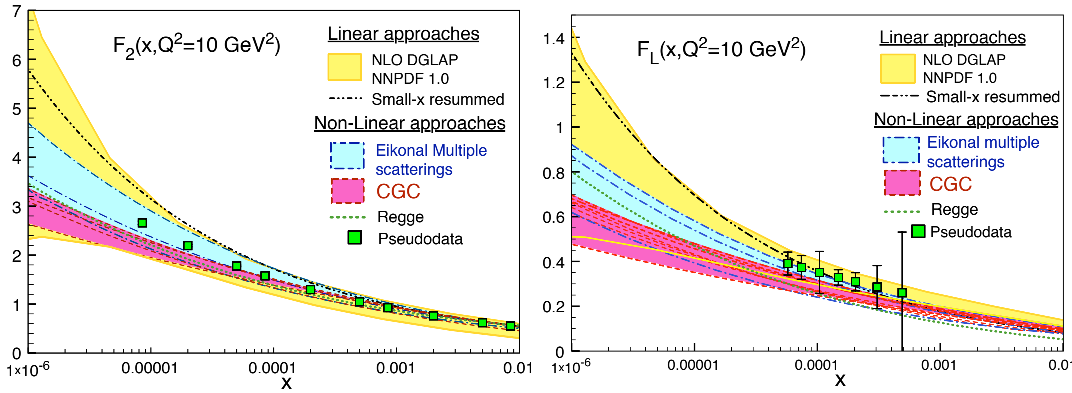

Figure 7.12: Predictions from different models for $F_2(x, Q^2 = 10 \text{ GeV}^2)$ (plot on the left) and $F_L(x, Q^2 = 10 \text{ GeV}^2)$ (plot on the right) versus x, together with the corresponding pseudodata. See the text for explanations.

categories: those based in linear evolution approaches and those that include non-linear small-x dynamics. Among the linear approaches we include extrapolation from the NLO DGLAP fit as performed by the NNPDF collaboration [203] (solid yellow bands) and the results from a combined DGLAP/BFKL approach that includes resummation of small-x effects [260] (black-dotted-dotted lines). The non-linear approaches are all formulated in terms of the dipole model. Here we distinguish two categories: those based in the eikonalization of multiple scatterings together with DGLAP evolution of the gluon distributions [192,193] (blue dashed-dotted lines) and those relying in the Color Glass Condensate effective theory of high-energy QCD scattering (red dashed lines). The latter include calculations based on solutions of the running coupling Balitsky-Kovchegov equation [261] and other more phenomenological modelings of the dipole amplitude without [179], or with impact parameter dependence [194]. Finally, we also include a hybrid approach, where initial conditions based on Regge theory and including non-linearities are evolved in Q^2 according to linear DGLAP evolution [141] (green dotted line). In all cases the error bands are generated by allowing variations of the free parameters in each subset of models. Green filled squares correspond to the LHeC pseudodata.

Clearly, the accuracy of the data at the LHeC will offer huge possibilities for discriminating different models and for constraining the dynamics underlying the small-x region.

Constraining small-x dynamics

Given the fact that in all fits presented above there are significant flexibilities in the initial parametrizations, it is conceivable that upon suitable changes of parameters it would be possible to obtain the satisfactory fits of different models to the LHeC data. It is therefore essential to analyze in more detail the ability of the LHeC to discriminate different approaches and hence distinguishing different evolution dynamics.

To this aim, a PDF analysis was performed for the LHeC pseudodata which were generated using different scenarios for small-x QCD dynamics. We considered $F_2(x, Q^2)$ and $F_L(x, Q^2)$ simulated pseudodata at small x, in a scenario in which the LHeC machine has electron energy of $E_e = 70$ GeV and electron acceptance of $\theta_e \leq 179^o$, for an integrated luminosity of $\int \mathcal{L} = 1$

fb^{-1}. The reference baseline for these studies is the NNPDF1.0 parton set [262]. The kinematics of the LHeC pseudodata included in the fit (together with that of the NNPDF1.0 analysis) are shown in Fig. 7.13. The average total uncertainty of the simulated F_2 pseudodata is $\sim 2\%$, while that of F_L is $\sim 8\%$.

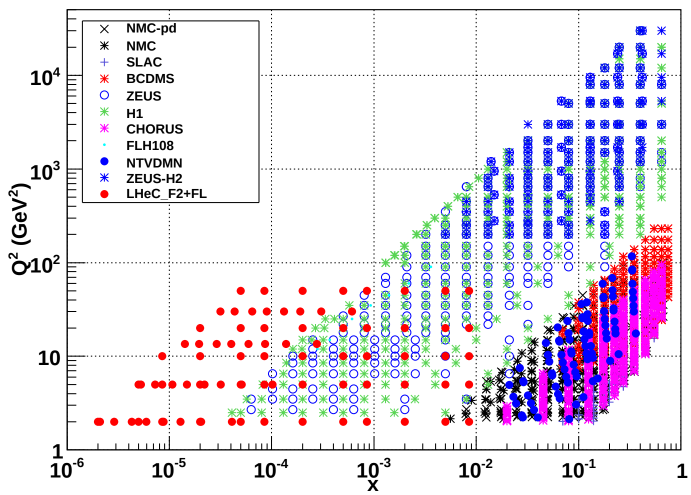

Figure 7.13: The kinematical coverage of the LHeC pseudodata used in the present studies, together with the data already included in the reference NNPDF1.0 dataset.

LHeC pseudodata have been generated not within the DGLAP framework, but rather from two different models: the AAMS09 model [261], which is based on the non-linear Balitsky-Kovchegov evolution with running coupling, and the FS04 model [180], based on the dipole model. Both of these models deviate significantly from the linear DGLAP evolution since they include saturation effects in the gluon density.

Next, the global analysis using the NNPDF1.0 framework with fixed-order DGLAP evolution was performed but now including LHeC pseudodata generated using the scenarios with saturation. This procedure provides an illustration of a potential analysis technique which ultimately should be applied to experimental data.

Such study offers the possibility of checking the sensitivity to parton dynamics beyond fixed-order DGLAP. In this respect, for both the AAMS09 and the FS04 models the conclusions are the same: the DGLAP analysis reproduces perfectly the $F_2(x, Q^2)$ pseudodata. This implies that although the underlying physical theories are different, from a practical point of view the small-x extrapolations of AAMS09 and FS04 for F_2 are rather similar to DGLAP-based extrapolations, and their differences can be absorbed as modifications of the shape of the non-perturbative initial conditions. Note that, in this scenario, the more sophisticated analysis based on sequential kinematical cuts and backwards DGLAP evolution presented in Sect. 7.1.2 should be applied.

However, the situation is very different for the longitudinal structure function $F_L(x, Q^2)$, provided the level arm in Q^2 is large enough. The analysis based on the linear DGLAP evolution

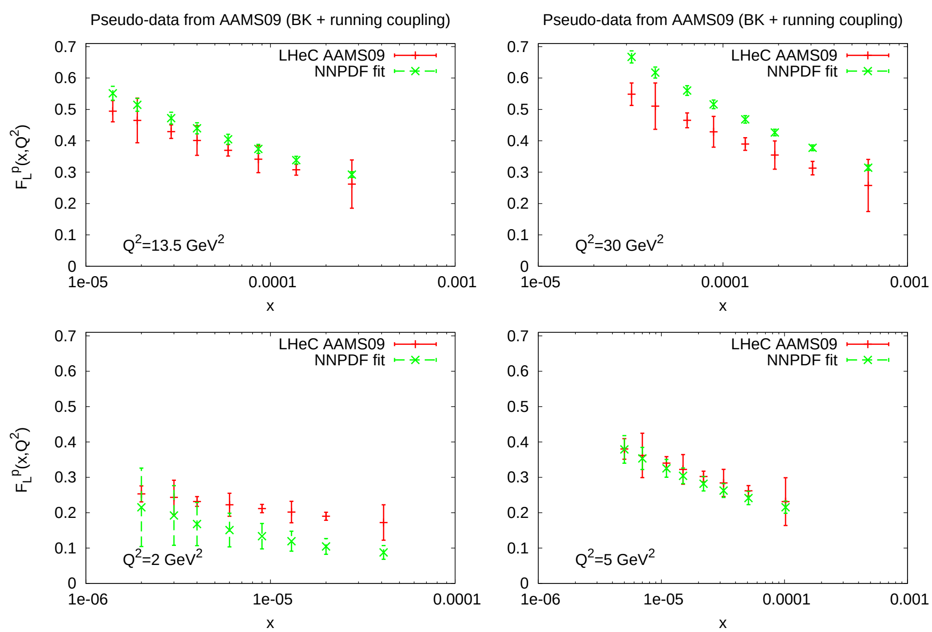

Figure 7.14: The results of the combined DGLAP analysis of the NNPDF1.2 data set and the LHeC pseudodata for $F_L(x, Q^2)$ in various Q^2 bins generated with the AAMS09 model.

fails to reproduce simultaneously F_2 and F_L in all the Q^2 bins, and thus the overall χ^2 is very large. This is a clear signal of the departure from fixed-order DGLAP of the simulated pseudodata. This effect is illustrated in Fig. 7.14, where the results of the DGLAP analysis are compared with the LHeC pseudodata generated from the AAMS09 model. Our analysis shows therefore that F_L data is a very sensitive probe of novel small-x QCD dynamics, and that their measurement would allow to discriminate uniquely between different theoretical scenarios.

The importance of the measurement of the longitudinal structure function is better illustrated in Fig. 7.15. It shows the uncertainties in the gluon distribution function in two different scenarios. In one case only F_2 data were used in the fit, and in the second case the pseudodat on F_L were added also. Clearly the inclusion of the pseudotata on F_L markedly improves the determination of the gluon density.

As is however well known from experience at HERA the measurement of the longitudinal structure function presents certain experimental challenges. An alternative possibility of using the charmed structure function F_2^c to constrain the PDFs was also investigated, and it gave similar results to F_L. In Fig. 7.16 the gluon distribution function is shown, obtained from the NNPDF2.0 analysis. The green band corresponds to the standard analysis using the F_2 structure function data and the red band to the analysis where additionally measurements on F_2^c from the LHeC were used. This has been studied using a novel technique based on Bayesian reweighting [263]. It is observed that the charmed structure function greatly constraints the gluon distribution function at small values of x, especially between $10^{-2} - 10^{-4}$. The advantage

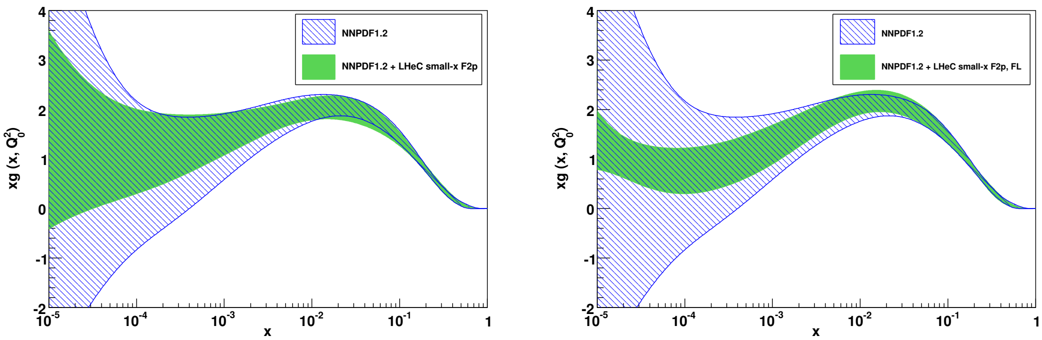

Figure 7.15: The results for the gluon distribution in the combined DGLAP analysis of the NNPDF1.2 data set [203] and when including LHeC pseudodata for F_2 (left) and $F_2 + F_L$ (right).

of having 1 degree acceptance is also illustrated. Using simultaneously F_2 and F_2^c LHeC pseudodata one can precisely pin down the deviations from the fixed-order linear DGLAP evolution at small x.

Predictions for nuclei: impact on nuclear parton distribution functions

LHeC will be the first electron-ion collider machine, and hence it will have enormous potential for measuring the nuclear parton distribution functions at small x.

Let us start by a brief explanation of how the pseudodata for inclusive observables in ePb collisions are obtained: For generating F_2 in electron-nucleus collisions, the points (x, Q^2), generated for e(50) + p(7000) collisions as explained in Subsection 5.1, are considered. Among them, we keep only those points at small $x \leq 0.01$ and not too large $Q^2 < 1000$ GeV^2 with $Q^2 \leq sx$, for a Pb beam energy of 2750 GeV per nucleon. Under the assumption that the luminosity per nucleon is the same in ep and eA, the statistics is scaled by a factor $1/(5 \times 50 \times A)$, with 50 coming from the transition from a high luminosity to a low luminosity scenario, and 5 being a conservative reduction factor (e.g. for the probably shorter running time for ions than for proton).

In each point of the grid, σ_r and F_2 are generated using the dipole model of [175, 264] to get the central value. Then, for every point, the statistical error in ep is scaled by the mentioned factor $1/(5 \times 50 \times A)$, and corrected by the difference in F_2 or σ_r between the (Glauberized) 5-flavor GBW model [264] and the model used for the ep simulation. The fractional systematic errors are taken, for the same grid point, to be the same as for ep - as obtained in previous DIS experiments on nuclear targets[5]. An analogous procedure is applied for obtaining the pseudodata for F_2^c and F_2^b, considering the same tag and background rejection efficiencies as in the ep simulation.

For extracting F_L, a dedicated simulation of e+p(2750) collisions has been performed, at three different energies: 10, 25 and 50 GeV for the electron, with assumed luminosities 5, 10 and 100 pb^{-1} respectively, see Sec. 5.1. Then, for each point in the simulated grid, F_L values

[5]The main difference in the systematics would eventually come from the different size of the radiative corrections in proton and nuclei, an important point which remains to be addressed in future studies.

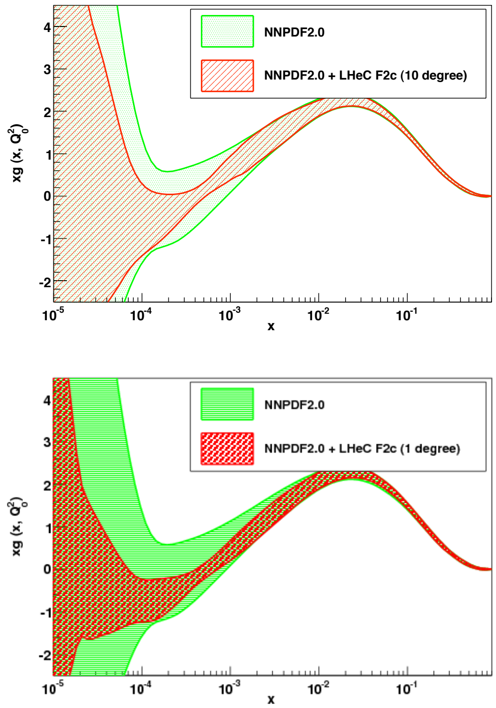

Figure 7.16: The effects of the inclusion of the data on charmed structure function pseudodata from the LHeC in the NNPDF global analysis on constraining the gluon distribution function. Left plot: 10 degree scenario, right plot: 1 degree scenario.

in proton and nuclei are generated using the (Glauberized) 5-flavor GBW model [264]. The relative uncertainties are taken to be exactly the same as in the ep simulation, as explained above.

In Fig. 7.17 we show several predictions for the nuclear suppression factor, Eq. (7.6), with respect to the proton, for the total and longitudinal structure functions, F_2 and F_L respectively, in ePb collisions at $Q^2 = 5$ GeV^2 and for $10^{-5} \le x \le 0.1$. Results from global DGLAP analyses at NLO: nDS, HKN07 and EPS09 [218, 245, 246], plus those from models using the relation between diffraction and nuclear shadowing, AKST and FGS10 [142, 249], are shown together with the LHeC pseudodata. Brief explanations on the different models can be found in Sec. 7.1.4. Clearly, the accuracy of the data at the LHeC will offer huge possibilities for discriminating between different models and for constraining the dynamics underlying nuclear shadowing at small x.

In order to better quantify how the LHeC would improve the present situation concerning nuclear PDFs in global DGLAP analyses (see the uncertainty band in Fig. 7.11), nuclear LHeC pseudodata have been included in the global EPS09 analysis in [218]. The DGLAP evolution was carried out at the NLO accuracy, in the variable-flavor-number scheme (SACOT prescription) with the CTEQ6.6 [197] set for free proton PDFs as a baseline. For more details the reader may

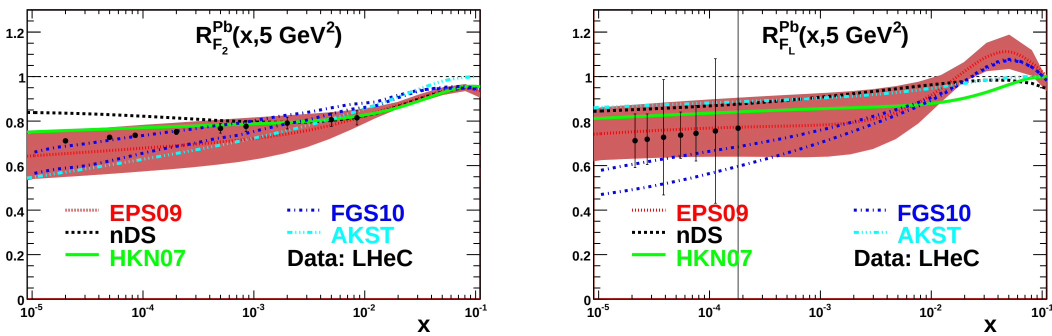

Figure 7.17: Predictions from different models for the nuclear modification factor, Eq. (7.6) for Pb with respect to the proton, for $F_2(x, Q^2 = 5\ \text{GeV}^2)$ (plot on the left) and $F_L(x, Q^2 = 5\ \text{GeV}^2)$ (plot on the right) versus x, together with the corrresponding pseudodata. Dotted lines correspond to the nuclear PDF set EPS09 [218], dashed ones to nDS [245], solid ones to HKN07 [246], dashed-dotted ones to FGS10 [249] and dashed-dotted-dotted ones to AKST [142]. The band correspond to the uncertainty in the Hessian analysis in EPS09 [218].

consult the original EPS09 paper [218] and references therein. The only difference compared to the original EPS09 setup is that one additional gluon parameter, x_a, has been varied (this parameter was originally frozen in EPS09), and the only additionally weighted data set was the PHENIX data on π^0 production at midrapidity [265] in dAu collisions at RHIC.

Two different fits have been performed: the first one (Fit 1) includes pseudodata on the total reduced cross section. The results of the fit for the ratios of parton densities are shown in Fig. 7.18. A large improvement in the determination of sea quark and gluon parton densities at small x is evident.

The second fit (Fit 2) includes not only nuclear LHeC pseudodata on the total reduced cross section but also on its charm and beauty components. These data provide a possibility of getting direct information on the nuclear effects on charm and beauty parton densities which are mainly dynamically generated from the gluons through the DGLAP evolution. Thus, the inclusion of such pseudodata further improves the determination of the nuclear effects on the gluon at small x, as illustrated in Fig. 7.19.

In conclusion, the accuracy and large lever arm in x and Q^2 of the nuclear data at the LHeC will offer huge possibilities for discriminating different models and for constraining the parton densities in global DGLAP analyses. Besides measurements of the reduced cross section, data on its charm and bottom components and on F_L will help to constrain the nuclear effects on PDFs, see e.g. the recent works [266, 267].

7.2.3 Exclusive Production

Introduction

Exclusive processes such as electroproduction of vector mesons and photons, $\gamma^* N \to V + N (V = \rho^0, \phi, \gamma)$, or photoproduction of heavy quarkonia, $\gamma N \to V + N (V = J/\psi, \Upsilon)$ - see figure 7.20 - provide information on nucleon structure and small-x dynamics complementary to that obtained

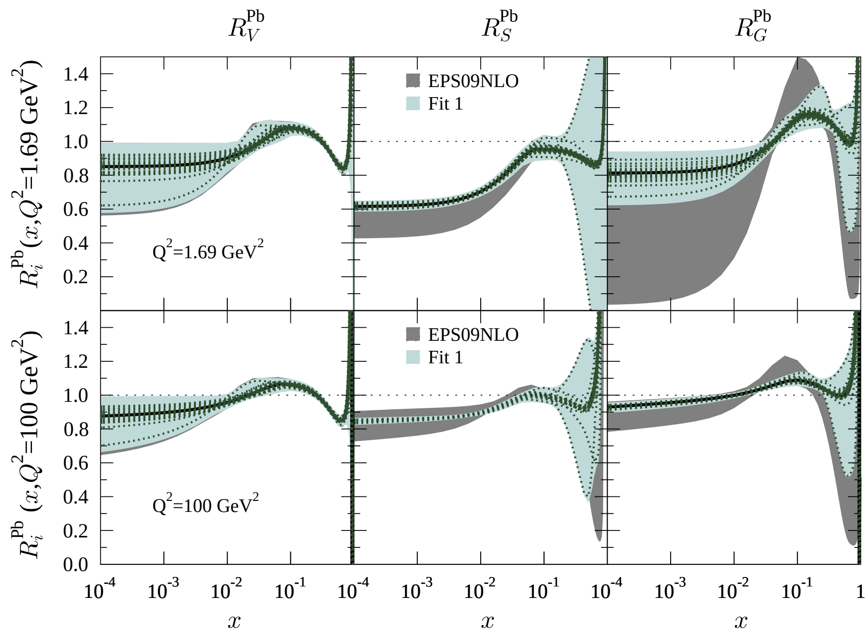

Figure 7.18: Ratio of parton densities in a bound proton in Pb over those in a free proton, for valence u (left), $\bar{u}$ (middle) and g (right), at $Q^2 = 1.69$ (top) and 100 (bottom) GeV^2. The dark grey band corresponds to the uncertainty band using the Hessian method in the original EPS09 analysis [218], while the light blue one corresponds to the uncertainty band obtained after including nuclear LHeC pseudodata on the total reduced cross sections (Fit 1). The dotted lines indicate the values corresponding to the different nPDF sets in the EPS09 analysis [218].

in inclusive measurements [178]. Experimentally the cleanest processes are exclusive vector meson production ($ep \to eVp$) and Deeply-Virtual Compton Scattering (DVCS, $ep \to e\gamma p$), which have both played a major role at HERA [268].

Diffractive channels are favourable, since the underlying exchange crudely equates to a pair of gluons, making the process sensitive to the square of the gluon density [269], in place of the linear dependence for F_2 or F_L. This enhances substantially the sensitivity to non-linear evolution and saturation phenomena. As already shown at HERA, J/Ψ production is a particularly clean probe of the gluonic structure of the hadron [194, 269]. The same exclusive processes can be measured in deep inelastic scattering off nuclei, where the gluon density is modified by nuclear effects. In addition, exclusive processes give access to the spatial distribution of the gluon density, parametrized by the impact parameter [270] of the collision. The correlations between the gluons coupling to the proton contain information on the three-dimensional structure of the nucleon or nucleus, which is encoded in the Generalised Parton Densities (GPDs). The GPDs combine aspects of parton densities and elastic form factors and have emerged as a key concept for describing nucleon structure in QCD (see [271–273] for a review).

Exclusive processes can be treated conveniently within the dipole picture described in Sec. 7.1.2. In this framework, the cross section can be represented as a product of three fac-

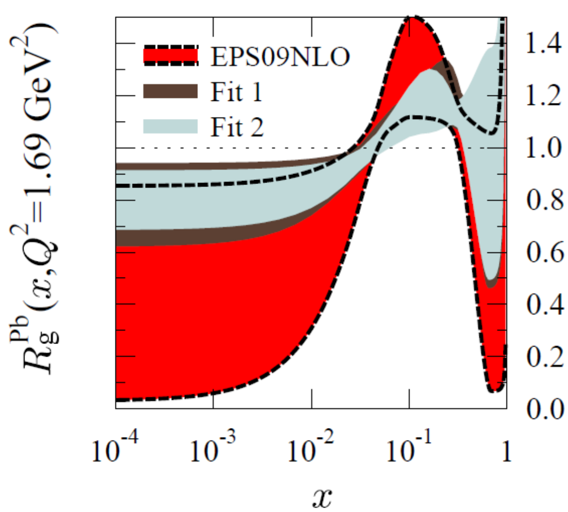

Figure 7.19: Ratio of the gluon densities in a bound proton in Pb over that in a free proton at $Q^2 = 1.69$ GeV^2. The red band corresponds to the uncertainty band using the Hessian method in the original EPS09 analysis [218], while the dark brown one corresponds to the uncertainty band obtained after including nuclear LHeC pseudodata on the total reduced cross sections (Fit 1), and the light blue one to the uncertainty band obtained after further including pseudodata on charm and beauty reduced cross sections (Fit 2).

torizable terms: the splitting of an incoming photon into a $q\bar{q}$ dipole; the 'dipole' cross section for the interaction of this $q\bar{q}$ pair with the proton and, in the case of vector mesons, a wave function term for the projection of the dipole into the meson. As discussed in Sec. 7.1.2 the dipole formalism is particularly convenient since saturation effects can be easily incorporated.

Generalised Parton Densities and Spatial Structure

At sufficiently large Q^2 the exclusively produced meson or photon is in a configuration of transverse size much smaller than the typical hadronic size, $r_\perp \ll R_{\mathrm{hadron}}$. As a result its interaction with the target can be described using perturbative QCD [274]. A QCD factorization theorem [275] states that the exclusive amplitudes in this regime can be factorized into a perturbative QCD scattering process and certain universal process-independent functions describing the emission and absorption of the active partons by the target, the generalized parton distributions (GPDs).

The Fourier transform of the GPDs with respect to the transverse momentum transferred to the nucleon describes the transverse spatial distribution of partons with a given longitudinal momentum fraction, x [276]. The transverse spatial distributions of quarks and gluons are fundamental characteristics of the nucleon, which reveal the size of the configurations in its

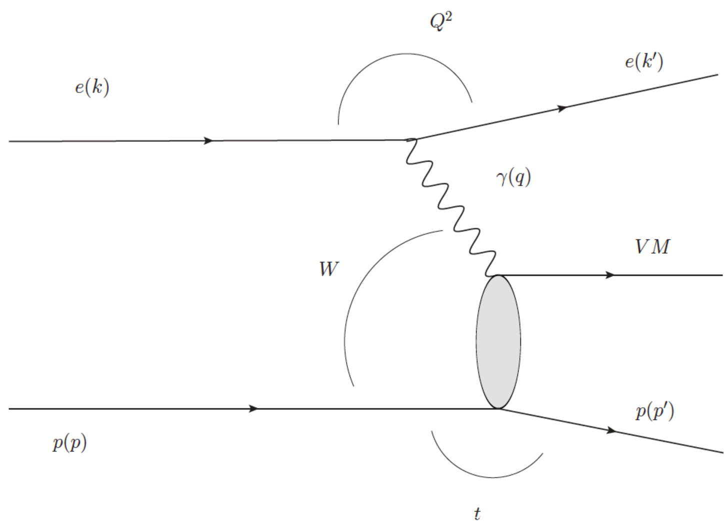

Figure 7.20: Schematic illustration of the exclusive vector meson production process and the kinematic variables used to describe it in photoproduction ($Q^2 \to 0$) and DIS (large Q^2). The outgoing particle labelled 'VM', may be either a vector meson with $J^{PC} = 1^{--}$ or a photon.

partonic wave function and allow one to study the non-perturbative dynamics governing their change with x, such as Gribov diffusion, chiral dynamics, and other phenomena. The nucleon transverse gluonic size is also an essential input in studies of saturation at small x. It determines the initial conditions of the non-linear QCD evolution equations and thus directly influences the impact parameter dependence of the saturation scale for the nucleon [193, 277], which in turn predicates its nuclear enhancement [278]. Information on the nucleon transverse quark and gluon distributions is further required in the phenomenology of high-energy pp collisions with hard processes, including those with new particle production, where it determines the underlying event structure (centrality dependence) in inclusive scattering [279] and the rapidity gap survival probability in central exclusive diffraction [280, 281]. In view of its considerable interest, the transverse quark/gluon imaging of the nucleon with exclusive processes has been recognized as an important objective of nucleon structure and small-x physics.

Mapping the transverse spatial distribution of quarks and gluons requires measurement of the (relative) t-dependence of hard exclusive processes up to large values of $|t|$, of the order of $|t| < 1\,\mathrm{GeV}^2$. Studies of the Q^2-dependence and comparisons between different channels provide crucial tests of the reaction mechanism and the universality of GPDs. Vector meson production at small x and heavy quarkonium photoproduction at high energies probe the gluon GPD of the target, while real photon production (deeply-virtual Compton scattering, or DVCS) involves the singlet quark as well as gluon GPDs. Measurements of exclusive J/ψ photo/electroproduction [282, 283] and ρ^0 and ϕ electroproduction at HERA have confirmed the applicability of the factorized QCD description through several model-independent tests, and have provided basic information of the nucleon gluonic size in the region $10^{-4} < x < 10^{-2}$ and its change with x [178]. Measurements of DVCS at HERA [284, 285] hint that the transverse distribution of singlet quarks may be larger than that of gluons. While these experiments have given important insight in nucleon structure, the interpretation of the HERA data is limited by the low statistics which precludes fully differential analysis. The lack of recoil detection necessitates model-dependent corrections for proton break-up at larger t.

As discussed in the following, the LHeC would enable a comprehensive program of gluon and singlet quark transverse imaging through exclusive processes, with numerous applications to nucleon structure and small-x physics. The high statistics would permit fully differential measurements of exclusive channels as needed to control the reaction mechanism, e.g. measurements of the t-distributions for fixed x differentially in Q^2, to demonstrate dominance of small-size configurations. It would also allow one to push such measurements to the region $Q^2 \sim \text{few} \times 10\,\text{GeV}^2$ where finite-size (higher-twist) effects are small and the effects of QCD evolution can be cleanly identified. Measurements of gluonic exclusive channels $(J/\psi, \phi, \rho^0)$ at the LHeC would provide gluonic transverse images of the nucleon down to $x \sim 10^{-6}$ with unprecedented accuracy, testing theoretical ideas about diffusion dynamics in the wave function. Because exclusive cross sections are proportional to the square of the gluon GPD (i.e. the gluon density), such measurements would also offer new insight into non-linear effects in QCD evolution, and enable new tests of the approach to saturation by measuring the impact parameter dependence of the saturation scale. Along these lines, saturation effects on exclusive vector meson production on protons and nuclei have been studied in [286–288]. Furthermore, measurements of DVCS would provide additional information on the nucleon singlet quark size and its dependence on x. Besides its intrinsic interest for nucleon structure and small-x physics, this information would greatly advance our theoretical understanding of the transverse geometry of high-energy pp collisions at the LHC. We note that these exlcusive measurements at the LHeC would complement similar measurements at moderately small x $(0.003 < x < 0.2)$ with the COMPASS experiment at CERN and in the valence region $x > 0.1$ with the JLab 12 GeV Upgrade, providing a comprehensive picture of the nucleon spatial structure.

Other interesting information comes from hard exclusive measurements accompanied by diffractive dissociation of the nucleon, $\gamma^* N \to V + X$ (X = low-mass diffractive state). The ratio of inelastic to elastic diffraction in these processes provides information on the quantum fluctuations of the gluon density, which reveals the quantum-mechanical nature of the non-perturbative color fields in the nucleon and can be related to dynamical models of low-energy nucleon structure [289]. HERA results are in qualitative agreement with such model predictions but do not permit a quantitative analysis. Diffractive measurements at the LHeC would allow for detailed quantitative studies of all these new aspects of nucleon and nuclear structure.

Exclusive Production in the Dipole Approach

For the exclusive production of the vector mesons, a QCD factorization theorem has been demonstrated (for σ_L) in [274]. The dipole model follows from this QCD factorization theorem in the LO approximation. Within the dipole model, see Sec. 7.1.2, the amplitude for an exclusive diffractive process, $\gamma^* p \to E + p$, shown in Fig. 7.21(a), can be expressed as

$$\mathcal{A}_{T,L}^{\gamma^* p \to E+p}(x, Q, \Delta) = \mathrm{i} \int \mathrm{d}^2\boldsymbol{r} \int_0^1 \frac{\mathrm{d}z}{4\pi} \int \mathrm{d}^2\boldsymbol{b}\; (\Psi_E^* \Psi)_{T,L}\; \mathrm{e}^{-\mathrm{i}[\boldsymbol{b}-(1-z)\boldsymbol{r}]\cdot\boldsymbol{\Delta}}\; \frac{\mathrm{d}\sigma_{q\bar{q}}}{\mathrm{d}^2\boldsymbol{b}}\,. \tag{7.7}$$

Here $E = V$ for vector meson production, or $E = \gamma$ for deeply virtual Compton scattering (DVCS). In Eq.(7.7), z is the fraction of the photon's light-cone momentum carried by the quark, $r = |\boldsymbol{r}|$ is the transverse size of the $q\bar{q}$ dipole, while $\boldsymbol{b}$ is the impact parameter, that

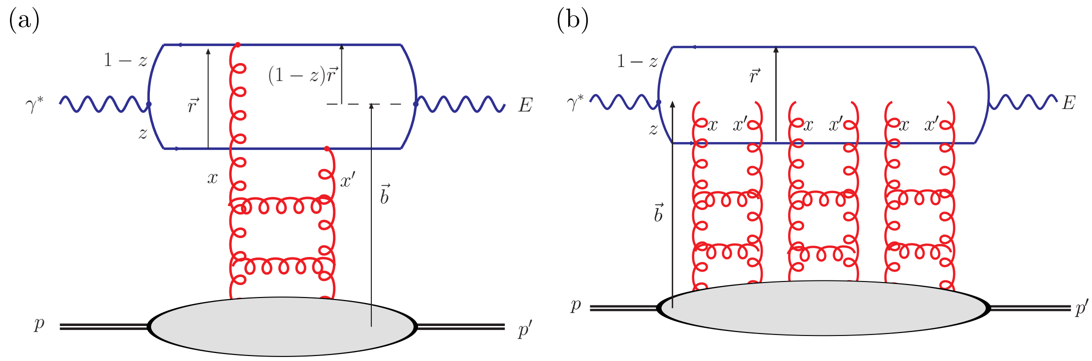

Figure 7.21: Diagrams representing the $\gamma^* p$ scattering amplitude proceeding via (a) single-Pomeron and (b) multi-Pomeron exchange, where the perturbative QCD Pomeron is represented by a gluon ladder. For exclusive diffractive processes, such as vector meson production ($E = V$) or DVCS ($E = \gamma$), we have $x' \ll x \ll 1$ and $t = (p - p')^2$. For inclusive DIS, we have $E = \gamma^*$, $x' = x \ll 1$ and $p' = p$.

is, $b = |\boldsymbol{b}|$ is the transverse distance from the centre of the proton to the centre-of-mass of the $q\bar{q}$ dipole; see Fig. 7.21(a). The transverse momentum lost by the outgoing proton, $\boldsymbol{\Delta}$, is the Fourier conjugate variable to the impact parameter $\boldsymbol{b}$, and $t \equiv (p - p')^2 = -\Delta^2$. The forward overlap function between the initial-state photon wave function and the final-state vector meson or photon wave function in Eq. (7.7) is denoted $(\Psi_E^* \Psi)_{T,L}$, while the factor $\exp[\mathrm{i}(1-z)\boldsymbol{r} \cdot \boldsymbol{\Delta}]$ in Eq. (7.7) originates from the non-forward wave functions [290]. The differential cross section for an exclusive diffractive process is obtained from the amplitude, Eq. (7.7), by

$$\frac{\mathrm{d}\sigma_{T,L}^{\gamma^* p \to E + p}}{\mathrm{d}t} = \frac{1}{16\pi} \left| \mathcal{A}_{T,L}^{\gamma^* p \to E + p} \right|^2 , \tag{7.8}$$

up to corrections from the real part of the amplitude and from skewedness ($x' \ll x \ll 1$). Taking the imaginary part of the forward scattering amplitude immediately gives the formula for the total $\gamma^* p$ cross section (or equivalently, the proton structure function $F_2 = F_T + F_L$):

$$\sigma_{T,L}^{\gamma^* p}(x, Q) = \mathrm{Im}\, \mathcal{A}_{T,L}^{\gamma^* p \to \gamma^* p}(x, Q, \Delta = 0) = \sum_f \int \mathrm{d}^2\boldsymbol{r} \int_0^1 \frac{\mathrm{d}z}{4\pi} (\Psi^* \Psi)_{T,L}^f \int \mathrm{d}^2\boldsymbol{b}\, \frac{\mathrm{d}\sigma_{q\bar{q}}}{\mathrm{d}^2\boldsymbol{b}} \, . \tag{7.9}$$

The dipole picture therefore provides a unified description of both exclusive diffractive processes and inclusive deep-inelastic scattering (DIS) at small x.

The unknown quantity common to Eqs. (7.7) and (7.9) is the b-dependent dipole–proton cross section,

$$\frac{\mathrm{d}\sigma_{q\bar{q}}}{\mathrm{d}^2\boldsymbol{b}} = 2\, \mathcal{N}(x, r, b) \, , \tag{7.10}$$

where $\mathcal{N}$ is the imaginary part of the dipole–proton scattering amplitude, which can vary between zero and one, where $\mathcal{N} = 1$ corresponds to the unitarity ("black disc") limit. The scattering amplitude $\mathcal{N}$ encodes the information about the details of the strong interaction between the dipole and the target (proton or nucleus). It is generally parameterised according to some theoretically-motivated functional form, with the parameters fitted to data. Most dipole models assume a factorised b dependence, $\mathcal{N}(x,r,b) = T(b)\,\mathcal{N}(x,r)$, with $\mathcal{N}(x,r) \in [0,1]$ and, for example, $T(b) = \Theta(R_p - b)$, so that the b-integrated $\sigma_{q\bar{q}} = (2\pi R_p^2)\,\mathcal{N}(x,r)$. However, (i) the "saturation scale" is strongly dependent on impact parameter, (ii) the b-dependence should be made consistent with the t-dependence of exclusive diffraction at HERA, and (iii) the non-zero effective "Pomeron slope" $\alpha'_{\mathbb{P}}$ measured at HERA implies a correlation between the x- and b-dependences of $\mathcal{N}(x,r,b)$. Therefore, $\mathcal{N}(x,r,b)$ should be determined from the simultaneous description of inclusive DIS and exclusive diffractive processes measured at HERA.

An impact-parameter-dependent saturation ("b-sat") model [193, 194] has been shown to be very successful in describing a broad range of HERA data on exclusive diffractive vector meson (J/ψ, ϕ, ρ) production and DVCS (see other quite different approach in [291]), including almost all aspects of the Q^2, W and t dependence with the exception of $\alpha'_{\mathbb{P}}$, together with the inclusive structure functions F_2, $F_2^{c\bar{c}}$, $F_2^{b\bar{b}}$ and F_L. The "b-Sat" parameterisation is based on LO DGLAP evolution of an initial gluon density, $xg(x,\mu_0^2) = A_g\, x^{-\lambda_g}\,(1-x)^{5.6}$, with a Gaussian b dependence, $T(b) \propto \exp(-b^2/2B_G)$. The dipole scattering amplitude is parametrized as

$$\mathcal{N}(x,r,b) = 1 - \exp\left(-\frac{\pi^2}{2N_c} r^2 \alpha_S(\mu^2)\, xg(x,\mu^2)\, T(b)\right), \tag{7.11}$$

where the scale $\mu^2 = 4/r^2 + \mu_0^2$, $B_G = 4\ \text{GeV}^{-2}$ was fixed from the t-slope of exclusive J/ψ photoproduction at HERA, and the other three parameters ($\mu_0^2 = 1.17\ \text{GeV}^2$, $A_g = 2.55$, $\lambda_g = 0.020$) were fitted to ZEUS F_2 data with $x_{\text{Bj}} \leq 0.01$ and $Q^2 \in [0.25, 650]\ \text{GeV}^2$ [194]. The eikonalised dipole scattering amplitude of Eq. (7.11) can be expanded as

$$\mathcal{N}(x,r,b) = \sum_{n=1}^{\infty} \frac{(-1)^{n+1}}{n!} \left[\frac{\pi^2}{2N_c} r^2 \alpha_S(\mu^2)\, xg(x,\mu^2)\, T(b)\right]^n, \tag{7.12}$$

where the n-th term in the expansion corresponds to n-Pomeron exchange; for example, the case $n = 3$ is illustrated in Fig. 7.21(b). The terms with $n > 1$ are necessary to ensure unitarity.

Simulations of LHeC Elastic J/ψ Production

Due to its extremely clean final states, the relatively low effective x values ($x_{\text{eff}} \sim (Q^2 + m_V^2)/(Q^2 + W^2)$) and scales ($Q^2_{\text{eff}} \sim (Q^2 + m_V^2)/4$) accessed [269, 292], and the experimental possibility of varying both W and t over wide ranges, the dynamics of J/ψ photoproduction ($Q^2 \to 0$) may offer the cleanest available signatures of the transition between the dilute and dense regimes of small-x partons. Even if the LHeC detector tracking and calorimetry extend only to within 10° of the beampipe, it should be possible to detect the muons from J/ψ or Υ decays with acceptances extending to within 1° of the beampipe with dedicated muon chambers on the outside of the experiment. Depending on the electron beam energy, this makes invariant photon-proton masses W of well beyond 1 TeV accessible.

For the analysis presented here we concentrate on the photoproduction limit, where the HERA data are most precise due to the largest cross sections and where unitarity effects are most important. Studies have also been made at larger Q^2 [293], where the extra hard scale additionally allows a perturbative treatment of exclusive light vector meson (e.g. ρ, ω, ϕ) production. Again, perturbative unitarity effects are expected to be important for light vector meson production when $Q^2 \gtrsim 1\ \text{GeV}^2$ is not too large.

LHeC pseudodata for elastic J/ψ and Υ photoproduction and electroproduction have been generated under the assumption of 1° acceptance and a variety of luminosity scenarios based on

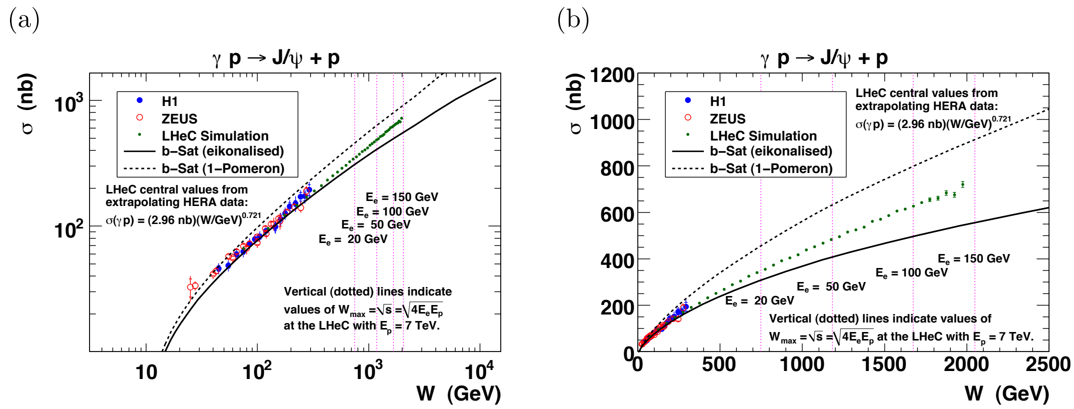

Figure 7.22: Exclusive J/ψ photoproduction at the LHeC, as a function of the γp centre-of-mass energy W, plotted on a (a) log–log scale and (b) linear–linear scale. The difference between the solid and dashed curves indicates the size of unitarity corrections compared to pseudodata from the LHeC simulation.

simulations using the DIFFVM Monte Carlo generator [294]. This generator involves a simple Regge-based parameterization of the dynamics and a full treatment of decay angular distributions. Statistical uncertainties are estimated for each data point. Systematic uncertaintes are hard to estimate without a detailed simulation of the muon identification and reconstruction capabilities of the detector, but are likely to be at least as good as the 10% measurements typically achieved for the elastic J/ψ at HERA.

The plots in Fig. 7.22 show t-integrated predictions for exclusive J/ψ photoproduction ($Q^2 = 0$) obtained from Eqs. (7.7) and (7.8), using the eikonalised "b-Sat" dipole scattering amplitude given in Eq. (7.11) together with a "boosted Gaussian" vector meson wave function [194, 295]. Also shown is the single-Pomeron exchange contribution obtained by keeping just the first ($n = 1$) term in the expansion of Eq. (7.12), which is linearly dependent on the gluon density, without refitting any of the input parameters. The difference between the "eikonalised" and "1-Pomeron" predictions therefore indicates the importance of unitarity corrections, which increase significantly with rising γp centre-of-mass energy W. The maximum kinematic limit accessible at the LHeC, $W = \sqrt{s}$, is indicated with different options for electron beam energies (E_e) and not accounting for the angular acceptance of the detector. The precise HERA data [283, 296] are overlaid, together with sample LHeC pseudodata points, assuming 1° muon acceptance, with the errors (statistical only) given by an LHeC simulation with $E_e = 150$ GeV. The central values of the LHeC pseudodata points were obtained from a Gaussian distribution with the mean given by extrapolating a power-law fit to the HERA data [283, 296] and the standard deviation given by the statistical errors from the LHeC simulation. The plots in Fig. 7.22 show that the errors on the LHeC pseudodata are much smaller than the difference between the "eikonalised" and "1-Pomeron" predictions. Therefore, exclusive J/ψ photoproduction at the LHeC may be an ideal observable for investigating unitarity corrections at a perturbative scale provided by the charm-quark mass.

Similar plots for exclusive Υ photoproduction are shown in Fig. 7.23. Here, the unitarity corrections are smaller than for J/ψ production due to the larger scale provided by the bottom-quark mass and therefore the smaller typical dipole sizes r being probed. The simu-

(a) (b)

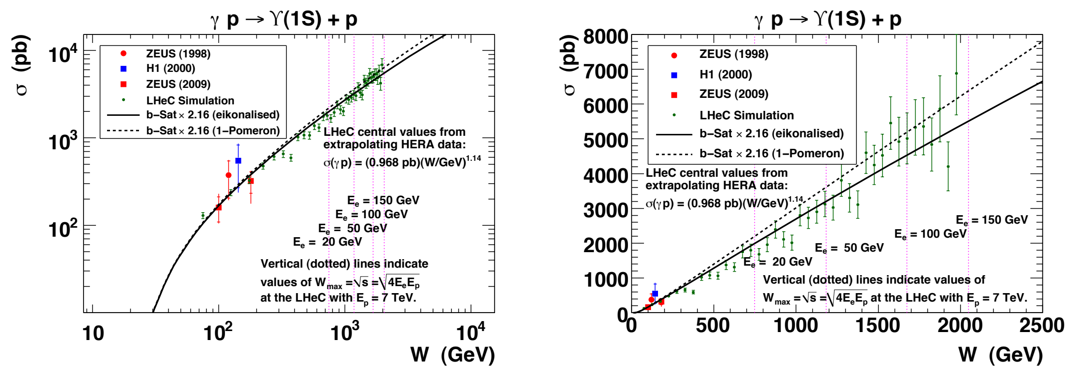

Figure 7.23: Exclusive Υ photoproduction at the LHeC, as a function of the γp centre-of-mass energy W, plotted on a (a) log–log scale and (b) linear–linear scale. The difference between the solid and dashed curves indicates the size of unitarity corrections compared to pseudodata from an LHeC simulation. The "b-Sat" theory predictions have been scaled by a factor 2.16 to best-fit the existing HERA data.

lated LHeC pseudodata points also have larger statistical errors than for J/ψ production due to the much smaller cross sections. Nonetheless, the simulations indicate that a huge improvement in kinematic range and precision is possible compared with the very sparse Υ data from HERA [297–299].

It is essential to note that, in order to achieve a satisfactory description of the experimental data, an additional normalization factor of ~ 2 has to be included in the dipole calculation (a similar factor is required for other calculations using the dipole model, see for example Ref. [300]). This normalization factor does not arise from any theoretical considerations. Therefore one needs to be aware that the dipole model prediction for the Υ in diffractive exclusive processes in DIS still poses significant theoretical challenges.

The cross sections shown in Figs. 7.22 and 7.23 are integrated over $t \equiv (p - p')^2 = -\Delta^2$, where $\boldsymbol{\Delta}$ is the Fourier conjugate variable to the impact parameter $\boldsymbol{b}$. One expects that at higher centre-of-mass energies (smaller x), saturation effects are more important closer to the centre of the proton (smaller b), where the interaction region is more dense. This is illustrated in Fig. 7.24(a) where the dipole scattering amplitude is shown as a function of b for various x values. By measuring exclusive diffraction in bins of $|t|$ one can extract the impact parameter profile of the interaction region. This is illustrated in Fig. 7.24(b) where the integrand of Eq. (7.7) is shown for different values of t as a function of impact parameter. Clearly for larger values of $|t|$, smaller values of b are probed in the impact parameter profile. This region is expected to be more densely populated and therefore the saturation effects should be more important there. Indeed, the eikonalised dipole model of Eq. (7.11) leads to "diffractive dips" in the t-distribution of exclusive J/ψ photoproduction at large $|t|$ (reminiscent of the dips seen in the t-distributions of proton-proton elastic cross sections), departing from the exponential fall-off in the t-distribution seen with single-Pomeron exchange [193]. The HERA experiments have only been able to make precise measurements of exclusive J/ψ photoproduction at relatively small $|t| \lesssim 1$ GeV^2, and no significant departure from the exponential fall-off behaviour, $\mathrm{d}\sigma/\mathrm{d}t \sim \exp(-B_D|t|)$, has been observed.

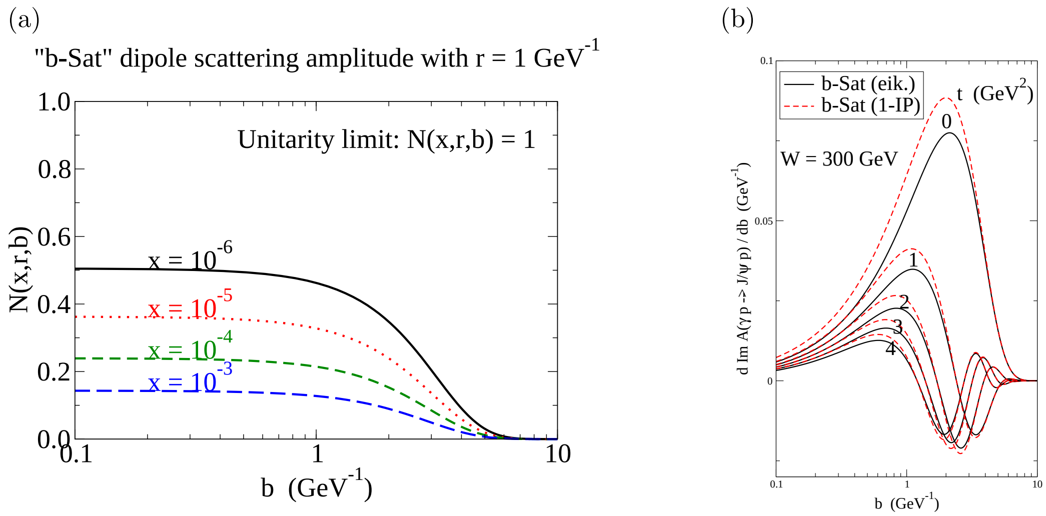

Figure 7.24: (a) The (imaginary part of the) dipole scattering amplitude, $\mathcal{N}(x, r, b)$, as a function of the impact parameter b, for fixed values of dipole size $r = 1$ GeV^{-1} (typical for exclusive J/ψ photoproduction) and different x values. (b) The (r-integrated) amplitude for exclusive J/ψ photoproduction as a function of b, for $W = 300$ GeV and $|t| = 0, 1, 2, 3, 4$ GeV^2.

In Fig. 7.25 the differential cross section $d\sigma/dt$ is shown as a function of the energy W in different bins of t for the case of the exclusive J/Ψ production. Again two different scenarios are shown, with unitarisation effects and with single Pomeron exchange. Already for small values of $|t| \sim 0.2$ GeV^2 and low values of electron energies there is a large discrepancy between the models. The LHeC simulated data still have very small errors in this regime, and can clearly distinguish between the different models. The differences are of course amplified for larger t and large energies. However the precision of the data deteriorates at large t.

Summarizing, it is clear that the precise measurements of large-$|t|$ exclusive J/ψ photoproduction at the LHeC would have significant sensitivity to unitarity effects.

Simulations of Deeply Virtual Compton Scattering at the LHeC

Simulations have been made of the DVCS measurement possibilities with the LHeC using the Monte Carlo generator, MILOU [301], in the 'FFS option', for which the DVCS cross section is estimated using the model of Frankfurt, Freund and Strikman [302]. A t-slope of $B = 6$ GeV^{-2} is assumed.

The $ep \to e\gamma p$ DVCS cross section is estimated in various scenarios for the electron beam energy and the statistical precision of the measurement is estimated for different integrated luminosity and detector acceptance choices. Detector acceptance cuts at either 1° or 10° are placed on the polar angle of the final state electron and photon. Based on experience with controlling backgrounds in HERA DVCS measurements [284, 285, 303], an additional cut is placed on the transverse momentum P_T^γ of the final state photon.

The acceptance restrictions on the scattered electron follow the same patterns as for the inclusive cross section (see Sec. 7.2.2). The photon P_T^γ cut is found to be a further important

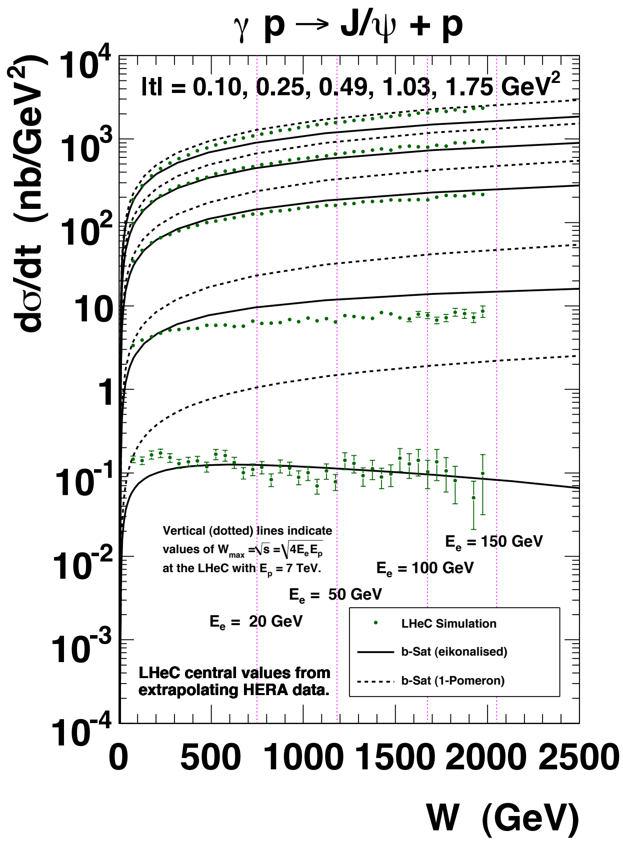

Figure 7.25: W-distributions of exclusive J/ψ photoproduction at the LHeC in bins of $t = 0.10, 0.20, 0.49, 1.03, 1.75$ GeV^2. The difference between the solid and dashed curves indicates the size of unitarity corrections compared to pseudodata from an LHeC simulation. The central values of the LHeC pseudodata points were obtained from a Gaussian distribution with the mean given by extrapolating a parameterization of HERA data and the standard deviation given by the statistical errors from the LHeC simulation with $E_e = 150$ GeV. The t-integrated cross section (σ) as a function of W for the HERA parameterization was obtained from a power-law fit to the data from both ZEUS [296] and H1 [283], then the t-distribution was assumed to behave as $\mathrm{d}\sigma/\mathrm{d}t = \sigma \cdot B_D \exp(-B_D|t|)$, with $B_D = [4.400 + 4 \cdot 0.137 \log(W/90 \text{ GeV})]$ GeV^{-2} obtained from a linear fit to the values of B_D versus W given by both ZEUS [296] and H1 [283].

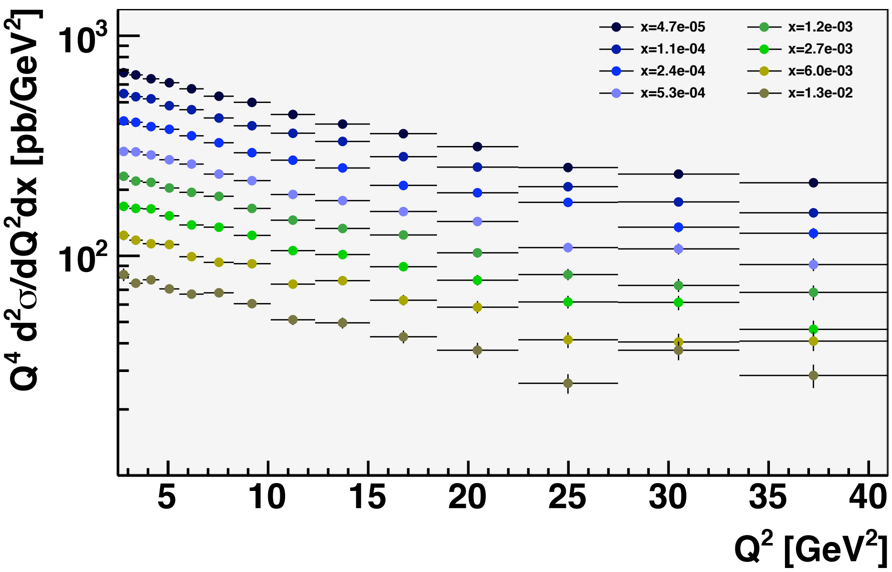

Figure 7.26: Simulated LHeC measurement of the DVCS cross section multiplied by Q^4 for different x values for a luminosity of 1 fb^{-1}, with $E_e = 50$ GeV, electron and photon acceptance extending to within 1° of the beampipe with a cut at $P_T^\gamma = 2$ GeV. Only statistical uncertainties are considered.

factor in the Q^2 acceptance, with measurements at $Q^2 < 20$ GeV^2 almost completely impossible for a cut at $P_T^\gamma > 5$ GeV, even in the scenario with detector acceptances reaching 1°. If the cut is relaxed to $P_T^\gamma > 2$ GeV, it opens the acceptances towards the lowest Q^2 and x values permitted by the electron acceptance.

A simulation of a possible LHeC DVCS measurement double differentially in x and Q^2 is shown in Fig. 7.26 for a modest luminosity scenario in which the electron beam energy is 50 GeV, the detector acceptance extends to 1° and photon measurements are possible down to $P_T^\gamma = 2$ GeV. High precision is possible throughout the region $2.5 < Q^2 < 40$ GeV^2 for x values extending down to $\sim 5 \times 10^{-5}$. DVCS therefore places constraints on the detector performance for low transverse momentum photons, which in practice translates into the electromagnetic calorimetry noise conditions and response linearity at low energies.

If the detector acceptance extends to only 10°, the P_T^γ cut no longer plays such an important role. Although the low Q^2 acceptance is lost in this scenario, the much larger luminosity will allow precise measurements for $Q^2 \gtrsim 50$ GeV^2, a region which is not well covered in the 1 degree acceptance scenario due to the small cross section. In the simulation shown in Fig. 7.27, a factor of 100 increase in luminosity is considered, resulting in precise measurements extending to $Q^2 > 500$ GeV^2, well beyond the range explored for DVCS or other GPD-sensitive processes to date.

Maximising the lepton beam energy potentially gives access to the largest W and smallest

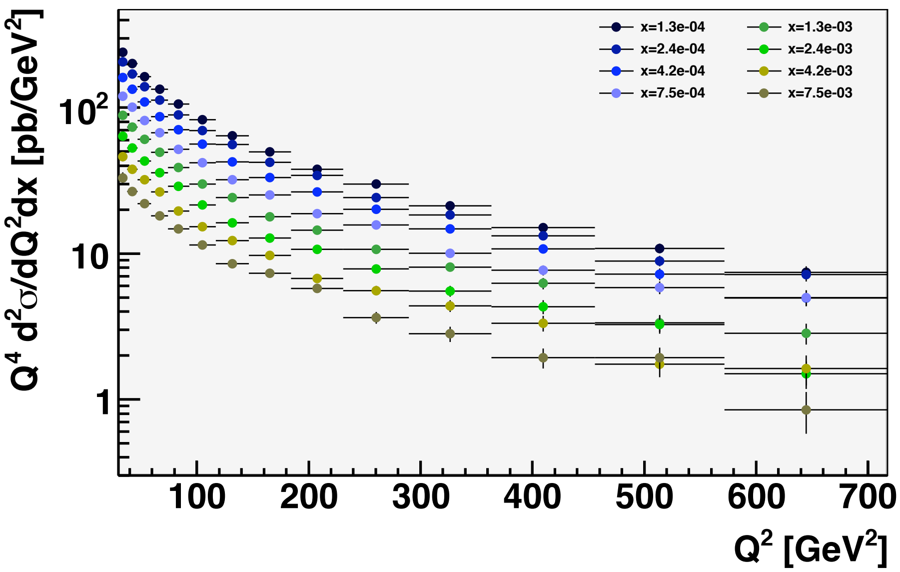

Figure 7.27: Simulated LHeC measurement of the DVCS cross section multiplied by Q^4 for different x values for a luminosity of 100 fb^{-1}, with $E_e = 50$ GeV, electron and photon acceptance extending to within 10° of the beampipe with a cut at $P_T^\gamma = 5$ GeV. Only statistical uncertainties are considered.

x values, provided the low P_T^γ region can be accessed. However, the higher beam lepton energy boosts the final state photon in the scattered lepton direction resulting in an additional acceptance limitation.

Further studies of this process will require a better understanding of the detector in order to estimate systematic uncertainties. A particularly interesting extension would be to investigate possible beam charge [284, 303] and polarisation asymmetry measurements at lower x or larger Q^2 than was possible at HERA. With the addition of such information, a full study of the potential of the LHeC to constrain GPDs could be performed.

Diffractive Vector Meson Production off Nuclei

Exclusive diffractive processes are similarly promising as a source of information on the gluon density in the nucleus. DIS off nuclei at small x can also be treated within the same theoretical framework making the comparisons with the proton case relatively straightforward. The interaction of the dipole with the nucleus can be viewed as a sum of dipole scatterings off the nucleons forming the nucleus. Nuclear effects can be incorporated into the dipole cross section by modifying the transverse gluon distribution and adding the corrections due to Glauber rescattering from multiple nucleons [193, 287].

There is one aspect of diffraction which is specific to nuclei that one should mention. The

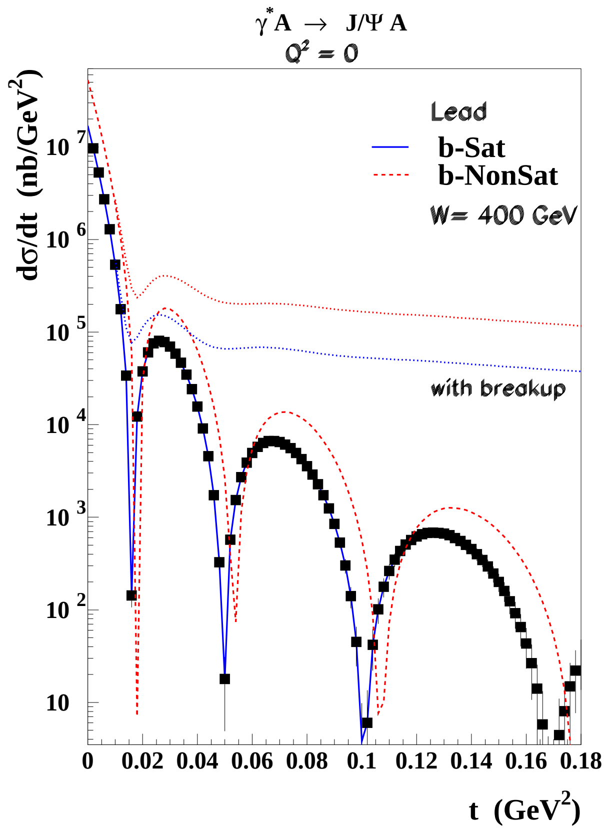

Figure 7.28: Differential cross section for diffractive production of J/Ψ on a lead nucleus for as a function of the momentum transfer $|t|$. Dashed-red and solid-blue lines correspond to the predictions on the coherent production without and with the saturation effects respectively. Dotted lines correspond to the predictions for the incoherent case.

structure of incoherent diffraction eA→eXY is more complex than with a proton target, and it can also be much more informative. In the case of a target nucleus, we expect the following qualitative changes in the t-dependence. First, the low-$|t|$ regime of coherent diffraction illustrated in Fig. **??** in which the nucleus scatters elastically and remains in its ground state, will be dominant up to a smaller value of $|t|$ (to about $|t| = 0.05$ GeV^2) compared to the proton case, reflecting the larger size of the nucleus. Then, the nucleus dissociative regime, see Fig. **??**, will consist on two parts: an intermediate regime in momentum transfer up to about 0.7 GeV^2 where the nucleus will predominantly break up into its constituents nucleons, and a large-$|t|$ regime where the nucleons inside the nucleus will also break up, implying - for instance - pion production in the Y system. While these are only qualitative expectations, it is crucial to study this aspect of diffraction quantitatively in order to complete our understanding of the structure of nuclei.

Fig. 7.28 shows the diffractive cross sections for exclusive J/Ψ production off a lead nucleus with (b-Sat) and without (b-NonSat) saturation effects. The figure shows the coherent and incoherent cross sections.

The cross section around $t \sim 0$ is dominated by coherent production. It can be easily related to the properties of dipole-nucleon interactions because all the nuclear effects can be absorbed into the nuclear wave functions and only the average gluon density of nucleus enters[6]. The t-averaged gluon density and the saturation effects can be studied here in a very clean way. Fig. 7.29 shows this cross sections for J/Ψ production as a function of W for different nuclei. The cross section varies substantially as a function of the $\gamma^* - p$ CMS energy W and the nuclear mass number A. It is also very sensitive to shadowing or saturation effects due to the fact that the differential cross section at $t = 0$ has a quadratic dependence on the gluon density and A. Due to this fact the ratio of the cross sections for nuclei and protons are roughly proportional to the ratios of the gluon densities squared. This has been exploited in the calculation [304] presented in Fig. 7.30 where the ratio R for the gluon densities squared is shown, with values consistent with that could be obtained from Fig. 7.29.

Therefore, a precise measurement of this cross section around $t = 0$ is an invaluable source of information on the gluon density and in particular on non-linear effects.

Another region of interest is the measurement at larger $|t|$, $|t| \gtrsim 0.15\text{GeV}^2$. Here the reaction is fully dominated by the incoherent processes in which the nucleus breaks up. The shadowing or saturation effects should be stronger in this region than in the coherent case [278] and the shape of the diffractive cross section should be only weakly sensitive to nuclear effects [287]. Finally, the intermediate region, between $|t| \sim 0.01$ GeV^2 and $|t| \sim 0.1$ GeV^2 is also very interesting because here the barely known gluonic nuclear effects can be studied.

7.2.4 Inclusive diffraction

Introduction to Diffractive Deep Inelastic Scattering

Approximately 10% of low-x DIS events are of the diffractive type, $ep \to eXp$, with the proton surviving the collision intact despite the large momentum transfer from the electron (Fig. 7.31). This process is usually interpreted as the diffractive dissociation of the exchanged virtual photon to produce any hadronic final state system X with mass much smaller than W and the same net quantum numbers as the exchanged photon ($J^{PC} = 1^{--}$). Due to the lack of colour flow, diffractive DIS events are characterised by a large gap in the rapidity distribution of final state hadrons between the scattered proton and the diffractive final state X.

Similar processes exist in electron-ion scattering, as has been discussed previously, where they can be sub-divided into fully coherent diffraction, where the nucleus stays intact ($eA \to eXA$) and incoherent diffraction, where the nucleons within the nucleus are resolved and the nucleus breaks up ($eA \to eXY$, Y being a nuclear excitation with the same quantum numbers as A).

Theoretically, rapidity gap production is usually described in terms of the exchange of a net colourless object in the t-channel, which is often referred to as a pomeron [305, 306]. In the simplest models [307, 308], this pomeron has a universal structure and its vertex couplings factorise, such that it is applicable for example to proton-(anti)proton scattering as well as DIS. One of the main achievements at HERA has been the development of an understanding

[6] Note that for this forward cross section the exact shape of the nuclear wave function is not important, in contrast to what happens with the t-distribution which reflects the functional form of the nuclear density.

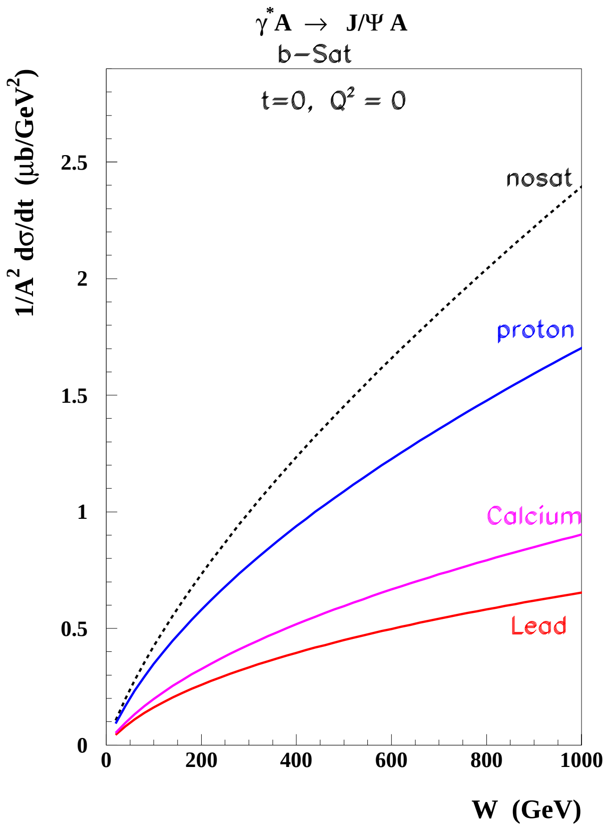

Figure 7.29: Energy dependence of the coherent photoproduction of the J/Ψ on a proton and different nuclei in the forward case $t = 0$. The cross sections are normalized by a factor $1/A^2$ as corresponding to the dependence on the gluon density squared if no nuclear effects are present.

of diffractive DIS in terms of parton dynamics and QCD [309]. Events are selected using the experimental signatures of either a leading proton [310–312] or the presence of a large rapidity gap [311, 313]. The factorisable pomeron picture has proved remarkably successful for the description of most of these data.

The kinematic variables used to describe diffractive DIS are illustrated in Fig. 7.31. In addition to x and Q^2, two additional invariants are introduced: the squared four-momentum transfer t at the hadronic vertex ($t < 0$), and the mass M_X of the diffractive final state. In practice, the variable M_X is often replaced by

$$\beta \; = \; \frac{Q^2}{Q^2 + M_X^2 - t} \; . \tag{7.13}$$

Small values of β refer to events with diffractive masses much bigger than the photon virtuality, while values of β close to unity refer to the opposite situation. In models based on a factorisable

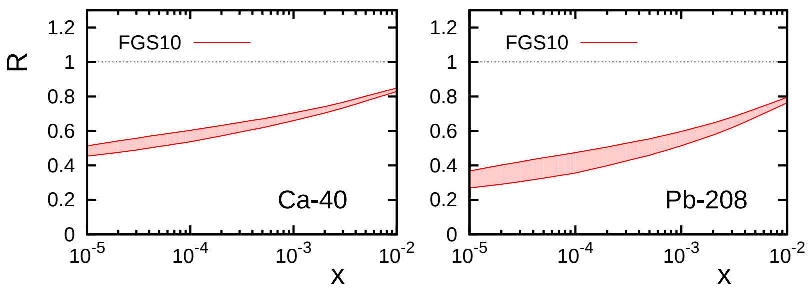

Figure 7.30: The x dependence of the ratio of the gluon densities squared, from nuclei to protons (rescaled by A^2), for the scale corresponding to the exclusive production of the J/Ψ. Models taken from [304].

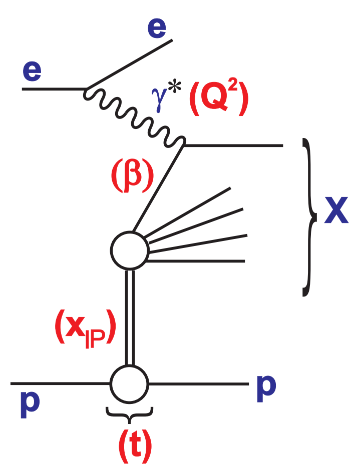

Figure 7.31: Illustration of the kinematic variables used to describe the diffractive DIS process $ep \to eXp$.

pomeron, β may be interpreted as the fraction of the pomeron longitudinal momentum which is carried by the struck parton. The variable

$$x_{\mathbb{P}} = \frac{x}{\beta} = \frac{Q^2 + M_X^2 - t}{Q^2 + W^2 - M^2} \,, \tag{7.14}$$

with M the nucleon mass, is then interpreted as the longitudinal momentum fraction of the Pomeron with respect to the incoming proton or ion. It also characterises the size of the rapidity gap as $\Delta\eta \simeq \ln(1/x_{\mathbb{P}})$.

Measuring Diffractive Deep Inelastic Scattering at the LHeC

Diffractive DIS can be studied in a substantially increased kinematic range at the LHeC, which will allow a whole new level of investigations of the factorization properties of inclusive diffraction, will lead to new insights into low-x dynamics and will provide a subset of final states with known quantum numbers for use in searches for new physics and elsewhere.

As shown in [174], collinear QCD factorization holds in the leading-twist approximation in diffractive DIS and can be used to define diffractive parton distribution functions for the proton or ion. That is, within the collinear framework, the diffractive structure functions [314] can be expressed as convolutions of the appropriate coefficient functions with diffractive quark and gluon distribution functions, which in general depend on all of β , Q^2, $x_{\mathbb{P}}$ and t. The diffractive parton distribution functions (DPDFs) are physically interpreted as probabilities for finding a parton with a small fraction of the proton momentum $x = \beta x_{\mathbb{P}}$, under the condition that the proton stays intact with a final state four-momentum which is specified up to an azimuthal angle by $x_{\mathbb{P}}$ and t. The DPDFs may then be evolved in Q^2 with the DGLAP evolution equations, with β playing the role of the Bjorken variable in diffractive DIS. The other two variables $x_{\mathbb{P}}$ and t play the role of external parameters to the DGLAP evolution.

In various extractions using HERA DDIS data [313, 315–317] the DPDFs have been found to be dominated by gluons. Proton vertex factorisation holds to good approximation, such that the DPDFs vary only in normalisation with the four-momentum of the final state proton, the normalisation being well modelled using Regge phenomenology [306].

The LHeC will offer the opportunity to study diffractive DIS in an unprecedented kinematic range. The diffractive kinematic plane is illustrated in Fig. 7.32 for two different values of the Pomeron momentum fraction, $x_{\mathbb{P}} = 0.01$ and $x_{\mathbb{P}} = 0.0001$. In each plot, accessible kinematic ranges are shown for three different electron energies in collision with the 7 TeV proton beam. Figure 7.32a corresponds to the coverage that will be possible based on leading proton detection (see Chapter 13). Figure 7.32b is more represetative of possibilities using the large rapidity gap technique (see the following). It is clear that the LHeC will have a much increased reach compared to HERA towards low values of $x_{\mathbb{P}}$, where the interpretation of diffractive events is not complicated by the presence of sub-leading meson exchanges, rapidity gaps are large and diffractive event selection systematics are correspondingly small. The range in the fractional struck quark momentum β extends by a factor of around 20 below that accessible at HERA.

Figure 7.33 indicates the achievable kinematic range of diffractive DIS measurements at the LHeC for the example of a 150 GeV electron beam combining large rapidity gap and proton tagging acceptance, compared with an estimation of the final HERA performance. For ease of illustration, a binning scheme is chosen in which the β dependence is emphasized and very large bins in $x_{\mathbb{P}}$ and Q^2 are taken. There is a large difference between the kinematically accessible ranges with backward acceptance cuts of 1° and 10°. Statistical uncertainties are typically much smaller than 1% for a luminosity of 1 fb^{-1}, so a much finer binning is possible if required. The data points are plotted according to the H1 Fit B DPDF predictions [313], which amounts to a crude extrapolation based on dependences in the HERA range.

Systematic uncertainties are difficult to estimate without a detailed knowledge of the forward detectors and their acceptances. At HERA, sub-5% systematics have been achieved in the bulk of the phase space and it is likely that the LHeC could do at least as well.

The limitations in the kinematic range accessible with the large rapidity gap technique are investigated in Fig. 7.34. This shows the correlation between $x_{\mathbb{P}}$ and the pseudorapidity $\eta_{\max}$ of the most forward particle in the hadronic final state system X, in simulated samples with LHeC and HERA beam energies, according to the RAPGAP event generator [18]. This correlation depends only on the proton beam energy and is thus the same for all LHeC running scenarios. At HERA, a cut at $\eta_{\max} \sim 3.2$ has been used to select diffractive events. Assuming LHeC forward instrumentation extending to around $\theta = 1^\circ$, a cut at $\eta_{\max} = 5$ may be possible, which would allow measurements to be made comfortably up to $x_{\mathbb{P}} \sim 0.001$, with some limited sensitivity at larger $x_{\mathbb{P}}$, a region where the proton tagging acceptance takes over (see Chapter 13). The two

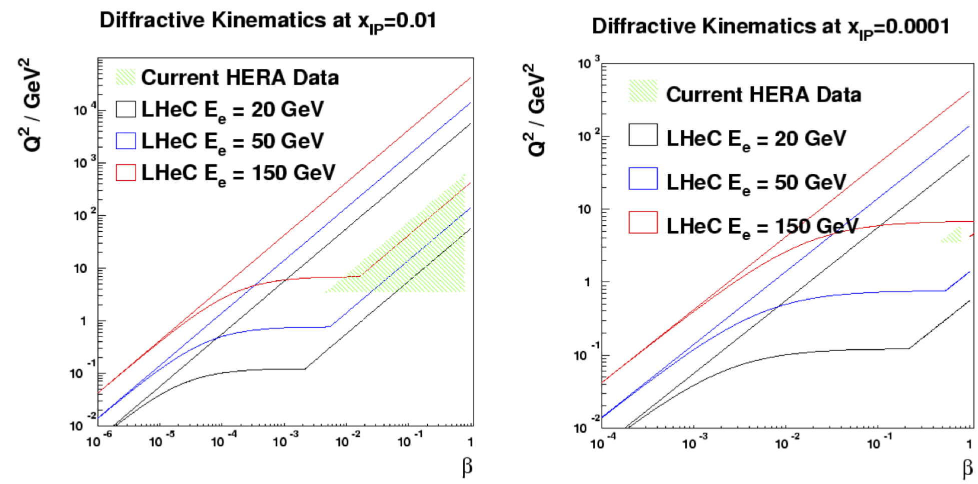

Figure 7.32: Kinematic ranges in Q^2 and β of HERA and of the LHeC for different electron energies $E_e = 20, 50, 150$ GeV at $x_{\mathbb{P}} = 0.01$ (left plot), and $x_{\mathbb{P}} = 0.0001$ (right plot). In both cases, 1° acceptance is assumed for the scattered electron and the typical experimental restriction $y > 0.01$ is imposed. No rapidity gap restrictions are applied.

methods are thus complementary, and offer some common acceptance in an overlap region of $x_{\mathbb{P}}$, which redundancy could be used for cross-calibration of the two methods and their systematics.

Diffractive Final States and Parton Densities

The previously unexplored diffractive DIS region of very low β is of particular interest. Here, diffractively produced systems will be created with unprecedented invariant masses. Figure 7.35 shows a comparison between HERA and the LHeC in terms of the M_X distribution which could be produced in diffractive processes with $x_{I\!P} < 0.05$ (using the RAPGAP Monte Carlo model [18]). Diffractive masses up to several hundred GeV are accessible with reasonable rates, such that diffractive final states involving beauty quarks and W and Z bosons, or even exotic states with 1^- quantum numbers, could be produced.

Large improvements in DPDFs are likely to be possible from NLO DGLAP fits to diffractive structure function data. In addition to the extended phase space in β, the extension of the kinematic range towards larger Q^2 increases the lever-arm for extracting the diffractive gluon density and opens the possibility of significant weak gauge boson exchange, which would allow a quark flavour decomposition for the first time.

Proton vertex factorisation can be tested precisely by comparing the LHeC β and Q^2 dependences at different small $x_{\mathbb{P}}$ values in their considerable regions of overlap. The production of dijets or heavy quarks as components of the diffractive system X will provide a means of testing QCD collinear factorisation. These processes are driven by boson-gluon fusion ($\gamma^* g \to q\bar{q}$) and thus provide complementary sensitivity to the diffractive gluon density to be compared with that from the scaling violations of the inclusive cross section. Factorisation tests of this sort have been carried out on many occasions at HERA, with NLO calculations based on DPDFs predicting jet and heavy flavour cross sections which are in good agreement with data [318,319].

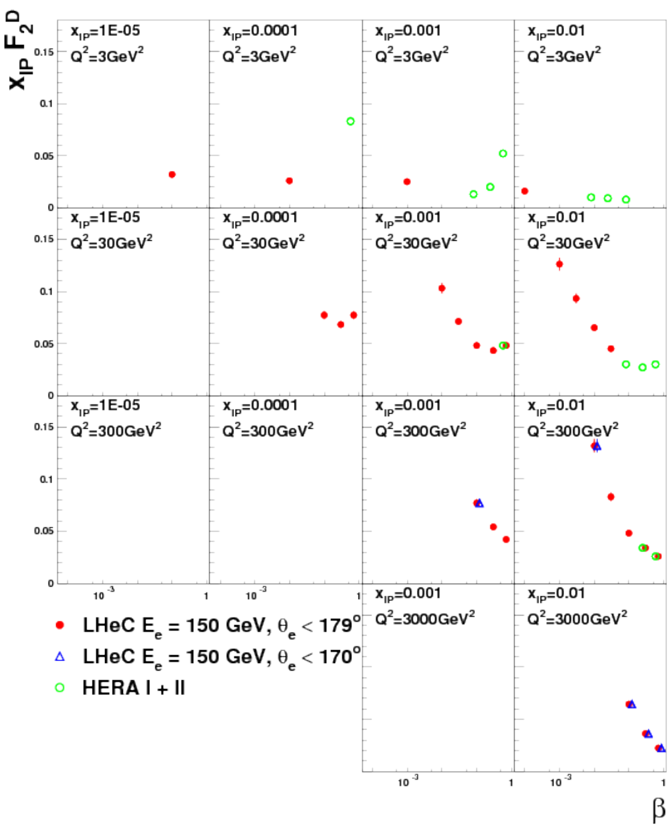

Figure 7.33: Simulation of a possible LHeC measurement of the diffractive structure function, F_2^D, compared with an estimate of the optimum results achievable at HERA using the full luminosity for a single experiment (500 pb^{-1}). The loss of kinematic region if the LHeC scattered electron acceptance extends to within 10° of the beam-pipe, rather than 1° is also illustrated.

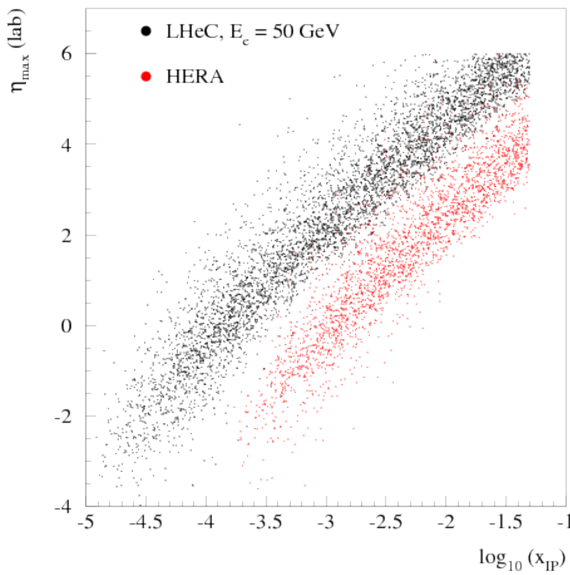

Figure 7.34: Comparison of the correlation between the rapidity gap selection variable, $\eta_{\max}$ and $x_{\mathbb{P}}$ at HERA and at the LHeC, using events simulated with the RAPGAP Monte Carlo generator.

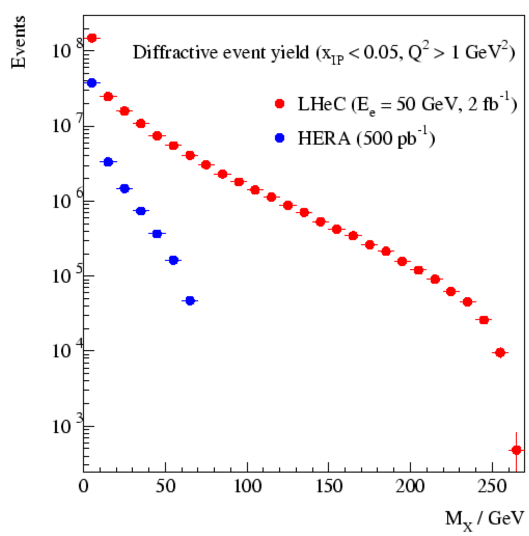

Figure 7.35: Simulated distributions in the invariant mass M_X according to the RAPGAP Monte Carlo model for samples of events obtainable with $x_{\mathbb{P}} < 0.05$ at HERA (full luminosity for a single experiment) and the LHeC (one year running at high acceptance).

However, due to the relatively small accessible jet transverse momenta, the precision is limited by scale uncertainties on the theoretical predictions. At the LHeC, much larger diffractive jet transverse momenta are measurable ($p_T \lesssim M_X/2$), which should lead to much more precise tests [320].

In contrast to leading proton production, the production of leading neutrons in DIS ($ep \to eXn$) requires the exchange of a net isovector system. Data from HERA have supported the view that this process is driven dominantly by charged pion exchange over a wide range of neutron energies [321]. With the planned emphasis on zero degree calorimetry for leading neutron measurements (see Chapter. 13), LHeC data will thus constrain the structure of the pion at much lower x and larger Q^2 values than has been possible hitherto. Note that the combination of rapidity gap detection and zero degree calorimetry offers the possibility of disentangling coherent from incoherent nuclear diffraction.

Diffractive DIS, Dipole Models and Sensitivity to Non-linear Effects

Diffractive DIS at the LHeC will give us an opportunity to test the predictions of collinear factorisation and the possible onset of non-linear or higher-twist effects in the evolution. Of particular importance is the semi-hard regime $Q^2 < 10$ GeV^2 and x as small as possible. It is possible that the non-linear saturation regime will be easier to reach with diffractive than with inclusive measurements, since diffractive processes are mostly sensitive to quantum fluctuations in the proton wave function that have a virtuality of order of the saturation scale Q_s^2, instead of Q^2. As a result, power corrections (not the generic Λ_{QCD}^2/Q^2 corrections, but rather the sub-class of them of order Q_s^2/Q^2) are expected to come into play starting from a higher value of Q^2 in diffractive than in inclusive DIS. Indeed, there is already a hint of this at HERA: collinear factorization starts to fail below about 3 GeV^2 in the case of F_2 [202], while it breaks down already around 8 GeV^2 in the case of F_2^D [313]. This fact can alternatively be observed in the feature that models which in principle should only work for small Q^2, can in practice be used up to larger Q^2 for diffractive than for inclusive observables (see e.g. [141]).

With the sort of measurement precision for F_2^D possible at the LHeC, it ought to be possible to distinguish between different models, as illustrated in Fig. 7.36. For the simulated data shown here, a conservative situation is assumed, in which the electron beam energy is 50 GeV and the rapidity gap method is used with modest forward detector requirements such that the highest $x_{\mathbb{P}}$ bin is at 0.001. H1 Fit B [313] extrapolations (as in Fig. 7.33) are compared with the "b-sat" [193, 194] and bCGC [322] dipole models. Photon fluctuations to $q\bar{q}g$ states are included in addition to the usual $q\bar{q}$ dipoles used to describe inclusive and vector meson cross sections at low x. Both dipole models differ substantially from the H1 Fit B extrapolation. The LHeC simulated precision and kinematic range are sufficient to distinguish between range of models with and without saturation effects, and also between different models which incorporate saturation.

Predicting nuclear shadowing from inclusive diffraction in ep

The connection between nuclear shadowing and diffraction was established a long time ago [139]. Its key approximation is that the nucleus can be described as a dilute system of nucleons in the nucleus rest frame. The accuracy of such approximation for hadron-nucleus interactions is on the level of a few %, which reflects the small admixture of non-nucleonic degrees of freedom in nuclei and the small off-shellness of the nucleons in nuclei as compared to the soft strong

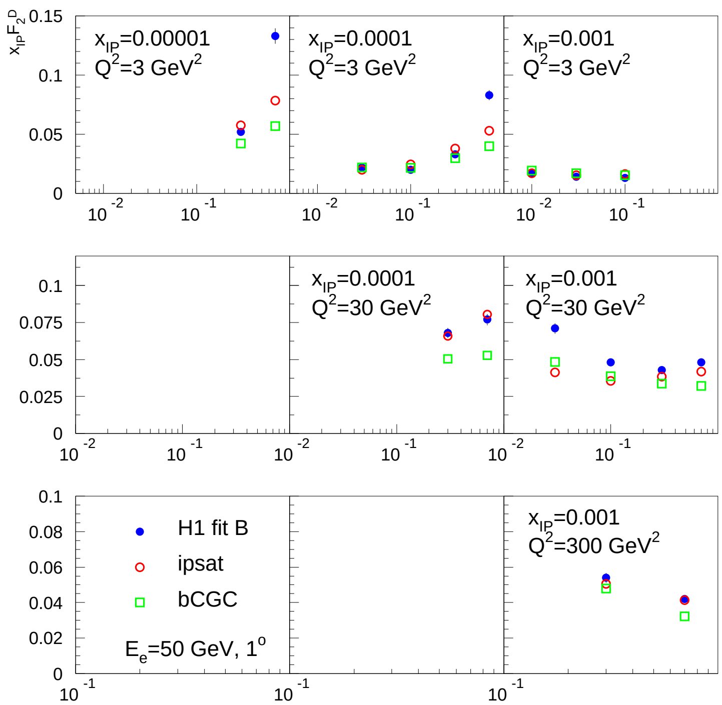

Figure 7.36: Simulated F_2^D measurements in selected $x_{\mathbb{P}}$, β and Q^2 bins. An extrapolation of the H1 Fit B DPDF fit to HERA data is compared with two different implementations of the dipole model, which include $q\bar{q}g$ photon fluctuations in addition to $q\bar{q}$ ones.

interaction scale. Gribov's result can be derived using the AGK cutting rules [323] and hence it is a manifestation of unitarity [324, 325]. The formalism can be used to calculate directly cross sections of $\gamma(\gamma^*)$-nucleus scattering for the interaction with $N = 2$ nucleons, but has to be supplemented by additional considerations to account for the contribution of the interactions with $N \geq 3$ nucleons.

In this context, nuclear PDFs at small x can be calculated [324, 325] combining unitarity relations for different cuts of the shadowing diagrams corresponding to diffractive and inelastic final states, with the QCD factorization theorem for hard diffraction [174]. A *model-independent* expression for the nuclear PDF at fixed impact parameter b, valid for the case $N = 2$ [324], reads:

$$\begin{aligned}
\Delta\left[x f_{j/A}(x,Q^2,b)\right] &= x f_{j/N}(x,Q^2,b) - x f_{j/A}(x,Q^2,b) \\
&= 8\pi A(A-1)\Re e\left[\frac{(1-i\eta)^2}{1+\eta^2}\int_x^{0.1} dx_{\mathbb{P}}\beta f_j^{D(4)}(\beta,Q^2,x_{\mathbb{P}},t_{\min})\right. \\
&\times \left.\int_{-\infty}^{\infty} dz_1 \int_{z_1}^{\infty} dz_2\, \rho_A(\mathbf{b},z_1)\rho_A(\mathbf{b},z_2) e^{i(z_1-z_2)x_{\mathbb{P}} m_N}\right], \qquad (7.15)
\end{aligned}$$

where $f_{j/A}(x,Q^2), f_{j/N}(x,Q^2)$ are nuclear and nucleon PDFs respectively, $f_j^{D(4)}(\beta,Q^2,x_{\mathbb{P}},t_{\min})$ are diffractive PDFs, $\eta = \Re e\, A^{diff}/\Im m\, A^{diff} \approx 0.17$, $\rho_A(r)$ is the nuclear matter density, and $t_{\min} = -m_N^2 x_{\mathbb{P}}^2$ with m_N the nucleon mass. Eq. (7.15) satisfies the QCD evolution equations to all orders in α_s. Numerical studies indicate that the dominant contribution to the shadowing probed by present experiments - corresponding to not very small x - comes from the region of relatively large β, corresponding to rapidity intervals of length ≤ 3 for which small-x approximations which involve summation of $\ln x$ terms are not applicable.

In Eq. (7.15), the interaction of different configurations of the hard probe (e.g. $q\bar{q}$, $q\bar{q}g$, vector meson resonances,...) are encoded in $f_j^{D(4)}(\beta,Q^2,x_{\mathbb{P}},t_{\min})$. Furthermore, for the case of more than $N = 2$ nucleons, there are two or more intermediate nucleon diffractive states which may be different and thus result in a different interaction between the the virtual photon and the nucleus. Therefore the interaction of the hard probe with $N \geq 3$ nucleons is sensitive to finer details of the diffractive dynamics, namely the interplay between the interactions of the hard probe with N nucleons with different cross sections. This (colour) fluctuation effect is analogous to the inelastic shadowing phenomenon for hA scattering, with the important difference that the dispersion of the interaction cross sections for the configurations in the projectile is much smaller in the hadronic case than in DIS.

In order to estimate such effect one should note that, experimentally, the energy dependence of hard diffraction is close to that of the soft Pomeron dynamics (the soft Pomeron intercept intercept $\alpha_{\mathbb{P}} \approx 1.11$) with the hard Pomeron contribution ($\alpha_{\mathbb{P}} \approx 1.25$) being a small correction. This fact indicates that hadron-like (aligned jet) configurations [326], evolved via DGLAP evolution to large Q^2, dominate hard diffraction in DIS, while point-like configurations give an important, and increasing with Q^2, contribution to small-x PDFs. This reduces the uncertainties in the treatment of $N \geq 3$ contributions [249, 304]. Calculations show that the difference between two extreme scenarios of colour fluctuations is $\leq 20\%$ for $A \sim 200$ and much smaller for lighter nuclei, see the two FGS10 curves in Figs. 7.11 and 7.17. Besides, fluctuations tend to reduce somewhat the shadowing as compared to the approximations neglecting them [142, 324, 327, 328], compare the FGS10 results in Fig. 7.17 left with those named AKST. Note that the gluon density, see Fig. 7.11 and Fig. 7.17 right, is more sensitive to the magnitude of fluctuations than F_2.

Finally, the AGK technique also allows to calculate nuclear diffractive PDFs, see below, and fluctuations of multiplicity in nondiffractive DIS [304, 324, 329]. Both observables turn out to be sensitive to the pattern of colour fluctuations.

Predictions for inclusive diffraction on nuclear targets

Diffractive DIS events were first discovered in ep collisions at the HERA collider. Since no eA collider has ever been built, diffraction in eA has simply never been measured. Thus, DDIS off nuclei at the LHeC will be a completely unexplored territory throughout the whole kinematic domain accessed, implying a huge discovery potential.

In spite of this lack of experimental information on DDIS off nuclei, we have expectations, based on our current understanding of QCD, of how it should look like. For instance, the theory of nuclear shadowing allows to construct nuclear diffractive PDFs for large Q^2 (see the previous item) while, within the Color Glass Condensate framework, nuclear diffractive structure functions can be predicted at small x. Depending on kinematics, different patterns of nuclear shadowing or antishadowing as a function of β and $x_{\mathbb{P}}$ are expected. This is just one example, out of many, of what should be checked with an eA collider. Others are the impact parameter dependence introduced in the models, or the relation between nuclear shadowing and diffraction in ep which relies on what we know on DDIS from HERA. Therefore, in the larger kinematical domain accessible at the LHeC there are many things to discover about the structure of nuclei with diffractive measurements.

Predictions from a variety of models for nuclear coherent diffraction are shown in Figs. 7.37 and 7.38. Models are FGS10 [304] and KLMV [330, 331]. Both plots show $x_{IP}F_2^D$ as a function of β in bins of Q^2 and x_{IP}. Statistical and systematic errors are added in quadrature, with systematic errors are estimated to be on the level of 5%. The models give very different predictions both in absolute value and in their detailed dependence on x_{IP} and Q^2.

Also shown in Fig. 7.39 are the diffractive-to-total ratios of the structure functions as a function of the collision energy W. It was demonstrated in [176] that the constancy of this ratio with energy can be naturally explained in the models which include saturation effects, because in the black disk regime the ratio of the diffractive to total cross sections tends to a constant value. At fixed impact parameter the ratio should be $\leq 50\%$, but the integration in impact parameter results in a smaller value. HERA data showed a relative constancy of this ratio that could be easily obtained within the GBW model [176]. In Fig.. 7.39 these ratios for proton and for lead (in the coherent case) are shown as a function of the c.m. γ^*-nucleon energy W. Within the given energy range the models predict a slight variation with energy. Note however the rather substantial difference between predictions coming from the different models. The uncertainty of modeling the impact parameter is one of the main sources of these differences.

7.2.5 Jet and multi-jet observables, parton dynamics and fragmentation

Introduction

Inclusive measurements provide essential information about the integrated distributions of partons in a proton. However, as was discussed in previous sections, more exclusive measurements

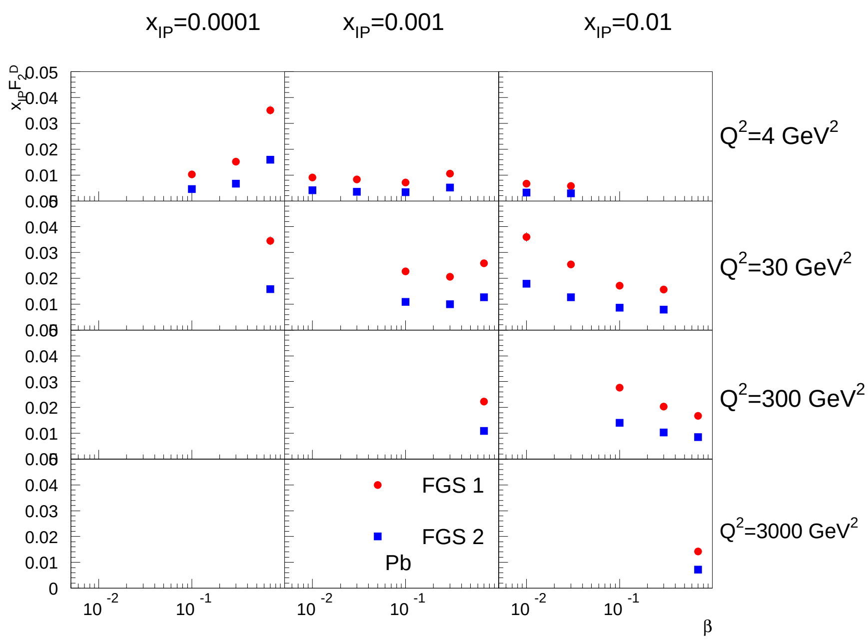

Figure 7.37: Diffractive structure function $x_{\mathbb{P}}F_2^D$ for Pb in bins of Q^2 and $x_{\mathbb{P}}$ as a function of β. Model calculations are taken from [304].

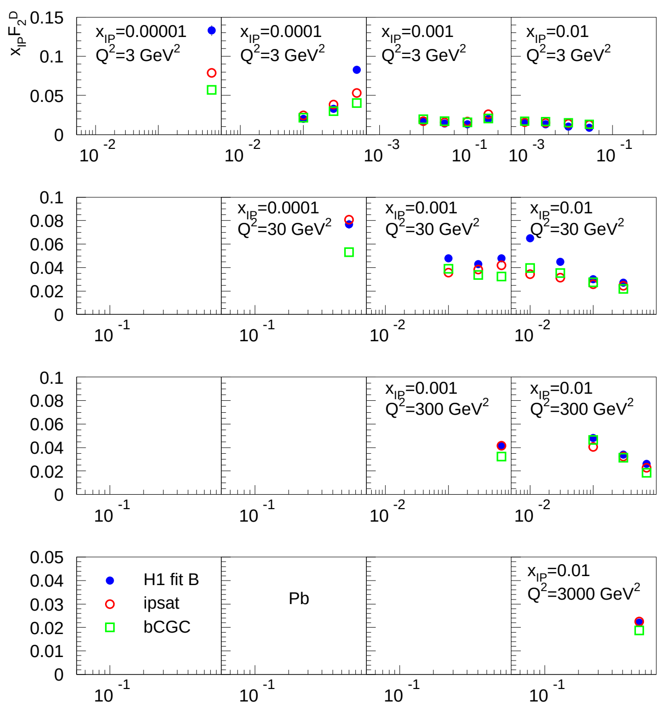

Figure 7.38: Diffractive structure function $x_{\mathbb{P}}F_2^D$ for Pb in bins of Q^2 and $x_{\mathbb{P}}$ as a function of β. Model calculations are based on the dipole framework [330, 331].

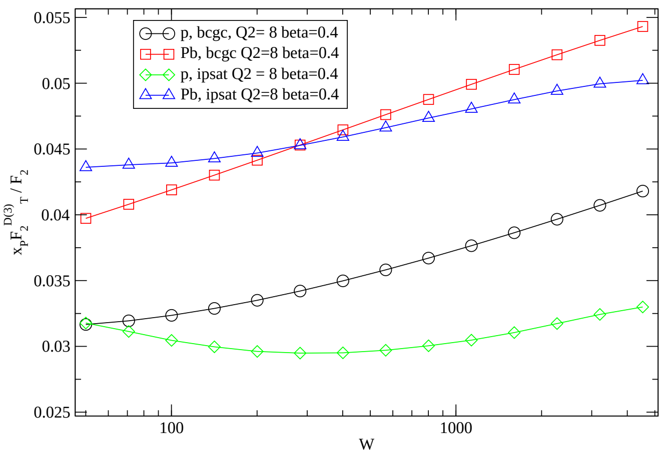

Figure 7.39: Ratio of the diffractive structure function $x_{\mathbb{P}} F_2^D$ to the inclusive structure function in p and Pb for fixed values of Q^2 and β as a function of the energy W. Model calculations are based on the dipole framework [330, 331].

are needed to pin down the essential details of the small-x dynamics. For example, a unique prediction of the BFKL framework at small x is the diffusion of the transverse momenta of the emitted partons between the photon and the proton: In the standard collinear approach with integrated parton densities the information about the transverse momentum is not accessible. It can be however recovered within a different framework which utilizes unintegrated parton distribution functions. Unintegrated parton distribution functions are natural in the BFKL approach to small-x physics. A general, fundamental expectation is that as x decreases, the distribution in transverse momentum of the emitted partons broadens. Thus the resulting effect is the characteristic diffusion of the transverse momenta.

The specific parton dynamics can be tested by a number of exclusive measurements. These in turn can provide valuable information about the distribution of transverse momentum in the proton. As discussed in [332], for many inclusive observables the collinear approximation with integrated parton distribution functions is completely insufficient, and even just including parton transverse momentum effects may not be sufficient. In DIS, for example, processes needing unintegrated distributions include the transverse momentum distribution of heavy quarks. Similar problems are encountered in hadron collisions when studying heavy quark and Higgs production. The natural framework using unintegrated parton distribution functions (updfs) gives a much more reliable description. Lowest-order calculations in the framework with updfs provide a much more realistic description of cross sections concerning kinematics. This may well lead to NLO and higher corrections being much smaller numerically than they typically are at present in standard collinear factorization, since the LO description is better.

This approach however calls for a precise measurements of a variety of relatively exclusive processes in a wide kinematic range. As we shall see below, measurements of dijets, forward jets and particles, as well as transverse energy flow, are compulsory to constrain the unintegrated parton distributions and will give a valuable information about parton dynamics at small x. While we will discuss the case of DIS on a proton, all conclusions can be paralleled for DIS on nuclei.

Unintegrated PDFs

The standard integrated parton densities are functions of the longitudinal momentum fraction of a parton relative to its parent hadron, with an integral over the parton transverse momentum. In contrast, unintegrated, or transverse-momentum-dependent (TMD), parton densities depend on both parton momentum fraction and parton transverse momentum. Processes for which unintegrated densities are natural include the Drell-Yan process (and its generalization to Higgs production), and semi-inclusive DIS (SIDIS). In SIDIS, we need TMD fragmentation functions as well as TMD parton densities.

In the literature there are several apparently different approaches to TMD parton densities, with varying degrees of explicitness in the definitions and derivations.

- The CSS approach [333–336] and some further developments [337].
- The CCFM approach [338–341] for small x.
- Related BFKL associated works [156, 342].

Central to this subject is the concrete definition of TMD densities, and complications arise because QCD is a gauge theory. A natural initial definition uses light-front quantization: the unintegrated density of parton j in hadron h would be

$$f_{j/h}(x, \boldsymbol{k}_\perp) \stackrel{?}{=} \frac{1}{2x(2\pi)^3} \sum_\lambda \frac{\langle P, h| b^\dagger_{k,\lambda,j} b_{k,\lambda,j} |P, h\rangle_{\mathrm{c}}}{\langle P, h|P, h\rangle}\,, \tag{7.16}$$

where $b_{k,\lambda,j}$ and $b^\dagger_{k,\lambda,j}$ are light-front annihilation and creation operators, j and λ label parton flavor and helicity, while $k = (k^+, \boldsymbol{k}_\perp)$ is its momentum, and only connected graphs 'c' are considered. The '?' over the equality sign warns that the formula does not apply literally in QCD. Expressing $b_{k,\lambda,j}$ and $b^\dagger_{k,\lambda,j}$ in terms of fields gives the TMD density as the Fourier transform of a light-front parton correlator. For example for a quark

$$f_j(x, \boldsymbol{k}_\perp) \stackrel{?}{=} \int \frac{\mathrm{d}w^- \, \mathrm{d}^2\boldsymbol{w}_\perp}{(2\pi)^3} \, e^{-ixP^+w^- + i\boldsymbol{k}_\perp\cdot\boldsymbol{w}_\perp} \, \langle P| \, \overline{\psi}_j(0, w^-, \boldsymbol{w}_\perp) \, \frac{\gamma^+}{2} \, \psi_j(0) \, |P\rangle_{\mathrm{c}}\,. \tag{7.17}$$

One can similarly define a TMD fragmentation function [334] $d_{h/j}(z, \boldsymbol{p}_\perp)$, for the probability density of final-state hadron h in an outgoing parton j.

The corresponding factorization formula for SIDIS $e + A(P_A) \to e + B(p_B) + X$ is [337]

$$\frac{\mathrm{d}\sigma}{\mathrm{d}x \, \mathrm{d}Q^2 \, \mathrm{d}z \, \mathrm{d}^2\boldsymbol{P}_{B\,\perp}} = \sum_j \int \mathrm{d}^2\boldsymbol{k}_\perp \, H_j f_{j/A}(x, \boldsymbol{k}_\perp) d_{B/j}(z, \boldsymbol{p}_{B\,\perp} + z\boldsymbol{k}_\perp), \tag{7.18}$$

where z and $\boldsymbol{P}_{B\,\perp}$ are the fractional longitudinal momentum and the transverse momentum of the detected hadron relative to the simplest parton-model calculation of the outgoing jet, while H_j is the hard-scattering factor for electron-quark elastic scattering; see Fig. 7.40(a). In the fragmentation function in Eq. (7.18), the use of $z\boldsymbol{k}_\perp$ with its factor of z is because the transverse-momentum argument of the fragmentation function is a transverse momentum of the outgoing hadron relative to the parton initiating the jet, whereas $\boldsymbol{k}_\perp$ is the transverse momentum of a parton relative to a hadron.

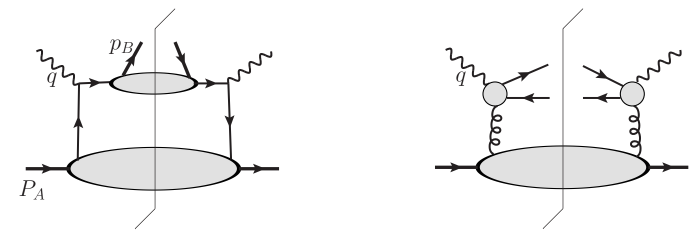

(a) (b)

Figure 7.40: (a) Parton model factorization for SIDIS cross section. (b) Factorization for high-energy $q\bar{q}$ photoproduction.

The most obvious way of applying (7.17) in QCD is to define the operators in light-cone gauge $A^+ = 0$, or, equivalently, to attach Wilson lines to the quark fields with a light-like direction for the Wilson lines. One minor problem in QCD is that, because of infinite wave function, the exact probability interpretation of parton densities cannot be maintained.

A much harder problem occurs because QCD is a gauge theory. Evaluating TMD densities defined by (7.17) in light-cone gauge gives divergences from where internal gluons have infinite negative rapidity [333]. These cancel only in the integrated density. The physical problem is that any colored parton entering (or leaving) the hard scattering is accompanied by a cloud of soft gluons, and the soft gluons of a given transverse momentum are distributed uniformly in rapidity. A parton density defined in light-cone gauge corresponds to the asymptotic situation of infinite available rapidity.

A quark in a realizable hard scattering can be considered as having a transverse recoil against the soft glue, but with a physically restricted range of rapidity. So a proper definition of a TMD density must implement a rapidity cutoff on gluon momenta. Evolution equations must take into account the rapidity cutoff. The CSS formalism [333] has an explicit form of the rapidity cutoff and an equation for dependence of TMD functions on the cutoff. But in any alternative formalism the need in the definitions for a cutoff on rapidity divergences is non-negotiable.

Parton densities and fragmentation functions are only useful because they appear in factorization theorems, so a useful definition must allow useful factorization theorems to be formulated and derived. An improved definition involving Wilson line operators has recently been given in [343]; see also [344].

A second train of argument leads to a related kind of factorization (the so-called $k_\perp$-factorization) for processes at small x [163]. A classic process is photo- or electro-production of charm pairs $\gamma(p_1) + h(p_2) \to Q(p_3) + \bar{Q}(p_4) + X$, for which $k_\perp$-factorization has the form

$$4M^2\sigma_{\gamma g}(\rho, M^2/Q_0^2) = \int \mathrm{d}^2\boldsymbol{k}_\perp \int_0^1 \frac{\mathrm{d}z}{z}\hat{\sigma}(\rho/z, \boldsymbol{k}_\perp^2/M^2) f_{g/h}(x, \boldsymbol{k}_\perp), \tag{7.19}$$

see Fig. 7.40(b). Here $\rho = M^2/(p_1+p_2)^2 \ll 1$, and M is the mass of the heavy quark. The corresponding definition of the TMD gluon density [338] is said to use light-cone gauge, but there is in fact a hidden rapidity cutoff resulting from the use of the BFKL formalism.

Although both (7.18) and (7.19) use $k_\perp$-dependent parton densities, there are important differences. In (7.19), the hard scattering $\hat{\sigma}$ has the incoming gluon *off*-shell, whereas in (7.18), the hard scattering H_j uses on-shell partons. This is associated with a substantial difference in the kinematics. In (7.18) for SIDIS, the transverse momenta of the partons relative to their hadrons are less than Q, which allows the neglect of parton virtuality in the hard scattering. This approximation fails at large partonic transverse momentum, $\boldsymbol{k}_\perp \sim Q$, but there ordinary collinear factorization is valid. So the factorization formula is readily corrected, by adding a suitable matching term [333].

In contrast, in the small-x formula (7.19), the gluon transverse momentum is comparable with the hard scale M. So it is not appropriate to neglect $\boldsymbol{k}_\perp$ with respect to M, and the hard scattering is computed with an off-shell gluon. Factorization is actually obtained from BFKL physics, where the gluons in Fig. 7.40(b) couple the charm quark subgraph to a subgraph where the lines have much larger rapidity.

The evolution equation of the CS-style TMD functions used in (7.18) gives the dependence of the TMD functions on the rapidity difference between the hadron and the virtual photon momenta. The results for TMD functions and for the cross sections can finally be obtained [337] in terms of (a) ordinary integrated parton densities and fragmentation functions, (b) perturbatively calculable quantities, and (c) a restricted set of non-perturbative quantities. The most important of these non-perturbative quantities is the distribution in recoil transverse momentum per unit rapidity against emission of soft interacting glue which is exponentiated after evolution. Importantly, it is independent of x and z, and it is universal between processes [345], and different only between gluons (color octet) and quarks (color triplet). There is also what can be characterized as a non-perturbative intrinsic transverse momentum distribution in both parton densities and fragmentation functions. In the quark sector, all but the fragmentation function are well measured in Drell-Yan processes [346].

On the other hand, evolution for the small-x formalism in (7.19) is given by the BFKL method.

The avenues for further improvement on this subject are both theoretical and experimental. On the theory side, these concern the relation between different formalisms for evolution [156, 333, 337, 342, 347], the extension of factorization theorems to a larger number of particles in the final state, and the matching to Monte Carlo generators. On the experimental side, the sensitivity to TMD functions is linked to a sensitivity to parton transverse momentum. This is the case of SIDIS at low transverse momentum. Another interesting process which would enable the TMD gluon functions to be probed is $ep \to \pi\pi X$, with the pions being in different directions (different jets), but such that they are close to back-to-back in the (q, p_i) (the so-called brick wall) frame.

Finally, measuring SIDIS and dijet production off protons or nuclei at the LHeC will allow detailed investigations of non-linear parton evolution in QCD. In this respect, the SIDIS cross section [348] and dihadron production [349] have been studied in the CGC framework. It turns out that, for small x, one is sensitive to the saturation regime of the target (proton or nucleus) wave function if the transverse momentum of the produced hadron is of the order of the saturation momentum.

Dijet production and angular decorrelation

Dijet production in high energy deep inelastic electron-proton scattering is a very valuable process which is excellent for studying properties of the small-x behavior in QCD. The dominant process is illustrated in Fig. 7.41, which is that of the $\gamma^* g \to q\bar{q} \to$ dijet production. The incoming gluon can have sizeable transverse momentum accumulated from diffusion in k_T along the gluon chain. As Bjorken-x becomes smaller, and therefore the longitudinal momentum of the gluon also decreases, larger values of the transverse momentum k_T can be sampled. This will lead to an azimuthal decorrelation between the jets which increases with decreasing x. The definition of $\Delta\phi$ is indicated in Fig. 7.41. That is, the jets are no longer back-to-back since they must balance the sizable transverse momentum k_T of the incoming virtual gluon.

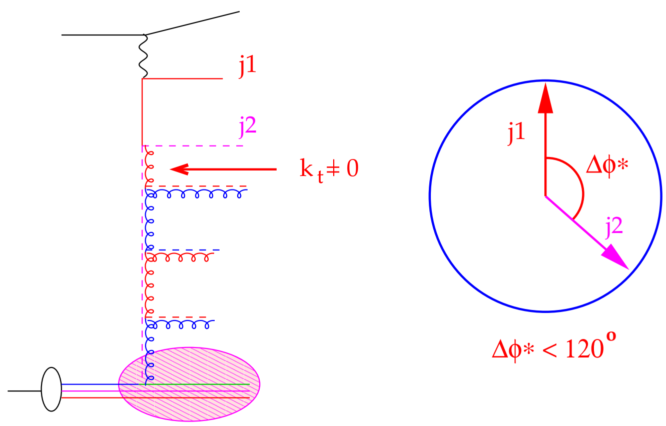

Figure 7.41: Schematic representation of the production of the system of two jets in the process of virtual photon-gluon fusion. The incoming gluon has nonvanishing transverse momentum $k_T \neq 0$ which leads to the decorrelation of the jets. $\Delta\phi$ is the angle between two jets.

This has to be contrasted with the conventional picture which uses integrated parton distributions, and typically leads to a narrow distribution about the back-to-back jet configuration. Higher orders usually broaden the distribution. However, as shown by direct measurements of DIS dijet data [350], NLO DGLAP calculations are not able to accommodate the pronounced effect of the decorrelation.

Explicit calculations for HERA kinematics show that the models which include the resummation of powers of $\log 1/x$ compare favourably to the experimental data [351–355]. The proposal and calculations to extend such studies to diffractive DIS also exist [356, 357].

In Fig. 7.42 we show the differential cross section as a function of $\Delta\phi$ for jets in $-1 < \eta_{jet} < 2.5$ with $E_{1T} > 7$ GeV and $E_{2T} > 5$ GeV found with the k_t jet algorithm in the kinematic range $Q^2 > 5$ GeV, $0.1 < y < 0.6$ for different regions in x. Predictions from MEPS [18], CDM [358] and CASCADE [359] are shown. At large x all predictions agree, both in shape and in normalization. At smaller x the $\Delta\phi$-distribution becomes flatter for CDM and CASCADE, indicating higher order effects leading to a larger decorrelation of the produced jets. Whereas a decorrelation is observed, its size depends on the details of the parton evolution and thus a measurement of the $\Delta\phi$ cross section provides a direct measurement of higher order effects which need to be taken into account at small x.

Thus, in principle, a measurement of the azimuthal dijet distribution offers a direct determination of the k_T-dependence of the unintegrated gluon distribution. When additionally supplemented by inclusive measurements, it can serve as an important constraint for the precise determination of the fully unintegrated parton distribution, with the transverse momentum dynamics in the proton completely unfolded.

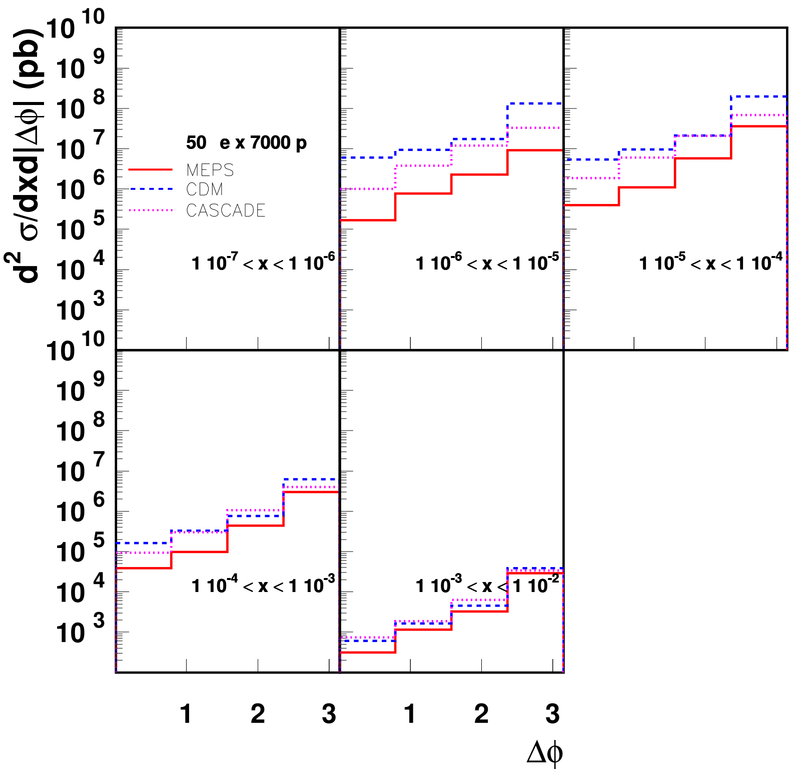

Figure 7.42: Differential cross section for dijet production as a function of the azimuthal separation $\Delta\phi$ for dijets with $E_{1T} > 7$ GeV and $E_{2T} > 5$ GeV.

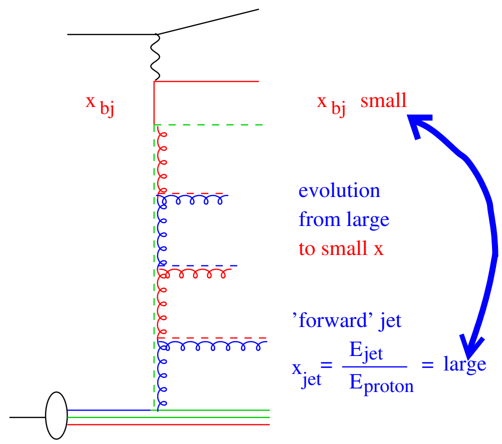

Figure 7.43: Schematic representation of the production of forward jet in DIS.

Forward observables

It was proposed some time ago [360, 361] that an excellent process which would be very sensitive to the parton dynamics and the transverse momentum distribution was that of the production of forward jets in DIS. According to [360, 361], DIS events containing identified forward jets provide a particularly clean window to the small-x dynamics. The schematic view of the process is illustrated in Fig. 7.43. The jet transverse momentum provides the second hard scale p_T. Hence one has a process with two hard scales: the photon virtuality Q and the transverse momentum of the forward jet p_T. As a result the collinear (DGLAP) configurations (with strongly ordered transverse momenta) can be eliminated by choosing the scales to be of comparable size, $Q^2 \simeq p_T^2$. Additionally, the jet is required to be produced in the forward direction, that is, x_J, the longitudinal momentum fraction of the produced jet, is as large as possible, and x/x_J as small as possible. This requirement selects the events with the large sub-energy between the jet and the virtual photon where the BFKL framework should be applicable. There have been dedicated measurements of forward jets at HERA [362–367], which demonstrated that the DGLAP dynamics at NLO order is indeed incompatible with the experimental measurements. On the other hand, the calculations based on resummations of powers of $\log 1/x$ (BFKL and others) [359,368–373] are consistent with the data. The azimuthal dependence of forward jet production has also been studied [374, 375] as a sensitive probe of the small-x dynamics.

Another process that provides a valuable insight into the features of small-x physics, is the measurement of the transverse energy E_T-flow accompanying DIS events at small x. The diffusion of the transverse momenta in this region, leads to a strongly enhanced distribution of E_T at small x. As shown in analysis [376, 377], the small-x evolution results in a broad Gaussian E_T-distribution as a function of rapidity. This should be contrasted with the much smaller E_T-flow obtained assuming strong k_T-ordering as in DGLAP-based approaches, which give an E_T-distribution that decreases with decreasing x, for fixed Q^2.

The first experimental measurements of the E_T-flow in small-x DIS events indicate that there is significantly more E_T than is given by conventional QCD cascade models based on DGLAP evolution. Instead we find that they are in much better agreement with estimates which incorporate dynamics beyond fixed-order DGLAP [358, 359, 378] like BFKL evolution. The latter dynamics are characterized by an increase of the E_T-flow in the central region with decreasing x.

However, the experimental data from HERA do not enable a detailed analysis due to their constrained kinematics. At the LHeC one could perform measurements with large separations in rapidity and for different selections of the scales (Q, p_T). In particular, there is a possibility of varying scales so to test systematically the parton dynamics from the collinear (strongly ordered) regime $Q^2 \gg p_T^2$ to the BFKL (equal scale, Regge kinematics) regime $Q^2 \simeq p_T^2$. Measurements of the energy flow in different x-intervals, in the small-x regime, should therefore allow a definitive check of the applicability of BFKL dynamics and of the eventual presence of more involved, non-linear effects.

The simulation of the forward jet production at the LHeC is shown in Figs. 7.44 and 7.45. The jets are required to have $E_T > 10$ GeV with a polar angle $\Theta_{jet} > 1^o$ and 3^o in the laboratory frame. Jets are found with the SISCone jet-algorithm [379]. The DIS phase space is defined by $Q^2 > 5$ GeV, $0.05 < y < 0.85$.

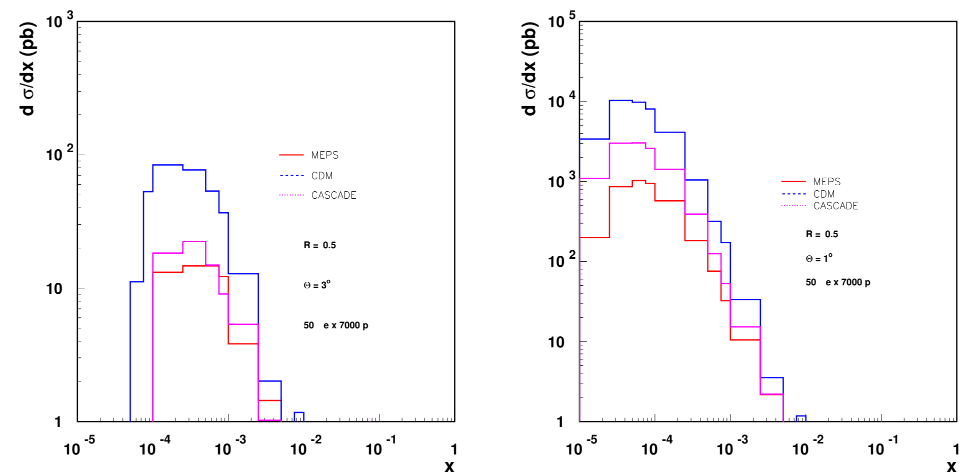

Figure 7.44: Cross section for forward jets with $\Theta_{jet} > 3^o$ (left) and $\Theta_{jet} > 1^o$ (right). Predictions from MEPS, CDM and CASCADE are shown. Jets are found with the SISCone algorithm using $R = 0.5$.

In Fig. 7.44 the differential cross section as a function of x for an electron energy of $E_e = 50$ GeV is shown. The predictions come from a Monte Carlo generator [18] using $\mathcal{O}(\alpha_s)$ matrix elements with a DGLAP type parton shower (MEPS), with higher order parton radiation as simulated with the Colour Dipole Model [358] and from CASCADE [380], which uses off-shell matrix elements convoluted with the unintegrated gluon distribution function (CCFM set A) and subsequent parton shower according to the CCFM evolution equation. Predictions for $\Theta_{jet} > 5^o$ and $\Theta_{jet} > 1^o$ are shown. One can clearly see that the small-x range is explored with the small angle scenario. In Fig. 7.45 the forward jet cross section is shown when using $R = 1$ instead of $R = 0.5$ (Fig. 7.44). It is important to note that the angular acceptance of the detector is crucial for the measurement of forward jets. The dependence of the cross section on

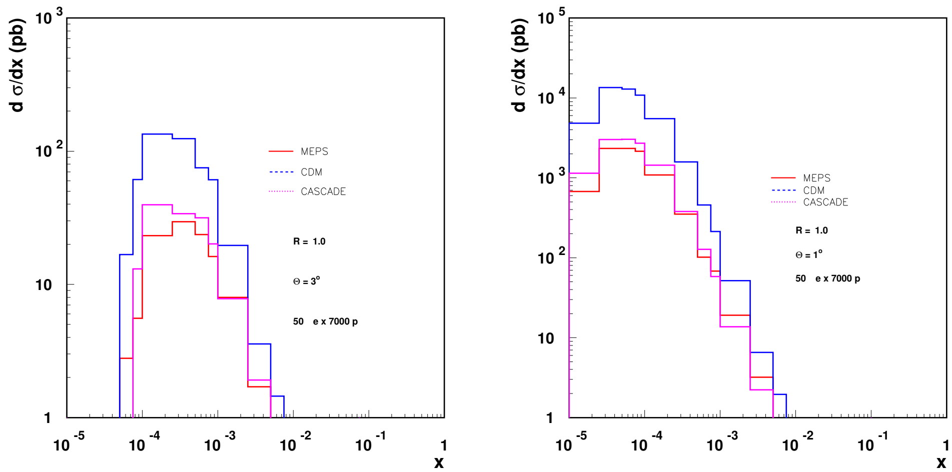

Figure 7.45: Cross section for forward jets with $\Theta_{jet} > 3^o$ (left) and $\Theta_{jet} > 1^o$ (right). Predictions from MEPS, CDM and CASCADE are shown. Jets are found with the SISCone algorithm using $R = 1.0$.

the acceptance angle is very strong as is evident from Figs. 7.44 and 7.45. In case of the 10^o acceptance, almost all of the forward jet signal is lost.

A complementary reaction to that of forward jets is the production of forward π^0 in DIS. Albeit having a lower rate, this process offers some advantages over forward jet production. By looking onto single particle production the dependencies on the jet finding algorithms can be eliminated. Also, the non-perturbative hadronisation effects can be effectively encompassed into the fragmentation functions [369].

Perturbative and non-perturbative aspects of final state radiation and hadronization

The mechanism through which a highly virtual parton produced in a hard scattering gets rid of its virtuality and color and finally projects onto a observable, final state hadron, is unknown to a great extent (see [256] and references therein). The different postulated stages of the parton in its way to becoming a hadron are shown in Fig. 7.46: colored parton which undergoes QCD radiation, colored excited bound state (pre-hadron), colorless pre-hadron and final hadron, are characterized by different time scales. While the first stage can be described in perturbative QCD [381], subsequent ones require models (e.g. the QCD dipole model for the pre-hadron stages) and nonperturbative information.

The LHeC offers great opportunities to study these aspects and improve our understanding on all of them. The energy of the parton which is kicked by the virtual photon implies a Lorentz dilation of the mentioned time scales for the different stages of the radiation and hadronization processes. All of them will be influenced by the fact that they do not take place in the vacuum but within the QCD field created by the other components of the hadron or nucleus. While at fixed target SIDIS or DY experiments, the lever arm in energy has been quite reduced ($\nu < 100$

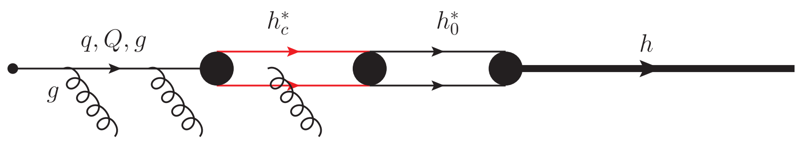

Figure 7.46: Sketch of the different postulated stages (from left to right): radiating parton, radiating pre-hadron, colorless pre-hadron and final hadron, of the projection of a highly virtual parton onto a final state hadron.

GeV), at the LHeC this lever arm will be huge ($\nu < 10^5$ GeV), implying that the different stages can be studied to happen in or out the hadron field by scanning increasing values of the parton energy. Furthermore, the fact that we can introduce a piece of colored matter of controlled length and density - a nucleus - by doing ePb collisions at different centralities, allows a controlable perturbation of the different processes. The induced differences in the final distributions of hadrons, both on their momenta and on their relative abundance, will provide most important information about the time scales and of the detailed physical mechanisms at work in every stage. Dramatic effects are predicted in some models [382], with the significant suppression of the forward hadron spectra due to the creation of the dense partonic system. Note that SIDIS experiments already provide most important information for the determination of standard fragmentation functions (see [383, 384] for a recent analysis). The other pieces of information, coming from e^+e^- experiments, will not be improved until linear colliders become available.

Furthermore, these studies will shed light on two aspects already commented in Sec. 7.1.4 related with the study of ultrarelativistic heavy-ion collisions: the characterization of the medium created in such collisions through hard probes, and the details of particle production in a dense situation which will define the initial conditions for the collective behavior of this medium. Concerning the latter, eA is a system in which our theoretical tools for computing particle production are more advanced e.g. within the CGC framework, and on a safer ground that in nucleus-nucleus collisions (see Sec. 7.1.1 and e.g. [255] and refs. therein.). The possibility of disentangling the different mechanisms through which the factorization that is used in dilute systems - collinear factorization [126] - becomes broken by density effects (i.e. initial and final state energy loss, final state absorption, . . .) will be possible at the LHeC and complement existing studies done in fixed target SIDIS and DY experiments [256].

7.2.6 Photoproduction Physics

Due to the $1/Q^4$ propagator term, the LHeC ep cross section is dominated by very low Q^2 quasi-real photons. With a knowledge of the effective photon flux [385], measurements in this kinematic region can be used to obtain real photoproduction (γp) cross sections. The real photon has a dual nature, sometimes interacting in a point-like manner and sometimes interacting through its effective partonic structure, resulting from $\gamma \to q\bar{q}$ and higher multiplicity splittings well in advance of the target [386, 387], the details of which are fundamental to the understanding of QCD evolution.

The total photoproduction cross section

The behaviour of the total photoproduction cross section at high energy is a topic of a major interest. It is now firmly established experimentally that all the hadronic cross sections rise with the energy for large energies. The Froissart-Martin bound has been derived for hadronic probes. It therefore remains to be seen whether this bound is applicable to the γp scattering. For example in Refs. [382, 388] it has been argued that the bound for the real photon-hadron interactions should be of the different functional form, namely $\ln^3 s$. This would imply that the universality of the asymptotic behavior hadronic cross sections does not hold. Therefore the measurement of the total photoproduction cross section at high energies will bring an important insight into the problems of universality of hadronic cross sections, unitarity constraints, the role of diffraction and the interface between hard and soft physics.

In Fig. 7.47, available data on the total cross section are shown [389–392][7], together with a variety of models. More specifically, the dot-dashed black line labeled 'FF model GRS' is a minijet model [394], the yellow band labeled 'Godbole et al.' is an eikonalized minijet model with soft gluon resummation [394] with the band defined by different choices of the parameters in the model, the red solid line labeled 'Block & Halzen' is based on a low energy parametrization of resonances joined with Finite Energy Sum Rules and asymptotic $\ln^2 s$-behaviour [395, 396], and the dashed blue line labeled 'Aspen model' is a QCD inspired model [397].

The theoretical predictions diverge at energies beyond those reached at HERA, where cross sections were measured by tagging and measuring the energies of electrons scattered through very small angles in dedicated calorimeters located well down the beampipe in the outgoing electron direction [389,390]. As discussed in Chapter 13, the most promising location for similar small angle electron detectors at the LHeC is in the region around 62 m from the interaction point, which could be used to tag scattered electrons in events with $Q^2 < 0.01$ GeV^2 and $y \sim 0.3$. This naturally leads to measurements of the total photoproduction cross section at γp center-of-mass energies $W \sim 0.5\sqrt{s}$. The measurements would be strongly limited by systematics. In the absence of a detailed simulation of an LHeC detector these uncertainties are hard to estimate. For the simulated data in Fig. 7.47, uncertainties of 7% have been assumed, matching the precision of the H1 and ZEUS data. This would clearly be more than adequate to distinguish between many of the available models. The HERA uncertainties were dominated by the invisible contributions from diffractive channels in which the diffractive masses were too small to leave visible traces in the main detector. If acceptances to 1° are achieved at the LHeC, better precision may be possible.

Jet photoproduction

Another important observable is jet photoproduction. It provides an abundant yield of high-energy probes of the nuclear medium that could be achieved at the LHeC. It has been computed using the simulations from [398, 399], for an electron beam of 50 GeV colliding with the LHC beams. For the nuclear case the same integrated luminosity was assumed per nucleon of 2 fb^{-1} as for ep. Only jets with $E_{Tjet} > 20$ GeV are considered, and for the distribution in E_{Tjet} the pseudorapidity acceptance is $|\eta_{jet}| < 3.1$, corresponding to $5^\circ < \theta_{jet} < 175^\circ$ angular acceptance.

[7] The recent results by ZEUS [393] refer only to the energy behavior of the cross section in the range 194 $< W <$ 296 GeV but do not provide absolute values.

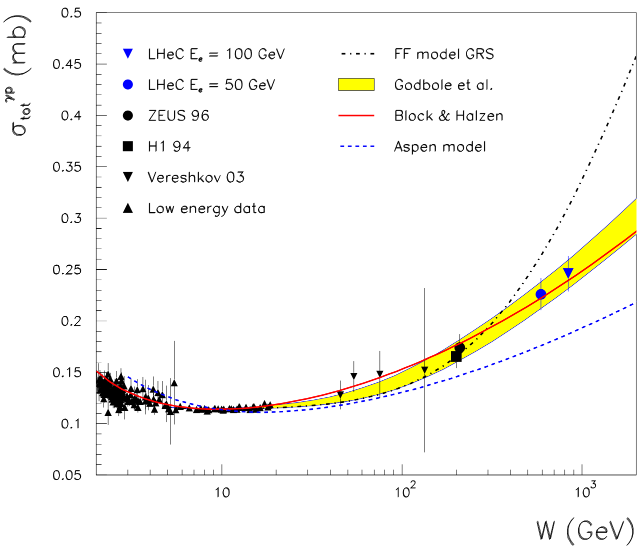

Figure 7.47: Simulated LHeC measurements of the total photoproduction cross section with $E_e = 50$ GeV or $E_e = 100$ GeV, compared with previous data and a variety of models (see text for details). This is derived from a similar figure in [394].

The simulations were performed using following assumptions: (i) For the Weizsäcker-Williams distribution of the electron, the standard option in [398, 399]; (ii) For the photon parton densities, GRV-HO [400]; (iii) For the proton parton densities, CTEQ6.1M [26]; (iv) For the nuclear modification of nucleon parton densities, EPS09 [218]; (v) For the renormalization and factorization scales, $\mu_R = \mu_F = \sum_{jets} E_{Tjet}/2$; and (vi) For the jet definition algorithm, inclusive k_T [401] with $D = 1$. The statistical uncertainty in the computation (i.e. in the Monte Carlo integration) is smaller than 10 % for all shown results. The limiting statistical uncertainty is for the largest E_{Tjet} and is usually much smaller for the lower values of E_T. No attempt has been done to estimate the uncertainties due to different choices of Weizsäcker-Williams distribution of photons in the electron, photon or proton parton densities, scales or jet definitions (see [402, 403] for such considerations at HERA). Nor the eventual problems of background subtraction, experimental efficiencies in jet reconstruction or energy calibration, have been addressed. The only studied uncertainty is that due to the uncertainties in the nuclear parton densities, extracted in EPS09 [218] using the Hessian method, see that reference for details.

The results are shown in Fig. 7.48. One observes that rates around 10^3 jets per GeV are expected with $E_{Tjet} \sim 95$ (80) GeV in ep (ePb), for $|\eta_{jet}| < 3.1$ and the considered integrated luminosity of 2 fb^{-1} per nucleon. Also the effects of the nuclear modification of parton densities and their uncertainties are smaller than 10 %. Finally we note that, the two-peak structure in the η_{jet}-plot results from the sum of the direct plus resolved contributions, each of them with a single maximum but located in opposite hemispheres: positive η_{jet} (photon side) for direct, negative η_{jet} (nucleon side) for resolved.

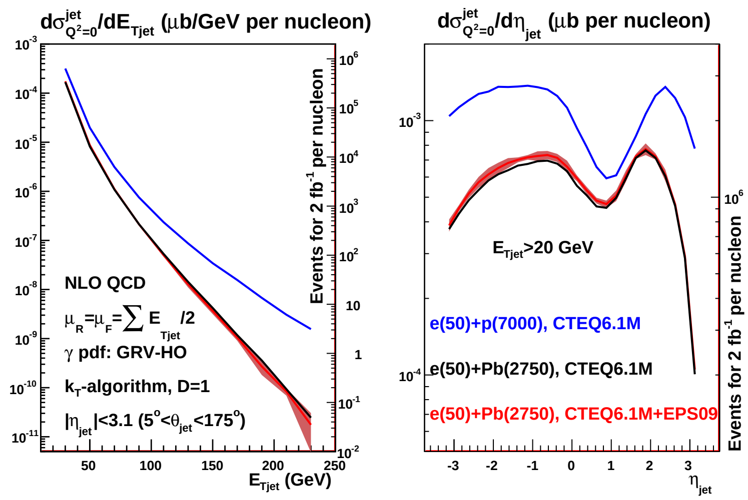

Figure 7.48: Results for the inclusive jet distribution in photoproduction versus E_{Tjet} (plot on the left) and η_{jet} (plot on the right) for $e(50)$+p(7000) (blue lines), $e(50)$+Pb(2750) without nuclear modification of parton densities (black lines), and $e(50)$+Pb(2750) with EPS09 nuclear modification of parton densities (red lines for the central value and bands for the uncertainty coming from the nuclear modification of parton densities). See the text and the legends on the plots for information about choices in the calculation and kinematical cuts. In both plots, the axis on the left corresponds to the cross section in μb, while the axis on the right provides the number of jets to be observed for an integrated luminosity of 2 fb^{-1} per nucleon, per unit of E_{Tjet} (η_{jet}) in the plot on the left (right).

7.2.7 Implications for ultra-high energy neutrino interactions and detection

The stringent constraints of the parton distributions at very small x from the future Large Hadron Electron Collider will have extremely important implications on neutrino astronomy. Ultra-high energy neutrinos can provide important information about the distant astronomical objects and the origin of the Universe. They have attracted a lot of attention during recent years, see the reviews [404,405]. Neutrino astronomy has many advantages over the conventional photon astronomy. This is due to the fact that the neutrinos, unlike photons, interact only weakly, so they can travel long distances being practically undisturbed. The typical interaction lengths for neutrinos and photons at energy $E \sim 1$ TeV are about

$$\mathcal{L}_{int}^{\nu} \sim 250 \times 10^9 \text{ g/cm}^2 \,, \qquad\qquad \mathcal{L}_{int}^{\gamma} \sim 100 \text{ g/cm}^2 \,.$$

Thus, very energetic photons with energy bigger than ~ 10 TeV cannot reach the Earth from the very distant corners of our Universe without being rescattered. On the contrary, neutrinos can travel very long distances. Besides, they are also not deflected by galactic magnetic fields, and therefore at ultra-high energies the angular distortion of the neutrino is very small. As a result, highly energetic neutrinos point back to their sources. The interest in the neutrinos at these high energies has led to the development of several neutrino observatories, see [405] and references therein.

For the reliable observation of neutrinos, precise knowledge about their production rates and interactions is essential for estimating the background, the expected fluxes and the detection probabilities. Even though neutrinos interact only weakly with other particles, strong interactions play an essential role in the calculations of their production rates and interaction cross section. This is due to the fact that neutrinos are coming from the decays of various mesons such as π, K, D and even B which are produced in high-energy proton-proton (or proton-nucleus or nucleus-nucleus) collisions. These hadronic processes occur mainly in the atmosphere though, possibly, also in the accretion discs in the remote Active Galactic Nuclei. Besides, the interactions of highly energetic neutrinos with matter are dominated by the deep inelastic cross section with nucleons or nuclei. This is why the knowledge about QCD from high-energy collider experiments such as HERA, Tevatron, LHC and, most importantly, the future LHeC, is invaluable.

One of the main uncertainties (if not the dominant one) in the current limits on high-energy neutrino production is due to the neutrino-nucleon or nucleus cross section. In fact, event rates are proportional to the neutrino cross section in many experiments. This cross section involves the gluon distribution probed at very small values of Bjorken variable x, down to even $\sim 10^{-9}$, which corresponds to a very high c.m.s. energy.

To visualize the kinematic regime probed in ultrahigh energy neutrino-nucleon interactions the contour plot is shown in Fig. 7.49, of the differential cross section $\frac{d^2\sigma}{d \ln 1/x d \ln Q^2/\Lambda^2}$ in the (x, Q^2) plane. The contours enclose the regions with different contributions to the total cross section $\sigma(E_\nu)$. We see that for very high energy $E = 10^{11}$ GeV the dominant contribution comes from the domain $Q^2 \simeq M_W^2$ and $x_{\min} \simeq M_W^2/(2M_N E) \sim 10^{-8} - 10^{-7}$ where M_N is the nucleon mass, currently inaccessible in accelerators.

On the other hand, another process which has been proposed for neutrino detection comes from the discovery of neutrino flavor oscillations, which makes it possible that also tau neutrinos reach the Earth in spite of being heavily suppressed in most postulated production mechanisms.

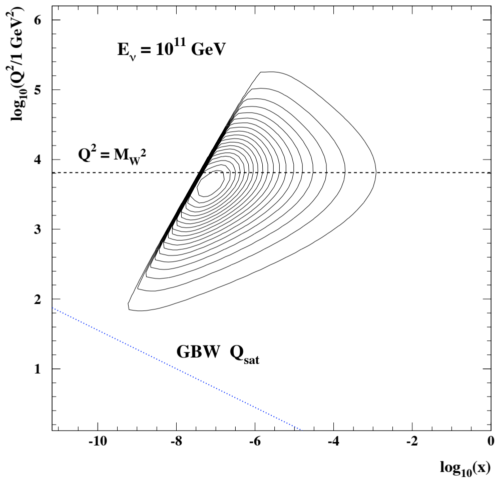

Figure 7.49: Contour plot showing the x, Q^2 domain of the dominant contribution to the $d\sigma/d\ln(1/x)d\log Q^2$ for the total ν-nucleon interaction at a value of the neutrino laboratory momentum equal to $E_\nu = 10^{11}$ GeV. The 20 contours are such that they enclose a contribution of 5, 10, 15 $\cdots$ % of the above differential cross section. The saturation scale in the model in [175] is shown by a dashed line. See the text for further explanations.

The possibility to search for tau neutrinos by looking for tau leptons that exit the Earth, Earth-skimming neutrinos, has been shown to be particularly advantageous to detect neutrinos of energies in the EeV range [406]. The short lifetime of the tau lepton originated in the neutrino charged current interaction allows the tau to decay in flight while still close to the Earth surface, producing an outcoming air shower detectable, in principle, by different techniques. This same channel yields negligible contributions for other neutrino flavors. The sensitivity to tau neutrinos through the Earth-skimming channel directly depends both on the neutrino charged current cross section and on the tau range (the energy loss) which determine the amount of matter with which the neutrino has to interact to produce an emerging tau. It turns out that the tau energy loss is also determined by the behavior of the proton and nucleus structure functions at very small values of x, see e.g. [407]. The average energy loss per unit depth, X, of taus is conveniently represented by:

$$-\left\langle \frac{dE}{dX} \right\rangle = a(E) + b(E)E, \quad b(E) = \frac{N_A}{A} \int dy\, y \int dQ^2 \frac{d\sigma^{lA}}{dQ^2 dy} \ , \tag{7.20}$$

where $a(E)$ is due to ionization and $b(E)$ is the sum of fractional losses due to e^+e^- pair production, bremsstrahlung and photonuclear interactions, N_A is Avogadro's number and A the mass number. The parameter $a(E)$ is nearly constant and the term $b(E)E$ dominates the energy loss above a critical energy that for tau leptons is of a few TeV, with the photonuclear interaction being dominant for tau energies exceeding $E = 10^7$ GeV (as already assumed in Eq. (7.20)). In Fig. 7.50 the relative contribution to $b(E)$ of different x and Q^2 regions is shown. It can be observed that the energy loss is dominated by very small x and, complementary to the case of the neutrino cross section, by small and moderate $Q^2 \lesssim m_\tau^2$.

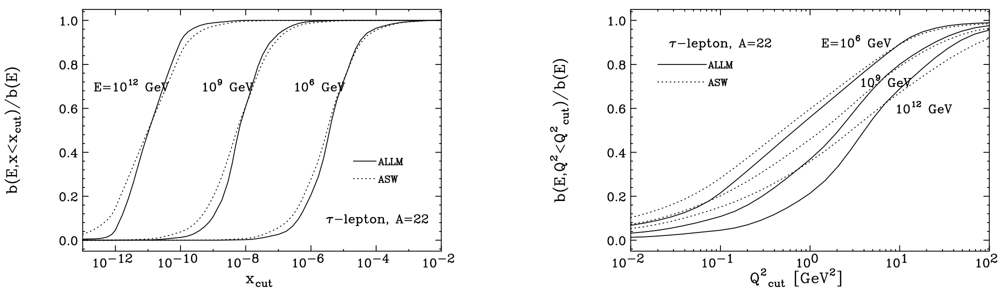

Figure 7.50: The relative contribution of $x < x_{cut}$ (plot on the left) and of $Q^2 < Q^2_{cut}$ (plot on the right) to the photonuclear energy loss rate, $b(E)$, for different neutrino energies $E = 10^6$, 10^9 and 10^{12} GeV, in two different models for the extrapolation of structure functions to very small x. See the text and [407] - from which these plots were taken - for explanations.

As the LHeC will be able to explore a new regime of low x and high Q^2 and constrain the parton distributions, the measurements performed at this collider will be invaluable for the precise evaluation of the neutrino-nucleon (or nucleus) scattering cross sections and tau energy loss necessary for ultra-high energy neutrino astronomy.

Part III

Accelerator

Chapter 8

Ring-Ring Collider

8.1 Baseline Parameters and Configuration

8.1.1 General Considerations

8.1.2 Design Parameters for ep

8.1.3 Design Parameters for eA / eD

8.1.4 Variation of beam energies

8.1.5 Layout Overview

8.2 Lattice Layout and Geometry

All lattice descriptions in this chapter are based on the LHeC lattice Version 1.1.

8.2.1 General Layout

The general layout of the LHeC consists of eight arcs and six straight sections plus two bypasses. The e-p collision experiment is located in point 2, which is also the only crossing of the beams. All straight sections exclusive the straight sections in the bypasses have the same length as the LHC straight sections: 538.8 m at even points and 537.8 m at odd points. Due to the geometric symmetry of the straight sections, all even and odd insertions have the same layout, except at point 2 and in the bypasses around point 1 and point 5.
The insertions shared with the LHC are already used for the experiments or for LHC equipement. Therefore the RF for the electron ring is installed in the straight sections of the bypasses. Out of the same reason the beam is injected in the bypass around point 1. Point 1 is preferred over point 5 out of geological and infrastructural reasons. The overall layout of the LHeC is shown in Fig. 8.1.

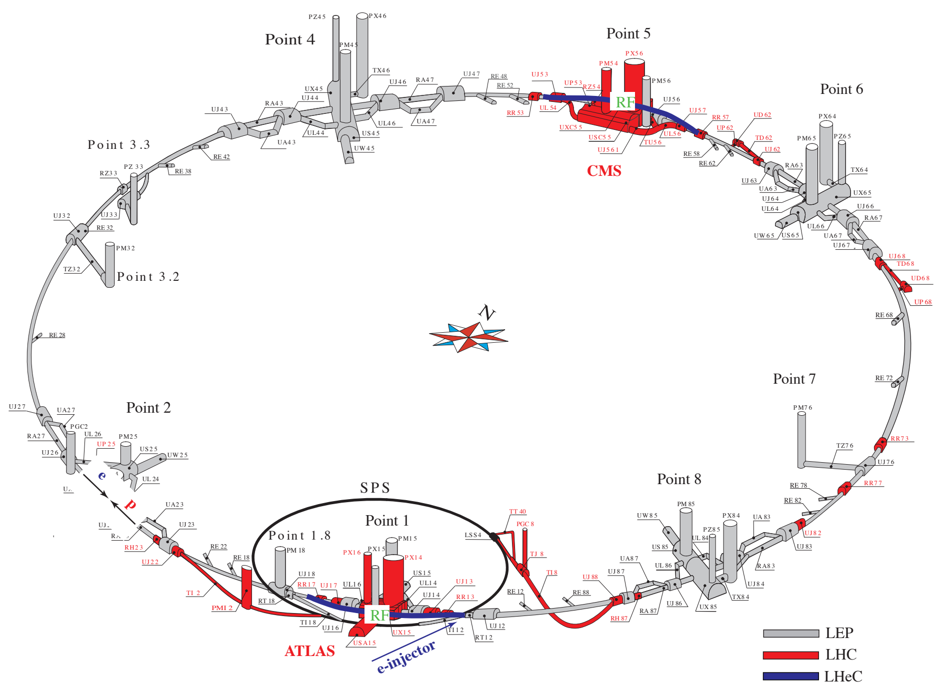

Figure 8.1: Schematic Layout of the LHeC: In grey the LEP tunnel now used for the LHC, in red the LHC extensions. The two LHeC bypasses are shown in blue. The RF is installed in the two bypasses. The bypass around point 1 hosts in addition the injection.

8.2.2 Electron Ring Circumference

The LHeC electron beam collides only in one point (point 2) with the protons of the LHC. This leaves the option to whether exactly match the circumferences of the proton and electron ring or to allow a difference of a multiple of the LHC bunch spacing. In the case of different circumferences the proton beam could become heated up due to beam-beam interactions with the electrons [408]. To avoid this possible effect, the electron ring circumference is matched exactly to the proton ring circumference.
The adjustment of the circumference can principally be achieved in two different ways:

1. Different bypass designs, e.g. inner and outer bypass, which compensate each other.

2. Placement of the electron ring to the inside or outside of the LHC in the places where the two rings share the same tunnel to compensate for the path length difference caused by the bypasses.

The different design possibilities for the bypasses are discussed in Sec. **??**. Considering the different bypass options and their characteristics, the best choice seems to be option 2 with an outer bypass around both experiments.

8.2.3 Idealized Ring

General Layout

To compensate the path length difference from the bypasses the electron ring is placed in average 61 cm to the inside of the LHC in the sections where both rings share the tunnel. To construct these sections it is easiest to design a whole ring parallel to the LHC and with a displacement of ideally 61 cm to the inside. In the following we refer to the lattice of this ring as the *Idealized Lattice*.
In addition to the horizontal displacement, the electron ring is set 1 m above the LHC in order to minimize the interference with the LHC elements. The main remaining conflict are then the cables of the cryostats (DFBMs and DFBAs) and jumper connections. A representative cross section of the LHC tunnel is shown in Fig. 8.2.
In the main arcs the DFBMs have a length of 6.62 m and are installed at the beginning of each LHC arc cell, whereas the insertions host a different number of cryostats with a varying placement and length. The idealized ring lattice avoids all DFBMs in the main arcs. In order to show that it is possible to also find a lattice, which avoids all cryostats in the insertions, the design of the dispersion suppressor is adapted to the DFBM positions and lengths in the insertions, where IR2 and IR3 are taken exemplarily for all even and odd insertions. The straight sections are filled with a regular FODO cell structure, which would still have to be slightly changed in case of interference with LHC elements, but is for simplicity not done in this version of the lattice.

Geometry

The reappearance of the DFBMs at the beginning of each LHC arc cell suggests a multiple or $1/n$th, $n \in \mathbb{N}$, of the LHC arc cell length as LHeC FODO cell length. Beside the integration constraints, the cell has to provide the right emittance. Taking half the LHC arc cell length as LHeC FODO cell length already fulfills this second criterion (Sec. 8.3.1).

As the LHC arc cell is symmetric, the best geometrical agreement with the LHC main arc would be achieved, if the LHeC cell had as well a symmetrical layout. Because of the DFBMs, no elements can be placed in the first approx. 6.9 m of each cell, especially no dipoles. If the cell would now be built symmetrically, another 6.9 m would be lost after the first FODO cell. This would result in additional and therefore unwanted synchrotron radiation losses as the energy loss in a dipole magnet is proportional to the inverse length of the dipole

$$U_{\text{dipole}} = \frac{C_\gamma}{2\pi} E_0^4 \frac{\theta^2}{l} \ , \ C_\gamma = \frac{4\pi}{3} \frac{r_e}{(m_e c^2)^3} \tag{8.1}$$

where θ is the bending angle, l the length of the dipole and E_0 the beam energy. In order to avoid this, the LHeC double FODO cell is symmetric in the placement of the quadrupoles but asymmetric in the placement of the dipoles (Fig. 8.3).

The bending angle in the arc cells and also in the DS is determined by the LHC geometry. In the following we refer to the LHC DS as the section from the end of the arc to the end of the DS. With this definition the LHC DS consists of two cells. Keeping the same converting rule as in the arc (one LHC FODO cell is transferred into two LHeC FODO cells), the LHeC DS would then ideally consist of 4 equal cells. Consistently the ratio between the LHeC DS and arc cell is the same as between the LHC DS and arc cell. For the LHC this ratio is 2/3. This leaves the following choices for the number of dipoles in the arc and DS cell:

$$N_{\text{Dipole, arc cell}} = \frac{3}{2} N_{\text{Dipole, DS cell}} = 3, 6, 9, 12, 15 \ \ldots \tag{8.2}$$

A good compromise between a reasonable dipole length and an optimal usage of the available space for the bending are 15 dipoles per arc cell. The dipoles are then split up in packages of $3+4+4+4$ in one arc cell and $2+3$ in one DS cell.
Beside the bending angle also the module length of the electron ring has to be matched to the LHC geometry. Because the electron ring runs on the inside of the proton ring all e-ring modules are shorter than their proton ring equivalents (Table 8.1).

The above considerations already fix the bending angle of the dipoles and the length of the

	Proton Ring	Electron Ring
Arc Cell Length	106.9 m	106.881 m
DSL Length (even points)	172.80 m	172.78 m
DSR Length (even points)	161.60 m	161.57 m
DSL Length (odd points)	173.74 m	173.72 m
DSR Length (odd points)	162.54 m	162.51 m

Table 8.1: Proton and Electron-Ring Module Lengths

different modules. The only degree of freedom left is the position and length. Ideally the dipole length would be chosen as long as possible, but due to the asymmetry of the arc cell, the dipoles have to be shortened and moved to the right in order to fit the LHC geometry. The only variable left for the DS is then the position of the dipoles. Different well known standard DS designs like the missing bend or half bend scheme exist, but they are all based on specific placement of the dipoles. In the case of the LHeC the position of the dipoles is strongly determined by

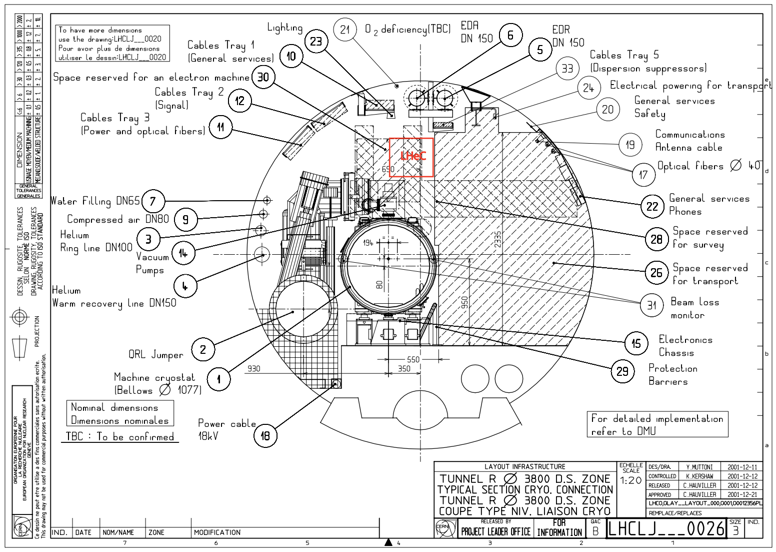

Figure 8.2: Representative cross section of the LHC tunnel. The location of the electron ring is indicated in red.

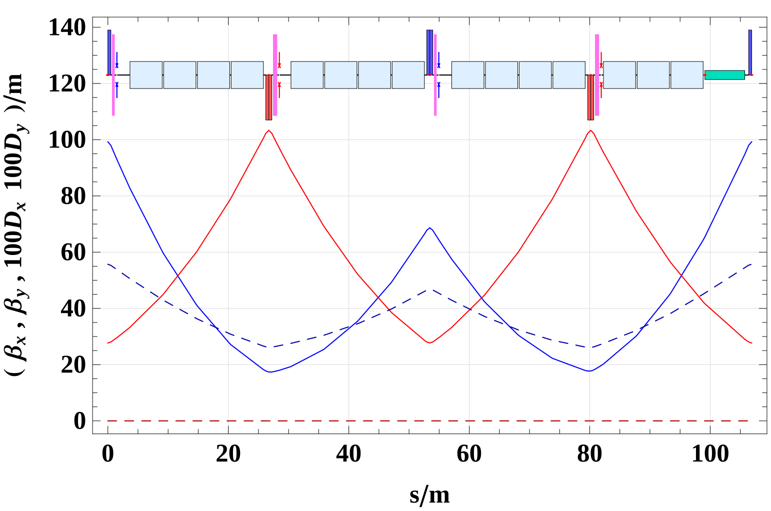

Figure 8.3: Electron ring arc cell optics.

the LHC geometry and does not match any of these standard schemes. Therefore the starting point for the DS layout is a layout with 4 DS cells similar to the LHC DS shown in Fig. 8.4. Because of the DFBMs in the region of the DS, the dipoles had to be placed differently from

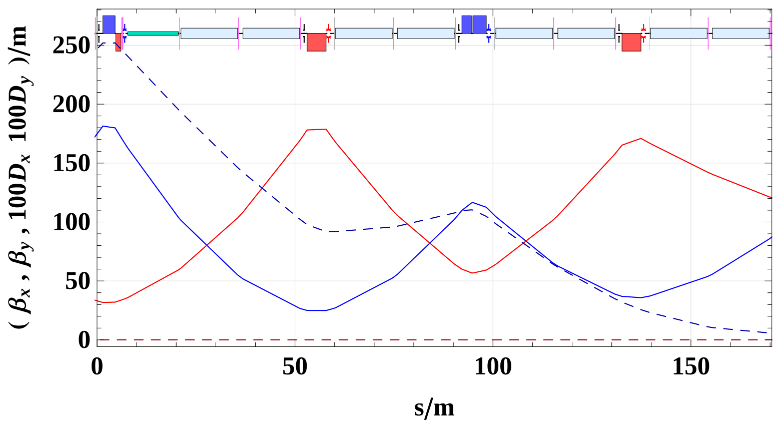

Figure 8.4: LHC DS on the left side or IP2.

this ideal configuration. In the final design as shown in Fig. 8.5 and 8.6, the dipoles are placed as symmetrically as possible between the regular arrangement of the quadrupoles.

The resulting difference between the LHC proton ring and the idealized LHeC electron ring is

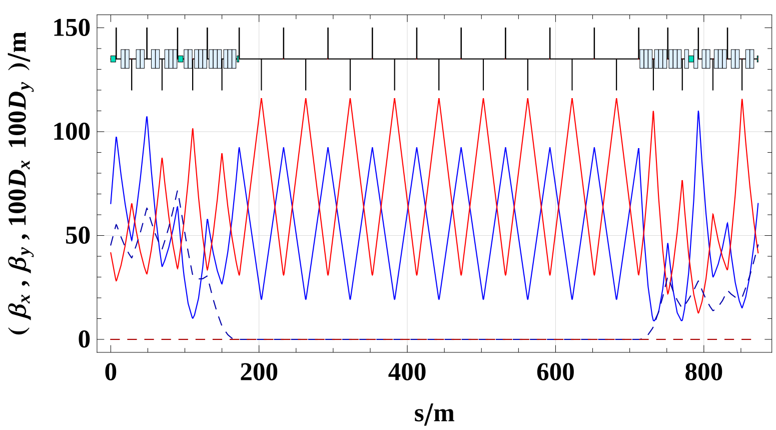

Figure 8.5: LHeC IR for even IRs, based on the DFBM configuration in point 2.

shown in Fig. 8.7, 8.8 and 8.9.

8.2.4 Different Bypass Options

It is foreseen to bypass the LHC experiments at point 1 and point 5. The main requirements for both bypasses are, that all integration constraints are respected and that the synchrotron radiation losses are not considerably increased by the bypasses. This implies that the separation

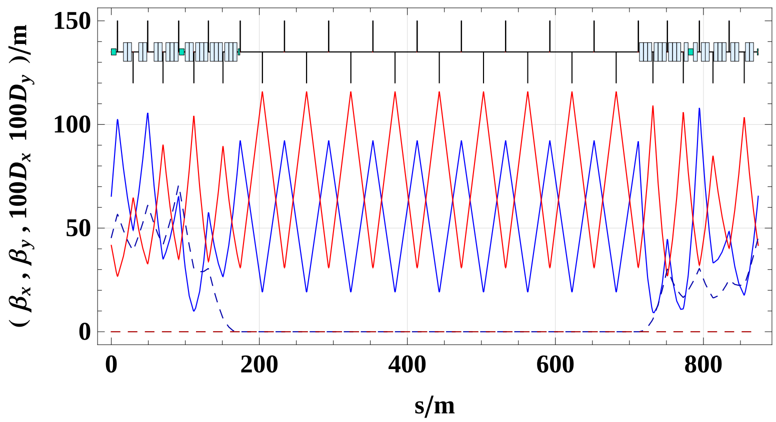

Figure 8.6: LHeC IR for odd IRs, based on the DFBM configuration in point 3.

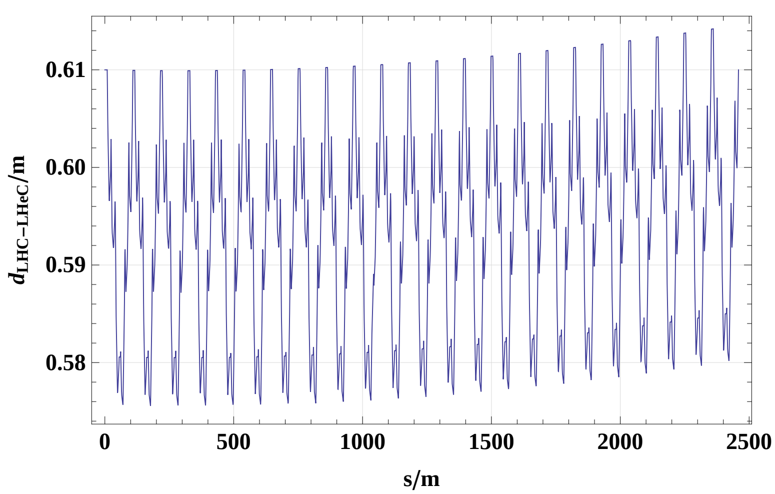

Figure 8.7: Horizontal distance between the proton and electron ring main arc.

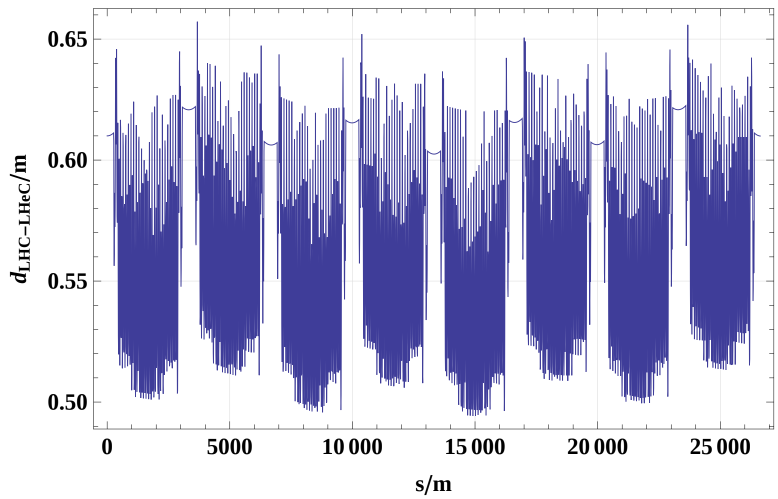

Figure 8.8: Distance between the idealized electron ring and the proton ring

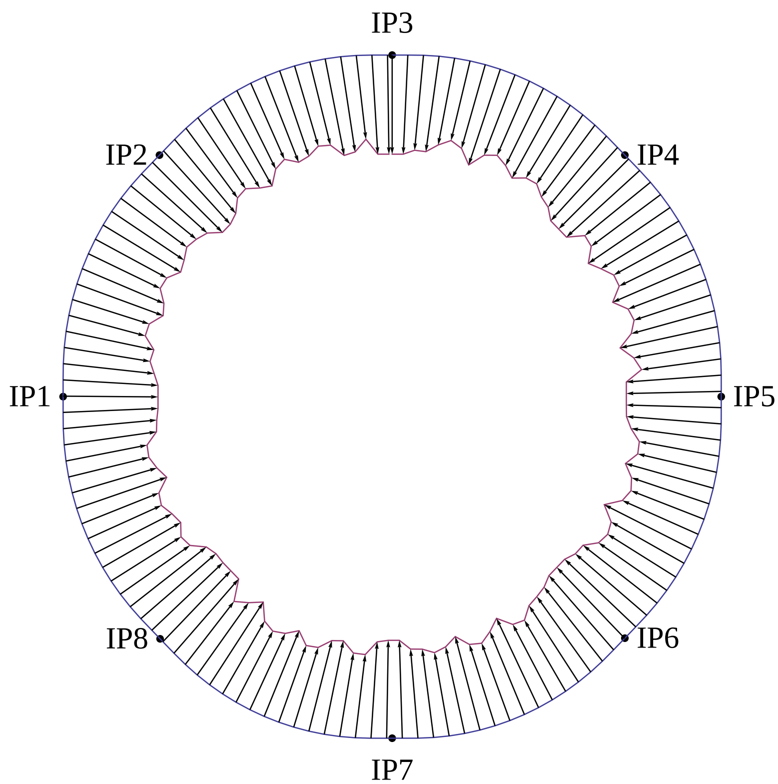

Figure 8.9: LHC and LHeC. The distance between the two rings is exaggerated by a factor 2000.

has to be small enough, so that the change in circumference can be compensated by the reduction or increase of the radius of the ring. Three different options have been considered as basic bypass design:

Vertical Bypass: A vertical bypass would have to be a vertically upwards bypass as downwards would imply to cross the LHC magnets and other elements, which is very difficult. For this a separation of about 20 to 25 m would be required [409], which could only be achieved by considerable strong additional vertical bending as the arcs and DS could not be used for the separation as there the bending is only in the horizontal plane. In general a vertical bypass would be rather long, increase the synchrotron radiation and decrease the polarization compared to a horizontal bypass. Due to this arguments we consider vertical bypasses only as an option, if horizontal bypasses are not possible.

Horizontal Inner Bypass: A horizontal inner bypass can be constructed by simply decreasing the bending radius of the main bends. Consequently the synchrotron radiation losses in an inner bypass are larger than in a comparable outer bypass. The advantage of an inner bypass is, if used in combination with an outer one, that it reduces the circumference and the two bypasses could compensate each others path length differences.

Horizontal Outer Bypass: A horizontal outer bypass optimizes most in respect to using the existing curvature of the ring and consequently reducing the synchrotron radiation losses. In general this is the preferred option.

8.2.5 Bypass Point 1

The cavern in point 1 reaches far to the outside of the LHC, so that a separation of about 100 m would be necessary in order to fully bypass the experimental hall. For a bypass on the inside a smaller separation of about 39 m would be required. For an inner bypass with minimal separation, the bending strength in three normal arc cells would have to be doubled resulting in a bypass of more than 2 km length. A sketch of an inner bypass is shown in Fig. 8.10. Because the required separation for a fully decoupled outer bypass as well as inner bypass is large, the bypass in Point 1 uses the existing survey gallery to bypass the experiment. The needed separation is then 16.25 m. The final bypass design is shown in Fig. 8.11. The RF is installed in the straight section next parallel to the straight section of the proton ring. The electron beam is injected into the arc on the right side of the bypass.

8.2.6 Bypasses Point 5

In point 5 only a separation of approx. 20 m is needed to completely bypass the experiment on the outside (Fig. 8.12). The separation in the case of an inner horizontal bypass or a vertical bypass would be the same or larger and therefore are the fully decoupled bypass is preferred over these two options. The RF is installed in the straight section parallel to the proton ring straight section.

8.2.7 Matching Proton and Electron Ring Circumference

Both bypasses require approximately the same separation and a similar design was chosen for both. To obtain the necessary separation Δ_{BP} a straight section of length s_{BP} is inserted into

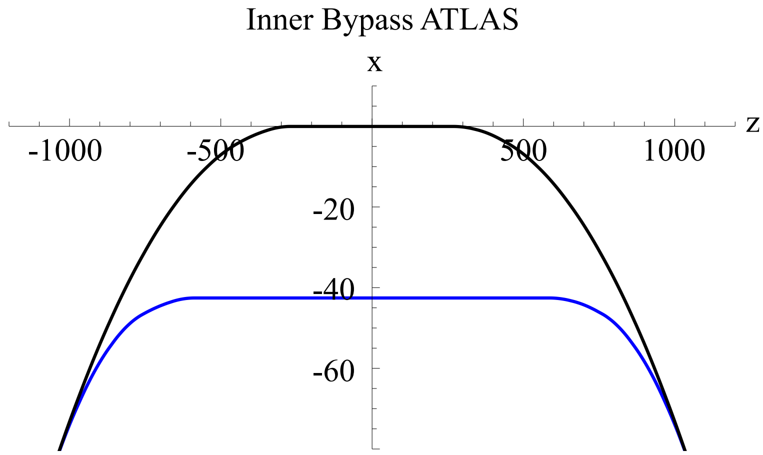

Figure 8.10: Inner Bypass around Point 1. The Bypass is shown in blue, The LHC proton ring in black.

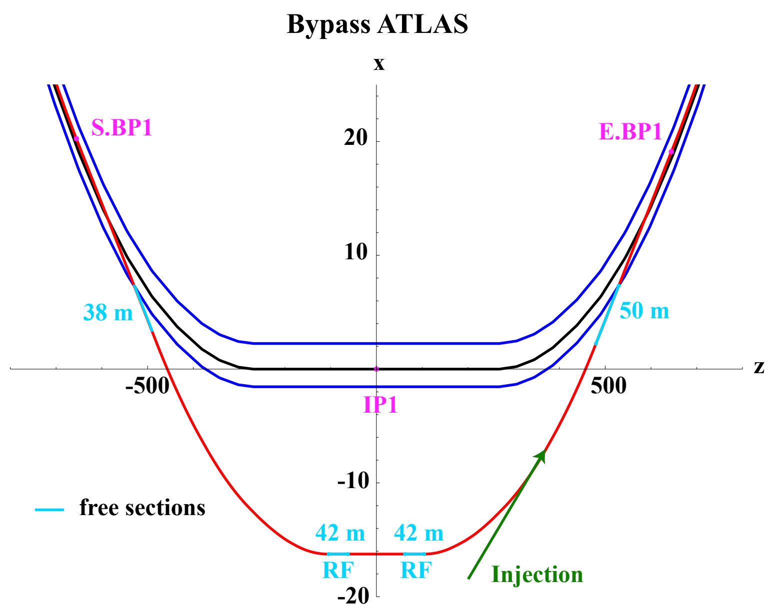

Figure 8.11: Bypass using the survey gallery in point 1. The LHC proton ring is shown in black, the electron ring in red and the tunnel walls in blue. Dispersion free sections reserved for the installation of RF, wiggler(s), injection and other equipment are marked in light blue. The injection is marked in green and is located in the right arc of the bypass. Beginning and end of the bypass are marked with S.BP1 and E.BP1

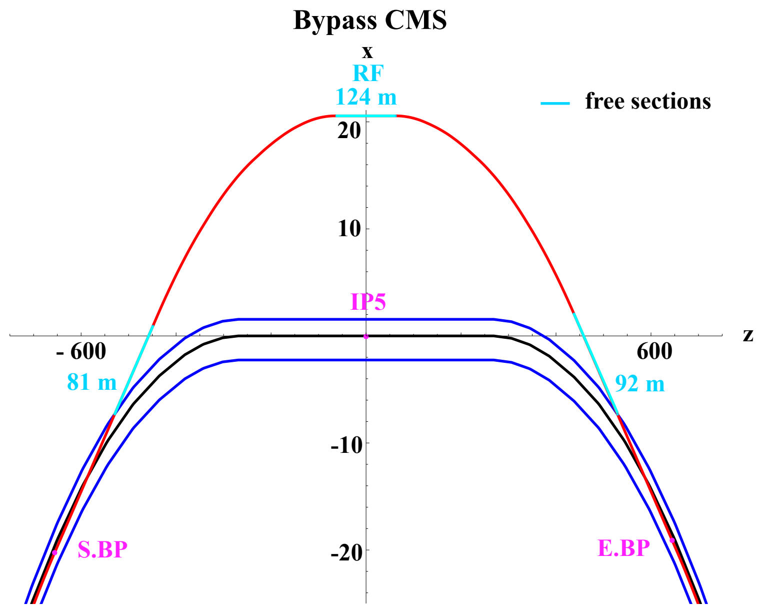

Figure 8.12: Fully decoupled bypasses in point 5. The LHC proton ring is shown in black, the electron ring in red and the tunnel walls in blue. Dispersion free sections reserved for the installation of RF, wiggler(s), injection and other equipment are marked in light blue. Beginning and end of the bypass are marked with S.BP1 and E.BP1

the lattice of the idealized ring (Sec. 8.2.3) before the last two arc cells. The separation Δ_{BP}, the remaining angel θ_{BP} and the inserted straight section s_{BP} are related by (Fig. 8.13):

$$\Delta_{\mathrm{BP}} = s_{\mathrm{BP}} \sin \theta_{\mathrm{BP}} \tag{8.3}$$

As indicated in Fig. 8.13 the separation could be increased by inserting a S-shaped chicane including negative bends. The advantage of additional bends would be the faster separation of the electron and proton ring and therefore probably less interference between the two rings. On the other hand these additional bends would need to be placed in the LHC tunnel which could conflict with the proton ring equipment, the straight sections of the bypass would be reduced and the synchrotron radiation losses increased.
In the following the estimates for the current bypass design, which does not include any extra bends, are presented. Given the separation, angle and length of the inserted straight section, the induced change in circumference is then:

$$\Delta s_{\mathrm{BP}} = s_{\mathrm{BP}} - x_{\mathrm{BP}} = 2\Delta_{\mathrm{BP}} \tan\left(\frac{\theta_{\mathrm{BP}}}{2}\right) \tag{8.4}$$

This change can be compensated by a change of radius of the idealized ring by:

$$\Delta s_{\mathrm{BP}} = 2\pi \Delta R \tag{8.5}$$

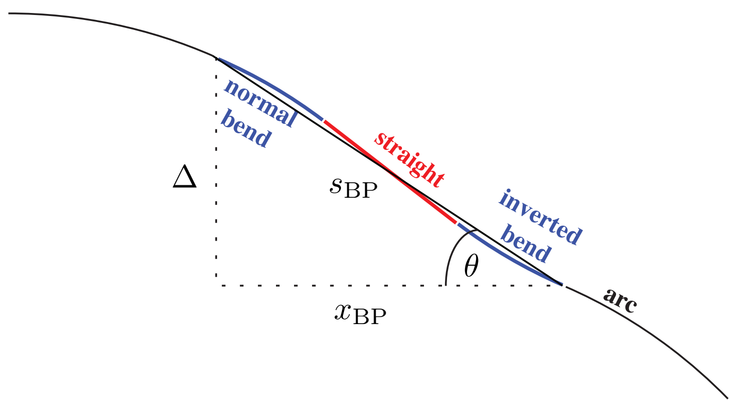

Figure 8.13: Outer bypass: a straight section is inserted to obtain the required separation. A larger separation could be achieved by inserting negative bends.

Taking the change in radius into account, the separation Δ_{BP} has to be substituted by $\Delta_{\mathrm{BP}} + \Delta R =: \Delta_{\mathrm{BP,tot}}$. The radius change and the total separation are then related by:

$$\Delta R = \frac{\Delta_{\mathrm{BP}}}{\pi \cot\left(\frac{\theta_{\mathrm{BP}}}{2}\right) - 2}\,, \quad \text{with } \Delta_{\mathrm{BP}} = \Delta_{\mathrm{BP1}} + \Delta_{\mathrm{BP5}} \tag{8.6}$$

The separation in point 1 can not be changed as the bypass uses the survey gallery, but point 5 can be used for the fine adjustment of the circumference. The design values of both bypasses are summarized in Table 8.2.

	Point 1	Point 5
Total bypass length	1303.3 m	1303.7 m
Separation	16.25 m	20.56 m
Dispersion free straight section	172 m	297 m
Ideal radius change of the idealized ring	61 cm	

Table 8.2: Bypass Figures

8.3 Optics

Throughout the whole electron ring lattice, the choice of the optics is strongly influenced by the geometrical constraints and shortage of space in the LHC tunnel. The main interference with the LHC beside point 1 and point 5, which have to be bypassed, are the cryostats in the tunnel, where no electron ring elements can be placed.

8.3.1 Arc Cell Optics

The LHC cryostats are placed at the beginning of each LHC main arc cell. For a periodic solution of the lattice, the electron ring arc cell length can therefore be only a multiple or $1/n$th, $n \in \mathsf{N}$, of the LHC FODO cell length. In general the emittance increases approx. with L^3 in a FODO cell assuming the same phase advance and bending radius per cell. In the case of the LHeC electron ring half the LHC FODO cell length delivers a emittance close to the design value, whereas the emittance of a cell with the full LHC FODO cell length is at least by approx. a factor of 4 too large. Choosing half the LHC FODO cell length divides the arc into 23 equal double FODO cells with a symmetric configuration of the quadrupoles and an asymmetric distribution of the dipoles, precisely 8 dipoles in the first FODO cell and 7 in the second. The dipole configuration is asymmetric in order to use all available space for the bending of the e-beam and consequently minimize the synchrotron radiation losses. With a phase advance of 180° horizontally and 120° vertically over the complete cell, which corresponds to a phase advance of 90°/60° per FODO cell, the horizontal emittance lies with 4.70 nm well below the design value of 5 nm. Because of the asymmetry of the dipole configuration, the phase advance in the horizontal plane is also not equally distributed. In the first half it is with 90.6°/60° slightly larger than in the second half with 89.4°/60°. The optics of one arc cell is shown in Fig. 8.3 and the parameters listed in Table 8.3.

8.3.2 Insertion Optics

For simplicity all even and all odd insertions of the electron ring have the same layout as described in Sec. 8.2.1. Each insertion is divided in three parts: the dispersion suppressor on the left side (DSL), the straight section and the dispersion suppressor on the right side (DSR).

Dispersion Suppressor

The dipole configuration of the DS can not be freely chosen out of geometrical reasons. Therefore the matching has to be done with quadrupoles slightly supported by the dipoles. For this each DS contains 8 matching quadrupoles. The DS on the left side is split into two DS

Beam Energy	60 GeV
Phase Advance per Cell	180°/120°
Cell length	106.881 m
Dipole Fill factor	0.75
Damping Partition $J_x/J_y/J_e$	1.5/1/1.5
Coupling constant κ	0.5
Horizontal Emittance (no coupling)	4.70 nm
Horizontal Emittance ($\kappa = 0.5$)	3.52 nm
Vertical Emittance ($\kappa = 0.5$)	1.76 nm

Table 8.3: Optics Parameters of one LHeC arc cell with a phase advance of 180°/120°.

sections, reaching from the first DFBM to the second and from the second to the beginning of the straight section. In the DSL the quadrupoles are distributed equally in each section. In the DSR they are placed with equal distances from each other throughout the complete DS. This layout turned out to be better for the right side due to the different arrangement of the DFBMs. The DS of the even and odd points differ slightly in their length but have in general the same layout. The length of the DS is listed in Table 8.1. The DS optics are shown in Fig. 8.5 and 8.6.

Straight Section

The straight sections consist in this lattice of a regular FODO lattice with a phase advance of 90°/60°. In a later stage the lattice of the straight sections will have to be adjusted to the different insertions.

8.3.3 Bypass Optics

The general layout and nomenclature of the bypasses is illustrated in Fig. 8.14. The straight sections LSSL, LSSR and IR are dispersion free sections reserved for the installation of RF, wiggler(s), injection etc. As dispersion suppressor before the fist straight section LSSL and after the last straight section LSSR two normal arc cells with 8 individual quadrupoles are used. In the sections TLIR and TRIR the same configuration of dipoles is kept as in the idealized lattice out of geomteric reasons. Between this fixed arrangement of dipoles 14 matching quadrupoles per side are placed as equally as possible.
The straight sections consist of a regular FODO lattice with a phase advance of 90°/60°.
The complete bypass optics in Point 1 and Point 5 are shown in Fig. 8.15 and 8.16.

8.3.4 Complete Optics

Combining all the lattice parts discussed in section 8.3.1 to 8.3.3 one obtains a lattice with the parameters listed in Table 8.4

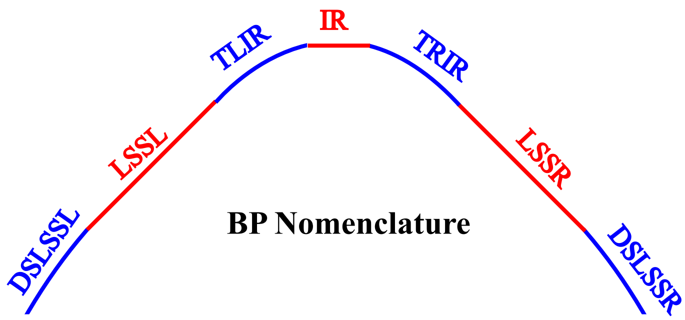

Figure 8.14: Bypass layout and nomenclature.

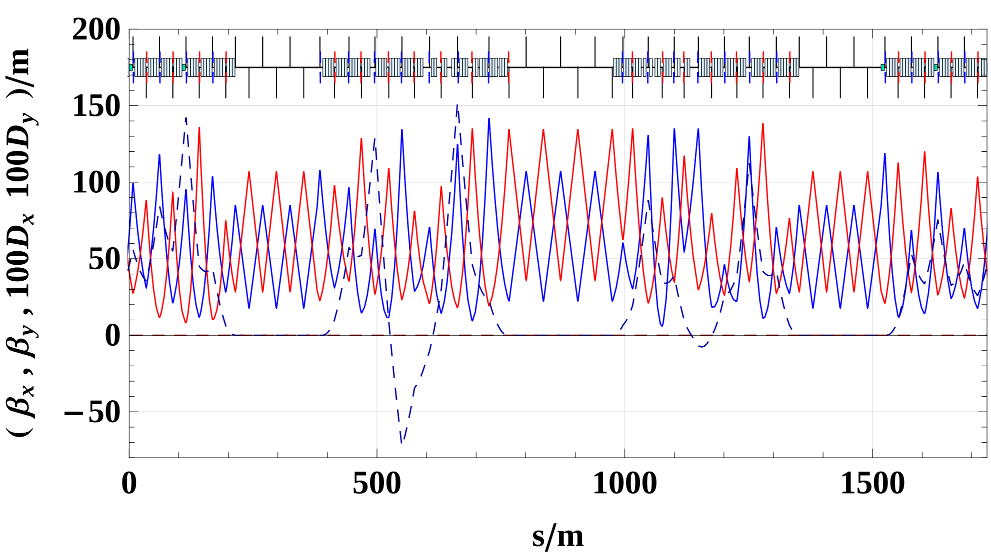

Figure 8.15: Bypass optics Point 1.

Beam Energy	60 GeV
Numb. of Part. per Bunch	2.0×10^{10}
Numb. of Bunches	2808
Circumference	26658.8832 m
Syn. Rad. Loss per Turn	437.2 MeV
Power	43.72 MW
Damping Partition $J_x/J_y/J_e$	1.5/1/1.5
Damping Time τ_x	0.016 s
Damping Time τ_y	0.025 s
Damping Time τ_e	0.016 s
Polarization Time	61.7 min
Coupling Constant κ	0.5
Horizontal Emittance (no coupling)	5.49 nm
Horizontal Emittance ($\kappa = 0.5$)	4.11 nm
Vertical Emittance ($\kappa = 0.5$)	2.06 nm
RF Voltage V_{RF}	720 MV
RF frequency f_{RF}	359.856 MHz
Bunch Length	6.05 mm
Max. Hor. Beta	141.26 m
Max. Ver. Beta	135.25 m

Table 8.4: Optics Parameters of one LHeC arc cell with a phase advance of 180°/120°.

8.4 Layout

The design of the Interaction Region (IR) of the LHeC is one of the most crucial parts of the project. It has to consider boundary conditions from

- the lattice design and beam optics of the electron and proton beam
- the geometry of the LHC experimental cavern and the tunnel
- the beam separation scheme which is determined by the bunch pattern of the LHC standard proton operation and related to this the optimisation of the synchrotron light emission and collimation
- and finally the technical feasibility of the hardware.

The design of the interaction region of the ring-ring electron-proton collider is particularly challenging: It has to be optimised with respect to a well matched beam optics that adapts the optical parameters from the new electron-proton interaction point to the standard LHC proton beam optics in the arc and to the newly established beam optics of the electron ring respectively. At the same time the two beams have to be separated efficiently and guided into their corresponding magnet lattice. As a general rule that has been established in the context of this study any modification in the standard LHC lattice and any impact on the LHC proton beam parameters had to be chosen moderately to avoid detrimental effects on the performance of the LHC proton-proton operation.

The layout and parameters of the new e/p interaction point are defined by the particle physics reqirements. At present the physics programme that has been proposed for the LHeC [1] follows two themes - a high luminosity, high Q^2 programme requiring a forward and backward detector acceptance of around 10° and a low x, low Q^2 programme, which requires an increased detector acceptance in forward and backward direction of at least 1° and could proceed with reduced luminosity. Accordingly two machine scenarios have been studied for the interaction region design. Firstly, a design that has been optimised for high luminosity with an acceptance of 10° and secondly, a high acceptance design that allows for a smaller opening angle of the detector. In both cases the goal for the machine luminosity is in the range of $10^{33}\,\mathrm{cm}^{-1}\,\mathrm{s}^{-1}$ but the layout differ in the magnet lattice, the achievable absolute luminosity and mainly the synchrotron radiation that is emitted during the beam separation process. Both options will be presented here in detail and the corresponding design luminosity, the technical requirements and the synchrotron radiation load will be compared. In both cases however, a well matched spot size of the electron and proton beam had to be established at the collision point: Experience in SPS and HERA [2] showed that matched beam cross sections $\sigma_x(p) = \sigma_x(e)$, $\sigma_y(p) = \sigma_y(e)$ have to be established between the two colliding beams to guarantee stable beam conditions. Considering the different nature of the beams, namely the emittances in the two planes the interaction region design has to consider this boundary condition and the beam optics has to be established according to this goal.

The basic beam parameters however like energy, particle intensity and beam emittances are identical for both designs, determined by the electron and proton ring lattices and the pre-accelerators. They are summarised in Table 8.5.

Table 8.5: Main parameters for e/p collisions.

Quantity	unit	e	p
Beam energy	GeV	60	7000
Total beam current	mA	100	860
Number of bunches		2808	2808
Particles/bunch N_b	10^{10}	2.0	17
Horiz. emittance	nm	5.0	0.5
Vert. emittance	nm	2.5	0.5
Bunch distance	ns	25	

Colliding two beams of different characteristics, the luminosity obtained is given by the equation

$$L = \sum_{i=1}^{n_b} (I_e * I_p) \frac{1}{e^2 f_0 2\pi \sqrt{\sigma_{xp}^2 + \sigma_{xe}^2} \sqrt{\sigma_{yp}^2 + \sigma_{ye}^2}}, \tag{8.7}$$

where $\sigma_{x,y}$ denotes the beam size of the electron and proton beam in the horizontal and vertical plane and I_e, I_p the electron and proton single bunch currents. In all IR layouts the electron beam size at the IP is matched to the proton beam size in order to optimise the delivered luminosity and minimise detrimental beam beam effects.

The main difference of the IR design for the electron proton collisions with respect to the existing LHC interaction regions is the fact that the two beams of LHeC cannot be focussed and / or guided at the same time. The different nature of the two beams, the fact that the electrons emit synchrotron radiation and mainly the large difference in the particle momentum make a simultaneous focusing of the two beams impossible. The strong gradients of the proton quadrupoles in the LHC triplet structure cannot be tolerated nor compensated by the electron lattice and a stable optical solution for the electrons is not achievable under the influence of the proton magnet fields. After the collision point the electron beam therefore has to be separated from the proton beam before any strong " 7 TeV like" magnet field is applied.
In order to obtain still a compact design and to optimize the achievable luminosity of the new e/p interaction region, the beam separation scheme has to be combined with the electron mini-beta focusing structure.

Figure 8.17 shows a schematic layout of the interaction region. It refers to the 10 degree option and shows a compact triplet structure that is used for early focusing of the electron beam. The quadrupoles are embedded into the detector opening angle and to obtain the required separation effect they are shifted in the horizontal plane and act as combined function magnets: Thus focusing and separation of the electron beam are combind in a very compact lattice structure, which is the prerequisite to achieve luminosity values in the 10^{33} range.

8.4.1 Beam Separation Scheme

The separation scheme of the two beams has to be optimised with respect to an efficient (i.e. fast) beam separation and a synchrotron radiation power and critical energy of the emitted photons that can be tolerated by a decent absorber design. Two main issues have to be accomplished: a sufficient horizontal distance between the beams has to be generated at the position of the first proton (half) quadrupole, located at a distance of s=22m from the interaction point (the nominal value of the LHC proton lattice). In addition to that, harmful beam beam effects have to be avoided at the first parasitic bunch encounters which will take place at s = 3.75m, as the nominal bunch distance in LHC corresponds to $\Delta t = 25ns$. These secondary bunch crossings have to be avoided as they would lead to intolerable beam-beam effects in both storage rings. As a consequence the separation scheme has to deliver a sufficiently large horizontal distance between the two counter rotating bunches at these locations.

To achieve the first requirement a separation effect is created inside the mini beta quadrupoles of the electron beam: For the design of the ep interaction region a special lattice has been chosen: The large momentum difference of the two colliding beams provides a very elegant way to separate the lepton and the hadron beam: The focusing scheme that leads to well matched electron and proton beams has been combined with a fast beam separation. Shifting the mini-beta quadrupoles of the electron beam and installing a 15.8m long but weak separator dipole magnet close to the IP provides the gentle separation scheme needed to keep the synchrotron radiation level in the IR within reasonable limits.
The nearest proton quadrupole to the IP is designed as a half-quadrupole to ease the extraction of the outgoing electron beam. At this location (at s=22 m) a minimum separation of $\Delta x = 55mm$ is needed to guide the electron beam along the mirror plate of a sc. proton half quadrupole [4]. A first layout of this magnet is sketched in figure 8.18

The horizontal offsets of the mini beta lenses are chosen individually in a way that the

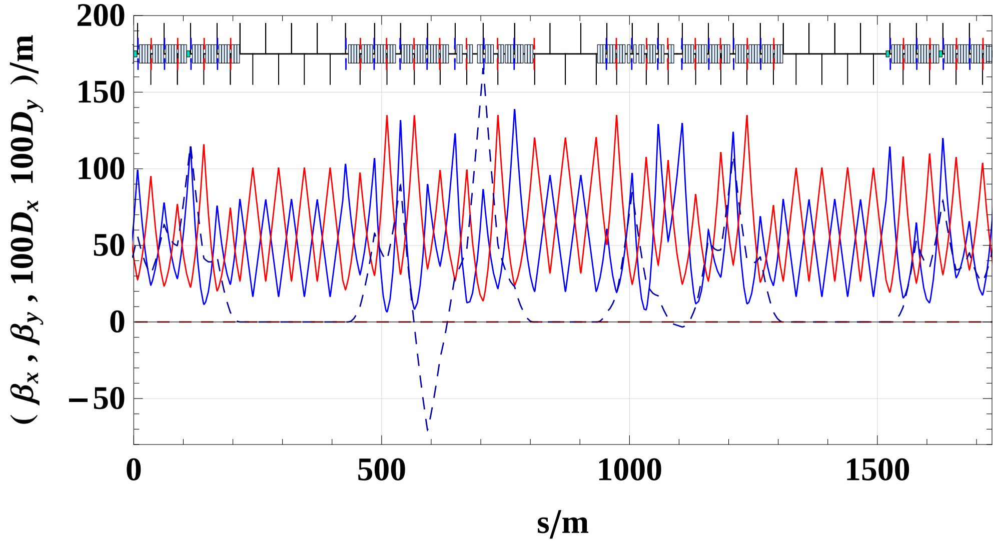

Figure 8.16: Bypass Optics Point 5.

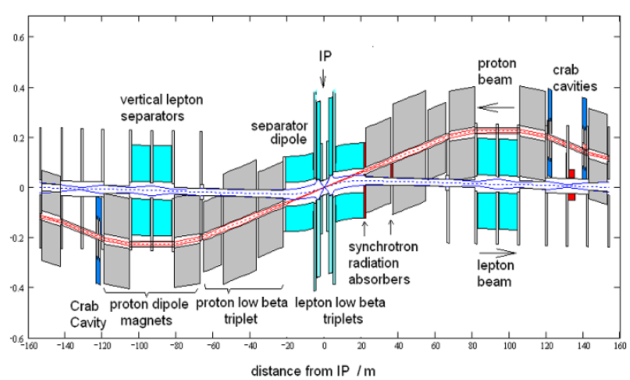

Figure 8.17: Schematic layout of the LHeC interaction region

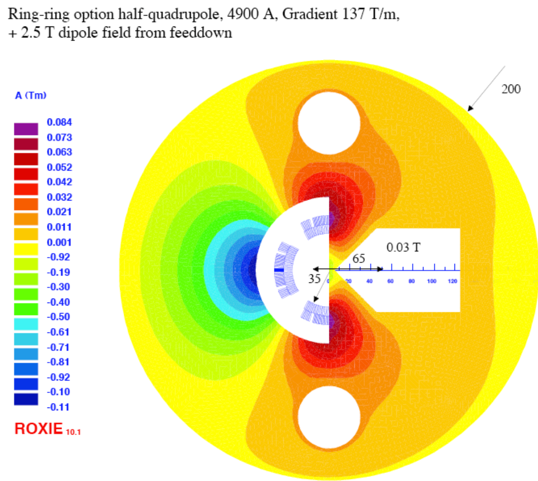

Figure 8.18: Super conducting half quadrupole in the proton lattice: The electron beam will pass on the right and side of the mirror plate in a quasi field free region.

resulting bending strength in the complete separation scheme (quadrupole triplet / dublet and separator dipole) is constant. In this way a moderate separation strength is created with a constant bending radius of $\rho = 6757m$ for the 10 degree option. In the case of the 1 degree option the quadrupole lenses of the electron lattice cannot be included inside the detector design as the opening angle of the detector does not provide enough space for the hardware of the machine lattice. Therefore a much larger distance between the IP and the location of the first electron lens had to be chosen (Δ s =6.2m instead of Δ s =1.2m). As a consequence - to achieve the same overall beam separation - stronger magnetic separation fields have to be applied resulting in a a bending radius of $\rho = 4057m$ in this case. In both cases the electron quadrupoles are aligned along the design orbit of the electron beam to avoid local strong bending fields and keep the synchrotron radiation power to a minimum. This technique has already been succesfuly applied at the layout of the HERA electron-proton collider [3].

Still the separation at the location of the first proton magnet is small and at this point a half quadrupole design for this super conducting magnet has been chosen. The resulting beam parameters - including the expected luminosity for this ring ring option - are summarised in table 2.

It has to be pointed out in this context that the arrangement of the off centre quadrupoles as well as the strength of the separator dipole depend on the beam optics of the electron beam. The beam size at the parasitic crossings as well as at the proton quadrupole will determine the required horizontal distance between the electron and proton bunches. The strength and position of these magnets however will determine the optical parameters, including the dispersion function that is created during the separation process itself. Therefore a self-consistent layout concerning optics, beam separation and geometry of the synchrotron light absorbers has to be found.

It is obvious that these boundary conditions have to be fulfilled not only during luminosity

Table 8.6: Parameters of the mini beta optics for the 1° and 10° options of the LHeC Interaction Region.

Detector Option		1°		10°	
Quantity	unit	electrons	protons	electrons	protons
Number of bunches		2808			
Particles/bunch N_b	10^{10}	1.96	17	1.96	17
Horiz. beta-function	m	0.4	4.0	0.18	1.8
Vert. beta-function	m	0.2	1.0	0.1	0.5
Horiz. emittance	nm	5.0	0.5	5.0	0.5
Vert. emittance	nm	2.5	0.5	2.5	0.5
Distance to IP	m	6.2	22	1.2	22
Crossing angle	mrad	1.0		1.0	
absolute Luminosity	$m^{-2}s^{-1}$	$8.54 * 10^{32}$		$1.8 * 10^{33}$	
Loss-Factor S		0.86		0.75	
effective Luminosity	$m^{-2}s^{-1}$	$7.33 * 10^{32}$		$1.34 * 10^{33}$	

operation of the e/p rings. During injection and the complete acceleration procedure of the electron ring the influence of the electron quadrupoles on the proton beam has to be compensated with respect to the proton beam orbit (as a result of the separation fields) as well as to the proton beam optics: The changing deflecting fields and gradients of the electron magnets will require correction procedures in the proton lattice that will compensate this influence at any moment.

8.4.2 Crossing Angle

A central aspect of the LHeC IR design is the beam-beam interaction of the colliding elecron and proton bunches. The bunch structure of the electron beam will match the pattern of the LHC proton filling scheme for maximal luminosity, giving equal bunch spacings of 25 ns to both beams. The IR design therefore is required to separate the bunches as quickly as possible to avoid additional bunch interactions at these positions and limit the beam beam effect to the unavoidable interactions at the IP. The design bunch distance in the LHC proton bunch chain corresponds to $\Delta t = 25ns$ or $\Delta s = 7.5m$. The counter rotating bunches therefore meet after the crossing at the interaction point again at a distance s=3.75m from the IP in a so-called parasitic encounter. To avoid detrimental effects from these parasitic crossings the above mentioned separation scheme has to be supported by a crossing angle that will deliver the required horizontal distance between the bunches at the first parasitic bunch crossings. This technique is used in all LHC interaction points. In the case of LHeC however the crossing angle is determined by the emittance of the electron beam and the resulting beam size which is considerably larger than the usual proton beams in the storage ring. In the case of the LHeC IR a crossing angle of $\theta = 1mrad$ is considered as sufficient to avoid beam-beam effects from this parasitic crossings. Figure 8.19 shows the position of the first possible parasitic encounters and the effect of the crossing angle to deliver a sufficient separation at these places.

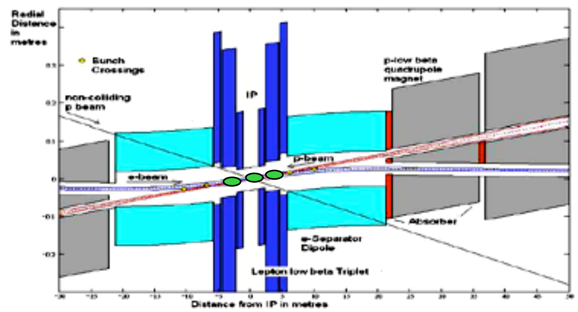

Figure 8.19: LHeC interaction region including the location of the first parasitic bunch encounters where due to the crossing angle of 1 mrad a sufficient beam separation is achieved.

The detailed impact of one beam on another is evaluated from a dedicated beam-beam interaction study, and the absolute requirement is a minimum of $5\sigma_e + 5\sigma_p$ separation at every parasitic crossing node. Due to the larger electron emittance the separation is mainly dominated by the electron beam parameters, and the rapid growth of the β-function in the drift around the IP,

$$\beta(s) = \beta^* + \frac{l^2}{\beta^*}, \tag{8.8}$$

where the asterix refers to the values at the IP. Therefore optical layouts with smaller β^* and larger l* are harder to separate the beams due to the large growth of β and the increased beam separation requirement.

Beside this beneficial effect, a crossing angle will help to reduce the required strength in the separation scheme and minimise the synchrotron radiation power that is created inside the interaction region. However due to the geometric effect at the IP the luminosity is reduced due to the fact that the bunches will not collide head on anymore. This reduction is expressed in a geometric luminosity reduction factor "S", that depends on the crossing angle θ, the length of the electron and proton bunches σ_{ze} and σ_{zp} and the transverse beam dimension in the pane of the bunch crossing σ_x^*:

$$S(\theta) = \left[1 + \left(\frac{\sigma_{sp}^2 + \sigma_{se}^2}{2\sigma_x^{*2}}\right)\tan^2\frac{\theta}{2}\right]^{-\frac{1}{2}} \quad . \tag{8.9}$$

Accordingly the effective luminosity that can be expected for a given IR layout is obtained by

$$L = S(\theta) * L_0 \tag{8.10}$$

For the beam optics that have been chosen and the crossing angle of $\theta = 1mrad$ the loss factor amounts to $S = 74\%$

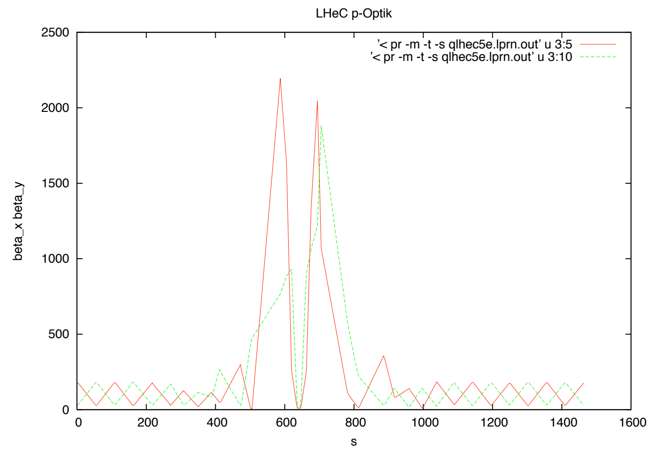

Figure 8.20: Proton optics for the LHeC interaction region. The gradients of the antisymmetric triplet lattice in the standard LHC have been modified to adopt for the requirements of the LHeC flat beam parameters.

8.4.3 Beam Optics and Luminosity

For the design of the proton beam optics in LHeC a special boundary condition had to be observed: For the layout of the four present proton-proton interaction regions in the LHC machine an anti-symmetric option had been chosen: A solution that is appropriate for a round beam optics ($\sigma_x = \sigma_y$). An optimised design for collisions with the flat $e^{\pm}$ beams however requires unequal β -functions for the hadron beam and the existing LHC optics can no longer be maintained. Therefore the optical layout of the existing triplet structure in the LHC had to be modified to match the required beta functions ($\beta_x = 1.8m, \beta_y = 0.5m$) to the regular optics of the FoDo in the arc (Figure 8.20).

In the case of the electron beam optics, two different layouts of the interaction region are considered: As mentioned above according to the preferences of the high energy physics an optical concept for highest achievable luminosity has been studied as well as a solution for maximum detector acceptance. In the first case an opening angle of 10° is available inside the detector geometry and allows to install an embedded magnet structure where the first electron quadrupole lenses can be placed as close as $s = 1.2m$ from the IP. This early focusing scheme leads to moderate values of the β function inside the mini beta quadrupoles and therefore allows for a smaller spot size at the IP and larger luminosity values can be achieved. Still however the quadrupoles require a compact design: While the gradients required by the optical solution are small (for a super conducting design) the outer radius of the first lectron quadrupole is limited to $r_{max} = 210mm$.

In the case of the 1° option the detector design is optimised for largest detector acceptance. Accodingly the opening angle of the detector hardware is too small to deliver space for accelerator magnets. The mini beta quadrupoles therefore have to be located outside the detector,

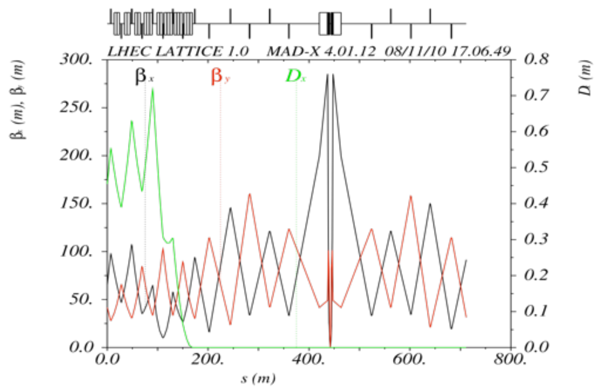

Figure 8.21: Electron optics for the LHeC interaction region. The plot corresponds to the 10 degree option where a triplet structure combined with a separation dipole has ben chosen to separate the two beams.

and a distance $s = 6m$ from the IP had to be chosen in this case. Even if in this case the magnet dimensions are not limited by the detector design the achievable luminosity is about a factor of two smaller than in the 10° case.

The two beam optics that are based on these considerations are discused in detail in the next chapter of this report. Here we refer to the main parameters that are compared in table Table 8.6. In the case of the 10° option a triplet structure has been chosen to allow for moderate values of the beta functions inside the mini beta quadrupoles. The corresponding optics is shown in Figure 8.21. The table includes as well the overall synchrotron radiation power that is produced inside the IR. Due to the larger bending radius (i.e. smaller bending forces) in the case of the 10° option the produced synchrotron radiation power is limited to about 30 kW, while the alternative - high acceptance - option has to handle 50kW synchrotron light.
The details of the synchrotron light characteristics in both cases, including the critical energies and the design for the required absorbers are covered in the next chapters of this report.

For the 1° option the mini beta focusing is based on a quadrupole dublet as the space limitations in the transverse plane are much more relaxed compared to the alternative option and the main issue here was to find a compact design in the longitudinal coordinate: Due to the larger distcance of the focusing and separating magnets from the IP the magnet structure has to be more compact and the separating field stronger to obtain the required horizontal beam distance at the location s=22m of the first proton quadrupole. The corresponding beam optics for both options are explained in full detail below.

Bibliography

[1] U. Schneekloth,*Boundary Conditions for the Interaction Region Design*, 1st ECFA-CERN LHeC workshop, Divonne, France (2008).

[2] M. Bieler *et al.*,*Recent and past experiences with beam beam effects at HERA*, LHC beam-beam workshop, CERN, Geneva (1999).

[3] J. Rossbach, R. Brinkmann,*HERA straight sections for elctron-proton interactions*, IEEE Trans Nucl Science, Vol NS-32,5 (1985).

[4] S. Russenschuck,*super conducing magnet design for the LHeC*, this report

8.5 Interaction Regions

A successful interaction region in an e-p collider must primarily deliver luminosity and detector coverage. Luminosity, both instantaneous and integrated, must be maximised to ensure useful amounts of data are collected. However this should not be pursued at the expense of detector coverage, which is needed to ensure sensitivity to a wide range of processes.

8.5.1 Design Requirements

Detector Coverage and Acceptance

Acceptance describes the amount of angular obstruction of the detector due to the presence of machine elements, as shown in figure 8.22. For example, an acceptance of 10° implies a protrusion of machine elements into the detector such that a cone of 10° half-angle along the beam axis is blocked. The detector is thus unable to see particles emitted at less than this angle, and event data is lost at high pseudo-rapidities. Note that throughout this section, smaller angles denote higher acceptance.

Lower acceptance allows machine elements closer to the IP. Since β grows quadratically with distance, a smaller l^* generally allows stronger focusing of a beam and thus higher luminosity. While there is no direct relationship between l^* and luminosity, a balance must be found to optimise both luminosity and acceptance. Two IR designs are proposed as solutions to the balance between luminosity and acceptance. Both designs aim to achieve a luminosity of $\sim 10^{33}$ cm^{-2}s^{-1}.

1. High Luminosity Layout (HL)

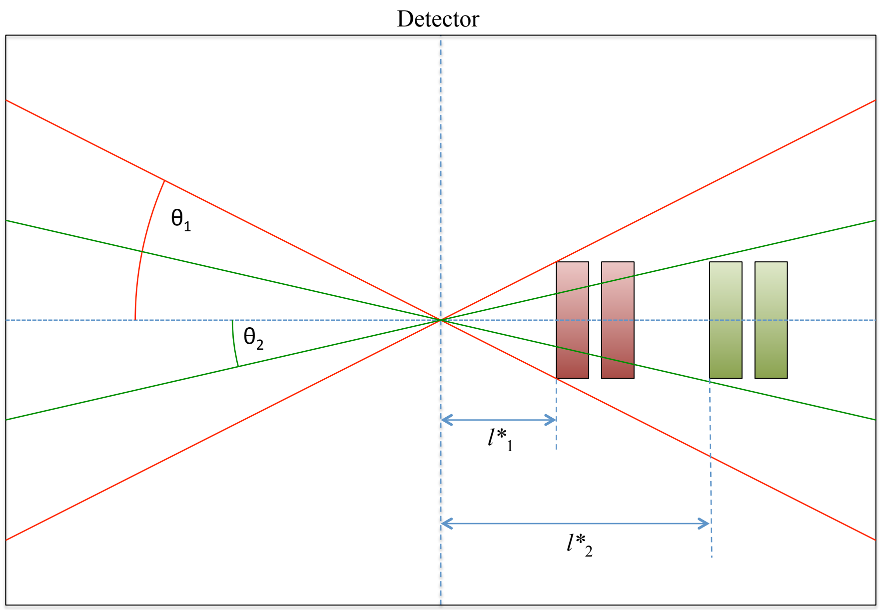

Figure 8.22: Graphical representation of acceptance. θ_1 shows a lower acceptance cone, while θ_2 shows a higher acceptance cone. For machine elements of constant diameter, higher acceptance increases l^*.

- 10° acceptance
- Higher luminosity

2. High Acceptance Layout (HA)

   - 1° acceptance
   - Lower luminosity

In concert with these designs, two plans are proposed for running LHeC. One option is to run with the HL layout, then switch to the HA layout during a shutdown. The second option is to optimise the HA layout for sufficient luminosity to replace the HL layout entirely.

Beam Separation

In an e-p collider IR, there are at least two dissimilar beams. In the case of LHeC, there are two proton beams and an electron beam. One proton beam is brought into collision with the electron beam, while the other, left unsqueezed, is diverted. Unwanted interactions between all these beams must be avoided. To avoid excessive beam-beam interaction other than at the IP, the beams must be separated quickly. The bunch spacing of 25 ns gives rise to parasitic interaction nodes every 3.75 m before and after the IP. Therefore a separation scheme must be implemented which provides sufficient distance between the beams at these points. A minimum separation of $5\sigma_e + 5\sigma_p$ is specified at each parasitic node. Beam-beam interactions are discussed in section [TATIANA].

A further requirement is imposed by the geometry of the IR. An interaction region for an e-p collider involves optics for both the proton and the electron beam. Due to the significantly larger rigidity of the proton beam, the fields used in the proton optics are much stronger than those in the electron optics. While the electron optics do not strongly affect the proton beam, the electron beam will be lost if allowed to pass though the proton optics.

However the electron beam emits far more synchrotron radiation for a given bending angle than does the proton beam, and as such the amount by which the electron beam may be deflected inside the IR is limited. Since the electron IR optics are all situated between the IP and the proton IR optics, this constrains the separation which can be obtained by the time the electron beam reaches the proton optics, at s = 22.96 m.

Due to the large proton focusing magnets, it is infeasible to deflect the electron beam sufficiently to complete avoid them. Instead, a half-quadrupole is designed and employed, such that a second aperture with relatively low field may be included for the electron beam to pass through. After this, further bending is applied to the electron beam to extract it back into the electron accelerator ring lattice.

Lower fields may be obtained in the electron aperture if the distance between the electron aperture and the proton aperture is increased. Thus separation between the two beams at s = 22.96 m must still be maximised, whilst not increasing SR power and ϵ_c to infeasible levels. While this is somewhat flexible, a separation of 55 mm at s = 23 m has been chosen as an attainable target from optical, radiation [NATHAN] and magnet design [RUSSENSCHUCK]standpoints.

Separation Methods The combined requirements of minimising beam-beam interactions and achieving sufficient separation at the proton final quadrupole necessitate the use of multiple separation methods. There are three primary components of the IR separation schemes. Dipoles are used to deflect the electron beam. Due to the limited amount of available space for bending, the electron quadrupoles are offset to induce an additional dipole field, effectively increasing the length of dipole used in the IR. Generally a constant bending radius is used to minimise ϵ_c, although non-constant bends may allow greater control in placement of SR.

A crossing angle is also required at the IP to ensure sufficient separation at the first parasitic crossing. However the crossing angle introduces a loss factor in the instantaneous luminosity, given by

$$L(\theta) = L_0 S(\theta) \tag{8.11}$$

$$S(\theta) = \left[1 + \left(\frac{\sigma_{sp}^2 + \sigma_{se}^2}{2\sigma_x^{*2}}\right)\tan^2\frac{\theta}{2}\right]^{-\frac{1}{2}} \quad . \tag{8.12}$$

where σ_{sp} is the one-sigma width of the proton bunch in the longitudinal direction and σ_{se} that of the electron bunch. Beam separation therefore introduces a further optimisation problem with respect to both luminosity and SR. Note the dependence on beam spot size; due to this a more tightly focussed beam will suffer greater losses than a larger beam.

Lattice Matching and IR Geometry

Once the beams are separated into independent beam pipes, the electron beam must be transported into the ring lattice. Quadrupoles are used in the electron machine LSS to transport the beam from the IP to the dispersion suppressor and match twiss parameters at either end. This matching must be smooth and not require infeasible apertures. Space must be available to insert dipoles and further quadrupoles to allow the orbit of the beam to be designed with regard to the physical layout of the ring and the IR.

The IR and LSS geometries must be designed around a number of further constraints. As well as beam separation, the electron beam must be steered from the electron ring into the IR and back out again. The colliding proton beam must be largely undisturbed by the electron beam. The non-colliding proton beam must be guided through the IR without interacting with either of the other beams.

Proton Beam Matching

Parameters at the IP must be such that the existing proton optics may be altered to produce a matched proton beam. Generally an electron beam is flat, with ϵ_x significantly larger than ϵ_y. However proton beams are generally round, and as such a compromise must be found. In this case, the electron beam's physical cross-section is designed to have an aspect ratio of roughly 2:1. The electron beam spot size is also larger than the existing proton beam spot size, and relaxation of the proton optics is simpler than increasing focusing.

8.5.2 High Luminosity IR Layout

Parameters

Table 8.7 details the interaction point parameters and other parameters for this design. To optimise for luminosity, a small l^* is desired. An acceptance angle of 10° is therefore chosen, which gives an l^* of 1.2m for final focusing quadrupoles of reasonable size.
SR calculations are detailed in section [NATHAN]. The total power emitted in the IR is similar to that in the HERA-2 IR [reference] and as such appears to be reasonable, given enough space for absorbers.

$L(0)$	$1.8{\times}10^{33}$
θ	$1{\times}10^{-3}$
$S(\theta)$	0.746
$L(\theta)$	$1.34{\times}10^{33}$
β_x*	0.18 m
β_y*	0.1 m
σ_x*	$3.00{\times}10^{-5}$ m
σ_y*	$1.58{\times}10^{-5}$ m
SR Power	33 kW
E_c	126 keV

Table 8.7: Parameters for the High Luminosity IR.

Layout

A symmetric final quadrupole triplet layout has been chosen for this design, due to the relatively round beam spot aspect ratio of 1.8:1. Figure 8.23 and table 8.8 detail the layout.

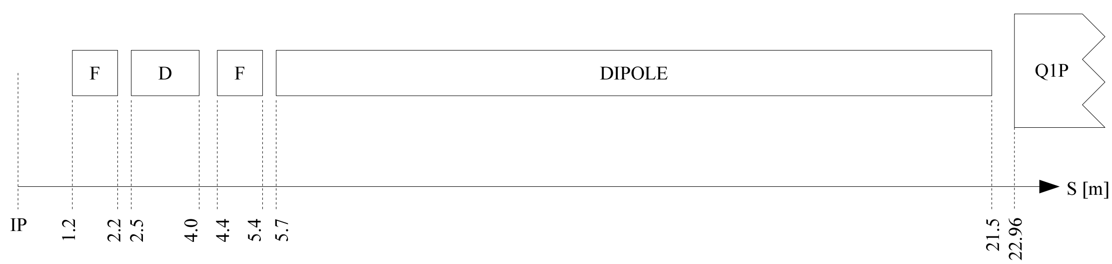

Figure 8.23: Layout of machine elements in the High Luminosity IR. Note that the left side of the IR is symmetric.

The $l*$ of 1.2 m allows both strong focusing of the beam, and constant bending of the beam from 1.2 m to 21.5 m. This is achieved with offset quadrupoles and a separation dipole.

Figure 8.24 shows the β functions of the beam in both planes from the IP to the face of the final proton quadrupole at s = 23 m.

Separation Scheme

An FDF electron triplet is used. This has the effect of generating a large peak in β_x, but is designed such that the peak is between parasitic crossings. The first F quadrupole reduces β_x at s = 3.75 m compared to an initial D quadrupole. The third F quadrupole then brings β_x down from the peak sufficiently to avoid large beam-beam interactions at the second parasitic crossing, s = 7.5 m.

Element	S_{entry} [m]	L [m]	Gradient [T/m]	Dipole Field [T]	Offset [m]
BS.L	-21.5	15.8	-	-0.0296	-
Q3E.L	-5.4	1.0	89.09228878	-0.0296	-3.32240×10^{-4}
Q2E.L	-4	1.5	-102.2013150	-0.0296	2.89624×10^{-4}
Q1E.L	-2.2	1.0	54.34070578	-0.0296	-5.44711×10^{-4}
IP	0.0	-	-	-	-
Q1E.R	1.2	1.0	54.34070578	0.0296	5.44711×10^{-4}
Q2E.R	2.5	1.5	-102.2013150	0.0296	-2.89624×10^{-4}
Q3E.R	4.4	1.0	89.09228878	0.0296	3.32240×10^{-4}
BS.R	5.7	15.8	-	-0.0296	-

Table 8.8: Machine elements for the High Luminosity IR. S_{entry} gives the leftmost point of the idealised magnetic field of an element. Note that S is relative to the IP.

This is aided by the bending provided by the offset quadrupoles, and also the IP crossing angle of 1 mrad. These elements ensure that the separation between the beams, normalised to beam size, increases at each parasitic crossing. Note that 1 mrad is not a minimum crossing angle required by beam-beam interaction separation criteria; it is simply a chosen balance between luminosity loss and minimising bend strength. In theory, this layout could support an IP with no crossing angle; however the bend strength required to achieve this would generate an undesirable level of SR power.

Lattice Matching and IR Geometry

The IR is matched into the ring arc lattice by means of matching quads in the LSS. The quads are roughly evenly spaced, with enough space left after the IR section to accommodate the proton optics and the remaining electron ring geometry, which has yet to be designed fully. The solution is nearly symmetric about the IP; however due to the geometry of the LHC machinery, the electron ring itself is not exactly symmetric. As such the solution differs slightly on either side of the LSS. Table 8.9 details the layout of machine elements in the LSS. Five matching quadrupoles are used on either side of the IP. However a sixth quadrupole is also used on the left side, next to the dispersion suppressor. Due to the asymmetric design of the dispersion suppressors, a quadrupole (MQDSF.L2) is included at the same distance from the IP on the right side as part of the dispersion suppressor, while one is not included on the left. MQDSF.L2 is required to match the optics, but is more constrained than the other matching quadrupoles. Figure 8.25 shows the β functions of the matching from the IP to the dispersion suppressor, on both sides of the IP. Figure 8.26 shows this on one side of the IP only for detail.

A smooth matching is obtained, with the IR β peaks being brought down and controlled before being matched into the arc solution. The beam envelopes in the LSS are of reasonable size and do not require excessive aperture.

Note that this solution is not matched for dispersion as the rest of the ring geometry in the LSS and IR areas is yet to be designed. As it stands, having a non-zero bend strength in the

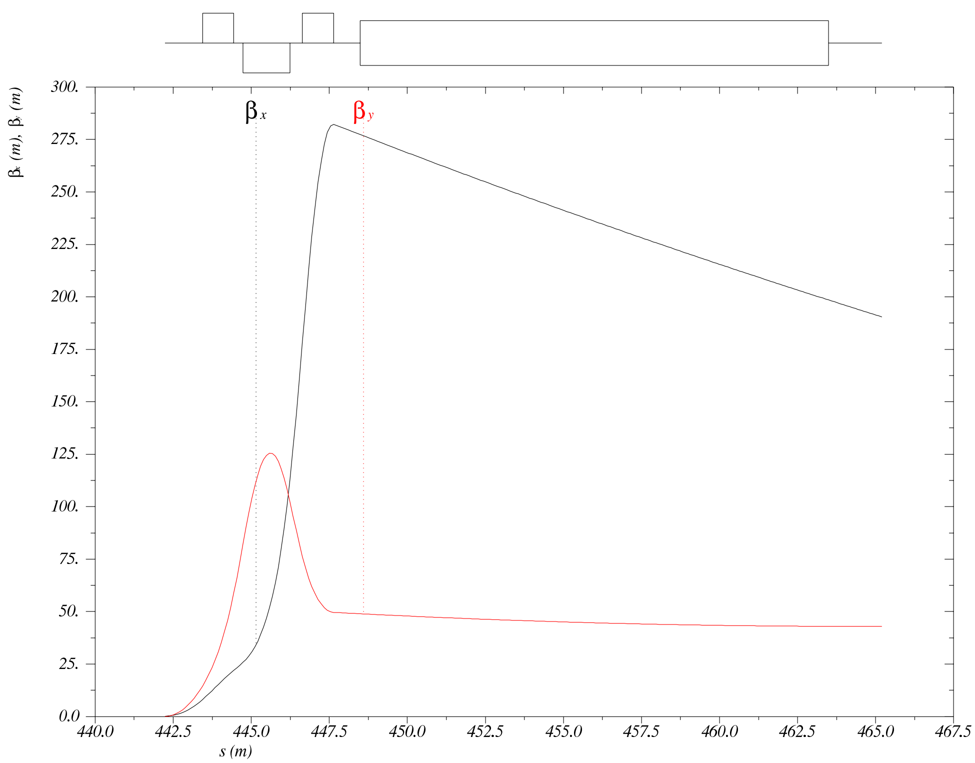

Figure 8.24: β functions in both planes for the High Luminosity IR layout, from the IP to the face of the final proton quadrupole at s = 23 m. Note that s is relative to the ring, which begins at the left side of the left dispersion suppressor of IP2.

IR dipoles and offset quads results in a non-physical lattice; in real space the ring will not join up, as demonstrated in figure 8.27.

Plans for the remaining IR geometry include a second horizontal dipole, and quadrupoles, on either side to turn each separation dipole into a dispersion-free S-shaped bend. This will be used to extract the beam into the electron machine. However other challenges are to be considered as vertical separation must also be achieved.

Element	S_{entry} [m]	L [m]	Gradient [T/m]
MQDSF.L2	-268.8944	1.0	9.611358758
MQDM5.L2	-240.5	1.0	-7.435432612
MQFM4.L2	-198.5	1.0	7.148957108
MQDM3.L2	-160.5	1.0	-6.493088294
MQFM2.L2	-120.5	1.0	6.057685328
MQDM1.L2	-82.5	1.0	-4.962254798
MQDM1.R2	81.5	1.0	-4.977379112
MQFM2.R2	119.5	1.0	6.030944724
MQDM3.R2	159.5	1.0	-6.63145508
MQFM4.R2	197.5	1.0	6.884472924
MQDM5.R2	239.5	1.0	-7.439587356

Table 8.9: Machine elements for the High Luminosity LSS layout. S_{entry} gives the leftmost point of the idealised magnetic field of an element. Note that S is relative to the IP.

8.5.3 High Acceptance IR Layout

Parameters

Table 8.10 details the interaction point parameters and other parameters for this design. The chosen acceptance for this layout is 1°. For final electron focusing magnets of reasonable strength this places all elements outside the limits of the detector, at z = ±6.2m, where z the is longitudinal axis of the detector. Due to the small crossing angle the magnets are thus placed at s = ±6.2m. As such, the actual acceptance of the layout is limited by the beam pipe rather than the size of machine elements. This also gives further flexibility in the strengths and designs of the final focusing quadrupoles, although this flexibility is not exploited in the design.

$L(0)$	8.54×10^{32}
θ	1×10^{-3}
$S(\theta)$	0.858
$L(\theta)$	7.33×10^{32}
β_x*	0.4 m
β_y*	0.2 m
σ_x*	4.47×10^{-5} m
σ_y*	2.24×10^{-5} m
SR Power	51 kW
E_c	163 keV

Table 8.10: Parameters for the High Acceptance IR.

SR calculations are detailed in section [NATHAN]. The total power emitted in the IR is similar

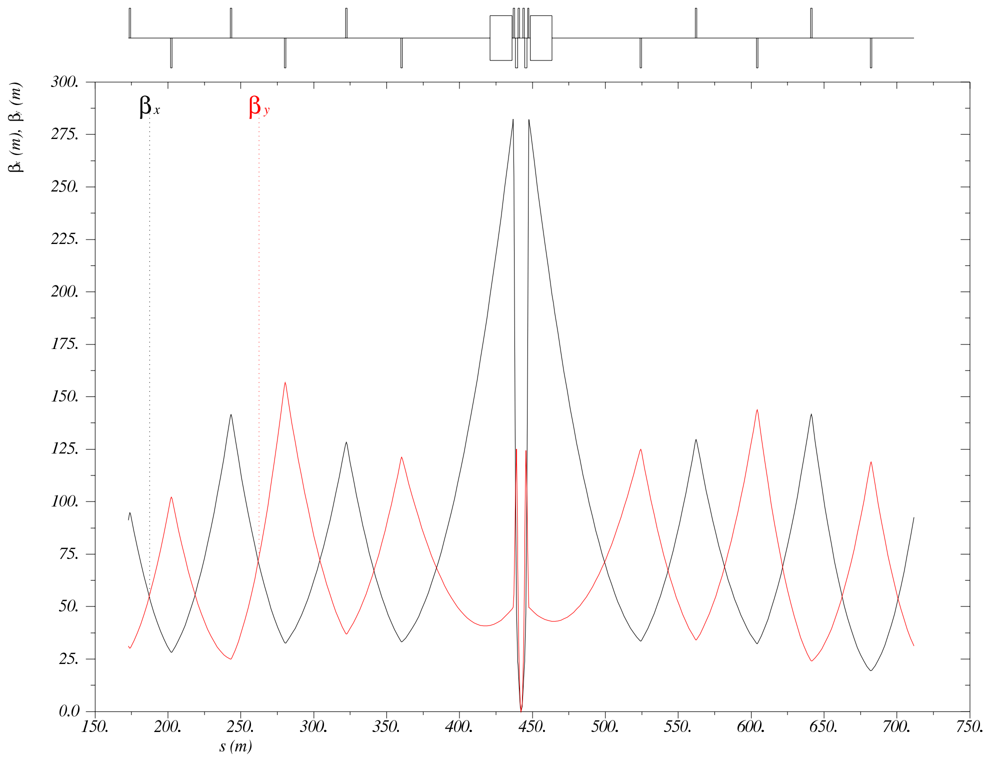

Figure 8.25: β functions in both planes for the High Luminosity IR layout, from the end of the left dispersion suppressor to the start of the right dispersion suppressor. Note that s is relative to the ring, which begins at the left side of the left dispersion suppressor of IP2.

to that in the HERA-2 IR [reference] and as such appears to be reasonable, given enough space for absorbers. However it is significantly higher than that in the high luminosity layout. As discussed in section [NATHAN], an option exists to reduce the total SR power by including a dipole field in the detector, thus mitigating the limitation imposed on dipole length by the larger l^*.

Layout

A symmetric final quadrupole doublet layout has been chosen for this design. The beam spot aspect ratio of 2:1 is marginally flatter than the High Luminosity layout, and as such a triplet is less suitable. Figure 8.28 and table 8.11 detail the layout.

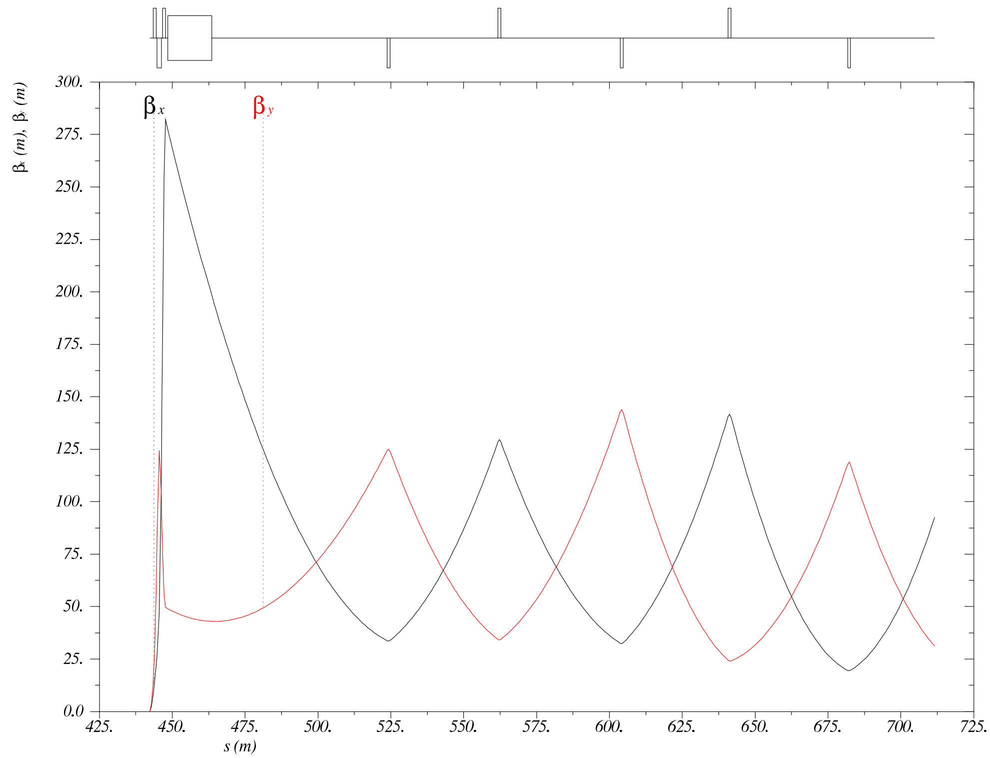

Figure 8.26: β functions in both planes for the High Luminosity IR layout, from the IP to the start of the right dispersion suppressor. Note that s is relative to the ring, which begins at the left side of the left dispersion suppressor of IP2.

The l^* of 6.2m imposes limitations on focusing and bending in this layout. Focusing is limited by quadratic β growth through a drift space, which is increased for smaller β^*. As such, lower instantaneous luminosity is attainable.

Since offset quadrupoles are used to separate the beams, this layout has less total dipole length available. Additionally, the first parasitic crossing occurs before the beam is focused in the first quadrupole. This further limits final focusing as the beam cannot be permitted to grow too large by this time. The loss of dipole length also means stronger bending must be used later, increasing SR power generation.

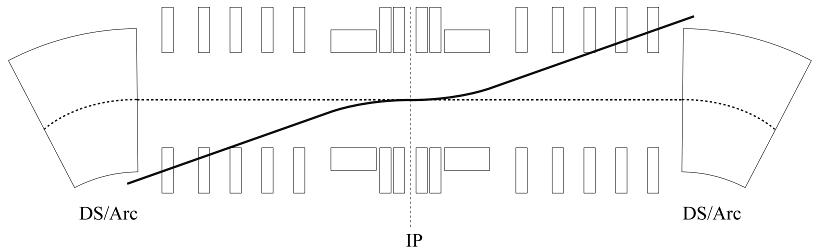

Figure 8.27: Graphical representation of misaligned LSS/IR geometry. With beam steering in the IR and no compensation in the LSS, the electron beam no longer lines up with the ring lattice reference orbit. Diagram is not to scale and does not represent the correct optical layout of the IR nor the LSS.

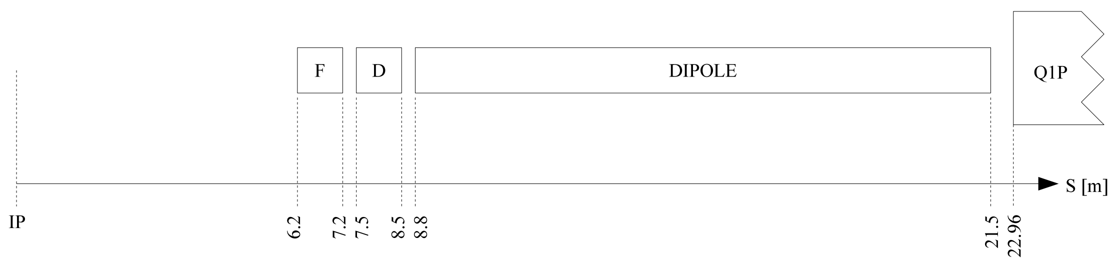

Figure 8.28: Layout of machine elements in the High Acceptance IR. Note that the left side of the IR is symmetric.

Element	S_{entry} [m]	L [m]	Gradient [T/m]	Dipole Field [T]	Offset [m]
BS.L	-21.5	12.7	-	-0.0493	-
Q2E.L	-8.5	1.0	-77.31019000	-0.0493	6.37691×10^{-4}
Q1E.L	-7.2	1.0	90.40354154	-0.0493	-5.45333×10^{-4}
IP	0.0	-	-	-	-
Q1E.R	6.2	1.0	90.40354154	0.0493	5.45333×10^{-4}
Q2E.R	7.5	1.0	-77.31019000	0.0493	-6.37691×10^{-4}
BS.R	8.8	12.7	-	0.0493	-

Table 8.11: Machine elements for the High Acceptance IR. S_{entry} gives the leftmost point of the idealised magnetic field of an element. Note that S is relative to the IP.

Figure 8.29 shows the β functions of the beam in both planes from the IP to the face of the final proton quadrupole at s = 23 m.

Separation Scheme

The final electron doublet is arranged such that the peak in β_y is large, while the peak in β_x is controlled and kept small. Unlike the High Luminosity layout, the first parasitic crossing is

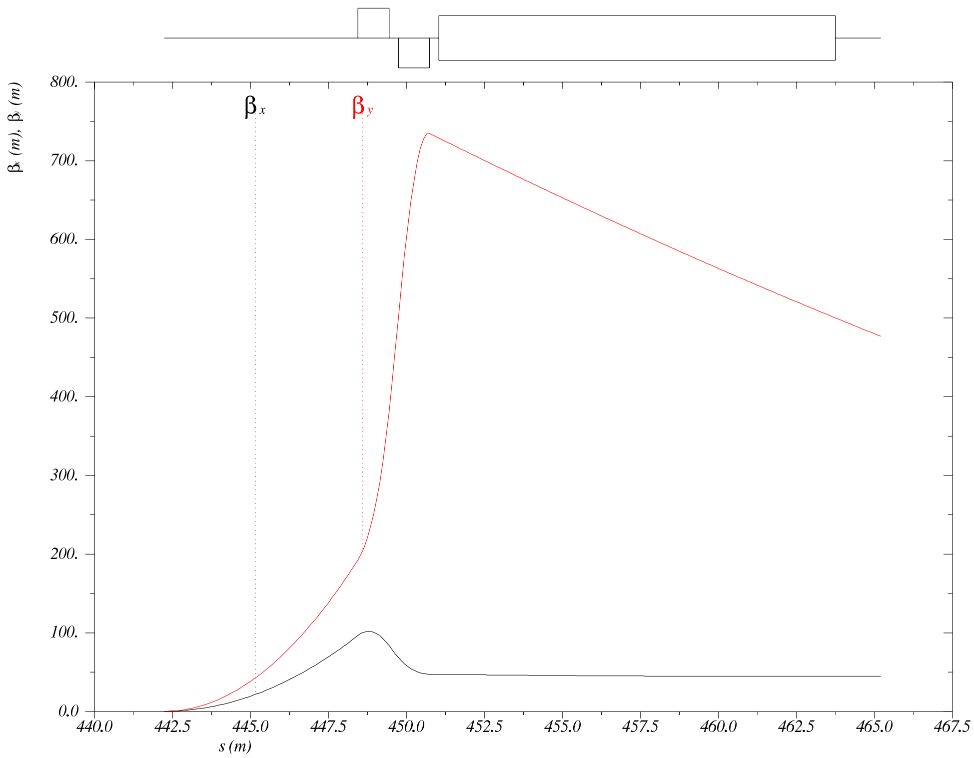

Figure 8.29: β functions in both planes for the High Acceptance IR layout, from the IP to the face of the final proton quadrupole at s = 23 m. Note that s is relative to the ring, which begins at the left side of the left dispersion suppressor of IP2.

reached before focusing begins. As such there is a minimum crossing angle of roughly 0.7 mrad, which is dependent solely upon β growth in the drift space. For comparison with the High Luminosity layout, and as a balance between luminosity loss and SR power generation, a crossing angle of 1 mrad has been chosen.

Lattice Matching and IR Geometry

The IR is matched into the ring arc lattice by means of matching quads in the LSS. The quads are roughly evenly spaced, with enough space left after the IR section to accommodate the proton optics and the remaining electron ring geometry, which has yet to be designed fully. The solution is nearly symmetric about the IP; however due to the geometry of the LHC ma-

Element	S_{entry} [m]	L [m]	Gradient [T/m]
MQDSF.L2	-268.8944	1.0	9.643324144
MQFM6.L2	-237.5	1.0	-7.513288936
MQDM5.L2	-205.5	1.0	7.74537173
MQFM4.L2	-174.5	1.0	-6.18152704
MQDM3.L2	-143.5	1.0	6.475404012
MQFM2.L2	-111.5	1.0	-9.254556824
MQDM1.L2	-80.5	1.0	5.843405232
MQDM1.R2	79.5	1.0	5.843405232
MQFM2.R2	110.5	1.0	-9.254556824
MQDM3.R2	142.5	1.0	6.475404012
MQFM4.R2	173.5	1.0	-6.048380018
MQDM5.R2	204.5	1.0	7.360488416
MQFM6.R2	236.5	1.0	-7.225547436

Table 8.12: Machine elements for the High Acceptance LSS layout. S_{entry} gives the leftmost point of the idealised magnetic field of an element. Note that S is relative to the IP.

chinery, the electron ring itself is not exactly symmetric. As such the solution differs slightly on either side of the LSS. Table 8.12 details the layout of machine elements in the LSS. Six matching quadrupoles are used on either side of the IP. As in the High Luminosity layout, an extra quadrupole (MQDSF.L2) is employed on the left side to account for the asymmetry of the dispersion suppressors. Figure 8.30 shows the β functions of the matching from the IP to the dispersion suppressor, on both sides of the IP. Figure 8.31 shows this on one side of the IP only for detail.

As with the High Luminosity layout, a smooth matching is obtained, with the IR β peaks being brought down and controlled before being matched into the arc solution. The beam envelopes in the LSS are of reasonable size and do not require excessive aperture.

Other geometric issues must again be addressed, which are briefly discussed in section 8.5.2.

8.5.4 Comparison of Layouts

Table 8.13 shows a direct comparison of various parameters of the two layouts.

The difference in luminosity after considering losses due to the crossing angle is a factor of 1.8. However it should be noted that this design strives for technical feasibility and both layouts could be squeezed further to decrease β^* in both planes. The High Luminosity layout could likely be squeezed further than the High Acceptance layout due to the large difference in l^*, as shown in figure 8.32 which compares the two IR layouts. At this stage both designs deliver their required IP parameters of luminosity and acceptance and appear to be feasible.

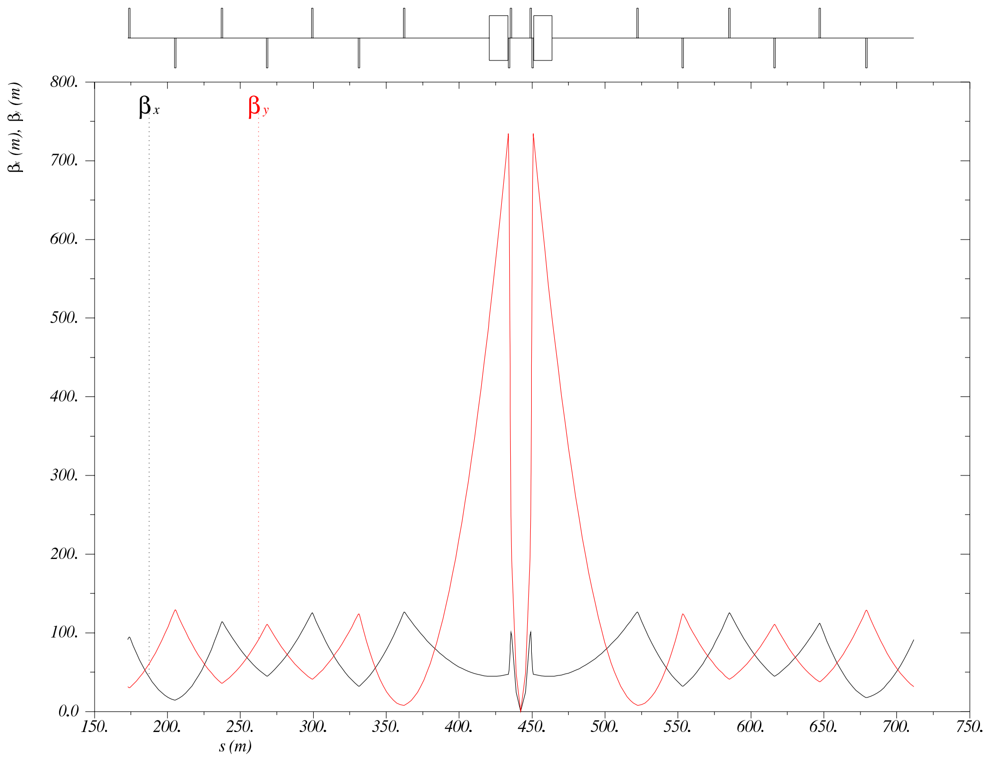

Figure 8.30: β functions in both planes for the High Acceptance IR layout, from the end of the left dispersion suppressor to the start of the right dispersion suppressor. Note that s is relative to the ring, which begins at the left side of the left dispersion suppressor of IP2.

The High Acceptance design generates a significantly higher level of SR power. This still appears to be within reasonable limits and is discussed in section [NATHAN]. Furthermore, an option is discussed to install a dipole magnet in the detector. This early separation would reduce the required strength of the dipole fields in the IR, significantly reducing total SR power.

8.5.5 Synchrotron radiation and absorbers

Introduction

The synchrotron radiation (SR) in the interaction region has been analyzed in three ways. The SR was simulated in depth using a program made with the Geant4 (G4) toolkit. In addition a cross check of the total power and average critical energy was done in IRSYN, a Monte Carlo

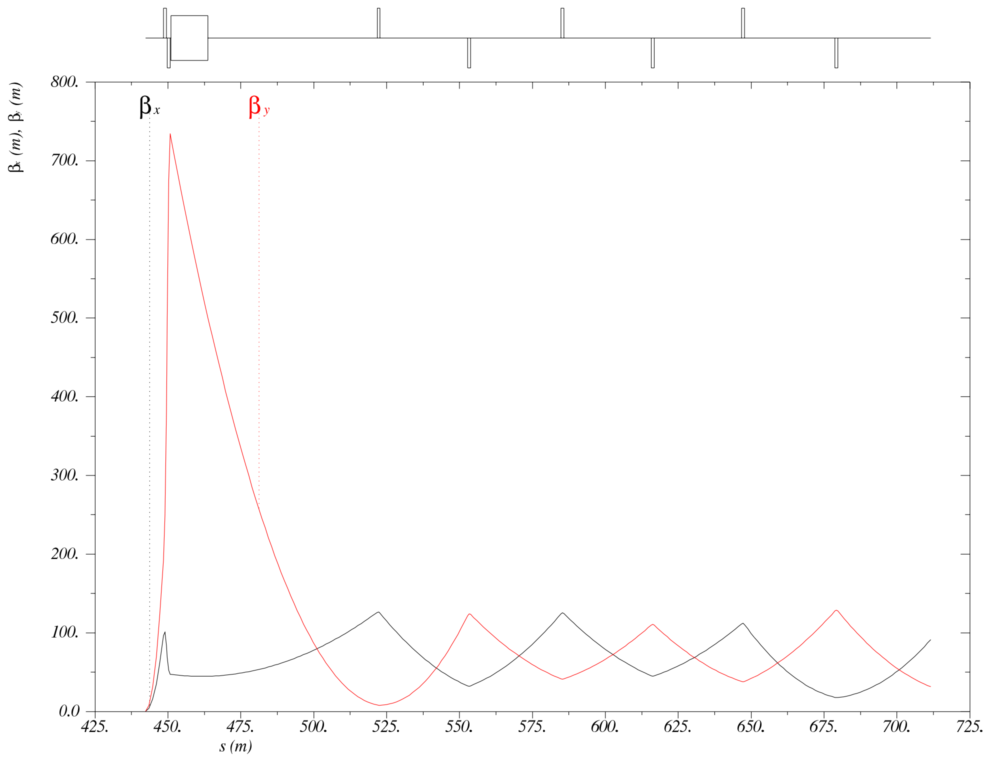

Figure 8.31: β functions in both planes for the High Luminosity IR layout, from the IP to the start of the right dispersion suppressor. Note that s is relative to the ring, which begins at the left side of the left dispersion suppressor of IP2.

simulation package written by R. Appleby. [410] A final cross check has been made for the radiated power per element using an analytic method. These other methods confirmed the results seen using G4. The G4 program uses Monte Carlo methods to create gaussian spatial and angular distributions for the electron beam. The electron beam is then guided through vacuum volumes that contain the magnetic fields for the separator dipoles and electron final focusing quadrupoles.

The SR is generated in these volumes using the appropriate G4 process classes. The G4 SR class was written for a uniform magnetic field, and therefore the quadrupole volumes were divided such that the field remained approximately constant in each volume. This created agreement between upstream and downstream quadrupoles since for a downstream quadrupole the beta function at the entrance and exit are reversed from its upstream counterpart. This

Parameter	HL	HA
$L(0)$	$1.8{\times}10^{33}$	$8.54{\times}10^{32}$
θ	$1{\times}10^{-3}$	$1{\times}10^{-3}$
$S(\theta)$	0.746	0.858
$L(\theta)$	$1.34{\times}10^{33}$	$7.33{\times}10^{32}$
β_x*	0.18 m	0.4 m
β_y*	0.1 m	0.2 m
σ_x*	$3.00{\times}10^{-5}$ m	$4.47{\times}10^{-5}$ m
σ_y*	$1.58{\times}10^{-5}$ m	$2.24{\times}10^{-5}$ m
SR Power	33 kW	51 kW
E_c	126 keV	163 keV

Table 8.13: Parameters for the High Luminosity IR.

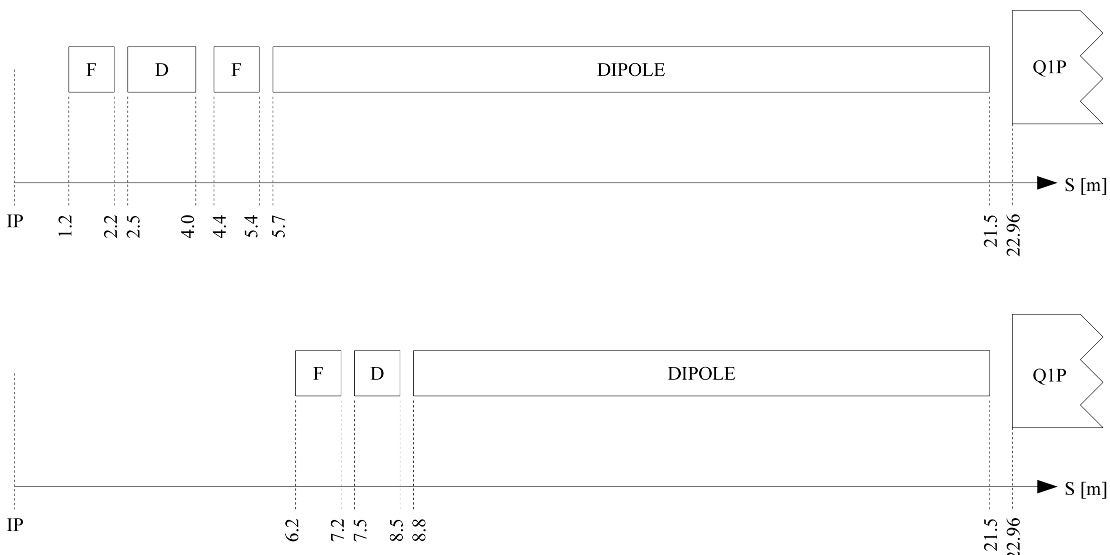

Figure 8.32: Scale comparison of the layouts for the High Luminosity and High Acceptance designs. Note the large difference in $l*$.

agreement confirms that the field was approximately constant in each volume.

The position, direction, and energy of each photon created is written as ntuples at user defined Z values. These ntuples are then used to analyze the SR fan as it evolves in Z. The analysis was done primarily through the use of MATLAB scripts. It was necessary to make two versions of this program. One for the high luminosity design and one for the high detector acceptance design.

Before going further I will explain some conventions used for this section. I will refer to the electron beam as *the beam* and the proton beams will be referred to as either the interacting or non interacting proton beams. The beam propagates in the -Z direction and the interacting proton beam propagates in the +Z direction, I will use a right handed coordinate system where the X axis is horizontal and the Y axis is vertical. The beam centroid always remains in the Y = 0 plane. The *angle of the beam* will be used to refer to the angle between the beam centroid's velocity vector and the Z axis, in the Y = 0 plane. This angle is set such that the beam propagates in the -X direction as it traverses Z.

The SR fans extension in the horizontal direction is driven by the angle of the beam at the entrance of the upstream separator dipole. Because the direction of emitted photons is parallel to the direction of the electron that emitted it, the angle of the beam and the distance to the absorber are both greatest at the entrance of the upstream separator dipole and therefore this defines one of the edges of the synchrotron fan on the absorber. The other edge is defined by the crossing angle and the distance from the IP to the absorber. The S shaped trajectory of the beam means that the smallest angle of the beam will be reached at the IP. Therefore the photons emitted at this point will have the lowest angle and for this given angle the smallest distance to the absorber. This defines the other edge of the fan in the horizontal direction.

The SR fans extension in the vertical direction is driven by the beta function and angular spread of the beam. The beta function along with the emittance defines the r.m.s. spot size of the beam. The vertical spot size defines the Y position at which photons are emitted. On top of this the vertical angular spread defines the angle between the velocity vector of these photons and the Z axis. Both of these values produce complicated effects as they are functions of Z. These effects also affect the horizontal extension of the fan however are of second order when compared to the angle of the beam. Since the beam moves in the Y = 0 plane these effects dominate the vertical extension of the beam.

The number density distribution of the fan is a complicated issue. The number density at the absorber is highest between the interacting beams. The reason for this is that although the separator dipoles create significantly more photons the number of photons generated per unit length in Z is much lower for the dipoles as opposed to the quadrupoles due to the high fields experienced in the quadrupoles. The position of the quadrupole magnets then causes the light radiated from them to hit the absorber in the area between the two interacting beams.

High Luminosity

Parameters: The parameters for the high luminosity option are listed in Table 8.14. The separation refers to the displacement between the two interacting beams at the face of the proton triplet.

The energy, current, and crossing angle (θ_c) are common values used in all RR calculations. The dipole field value refers to the constant dipole field created throughout all dipole elements in the IR. The direction of this field is opposite on either side of the IP. The quadrupole elements have an effective dipole field created by placing the quadrupole off axis, which is the same as this constant dipole field. The field is chosen such that 55 mm of separation is reached by the face of the proton triplet. This separation was chosen based on S. Russenschuck's SC quadrupole design for the proton final focusing triplet. [411] The separation between the interacting beams can be increased by raising the constant dipole field. However, for a dipole magnet $P_{SR} \propto |B^2|$, [412] therefore an optimization of the design will need to be discussed. The chosen parameters give a flux of 5.39×10^{18} photons per second at Z = -21.5 m.

Characteristic	Value
Electron Energy [GeV]	60
Electron Current [mA]	100
Crossing Angle [mrad]	1
Absorber Position [m]	-21.5
Dipole Field [T]	0.0296
Separation [mm]	55
γ/s	5.39×10^{18}

Table 8.14: High Luminosity: Parameters

Power and Critical Energy: Table 8.15 shows the power of the SR produced by each element along with the average critical energy produced per element. This is followed by the total power produced in the IR and the average critical energy. Since the G4 simulations utilize Monte Carlo, multiple runs should be made with various seeds to get an estimate for the standard error.

Element	Power [kW]	Critical Energy [keV]
DL	6.4	71
QL3	5.3	308
QL2	4.3	218
QL1	0.6	95
QR1	0.6	95
QR2	4.4	220
QR3	5.2	310
DR	6.4	71
Total/Avg	33.2	126

Table 8.15: High Luminosity: Power and Critical Energies [Geant4]

The power from the dipoles is greater than any one quadrupole however the critical energies of the quadrupoles are significantly higher than in the dipoles. It is expected that the dipole and quadrupole elements can create power on the same order however have very different critical energies. This is because the dipole is an order of magnitude longer than the quadrupole elements. Since the SR power created for both the quadrupole and dipoles are linearly dependent on length [412] one needs to have a much higher average critical energy to create comparable amounts of power.

Comparison: The IRSYN cross check of the power and critical energies is shown in Table 8.16. This comparison was done for the total power and the average critical energy.

A third cross check to the G4 simulations was made for the power as shown in Table 8.17. This was done using an analytic method for calculating power in dipole and quadrupole

	Power [kW]		Critical Energy [keV]	
	Geant4	IRSYN	Geant4	IRSYN
Total/Avg	33.2	X	126	X

Table 8.16: High Luminosity: Geant4 and IRSYN comparison

magnets. [412] This was done for every element which provides confidence in the distribution of this power throughout the IR.

	Power [kW]	
Element	Geant4	Analytic
DL	6.4	6.3
QL3	5.3	5.4
QL2	4.3	4.6
QL1	0.6	0.6
QR1	0.6	0.6
QR2	4.4	4.6
QR3	5.2	5.4
DR	6.4	6.3
Total/Avg	33.2	33.8

Table 8.17: High Luminosity: Geant4 and Analytic method comparison

Number Density and Envelopes: The number density of photons as a function of Z is shown in Figure 8.33. Each graph displays the density of photons in the $Z = Z_o$ plane for various values of Z_o. The first three figures give the growth of the SR fan inside the detector area. This is crucial for determining the dimensions of the beam pipe. Since the fan grows asymmetrically in the -Z direction an asymmetric elliptical cone geometry will minimize these dimensions, allowing the tracking to be placed as close to the beam as possible. The horizontal extension of the fan in the high luminosity case is the minimum for the two Ring Ring options as well as the Linac Ring option, which is most important inside the detector region. This is due to the lower value of l^*. Because the quadrupoles are closer to the IP and contain effective dipole fields the angle of the beam at the entrance of the upstream dipole can be lower as the angle of the beam doesnt need to equal the crossing angle until $Z = l^*$. The number density of this fan appears as expected. There exists the highest density between the two beams at the absorber.

In Figure 8.33 the distribution was given at various Z values however a continuous envelope distribution is also important to see everything at once. This can be seen in Figure 8.34, where the beam and fan envelopes are shown in the Y = 0 plane. This makes it clear that the fan is antisymmetric which comes from the S shape of the electron beam as previously mentioned.

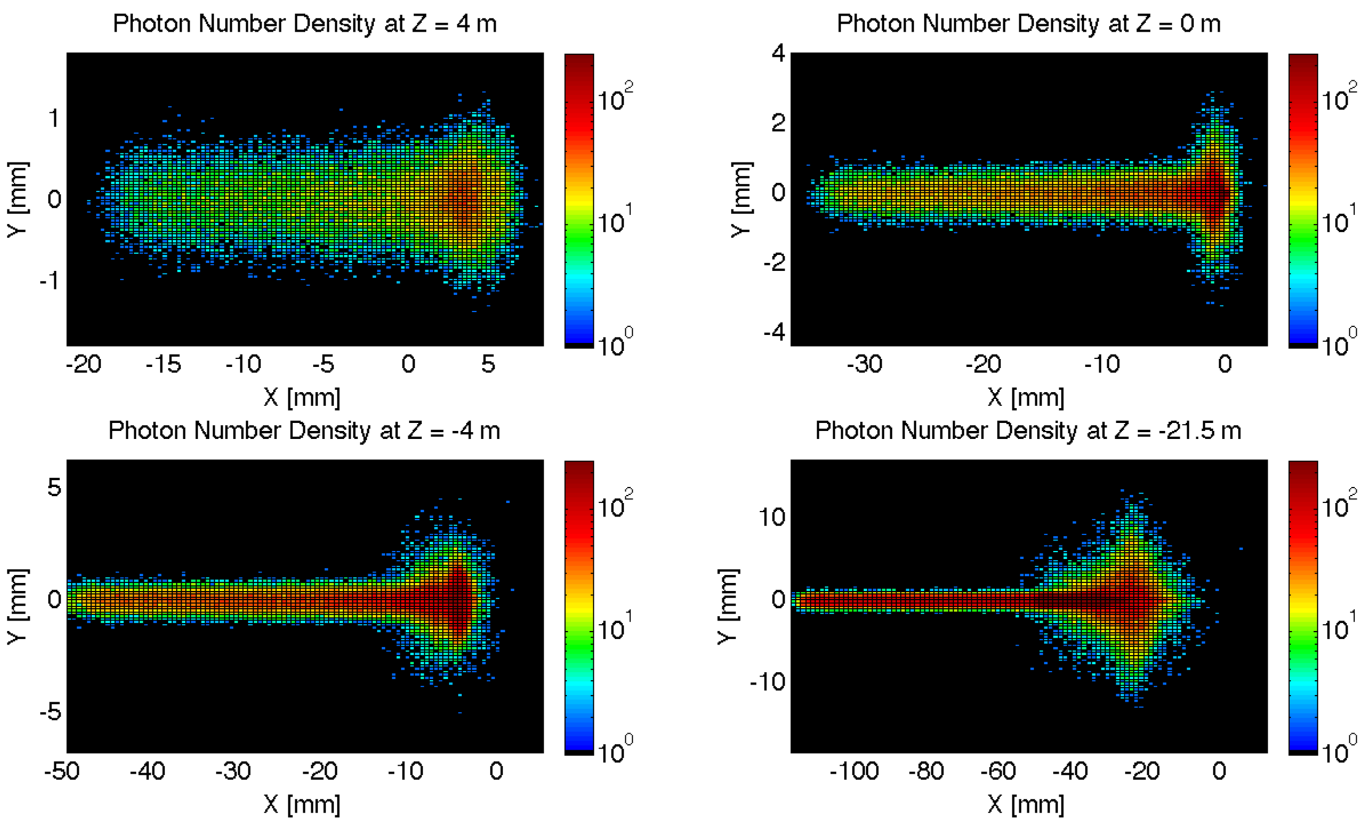

Figure 8.33: High Luminosity: Number Density Growth in Z

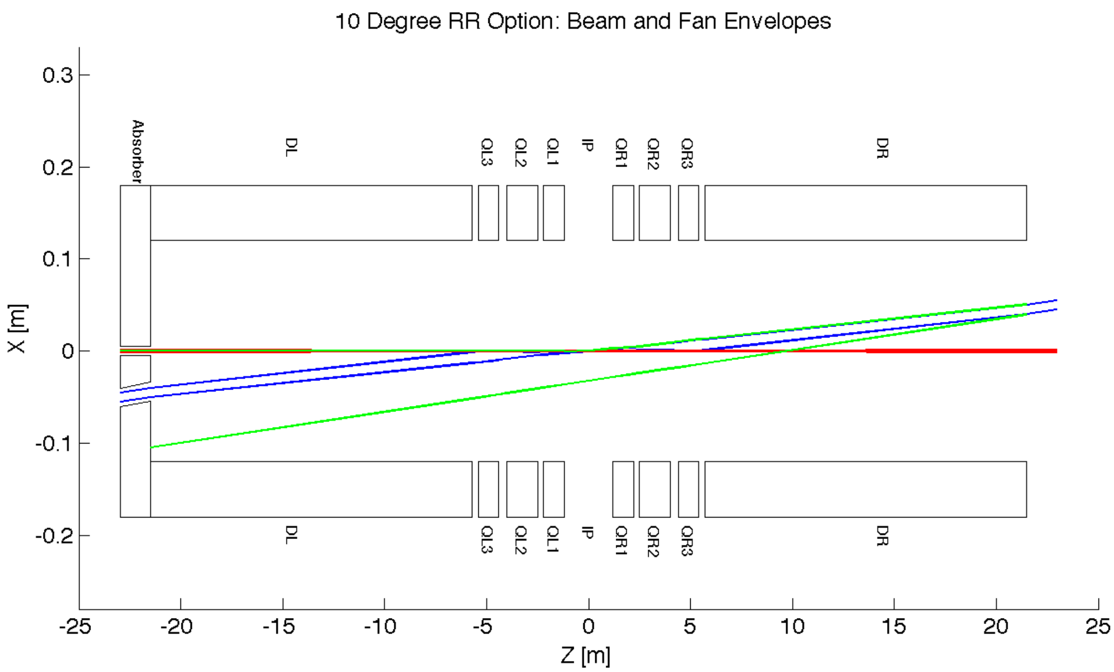

Figure 8.34: High Luminosity: Beam Envelopes in Z

Critical Energy Distribution: The Critical Energy is dependent upon the element in which the SR is generated, and for the quadrupole magnets it is also dependent upon Z. This is a result of the fact that the critical energy is proportional to the magnetic field component that is perpendicular to the particle direction. i.e. $E_c \propto B_\perp$. [413] Since the magnitude of the magnetic field is dependent upon x and y, then for a gaussian beam in position particles will experience different magnetic fields and therefore have a spectrum of critical energies. In a dipole the field is constant and therefore regardless of the position of the particles as long as they are in the uniform field area of the magnet they have a constant critical energy. Since the magnetic field is dependent upon x and y it is clear that as the r.m.s. spot size of the beam decreases there will be a decrease in critical energies. The opposite will occur for an increasing spot size. This is evident from Figure 8.35.

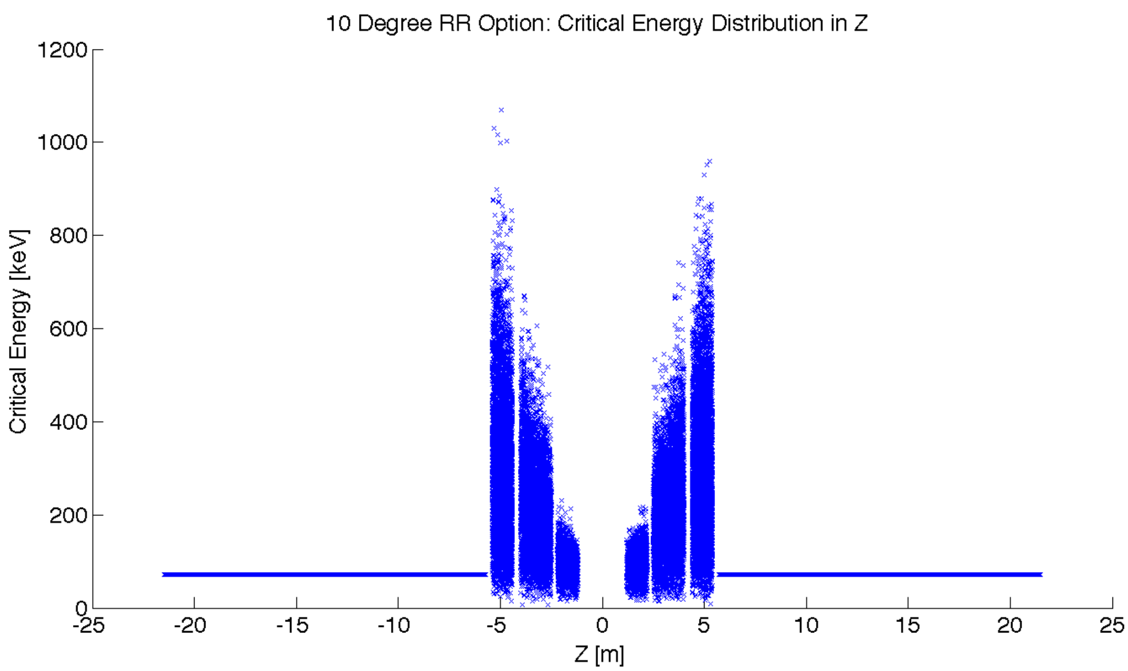

Figure 8.35: High Luminosity: Critical Energy Distribution in Z

Absorber: The Photon distribution on the absorber surface is crucial. The distribution decides how the absorber must be shaped. The shape of the absorber in addition to the distribution on the surface then decides how much SR is backscattered into the detector region. In HERA backscattered SR was a significant source of background that required careful attention. [414] Looking at Figure 8.36 it is shown that for the high luminosity option 19.2 kW of power from the SR light will fall on the face of the absorber which is 58% of the total power. This gives a general idea of the amount of power that will be absorbed. However, backscattering and IR photons will lower the percent that is actually absorbed.

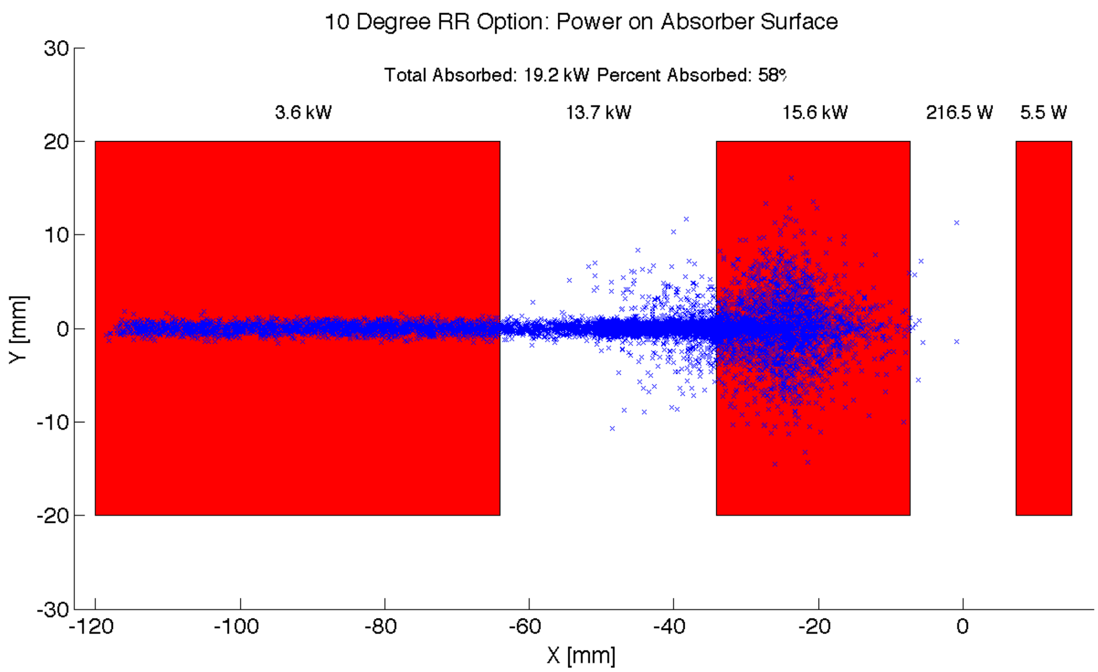

Figure 8.36: High Luminosity: Photon distribution on Absorber Surface

Proton Triplet: The super conducting final focusing triplet for the protons needs to be protected from radiation by the absorber. Some of the radiation produced upstream of the absorber however will either pass through the absorber or pass through the apertures for the two interacting beams. This is most concerning for the interacting proton beam aperture which will have the superconducting coils. A rough upper bound for the amount of power the coils can absorb before quenching is 100 W. [415] There is approximately 217 W entering into the interacting proton beam aperture as is shown in Figure 8.36. This doesnt mean that all this power will hit the coils but simulations need to be made to determine how much of this will hit the coils. The amount of power that will pass through the absorber can be disregarded as it is not enough to cause any effects. The main source of power moving downstream of the absorber will be the photons passing through the beams aperture. This was approximately 13.7 kW as can be seen from Figure 8.36. Most of this radiation can be absorbed in a secondary absorber placed after the first downstream proton quadrupole. Overall protecting the proton triplet is important and although the absorber will minimize the radiation continuing downstream this needs to be studied in depth.

Backscattering: Another Geant4 program was written to simulate the backscattering of photons into the detector region. The ntuple with the photon information written at the absorber surface is used as the input for this program. An absorber geometry made of copper is described, and general physics processes are set up. A detector volume is then described and set to record the information of all the photons which enter in an ntuple. The first step in minimizing the backscattering was to optimize the absorber shape. Although the simulation didnt include a beam pipe the backscattering for different absorber geometries was compared against one another to find a minimum. The most basic shape was a block of copper that had cylinders removed for the interacting beams. This was used as a benchmark to see the maximum possible backscattering. In HERA a wedge shape was used for heat dissipation and minimizing backscattering. [414] The profile of two possible wedge shapes in the YZ plane is shown in Figure 8.37. It was found that this is the optimum shape for the absorber. The reason for this is that a backscattered electron would have to have its velocity vector be almost parallel to the wedge surface to escape from the wedge and therefore it works as a trap. As can be seen from Table 8.18 utilizing the wedge shaped absorber did not reduce the power by much. This appears to be a statistical limitation. This needs to be redone with higher statistics to get a better opinion on the difference between the two geometries.

After the absorber was optimized it was possible to set up a beam pipe geometry. An asymmetric elliptical cone beam pipe geometry made of beryllium was used since it would minimize the necessary size of the beam pipe as previously mentioned. The next step was to place the lead shield and masks inside this beam pipe. To determine placement a simulation was run with just the beam pipe. Then it was recorded where each backscattered photon would hit the beam pipe in Z. A histogram of this data was made. This determined that the shield should be placed in the Z region ranging from -20 m until the absorber (-21.5 m). The shields were then placed at -21.2 m and -20.5 m. This decreased the backscattered power to zero as can be seen from Table 8.18. Although this is promising this number should be checked again with higher statistics to judge its accuracy. Overall there is still more optimization that can occur with this placement.

Cross sections of the beam pipe in the $Y = 0$ and $X = 0$ planes with the shields and masks included can be seen in Figure 8.38.

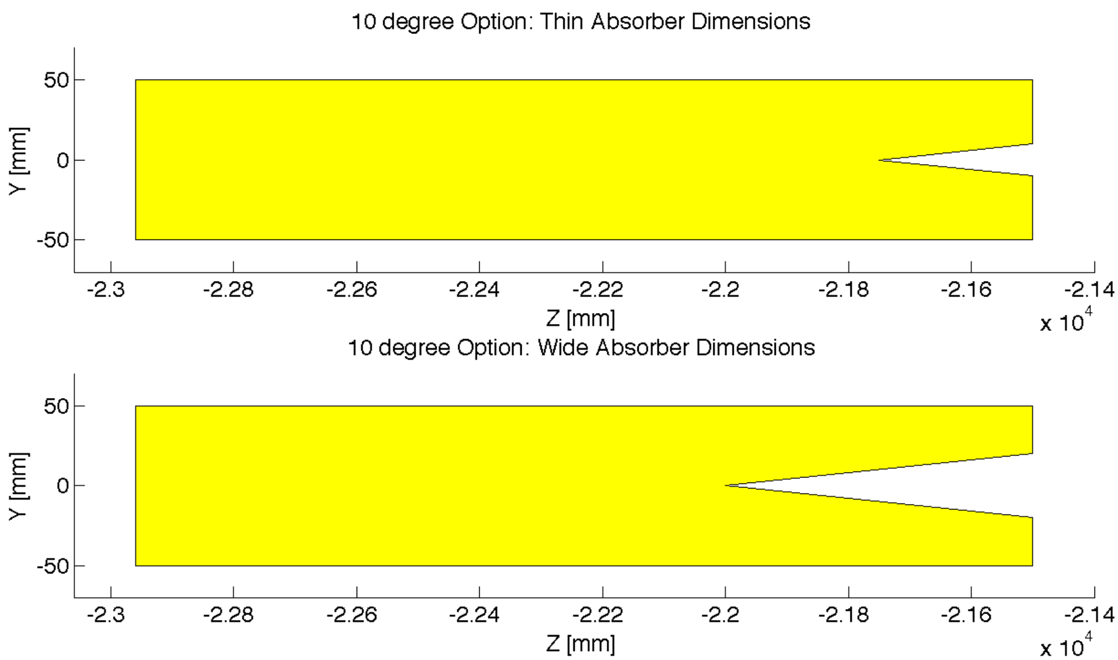

Figure 8.37: 10 deg: Absorber Dimensions

Absorber Type	Power [W]
Flat	22
Wedge	18.5
Wedge & Mask/Shield	0

Table 8.18: High Luminosity: Backscattering/Mask

High Detector Acceptance

Parameters: For the Ring Ring high acceptance option the basic parameters are listed in Table 8.19. The separation refers to the displacement between the two interacting beams at the face of the proton triplet.

The energy, current, and crossing angle (θ_c) are common values used in all RR calculations. The dipole field value refers to the constant dipole field created throughout all dipole elements in the IR. The separation is the same as in the high luminosity case and can be altered for the same reasons with the same ramifications.The chosen parameters give a flux of 6.41×10^{18} photons per second at Z = -21.5 m, which is slightly higher than in the high luminosity case. This is expected as the fields experienced in the high acceptance case are higher.

Power and Critical Energy: Table 8.20 shows the power of the SR produced by each element along with the average critical energy produced per element. This is followed by the

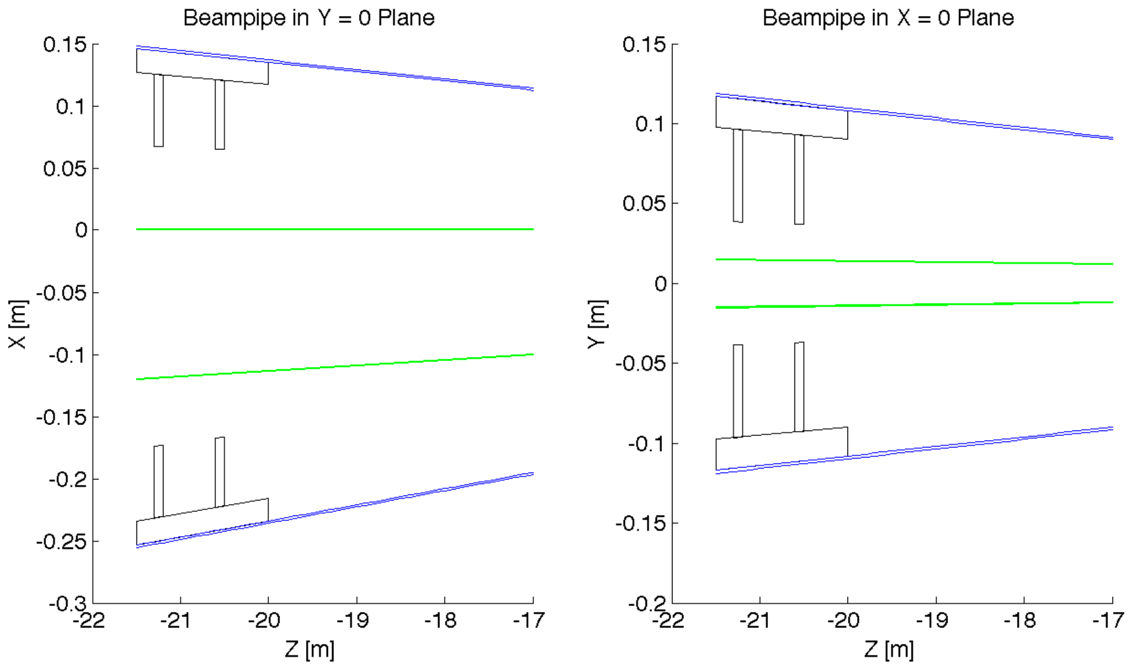

Figure 8.38: High Luminosity: Beampipe Cross Sections

Characteristic	Value
Electron Energy [GeV]	60
Electron Current [mA]	100
Crossing Angle [mrad]	1
Absorber Position [m]	-21.5
Dipole Field [T]	0.0493
Separation [mm]	55.16
γ/s	6.41×10^{18}

Table 8.19: High Acceptance: Parameters

total power produced in the IR and the average critical energy. Since the G4 simulations utilize Monte Carlo, multiple runs should be made with various seeds to get an estimate for the standard error.

The distribution of power and critical energy over the IR elements is similar to that of the high acceptance option with the exception of the upstream and downstream separator dipole magnets. The power and critical energies are significantly higher than before. This is due to the higher dipole field and the quadratic dependence of power on magnetic field and linear dependence of critical energy on magnetic field. [413]

Element	Power [kW]	Critical Energy [keV]
DL	13.9	118
QL2	6.2	318
QL1	5.4	294
QR1	5.4	293
QR2	6.3	318
DR	13.9	118
Total/Avg	51.1	163

Table 8.20: High Acceptance: Power and Critical Energies [Geant4]

Comparison: The IRSYN cross check of the power and critical energies is shown in Table 8.21. This comparison was done for the total power and the critical energy.

	Power [kW]		Critical Energy [keV]	
	Geant4	IRSYN	Geant4	IRSYN
Total/Avg	51.1	51.3	163	162

Table 8.21: High Acceptance: Geant4 and IRSYN comparison

A third cross check to the G4 simulations was also made for the power as shown in Table 8.22. This was done using an analytic method for calculating power in dipole and quadrupole magnets. [412] This comparison provides confidence in the distribution of the power throughout the IR.

	Power [kW]	
Element	Geant4	Analytic
DL	13.9	14
QL2	6.2	6.2
QL1	5.4	5.3
QR1	5.4	5.3
QR2	6.3	6.2
DR	13.9	14
Total	51.1	51

Table 8.22: High Acceptance: Geant4 and Analytic method comparison

Number Density and Envelopes: The number density of photons as a function of Z is shown in Figure 8.39. The horizontal extension of the fan in the high acceptance case is larger than in the high luminosity case however still lower than in the LR option. Since the beam

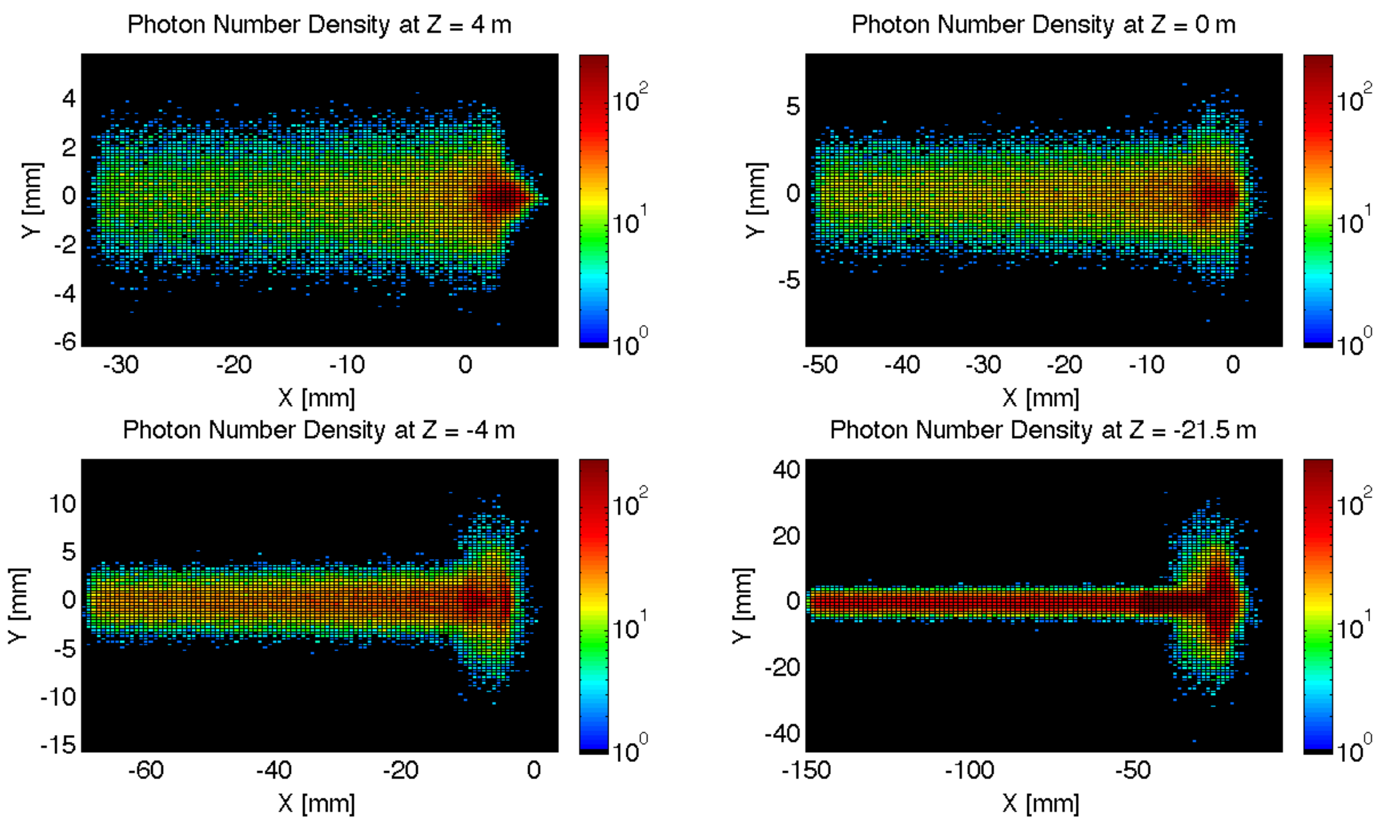

Figure 8.39: High Acceptance: Number Density Growth in Z

stays at a constant angle for the first 6.2 m after the IP it requires larger fields to bend in order to reach the desired separation. This means that an overall larger angle is reached near the absorber, and since the S shaped trajectory is symmetric in Z the angle of the beam at the entrance of the upstream quadrupoles is also larger and therefore the fan extends further in X.

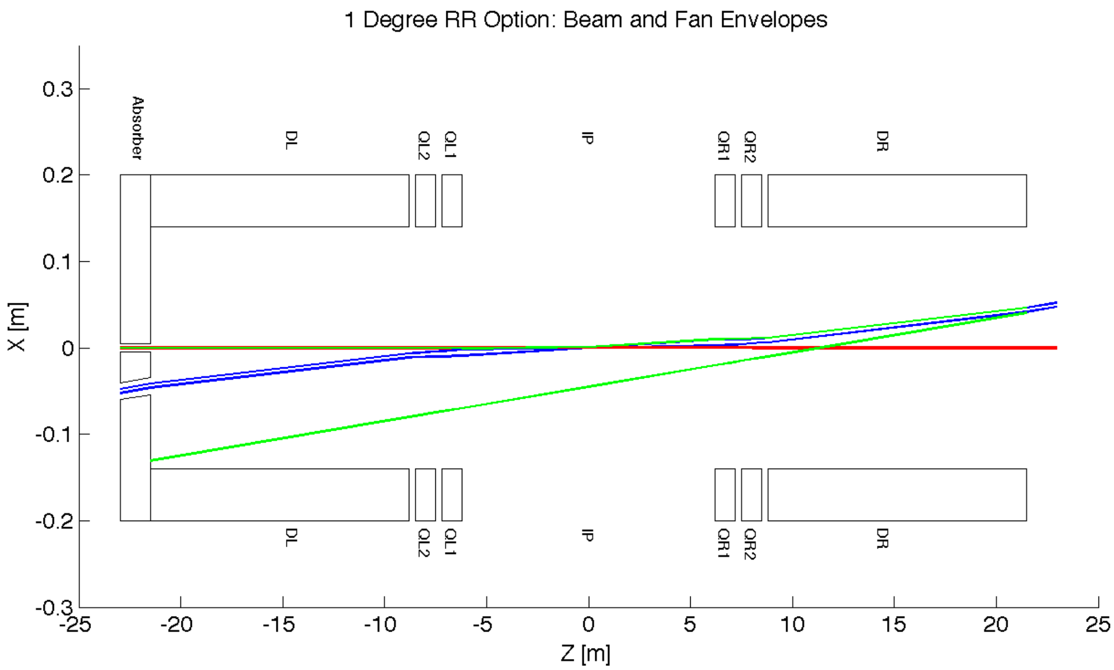

Figure 8.40: High Acceptance: Beam Envelopes in Z

The envelope of the SR fan can be seen in Figure 8.40, where the XZ plane is shown at the value Y = 0. Once again the fan is antisymmetric due to the S shape of the electron beam.

Critical Energy Distribution: The critical energy distribution in Z is similar to that of the high luminosity case. This is due to the focusing of the beam in the IR. This is evident from Figure 8.41.

Absorber: Looking at Figure 8.42 it is shown that for the high acceptance option 38.5 kW of power from the SR light will fall on the face of the absorber which is 75% of the total power. This gives a general idea of the amount of power that will be absorbed. However, backscattering and IR photons will lower the percent that is actually absorbed.

Proton Triplet: The super conducting final focusing triplet for the protons needs to be protected from radiation by the absorber. Some of the radiation produced upstream of the absorber however will either pass through the absorber or pass through the apertures for the two interacting beams. This is most concerning for the interacting proton beam aperture which will have the superconducting coils. A rough upper bound for the amount of power the coils can

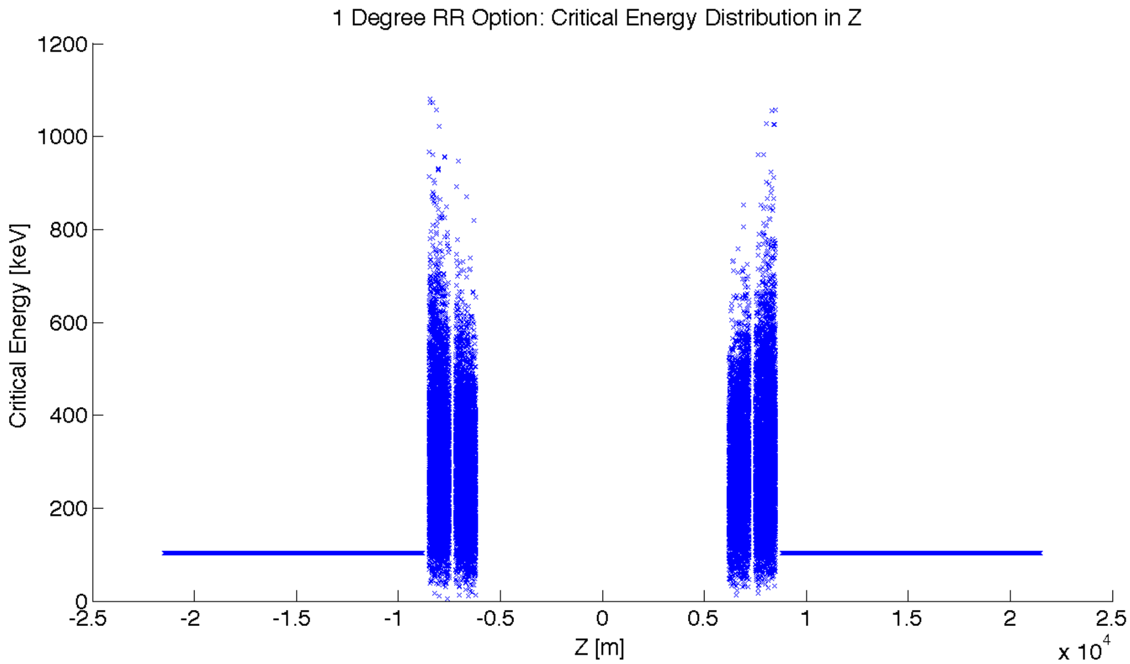

Figure 8.41: High Acceptance: Critical Energy Distribution in Z

absorb before quenching is 100 W. [415] In the high acceptance option there is approximately 0.4 W entering into the interacting proton beam aperture as is shown in Figure 8.42. Therefore for the high acceptance option this is not an issue. The amount of power that will pass through the absorber can be disregarded as it is not enough to cause any significant effects. The main source of power moving downstream of the absorber will be the photons passing through the beams aperture. This was approximately 12.7 kW as can be seen from Figure 8.42. Most of this radiation can be absorbed in a secondary absorber placed after the first downstream proton quadrupole. Overall protecting the proton triplet is important and although the absorber will minimize the radiation continuing downstream this needs to be studied in depth.

Backscattering: Another Geant4 program was written to simulate the backscattering of photons into the detector region. The ntuple with the photon information written at the absorber surface is used as the input for this program. An absorber geometry made of copper is described, and general physics processes are set up. A detector volume is then described and set to record the information of all the photons which enter in an ntuple. The first step in minimizing the backscattering was to optimize the absorber shape. Although the simulation didnt include a beam pipe the backscattering for different absorber geometries was compared against one another to find a minimum. The most basic shape was a block of copper that had cylinders removed for the interacting beams. This was used as a benchmark to see the maximum possible backscattering. In HERA a wedge shape was used for heat dissipation and minimizing backscattering. [414] The profile of two possible wedge shapes in the YZ plane is

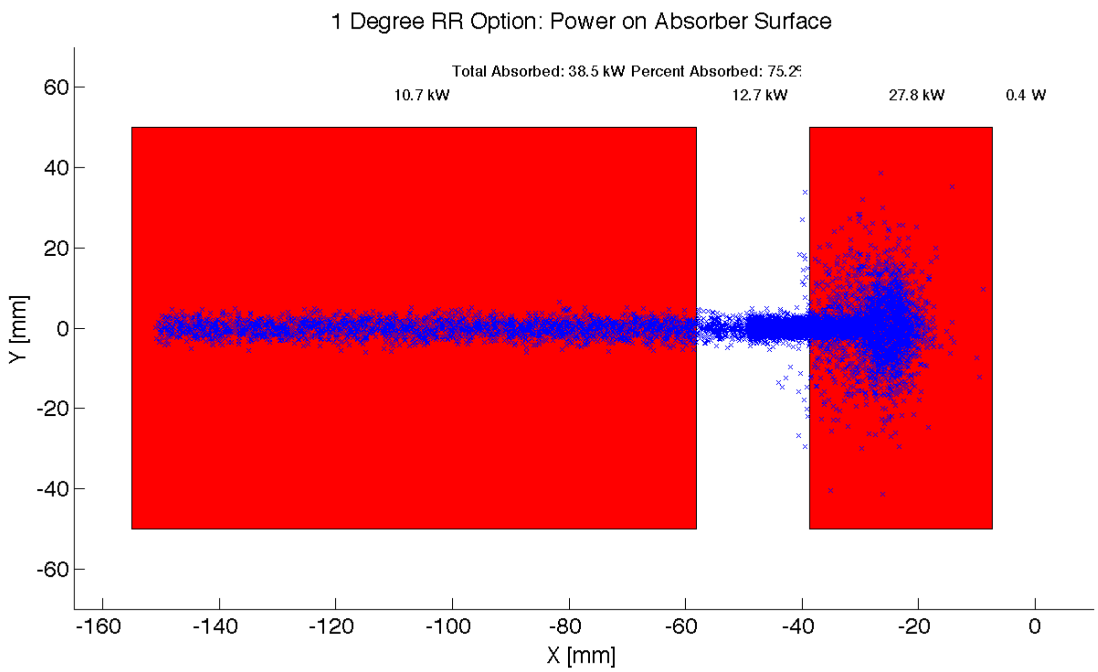

Figure 8.42: High Acceptance: Photon distribution on Absorber Surface

shown in Figure 8.43. It was found that this is the optimum shape for the absorber. The reason for this is that a backscattered electron would have to have its velocity vector be almost parallel to the wedge surface to escape from the wedge and therefore it works as a trap. As can be seen from Table 8.23 utilizing the wedge shaped absorber decreased the backscattered power by a factor of 9.

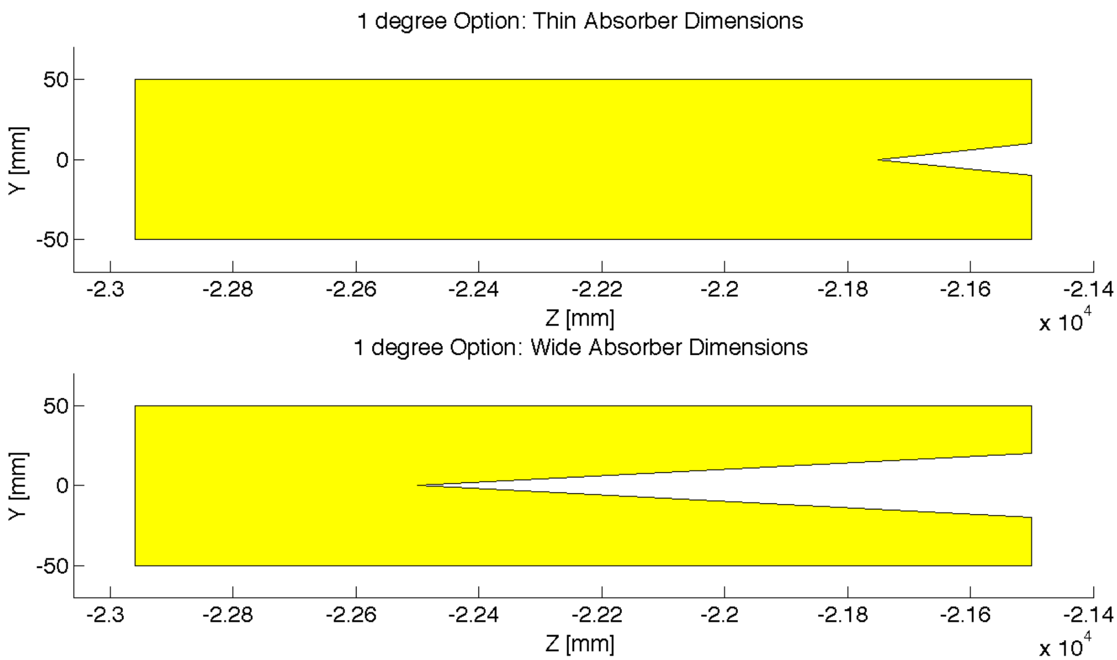

Figure 8.43: 1 deg: Absorber Dimensions

After the absorber was optimized it was possible to set up a beam pipe geometry. An asymmetric elliptical cone beam pipe geometry made of beryllium was used since it would minimize the necessary size of the beam pipe as previously mentioned. The next step was to place the lead shield and masks inside this beam pipe. To determine placement a simulation was run with just the beam pipe. Then it was recorded where each backscattered photon would hit the beam pipe in Z. This determined that the shield should be placed in the Z region ranging from -20 m until the absorber (-21.5 m). The shields were then placed at -21.2 m and -20.6 m. This decreased the backscattered power to zero as can be seen from Table 8.23. Although this is promising this number should be checked again with higher statistics to judge its accuracy. Overall there is still more optimization that can occur with this placement.

Cross sections of the beam pipe in the Y = 0 and X = 0 planes with the shields and masks included can be seen in Figure 8.44.

Absorber Type	Power [W]
Flat	91.1
Wedge	10
Wedge & Mask/Shield	0

Table 8.23: High Acceptance: Backscattering/Mask

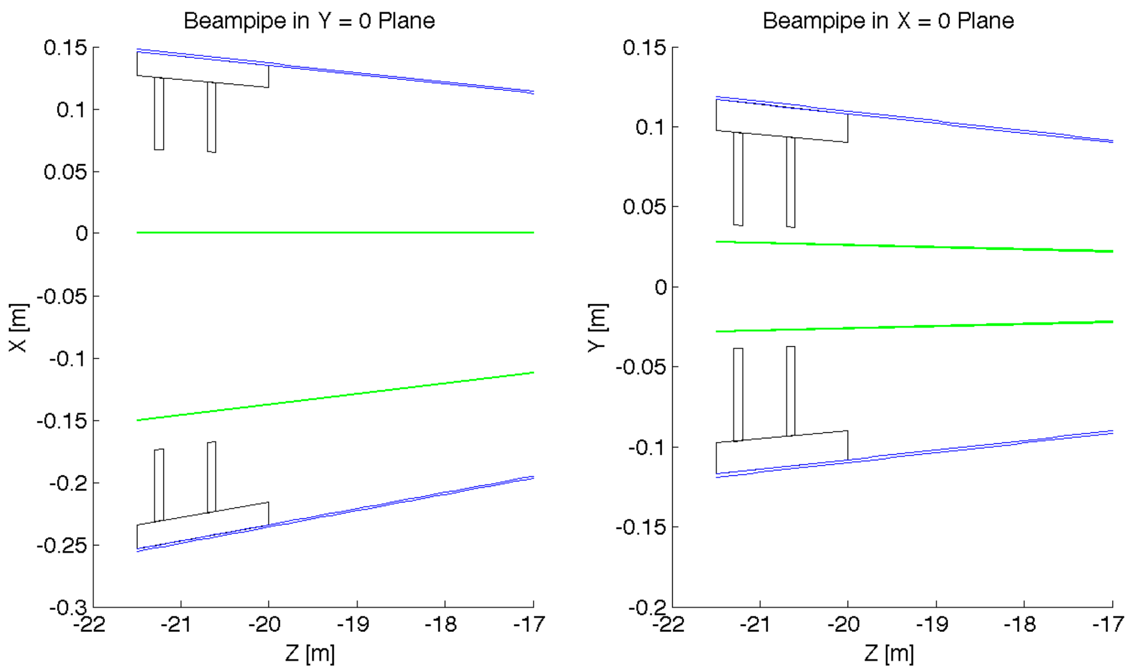

Figure 8.44: High Acceptance: Beampipe Cross Sections

8.6 Spin polarisation – an overview

Before describing concepts for attaining electron and positron spin polarisation for the ring-ring option of the LHeC we present a brief overview of the theory and phenomenology. We can then draw on this later as required. This overview is necessarily brief but more details can be found in [416, 417].

8.6.1 Self polarisation

The spin polarisation of an ensemble of spin–1/2 fermions with the same energies travelling in the same direction is defined as

$$\mathbf{P} = \langle \frac{2}{\hbar} \sigma \rangle \tag{8.13}$$

where σ is the spin operator in the rest frame and $\langle\ \rangle$ denotes the expectation value for the mixed spin state. We denote the single-particle rest-frame expectation value of $\frac{2}{\hbar}\sigma$ by $\mathbf{S}$ and we call this the "spin". The polarisation is then the average of $\mathbf{S}$ over an ensemble of particles such as that of a bunch of particles.

Relativistic $e^{\pm}$ circulating in the (vertical) guide field of a storage ring emit synchrotron radiation and a tiny fraction of the photons can cause spin flip from up to down and vice versa. However, the up–to–down and down–to–up rates differ, with the result that in ideal circumstances the electron (positron) beam can become spin polarised anti-parallel (parallel) to the field, reaching a maximum polarisation, P_{st}, of $\frac{8}{5\sqrt{3}} = 92.4\%$. This, the Sokolov-Ternov (S-T) polarising process, is very slow on the time scale of other dynamical phenomena occurring in storage rings, and the inverse time constant for the exponential build up is [418]:

$$\tau_{\mathrm{st}}^{-1} = \frac{5\sqrt{3}}{8}\frac{r_{\mathrm{e}}\gamma^5\hbar}{m_{\mathrm{e}}|\rho|^3} \tag{8.14}$$

where r_{e} is the classical electron radius, γ is the Lorentz factor, ρ is the radius of curvature in the magnets and the other symbols have their usual meanings. The time constant is usually in the range of a few minutes to a few hours.

However, even without radiative spin flip, the spins are not stationary but precess in the external fields. In particular, the motion of $\mathbf{S}$ for a relativistic charged particle travelling in electric and magnetic fields is governed by the Thomas-BMT equation $d\mathbf{S}/ds = \mathbf{\Omega} \times \mathbf{S}$ where s is the distance around the ring [417, 419]. The vector $\mathbf{\Omega}$ depends on the electric ($\mathbf{E}$) and magnetic ($\mathbf{B}$) fields, the energy and the velocity ($\mathbf{v}$) which evolves according to the Lorentz equation:

$$\begin{aligned}\mathbf{\Omega} &= \frac{e}{m_{\mathrm{e}}c}\left[-\left(\frac{1}{\gamma}+a\right)\mathbf{B} + \frac{a\gamma}{1+\gamma}\frac{1}{c^2}(\mathbf{v}\cdot\mathbf{B})\mathbf{v} + \frac{1}{c^2}\left(a+\frac{1}{1+\gamma}\right)(\mathbf{v}\times\mathbf{E})\right] &(8.15)\\ &= \frac{e}{m_{\mathrm{e}}c}\left[-\left(\frac{1}{\gamma}+a\right)\mathbf{B}_{\perp} - \frac{g}{2\gamma}\mathbf{B}_{\parallel} + \frac{1}{c^2}\left(a+\frac{1}{1+\gamma}\right)(\mathbf{v}\times\mathbf{E})\right]. &(8.16)\end{aligned}$$

Thus $\mathbf{\Omega}$ depends on s and on the position of the particle $u \equiv (x, p_x, y, p_y, l, \delta)$ in the 6-D phase space of the motion. The coordinate δ is the fractional deviation of the energy from the energy of a synchronous particle ("the beam energy") and l is the distance from the centre of the bunch. The coordinates x and y are the horizontal and vertical positions of the particle relative to the reference trajectory and $p_x = x', p_y = y'$ (except in solenoids) are their conjugate momenta. The quantity g is the appropriate gyromagnetic factor and $a = (g-2)/2$ is the gyromagnetic anomaly. For $e^{\pm}$, $a \approx 0.0011596$. $\mathbf{B}_{\parallel}$ and $\mathbf{B}_{\perp}$ are the magnetic fields parallel and perpendicular to the velocity.

In a simplified picture, the majority of the photons in the synchrotron radiation do not cause spin flip but tend instead to randomise the $e^{\pm}$ orbital motion in the (inhomogeneous) magnetic fields. Then, if the ring is insufficiently-well geometrically aligned and/or if it contains special magnet systems like the "spin rotators" needed to produce longitudinal polarisation at a detector (see below), the spin-orbit coupling embodied in the Thomas-BMT equation can cause spin diffusion, i.e. depolarisation. Compared to the S-T polarising effect the depolarisation tends to rise very strongly with beam energy. The equilibrium polarisation is then less than 92.4% and will depend on the relative strengths of the polarisation and depolarisation processes. As we shall see later, even without depolarisation certain dipole layouts can reduce the equilibrium polarisation to below 92.4 %.

Analytical estimates of the attainable equilibrium polarisation are best based on the Derbenev-Kondratenko (D-K) formalism [420, 421]. This implicitly asserts that the value of the equilibrium polarisation in an $e^{\pm}$ storage ring is the same at all points in phase space and is given by

$$P_{\rm dk} \;=\; \mp\frac{8}{5\sqrt{3}}\frac{\oint ds\left\langle \frac{1}{|\rho(s)|^3}\hat{b}\cdot(\hat{n}-\frac{\partial\hat{n}}{\partial\delta})\right\rangle_s}{\oint ds\left\langle \frac{1}{|\rho(s)|^3}(1-\frac{2}{9}(\hat{n}\cdot\hat{s})^2+\frac{11}{18}|\frac{\partial\hat{n}}{\partial\delta}|^2)\right\rangle_s} \tag{8.17}$$

where $< >_s$ denotes an average over phase space at azimuth s, $\hat{s}$ is the direction of motion and $\hat{b}=(\hat{s}\times\dot{\hat{s}})/|\dot{\hat{s}}|$. $\hat{b}$ is the magnetic field direction if the electric field vanishes and the motion is perpendicular to the magnetic field. $\hat{n}(u;s)$ is a unit 3-vector field over the phase space satisfying the Thomas-BMT equation along particle trajectories $u(s)$ (which are assumed to be integrable), and it is 1-turn periodic: $\hat{n}(u;s+C)=\hat{n}(u;s)$ where C is the circumference of the ring.

The field $\hat{n}(u;s)$ is a key object for systematising spin dynamics in storage rings. It provides a reference direction for spin at each point in phase space and it is now called the *"invariant spin field"* [417, 422, 423]. At zero orbital amplitude, i.e. on the periodic ("closed") orbit, the $\hat{n}(0;s)$ is written as $\hat{n}_0(s)$. For $e^{\pm}$ rings and away from spin-orbit resonances (see below), $\hat{n}$ is normally at most a few milliradians away from $\hat{n}_0$.

A central ingredient of the D-K formalism is the implicit assumption that the $e^{\pm}$ polarisation at each point in phase space is parallel to $\hat{n}$ at that point. In the approximation that the particles have the same energies and are travelling in the same direction, the polarisation of a bunch measured in a polarimeter at s is then the ensemble average

$$\mathbf{P}_{\rm ens,dk}(s) \;=\; P_{\rm dk}\;\langle\hat{n}\rangle_s\;. \tag{8.18}$$

In conventional situations in $e^{\pm}$ rings, $\langle\hat{n}\rangle_s$ is very nearly aligned along $\hat{n}_0(s)$. The *value* of the ensemble average, $P_{\rm ens,dk}(s)$, is essentially independent of s.

Equation 8.17 can be viewed as having three components. The piece

$$P_{\rm bk} \;=\; \mp\frac{8}{5\sqrt{3}}\frac{\oint ds\left\langle \frac{1}{|\rho(s)|^3}\hat{b}\cdot\hat{n}\right\rangle_s}{\oint ds\left\langle \frac{1}{|\rho(s)|^3}(1-\frac{2}{9}(\hat{n}\cdot\hat{s})^2)\right\rangle_s} \approx \mp\frac{8}{5\sqrt{3}}\frac{\oint ds\frac{1}{|\rho(s)|^3}\hat{b}\cdot\hat{n}_0}{\oint ds\frac{1}{|\rho(s)|^3}(1-\frac{2}{9}n_{0s}^2)}\;. \tag{8.19}$$

gives the equilibrium polarisation due to radiative spin flip. The quantity n_{0s} is the component of $\hat{n}_0$ along the closed orbit. The subscript "bk" is used here instead of "st" to reflect the fact that this is the generalisation by Baier and Katkov [424, 425] of the original S-T expression to cover the case of piecewise homogeneous fields. Depolarisation is then accounted for by including the term with $\frac{11}{18}|\frac{\partial\hat{n}}{\partial\delta}|^2$ in the denominator. Finally, the term with $\frac{\partial\hat{n}}{\partial\delta}$ in the numerator is the so-called kinetic polarisation term. This results from the dependence of the radiation power on the initial spin direction and is not associated with spin flip. It can normally be neglected but is still of interest in rings with special layouts.

In the presence of radiative depolarisation the rate in Eq. 8.14 must be replaced by

$$\tau_{\rm dk}^{-1} \;=\; \frac{5\sqrt{3}}{8}\frac{r_{\rm e}\gamma^5\hbar}{m_{\rm e}}\frac{1}{C}\oint ds\left\langle\frac{1-\frac{2}{9}(\hat{n}\cdot\hat{s})^2+\frac{11}{18}|\frac{\partial\hat{n}}{\partial\delta}|^2}{|\rho(s)|^3}\right\rangle_s\;. \tag{8.20}$$

This can be written in terms of the spin-flip polarisation rate, $\tau_{\rm bk}^{-1}$, and the depolarisation rate, $\tau_{\rm dep}^{-1}$, as:

$$\frac{1}{\tau_{\rm dk}} \;=\; \frac{1}{\tau_{\rm bk}} + \frac{1}{\tau_{\rm dep}}\;, \tag{8.21}$$

where

$$\tau_{\rm dep}^{-1} \;=\; \frac{5\sqrt{3}}{8}\frac{r_{\rm e}\gamma^5\hbar}{m_{\rm e}}\frac{1}{C}\oint ds\,\left\langle \frac{\frac{11}{18}\,|\frac{\partial\hat{n}}{\partial\delta}|^2}{|\rho(s)|^3}\right\rangle_s \tag{8.22}$$

and

$$\tau_{\rm bk}^{-1} \;=\; \frac{5\sqrt{3}}{8}\frac{r_{\rm e}\gamma^5\hbar}{m_{\rm e}}\frac{1}{C}\oint ds\left\langle\frac{1-\frac{2}{9}(\hat{n}\cdot\hat{s})^2}{|\rho(s)|^3}\right\rangle_s\;. \tag{8.23}$$

The time dependence for build-up from an initial polarisation P_0 to equilibrium is

$$P(t) \;=\; P_{\rm ens,dk}\left[1-e^{-t/\tau_{\rm dk}}\right] + P_0 e^{-t/\tau_{\rm dk}}\;. \tag{8.24}$$

In perfectly aligned $e^{\pm}$ storage rings containing just horizontal bends, quadrupoles and accelerating cavities, there is no vertical betatron motion and $\hat{n}_0(s)$ is vertical. Since the spins do not "see" radial quadrupole fields and since the electric fields in the cavities are essentially parallel to the particle motion, $\hat{n}$ is vertical, parallel to the guide fields and to $\hat{n}_0(s)$ at all u and s. Then the derivative $\frac{\partial\hat{n}}{\partial\delta}$ vanishes and there is no depolarisation. However, real rings have misalignments. Then there is vertical betatron motion so that the spins also see radial fields which tilt them from the vertical. Moreover, $\hat{n}_0(s)$ is also tilted and the spins can couple to vertical quadrupole fields too. As a result $\hat{n}$ becomes dependent on u and "fans out" away from $\hat{n}_0(s)$ by an amount which usually increases with the orbit amplitudes. Then in general $\frac{\partial\hat{n}}{\partial\delta}$ no longer vanishes in the dipoles (where $1/|\rho(s)|^3$ is large) and depolarisation occurs. In the presence of skew quadrupoles and solenoids and, in particular, in the presence of spin rotators, $\frac{\partial\hat{n}}{\partial\delta}$ can be non-zero in dipoles even with perfect alignment. The deviation of $\hat{n}$ from $\hat{n}_0(s)$, and the depolarisation, tend to be particularly large near to the spin-orbit resonance condition

$$\nu_0 \;=\; k_0 + k_I Q_I + k_{II} Q_{II} + k_{III} Q_{III}\;. \tag{8.25}$$

Here $k_0, k_I, k_{II}, k_{III}$ are integers, Q_I, Q_{II}, Q_{III} are the three tunes of the synchrobetatron motion and ν_0 is the spin tune on the closed orbit, i.e. the number of precessions around $\hat{n}_0(s)$ per turn, made by a spin on the closed orbit [1]. In the special case, or in the approximation, of no synchrobetatron coupling one can make the associations: $I \to x$, $II \to y$ and $III \to s$, where, here, the subscript s labels the synchrotron mode. In a simple flat ring with no closed-orbit distortion, $\nu_0 = a\gamma$ where γ is the Lorentz factor for the nominal beam energy. For $e^{\pm}$, $a\gamma$ increments by 1 for every 441 MeV increase in beam energy. In the presence of misalignments and special elements like rotators, ν_0 is usually still approximately proportional to the beam energy. Thus an energy scan will show peaks in $\tau_{\rm dep}^{-1}$ and dips in $P_{\rm ens,dk}(s)$, namely at around the resonances. Examples can be seen in figures 3.1 and 3.2 below. The resonance condition expresses

[1] In fact the resonance condition should be more precisely expressed in terms of the so-called amplitude dependent spin tune [417, 422, 423]. But for typical $e^{\pm}$ rings, the amplitude dependent spin tune differs only insignificantly from ν_0.

the fact that the disturbance to spins is greatest when the $|\mathbf{\Omega}(u;s) - \mathbf{\Omega}(0;s)|$ along a trajectory is coherent ("in step") with the natural spin precession. The quantity $(|k_{_I}| + |k_{_{II}}| + |k_{_{III}}|)$ is called the order of the resonance. Usually, the strongest resonances are those for which $|k_{_I}| + |k_{_{II}}| + |k_{_{III}}| = 1$, i.e. the first-order resonances. The next strongest are usually the so-called *"synchrotron sideband resonances"* of parent first-order resonances, i.e. resonances for which $\nu_0 = k_{_0} \pm Q_{_{I,II,III}} + \tilde{k}_{_{III}} Q_{_{III}}$ where $\tilde{k}_{_{III}}$ is an integer and mode III is associated with synchrotron motion. All resonances are due to the non-commutation of successive spin rotations in 3-D and they therefore occur even with purely linear orbital motion.

We now list some keys points.

- The approximation on the r.h.s. of Eq. 8.19 makes it clear that if there are dipole magnets with fields not parallel to $\hat{n}_0$, as is the case, for example, when spin rotators are used, then $P_{\rm bk}$ can be lower than the 92.4% achievable in the case of a simple ring with no solenoids and where all dipole fields and $\hat{n}_0(s)$ are vertical.

- If, as is usual, the kinetic polarisation term makes just a small contribution, the above formulae can be combined to give

$$P_{\rm ens,dk} \quad \approx \quad P_{\rm bk} \frac{\tau_{\rm dk}}{\tau_{\rm bk}} \, . \tag{8.26}$$

  From Eq. 8.21 it is clear that $\tau_{\rm dk} \leq \tau_{\rm bk}$.

- The underlying rate of polarisation due to the S-T effect, $\tau_{\rm bk}^{-1}$, increases with the fifth power of the energy and decreases with the third power of the bending radii.

- It can be shown that as a general rule the "normalised" strength of the depolarisation, $\tau_{\rm dep}^{-1}/\tau_{\rm bk}^{-1}$, increases with beam energy according to a tune-dependent polynomial in even powers of the beam energy. So we expect that the attainable equilibrium polarisation decreases as the energy increases. This was confirmed LEP, where with the tools available, little polarisation could be obtained at 60 GeV [426].

8.6.2 Suppression of depolarisation – spin matching

Although the S-T effect offers a convenient way to obtain stored high energy $e^{\pm}$ beams, it is only useful in practice if there is not too much depolarisation. Depolarisation can be significant if the ring is misaligned, if it contains spin rotators or if it contains uncompensated solenoids or skew quadrupoles. Then if $P_{\rm ens,dk}$ and/or $\tau_{\rm dk}$ are too small, the layout and the optic must be adjusted so that $(|\frac{\partial \hat{n}}{\partial \delta}|)^2$ is small where $1/|\rho(s)|^3$ is large. So far it is only possible to do this within the linear approximation for spin motion. This technique is called *"linear spin matching"* and when successful, as for example at HERA [427], it immediately reduces the strengths of the first-order spin-orbit resonances. Spin matching requires two steps: *"strong synchrobeta spin matching"* is applied to the optics and layout of the perfectly aligned ring and then *"harmonic closed-orbit spin matching"* is applied to soften the effects of misalignments. This latter technique aims to adjust the closed orbit so as to reduce the tilt of $\hat{n}_0$ from the vertical in the arcs. Since the misalignments can vary in time and are usually not sufficiently well known, the adjustments are applied empirically while the polarisation is being measured.

Spin matching must be approached on a case–by–case basis. An overview can be found in [416].

8.6.3 Higher order resonances

Even if the beam energy is chosen so that first-order resonances are avoided and in linear approximation $P_{\mathrm{ens,dk}}$ and/or τ_{dk} are expected to be large, it can happen that that beam energy corresponds to a higher order resonance. As mentioned above, in practice the most intrusive higher order resonances are those for which $\nu_0 = k_0 \pm Q_k + \tilde{k}_s Q_s$ ($k \equiv I, II$ or III). These synchrotron sideband resonances of the first-order parent resonances are due to modulation by energy oscillations of the instantaneous rate of spin precession around $\hat{n}_0$. The depolarisation rates associated with sidebands of isolated parent resonances ($\nu_0 = k_0 \pm Q_k$) are related to the depolarisation rates for the parent resonances. For example, if the beam energy is such that the system is near to a dominant Q_y resonance we can approximate τ_{dep}^{-1} in the form

$$\tau_{\mathrm{dep}}^{-1} \propto \frac{A_y}{(\nu_0 - k_0 \pm Q_y)^2} \; . \tag{8.27}$$

This becomes

$$\tau_{\mathrm{dep}}^{-1} \propto \sum_{\tilde{k}_s=-\infty}^{\infty} \frac{A_y \, B_y(\zeta; \tilde{k}_s)}{\left(\nu_0 - k_0 \pm Q_y \pm \tilde{k}_s \, Q_s\right)^2}$$

if the synchrotron sidebands are included. The quantity A_y depends on the beam energy and the optics and is reduced by spin matching. The proportionality constants $B_y(\zeta; \tilde{k}_s)$ are called *enhancement factors*, and they contain modified Bessel functions $I_{|\tilde{k}_s|}(\zeta)$ and $I_{|\tilde{k}_s|+1}(\zeta)$ which depend on Q_s and the energy spread σ_δ through the *modulation index* $\zeta = (a\gamma \; \sigma_\delta / Q_s)^2$. More formulae can be found in [428, 429].

Thus the effects of synchrotron sideband resonances can be reduced by doing the spin matches described above. Note that these formulae are just meant as a guide since they are approximate and explicitly neglect interference between the first-order parent resonances. To get a complete impression, the Monte-Carlo simulation mentioned later must be used. The sideband strengths generally increase with the energy spread and the beam energy and the sidebands are a major contributor to the increase of $\tau_{\mathrm{dep}}^{-1}/\tau_{\mathrm{bk}}^{-1}$ with energy.

8.6.4 Spin rotators

The LHeC, like all analogous projects involving spin, needs longitudinal polarisation at the interaction point. However, if the S-T effect is to be the means of producing and maintaining the polarisation, then as is clear from Eq. 8.19, $\hat{n}_0$ must be close to vertical in most of the dipoles. We have seen at Eq. 8.18 that the polarisation is essentially parallel to $\hat{n}_0$. So to get longitudinal polarisation at a detector, it must be arranged that $\hat{n}_0$ is longitudinal at the detector but vertical in the rest of the ring. This can be achieved with magnet systems called spin rotators which rotate $\hat{n}_0$ from vertical to longitudinal on one side of the detector and back to vertical again on the other side.

Spin rotators use sequences of magnets which generate large spin rotations around different axes and exploit the non-commutation of successive large rotations around different axes. According to the T-BMT equation, the rate of spin precession in longitudinal fields is inversely proportional to the energy. However, for motion perpendicular to a magnetic field spins precess at a rate essentially proportional to the energy: $\delta\theta_{\mathrm{spin}} = (a\gamma + 1)\delta\theta_{\mathrm{orb}}$ in obvious notation.

Thus for the high-energy ring considered here, spin rotators should be based on dipoles as in HERA [427]. In that case the rotators consisted of interleaved horizontal and vertical bending magnets set up so as to generate interleaved, closed, horizontal and vertical bumps in the design orbit. The individual orbit deflections were small but the spin rotations were of the order of a radian. The success in obtaining high polarisation at HERA attests to the efficacy of such rotators.

Eq. 8.19 shows that $P_{\rm bk}$ essentially scales with the cosine of the angle of tilt of $\hat{n}_0$ from the vertical in the arc dipoles. Thus a rotation error resulting in a tilt of $\hat{n}_0$ of even a few degrees would not reduce $P_{\rm bk}$ by too much. However, as was mentioned above, a tilt of $\hat{n}_0$ in the arcs can lead to depolarisation. In fact the calculations below show that at 60 GeV, tilts of more than a few milliradians cause significant depolarisation. Thus well tuned rotators are essential for maintaining polarisation.

8.7 Calculations of the $e^{\pm}$ polarisation in the LHeC

As a first step towards assessing the attainable polarisation we have considered an early version of the LHeC lattice: a flat ring with no rotators, no interaction point and no bypasses. The tunes are $Q_x = 123.83$ and $Q_y = 85.62$. The horizontal emittance is 8 nm which agrees well with the on-momentum emittance calculated by MadX. The ring is therefore typical of the designs under consideration. With perfect alignment, $\hat{n}_0$ is vertical everywhere and there is no vertical dispersion. The polarisation will then reach 92.38%. At ≈ 60 GeV, $\tau_{\rm st} \approx 60$ minutes.

For the simple flat ring these values can be obtained by hand from Eq. 8.19 and Eq. 8.23. However, in general, e.g., in the presence of misalignments or rotators, the calculation of polarisation requires special software and for this study, the thick-lens code SLICKTRACK was used [430]. This essentially consists of four sections which carry out the following tasks:

(1) Simulation of misalignments followed by orbit correction with correction coils.

(2) Calculation of the optical properties of the beam and the beam sizes.

(3) Calculation of $\partial\hat{n}/\partial\delta$ for linearised spin motion with the thick-lens version (SLICK [431]) of the SLIM algorithm [416].

    The equilibrium polarisation is then obtained from Eq. 8.17. This provides a first impression and only exhibits the first order resonances.

(4) Calculation of the rate of depolarisation beyond the linear approximation of item 3.

    In general, the numerical calculation of the integrand in Eq. 8.22 beyond first order represents a difficult computational problem. Therefore a pragmatic approach is adopted, whereby the rate of depolarisation is obtained with a Monte-Carlo spin-orbit tracking algorithm which includes radiation emission. The algorithm employs full 3-D spin motion in order to see the effect of the higher order resonances. The Monte-Carlo algorithm can also handle the effect on the particles and on the spins of the non-linear beam-beam forces. An estimate of the equilibrium polarisation is then obtained from Eq. 8.26.

Some basic features of the polarisation for the misaligned flat ring are shown in figures 8.45 and 8.46 where polarisations are plotted against $a\gamma$ around 60 GeV. In both cases the r.m.s. vertical closed-orbit deviation is about 75μm. This is obtained after giving the quadrupoles

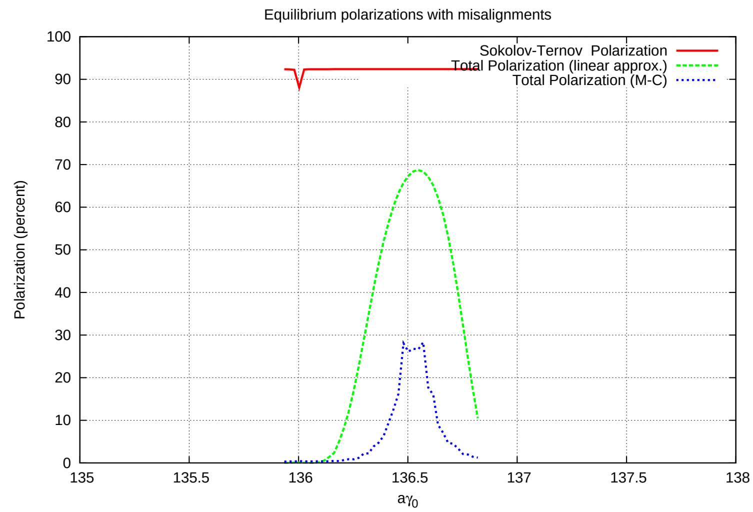

Figure 8.45: Estimated polarisation for the LHeC without spin rotators, $Q_s = 0.06$.

r.m.s. vertical misalignments of 150μm and assigning a correction coil to every quadrupole. The vector $\hat{n}_0$ has an r.m.s. tilt of about 4 milliradians from the vertical near $a\gamma = 136.5$. For figure 1 the synchrotron tune, Q_s, is 0.06 so that $\xi \approx 5$. For figure 2, $Q_s = 0.1$ so that $\xi \approx 1.9$.

The red curves depict the polarisation due to the Sokolov-Ternov effect alone. The dip to below 92.38 % at $a\gamma = 136$ is due to the characteristic very large tilt of $\hat{n}_0$ from the vertical at an integer value of $a\gamma$. See [416].

The green curves depict the equilibrium polarisation after taking into account the depolarisation associated with the misalignments and the consequent tilt of $\hat{n}_0$. The polarisation is calculated with the linearised spin motion as in item 3 above. In these examples the polarisation reaches about 68 %. The strong fall off on each side of the peak is mainly due to first-order "synchrotron" resonances $\nu_0 = k_0 \pm Q_s$. Since Q_s is small these curves are similar for the two values of Q_s.

The blue curves show the polarisation obtained as in item 4 above. Now, by going beyond the linearisation of the spin motion, the peak polarisation is about 27 %. The fall from 68 % is mainly due to synchrotron sideband resonances. With $Q_s = 0.06$ (Fig. 8.45) the resonances are overlapping. With $Q_s = 0.1$, (Fig. 8.46) the sidebands begin to separate. In any case these curves demonstrate the extreme sensitivity of the attainable polarisation to small tilts of $\hat{n}_0$ at high energy. Simulations for $Q_s = 0.1$ with a series of differently misaligned rings, all with r.m.s. vertical closed-orbit distortions of about 75μm, exhibit peak equilibrium polarisations ranging from about about 10 % to about 40 %. Experience at HERA suggests that harmonic closed-orbit spin matching can eliminate the cases of very low polarisation.

Figure 8.47 shows a typical energy dependence of the peak equilibrium polarisation for a fixed rf voltage and for one of the misaligned rings. The synchrotron tune varies from $Q_s = 0.093$ at 40 GeV to $Q_s = 0.053$ at 5 GeV due to the change in energy loss/turn. As expected the attainable polarisation falls steeply as the energy increases. However, although with this good alignment, a high polarisation is predicted at 45 GeV, $\tau_{\rm bk}$ would be about 5 hours as at LEP.

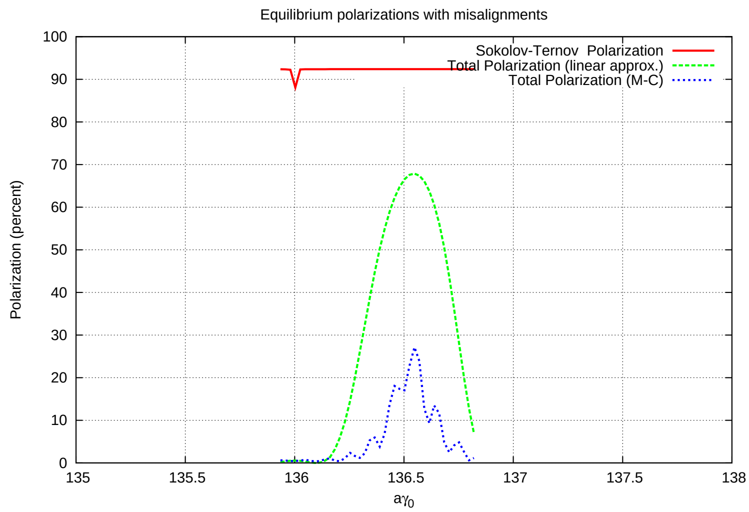

Figure 8.46: Estimated polarisation for the LHeC without spin rotators, $Q_s = 0.1$.

A small $\tau_{\rm bk}$ is not only essential for a programme of particle physics, but essential for the application of empirical harmonic closed-orbit spin matching.

As mentioned above it was difficult to get polarisation at 60 GeV at LEP. However, these calculations suggest that by adopting the levels of alignment that are now standard for synchrotron-radiation sources and by applying harmonic closed-orbit spin matching, there is reason to hope that high polarisation in a flat ring can still be obtained.

8.7.1 Further work

We now list the next steps towards obtaining longitudinal polarisation at the interaction point.

(1) A harmonic closed-orbit spin matching algorithm must be implemented for the LHeC to try to correct the remaining tilt of $\hat{n}_0$ and thereby increase the equilibrium polarisation.

(2) Practical spin rotators must be designed and appropriate strong synchrobeta spin matching must be implemented. The design of the rotators and spin matching are closely linked. Some preliminary numerical investigations (below) show, as expected, that without this spin matching, little polarisation will be obtained.

(3) If synchrotron sideband resonances are still overwhelming after items 1 and 2 are implemented, a scheme involving Siberian Snakes could be tried. Siberian Snakes are arrangements of magnets which manipulate spin on the design orbit so that the closed-orbit spin tune is independent of beam energy. Normally the spin tune is then 1/2 and heuristic arguments suggest that the sidebands should be suppressed. However, the two standard schemes [432] either cause $\hat{n}_0$ to lie in the machine plane (just one snake) or ensure that it is vertically up in one half of the ring and vertically down in the other half (two snakes). In both cases Eq. 8.19 shows that $P_{\rm bk}$ vanishes. In principle, this problem can be overcome

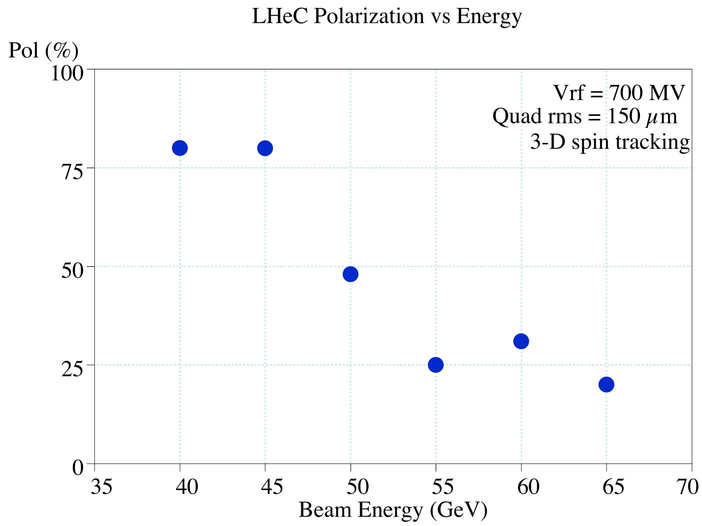

Figure 8.47: Equilibrium polarisation *vs* ring energy, full 3-D spin tracking results

for two snakes by again appealing to Eq. 8.19 and having short strong dipoles in the half of the ring where $\hat{n}_0$ points vertically up and long weaker dipoles in the half of the ring where $\hat{n}_0$ points vertically down (or vice versa). Of course, the dipoles must be chosen so that the total bend angle is π in each half of the ring. Moreover, Eq. 8.19 shows that the pure Sokolov-Ternov polarisation would be much less than 92.4%. One version of this concept [433] uses a pair of rotators which together form a snake while a complementary snake is inserted diametrically opposite to the interaction point. Each rotator comprises interleaved strings of vertical and horizontal bends which not only rotate the spins from vertical to horizontal, but also bring the $e^{\pm}$ beams down to the level of the proton beam and then up again. However, the use of short dipoles in the arcs increases the radiation losses.

Note that because of the energy dependence of spin rotations in the dipoles, $\hat{n}_0$ is vertical in the arcs at just one energy. This concept has been tested with SLICKTRACK but in the absence of a strong synchrobeta spin match, the equilibrium polarisation is very small as expected. Nevertheless the effects of misalignments and the tilt of $\hat{n}_0$ away from design energy, have been isolated by imposing an artificial spin match using standard facilities in SLICKTRACK. The snake in the arc has been represented as a thin element that has no influence on the orbital motion. Then it looks as if the synchrotron sidebands are indeed suppressed in the depolarisation associated with tilts of $\hat{n}_0$. In contrast to the rotators in HERA, this kind of rotator allows only one helicity for electrons and one for positrons.

(4) If a scheme can be found which delivers sufficient longitudinal polarisation, the effect of non-linear orbital motion, the effect of beam-beam forces and the effect of the magnetic fields of the detector must then be studied.

8.8 Summary

We have investigated the possibility of polarisation in the LHeC electron ring. At this stage of the work it appears a polarisation between 25 and 40% at 60 GeV can be reasonably aimed for, assuming the efficacy of harmonic closed-orbit spin matching. Attaining this degree of polarisation will require precision alignment of the magnets to better than 150μm rms, a challenging but achievable goal. The spin rotators necessary at the IP need to be properly spin matched to avoid additional depolarisation and this work is in progress. An interesting alternative involving the use of Siberian Snakes to try to avoid the depolarising synchrotron sidebands resonances is being investigated. At present, this appears to potentially yield a similar degree of polarisation, at the expense of increased energy dissipation in the arcs arising from the required differences of the bending radii in the two halves of the machine.

8.9 Integration and machine protection issues

Karl Hubert Meß and Yves Muttoni CERN

8.9.1 Space requirements

The integration of an additional electron accelerator into the LHC is a difficult task. For once,the LEP tunnel was designed for LEP and not for the LHC, which is now using up almost all space in the tunnel. It is not evident, how to place another accelerator into the limited space. Secondly, the LHC will run for several years, before the installation of a second machine can start. Meanwhile the tunnel will be irradiated and all installation work must proceed as fast as possible to limit the collective and individual doses. The activation after the planned high-luminosity-run of the LHC and after one month of cool-down is expected to be around 0.5...1$\mu Sv/h$ [**?**] on the proton magnets and many times more at exposed positions. Moreover the time windows for installation will be short and other work for the LHC will be going on, maybe with higher priority. Nevertheless, with careful preparation and advanced installation schemes an electron accelerator can be fitted in.

So far all heavy equipment had to pass the UJ2, while entering the tunnel. There the equipment has to be moved from TI2, which comes in from the outside, to the transport zone of LHC, which is on the inner side of the ring. Clearly, everything above the cold dipoles has to be removed. The new access shafts and the smaller size of the equipment for the electron ring may render this operation unnecessary.

General The new electron accelerator will be partially in the existing tunnel and partially in specially excavated tunnel sections and behind the experiments in existing underground areas. The excavation work will need special access shafts in the neighborhood of the experiments from where the stub-tunnels can be driven. The connection to the existing LEP tunnels will be very difficult. The new tunnel enters with a very small grazing angle, which means over a considerable length. Very likely the proton installation will have to be removed while the last meters of the new tunnel is bored.

Figure 8.48 [**?**] shows a typical cross section of the LHC tunnel, where the two machines are together. The LHC dipole dominates the picture. The transport zone is indicated at the right (inside of the ring). The cryogenic installations (QRL) and various pipes and cable trays are on the left. The dipole cross section shows two concentric circles. The larger circle corresponds to the largest extension at the re-enforcement rings and marks a very localized space restriction on a very long object. The inner circle is relevant for items shorter than about 10 m longitudinally. A hatched square above the dipole labeled *30* indicates the area, which was kept free in the beginning for an electron machine. Unfortunately, the center of this space is right above the proton beam. Any additional machine will, however, have to avoid the interaction points 1 and 5. In doing so additional length will be necessary, which can only be compensated for by shifting the electron machine in the arc about 60 cm to the inside (right). The limited space for compensation puts a constraint on the extra length created by the bypasses. The transport zone will, however, be affected. This requires an unconventional way to mount the electron machine. Nevertheless, there is clearly space to place an electron ring into the LHC, for most of the arc. Figure 8.49 gives the impression that the tunnel for most of its length is not too

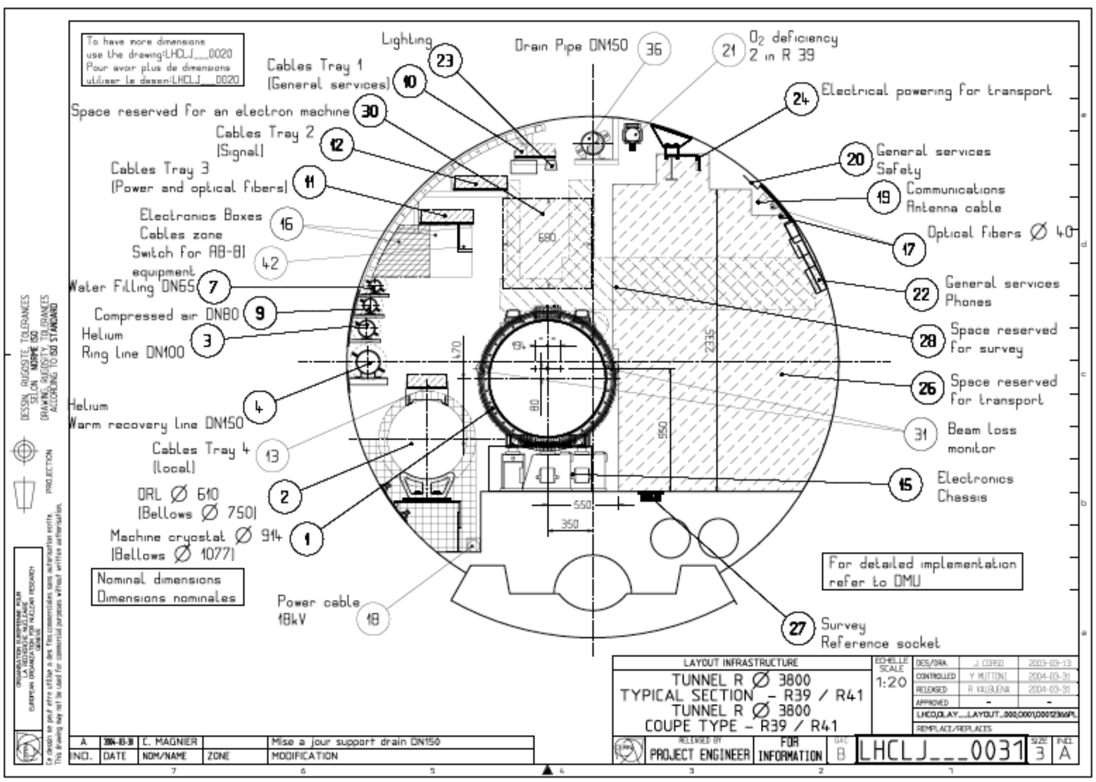

Figure 8.48: Cross-section of the LHC tunnel [?]

occupied.

In the arc In Fig. 8.49 one sees the chain of superconducting magnets and in the far distances the *QRL jumper*, the cryogenic connection between the superconducting machine and the cryogenic distribution line. The jumpers come always at the position of every second quadrupole. The optics of the LHeC foresees no e-ring magnet at these positions. The picture 8.49, taken

Figure 8.49: View of sector 4.

in sector 3, shows also the critical tunnel condition in this part of the machine. Clearly, heavy loads cannot be suspended from the tunnel ceiling. The limit is set to 100 kg per meter along the tunnel. The e-ring components have to rest on stands from the floor wherever possible. See **??** on page **??**. Normally there is enough space between the LHC dipoles and the QRL to place a vertical 10 cm quadratic or rectangular support. Alternatively a steel arch bolted to the tunnel walls and resting on the floor can support the components from above. This construction is required wherever the space for a stand is not available.

The electron machine, though partially in the transport zone, will be high up in the tunnel, high enough not to interfere with the transport of a proton magnet or alike. The transport of cryogenic equipment may need the full hight. Transports of that kind will only happen, when part of the LHC are warmed up. This gives enough time to shift the electron ring to the outside by 30 cm, if the stands are prepared for this operation. The outside movement causes also a small elongation of the inter-magnet connections. This effect is locally so small that the expansion joints, required anyway, can accommodate it. One could even think of moving large sections of the e-machine outwards in a semi-automatic way. Thus the time to clear the transport path can be kept in the shadow of the warm-up and cool-down times.

Dump area The most important space constraints for the electron machine are in the proton dump area, the proton RF cavities, point 3, and in particular the collimator sections.

Figure 8.50 [**?**] shows the situation at the dump kicker. The same area is also shown in a photo in Figure 8.51, while Figure 8.52 shows one of the outgoing dump-lines. The installation of the e-machine requires the proper rerouting of cables (which might be damaged by radiation

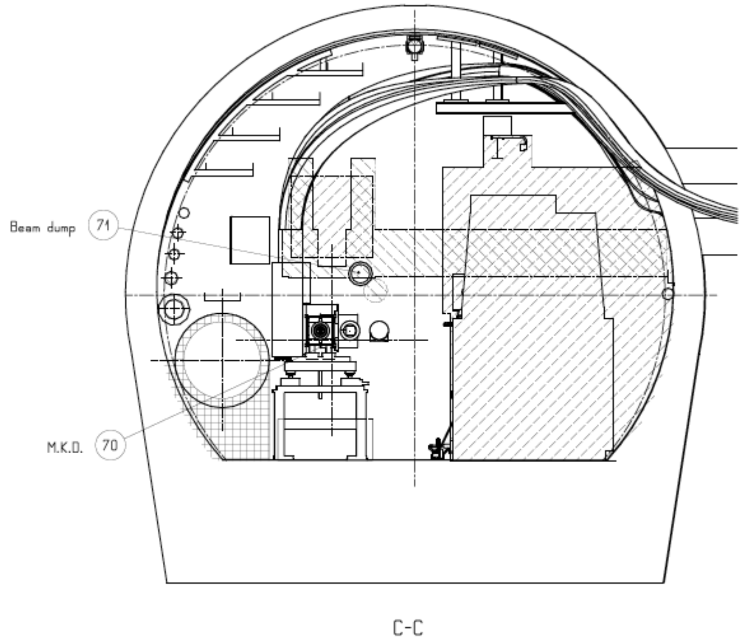

Figure 8.50: Dump kicker [?]

and in need of exchange anyhow), eventually turning of pumps by 90 degrees or straight sections in the electron optics to bridge particularly difficult stretches with a beam pipe only.

Point 4, proton RF The Figures 8.53 [**?**] and 8.54 illustrate the situation at the point 4, where the LHC RF is installed. Fortunately, the area is not very long. A short straight section could be created for the electron ring. This would allow to pass the area with just a shielded beam pipe.

Cryolink in point 3 The geography around point 3 did not permit to place there a cryoplant. The cryogenic cooling for the feedboxes is provided by a cryolink, as is shown in the figures 8.55 and 8.56. In particular above the Q6 proton quadrupole changes have to be made. There are other interferences with the cryogenics, as for example at the DFBAs (main feedboxes). An example is shown in figure 8.57. Eventually the electron optics has to be adapted to allow the beampipe to pass the cables, which may have to be moved a bit.

Long straight section 7 An extra air duct is mounted in the long straight section 7 (LSS7) as is indicated in Fig. 8.58 avoiding the air pollution of the area above point 7. The duct occupies the space planned for the electron machine. The air duct has to be replaced by a slightly different construction mounted further outside (to the right in the figure). There are also air ducts at points 1 and 5, but they are not an issue. The electron ring is passing behind the experiments in these points

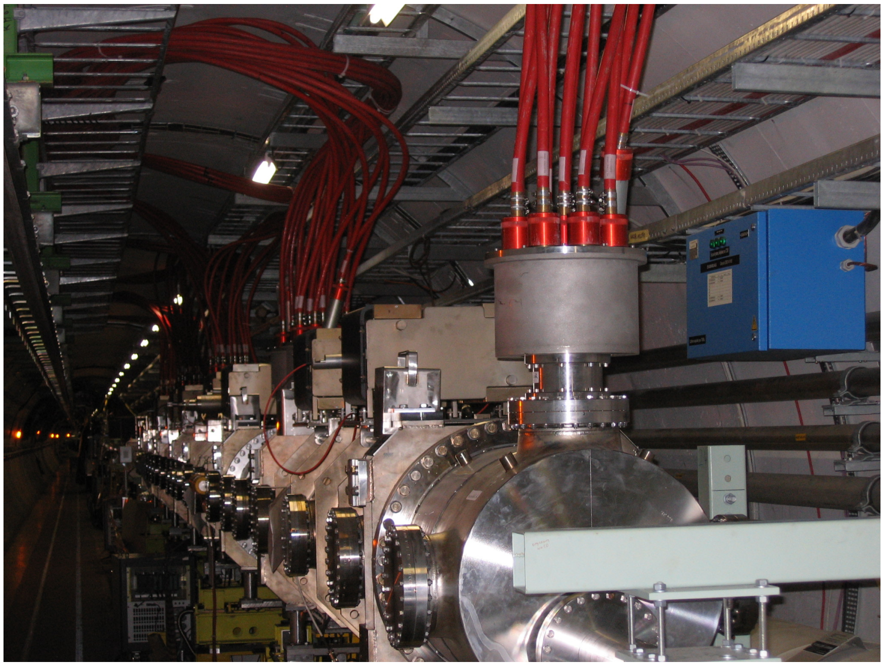

Figure 8.51: Dump kicker

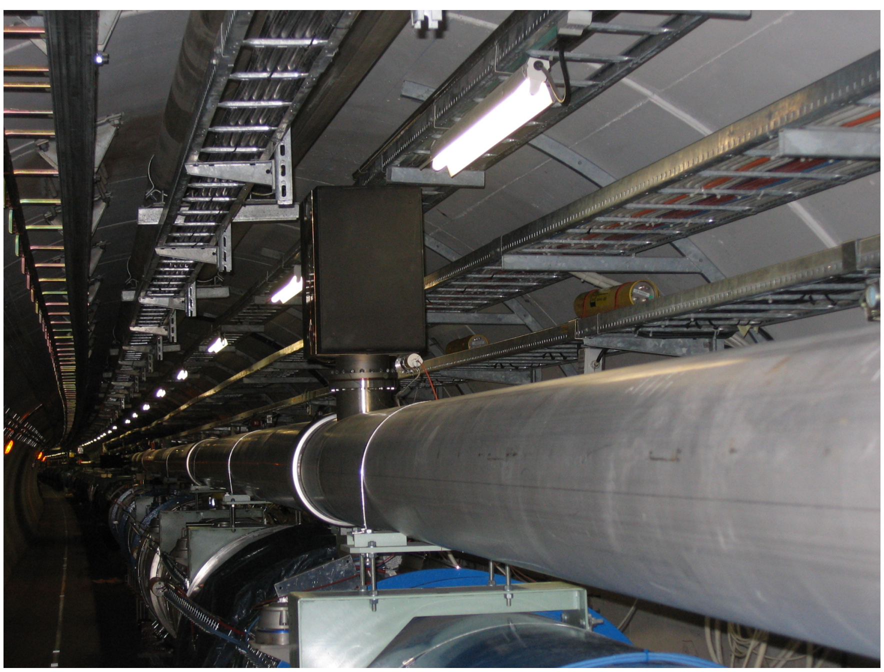

Figure 8.52: Dump line

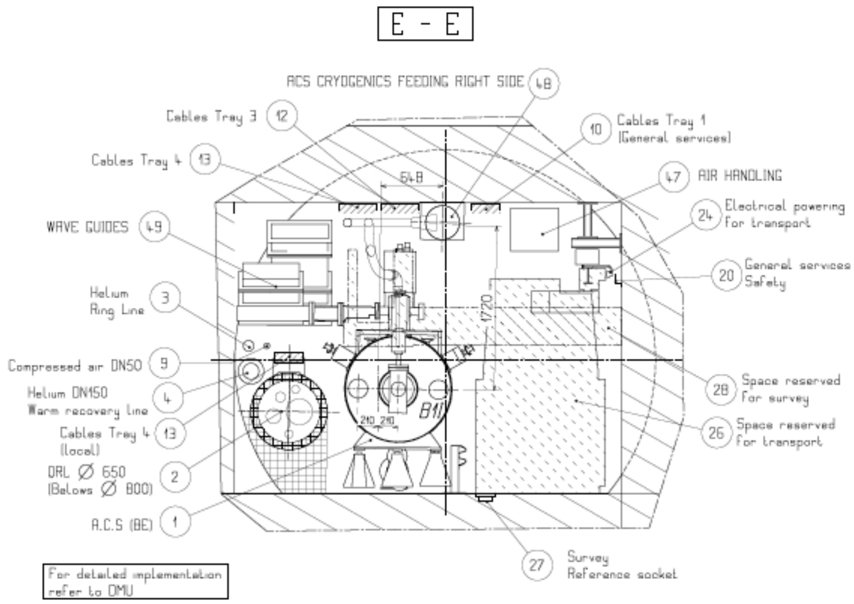

h

Figure 8.53: Proton RF in point 4 [?]

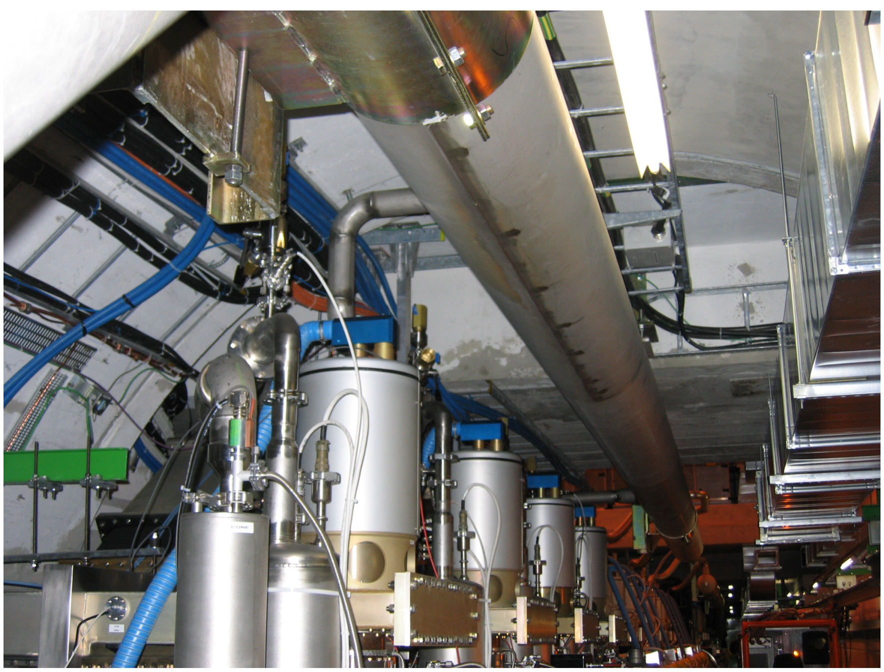

Figure 8.54: Point 4

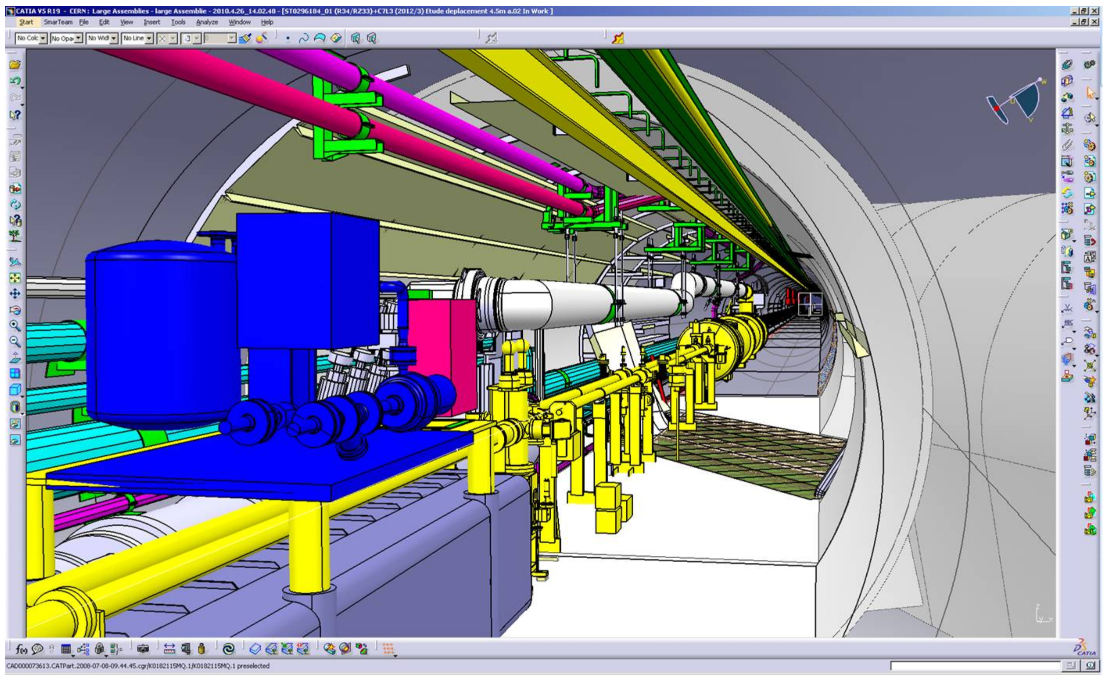

Figure 8.55: The cryogenic connection in point 3

Proton collimation The areas around point 3 (-62...+177m) and point 7 (-149...+205m) [**?**] are heavily used for the collimation of the proton beam. The high dose rate in the neighborhood of a collimator makes special precautions for the installation of new components or the exchange of a collimator necessary. Moreover, the collimator installation needs the full hight of the tunnel. Hence, the e-installation has to be suspended from the re-enforced tunnel roof. The e-machine components must be removable and installable, easy and fast. The re-alignment must be well prepared and fast, possibly in a remote fashion. It is uncommon to identify fast mounting and demounting as a major issue. However, with sufficient emphasis during the R&D phase of the project, this problem can be solved.

8.9.2 Impact of the synchrotron radiation on tunnel electronics

It is assumed that the main power converters of the LHC will have been moved out of the RRs because of the single event upsets, caused by proton losses.

The synchrotron radiation has to be intercepted at the source, as in all other electron accelerators. A few millimeter of lead are sufficient for the relatively low (critical) energies around 100 to 200 keV. The K-edge of lead is at 88 keV, the absorption coefficient is above 80/cm at this energy [**?**]. One centimeter of lead is sufficient to suppress 300 keV photons by a factor of 100. Detailed calculations of the optics will determine the amount of lead needed in the various places. The primary shielding needs an effective water cooling to avoid partial melting of the lead.

The electronics is placed below the proton magnets. Only backscattered photons with

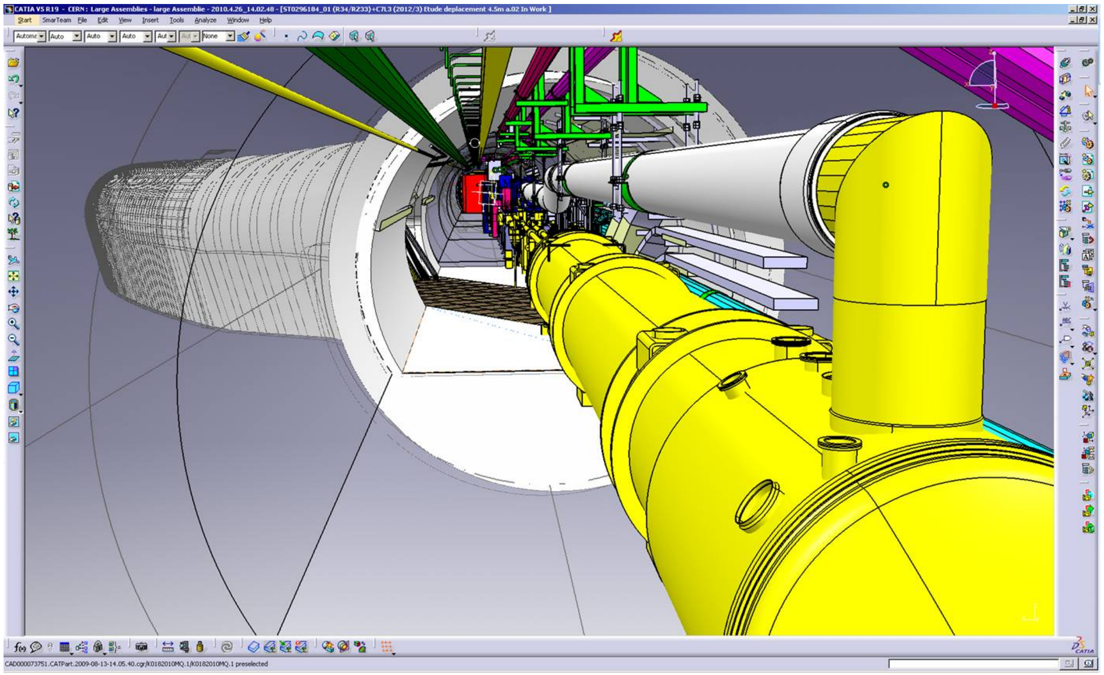

Figure 8.56: The cryogenic connection in point 3

correspondingly lower energy will reach the electronics. If necessary, a few millimeter of extra shielding could be added here.

The risk for additional single event upsets due to synchrotron radiation is negligible.

8.9.3 Compatibility with the proton beam loss system

The proton beam loss monitoring system works very satisfactory. It has been designed to detect proton losses by observing secondaries at the outside of the LHC magnets. The sensors are ionization chambers. Excessive synchrotron radiation (SR) background will presumably trigger the system and dump the proton beam. The SR background at the monitors has to be reduced by careful shielding of either the monitors or the electron ring. Alternatively, the impact of the photon background can be reduced by using a new loss monitoring system which is based on coincidences (as was done elsewhere [**?**]).

8.9.4 Space requirements for the electron dump

8.9.5 Protection of the p-machine against heavy electron losses

The existing proton loss detectors are placed, as mentioned above, at the LHC magnets. The trigger threshold requires certain number of detectors to be hit by a certain number of particles. The assumption is that the particles come from the inside of the magnets and the particle density there is much higher. Electron losses, creating a similar pattern in the proton loss detectors will result in a much lower particle density in the superconducting coils. Hence, still tolerable

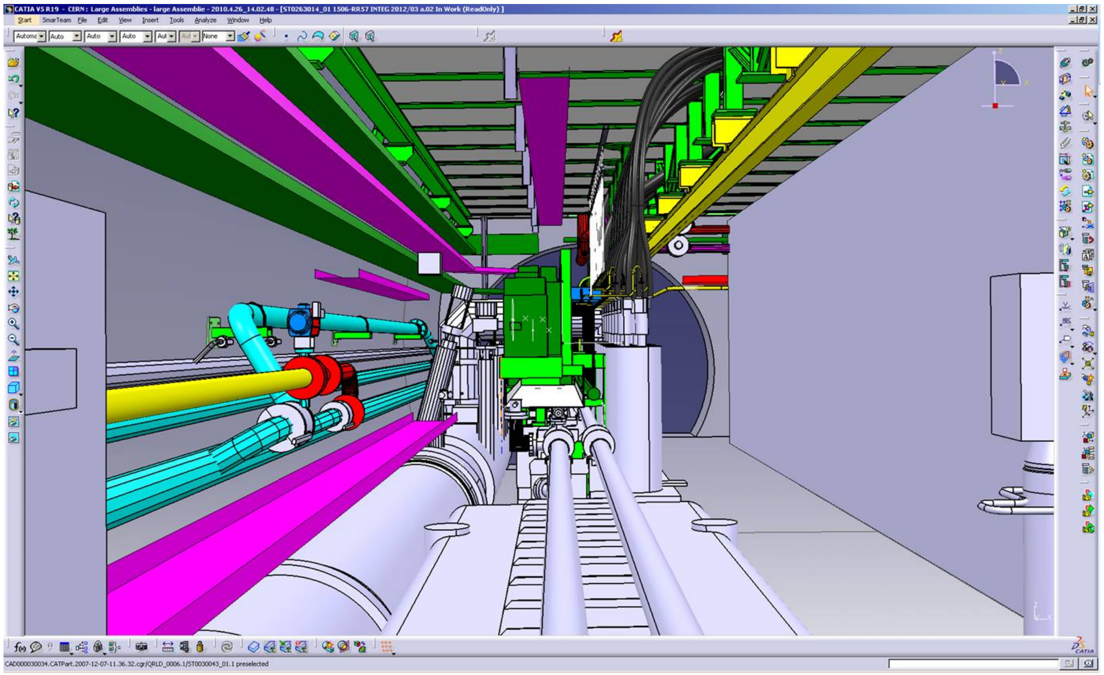

Figure 8.57: A typical big current feedbox (DFBA)

electron losses will unnecessarily trigger the proton loss system and dump the proton beam. The proton losses are kept at a low level by installing an advanced system of collimators and masks. Fast changes of magnet currents, which will result in a beam loss, are detected. A similar system is required for the electrons. An electron loss detection system, like the one mentioned in Ref. [?], combined with the proton loss system can be used to identify the source of the observed loss pattern and to minimize the electron losses by improved operation. It seems very optimistic to think of a hardware discrimination system, which determines very fast the source of the loss and acts correspondingly. Such a system could be envisaged only after several years of running.

8.9.6 How to combine the Machine Protection of both rings?

The existing machine-protection system combines many different subsystems. The proton loss system, the quench detection system, cryogenics, vacuum, access, and many other subsystems may signal a dangerous situation. This requirement lead to a very modular architecture, which could be expanded to include the electron accelerator.

.

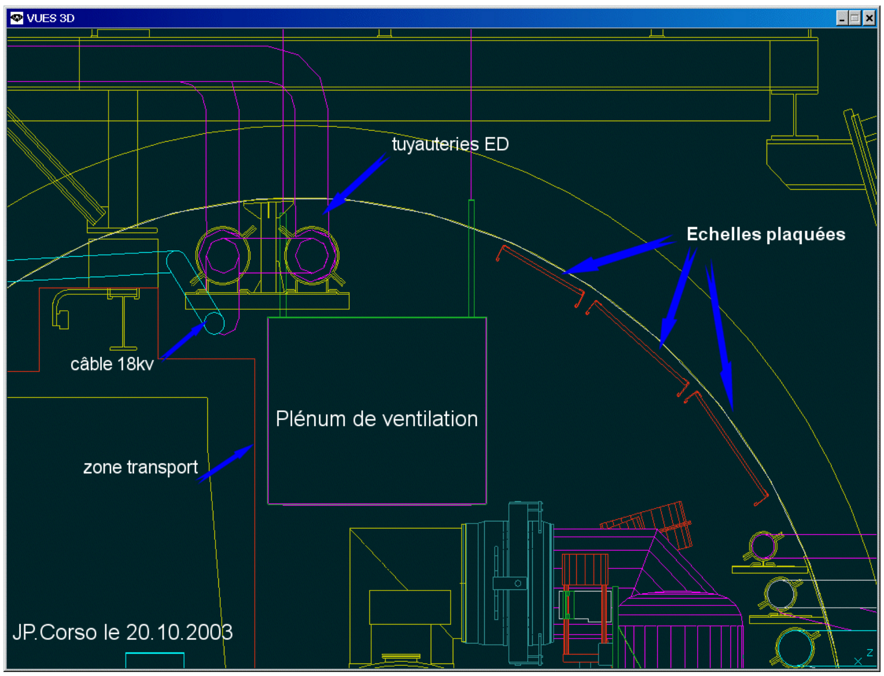

Figure 8.58: Air-duct in LSS7 [?]

Chapter 9

Linac-Ring Collider

9.1 Basic Parameters and Configurations

9.1.1 General Considerations

A high-energy electron-proton collider can be realized by accelerating electrons (or positrons) in a linear accelerator (linac) to 60–140 GeV and colliding them with the 7-TeV protons circulating in the LHC. Except for the collision point and the surrounding interaction region, the tunnel and the infrastructure for such a linac are separate and fully decoupled from the LHC operation, from the LHC maintenance work, and from other LHC upgrades (e.g., HL-LHC and HE-LHC).

The technical developments required for this type of collider can both benefit from and be used for many future projects. In particular, to deliver a long or continuous beam pulse, as required for high luminosity, the linac must be based on superconducting (SC) radiofrequency (RF) technology. The development and industrial production of its components can exploit synergies with numerous other advancing SC-RF projects around the world, such as the DESY XFEL, eRHIC, ESS, ILC, CEBAF upgrade, CESR-ERL, JLAMP, and the CERN HP-SPL.

For high luminosity operation at a beam energy of 50–70 GeV the linac should be operated in continuous wave (CW) mode, which restricts the maximum RF gradient through the associated cryogenics power, to a value of about 20 MV/m or less. In order to limit the active length of such a linac and to keep its construction and operating costs low, the linac should, and can, be recirculating. For the sake of energy efficiency and to limit the overall site power, while boosting the luminosity, the SC recirculating CW linac can be operated in energy-recovery (ER) mode. A 60-GeV recirculating energy-recovery linac represents the baseline scenario for a linac-ring LHeC.

Electron-beam energies higher than 70 GeV, e.g. 140 GeV, can be achieved by a pulsed SC linac, similar to the XFEL, ILC or SPL. In this case the accelerating gradient can be larger than for CW operation, i.e. above 30 MV/m, which minimizes the total length, but recirculation is no longer possible at this beam energy due to prohibitively high synchrotron-radiation energy losses in any return arc of reasonable dimension. As a consequence the standard energy recovery scheme using recirculation cannot be implemented and the luminosity of such a higher-energy lepton-hadron collider would be more than an order of magnitude lower than the one of the lower-energy CW ERL machine, at the same wall-plug power. An advanced energy-recovery option for the pulsed straight linac would employ two-beam technology, as developed for CLIC, in this case based on a decelerating linac and multiple energy-transfer beams, to boost the luminosity potentially by several orders of magnitude [?]. Such novel type of energy-recovery linac could later be converted into a linear collider, or vice versa.

While for a linac it is straightforward to deliver a 80–90% polarized electron beam, the production of a sufficient number of positrons is extremely challenging for a linac-ring collider. A conceivable path towards decent proton-positron luminosities would include a recycling of the spent positrons, together with the recovery of their energy.

The development of a CW SC recirculating energy-recovery linac (ERL) for LHeC would prepare the ground, the technology and the infrastructure for many possible future projects, e.g., for an International Linear Collider, for a Muon Collider[1], for a neutrino factory, or for a proton-driven plasma wake field accelerator. A ring-linac LHeC would, therefore, promote any conceivable future high-energy physics project, while pursuing an attractive forefront high-energy physics programme in its own right.

9.1.2 ERL Performance and Layout

Particle physics imposes the following performance requirements. The lepton beam energy should be 60 GeV or higher and the electron-proton luminosity of order 10^{33} cm^{-2}s^{-1}. Positron-proton collisions are also required, with at least a few percent of the electron-proton luminosity. Since the LHeC should operate simultaneously with LHC *pp* physics, it should not degrade the *pp* luminosity. Both electron and positron beams should be polarized. Lastly, the detector acceptance should extend down to 1° or less. In addition, the total electrical power for the lepton branch of the LHeC collider should stay below 100 MW.

For round-beam collisions, the luminosity of the linac-ring collider [?] is written as

$$L = \frac{1}{4\pi e}\frac{N_{b,p}}{\epsilon_p}\frac{1}{\beta_p^*} I_e H_{hg} H_D \ , \tag{9.1}$$

where e denotes the electron charge, $N_{b,p}$ the proton bunch population, β_p^* the proton IP beta function, I_e the average electron beam current, H_{hg} the geometric loss factor arising from crossing angle and hourglass effect, and H_D the disruption enhancement factor due to the electron pinch in collision, or luminosity reduction factor from the anti-pinch in the case of positrons. In the above formula, it is assumed that the electron bunch spacing is a multiple of the proton beam bunch spacing. The latter could be equal to 25, 50 or 75 ns, without changing the luminosity value.

The ratio $N_{b,p}/\epsilon_p$ is also called the proton beam brightness. Among other constraints, the LHC beam brightness is limited by the proton-proton beam-beam limit. For the LHeC design we assume the brightness value obtained for the ultimate bunch intensity, $N_{p,p} = 1.7 \times 10^{11}$, and the nominal proton beam emittance, $\epsilon_p = 0.5$ nm ($\gamma\epsilon_p = 3.75$ μm). This corresponds to a total *pp* beam-beam tune shift of 0.01. More than two times higher values have already been demonstrated, with good *pp* luminosity lifetime, during initial LHC beam commissioning, indicating a potential for higher *ep* luminosity.

To maximize the luminosity the proton IP beta function is chosen as 0.1 m. This is considerable smaller than the 0.55 m for the *pp* collisions of the nominal LHC. The reduced beta function can be achieved by reducing the free length between the IP and the first proton quadrupole (10

[1]The proposed Muon Collider heavily relies on SC recirculating linacs for muon acceleration as well as on a SC-linac proton driver.

m instead of 23 m), and by squeezing only one of the two proton beams, namely the one colliding with the leptons, which increases the aperture available for this beam in the last quadrupoles. In addition, we assume that the final quadrupoles could be based on Nb_3Sn superconductor technology instead of Nb-Ti. The critical field for Nb_3Sn is almost two times higher than for Nb-Ti, at the same temperature and current density, allowing for correspondingly larger aperture and higher quadrupole gradient. Nb_3Sn quadrupoles are presently under development for the High-Luminosity LHC upgrade (HL-LHC).

The geometric loss factor H_{hg} needs to be optimized as well. For round beams with $\sigma_{z,p} \gg \sigma_{z,e}$ (well fulfilled for $\sigma_{z,p} \approx 7.55$ cm, $\sigma_{z,e} \approx 300$ μm) and $\theta_c \ll 1$, it can be expressed as[2]

$$H_{hg} = \frac{\sqrt{\pi} z e^{z^2} \mathrm{erfc}(z)}{S} \ , \tag{9.2}$$

where

$$z \equiv 2 \frac{(\beta_e^*/\sigma_{z,p})(\epsilon_e/\epsilon_p)}{\sqrt{1+(\epsilon_e/\epsilon_p)^2}} S$$

and

$$S \equiv \sqrt{1 + \frac{\sigma_{x,p}^2 \theta_c^2}{8 \sigma_p^{*\,2}}} \ .$$

Luminosity loss from a crossing angle is avoided by head-on collisions. The luminosity loss from the hourglass effect, due to the long proton bunches and potentially small electron beta functions, is kept small, thanks to a "small" linac electron beam emittance of 0.43 nm ($\gamma\epsilon_e =$ 50 μm). We note that the assumed electron-beam emittance, though small when compared with a storage ring of comparable energy, is still very large by linear-collider standards.

The disruption enhancement factor for electron-proton collisions is about $H_D \approx 1.35$, according to Guinea-Pig simulations [?] and a simple estimate based on the fact that the average rms size of the electron beam during the collision approaches a value equal to $1/\sqrt{2}$ of the proton beam size. This additional luminosity increase from disruption is not taken into account in the numbers given below. On the other hand, for positron-proton collisions the disruption of the positrons leads to a significant luminosity reduction, by roughly a factor $H_D \approx 0.3$, similar to the case of electron-electron collisions [?].

The final parameter determining the luminosity is the average electron (or positron) beam current I_e. It is closely tied to the total electrical power available (taken to be 100 MW).

Crossing Angle and IR Layout

The colliding electron and proton beams need to be separated by 7 cm at a distance of 10 m from the IP in order to enter through separate holes in the first proton quadrupole magnet. This separation could be achieved with a crossing angle of 7 mrad and crab cavities. The required crab voltage would, however, need to be of order 200 MV, which is 20–30 times the voltage needed for *pp* crab crossing at the HL-LHC. Therefore, crab crossing is not considered

[2] The derivation of this formula is similar to the one for the LHC in Ref. [?], with the difference that here the two beams have different emittances and IP beta functions, and the electron bunch length is neglected. Curves obtained with formula (9.2) were first reported in [?].

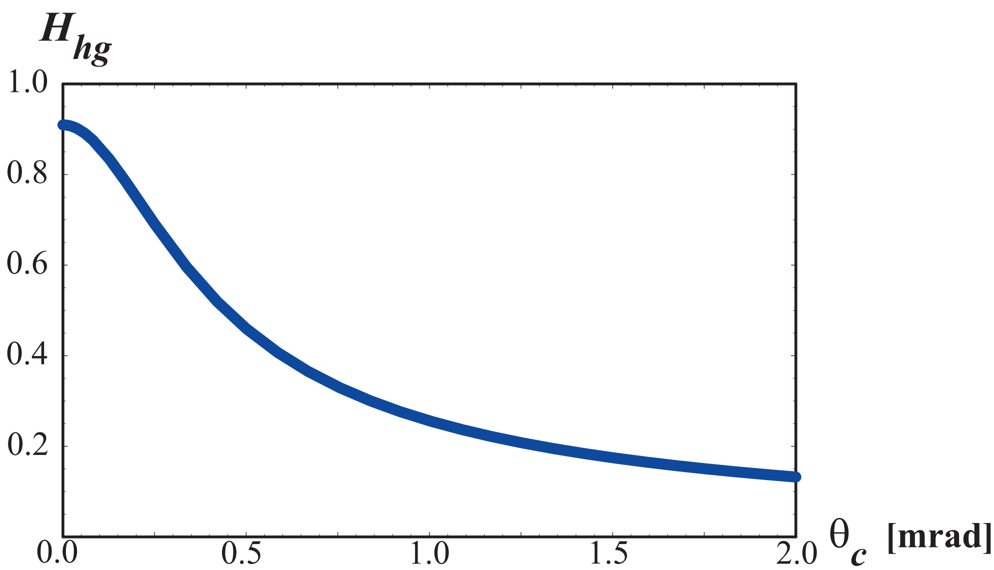

Figure 9.1: Geometric luminosity loss factor H_{hg}, (9.2), as a function of the total crossing angle

an option for the L-R LHeC. Without crab cavities, any crossing angle should be smaller than 0.3 mrad, as is illustrated in Fig. 9.1. Such small a crossing angle is not useful, compared with the 7 mrad angle required for the separation. The R-L interaction region (IR), therefore, uses detector-integrated dipole fields around the collision point, to provide head-on *ep* collisions ($\theta_c = 0$ mrad) and to separate the beams by the required amount. A dipole field of about 0.3 T over a length of ± 9 m accomplishes these goals.

The IR layout with separation dipoles and crossing angle is sketched in Fig. 9.2. Significant synchrotron radiation, with 48 kW average power, and a critical photon energy of 0.7 MeV, is emitted in the dipole fields. A large portion of this radiation is extracted through the electron and proton beam pipes. The SC proton magnets can be protected against the radiation heat load by an absorber placed in front of the first quadrupole and by a liner inside the beam pipe. Backscattering of synchrotron radiation into the detector is minimized by shaping the surface of absorbers and by additional masking.

The separation dipole fields modify, and enhance, the geometric acceptance of the detector. Figure 9.3 illustrates that scattered electrons with energies of 10–50 GeV might be detected at scattering angles down to zero degrees.

Electron Beam and the Case for Energy Recovery

The electron-beam emittance and the electron IP beta function are not critical, since the proton beam size is large by electron-beam standards (namely about 7 μm rms compared with nm beam-sizes for linear colliders). The most important parameter for high luminosity is the average beam current, I_e, which linearly enters into the luminosity formula (9.1). In addition to the electron beam curent, also the bunch spacing (which should be a multiple of the LHC 25-ns proton spacing) and polarization (80–90% for the electrons) need to be considered. Having pushed all other parameters in (9.1), Fig. 9.4 illustrates that an average electron current of

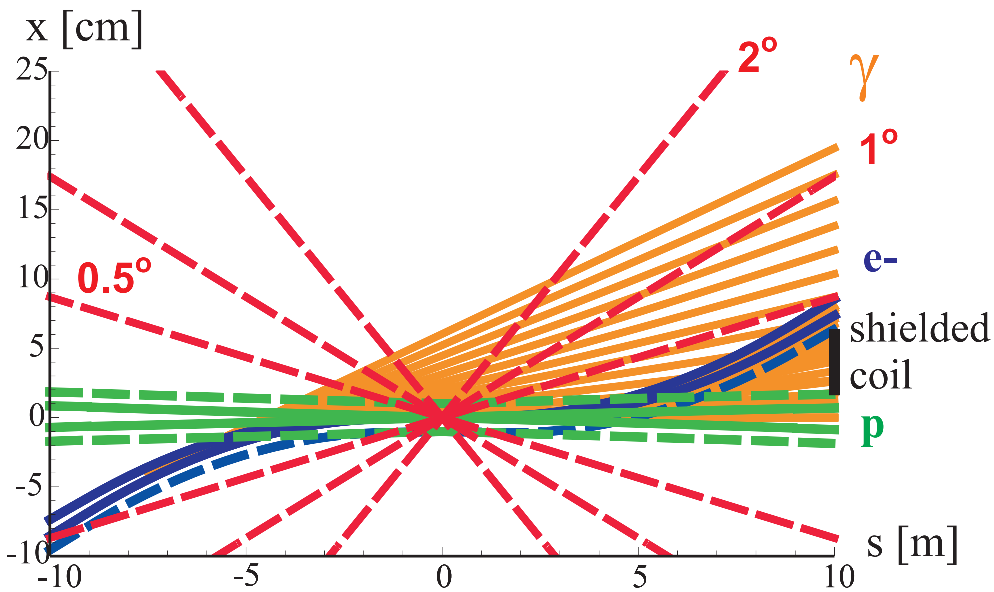

Figure 9.2: Linac-ring interaction-region layout. Shown are the beam enevelopes of 10σ (electrons) [solid blue] or 11σ (protons) [solid green], the same envelopes with an additional constant margin of 10 mm [dashed], the synchroton-radiation fan [orange], the approximate location of the magnet coil between incoming protons and outpgoing electron beam [black], and a "1 degree" line.

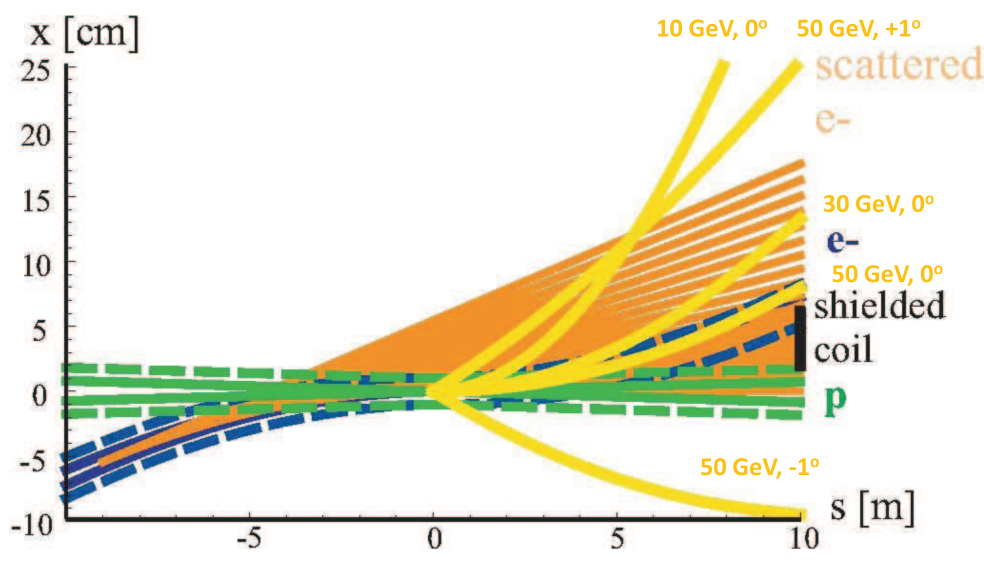

Figure 9.3: Example trajectories in the detector dipole fields for electrons of different energies and scattering angles, demonstrating an enhancement of the detector acceptance by the dipoles.

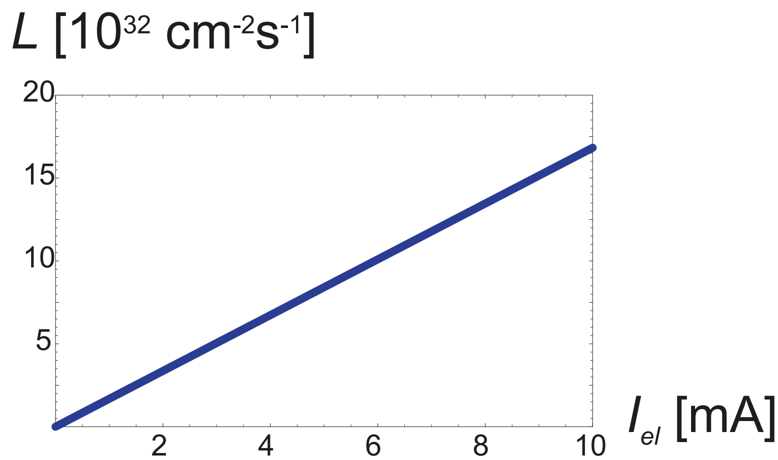

Figure 9.4: Linac-ring luminosity versus average electron beam current, according to (9.1).

about 6.4 mA is required to reach the target luminosity of 10^{33} cm^{-2}s^{-1}.

For comparison, the CLIC main beam has a design average current of 0.01 mA [**?**], so that it falls short by a factor 600 from the LHeC requirement. For other applications it has been proposed to raise the CLIC beam power by lowering the accelerating gradient, raising the bunch charge by a factor of two, and increasing the repetition rate up to three times, which raises the average beam current by a factor 6 to about 0.06 mA (this type of CLIC upgrade is described in [**?**]). This ultimate CLIC main beam current is still a factor 100 below the LHeC target. On the other hand, the CLIC drive beam would have a sufficiently high current, namely 30 mA, but at the low energy 2.37 GeV, which would not be useful for high-energy *ep* physics. Due to this low an energy, also the drive beam power is still a factor of 5 smaller than the one required by LHeC. Finally, the ILC design current is about 0.04 mA [**?**], which also falls more than a factor 100 short of the goal.

Fortunately, SC linacs can provide higher average current, e.g. by increasing the linac duty factor 10–100 times, or even running in continuous wave (CW) mode, at lower accelerating gradient. Example average currents for a few proposed designs illustrate this point: The CERN High-Power Superconducitng Proton Linac aims at about 1.5 mA average curent (with 50 Hz pulse rate) [**?**], the Cornell ERL design at 100 mA (cw) [**?**], and the eRHIC ERL at about 50 mA average current at 20 GeV beam energy (cw) [**?**]. All these designs are close to, or exceed, the LHeC requirements for average beam current and average beam power (6.4 mA at 60 GeV). It is worth noting that the JLAB UV/IR 4th Generation Light Source FEL is routinely operating with 10 mA average current (135 pC pulses at 75 MHz) [**?**].

The target LHeC IP electron-beam power is 384 MW. With a standard wall-plug-power to RF conversion efficiency around 50%, this would imply about 800 MW electrical power, far more than available. This highlights the need for energy recovery where the energy of the spent beam, after collision, is recuperated by returning the beam 180° out of phase through the same RF structure that had earlier been used for its acceleration, again with several recirculations. An energy recovery efficiency η_{ER} reduces the electrical power required for RF power generation at a given beam current by a factor $(1 - \eta_{\mathrm{ER}})$. We need an efficiency η_{ER} above 90% or higher to reach the beam-current goal of 6.4 mA with less than 100 MW total electrical power.

The above arguments have given birth to the LHeC Energy Recovery Linac high-luminosity baseline design, which is being presented in this chapter.

Choice of RF Frequency

Two candidate RF frequencies exist for the SC linac. One possibility is operating at the ILC and XFEL RF frequency around 1.3 GHz, the other choosing a frequency of about 720 MHz, close to the RF frequencies of the CERN High-Power SPL, eRHIC, and the European Spallation Source (ESS).

The ILC frequency would have the advantage of synergy with the XFEL infrastructure, of profiting from the high gradients reached with ILC accelerating cavities, and of smaller structure size, which could reduce the amount of high-purity niobium needed by a factor 2 to 4.

Despite these advantages, the present LHeC baseline frequency is 720 MHz, or, more precisely, 721 MHz to be compatible with the LHC bunch spacing. The arguments in favor of this lower frequency are the following:

- A frequency of 721 MHz requires less cryo-power (about two times less than at 1.3 GHz according to BCS theory; the exact difference will depend on the residual resistance [?]).
- The lower frequency will facilitate the design and operation of high-power couplers [?], though the couplers might not be critical [?].
- The smaller number of cells per module (of similar length) at lower RF frequency is preferred with regard to trapped modes [?].
- The lower-frequency structures reduce beam-loading effects and transverse wake fields.
- The project can benefit from synergy with SPL, eRHIC and ESS.

In case the cavity material costs at 721 MHz would turn out to be a major concern, they could be reduced by applying niobium as a thin film on a copper substrate, rather than using bulk niobium. The thin film technology may also enhance the intrinsic cavity properties, e.g. increase the Q value.

Linac RF parameters for both 720 MHz and 1.3 GHz in CW mode as well as for a pulsed 1.3-GHz option are compared in Table 9.1. The 721 MHz parameters are derived from eRHIC [?]. Pulsed-linac applications for LHeC are discussed in subsections 9.1.4 and 9.1.6.

ERL Electrical Site Power

The cryopower for two 10-GeV accelerating SC linacs is 28.9 MW, assuming pessimistically 37 W/m heat load at 1.8 K and 18 MV/m cavity gradient (this is a pessimistic estimate since the heat load could be up to 3 times smaller; see Table 9.1), and 700 "W per W" cryo efficiency as for the ILC. The RF power needed to control microphonics for the accelerating RF is estimated at 22.2 MW, considering that 10 kW/m RF power may be required, as for eRHIC, with 50% RF generation efficiency. The electrical power for the additional RF compensating the synchrotron-radiation energy loss is 24.1 MW, with an RF generation efficiency of 50%. The cryo power for

[1] The range of heat-load values quoted for 721 MHz reflects the measured parameters of eRHIC prototype cavity BNL-I and an extrapolation to the improved cavity BNL-III [?].

[2] The range of heat-load values indicated for 1.3 GHz refers to different assumptions on the cavity Q at 18 MV/m (or to two different extrapolations from [?]).

Table 9.1: Linac RF parameters for two different RF frequencies and two modes of operation.

	ERL 721 MHz	ERL 1.3 GHz	Pulsed
duty factor	CW	CW	0.05
RF frequency [GHz]	0.72	0.72	1.3
cavity length [m]	1	$\sim$1	$\sim$1
energy gain / cavity [MeV]	18	18	31.5
R/Q [100Ω]	400–500	1200	1200
Q_0 [10^{10}]	2.5–5.0	2?	1
power loss stat. [W/cav.]	5	< 0.5	< 0.5
power loss RF [W/cav.]	8–32[1]	13–27[2]	< 10
power loss total [W/cav.]	13–37	13–27	11
"W per W" (1.8 K to RT)	700	700	700
power loss / GeV at RT [MW]	0.51–1.44	0.6–1.1	0.24
length / GeV [m] (filling=0.57)	97	97	56

the compensating RF is 2.1 MW, provided in additional 1,44 GeV linacs, and the microphonics control for the compensating RF requires another 1.6 MW. In addition, with an injection energy of 50 MeV, 6.4 mA beam current, and as usual 50% efficiency, the electron injector consumes about 6.4 MW. A further 3 MW is budgeted for the recirculation-arc magnets [?]. Together this gives a grand total of 88.3 MW electrical power, some 10%.below the 100 MW limit.

ERL Configuration

The ERL configuration is depicted in Fig. 9.5. The shape, arc radius and number of passes have been optimized with respect to construction cost and with respect to synchrotron-radiation effects [?].

The ERL is of racetrack shape. A 500-MeV electron bunch coming from the injector is accelerated in each of the two 10-GeV SC linacs during three revolutions, after which it has obtained an energy of 60 GeV. The 60-GeV beam is focused and collided with the proton beam. It is then bent by 180° in the highest-energy arc beam line before it is sent back through the first linac, at a decelerating RF phase. After three revolutions with deceleration, re-converting the energy stored in the beam to RF energy, the beam energy is back at its original value of 500 MeV, and the beam is now disposed in a low-power 3.2-kW beam dump. A second, smaller (tune-up) dump could be installed behind the first linac.

Strictly speaking, with an injection energy into the first linac of 0.5 GeV, the energy gain in the two accelerating linacs need not be 10 GeV each, but about 9.92 GeV, in order to reach 60 GeV after three passages through each linac. Considering a rough value of 10 GeV means that we overestimate the electrical power required by about 1%.

Each arc contains three separate beam lines at energies of 10, 30 and 50 GeV on one side, and 20, 40 and 60 GeV on the other. Except for the highest energy level of 60 GeV, at which there is only one beam, in each of the other arc beam lines there always co-exist a decelerating

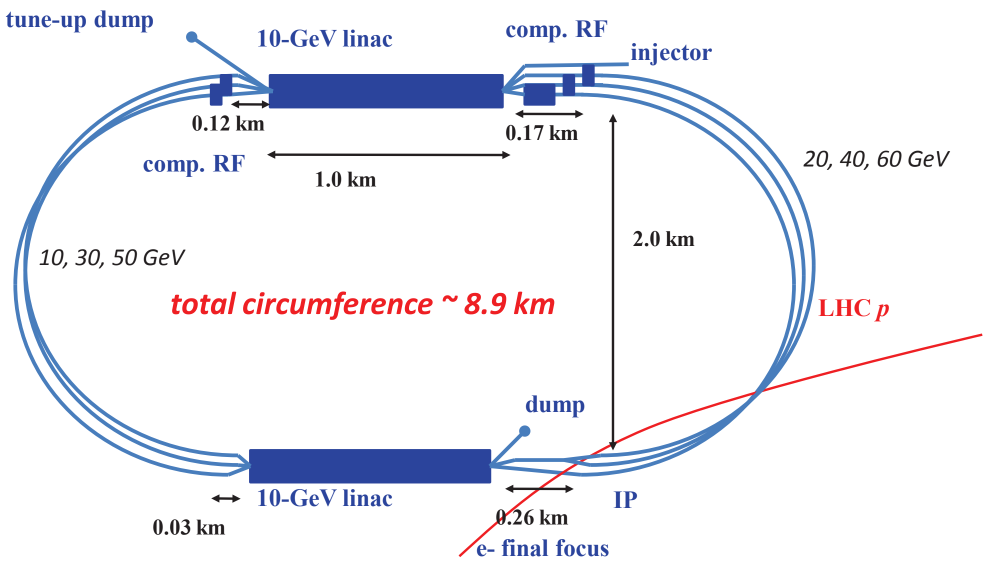

Figure 9.5: LHeC ERL layout including dimensions.

and an accelerating beam. The effective arc radius of curvature is 1 km, with a dipole bending radius of 764 m [**?**].

The two straight sections accommodate the 1-km long SC accelerating linacs. There is another 290 m section in each straight. In one straight of the racetrack 260 m of this additional length is allocated for the electron final focus (plus matching and splitting), the residual 30 m on the other side of the same straight allows for combining the beam and matching the optis into the arc. In the second straight section the additional RF compensating for 1.44 GeV energy loss is installed [**?**]. For the highest energy, 60 GeV, there is a single beam and the compensating RF (750 MV) can have the same frequency, 721 MHz, as in the main linac [?]. For the other energies, a higher harmonic RF system, e.g. at 1.442 GHz, can compensate the energy loss for both decelerating and accelerating beams, which are 180° out of phase at 721 MHz. On one side of the second straight one must compensate a total of about 907 MV (=750+148+9 MW, corresponding to the energy loss at 60, 40 and 20 GeV, repectively), which should easily fit within a length of 170 m. On the other side one has to compensate 409 MV (=362+47 MV), corresponding to SR energy losses at 50 and 30 GeV), for which a length of 120 m is available.

The total circumference of the ERL racetrack is chosen as 8.9 km, equal to one third of the LHC circumference. This choice has the advantage that one could introduce ion-clearing gaps in the electron beam which would match each other on successive revolutions (e.g. for efficient ion clearing in the linacs that are shared by six different parts of the beam) and which would also always coincide with the same proton bunch locations in the LHC, so that in the latter a given proton beam would either always collide or never collide with the electrons [**?**]. Ion clearing may be necessary to suppress ion-driven beam instabilities. The proposed implementation scheme would remove ions while minimizing the proton emittance growth which could otherwise arise when encountering collisions only on some of the turns. In addition, this arrangement can be useful for comparing the emittance growth of proton bunches which are colliding with the electrons and those which are not.

The length of individual components is as follows. The exact length of the 10-GeV linac is 1008 m. The individual cavity length is taken to be 1 m. The optics consists of 56-m long FODO cells with 32 cavities. The number of cavities per linac is 576. The linac cavity filling factor is 57.1%. The effective arc bending radius is set to be 1000 m. The bending radius of the dipole magnets is 764 m, corresponding to a dipole filling factor of 76.4% in the arcs. The longest SR compensation linac has a length of 84 m (replacing the energy lost by SR at 60 GeV). Combiners and splitters between straights and arcs require about 20–30 m space each. The electron final focus may have a length of 200–230 m.

IP Parameters and Beam-Beam Effects

Table 9.2 presents interaction-point (IP) parameters for the electron and proton beams.

Table 9.2: IP beam parameters

	protons	electrons
beam energy [GeV]	7000	60
Lorentz factor γ	7460	117400
normalizwed emittance $\gamma\epsilon_{x,y}$ [μm]	3.75	50
geometric emittance $\epsilon_{x,y}$ [nm]	0.,40	0.43
a IP beta function $\beta^*_{x,y}$ [m]	0.10	0.12
rms IP beam size $\sigma^*_{x,y}$ [μm]	7	7
initial rms IP beam divergence $\sigma^*_{x',y'}$ [μrad]	70	58
beam current [mA]	$\geq$430	6.4
bunch spacing [ns]	25 or 50	(25 or) 50
bunch population [ns]	1.7×10^{11}	(1 or) 2×10^9

Due to the low charge of the electron bunch, the proton head-on beam-beam tune shift is tiny, namely $\Delta Q_p = +0.0001$, which amounts to only about 1% of the LHC *pp* design tune shift (and is of opposite sign). Therefore, the proton-beam tune spread induced by the *ep* collisions is negligible. In fact, the electron beam acts like an electron lens and could conceivable increase the *pp* tune shift and luminosity, but only by about 1%. Long-range beam-beam effects are equally insignificant for both electrons and protons, since the detector-integrated dipoles separate the electron and proton bunches by about $36\sigma_p$ at the first parasitic encounter, 3.75 m away from the IP.

One further item to be looked at is the proton beam emittance growth. Past attempts at directly simulating the emittance growth from *ep* collisions were dominated by numerical noise from the finite number of macroparticles and could only set an upper bound [**?**], nevertheless indicating that the proton emittance growth due to the pinching electron beam might be acceptable for centered collisions. Proton emittance growth due to electron-beam position jitter and simultaneous *pp* collisions is another potential concern. For a 1σ offset between the electron and proton orbit at the IP, the proton bunch receives a deflection of about 10 nrad (approximately $10^{-4}\sigma^*_{x',y'}$). Beam-beam simulations for LHC *pp* collisions have determined the acceptable level for random white-noise dipole excitation as $\Delta x/\sigma_x \leq 0.1\%$ [**?**]. This translates into a very relaxed electron-beam random orbit jitter tolerance of more than 1σ. The tolerance on the orbit jitter will then not be set by beam-beam effects, but by the luminosity loss resulting from off-center collisions, which, without disruption, scales as $\exp(-(\Delta x)^2/(4\sigma_{x,y}^{*\,2})$. The random orbit jitter observed at the SLAC SLC had been of order 0.3–0.5σ [**?**, **?**]. A 0.1σ offset at LHeC would reduce the luminosity by at most 0.3%, a 0.3σ offset by 2.2%. Disruption further relaxes the tolerance.

The strongest beam-beam effect is encountered by the electron beam, which is heavily disrupted. The electron disruption parameter is $D_{x,y} \equiv N_{b,p} r_e \sigma_{z,p}/(\gamma_e \sigma^{*\,2}) \approx 6$, and the "nominal disruption angle" $\theta_0 \equiv D\sigma^*/\sigma_{z,p} = N_{b,p} r_e/(\gamma_e \sigma^*)$ [**?**] is about 600 μrad (roughly $10\sigma^*_{x',y'}$), which is huge. Simulations show that the actual maximum angle of the disrupted electrons is less than half θ_0.

Figure 9.6 illustrates the emittance growth and optics-parameter change for the electron beam due to head-on collision with a "strong" proton bunch. The intrinsic emittance grows by only 15%, but there is a 180% growth in the mismatch parameter "$B_{\rm mag}$" (defined as $B_{\rm mag} = (\beta\gamma_0 - 2\alpha\alpha_0 + \beta_0\gamma)/2$, where quantities with and without subindex "0" refer to the optics without and with collision, respectively. Without adjusting the extraction line optics to the parameters of the mismatched beam the emittance growth will be about 200%. This would be acceptable since the arc and linac physical apertures have been determined assuming up to 300% emittance growth for the decelerating beam [?]. However, if the optics of the extraction line is rematched for the colliding electron beam (corresponding to an effective β^* of about 3 cm rather than the nominal 12 cm; see Fig.9.6 bottom left), the net emittance growth can be much reduced, to only about 20%. The various optics parameters shown in Fig. 9.6 vary by no more than 10–20% for beam-beam orbit offsets up to 1σ.

Figure 9.7 presents the average electron deflection angle as a function of the beam-beam offset. The extraction channel for the electron beam must have sufficient aperture to accommodate both the larger emittance due to disruption and the average trajectory change due to off-center collisions.

9.1.3 Polarization

The electron beam can be produced from a polarized DC gun with about 90% polarization, and with, conservatively, 10–50 μm normalized emittance [**?**]. Spin-manipulation tools and measures for preserving polarization, like Wien filter and/or spin rotators, and polarimeters should be included in the optics design of the injector, the final focus, and the extraction line.

As for the positrons, up to about 60% polarization can be achieved either with an undulator [**?**] or with a Compton-based e^+ source [**?**, **?**][3].

9.1.4 Pulsed Linacs

For beam energies above about 140 GeV, due to the growing impact of synchrotron radiation, the construction of a single straight linac is cheaper than that of a recirculating linac [?]. Figure 9.8 shows the schematic of an LHeC collider based on a pulsed straight 140-GeV linac, including injector, final focus, and beam dump. The linac could be either of ILC type (1.3 GHz RF frequency) or operate at 721 MHz as the preferred ERL version. In both cases, ILC

[3] The primary challenge for positrons is to produce them in sufficient number and with a small enough emittance.

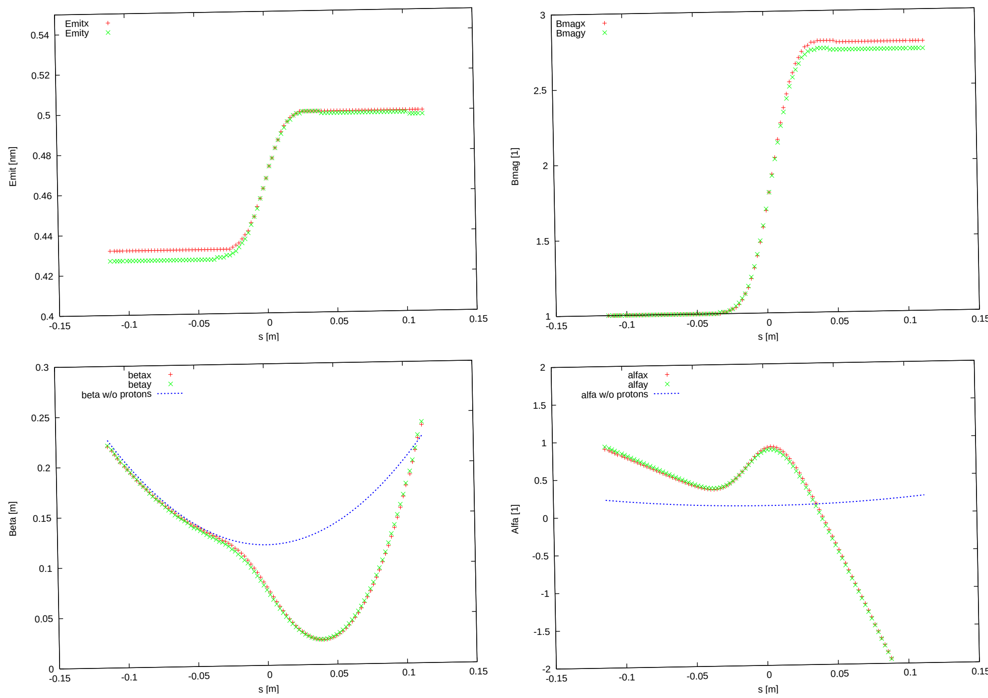

Figure 9.6: Simulated evolution of the electron beam emittance (top left), mismatch factor B_{mag} (top right) beta dfunction (bottom left) and alpha function (bottom right) during the collision with a proton bunch, as a function of distance from the IP.

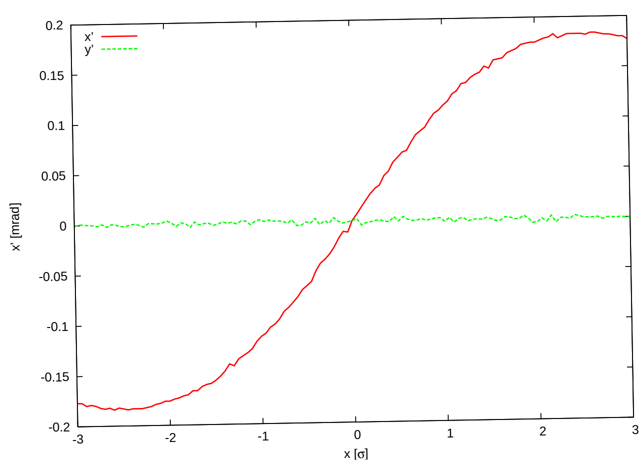

Figure 9.7: Simulated electron horizontal center-of-mass deflection angle as a function of the horizontal beam-beam offset.

Figure 9.8: Pulsed single straight 140-GeV linac for highest energy ep collisions.

values are assumed for the cavity gradient (31.5 MV/m) and for the cavity unloaded Q value ($Q_0 = 10^{10}$). This type of linac would be extendable to ever higher beam energies and could conceivably later become part of a linear collider. In its basic, simplest and conventional version no energy recovery is possible for this configuration, since it is impossible to bend the 140-GeV beam around. The lack of energy recovery leads to significantly lower luminosity. For example, with 10 Hz repetition rate, 5 ms pulse length (longer than ILC), a geometric reduction factor $H_g = 0.94$ and $N_b = 1.5 \times 10^9$ per bunch, the average electron current would be 0.27 mA and the luminosity 4×10^{31} cm^{-2}s^{-1}.

The construction of the 140-GeV pulsed straight linac could be staged, e.g. so as to first feature a pulsed linac at 60 GeV, which could also be used for γ-p/A collisions (see subsection 9.1.6). The linac length decreases directly in proportion to the beam energy. For example, at 140-GeV the pulsed linac measures 7.9 km, while at 60 GeV its length would be 3.4 km. For a given constant wall-plug power, of 100 MW, both the average electron current and the luminosity scale roughly inversely with the beam energy. At 60 GeV the average electron current becomes 0.63 mA and the pulsed-linac luminosity, without any energy recovery, would be more than 9×10^{31} cm^{-2}s^{-1}.

9.1.5 Highest-Energy LHeC ERL Option

The simple straight linac layout of Fig. 9.8 can be expanded as shown in Fig. 9.9 [?]. The main electron beam propagates from the left to the right. In the first linac it gains about 150 GeV, then collides with the hadron beam, and is then decelerated in the second linac. By transferring the RF energy back to the first accelerating linac, with the help of multiple, e.g. 15, 10-GeV "energy-transfer beams," a novel type of energy recovery is realized without bending the spent beam. With two straight linacs facing each other this configuratiom could easily be converted into a linear collider, or vice versa, pending on geometrical and geographical constraints of the LHC site. As there are no synchrotron-radiation losses the energy recovery can be nearly 100% efficient. Such novel form of ERL could push the LHeC luminosity to the 10^{35} cm^{-2}s^{-1} level. In addition, it offers ample synergy with the CLIC two-beam technology.

9.1.6 γ-p/A Option

In case of a (pulsed) linac without energy recovery the electron beam can be converted into a high-energy photon beam, by backscattering off a laser pulse, as is illustrated in Fig. 9.10. The rms laser spot size at the conversion point should be similar to the size of the electron beam at this location, that is $\sigma_\gamma \approx 10\mu$m.

With a laser wavelength around $\lambda_\gamma \approx 250$ nm ($E_{\gamma,0} \approx 5$ eV), obtained e.g. from a Nd:YAG

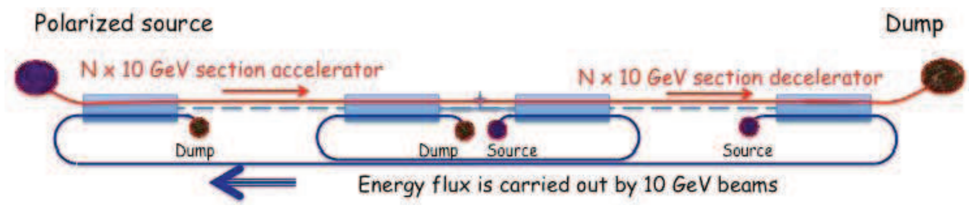

Figure 9.9: Highest-energy high-luminosity ERL option based on two straight linacs and multiple 10-GeV energy-transfer beams [?].

laser with frequency quadrupling, the Compton-scattering parameter x [?, ?],

$$x \approx 15.3 \left[\frac{E_{e,0}}{\mathrm{TeV}}\right] \left[\frac{E_{\gamma,0}}{\mathrm{eV}}\right] , \tag{9.3}$$

is close to the optimum value 4.8 for an electron energy of 60 GeV (for $x > 4.8$ high-energy photons get lost due to the creation of e^+e^- pairs). The maximum energy of the Compton scattered photons is given by $E_{\gamma,\max} = x/(x+1)E_0$, which is larger than 80% of the initial electron-beam energy $E_{e,0}$, for our parameters. The cross section and photon spectra depend on the longitudinal electron polarization λ_e and on the circular laser polarization P_c. With proper orientation ($2\lambda_e P_c = -1$) the photon spectrum is concentrated near the highest energy $E_{\gamma.\max}$.

The probability of scattering per individual electron is [?]

$$n_\gamma = 1 - \exp(-q) \tag{9.4}$$

with

$$q = \frac{\sigma_c A}{E_{\gamma,0} 2\pi\sigma_\gamma^2} , \tag{9.5}$$

where σ_c denotes the (polarized) Compton cross section and A the laser pulse energy. Using the formulae in [?], the Compton cross section for $x = 4.8$ and $2\lambda_e P_c = -1$ is computed to be $\sigma_c = 3.28\times10^{-25}$ cm^2. The pulse energy corresponding to $q = 1$, i.e. to a conversion efficiency of 65%, is estimated as $A \approx E_{\gamma,0}2\pi\sigma_\gamma^2/\sigma_c \approx 16$ J. To set this into perspective, for a $\gamma\gamma$ collider at the ILC, Ref. [?] considered a pulse energy of 9 J at a four times longer wavelength of $\lambda \approx 1$ μm.

The energies of the leftover electrons after conversion extend from about 10 to 60 GeV. This spent electron beam, with its enormous energy spread, must be safely extracted from the interaction region. The detector-integrated dipole magnets will assist in this process. They will also move the scattered electrons away from the interaction point. A beam dump for the neutral photons should also be installed, behind the downstream quadrupole channel.

Figure 9.11 presents an example photon energy spectrum after the conversion and a luminosity spectrum [?], obtained from a simulation with the Monte-Carlo code CAIN [?].

Differently from $\gamma\gamma$ collisions at a linear collider, thanks to the much larger IP spot size and smaller beam energy, the conversion point can be a much larger distance $\Delta s \approx \beta^* \sim 0.1$ m away from the interaction point, which could simplify the integration in the detector, and is also necessary as otherwise, with e.g. a mm-distance between CP and IP, the conversion would take place inside the proton bunch.

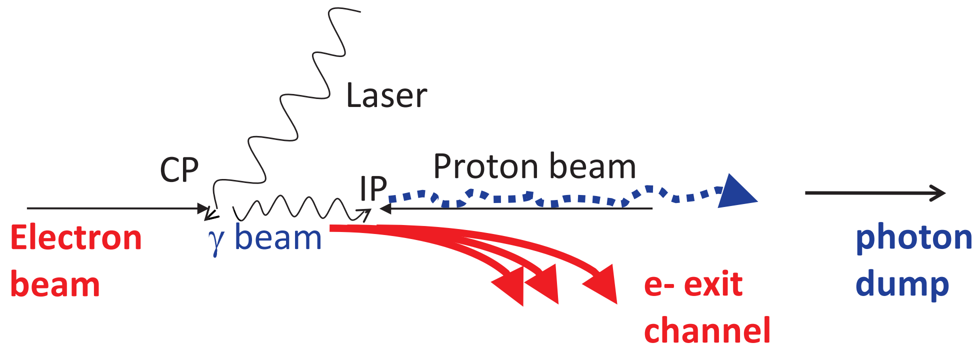

Figure 9.10: Schematic of γ-p/A collision; prior to the photon-hadron interaction point (IP), the electron beam is scattered off a several-J laser pulse at the conversion point (CP).

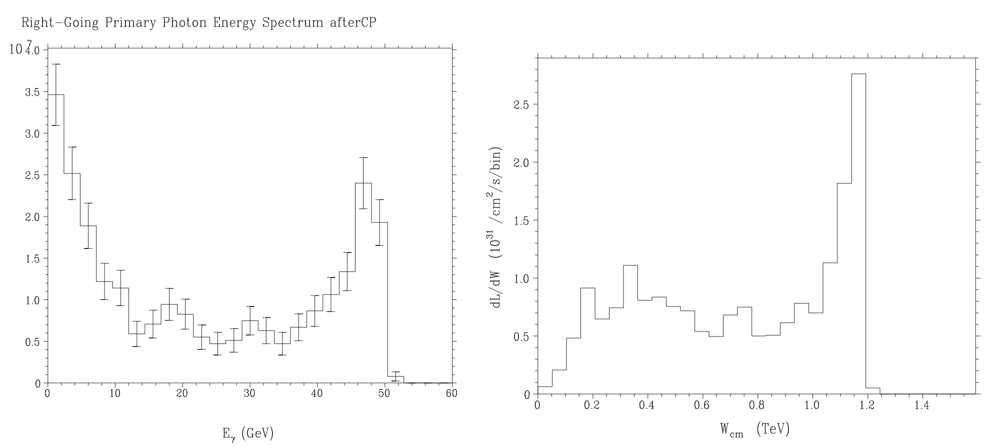

Figure 9.11: Simulated example photon spectrum after the conversion point (left) and γ-p luminosity spectrum [?].

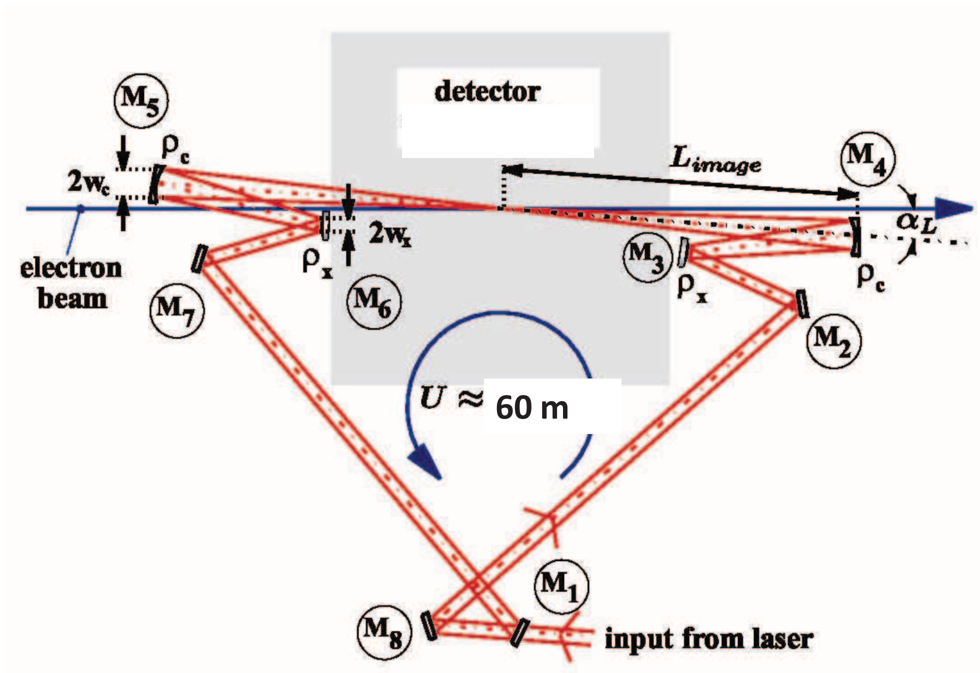

Figure 9.12: Recirculating mirror arrangement providing a laser-pulse path length of 60 m for pulse stacking synchronously with the arriving electron bunches (adapted from [?]).

To achieve the required laser pulse energy, external pulses can be stacked in a recirculating optical cavity. For an electron bunch spacing of e.g. 200 ns, the path length of the recirculation could be 60. A schematic of a possible mirror system is sketched in Fig. 9.12 (adapted from [?]).

9.1.7 Summary of Basic Parameters and Configurations

The baseline 60-GeV ERL option presented here can provide a *pe* luminosity of 10^{33} cm^{-2}s^{-1}, at less than 100 MW total electrical power for the electron branch of the collider, and with less than 9 km circumference. Its main hardware component is about 21 GV of SC-RF.

A pulsed 140-GeV linac, without energy recovery, could achieve a luminosity of 1.4×10^{31} cm^{-2}s^{-1}, at higher c.m. energy, again with less than 100 MW electrical power, and shorter than 9 km in length. The pulsed linac can accommodate a γ-p/A option. An advanced, novel type of energy recovery, proposed for the single straight high-energy linac case, includes a second decelating linac, and multiple 10-GeV "energy-transfer beams". This type of collider could potentially reach luminosities of 10^{35} cm^{-2}s^{-1}.

High polarization is possible for all linac-ring options. Beam-beam effects are benign, especially for the proton beam, which will not be affected by the presence of the electron beam.

Producing the required number of positrons needed for high-luminosity proton-positron collisions is the main open challenge for a linac-ring LHeC. Recovery of the positrons together with their energy, as well as fast transverse cooling schemes, are likely to be essential ingredients for any linac-based high-luminosity *ep* collider involving positrons.

9.2 Interaction region

This section presents a first conceptual design of the LHeC linac-ring Interaction Region (IR). The merits of the IR are a very low β^* of 0.1m with proton triplets as close as possible to the IP to minimize chromaticity. Head-on proton-electron collisions are achieved by means of dipoles around the Interaction Point (IP). The Nb_3Sn superconductor has been chosen for the proton triplets since it provides the largest gradient. If this technology proves not feasible in the timescale of the LHeC a new design of the IR can be pursued using standard technology.

The main goal of this first design is to evaluate potential obstacles, decide on the needs of special approaches for chromaticity correction and evaluate the impact of the IR synchrotron radiation.

9.2.1 Layout

A crossing angle of 6 mrad between the non-colliding proton beams allows enough separation to place the proton triplets. Only the proton beam colliding with the electrons is focused. A possible configuration in IR2 could be to inject the electrons parallel to the LHC beam 1 and collide them head-on with beam 2, see Fig. 9.13. The signs of the separation and recombination dipoles (D1 and D2) have to be changed to allow for the large crossing angle at the IP. The new D1 has one aperture per beam and is 4.5 times stronger than the LHC design D1. The new D2 is 1.5 times stronger than the LHC design D2. Both dipoles feature about a 6 T field. The lengths of the nominal LHC D1 and D2 dipoles have been left unchanged, 23 m and 9 m, respectively. However the final IR design will need to incorporate a escape line for the neutral particles coming from the IP, probably requiring to split D1 into two parts separated by tens of meters.

Bending dipoles around the IP are used to make the electrons collide head-on with beam 2 and to safely extract the disrupted electron beam. The required field of these dipoles is determined by the L^* and the minimum separation of the electron and the focused beam at the first quadrupole (Q1). A 0.3 T field extending over 9 m allows for a beams separation of 0.07 m at the entry of Q1. This separation distance is compatible with mirror quadrupole designs using Nb_3Sn technology. The electron beam radiates 48 kW in the IR dipoles. A sketch of the 3 beams, the synchrotron radiation fan and the proton triplets is shown in Fig. 9.14.

9.2.2 Optics

Colliding proton optics

The colliding beam triplet starts at L^*=10m from the IP. It consists of 3 quadrupoles with main parameters given in Table 9.3. The quadrupole aperture is computed as $11\max(\sigma_x,\sigma_y)+5$ mm. The 5 mm split into 1.5 mm for the beam pipe, 1.5 mm for mechanical tolerances and 2 mm for the closed orbit. These quadrupoles are consistent with Nb_3Sn technology. The total chromaticity from the two IP sides amounts to 960 units. The optics functions for the colliding beam are shown in Fig. 9.15

It was initially hoped that a compact Nb_3Sn triplet with L^*=10m would allow for a normal chromaticity correction using the arc sextupoles. However after matching this triplet to the LHC and correcting linear chromaticity the chromatic β-beating at dp/p=0.001 is about 100%. This is intolerable regarding collimation and machine protection issues. Therefore a dedicated chromaticity correction scheme has to be adopted. A large collection of studies exist showing

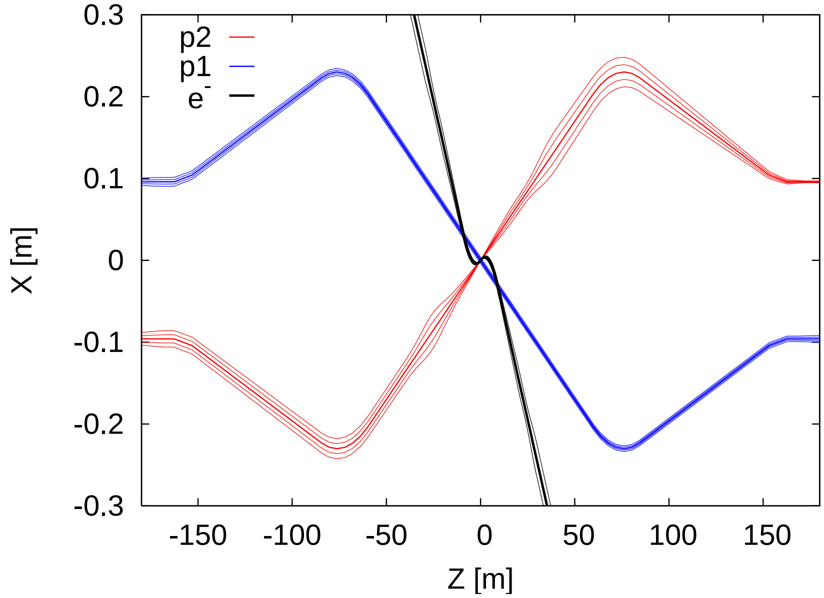

Figure 9.13: LHeC interaction region displaying the two proton beams and the electron beam trajectories with 5σ and 10σ envelopes.

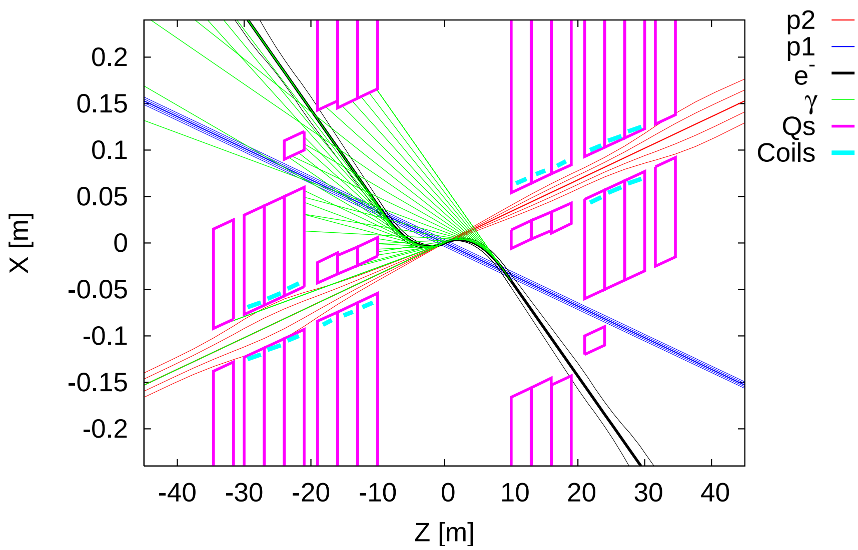

Figure 9.14: LHeC interaction region with a schematic view of synchrotron radiation. Beam trajectories with 5σ and 10σ envelopes are shown.

Name	Gradient [T/m]	Length [m]	Radius [mm]
Q1	187	9	22
Q2	308	9	30
Q3	185	9	32

Table 9.3: Parameters of the proton triplet quadrupoles. The radius is computed as $11\max(\sigma_x,\sigma_y)+5$ mm.

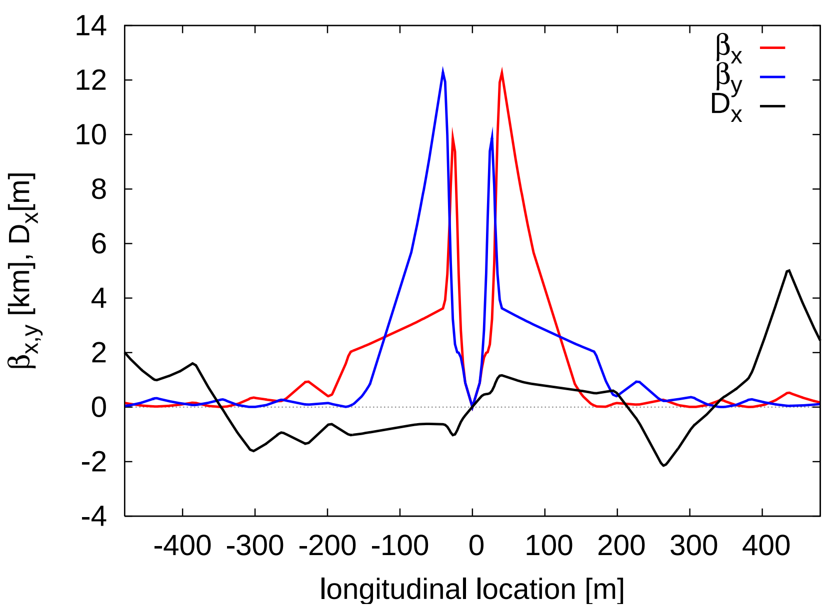

Figure 9.15: Optics functions for main proton beam.

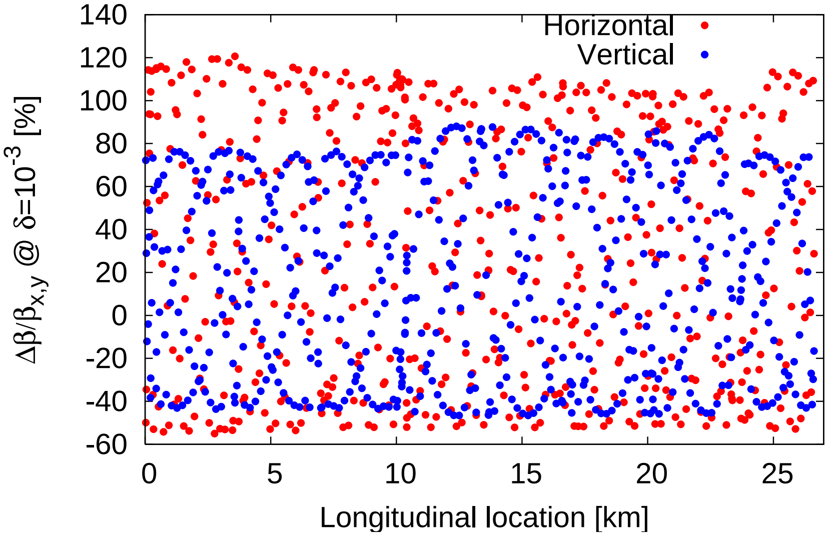

Figure 9.16: Chromatic beta-beating at dp/p=0.001.

the feasibility of correcting even larger chromaticities in the LHC [434–436]. Other local chromatic correction approaches as [437], where quadrupole doublets are used to provide the strong focusing, could also be considered for the LHeC.

Since LHeC anyhow requires a new dedicated chromaticity correction scheme, current NbTi technology could be pursued instead of Nb_3Sn and the L^* could also be slightly increased. The same conceptual three-beam crossing scheme as in Fig. 9.13 could be kept.

To achieve L^* below 23 m requires a cantilever supported on a large mass as proposed for the CLIC QD0 [438] to provide sub-nanometer stability at the IP. The LHeC vibration tolerances are much more relaxed, being on the sub-micrometer level.

Non-colliding proton optics

The non-colliding beam has no triplet quadrupoles since it does not need to be focused. The LHC "alignment optics" [439] was used as a starting point. Figure 9.17 shows the optics functions around the IP. The LHeC IP longitudinal location can be designed so as to completely avoid unwanted proton-proton collisions.

The non-colliding proton beam travels through dedicated holes in the proton triplet quadrupoles, in Q1 together with the electron beam. The Q1 hole dimensions are determined by the electron beam, see below. Instead the non-colliding proton beam travels alone trough the first module of the Q2 requiring about 30 mm full aperture. No fields are assumed in these apertures but the possible residual fields could easily be taken into account for the proton optics.

Electron optics

The electron L^*=30 m has been chosen to allow for enough separation between the proton and the electron final focusing quadrupoles. A first design of the optics already matched to the exit

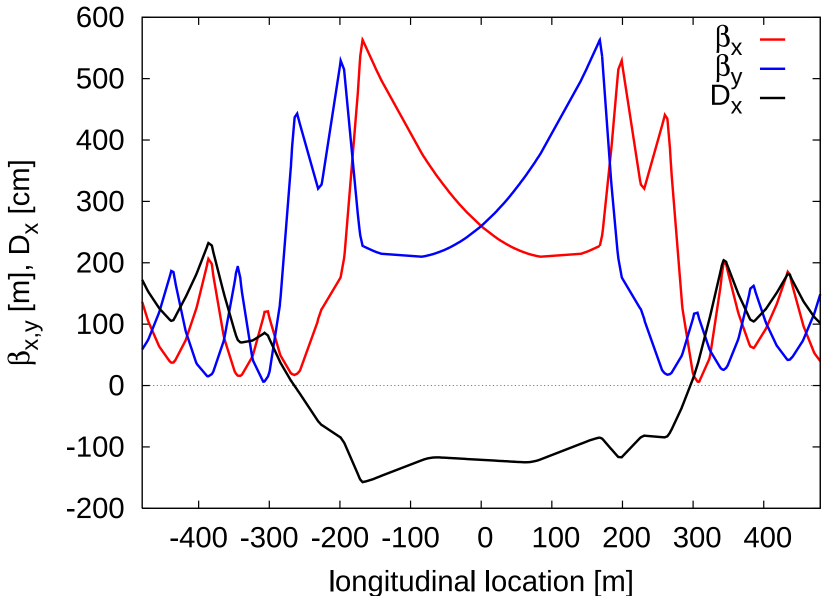

Figure 9.17: Optics functions for the non-colliding proton beam without triplets.

Name	Gradient [T/m]	Length [m]	Radius [mm]
Q1	19.7	1.34	20
Q2A	38.8	1.18	32
Q2B	3.46	1.18	20
Q3	22.3	1.34	22

Table 9.4: Parameters of the electron triplet quadrupoles. The radius is computed as 11max(σ_x,σ_y)+5 mm.

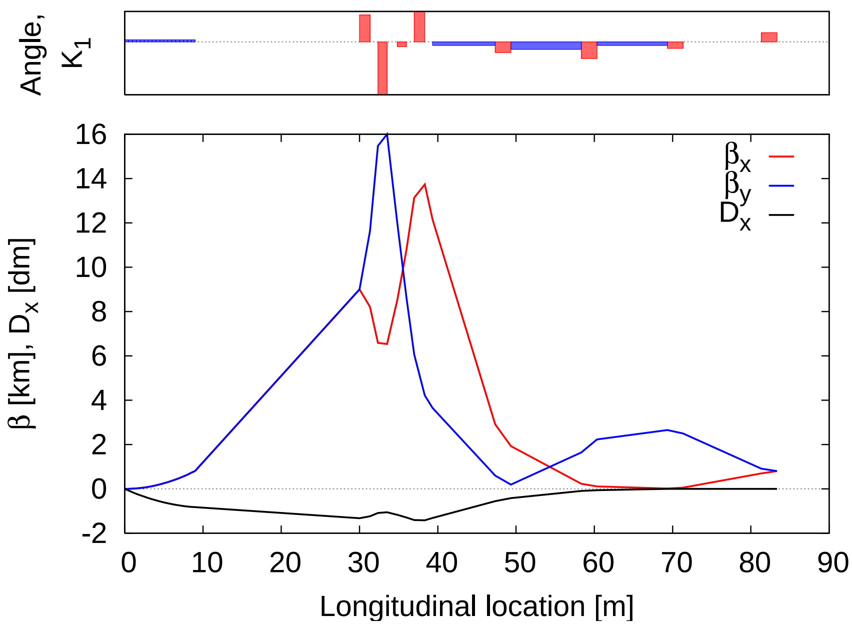

Figure 9.18: Optics of the electron beam.

of the linac is shown in Fig. 9.18. The electron focusing quadrupoles feature moderately low gradients as shown in Table 9.4. The IP beam size aberration versus the relative energy spread of the beam is shown in Fig. 9.19. Chromatic correction is mandatory for relative energy spreads above 3×10^{-4}. It is recommended to design a chromatic correction section. About 200 m are available between the exit of the linac and the IP while the current electron final focus is using only 90 m, leaving space for collimation and beam diagnostics.

The electrons travel through dedicated holes in the proton triplet quadrupoles. The electron hole in the proton Q1 must have about 160 mm full horizontal aperture to allow for the offcenter electron orbit (120 mm) and the usual beam aperture assumptions (20 mm). First design of mirror magnets for Q1 feature a field of 0.5 T in the electron beam pipe. This value is considered too large when compared to the IR dipole of 0.3 T, but new designs with active isolation or dedicated coils could considerably reduce this field. Migrating to NbTi technology would automatically reduce this field too.

Spent electron beam

The proton electromagnetic field provides extra focusing to the electron beam. This increases the divergence of the electron. Figure 9.20 shows the horizontal distribution of the electrons at 10 m from the IP (entry of Q1) as computed by Guineapig [440]. The dispersion has a small effect of the beam size. Therefore it is possible to linearly scale the sigmas at 10 m to estimate both the horizontal and vertical sigmas at any other longitudinal location. The simulation used 10^5 particles. No particles are observed beyond 4.5 mm from the beam centroid at 10 m from the IP and beyond 9 mm at 20 m. A radial aperture of 10 mm has been reserved for the beam size at the incoming electron Q1 hole. This 10 mm seem to be enough to also host the spent

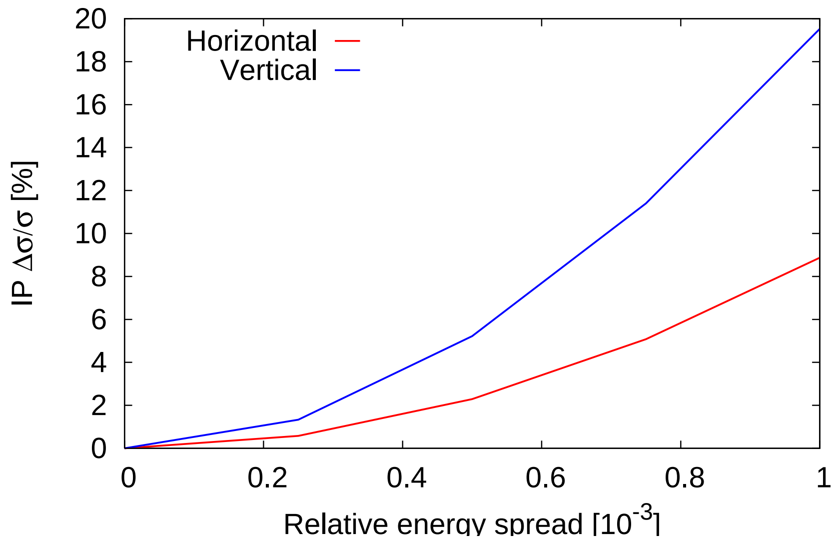

Figure 9.19: IP electron beam size versus relative energy spread of the beam.

electron beams, although it might be worth to allocate more aperture margin in the last block of Q1.

9.2.3 Modifications for γp

9.2.4 Synchrotron radiation and absorbers

Introduction

The synchrotron radiation (SR) in the interaction region has been analyzed in three ways. The SR was simulated in depth using a program made with the Geant4 (G4) toolkit. In addition a cross check of the total power and average critical energy was done in IRSYN, a Monte Carlo simulation package written by R. Appleby. [410] A final cross check has been made for the radiated power using an analytic method. These other methods confirmed the results found using G4. The G4 program uses Monte Carlo methods to create gaussian spatial and angular distributions for the electron beam. This electron beam is then guided through vacuum volumes that contain the magnetic fields for the separator dipoles. The SR is generated in these volumes using the appropriate G4 process classes. The position, direction, and energy of each photon created is written as ntuples at user defined Z values. These ntuples are then used to analyze the SR fan as it evolves in Z. The analysis was done primarily through the use of MATLAB scripts.

Before going further I will explain some conventions used for this section. I will refer to the electron beam as *the beam* and the proton beams will be referred to as either the interacting or non interacting proton beams. The beam propagates in the -Z direction and the interacting proton beam propagates in the +Z direction, I will use a right handed coordinate system where the X axis is horizontal and the Y axis is vertical. The beam centroid always remains in the Y = 0 plane. The *angle of the beam* will be used to refer to the angle between the beam centroid's

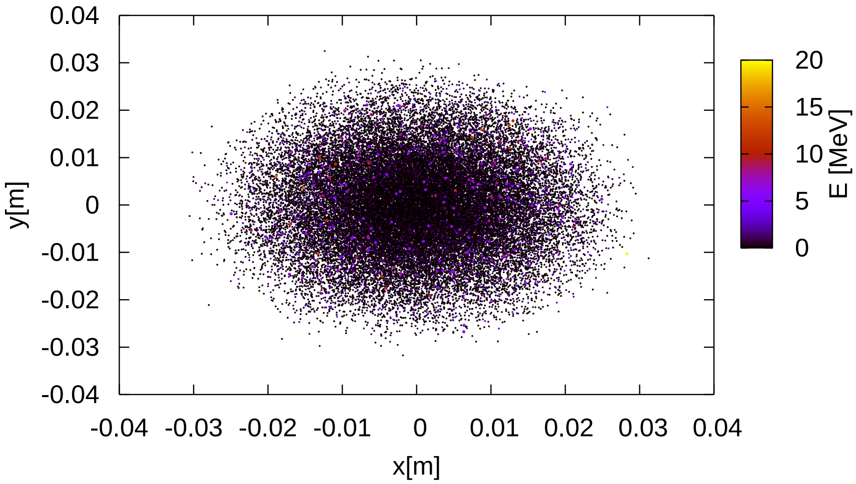

Figure 9.20: Distribution of the spent electron beam at 10 m from the IP. The Gaussian and rms sigmas are shown on the plot.

direction and the z axis, in the Y = 0 plane. This angle is set such that the beam propagates in the -X direction as it traverses Z.

The SR fans extension in the horizontal direction is driven by the angle of the beam at the entrance of the upstream separator dipole. Because the direction of emitted photons is parallel to the direction of the electron that emitted it, the angle of the beam and the distance to the absorber are both greatest at the entrance of the upstream separator dipole and therefore this defines one of the edges of the synchrotron fan on the absorber. The other edge is defined by the crossing angle. The S shaped trajectory of the beam means that the smallest angle of the beam will be reached at the IP. Therefore the photons emitted at this point will move along the Z axis due to having no crossing angle. This defines the other edge of the fan in the horizontal direction.

The SR fans extension in the vertical direction is driven by the beta function and angular spread of the beam. The beta function along with the emittance defines the r.m.s. spot size of the beam. The vertical spot size defines the Y position at which photons are emitted. On top of this the vertical angular spread defines the angle between the velocity vector of these photons and the Z axis. Both of these values produce complicated effects as they are functions of Z. These effects also affect the horizontal extension of the fan however are of second order when compared to the angle of the beam. Since the beam moves in the Y=0 plane these effects dominate the vertical extension of the beam.

The number density distribution of the fan is a complicated issue. The number density at the absorber is highest between the two interacting beams. This is due to the S shaped trajectory of the beam.

Parameters

The parameters for the Linac Ring option are listed in Table 9.5. The separation refers to the displacement between the two interacting beams at the face of the proton triplet.

Characteristic	Value
Electron Energy [GeV]	60
Electron Current [mA]	6.6
Crossing Angle [mrad]	0
Absorber Position [m]	-9
Dipole Field [T]	0.3
Separation [mm]	75
γ/s	1.37×10^{18}

Table 9.5: LR: Parameters

The energy, current, and crossing angle (θ_c) are the common values used in all LR calculations. The B value refers to the constant dipole field created throughout the two dipole magnets in the IR. The direction of this field is opposite on either side of the IP. The field is chosen such that 75 mm of separation is reached by the face of the proton triplet. This separation was chosen based on S. Russenschuck's SC quadrupole design. [411] The separation between the interacting beams can be increased by raising the constant dipole field however for a dipole magnet $P_{SR} \propto |B^2|$, [412] therefore an optimization of the design will need to be discussed. The chosen parameters give a flux of 1.37×10^{18} photons per second at Z = -9 m.

Power and Critical Energy

Table 9.6 shows the power of the SR produced in the IR along with the critical energy. This is followed by the total power produced in the IR and the critical energy. Since the G4 simulations utilize Monte Carlo, multiple runs were used to provide a standard error. This only caused fluctuations in the power since the critical energy is static for a constant field and constant energy.

Element	Power [kW]	Critical Energy [keV]
DL	24.4 +/- 0.1	718
DR	24.4 +/- 0.1	718
Total	48.8 +/- 0.1	718

Table 9.6: LR: Power and Critical Energies [Geant4]

These magnets have strong fields and therefore produce high critical energies and a substantial amount of power. Although the power is similar to that of the RR design the critical energy is much larger. This comes from the linear dependence of critical energy on magnetic field (*i.e.* $E_c \propto B$). [413] With the dipole field in the LR case being an order of magnitude larger than the dipole fields in the RR case the critical energies from the dipole magnets are also an order of magnitude larger in the LR case.

Comparison

The IRSYN cross check of the power and critical energies is shown in Table 9.7. This comparison was done for the total power and the critical energy.

	Power [kW]		Critical Energy [keV]	
	Geant4	IRSYN	Geant4	IRSYN
Total	48.8 +/- 0.1	X	718	718

Table 9.7: LR: Geant4 and IRSYN comparison

A third cross check to the Geant4 simulations was made for the power as shown in Table 9.8. This was done using an analytic method for calculating power in dipole magnets. [412]

	Power [kW]	
Element	Geant4	Analytic
DL	24.4 +/- 0.1	24.4
DR	24.4 +/- 0.1	24.4
Total/Avg	48.8 +/- 0.1	48.8

Table 9.8: LR: Geant4 and Analytic method comparison

Number Density and Envelopes

The number density of photons at different Z values is shown in Figure 9.21. Each graph displays the density of photons in the $Z = Z_o$ plane for various values of Z_o. The first three graphs give the growth of the SR fan inside the detector area. This is crucial for determining the dimensions of the beam pipe inside the detector area. Since the fan grows asymmetrically in the -Z direction an asymmetric elliptical cone shaped beam pipe will minimize these dimensions, allowing the tracking to be placed as close to the beam as possible. The horizontal extension of the fan in the LR option is larger than in the RR case. This is due to the large angle of the beam at the entrance of the upstream separator dipole. As mentioned in the introduction this angle defines the fans extension, and in the LR case this angle is the largest, hence the largest fan. The number density of this fan appears as expected. There exists the highest density between the two beams at the absorber.

In Figure 9.21 the distribution was given at various Z values however a continuous envelope distribution is also important to see everything at once. This can be seen in Figure 9.22, where the beam and fan envelopes are shown in the Y = 0 plane. This makes it clear that the fan is antisymmetric which comes from the S shape of the electron beam as previously mentioned.

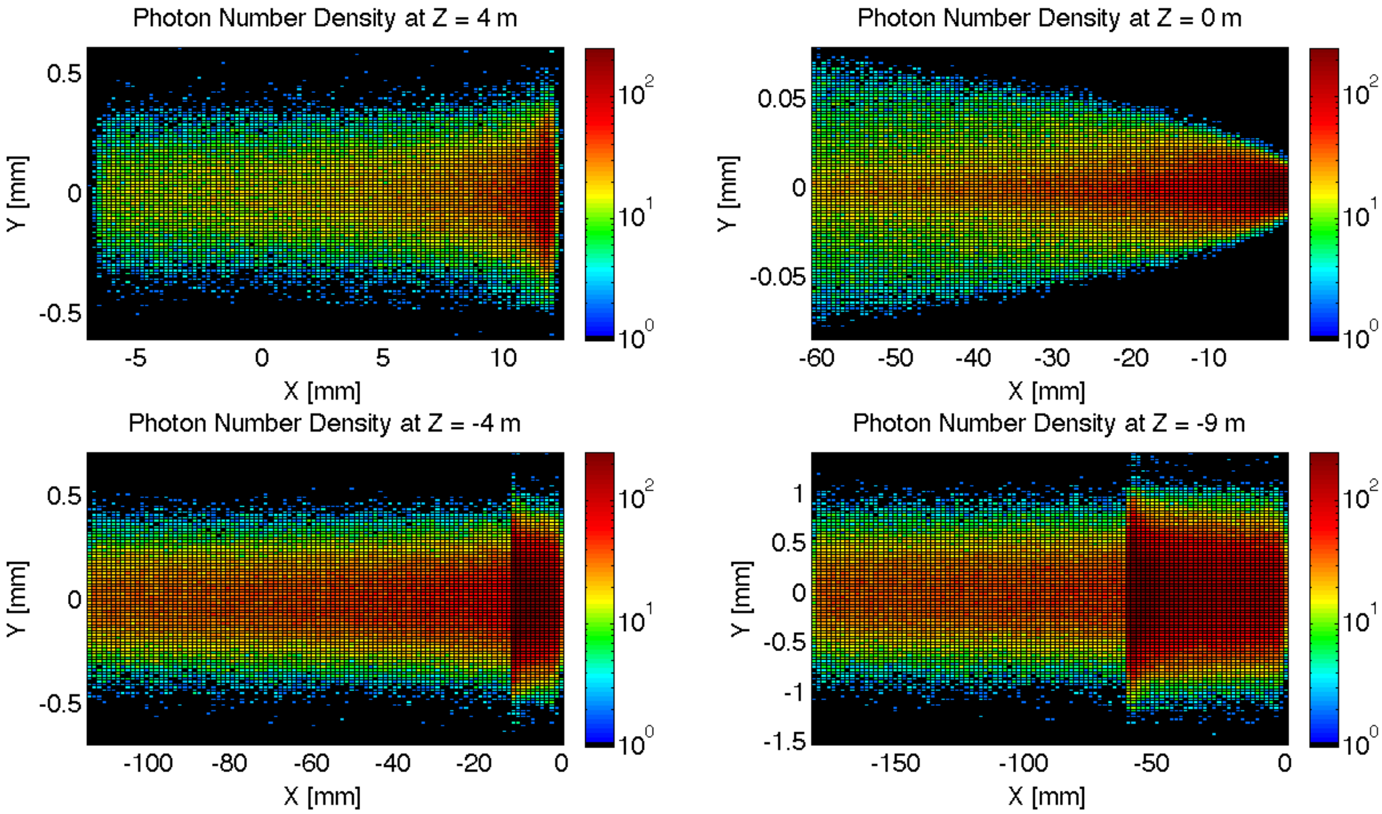

Figure 9.21: LR: Number Density Growth in Z

Absorber

The Photon distribution on the absorber surface is crucial. The distribution decides how the absorber must be shaped. The shape of the absorber in addition to the distribution on the surface then decides how much SR is backscattered into the detector region. In HERA backscattered SR was a significant source of background that required careful attention. [414] Looking at Figure 9.23 it is shown that for the LR option 35.15 kW of power from the SR light will fall on the face of the absorber which is 73% of the total power. This gives a general idea of the amount of power that will be absorbed. However, backscattering and IR photons will lower the percent that is actually absorbed.

Proton Triplet: The super conducting final focusing triplet for the protons needs to be protected from radiation by the absorber. Some of the radiation produced upstream of the absorber however will either pass through the absorber or pass through the apertures for the two interacting beams. This is most concerning for the interacting proton beam aperture which will have the superconducting coils. A rough upper bound for the amount of power the coils

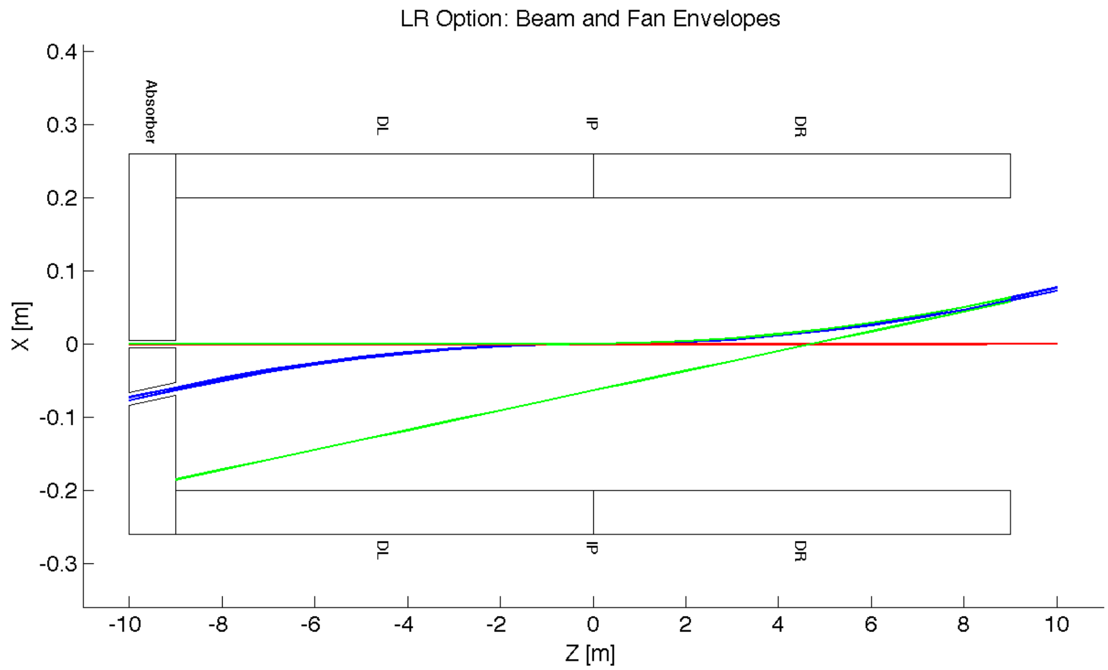

Figure 9.22: LR: Beam Envelopes in Z

can absorb before quenching is 100 W. [415] There is approximately 2 kW entering into the interacting proton beam aperture as is shown in Figure 9.23. This doesnt mean that all this power will hit the coils but simulations need to be made to determine how much of this will hit the coils. The amount of power that will pass through the absorber (0.25 W) can be disregarded as it is not enough to cause any significant effects. The main source of power moving downstream of the absorber will be the photons passing through the beams aperture. This was approximately 11 kW as can be seen from Figure 9.23. Most of this radiation can be absorbed in a secondary absorber placed after the first downstream proton quadrupole. Overall protecting the proton triplet is important and although the absorber will minimize the radiation continuing downstream this needs to be studied in depth.

Beamstrahlung The beamstrahlung photons travel parallel to the proton beam until the entrance of D1 without impacting the triplets. Figure 9.24 shows the transverse and energy distributions of the beamstralung photons at the entry of D1 as computed with Guineapig [440]. The maximum photon energy is about 20 MeV the average photon energy is 0.4 MeV. The beamstrahlung power is 980 W. D1 has to be designed to properly dispose the neutral debris from the IP. Splitting D1 into two parts could allow an escape line for the neutral particles.

Backscattering Another G4 program was written to simulate the backscattering of photons into the detector region. The ntuple with the photon information written at the absorber surface is used as the input for this program. An absorber geometry made of copper is de-

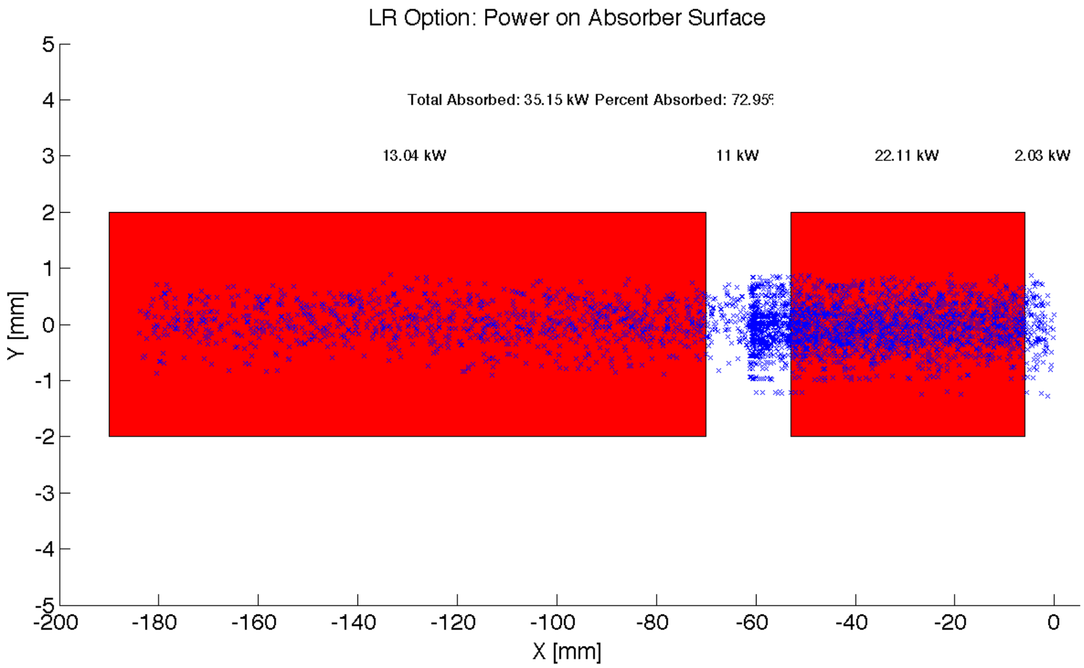

Figure 9.23: LR: Photon distribution on Absorber Surface

scribed, and general physics processes are set up. A detector volume is then described and set to record the information of all the photons which enter in an ntuple. The first step in minimizing the backscattering was to optimize the absorber shape. Although the simulation didnt include a beampipe the backscattering for different absorber geometries was compared against one another to find a minimum. The most basic shape was a block of copper that had cylinders removed for the interacting beams. This was used as a benchmark to see the maximum possible backscattering. In HERA a wedge shape was used for heat dissipation and minimizing backscattering. [414] The profile of this geometry in the YZ plane is shown in Figure 9.25. It was found that this is the optimum shape for the absorber. The reason for this is that a backscattered electron would have to have to have its velocity vector be almost parallel to the wedge surface to escape from the wedge and therefore it works as a trap. One can be seen from Table 9.9 utilizing the wedge shaped absorber decreased the backscattered power by a factor of 4. The energy distribution for the backscattered photons can be seen in Figure 9.26.

After the absorber was optimized it was possible to set up a beam pipe geometry. An asymmetric elliptical cone beam pipe geometry made of beryllium was used since it would minimize the necessary size of the beam pipe as previously mentioned. The next step was to place the lead shield and masks inside this beam pipe. To determine placement a simulation was run with just the beam pipe. Then it was recorded where each backscattered photon would hit the beam pipe in Z. A histogram of this data was made as shown in Figure 9.27. This determined that the shield should be placed in the Z region ranging from -8 m until the absorber (-9 m). The masks were then placed at -8.9 m and -8.3 m. This decreased the backscattered

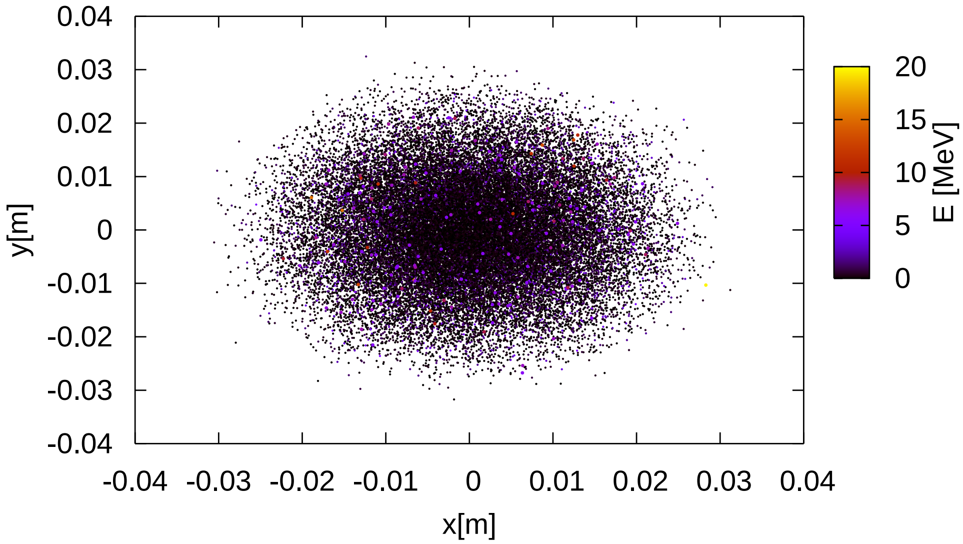

Figure 9.24: Beamstrahlung photons at the entrance of D1.

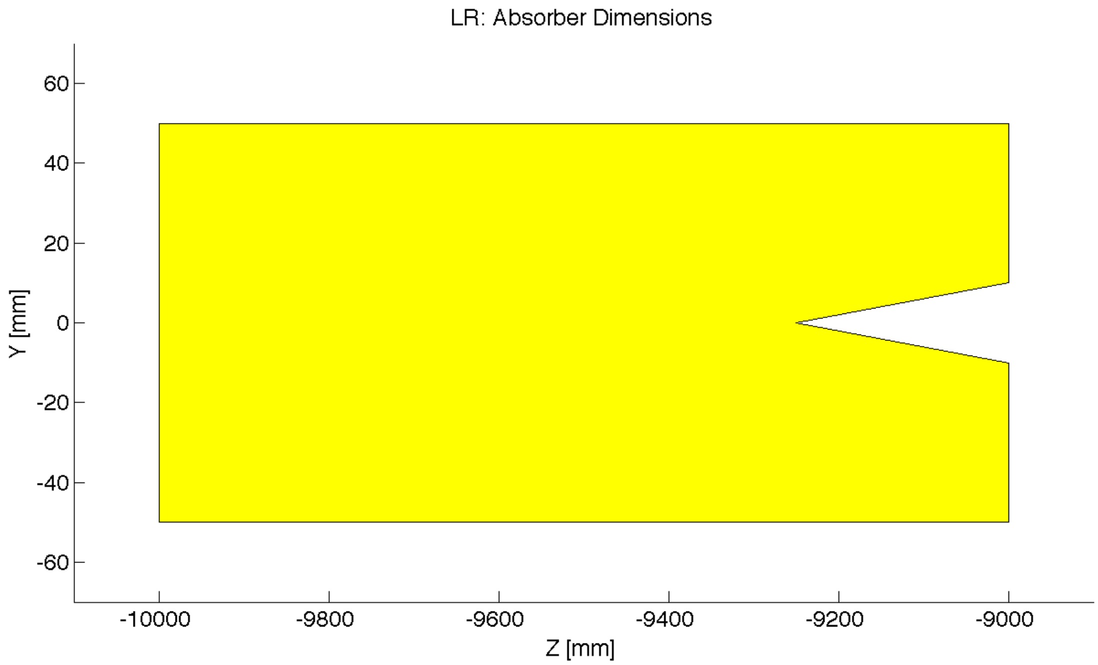

Figure 9.25: LR: Absorber Dimensions

power by a factor of 40 as can be seen from Table 9.9. Overall there is still more optimization that can occur with this placement.

Absorber Type	Power [W]
Flat	645.9
Wedge	159.1
Wedge & Mask/Shield	4.3

Table 9.9: LR: Backscattering/Mask

Cross sections of the beampipe in the Y = 0 and X = 0 planes with the shields and masks included can be seen in Figure 9.28.

9.3 Linac Lattice and Impedance

9.3.1 Overall Layout

The proposed layout of the recirculating linear accelerator complex (RLA) is illustrated schematically in Fig. 9.29. It consists of the following components:

- A 0.5 GeV injector with an injection chicane.

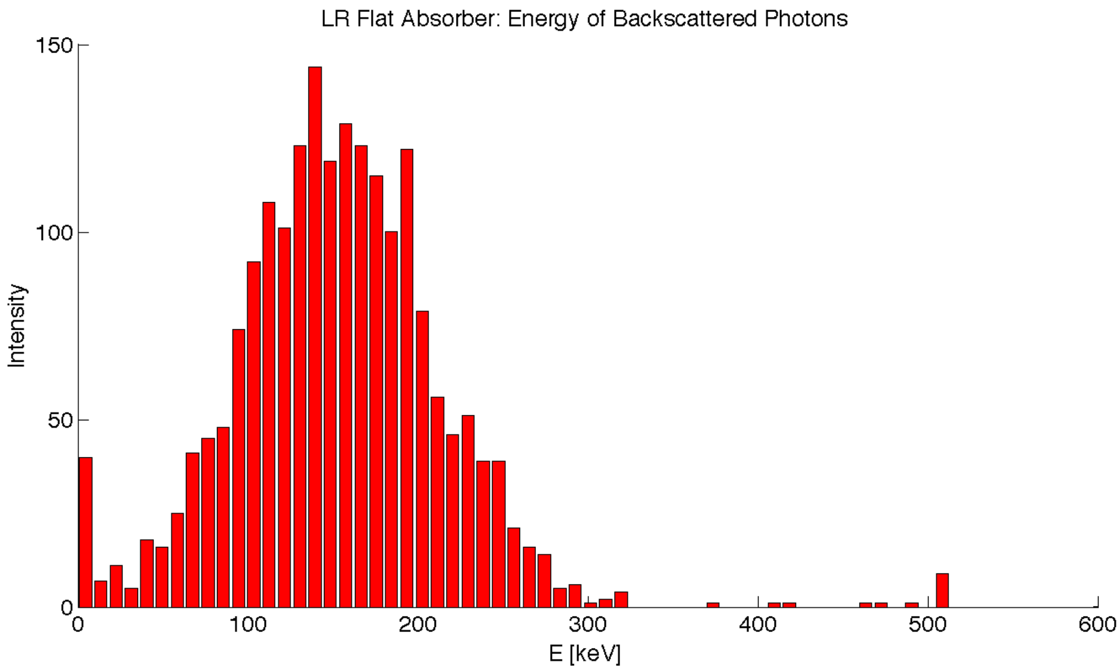

Figure 9.26: LR: Backscattered Energy Distribution

- A pair of 721.44MHz SCRF linacs. Each linac is one kilometer long with an energy gain 10GeV per pass.
- Six 180° arcs. Each arc has a radius of one kilometer.
- For each arc one re-accelerating station that compensates the synchrotron radiation emitted in this arc.
- A switching station at the beginning and end of each linac to combine the beams from different arcs and to distribute them over different arcs.
- An extraction dump at 0.5 GeV.

After injection, the beam makes three passes through the linacs before it collides with the LHC beam. The beam will then perform three additional turns in which the beam energy is almost completely extracted. The size of the complex is chosen such that each turn has the same length and that three turns correspond to the LHC circumference. This choice is motivated by the following considerations:

- To avoid the build-up of a significant ion density in the accelerator complex, clearing gaps may be required in the beam.
- The longitudinal position of these gaps must coincide for each of the six turns that a beam performs. This requires that the turns have the same length.

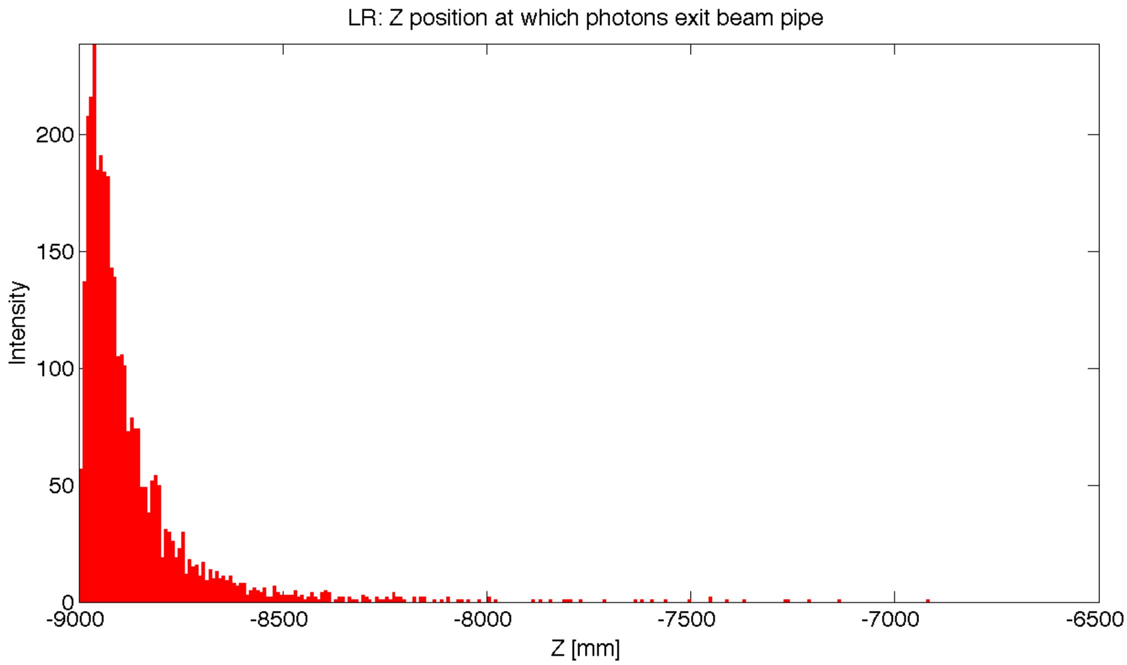

Figure 9.27: LR: Backscattered Photons Exiting the Beam Pipe

- Due to the gaps some LHC bunches will collide with an electron bunch but some will not. It is advantageous to have each LHC bunch either always collide with an electron bunch or to never collide. The choice of length for one turn in the RLA allows to achieve this.

Some key beam parameters are given in table 9.10.

9.3.2 Linac Layout and Lattice

The key element of the transverse beam dynamics in a multi-pass recirculating linac is an appropriate choice of multi-pass linac optics. The focusing strength of the quadrupoles along the linac needs to be set such that one can transport the beam at each pass. Obviously, one would like to optimize the focusing profile to accommodate a large number of passes through the RLA. In addition, the requirement of energy recovery puts a constraint on the exit/entrance

Parameter	Symbol	Value
Particles per bunch	N	$2 \cdot 10^9$
Initial normalised transverse emittance	ϵ_x, ϵ_y	30μm
Normalised transverse emittance at IP	ϵ_x, ϵ_y	50μm
Bunch length	σ_z	600μm

Table 9.10: Key beam parameters.

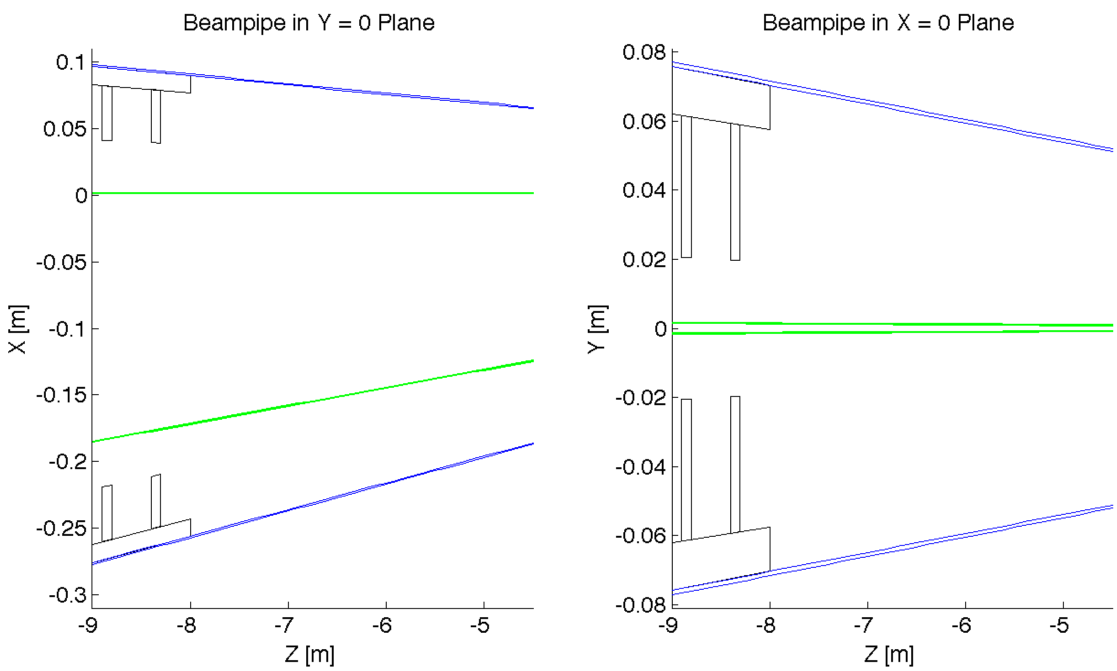

Figure 9.28: LR: Beampipe Cross Sections

Twiss functions for the two linacs. As a baseline we have chosen a FODO lattice with a phase advance of 130° for the beam that passes with the lowest energy and a quadrupole spacing of 28m [**?**]. Alternative choices are possible. An example is an optics that avoids any quadrupole in the linacs [**?**].

Linac Module Layout

The linac consists of a series of units, each consisting of two cryomodules and one quadrupole pack. See Fig. 9.30 for the layout. Each cryomodule is 12.8m and contains eight 1m-long accelerating cavities. The interconnect between two adjacent cryomodules is 0.8m long. The quadrupole pack is 1.6m long, including the interconnects to the adjacent cryomodules. The whole unit is 28m long.

Each quadrupole pack contains a quadrupole, a beam position monitor and a vertical and horizontal dipole corrector, see section 2.9.

Linac Optics

The linac consists of 36 units with a total length of 1008m. In the first linac, the strength of the quadrupoles has been chosen to provide a phase advance per cell of 130° for the beam in its first turn. In the second linac, the strength has been set to provide a phase advance of 130° for the last turn of the beam. The initial Twiss parameters of the beam and the return arcs are optimised to minimise the beta-functions of the beams in the following passages. The critrium

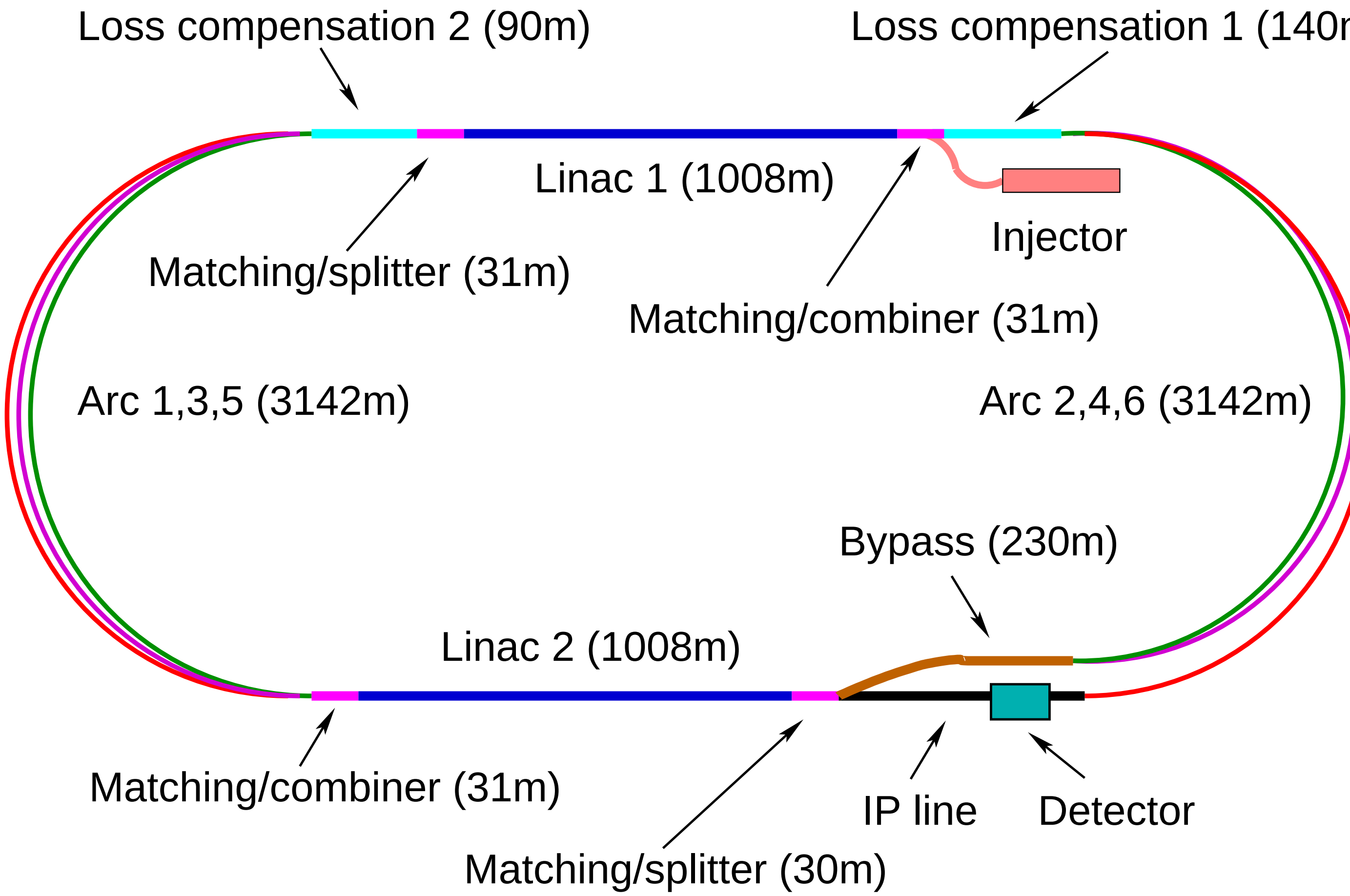

Figure 9.29: The schematic layout of the recirculating linear accelerator complex.

Figure 9.30: The schematic layout of a linac unit.

used has been to minimise the integral

$$\int_0^L \frac{\beta}{E} ds \tag{9.6}$$

Single bunch transverse wakefield effects and multi-bunch effects between bunches that have been injected shortly after each other are proportional to this integral [**?**]. The final solution is shown in Fig. 9.31. A significant beta-beating can be observed due to the weak focusing for the higher energy beams.

Return Arc Optics

At the ends of each linac the beams need to be directed into the appropriate energy-dependent arcs for recirculation. Each bunch will pass each arc twice, once when it is accelerated before the collision and once when it is decelerated after the collision. The only exception is the arc at highest energy that is passed only once. For practical reasons, horizontal rather than vertical beam separation was chosen. Rather than suppressing the horizontal dispersion created by the spreader, the horizontal dispersion can been smoothly matched to that of the arc, which results in a very compact, single dipole, spreader/recombiner system.

The initial choice of large arc radius (1 km) was dictated by limiting energy loss due to synchrotron radiation at top energy (60.5 GeV) to less than 1%. However other adverse effects of synchrotron radiation on beam phase-space such as cumulative emittance and momentum growth due to quantum excitations are of paramount importance for a high luminosity collider that requires normalized emittance of 50 mm mrad.

Three different arc designs have been developed [?]. In the design for the lowest energy turns, the beta-functions are kept small in order to limit the required vacuum chamber size and consequently the magnet aperture. At the higest energy, the lattice is optimised to keep the emittance growth limited, while the beta-functions are allowed to be larger. A cell of the lowest and one of the highest energy arc is shown in Fig. 9.32 All turns have a bending radius of 764m. The beam pipe diameter is 25mm, which corresponds to more than 12σ aperture.

An interesting alternative optics, which pushes towards a smaller beam pipe, has also been developed [?].

Synchrotron Radiation in Return Arcs

Synchrotron radiation in the arcs leads to a significant beam energy loss. This loss is compensated by the small linacs that are incorporated before or after each arc when the beams are already or still separated according to their energy, see Fig. 9.29. The energy loss at the 60GeV turn-round can be compensated by a linac with an RF frequency of 721.44MHz. The compensation at the other arcs is performed with an RF frequency of 1442.88MHz. In this way the bunches that are on their way to the collision point and the ones that already collided can both be accelerated. This ensures that the energy of these bunches are the same on the way to and from the interaction point, which simplifies the optics design. If the energy loss were not compensated the beams would have a different energy at each turn, so that the number of return arcs would need to be doubled.

The synchrotron radation is also generating an energy spread of the beam. In Tab. 9.11 the relative energy spread is shown as a function of the arc number that the beam has seen. At the interaction point, the synchrotron radiation induced RMS energy spread is only 2×10^{-4},

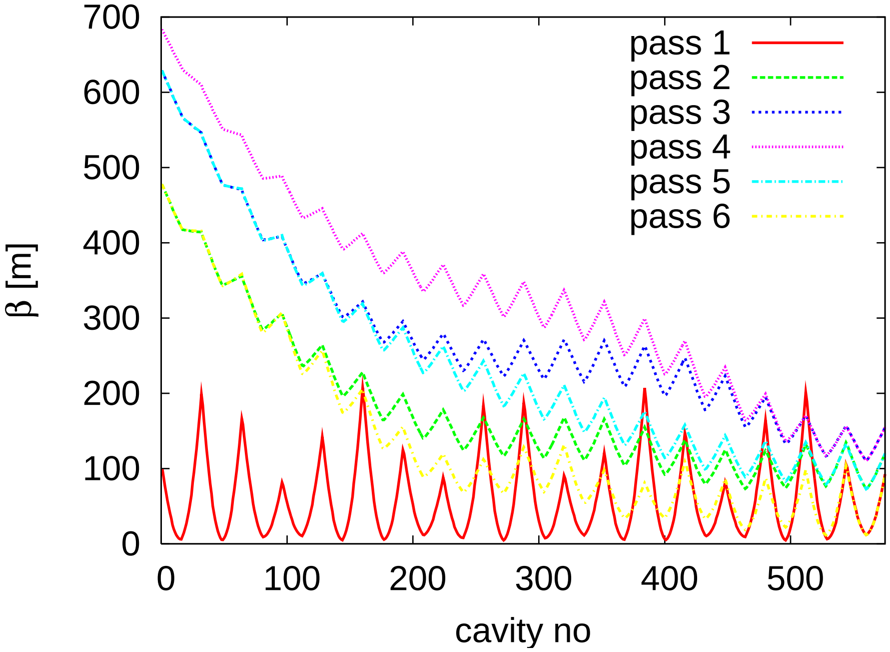

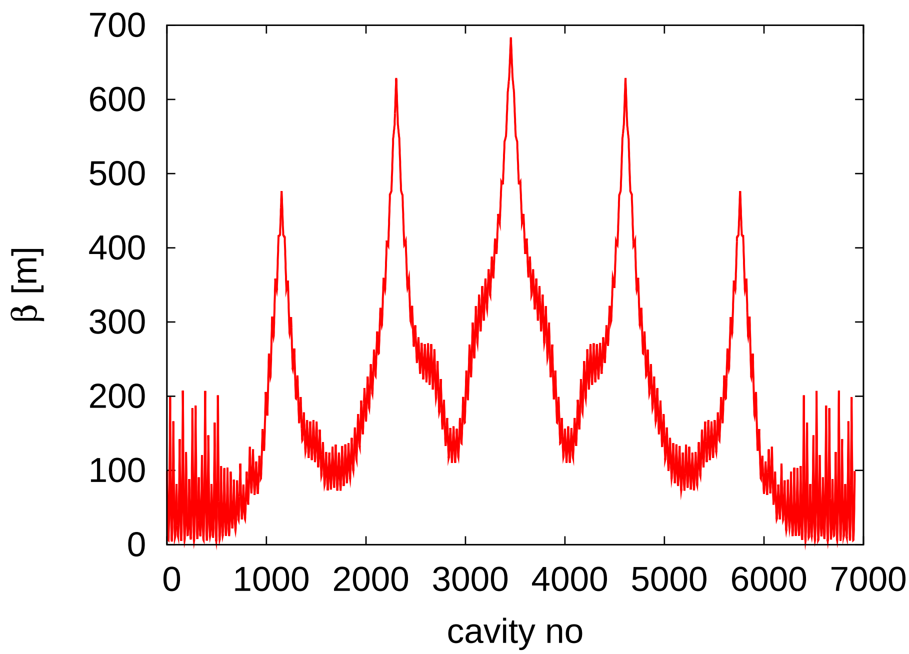

Figure 9.31: Beta-functions in the first linac. On the top, the beta-functions of the six different beam passages in the first linac are shown. On the bottom, the beta-function as seen by the beam during his stay in the linacs are shown.

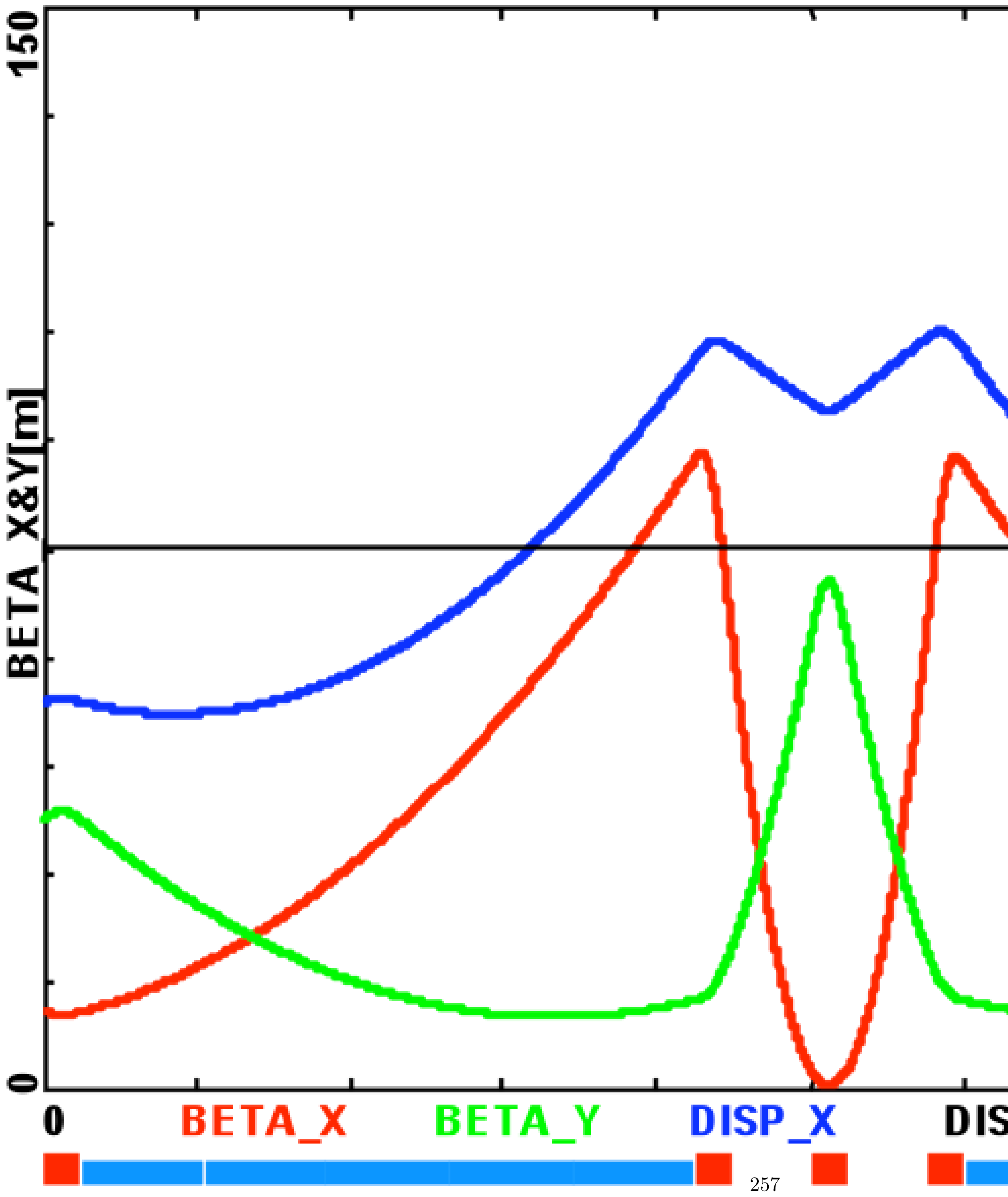

150
BETA_X&Y[m]
0
0
BETA_X
BETA_Y
DISP_X

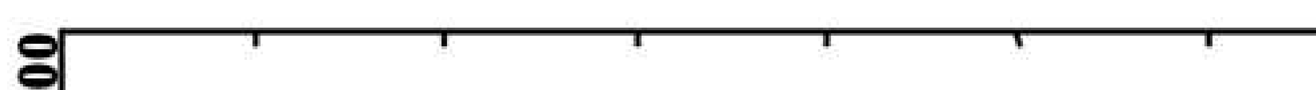

turn no	E [GeV]	ΔE [MeV]	σ_E/E [%]
1	10.5	0.7	0.00036
2	20.5	10.2	0.0019
3	30.5	49.8	0.0053
4	40.5	155	0.011
5	50.5	375	0.020
6	60.5	771	0.033
7	50.5	375	0.044
8	40.5	155	0.056
9	30.5	49.8	0.074
10	20.5	10.2	0.11
11	10.5	0.7	0.216
dump	0.5	0.0	4.53

Table 9.11: Energy loss due to synchrotron radiation in the arcs as a function of the arc number. The integrated energy spread induced by synchrotron radiation is also shown.

which adds to the energy spread of the wakefields. At the final arc the energy spread reaches about 0.22%, while at the beam dump it grows to a full 4.5%.

The growth of the normalised emittance is given by

$$\Delta\epsilon = \frac{55}{48\sqrt{3}}\frac{\hbar c}{mc^2} r_e \gamma^6 I_5 \tag{9.7}$$

Here, r_e is the classical electron radius, and I_5 is given by

$$I_5 = \int_0^L \frac{H}{|\rho|^3} ds = \frac{\langle H\rangle\theta}{\rho^2} \qquad H = \gamma D^2 + 2\alpha D D' + \beta D'^2 \tag{9.8}$$

For a return arc with a total bend angle $\theta = 180°$ one finds

$$\Delta\epsilon = \frac{55}{48\sqrt{3}}\frac{\hbar c}{mc^2} r_e \gamma^6 \pi \frac{\langle H\rangle\theta}{\rho^2} \tag{9.9}$$

The synchrotron radiation induced emittance growth is shown in table 9.12. Before the interaction point a total growth of about 7μm is accumulated. The final value is 26μm. While this growth is significant compared to the target emittance of 50μm at the collision point, it seems acceptable.

Matching Sections and Energy Compensation

Currently we do not have a design of the matching sections. However, we expect these sections to be straightforward. For the case of the linac optics without quadrupoles and the alternative return arc lattice design matching sections designs exist and exhibit no issues [?]. Also the sections that compensate the energy loss in the arcs have not been designed. But this again should be straightforward.

turn no	E [GeV]	$\Delta\epsilon_{arc}$ [μm]	$\Delta\epsilon_t$ [μm]
1	10.5	0.0025	0.0025
2	20.5	0.140	0.143
3	30.5	0.380	0.522
4	40.5	2.082	2.604
5	50.5	4.268	6.872
6	60.5	12.618	19.490
5	50.5	4.268	23.758
4	40.5	2.082	25.840
3	30.5	0.380	26.220
2	20.5	0.140	26.360
1	10.5	0.0025	26.362

Table 9.12: The emittance growth due to synchrotron radiation in the arcs.

9.3.3 Beam Break-Up

Single-Bunch Wakefield Effect

In order to evaluate the single bunch wakefield effects we used PLACET [**?**]. The full linac lattice has been implemented for all turns but the arcs have each been replaced by a simple transfer matrix, since the matching sections have not been available.

Single bunch wakefields were not available for the SPL cavities. We therefore used the wakefields in the ILC/TESLA cavities [**?**]. In order to adjust the wakefields to the lower frequency and larger iris radius (70mm vs. 39mm for the central irises) we used the following scaling

$$W_\perp(s) \approx \frac{1}{(70/39)^3} W_{\perp,ILC}(s/(70/39)) \qquad W_L(s) \approx \frac{1}{(70/39)^2} W_{L,ILC}(s/(70/39)) \tag{9.10}$$

First, the RMS energy spread along the linacs is determined. An initial uncorrelated RMS energy spread of 0.1% is assumed. Three different bunch lengths were studied, i.e. 300μm, 600μm and 900μm. This longest value yields the smallest final energy spread. The energy spread along during the beam life-time can be seen in Fig. 9.33. The wakefield induced energy spread is between 1×10^{-4} and 2×10^{-4} at the interaction point, 1–2×10^{-3} at the final arc and 3.5–4.5% at the beam dump.

Second, the single bunch beam-break-up is studied by tracking a bunch with an initial offset of $\Delta x = \sigma_x$. The resulting emittance growth of the bunch is very small, see Fig. 9.34.

Multi-Bunch Transverse Wakefield Effects

For a single pass through a linac the multi-bunch effects can easily be estimated analytically [?]. Another approach exists in case of two passes through one cavity [**?**]. It is less straightforward to find an analytic solution for multiple turns in linacs with wakefields that vary from one cavity

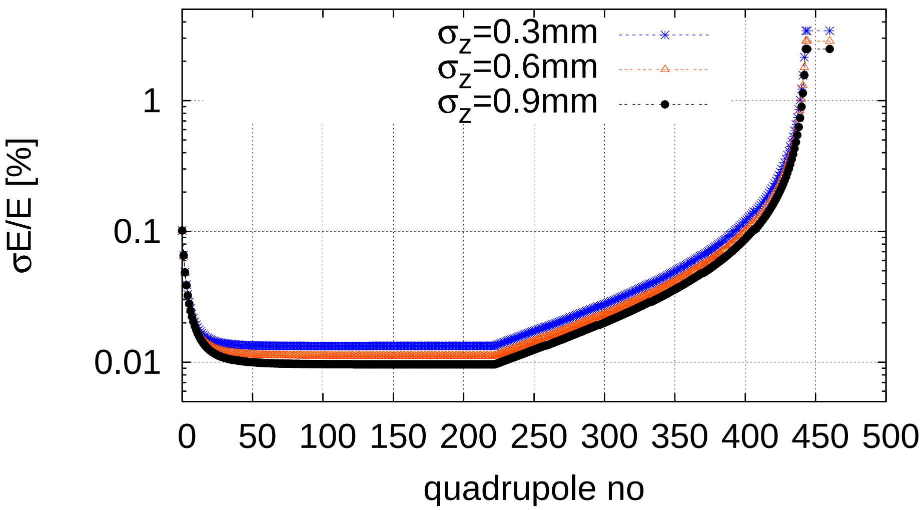

Figure 9.33: The RMS energy spread due to single bunch wakefields along the linacs. The bunch has been cut longitudinally at $\pm 3\sigma_z$ and at $\pm 3\sigma_E$ in the initial uncorrelated energy spread.

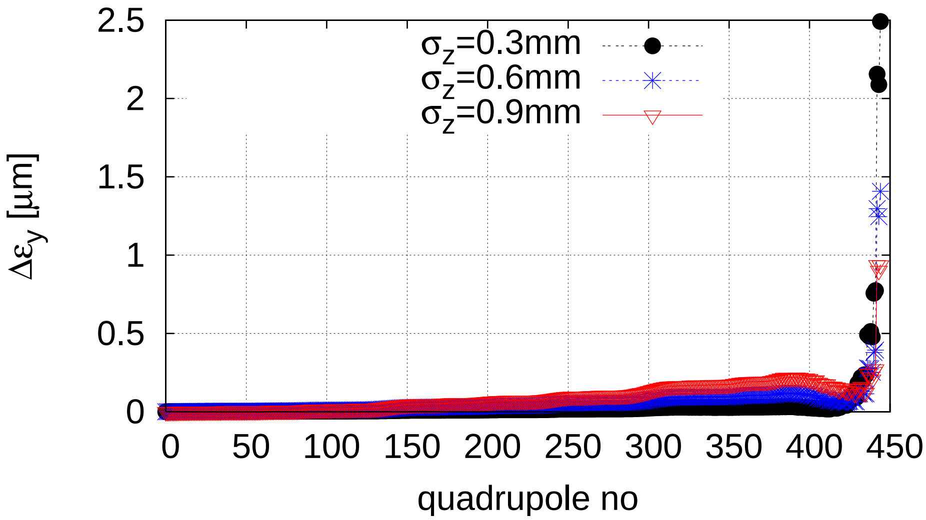

Figure 9.34: The single-bunch emittance growth along the LHeC linacs for a bunch with an initial offset of $\Delta x = \sigma_x$. The arcs have been represented by a simple transfer matrix.

f[GHz]	k[V/pCm^2]	f[GHz]	k[V/pCm^2]
0.9151	9.323	1.675	4.160
0.9398	19.095	2.101	1.447
0.9664	8.201	2.220	1.427
1.003	5.799	2.267	1.377
1.014	13.426	2.331	2.212
1.020	4.659	2.338	11.918
1.378	1.111	2.345	5.621
1.393	20.346	2.526	1.886
1.408	1.477	2.592	1.045
1.409	23.274	2.592	1.069
1.607	8.186	2.693	1.256
1.666	1.393	2.696	1.347
1.670	1.261	2.838	4.350

Table 9.13: The considered dipole modes of the SPL cavity design.

to the next. In this case the also phase advance from one passage through a cavity to the next passage depends on the position of the cavity within the linac.

We therefore have developed a code to simulate the multi-bunch effect in the case of recirculation and energy recovery [**?**]. It assumes point-like bunches and takes a number of dipole wake field modes into account. A cavity-to-cavity frequency spread of the wakefield modes can also be modeled. The arcs are replaced with simple transfer matrices. In the simulation, we offset a single bunch of a long train by one unit and determine the final position in phase space of all other bunches.

We evaluated the beam stability using the wakefield modes that have been calculated for the SPL cavity design [**?**]. The level of the Q-values of the transverse modes is not yet known. We assume $Q = 10^5$ for all modes, which is comparable to the larger of the Q-values found in the TESLA cavities. A random variation of the transverse mode frequencies of 0.1% has been assumed, which corresponds to the target for ILC [?]. The results in Fig. 9.35 indicate that the beam remains stable in our baseline design. Even in the alternative lattice with no focusing in the linacs, the beam would remain stable but with significantly less margin.

We also performed simulations, assuming that either only damping or detuning were present, see Fig. 9.36. The beam is unstable in both cases. Based on our results we conclude

- One has to ensure that transverse higher order cavity modes are detuned from one cavity to the next. While this detuning can naturally occur due to production tolerances, one has to find a method to ensure its presence. This problem exists similarly for the ILC.

- Damping of the transverse modes is required.

Further studies can give more precise limits on the maximum required Q and minimum mode detuning.

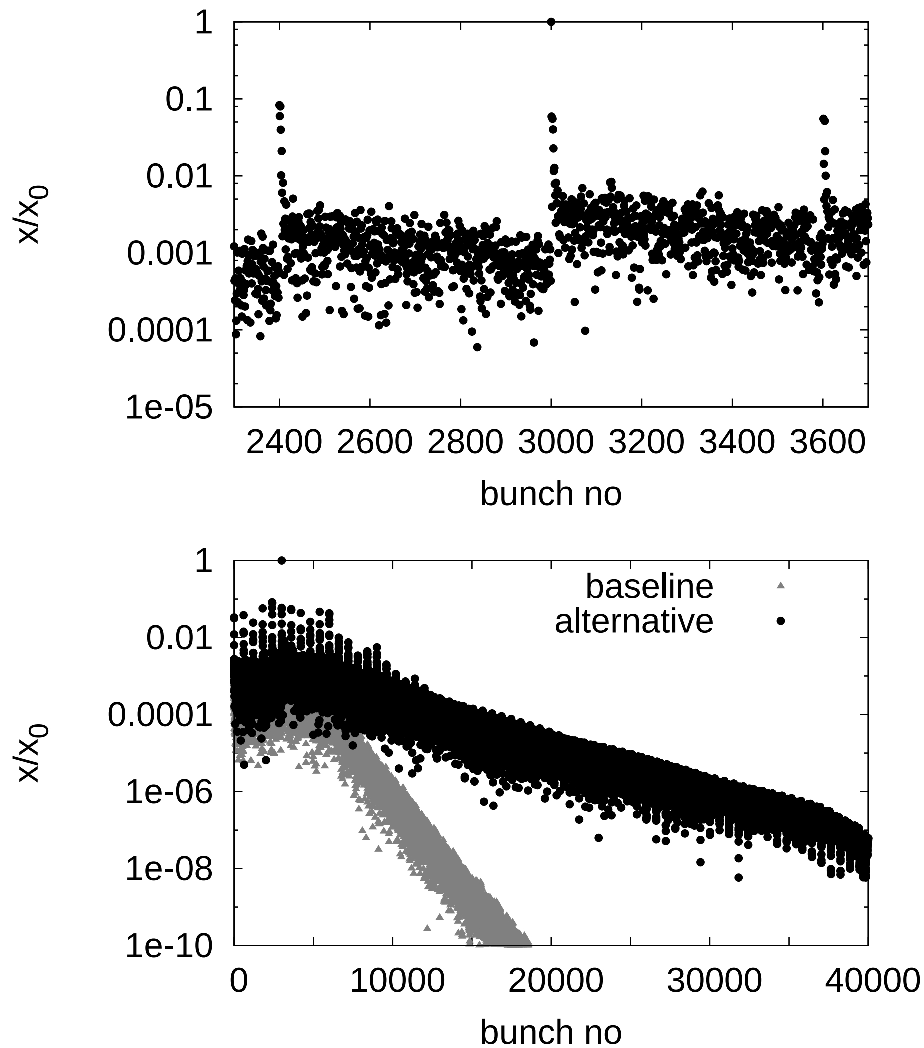

Figure 9.35: Multi-bunch beam break-up assuming the SPL cavity wakefields. One bunch has been offset at the beginning of the machine and the normalised amplitudes of the bunch oscillations are shown along the train at the end of the last turn. The upper plot shows a small number of bunches before and after the one that has been offset (i.e. bunch 3000). The lower plot shows the amplitudes along the full simulated train for the baseline lattice and the alternative design with no quadrupole focusing. One can see the fast decay of the amplitudes.

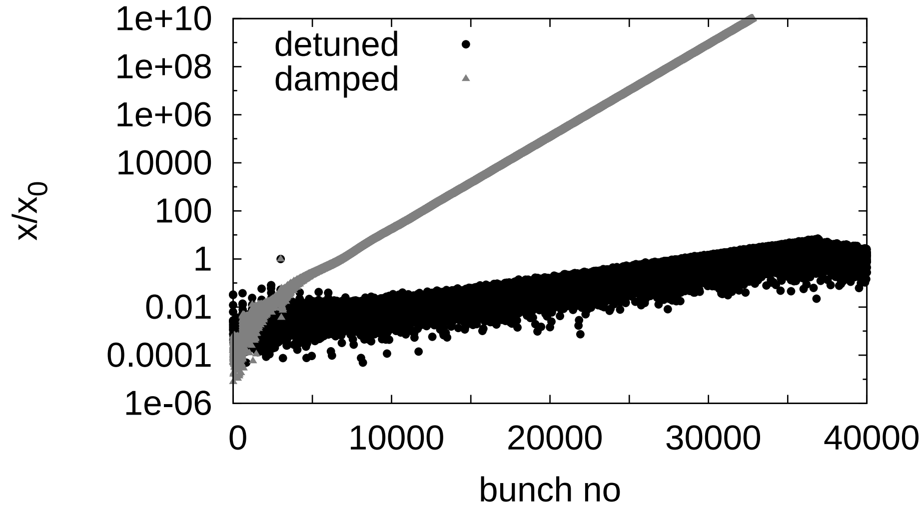

Figure 9.36: Multi-bunch beam break-up for the SPL cavities. In one case only damping, in the other case only cavity-to-cavity mode detuning is present.

Fast Beam-Ion Instability

Collision of beam particles with the residual gas in the beam pipe will lead to the production of positive ions. These ions can be trapped in the beam. There presence modifies the betatron function of the beam since the ions focus the beam. They can also lead to beam break-up, since bunches with an offset will induce a coherent motion in the ions. This can in turn lead to a kick of the ions on following bunches.

Trapping Condition in the beam pulse In order to estimate whether ions are trapped or not, one can replace each beam with a thin focusing lens, with the strength determined by the charge and transverse dimension of the beam. In this case the force is assumed to be linear with the ion offset, which is a good approximation for small offsets.

The coherent frequency f_i of the ions in the field of a beam of with bunches of similar size is given by [**?**]:

$$f_i = \frac{c}{\pi}\sqrt{\frac{Q_i N r_e \frac{m_e}{A m_p}}{3\sigma_y(\sigma_x+\sigma_y)\Delta L}} \tag{9.11}$$

Here, N is the number of electrons per bunch, ΔL the bunch spacing, r_e the classical electron radius, m_e the electron mass, Q_i the charge of the ions in units of e and A is their mass number and m_p the proton mass. The beam transverse beam size is given by σ_x and σ_y. The ions will be trapped in the beam if

$$f_i \leq f_{limit} = \frac{c}{4\Delta L} \tag{9.12}$$

In the following we will use $\Delta L \approx 2.5$m, i.e. assume that the bunches from the different turns are almost evenly spaced longitudinally.

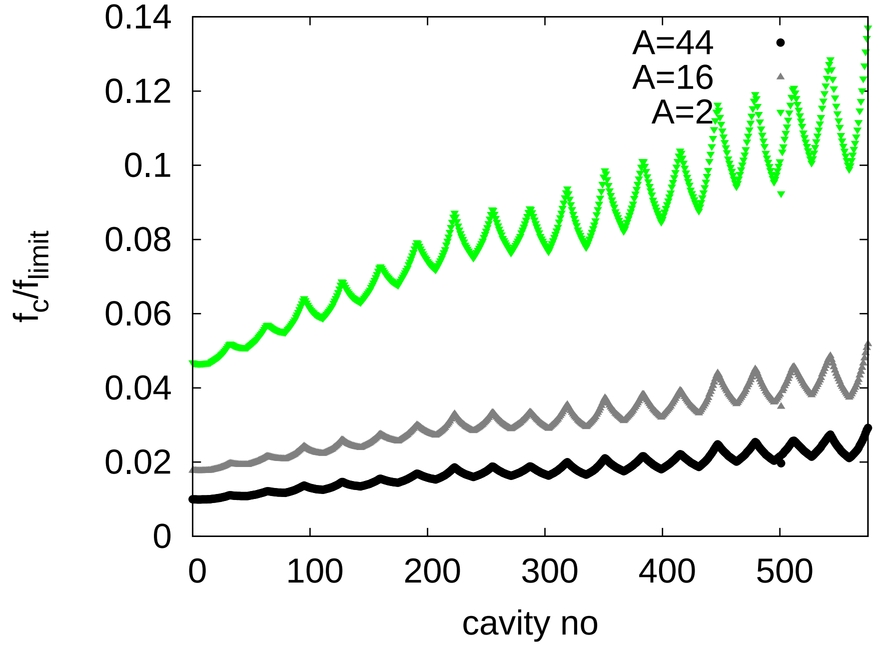

Figure 9.37: The oscillation frequency f_c of ions of different mass number A in the linacs using the average focusing strength of the bunches at different energy. The frequency is normalised to the limit frequency f_{limit} above which the ions would not be trapped any more.

In the linacs, the transverse size of the beam changes from one passage to the next while in each of the return arcs the beams have (approximately) the same size at both passages. But the variation from one turn to the next is not huge, so we use the average focusing strength of the six turns. The calculation shows that ions will be trapped for a continuous beam in the linacs. Since we are far from the limit of the trapping condition, the simplification in our model should not matter. As can be seen in Fig. 9.37 CO_2^+ ions are trapped all along the linacs. Even hydrogen ions H_2^+ would be trapped everywhere. If one places the bunches from the six turns very close to each other longitudinally, the limit freqeuncy f_{limit} is reduced. However, the ratio f_c/f_{limit} is not increased by more than a factor 6, which is not fully sufficient to remove the H_2^+.

Impact and Mitigation of Ion Effects Without any methods to remove ions, a continous beam would collect ions until they neutralise the beam current. This will render the beam unstable. Hence one needs to find methods to remove the ions. We will first quickly describe the mitigation techniques and then give a rough estimate of the expected ion effect.

A number of techniques can be used to reduce the fast beam-ion instability:

- An excellent vacuum quality will slow down the build-up of a significant ion density.
- Clearing gaps can be incorporated in the electron beam. During these gaps the ions can drift away from the beam orbit.
- Clearing electrodes can be used to extract the ions. They would apply a bias voltage that lets the ions slowly drift out of the beam.

Clearing Gaps In order to provide the gap for ion cleaning, the beam has to consist at injection of short trains of bunches with duration τ_{beam} separated by gaps τ_{gap}. If each turn of the beam in the machine takes τ_{cycle}, the beam parameters have to be adjusted such that $n(\tau_{beam} + \tau_{gap}) = \tau_{cycle}$. In this case the gaps of the different turns fall into the same location of the machine. This scheme will avoid beam loading during the gap and ensure that the gaps a fully empty. By chosing the time for one round trip in the electron machine to be an integer fraction of the LHC roundtrip time $\tau_{LHC} = m\tau_{cycle}$, one ensures that each bunch in the LHC will either always collide with an electron bunch or never. We chose to use $\tau_{cycle} = 1/3\tau_{LHC}$ and to use a single gap with $\tau_{gap} = 1/3\tau_{cycle} \approx 10\ \mu$s.

In order to evaluate the impact of a clearing gap in the beam, we model the beam as a thick focusing lens and the gap as a drift. The treatment follows [?], except that we use a thick lens approach and correct a factor two in the force. The focusing strength of the lens can be calculated as

$$k = \frac{2Nr_e m_e}{A_{ion} m_p \sigma_y(\sigma_x + \sigma_y)\Delta L} \tag{9.13}$$

The ions will not be collected if the following equation is fulfilled

$$\left|2\cos(\sqrt{k}(L_{erl} - L_g)) - \sqrt{k}L_g \sin(\sqrt{k}(L_{erl} - L_g))\right| \geq 2 \tag{9.14}$$

Since the beam size will vary as a function of the number of turns that the beam has performed, we replace the above defined k with the average value over the six turns using the average bunch

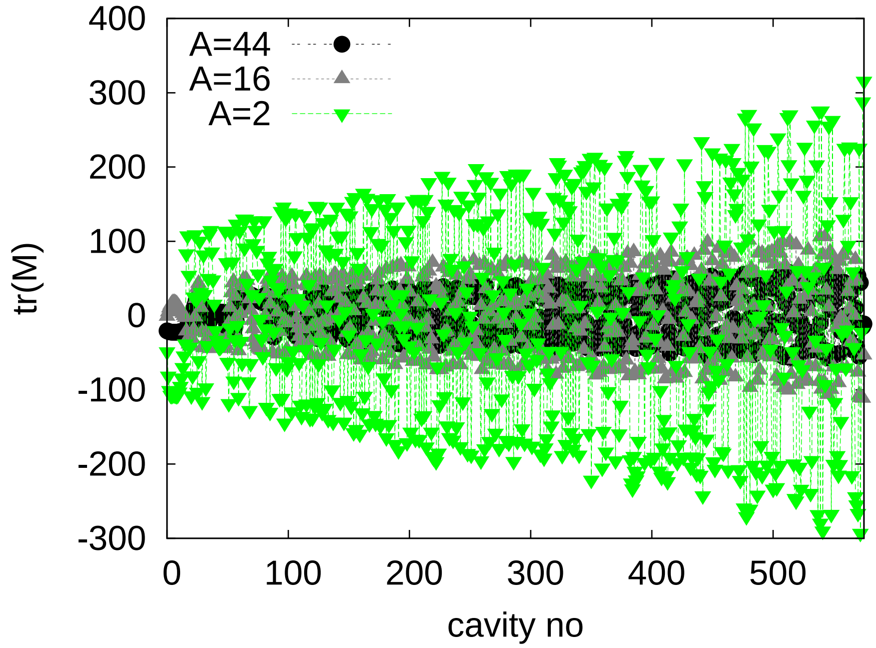

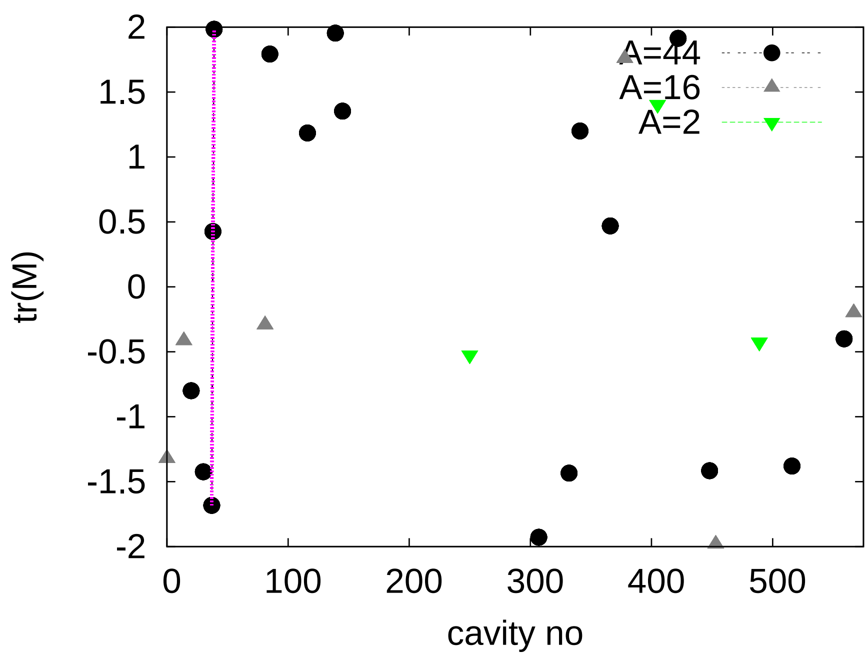

Figure 9.38: The trace of the transfer matrix for H_2^+, CH_4^+ and CO_2^+ ions in presence of a clearing gap. Values above 2 or below -2 indicate that the ions will not be trapped.

spacing ΔL,

$$k = \frac{1}{n}\sum_{i=1}^{n}\frac{2Nr_e m_e}{A_{ion}m_p\sigma_{y,i}(\sigma_{x,i}+\sigma_{y,i})\Delta L}. \tag{9.15}$$

The results of the calculation can be found in Fig. 9.38. As can be seen, in most locations the ions are not trapped. But small regions exist where ions will accumulate. More study is needed to understand which ion density is reached in these areas. Longitudinal motion of the ions will slowly move them into other regions where they are no longer trapped.

Ion Instability While the gap ensures that ions will be lost in the long run, they will still be trapped at least during the full train length of 20μs. We therefore evaluate the impact of ions on the beam during this time. This optmistically ignores that ions will not be completely removed from one turn to the next. However, the stability criteria we employ will be pessimistic. Clearly detailed simulations will be needed in the future to improve the predictive power of the estimates.

Different theoretical models exist for the rise time of a beam instability in the presence of ions. A pessimistic estimate is used in the following. The typical rise time of the beam-ion instability for the nth bunch can be estimated to be [?]

$$\tau_c = \frac{\sqrt{27}}{4}\left(\frac{\sigma_y(\sigma_x+\sigma_y)}{Nr_e}\right)^{\frac{3}{2}}\sqrt{\frac{A_{ion}m_p}{m}}\frac{kT}{p\sigma_{ion}}\frac{\gamma}{\beta_y cn^2\sqrt{L_{sep}}} \tag{9.16}$$

This estimate does not take into account that the ion frequency varies with transverse positon within the bunch and along the beam line.

We calculate the local instability rise length $c\tau_c$ for a pressure of $p = 10^{-11}$hPa at the position of the beam. As can be seen in Fig. 9.39 this instability rise length ranges from a few kilometers to several hundred. One can estimate the overall rise time of the ion instability by averaging over the local ion instability rates:

$$\langle\frac{1}{\tau_c}\rangle = \frac{\int\frac{1}{\tau_c(s)}ds}{\int ds} \tag{9.17}$$

For the worst case in the figure, i.e. CH_4^+, ones finds $c\tau_c \approx 14$ km and for H_2^+ $c\tau_c \approx 25$km. The beam will travel a total of 12km during the six passes through each of the two linacs. So the typical time scale of the rise of the instability is longer than the life time of the beam and we expect no issue. This estimate is conservative since it does not take into account that ion frequency varies within the beam and along the machine. Both effects will stabilise the beam. Hence we conclude that a partial pressure below 10^{-11} hPa is required for the LHeC linacs.

In the cold part of LEP a vacuum level of 0.5×10^{-9}hPa has been measured at room temperature, which corresponds to 0.6×10^{-10}hPa in the cold [**?**]. This is higher than required but this value "represents more the outgassing of warm adjacent parts of the vacuum system" [?] and can be considered a pessimistic upper limit. Measurements in the cold at HERA showed vacuum levels of 10^{-11}hPa [**?**], which would be sufficient but potentially marginal. Recent measurements at LHC show a hydrogen pressure of 5×10^{-12}hPa measured at room temperature, which corresponds to about 5×10^{-13}hPa in the cold [**?**]. For all other gasses a pressure of less than 10^{-13}hPa is expected measured in the warm [?], corresponding to 10^{-14}hPa in the cold. These levels are significantly better than the requirements. The shortest instability rise

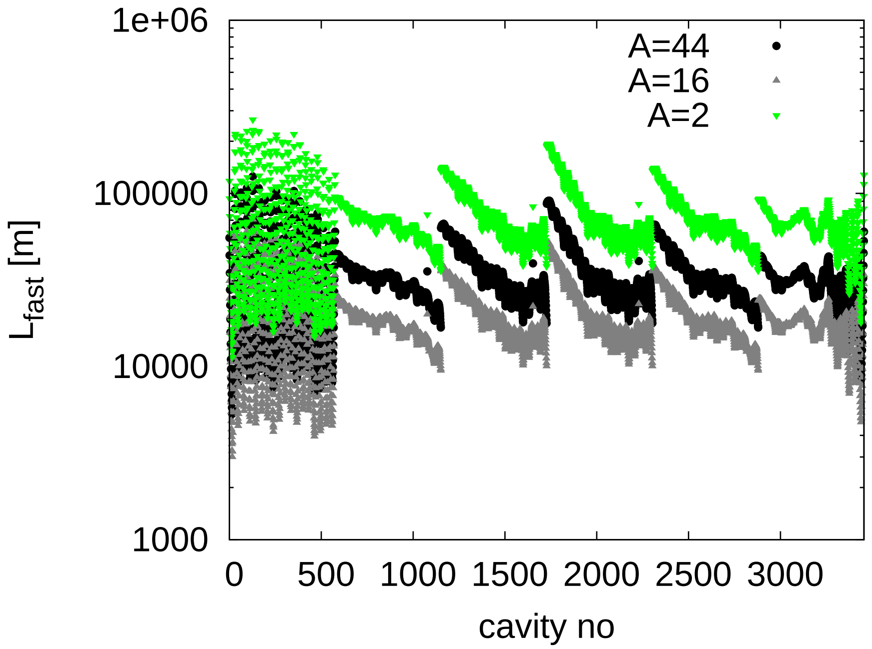

Figure 9.39: The instability length of the beam-ion instability assuming a very conservative partial pressure of 10^{-11}hPa for each gas.

length would be due to hydrogen. With a length of $c\tau_c \approx 500$km which is longer than 40 turns. Hence we do not expect a problem with the fast beam-ion instability in the linacs provided the vacuum system is designed accordingly.

The effect of the fast beam-ion instability in the arcs has been calculated in a similar way, taking into account the reduced beam current and the baseline lattice for each arc. Even H_2^+ will be trapped in the arcs. We calculate the instability rise length $c\tau_c$ for a partial pressure of $10^{-9\,\mathrm{hPa}}$ for each ion mass and find $c\tau_c \approx 70$km for H_2^+, $c\tau_c \approx 50$km for N_2^+ and CO^+ and $c\tau_c \approx 60$km forCO_2^+. The total distance the beam travels in the arcs is 15km. Hence we conclude that a partial pressure below 10^{-9} hPa should be sufficient for the arcs. More detailed work will be needed in the future to fully assess the ion effects in LHeC but we remain confident that they can be handled.

Ion Induced Phase Advance Error The relative phase advance error along a beam line can be calculated using [?] for a round beam:

$$\frac{\Delta\phi}{\phi} = \frac{1}{2}\frac{Nr_e}{\Delta L\epsilon_y}\frac{\theta}{\langle\beta_y^{-1}\rangle}$$

Here θ is the neutralisation of the beam by the ions. We use the maximum beta-function in the linac to make a conservative approximation $\langle\beta^{-1}\rangle = 1/700$m. At the end of the train we find $\rho \approx 3.3 \times 10^{-5}$ for $p = 10^{-11}$hPa in the cold and $p = 10^{-9}$hPa in the warm parts of the machine. This yields $\Delta\Phi/\Phi \approx 7 \times 10^{-4}$. Hence the phase advance error can be neglected.

Impact of the Gap on Beam Loading It should be notet that the gaps may create some beam-loading variation in the injector complex. We can estimate the associated gradient variation assuming that the same cavities and gradients are used in the injector as in the linacs. We use

$$\frac{\Delta G}{G} \approx \frac{1}{2}\frac{R}{Q}\omega\frac{\tau_{gap}\tau_{beam}I}{\tau_{gap}+\tau_{beam}}\frac{1}{G} \tag{9.18}$$

In this case the 10μs gaps in the bunch train correspond to a gradient variation of about 0.6%. This seems very acceptable.

9.3.4 Imperfections

Static imperfections can lead to emittance growth in the LHeC linacs and arcs. However, one can afford an emittance budget that is significantly larger than the one for the ILC, i.e. 10μm vs. 20nm. If the LHeC components are aligned with the accuracy of the ILC components, one would not expect emittance growth to be a serious issue. In particular in the linacs dispersion free steering can be used and should be very effective, since the energies of the different probe beams are much larger than they would be in ILC.

Gradient Jitter and Cavity Tilt

Since the cavities have titlts with respect to the beam line axis, dynamic variations of the gradient will lead to transverse beamdeflections. This effect can be easily calculated using the following expression:

$$\frac{\langle y^2\rangle}{\sigma_y^2} = \frac{\langle (y')^2\rangle}{\sigma_{y'}^2} = \frac{1}{2}\frac{1}{\epsilon}\int\frac{\beta}{E}ds\frac{L_{cav}\langle\Delta G^2\rangle\langle\langle (y'_{cav})^2\rangle}{mc^2}$$

For an RMS cavity tilt of 300μradian, an RMS gradient jitter of 1% and an emittance of 50μm we find

$$\frac{\langle y^2\rangle}{\sigma_y^2} = \frac{\langle (y')^2\rangle}{\sigma_{y'}^2} \approx 0.0125$$

i.e. an RMS beam jitter of $\approx 0.07\sigma_y$. At the interaction point the beam jitter would be $\approx 0.05\sigma_{y'}$.

Chapter 10

System Design

10.1 Magnets for the Interaction Region

10.1.1 Introduction

The technical requirements for the ring-ring options are easily achieved with superconducting magnets of proven technology. It is possible to make use of the wire and cable development for the LHC inner triplet magnets. We have studied all-together seven variants of which two are selected for this CDR. Although these magnets will require engineering design efforts, there are no challenges because the mechanical design will be very similar to the MQXA [**?**] magnet built for the LHC [**?**].

The requirements in terms of aperture and field gradient are much more difficult to obtain for the linac-ring option. We reverse the arguments and present the limitations for the field gradient and septum size, that is, the minimum distance between the proton and electron beams, for both Nb-Ti and Nb_3Sn superconducting technology. Here we limit ourselves to the two most promising conceptual designs.

10.1.2 Magnets for the ring-ring option

The interaction region requires a number of focussing magnets with apertures for the two proton beams and field-free regions to pass the electron beam after the collision point. The lattice design was presented in Section xx; the schematic layout is shown in Fig. 10.1.

The field requirements for the ring-ring option (gradient of 127 T/m, beam stay clear of 13 mm (12 σ), aperture radius of 21 mm for the proton beam, 30 mm for the electron beam) allow a number of different magnet designs using the well proven Nb-Ti superconductor technology and making use of the cable development for the LHC. In the simulations presented here, we have used the parameters (geometrical, critical surface, superconductor magnetization) of the cables used in the insertion quadrupole MQY of the LHC.

Fig. 10.2 shows a superferric magnet as built for the KEKb facility [**?**]. This design comes to its limits due to the saturation of the iron poles. Indeed, the fringe field in the aperture of the electron beam exceeds the limit tolerable for the electron beam optics, and the field quality required for proton beam stability, on the order of one unit in 10^{-4} at a reference radius of 2/3 the aperture, is difficult to achieve.

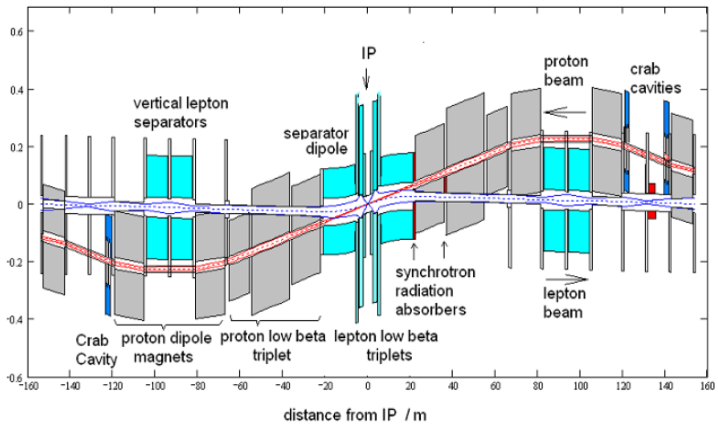

Figure 10.1: Layout of the LHeC interaction region (ring-ring option).

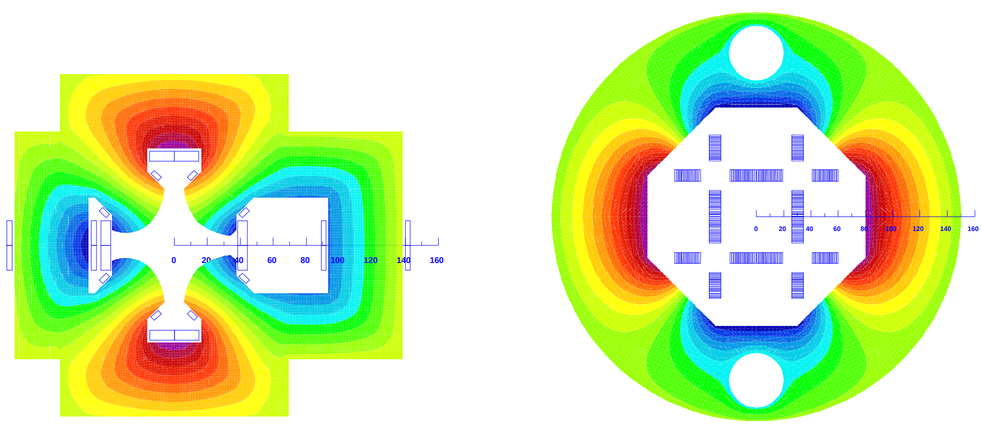

Figure 10.2: Cross-sections of insertion quadrupole magnets with iso-surfaces of the magnetic vector potential (field-lines). Left: Super-ferric, similar to the design presented in [?]. Right: Superconducting block-coil magnet as proposed in [?] for a coil-test facility.

The magnetic flux density in the low-field region of the design shown in Fig. 10.2 (right) is about 0.3 T. We therefore disregard this design as well. Moreover, the engineering design work required for the mechanical structure of this magnet would be higher than for the proven designs shown in Fig. 10.3.

Fig. 10.3 shows the three alternatives based on LHC magnet technology. In the case of the double aperture version the aperture for the proton beams is 21 mm in diameter, in the single aperture version the beam pipe is 26 mm. In all cases the 127 T/m field gradient can be achieved with a comfortable safety margin to quench (exceeding 30%) and using the cable(s) of

Table 10.1: Characteristic data for the superconducting cables ands strands. OL = outer layer, IL = inner layer

Magnet	MQY (OL)	MQY (IL)
Diameter of strands (mm)	0.48	0.735
Copper to SC area ratio	1.75	1.25
Filament diameter (μ m)	6	6
B_{ref} (T) @ T_{ref} (K)	8 @ 1.9	5 @ 4.5
$J_{\mathrm{c}}(B_{\mathrm{ref}}, T_{\mathrm{ref}})$ ($\mathrm{A\,mm^{-2}}$)	2872	2810
$-\mathrm{d}J_{\mathrm{c}}/\mathrm{d}B$ ($\mathrm{A\,mm^{-2}\,T}$)	600	606
ρ(293 K)/ρ(4.2 K) of Cu	80	80
Cable width (mm)	8.3	8.3
Cable thickness, thin edge (mm)	0.78	1.15
Cable thickness, thick edge (mm)	0.91	1.40
Keystone angle (degree)	0.89	1.72
Insulation thickn. narrow side (mm)	0.08	0.08
Insulation thickn. broad side (mm)	0.08	0.08
Cable transposition pitch length (mm)	66	66
Number of strands	34	22
Cross section of Cu (mm^2)	3.9	5.2
Cross section of SC (mm^2)	2.2	4.1

the MQY magnet of the LHC. The operation temperature is supposed to be 1.8 K, employing superfluid helium technology. The cable characteristic data are given in Table 10.1. The outer radii of the magnet coldmasses do not exceed the size of the triplet magnets installed in the LHC (diameter of 495 mm). The fringe field in the aperture of the electron beam is in all cases below 0.05 T.

Fig. 10.4 shows half-aperture quadrupoles (single and double-aperture versions for the proton beams) in a similar design as proposed in [?]. The reduced aperture requirement in the double-aperture version makes it possible to use a single layer coil and thus to reduce the beam-separation distance between the proton and the electron beams. The field-free regions is large enough to also accommodate the counter rotating proton beam. The version shown in Fig. 10.4 (left) employs a double-layer coil. In all cases the outer diameter of the coldmasses do not exceed the size of the triplet magnets currently installed in the LHC tunnel.

For this CDR we retain only the single aperture version for the Q2 (shown in Fig. 10.3, left) and the half-aperture quadrupole for the Q1 (shown in Fig. 10.4, top left). The separation distance between the electron and proton beams in Q1 requires the half-aperture quadrupole design to limit the overall synchrotron radiation power emitted by bending of the 60 GeV electron beam. The single aperture version for Q2 is retained in the present layout, because the counter rotating proton beam can guided outside the Q2 triplet magnet. The design of Q3 follows closely that of Q2, except for the size of the septum between the proton and the electron

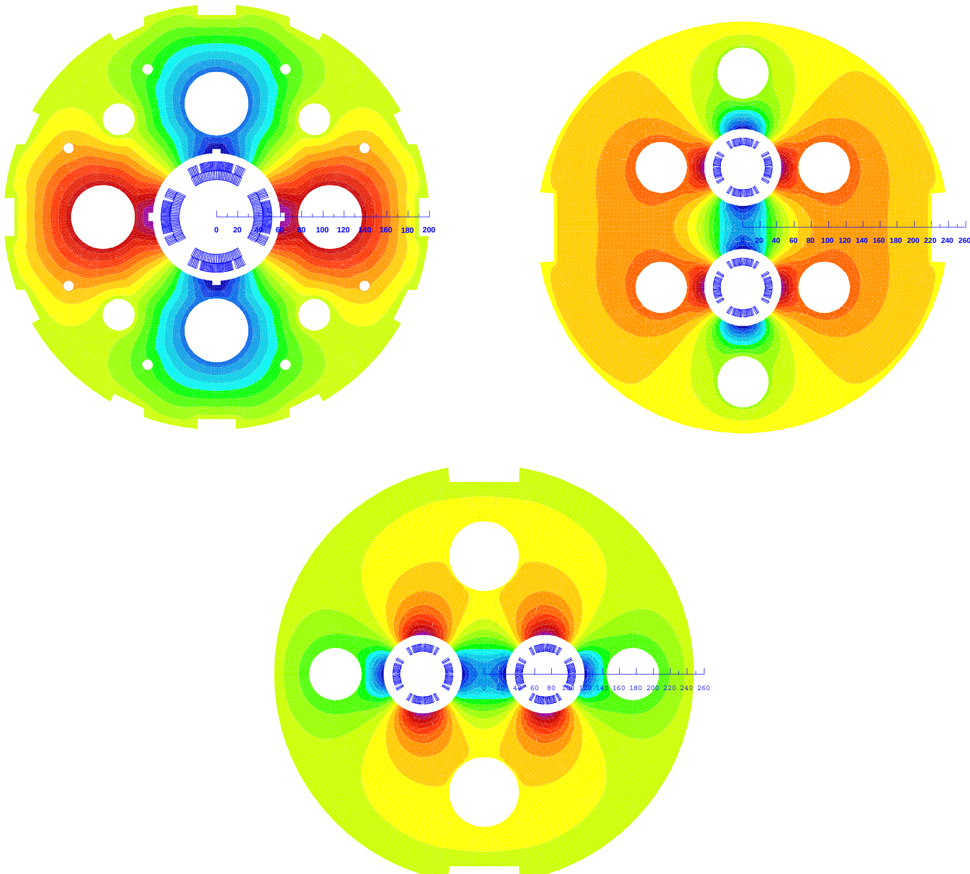

Figure 10.3: Cross-sections with field-lines of insertion quadrupole magnets. Classical designs similar to the LHC magnet technology. Top left: Single aperture with a double layer coil employing both cables listed in Table 10.1. Design chosen for Q2. Top right: Double aperture vertical. Bottom: Double aperture horizontal. The double-aperture magnets can be built with a single layer coil using only the MQY inner layer cable; see the right column of Table 10.1.

beams.

The coils in all three triplet magnets are made from two layers, using both Nb-Ti composite cables as specified in Table 10.1. The layers are individually optimized for field quality. This reduces the sensitivity to manufacturing tolerances and the effect of superconductor magnetization [**?**]. The mechanical design will be similar to the MQXA magnet where two kinds of interleaved yoke laminations are assembled under a hydraulic press and locked with keys in order to obtain the required pre-stress of the coil/collar structure. The main parameters of the magnets are given in Table 10.2.

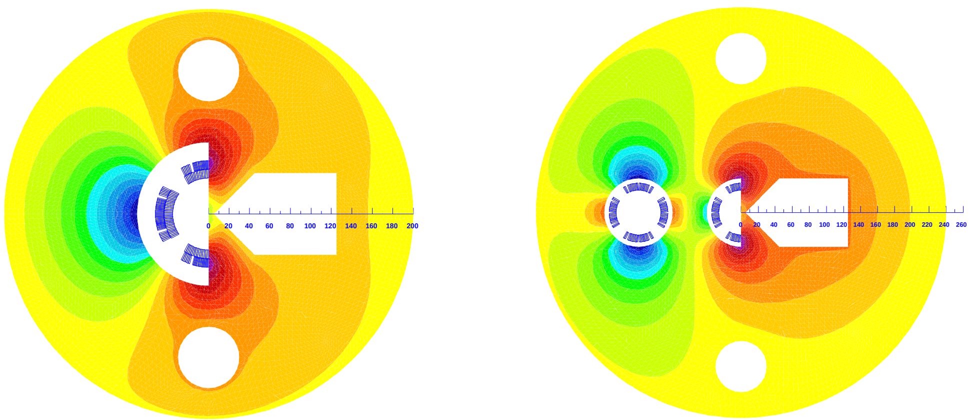

Figure 10.4: Cross-sections of insertion quadrupole magnets with field-lines. Left: Single half-aperture quadrupole with field-free domain [?]; design selected for Q1. Right: Double-aperture magnet composed of a quadrupole and half quadrupole.

10.1.3 Magnets for the linac-ring option

The requirements in terms of aperture and field gradient are more difficult to obtain for the linac-ring option. Consequently we present the limitations for the field gradient and septum size achievable with both Nb-Ti and Nb_3Sn superconducting technologies. We limit ourselves to the two conceptual designs already chosen for the ring-ring option. For the half quadrupole, shown in Fig. 10.6 (right), the working points on the load-line are given for both superconducting technologies in Fig. 10.5.

However, the conductor size must be increased and in case of the half quadrupole, a four layer coil must be used; see Fig. 10.6. The thickness of the coil is limited by the flexural rigidity of the cable, which will make the coil-end design difficult. Moreover, a thicker coil will also increase the beam separation between the proton and the electron beams. The results of the field computation are given in Table 10.2, column 3 and 4. Because of the higher iron saturation, the fringe fields in the electron beam channel are considerably higher than in the magnets for the ring-ring option.

For the Nb_3Sn option we assume composite wire produced with the internal Sn process (Nb rod extrusions), [**?**]. The non-Cu critical current density is 2900 A/mm^2 at 12 T and 4.2 K. The filament size of 46 μm in Nb_3Sn strands give rise to higher persistent current effects in the magnet. The choice of Nb_3Sn would impose a considerable R&D and engineering design effort, which is however, not more challenging than other accelerator magnet projects employing this technology [**?**].

Fig. 10.7 shows the conceptual design of the mechanical structure of these magnets. The necessary prestress in the coil-collar structure, which must be high enough to avoid unloading at full excitation, cannot be exerted with the stainless-steel collars alone. For the single aperture magnet as shown in Fig. 10.7 left, two interleaved sets of yoke laminations (a large one comprising the area of the yoke keys and a smaller, floating lamination with no structural function) provide the necessary mechanical stability of the magnet during cooldown and excitation.

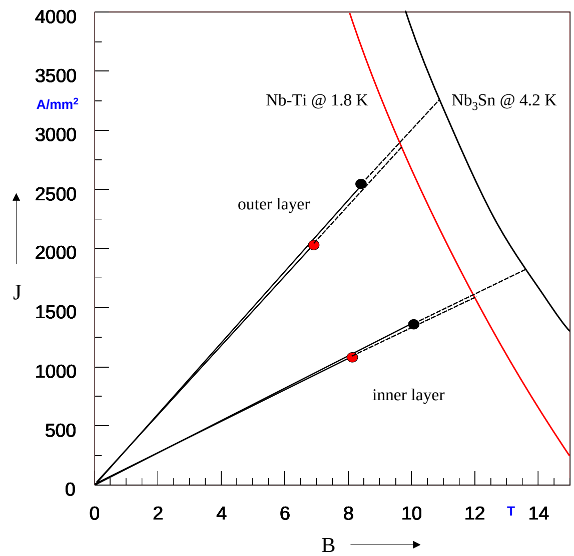

Figure 10.5: Working points on the load-line for both Nb-Ti and Nb_3Sn variants of the half quadrupole for Q1.

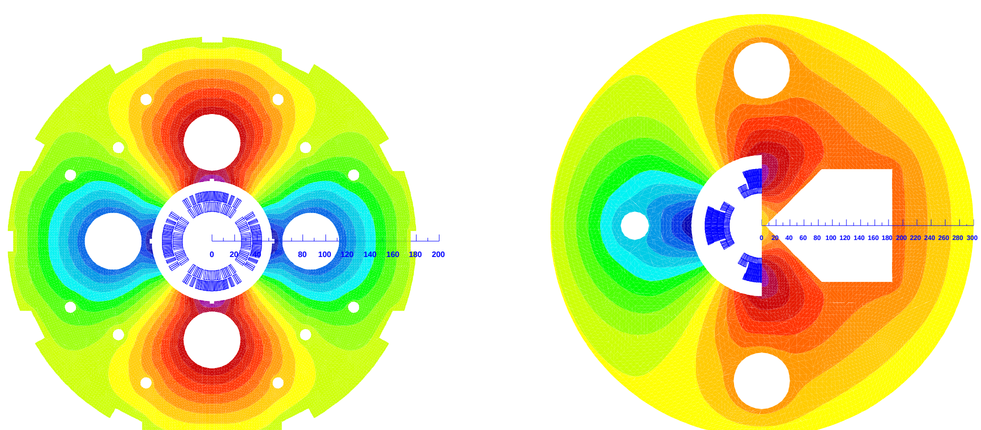

Figure 10.6: Cross-sections of the insertion quadrupole magnets for the linac-ring option. Left: Single aperture quadrupole. Right: Half quadrupole with field-free region.

Preassembled yoke packs are mounted around the collars and put under a hydraulic press, so that the keys can be inserted. The sizing of these keys and the amount of prestress before the cooldown will have to be calculated using mechanical FEM programs. This also depends on the elastic modulus of the coil, which has to be measured with a short-model equipped with

Table 10.2: SC = type of superconductor, g = field gradient, R = radius of the aperture (without coldbore and beam-screen), LL = operation percentage on the load line of the superconductor material, I_{nom} = operational current, B_0 = main dipole field, S_{beam} = beam separation distance, B_{fringe} = fringe field in the aperture for the electron beam, g_{fringe} = gradient field in the aperture for the electron beam.

Type		Ring-ring single aperture	Ring-ring half-quad	Linac-ring single aperture	Linac-ring half-quad
Function		Q2	Q1	Q2	Q1
SC		Nb-Ti at 1.8 K			
R	mm	36	35	23	46
I_{nom}	A	4600	4900	6700	4500
g	T/m	137	137	248	145
B_0	T	-	2.5	-	3.6
LL	%	73	77	88	87
S_{beam}	mm	107	65	87	63
B_{fringe}	T	0.016	0.03	0.03	0.37
g_{fringe}	T/m	0.5	0.8	3.5	18
SC		Nb_3Sn at 4.2 K			
I_{nom}	A			6700	4500
g	T/m			311	175
B_0	T			-	4.7
LL	%			83	82
B_{fringe}	T			0.09	0.5
g_{fringe}	T/m			9	25

pressure gauges. Special care must be taken to avoid nonallowed multipole harmonics because the four-fold symmetry of the quadrupole will not entirely be maintained.

The mechanical structure of the half-quadrupole magnet is somewhat similar, however, because of the left/right asymmetry four different yoke laminations must be produced. The minimum thickness of the septum will also have to be calculated with structural FEM programs.

10.1.4 Dipole Magnets

Two different types of bending magnets are considered in this document: the ones for the LR Option, used in the arcs of the recirculator, and the ones for the RR Option, to be installed in the LHC ring.

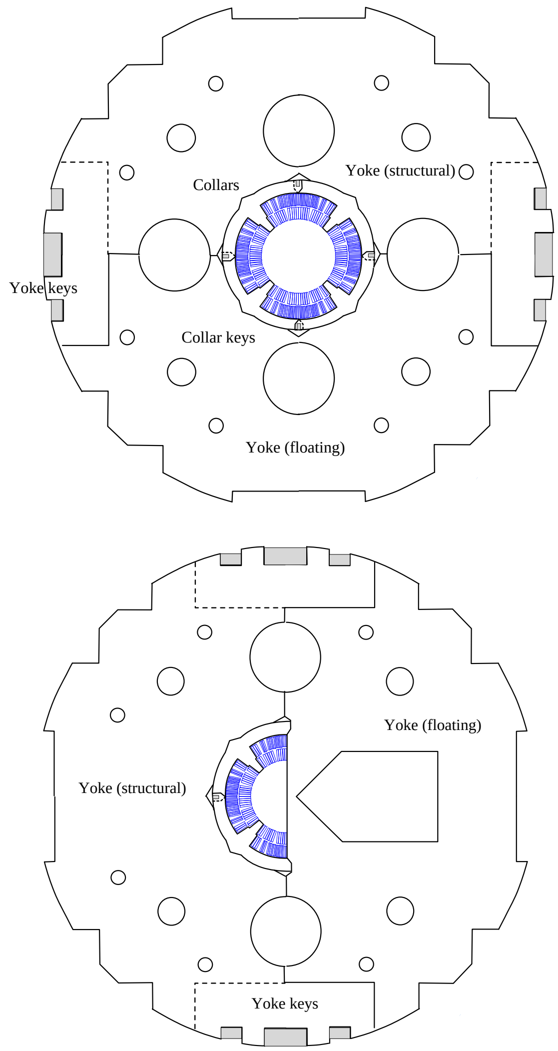

Figure 10.7: Sketch of the mechanical structure. Left: Single aperture magnet. Right: Half quadrupole with field-free region.

Dipole Magnets for the LR Option

Each of the 6 arcs of the recirculator needs 600 four-meter-long bending magnets, providing a magnetic field from 0.046 T to 0.264 T depending on the arc energy from 10.5 GeV to 60.5 GeV.

Considering the relatively low field strength required even for the highest energy arc, and the small required physical aperture of 25 mm only, it is proposed here to adopt the same cross section for all magnets, possibly with smaller conductors for the lowest energies.

This allows the design of very compact and relatively cheap magnets, running at low current densities to minimize the power consumption.

Table 10.3 summarizes the main parameters of the proposed magnet design illustrated in Figure 10.8.

Parameter	Value	Units
Beam Energy	10.5-60.5	GeV
Magnetic Length	4.0	Meters
Magnetic Field	0.046-0.264	Tesla
Number of magnets	6 x 600 = 3600	
Vertical aperture	25	mm
Pole width	80	mm
Number of turns	2	
Current @ 0.264 T	2200	Ampere
Conductor material	copper	
Magnet inductance	0.10	milli-Henry
Magnet resistance	0.10	milli-Ohm
Power @ 10.5 GeV	15	Watt
Power @ 20.5 GeV	55	Watt
Power @ 30.5 GeV	125	Watt
Power @ 40.5 GeV	225	Watt
Power @ 50.5 GeV	350	Watt
Power @ 60.5 GeV	500	Watt
Total power consumption 10-60 GeV	762	kW
Cooling	air or water	depends on energy

Table 10.3: Main parameters of bending magnets for the LR recirculator. Resistance and power refer to the same conductor size, however for the lowest energies conductors may be smaller.

Dipole Magnets for the RR Option

3080 bending magnets, 5.35-meter-long each, are needed in the LHC tunnel for the RR option. They shall provide a magnetic field ranging from 0.0127 T at 10 GeV to 0.0763 T at 60 GeV. The main issues in the design of these magnets are:

- the field range, situated in low field region, and in particular the very low injection field constitute a challenge for achieving a satisfactory field reproducibility from cycle to cycle and for making field quality relatively constant during the field ramp. These specific issues will be discussed further in the paragraphs dealing with the experimental work carried out at BINP and at CERN

- compactness, to fit in the present LHC

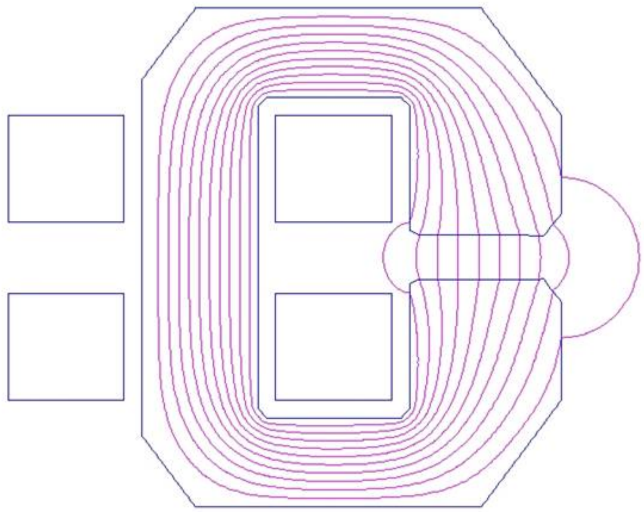

Figure 10.8: Bending magnets for the LR recirculator

- compatibility with synchrotron radiation power

The proposed design is constituted by compact C-Type dipoles, with the C-aperture on the external side of the ring to possibly allow the use of a vacuum pre-chamber and in any case to avoid the magnet intercepts the synchrotron radiation. The unusual poles shape allows minimizing the difference of flux lines length over the horizontal aperture, making magnetic field quality less dependent on the iron characteristics than in a C-type dipole of conventional shape. The coils are constituted by solid single bars of conductor, which after insulation are individually slit inside the magnet. The conductor can be in aluminium or in copper depending from economical reasons coming from a correct balance between investment cost and operation. The present design is based on an aluminium conductor, which among other has the advantage of making the magnet lighter than with a copper conductor. The conductor size is sufficiently large to reduce the dissipated power within levels which can be dealt by ventilation in the LHC tunnel: this is a considerable advantage in terms of simplicity of magnet manufacture, connections, reliability and of course of avoiding the installation of a water cooling circuit in the LHC arcs.

Table 10.4 summarizes the main parameters of the proposed magnet design illustrated in Figure 10.9.

10.1.5 BINP Model

Two different types of models have been manufactured, both aiming at demonstrating that a cycle-to-cycle reproducibility of the relatively low injection field (only 127 Gauss at an injection energy of 10 GeV) better than 0.1 Gauss can be achieved. Both models, pictured in Figure 10.10, showed a magnetic field reproducibility at injection field within +/- 0.075 Gauss when cycled between injection and maximum field. To achieve such results both models make use of the same iron laminations, which are 3408 type silicon steel grain oriented 0.35 mm thick.

Parameter	Value	Units
Beam Energy	10-60	GeV
Magnetic Length	5.35	Meters
Magnetic Field	0.0127-0.0763	Tesla
Number of magnets	3080	
Vertical aperture	40	mm
Pole width	150	mm
Number of turns	2	
Current @ 0.763 T	1300	Ampere
Conductor material	copper	
Magnet inductance	0.15	milli-Henry
Magnet resistance	0.16	milli-Ohm
Power @ 60 GeV	270	Watt
Total power consumption @ 60 GeV	0.8	MW
Cooling	air or water	depends on tunnel ventilation

Table 10.4: Main parameters of bending magnets for the RR Option.

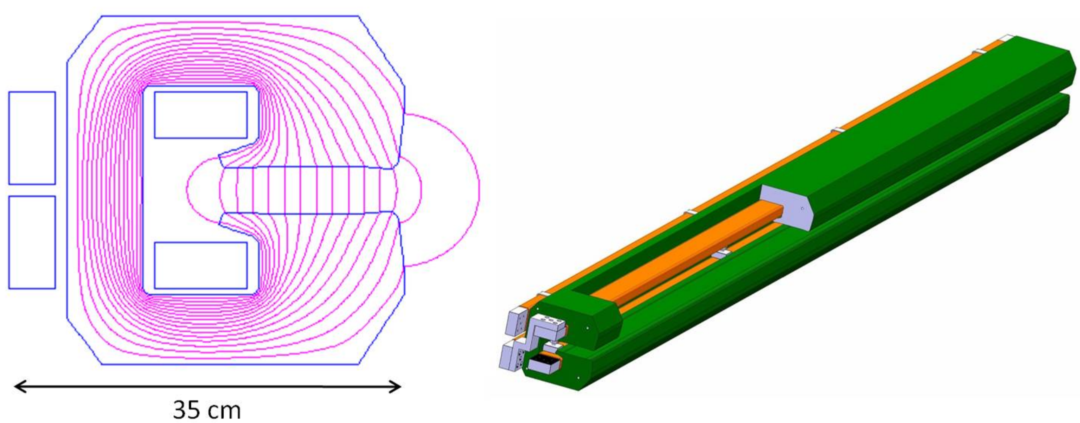

Figure 10.9: Bending magnets for the RR Option

Their coercive force in the direction of the orientation is about 6 A/m, and perpendicular to the direction of the orientation remains relatively low at about 22 A/m. The C-type model has been assembled in two variants, with the central iron part with grains oriented vertically and with grain oriented horizontally (both blocks are as shown in the picture). The relevant magnetic measurements did not show differences between the two versions.

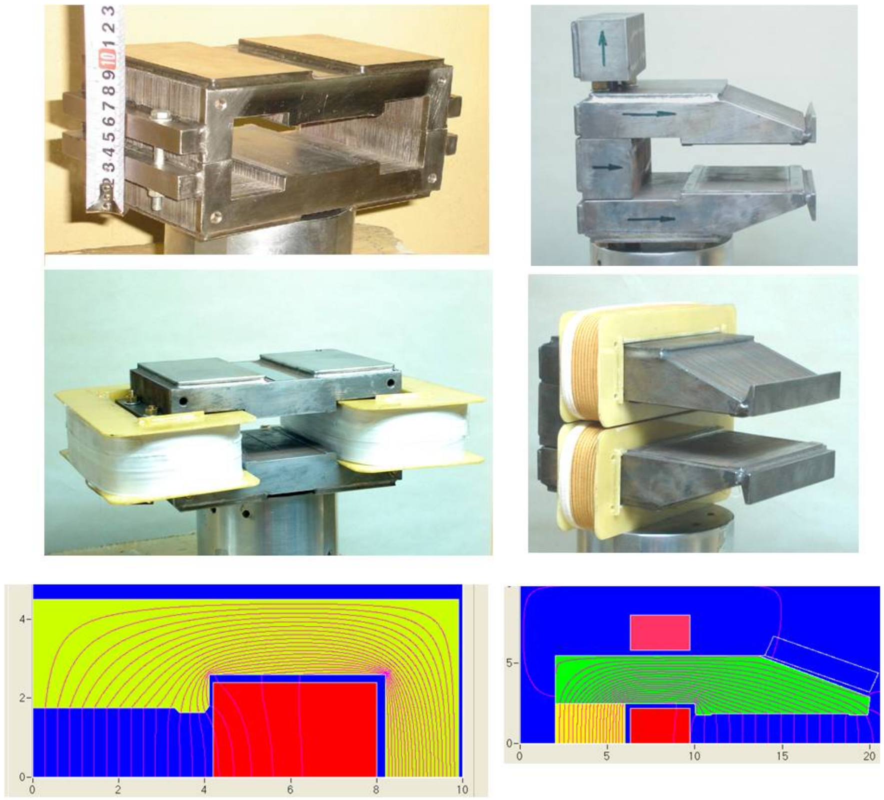

Figure 10.10: H and C-Type model magnets made by BINP

10.1.6 CERN Model

As a complementary study to the one made by BINP, the CERN model explores the manufacture of lighter magnets, with the yoke made by interleaved iron and plastic laminations. The magnetic flux produced in the magnet aperture is concentrated in the iron only, with a thickness ratio between plastic and iron of about 2:1 the magnetic field in the iron is about 3 times that in the magnet gap. In addition to a lighter assembly, this solution has the advantage of increasing the magnetic working point of the iron at injection fields, thus being less sensitive to the quality of the iron and in particular to the coercive force. To explore the whole potential of this solution three different lamination materials have been explored: an expensive NiFe 50 steel (Hc¡3 A/m) which will act as reference, a conventional grain oriented steel with similar characteristics as the one used by BINP, and a conventional low carbon steel with Hc 70 A/m. The model cross section reproduces the refence one described for the RR dipoles.

10.1.7 Quadrupole and Corrector Magnets

In case of the RR option we need, in the LHC tunnel:

- in the arcs, 368 QF each providing 10.28T integrated strength, and 368 QD each providing 8.40T integrated strength
- in the insertion and by-pass, 97 QF each providing 18T integrated strength, and 97 QD each providing 12.6T integrated strength

In case of the LR option we need:

- in the two 10 GeV linacs, 37+37 quadrupoles each providing 2.5T integrated strength
- again in the two 10 GeV linacs, 37+37 correctors each providing 10mTm integrated strength in both vertical and horizontal direction
- in the recirculator arcs 4 different quadrupole types, the Q0, Q1 and Q3 each providing about 35 T integrated strength, and the Q2 each providing about 50T integrated strength

RR: 368+368 quadrupoles in the arcs

Considering the integrated strength of QD and QF are not much different, we propose having the same type of magnets: the relevant parameters are summarized in Table 10.5 and the cross section is illustrated in Figure 10.11.

Parameter	Value	Units
Beam Energy	10-60	GeV
Magnetic Length	1.0	Meters
Field gradient @ 60 GeV	10.28 (QF) - 8.40 (QD)	T/m
Number of magnets	368 + 368	
Aperture radius	30	mm
Total length	1.2	meters
Weight	700	kg
Number of turns/pole	10	
Current @ 10.28 T/m	390	Ampere
Conductor material	copper	
Current density	4	A/mm2
Magnet inductance 3	milli-Henry	
Magnet resistance	16	milli-Ohm
Power @ 60 GeV	2500	Watt
Cooling	water	

Table 10.5: Main parameters of arc quadrupole magnets for the RR Option.

RR: 97 + 97 quadrupoles in the insertion and by-pass

In total 97 QF and 97 QD quadrupoles are needed in the insertion and by-pass. The required integrated strength is 18.0T for the QF and 11.9T for the QD. We propose having the same

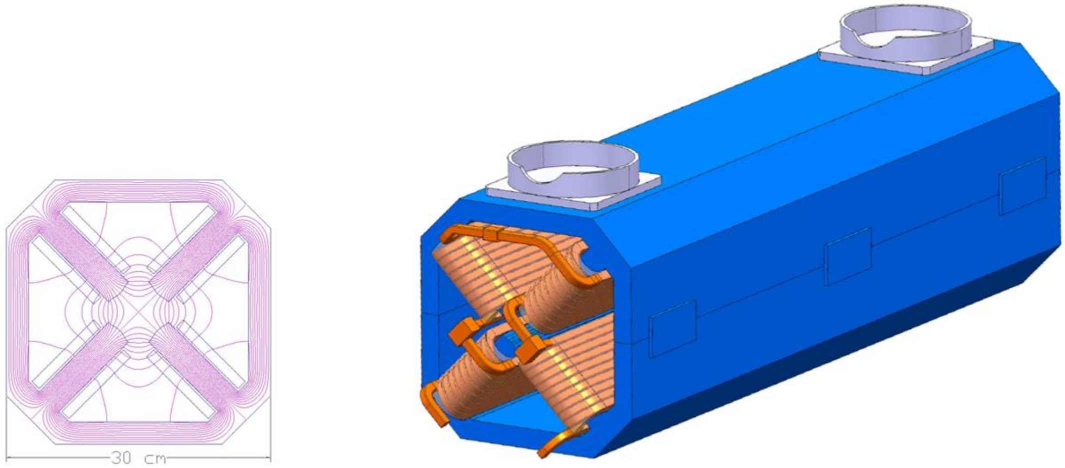

Figure 10.11: Arc quadrupole magnets for the RR Option

magnet cross section with two different length, 1.0 m the QF and 0.7 m the QD. The relevant parameters are summarized in table 10.9 and the cross section is illustrated in Figure 10.12.

Parameter	Value	Units
Beam Energy	10-60	GeV
Magnetic Length (QD/QF)	1.0/0.7	Meters
Field gradient @ 60 GeV	18	T/m
Number of magnets (QD+QF)	97 + 97	
Aperture radius	30	mm
Total length (QD/QF)	1.2/0.9	meters
Weight (QD/QF)	700/500	kg
Number of turns/pole	17	
Current @ 18 T/m	385	Ampere
Conductor material	copper	
Current density	5	A/mm2
Magnet inductance (QD/QF)	12/9	milli-Henry
Magnet resistance (QD/QF)	40/30	milli-Ohm
Power @ 60 GeV (QD/QF)	6.0/4.5	kWatt
Cooling	water	

Table 10.6: Main parameters of arc quadrupole magnets for the RR Option.

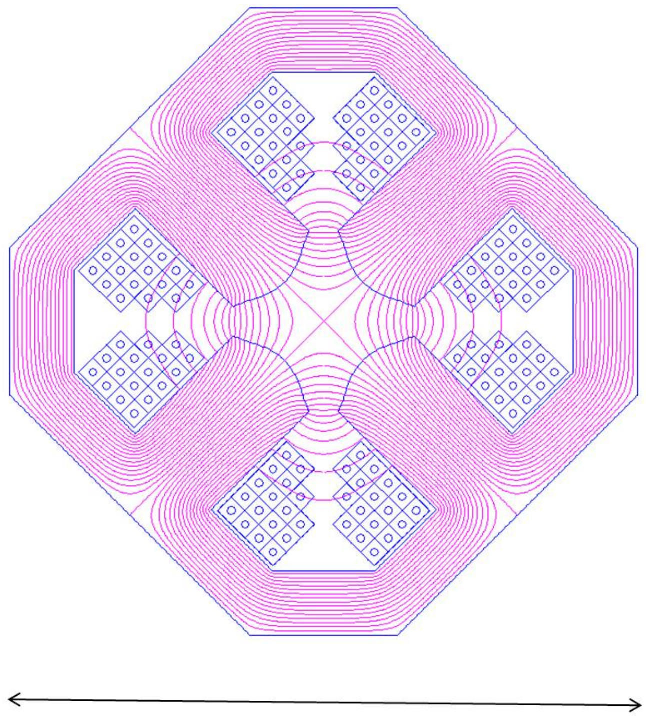

Figure 10.12: Insertion and by-pass quadrupole magnets for the RR Option

LR: 37 + 37 quadrupoles for the two 10 GeV Linacs

The present design solution considers 70 mm aperture radius magnets to be compatible with any possible aperture requirement. The relevant parameters are summarized in table **??** and the cross section is illustrated in Figure 10.13.

LR: 37 + 37 correctors for the two 10 GeV Linacs

The combined function correctors shall provide an integrated field of 10 mTm in an aperture of 140 mm. The relevant parameters are summarized in table 10.8 and the cross section is illustrated in Figure 10.14.

LR: 360 Q0 + 360 Q1+ 360 Q2 + 360 Q3 quadrupoles for the recirculator arcs

In each of the 6 arcs there are 4 types of quadrupoles, each type in 60 units, making 240 quadrupoles per arc. The required integrated strength can be met with one type of quadrupole manufactured in two different length: 1200 mm the Q2 and 900 mm the Q0-Q1-Q3. The quadrupoles of the low energy arcs may use a smaller conductor or less turns or the same conductor as the higher energy quadrupoles showing then ecological friendly power consumption. The relevant parameters are summarized in table **??** and the cross section is illustrated in Figure 10.15.

Parameter	Value	Units
Magnetic Length	250	mm
Field gradient	10	T/m
Number of magnets	37 + 37	
Aperture radius	70	mm
Weight (QD/QF)	300	kg
Number of turns/pole	44	
Current @ 10 T/m	500	Ampere
Conductor material	copper	
Current density	5	A/mm2
Magnet inductance	12	milli-Henry
Magnet resistance	24	milli-Ohm
Power @ 500 A	6	kWatt
Cooling	water	

Table 10.7: Main parameters of quadrupoles for the 10 GeV linacs of the LR option

Parameter	Value	Units
Magnetic Length	400	mm
Field induction	25	mT
Number of magnets (QD+QF)	37 + 37	
Free aperture	140 x 140	mm x mm
Yoke length	250	mm
Total length	350	mm
Weight	100	kg
Number of turns/circuit	2x100	
Current	40	Ampere
Conductor material	copper	
Current density	1.5	A/mm2
Magnet inductance per circuit	10	milli-Henry
Magnet resistance per circuit	0.1	Ohm
Power per circuit	160	Watt
Cooling	air	

Table 10.8: Main parameters of combined function corrector magnets for the LR Option.

10.2 RF Design

10.3 Vacuum

10.4 Cryogenics

10.5 Injection System

10.6 LHeC Injector for the Linac-Ring Option

10.6.1 Polarized electron beam

The Linac-Ring option is based on an ERL machine where the beam pattern, at IP, is shown

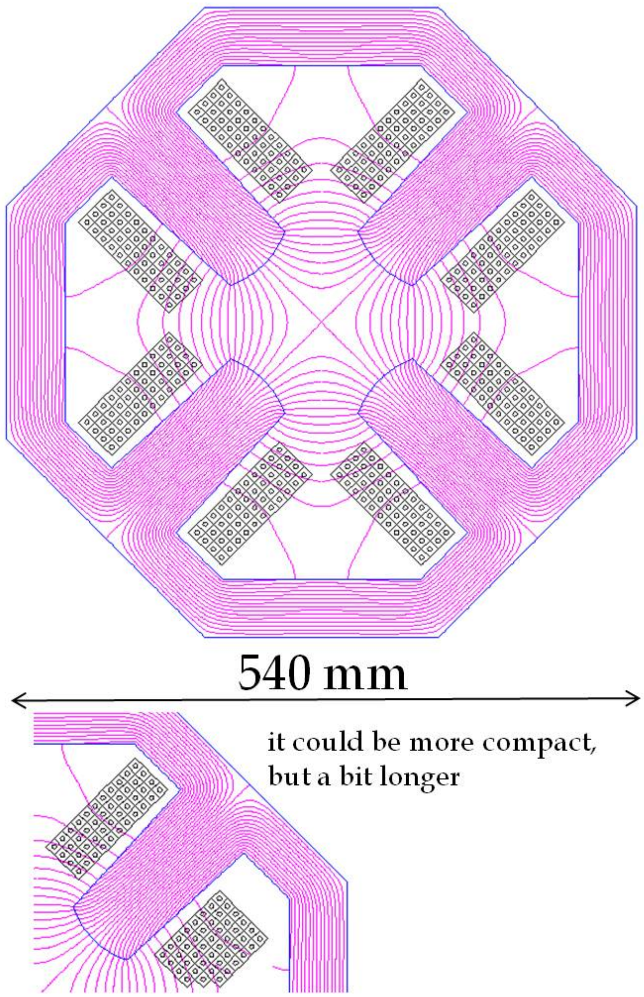

Figure 10.13: Quadrupoles for the 10 GeV linacs of the LR option

With this bunch spacing, one needs $20x10^9$ bunches/second and with the requested bunch charge, the average beam current is $20x10^9$ b/s x 0.33 nC/b = 6.6 mA.

Figure 10.17 shows a possible layout for the injector complex, as source of polarized electron beam.

The injector is composed of a DC gun where a photocathode is illuminated by a laser beam. Then a linac accelerates electron beam up to the requested energy before injection into the ERL. Downstream a bunch compressor system allows to compress the beam down to 1 ps and finally a spin rotator, brings the spin in the vertical plane.

Assuming 90% of transport efficiency between the source and the IP, the bunch charge at the photocathode should $2.2x10^9$ e-/b. According to the laser and photocathode performance, the laser pulse width, corresponding to the electron bunch length, will be between 10 and 100 ps.

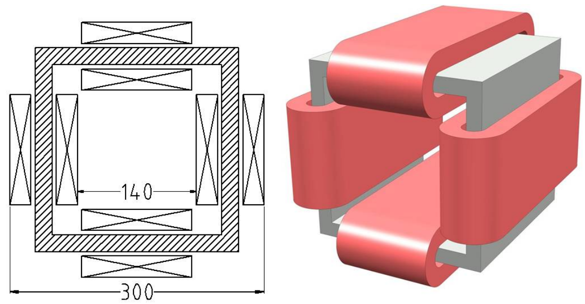

Figure 10.14: Combined function corrector magnets for the LR Option

Parameter	Value	Units
Beam Energy	10-60	GeV
Magnetic Length	0.9/1.2	Meters
Field gradient	41	T/m
Number of magnets (Q0+Q1+Q2+Q3)	1440	
Aperture radius	20	mm
Weight (QD/QF)	550/750	kg
Number of turns/pole	17	
Current @ 41 T/m	410	Ampere
Conductor material	copper	
Current density	5	A/mm2
Magnet inductance	15/20	milli-Henry
Magnet resistance	30/40	milli-Ohm
Power @ 410 A	5/7	kWatt
Cooling	water	

Table 10.9: Main parameters of quadrupoles for the recirculators of the LR option

Table 10.10 summarises the electron beam parameters at the exit of the DC gun. The challenges to produce the 7 mA beam current are the following:

- a very good vacuum ($< 10^{-12}$ mbar) is required in order to get a good lifetime.
- the issues related to the space charge limit and the surface charge limit should be considered. A peak current of 10 A with 4 ns pulse length has been demonstrated. Assuming a similar value for the DC gun, a laser pulse length of 35 ns would be sufficient to produce the requested LHeC charge.
- the high voltage (100 kV to 500 kV) of the DC gun could induce important field emissions.
- the design of the of the cathode/anode geometry is crucial for a beam transport close to 100%.

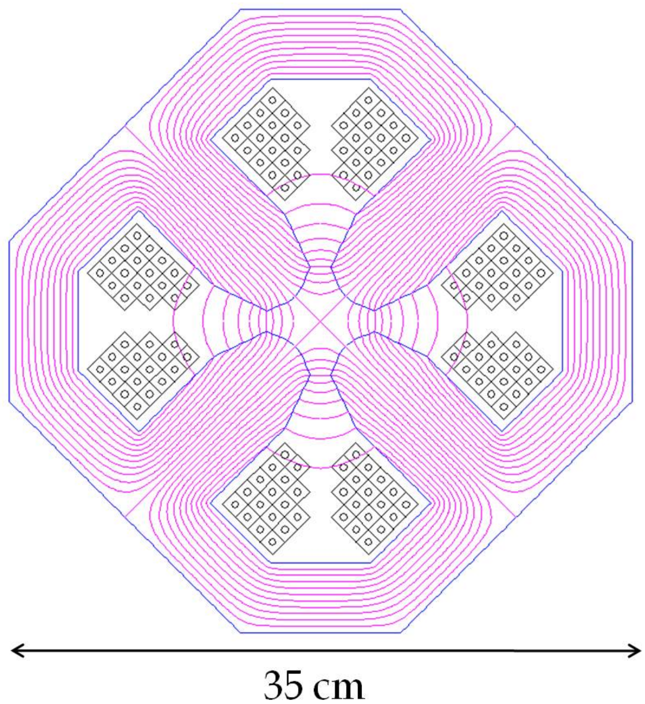

Figure 10.15: Quadrupoles for the recirculators of the LR option

- the quantum efficiency should be as high as possible for the photocathode ($\sim 1\%$ or more).
- the laser parameters (300 nJ/pulse on the photocathode, 20 MHz repetition rate) will need some R&D according to what is existing today on the market.
- the space charge could increase the transverse beam emittances.

In conclusion, a tradeoff between the photocathode, the gun and the laser seems reachable to get acceptable parameters at the gun exit. A classical Pre-Injector Linac accelerates electron beam to the requested ERL energy. Different stages of bunch compressor are used to compensate the initial laser pulse and the space charge effects inducing bunch lengthening. A classical spin rotator system rotates the spin before injection into the ERL.

10.6.2 Unpolarised positron beam

Table 10.11 shows the crucial challenges for the e^+ beam flux, foreseen for LHeC compared to the SLC and CLIC.

SLC (Stanford Linear Collider) was the only collider at high energy which has produced e^+ for the Physics. The flux for the CLIC project (a factor 20 compared to SLC) is very challenging and possible options with hybrid targets are under investigation on the paper. The requested LHeC flux (a factor 300 compared to SLC) for the pulsed option at 140 GeV could be obtained, in a first approximation, with 10 e^+ target stations working in parallel. The requested LHeC

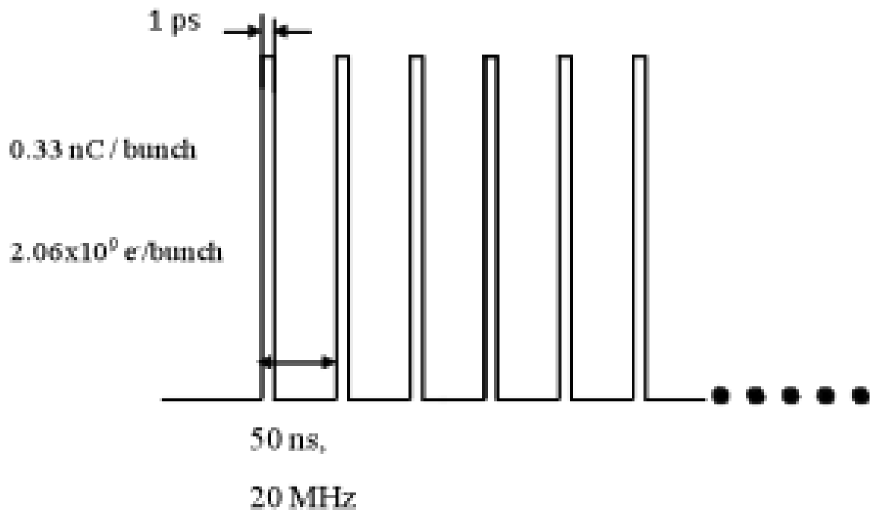

Figure 10.16: Beam pattern at IP

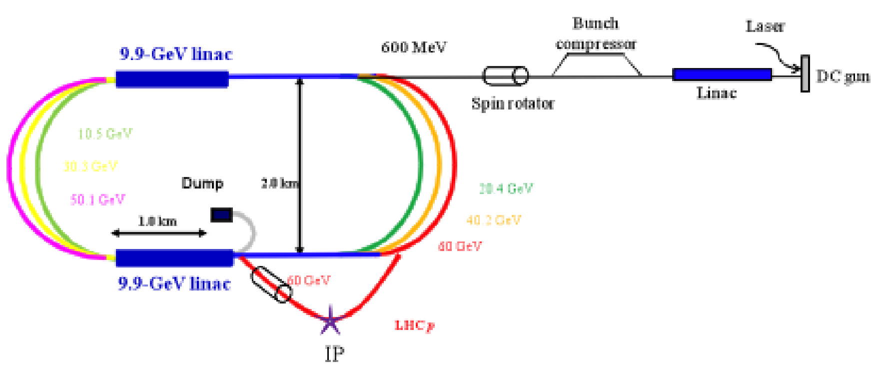

Figure 10.17: Layout of the injector assuming an injection at 600 MeV into the ERL.

Parameters	60 GeV ERL
Electrons /bunch	2.2×10^9
Charge /bunch	0.35 nC
Number bunches / s	20×10^9
Bunch length	$10 - 100$ ps
Bunch spacing	50 ns
Pulse repetition rate	CW
Average current	7 mA
Peak current of the bunch	$3.5 - 350$ A
Current density (1 cm)	$1.1 - 110$ A/cm^2
Polarization	$> 90\%$

Table 10.10: Beam parameters at the source.

	SLC	CLIC (3 TeV)	LHeC p= 140	LHeC ERL
Energy (GeV)	1.19	2.86	140	60
e^+/bunch at IP ($\times 10^9$)	40	3.72	1.6	2
e^+/bunch after capture ($\times 10^9$)	50	7.6	1.8	2.2
Bunches / macropulse	1	312	10^5	NA
Macropulse repetition rate	120	50	10	CW
Bunches / second	120	15600	10^6	20×10^6
e^+ / second ($\times 10^1 4$)	0.06	1.1	18	440

Table 10.11: Comparison of the e^+ flux.

flux (a factor 7300 compared to SLC) for the CW option, has no solution today and needs a very important study and investigation.

Figure 10.18 illustrates a possible option for the 140 GeV case, where the repetition rate is 10 Hz. The idea is to use 10 e^+ target stations in parallel. The consequence implies installing 2 RF deflectors upstream and same downstream. Experience exists for RF deflector at 3 GHz and 2 lines in parallel. Assuming that this configuration is acceptable from beam optics, it would be necessary to implement a Damping Ring because the emittances will be too high for the injection into the ERL.

Table 10.12 shows the beam characteristics at the end of the 10 GeV Primary beam Linac for electrons, before splitting the beam.

Table 10.13 shows the beam characteristics at the level of each e^+ target. One important parameter is the Peak Energy Deposition Density (PEDD) in the target. For Tungsten material, an experimental limit was found around 35 J/g as breakdown limit. In the proposed scheme, this constraint would be fulfilled. Another critical parameter is the relaxation time in the target (shock wave). The present estimation is established around 0.010 ms. With the proposed configuration, this should be acceptable. Last but not least is the total beam power deposition.

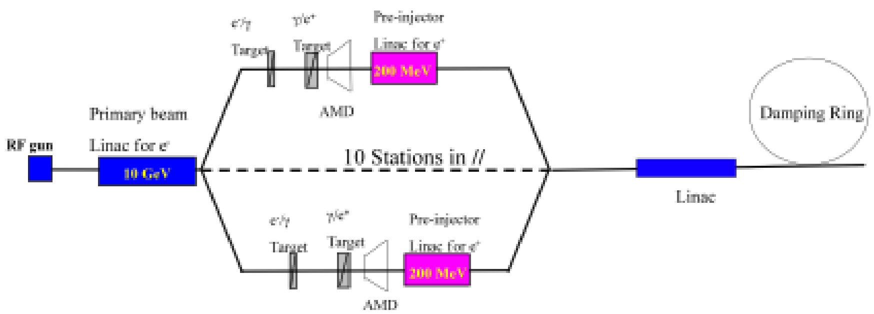

Figure 10.18: Possible layout with unpolarised e^+ for the LHeC injector (p-140 GeV).

Primary beam energy (e^-)	10 GeV
Number e^- / bunch	1.2×10^9
Number of bunches / pulse	100000
Number e^- / pulse	1.2×10^14
Pulse length	5 ms
Beam power	1900 kW
Bunch length	1 ps

Table 10.12: Electron beam parameters before splitting.

The 5.6 kW deposited in the target require to be verified experimentally. The limit is not well estimated today.

Yield (e^+/e^-)	1.5
Beam power (for e^-)	190 kW
Deposited power / target	5.6 kW
PEDD	0.3 J/g
Number e^+ / bunch	1.8×10^9
Number bunches / pulse	$10,000$
Number e^+ / pulse	1.8×10^{13}

Table 10.13: Beam parameters at each e^+ target.

Table 10.14 shows the beam characteristics after recombination at 200 MeV. The bunch lengthening will occur and will produce bunch length in the range between 20 and 100 ps. Therefore a bunch compressor system is also necessary.

Based on simulations, the transverse normalized rms beam emittances, in both planes, are in the range of 6000 to 10 000 mm.mrad. Therefore a Damping Ring (DR) is mandatory for the requested performance.

Therefore it is the necessity to design and implement a linac which will accelerate the

Secondary beam energy (e^+)	200 MeV
Number e^+ bunch	1.8×10^9
Number of bunches / pulse	$100,000$
Number of e^+ / pulse	1.8×10^{14}
Bunch spacing	50 ns
Repetition rate	10 Hz

Table 10.14: Positron beam parameters after recombination.

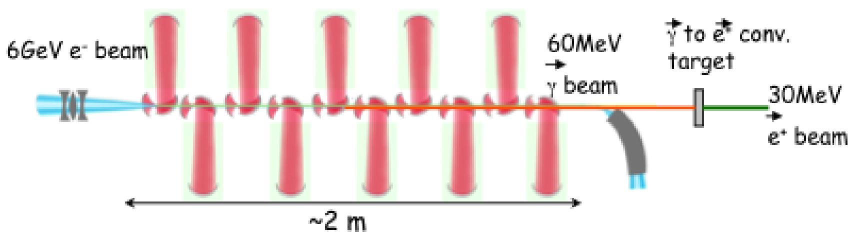

Figure 10.19: Layout based on Compton Linac for polarised e^+.

positron beam up to the DR energy optimised for the ERL injection.

10.6.3 Polarised positron beam

As discussed from Table 10.11, the challenge here is extremely demanding. The case of 140 GeV could be studied using either an undulator or a Compton process. However the flux is so high that a careful investigation is crucial.

For the CW- 60 GeV option, an approach could be the Compton process with a linac at high energy. Figure 10.19 shows a possible layout for such configuration.

At BNL, a ratio photon/electron close to 1 has been demonstrated. Assuming that a ratio photon/positron close to 2 % is achievable, then 50 photons are required to produce 1 e^+. For LHeC, one needs 0.35 nC/bunch (for e^+). Based on above estimations, it implies $\sim$ 18 nC/bunch (for e^-). Then with 10 optical cavities, the requested e^- charge is ~ 1,8 nC / bunch which is a reasonable value.

However many issues and challenges require a strong R&D program.

10.7 LHeC Injector for the Ring-Ring option

Figure 10.20 shows the layout of the LPI (LEP Pre-Injector) as it was working in 2000.

LPI was composed of the LIL (LEP Injector Linac) and the EPA (Electron Positron Accumulator).

Table 10.15 gives the beam characteristics at the end of LIL.

Figure 10.21 shows an electron beam profile at the end of LIL (500 MeV).

Table 10.16 gives the electron and positron beam parameters at the exit of EPA.

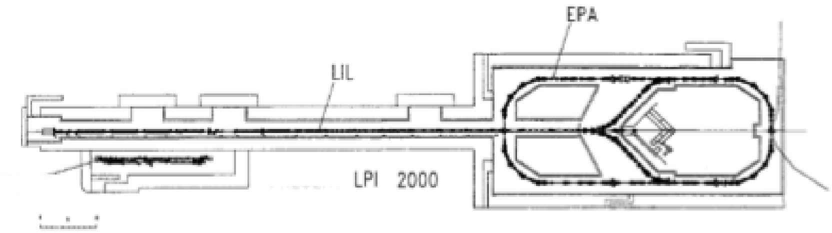

Figure 10.20: Layout of the LPI in 2000.

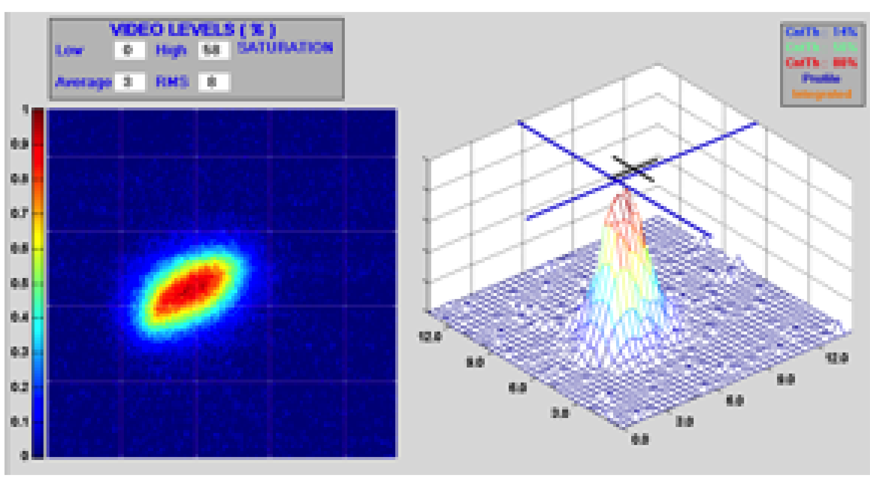

Figure 10.21: Electron beam profile at 500 MeV.

Beam energy	200 to 700 MeV
Charge	5×10^8 to $2 \times 10^{10} e^-$ / pulse
Pulse length	10 to 40 ns (FWHM)
Repetition frequency	1 to 100 Hz
Beam sizes (rms)	3 mm

Table 10.15: LIL beam parameters.

Energy	200 to 600 MeV
Charge	up to $4.5 \times 10^{11} e\pm$
Intensity	up to 0.172 A
Number of buckets	1 to 8
Emittance	0.1 mm.mrad
Tune	$Q_x = 4.537, Q_y = 4.298$

Table 10.16: The electron and positron beam parameters at the exit of EPA.

In summary, the LPI characteristics fulfils completely the requested performance for the LHeC injector based on Ring-Ring option.

10.8 Beam dumps

Beam Dump

10.9 Post collision line for 140 GeV option

The post collision line for the 140 GeV Linac option has to be designed taking care of minimising beam losses and irradiation. The production of beamsstrhalung photons and e^-e^+ pairs is negligible and the energy spread limited to 2×10^{-4}. A standard optics with FODO cells and a long field-free region allowing the beam to naturally grow before reaching the dump can be foreseen. The aperture of the post collision line is defined by the size of the spent beam and, in particular, by its largest horizontal and vertical angular divergence (to be calculated). A system of collimators could be used to keep losses below an acceptable level. Strong quadrupoles and/or kickers should be installed at the end of the line to dilute the beam in order to reduce the energy deposition at the dump window. Extraction line requirements:

- Acceptable radiation level in the tunnel
- Reasonably big transverse beam size at the dump window and energy dilution
- Beam line aperture big enough to host the beam: beta function and energy spread must be taken into account
- elements of the beam line must have enough clearance.

10.10 Absorber for 140 GeV option

Nominal operation with the 140 GeV Linac foresees to dump a 50 MW beam. This power corresponds to the average energy consumption of 69000 Europeans. An *Eco Dump* could be used to recover that energy; detailed studies are needed and are not presented here. Another option is to start from the concept of the ILC water dump and scale it linearly to the LHeC requirements. The ILC design is based on a water dump with a vortex-like flow pattern and is rated for 18 MW beam of electrons and positrons [441]. Cold pressurized water (18 m^3 at 10 bar) flows transversely with respect to the direction of the beam. The beam always encounters fresh water and dissipates the energy into it. The heat is then transmitted through heat exchangers. Solid material plates(Cu or W) are placed beyond the water vessel to absorb the tail of the beam energy spectrum and reduce the total length of the dump. This layer is followed by a stage of solid material, cooled by air natural convection and thermal radiation to ambient, plus several meters of shielding. The size of the LHeC dump, including the shielding, should be 36 m longitudinally and 21 m transversely and it should contain 36 m^3 of water. The water is separated from the vacuum of the extraction line by a thin Titanium Alloy (Ti-6Al-4V) window which has high temperature strength properties, low modulus of elasticity and low coefficient of thermal expansion. The window is primarily cooled by forced convection to water in order to reduce temperature rise and thermal stress during the passage of the beam. The window must be thin enough to minimise the energy absorption and the beam spot size of the undisrupted beam must be sufficiently large to prevent window damage. A combination of active dilution and optical means, like strong quadrupoles or increased length of the transfer line, can be use on this purpose. Further studies and challenges related to the dump design are:

- pressure wave formation and propagation into the water vessel
- remotely operable window exchange
- handling of tritium gas and tritiated water.

10.10.1 Energy deposition studies

Preliminary estimates, of the maximum temperature increase in the water and at the dump window, have been defined according to FLUKA simulation results performed for the ILC dump [442]. A 50 MW steady state power should induce a maximum temperature increase ΔT of 90° corresponding to a peak temperature of 215°. The water in the vessel should be kept at a pressure of about 35 bar in order to insure a 25° margin from the water boiling point.

FLUKA studies have been carried out for a 1 mm thick Ti window with a hemispherical shape. The beam size at the ILC window is $\sigma_x = 2.42$ mm and $\sigma_y = 0.27$ mm; an extraction line with 170 m drift and 6 cm sweep radius for beam dilution have been considered. A beam power of 25 W with a maximum heat source of 21 W/cm^3 deposited on the window have been calculated. This corresponds to a maximum temperature of 77° for the minimum ionisation particle (dE/dx = 2 MeV $\times$ cm^2/g), no shower is produced because the thickness of the window is significantly smaller than the radiation length. A maximum temperature lower than 100° would require a minimum beam size of $\sigma_{x,y} = 1.8$ mm. A minimum β function of 8877 m would be needed being the beam emittance $\varepsilon_{x,y} = 0.37$ nm for the undisrupted beam. The radius of the dump window depends on the size of the disrupted beam. The emittance of the disrupted beam is $\varepsilon_{x,y} = 0.74$ nm corresponding to a beam size $\sigma_{x,y}$ of 2.56 mm (for $\beta = 8877$ m); a radius R = 5 cm could then fit a 10σ envelope. The yield strength of the Ti alloy used for the window is $\sigma_{Ti} = 830$ MPa, this, according to the formula:

$$\sigma_{Ti} = 0.49 \times \Delta P \frac{R^2}{d^2} \tag{10.1}$$

where $\Delta P = 3.5$ MPa, imposes that the thickness of the window d is bigger than 2.3 mm.

Length of the transfer line drift space and possible dilution have to be estimated together with possible cooling.

10.11 Beam line dump for ERL Linac-Ring option

The main dump for the ERL Linac-ring option will be located downstream of the interaction point. Splitting magnets and switches have to be installed in the extraction region and the extracted beam has to be tilted away from the circulating beam by 0.03 rad to provide enough clearance for the first bending dipole of the LHeC arc (see Fig. 10.22). A 90 m transfer line, containing two recombination magnets and dilution kickers, is considered to be installed between the LHeC and the LHC arcs(see Fig. 10.23). The beam dump will be housed in a UD62/UD68

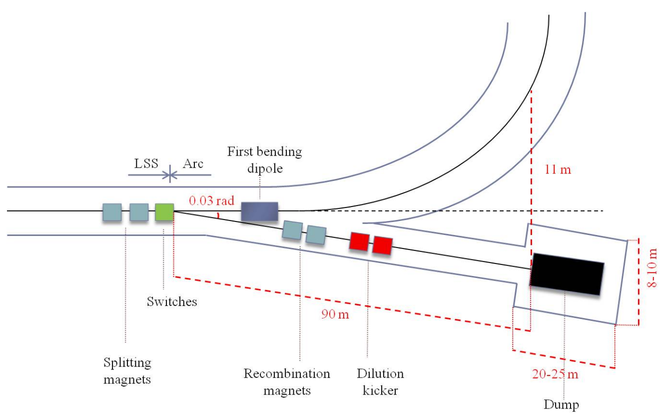

Figure 10.22: Scheme of the transfer line from end of long straight section of the linac and beam dump.

like cavern at the end of the TL and the option of having service caverns for water treatment and heat exchange is explored. An additional dump, and its extraction line, could be installed at the end of the first linac(see Fig. 10.23) for beam setup purposes at intermediate energy. The same design as for the nominal dump and extraction line would be applied.

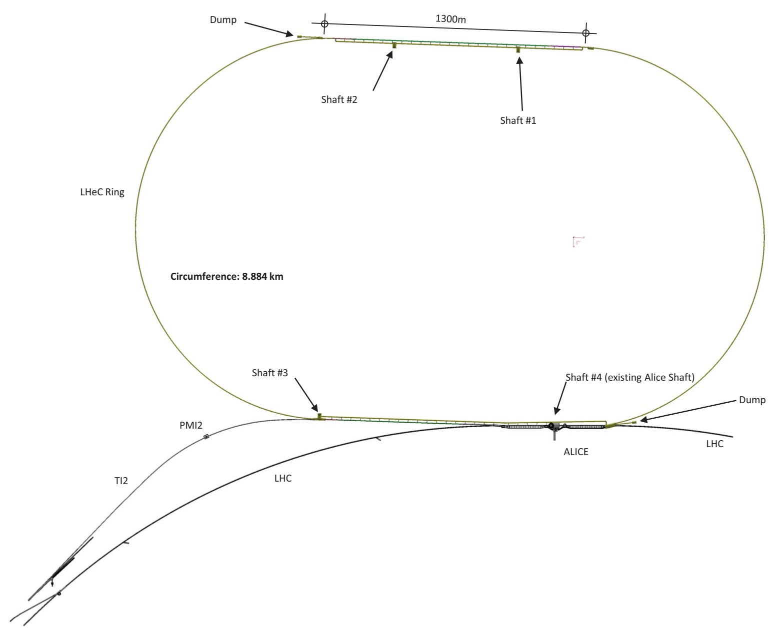

Figure 10.23: Two beam dumps are installed 90 m downstream the end of the long straight section of each linac for nominal operation and beam setup.

10.12 Absorber for ERL Linac-Ring option

During nominal operation a 0.5 GeV beam has to be dumped with a current of 6.6 mA. The setup beam will have a maximum current of 0.05 mA and an energy varying from 10 GeV to 60 GeV (10 GeV step size). Globally, a maximum beam power of 3 MW has to be dumped. The same design as for the 140 GeV option can be used by scaling linearly. In this case, a 3 m^3 water dump (0.5 m diameter and 8 m length) with a 3 m $\times$ 3 m $\times$ 10 m long shielding has to be implemented. No show stopper has been identified for the 18 MW ILC dump, same considerations are valid in this less critical case.

10.13 Injection Region Design for Ring-Ring Option

A 10 GeV recirculating Linac will be used to inject the electrons in the LHeC. This will be built on the surface or underground and a transfer line will connect the linac to the LHeC injection region. At this stage a purely horizontal injection is considered, since this will be easier to integrate into the accelerator. The electron beam will be injected in the bypass around ATLAS, with the baseline being injection into a dispersion free region (at the right side of ATLAS). Bunch-to-bucket injection is planned, as the individual bunch intensities are easily reachable in the injector and accumulation is not foreseen. Two options are considered: a simple septum plus kicker system where single bunches or short trains are injected directly onto the closed orbit; and a mismatched injection, where the bunches are injected with either a betatron or dispersion offset.

10.13.1 Injection onto the closed orbit

The baseline option is injection onto the orbit, where a kicker and a septum would be installed in the dispersion free region at the right side of ATLAS bypass (see Fig. 10.24). Injecting the beam onto the closed orbit has the advantage that the extra aperture requirements around the rest of the machine from injection oscillations or mismatch are minimised. The kicker and septum can be installed around a Defocusing quadrupole to minimise the kicker strength required. The kicker-septum phase advance is 75°.

Some assumptions made to define the required element apertures are made in Table 10.17.

For the septum, an opening between injected and circulating beam of 47 mm is required, taking into account some pessimistic assumptions on orbit, tolerances and with a 4 mm thick septum. This determines the kicker strength of about 1 mrad.

The septum strength should be about 33 mrad to provide enough clearance for the injected beam at the upstream lattice quadrupole, the yoke of which is assumed to have a full width of 0.6 m. This requires about 1.1 T m, and a 3.0 m long magnet at about 0.37 T is reasonable, of single turn coil construction with a vertical gap of 40 mm and a current of 12 kA.

The RF frequency of the linac is 1.3 GHz and a bunch spacing of 25 ns is considered, as the LHeC electron beam bunch structure is assumed to match with the LHC proton beam structure. Optimally a train of 72 bunches would be injected, which would require a 1.8 μs flattop for the kickers and a very relaxed 0.9 μs rise time (as for the LHC injection kickers [443]). However, this train length is too long for the recirculating linac to produce, and so the kicker rise time and fall time requirements are therefore assumed to be about 23 ns, to allow for the bunch length and some jitter.

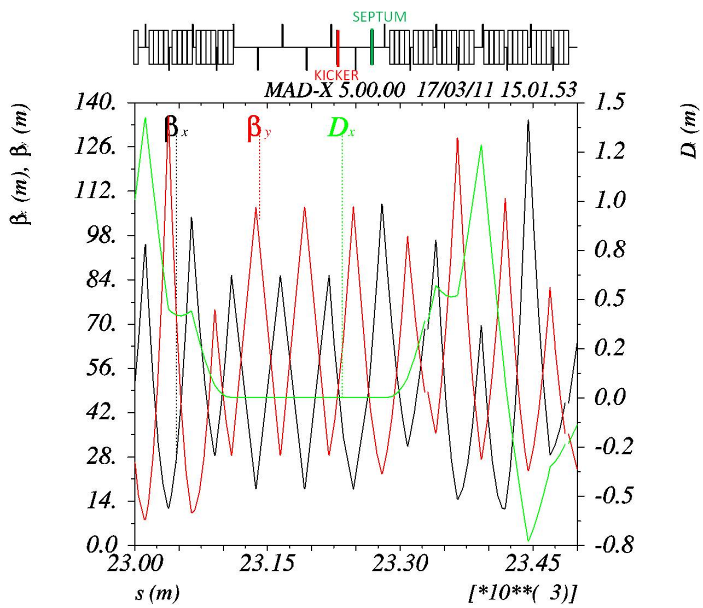

Figure 10.24: Injection optics is shown. The sequence starts (s=0) at the beginning of the dispersion suppressor at the left side of IP2 and proceeds clockwise, while the electron beam rotates counterclockwise (from right to left in the figure). The injection kicker and septum are installed in the dispersion free region of the bypass at the right side of ATLAS.

For a rise time $t_m = 23$ ns, a system impedance Z of 25 Ω is assumed, and a rather conservative system voltage U of 60 kV.

Assuming a full vertical opening h of 40 mm, and a full horizontal opening w of 60 mm (which allow $\pm 6\ \sigma$ beam envelopes with pessimistic assumptions on various tolerances and orbit), the magnetic length l_m of the individual magnets is:

$$l_m = h t_m Z / \mu_0 w = 0.31\ m$$

For a terminated system the gap field B is simply:

$$B = \frac{\mu_0 U}{2hZ} = 0.037\ T$$

As 0.03 Tm are required, the magnetic length should be 0.8 m, which requires 3 magnets. Assuming each magnet is 0.5 m long, including flanges and transitions the total installed kicker length is therefore about 1.5 m.

10.13.2 Mismatched injection

A mismatched injection is also possible, Figure 10.25 with a closed orbit bump used to bring the circulating beam orbit close to the septum, and then switched off before the next circulating bunch arrives.

Orbit variation	± 4 mm
Injection precision	± 3 mm
Mechanical/alignment tolerance	± 1 mm
Horizontal normalised emittance $\varepsilon_{n,x}$	0.58 mm
Vertical normalised emittance $\varepsilon_{n,y}$	0.29 mm
Injection mismatch (on emittance)	100 %
β_x, β_y @ Kicker	61.3 m, 39.7 m
β_x, β_y @ Septum	57.3 m, 42.3 m
σ_x, σ_y @ Kicker and Septum	0.8 mm, 0.4 mm

Table 10.17: Assumptions for beam parameters used to define the septum and kicker apertures

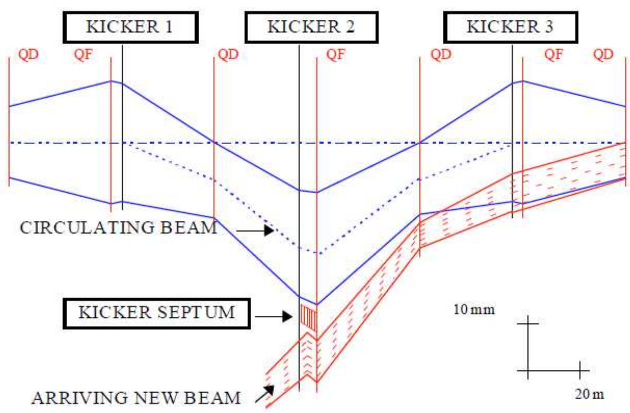

Figure 10.25: layout of mismatched injection system. To minimise kicker strengths the magnets are located near focusing quadrupoles.

The injected beam then performs damped betatron or synchrotron oscillations, depending on the type of mismatch used. In LHeC the damping time is about 3 seconds, so that to achieve the suggested 0.2 s period between injections, a damping wiggler would certainly be needed - the design of such a wiggler needs to be investigated.

Three kickers (KICKER 1, KICKER 2 and KICKER 3 in Fig. 10.25) are used to generate a closed orbit bump of 20 mm at the injection point. The kicker parameters are summarized in table 10.18. In case of betatron mismatch, the bumpers can be installed in the dispersion free region considered for the injection onto the closed orbit case discussed in the previous section (see Fig. 10.26). The installed magnet lengths of the kickers should be 2 m, 3.5 m and 1 m respectively, for the kickers size,Z and U parameters given above. Overall the kicker system is not very different to the system needed to inject onto the orbit.

To allow for the possibility of synchrotron injection, the injection kicker-septum would need to be located where the horizontal dispersion D_x is large. The beam is then injected with a

Magnet	θ_x [mrad]	B dl [Tm]
KICKER1	1.35	0.04
KICKER2	2.37	0.08
KICKER3	0.55	0.02

Table 10.18: Kickers strength and integrated magnetic field needed to generate an orbit bump of 20 mm at the injection point.

position offset x and a momentum offset δp, such that:

$$x = D_x \delta p$$

The beam then performs damped synchrotron oscillations around the ring, which can have an advantage in terms of faster damping time and also smaller orbit excursions in the long straight sections, particularly experimental ones, where the dispersion functions are small.

As an alternative to the fast (23 ns rise time) kicker for both types of mismatched injection, the kicker rise- and fall-time could be increased to almost a full turn, so that the bump is off when the mismatched bunch arrives back at the septum. This relaxes considerably the requirements on the injection kicker in terms of fall time. However, this does introduce extra complexity in terms of synchronizing the individual kicker pulse lengths and waveform shapes, since for the faster kicker once the synchronization is reasonably well corrected only the strengths need to be adjusted to close the injection bump for the single bunch.

10.13.3 Injection transfer line

The injection transfer line from the 10 GeV injection recirculating linac is expected to be straightforward. A transfer line of about 900 m, constituted by 15 FODO cells, has been considered. The phase advance of each cell corresponds to about 100°.

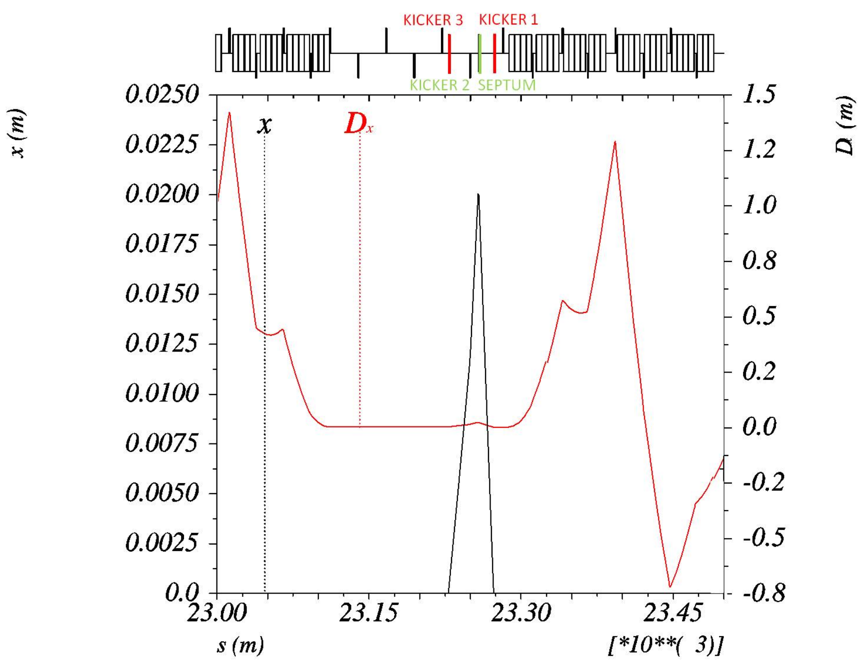

Figure 10.26: A closed orbit bump of 20 mm is generated by three kickers installed in the dispersion free region located at the right side of the bypass around ATLAS (electron beam moves from right to left in the Figure).

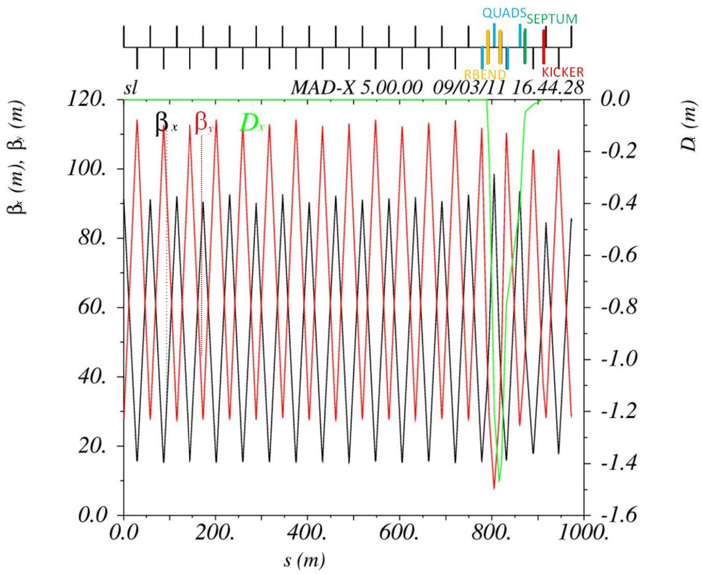

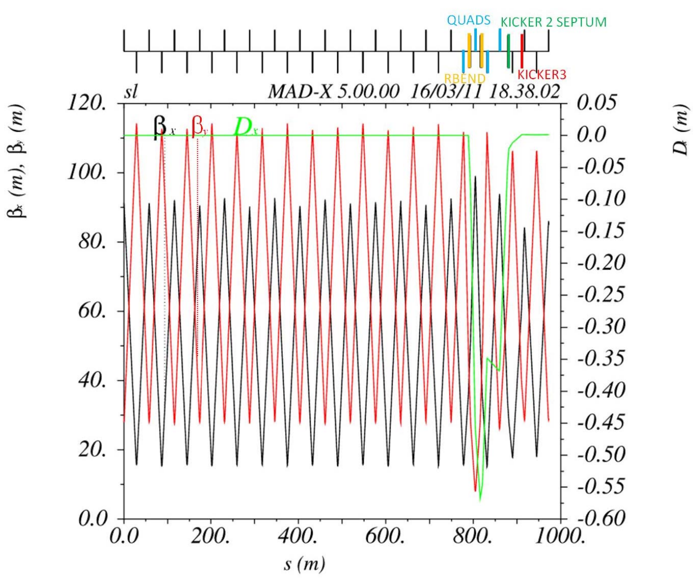

Figure 10.27: Transfer line optics for the injection onto orbit case (top) and mismatched injection case (bottom).

The last two cells are used for optics matching. In particular, four quadrupoles, 1 m long each, are used for β_x and β_y matching, while two rectangular bending magnets, 5 m long each, are used for matching the horizontal dispersion D_x to 0 (maximum D_x = -1.48 m for the injection onto closed orbit case and maximum D_x = -0.57 m for the mismatched injection case). The "good field region" for a 6σ beam envelope requires a minimum half-aperture, in the matching insertion, of 15 mm and 10 mm for the focusing and defocusing quadrupoles respectively, corresponding to a pole tip field of about 0.02 T. The maximum strength of the bending magnets, which are used for dispersion matching, corresponds to about 39 mrad. This requires 1.3 T m and a maximum field of 0.3 T. A single turn coil of 9.5 kA with a vertical gap of 40 mm could be used.

10.14 60 GeV internal dump

An internal dump will be needed for electron beam abort. The design for LEP [444] consisted of a boron carbide spoiler and an Aluminum alloy (6% copper, low magnesium) absorbing block (0.4 m $\times$ 0.4 m $\times$ 2.1 m long). A fast kicker was used to sweep eight bunches, of 8.3×10^{11} electrons at 100 GeV, onto the absorber. The first bunch was deflected by 65 mm and the last by 45 mm, inducing a temperature increase ΔT of 165°.

The bunch intensity for the LHeC is about a factor of 20 lower than for LEP and beam size is double (σ = 0.5 mm in LEP and σ = 1 mm in LHeC).

The lower energy (60 GeV) and energy density permit to dump 160 bunches in 20 mm to obtain the same ΔT as for LEP. However, in total LHeC will be filled with 2808 bunches, which means that significant additional dilution will be required. A combination of a horizontal and a vertical kicker magnet can be used, as an active dilution system, to paint the beam on the absorber block and increase the effective sweep length. The kickers and the dump can be located in the bypass around CMS, in a dispersion free region (see fig. 10.28).

It is envisaged to use Carbon-composite for the absorber block, since this has much better thermal and mechanical properties than aluminum. The required sweep length is then assumed to be about 100 mm, from scaling of the LEP design. The minimum sweep speed in this case is about 0.6 mm per μs, which means about 54 bunches per mm. Taking into account the energy and the beam size, this represents less than a factor 2 higher energy density on the dump block, compared to the average determined by the simple scaling, that should be feasible using carbon. More detailed studies are required to optimise the diluter and block designs. Vacuum containment, shielding and a water cooling system has to be incorporated. A beam profile monitor can be implemented in front of each absorber to observe the correct functioning of the beam dump system.

The vertical kicker would provide a nominal deflection of about 55 mm (see fig. 10.29), modulated by $\pm$13% for three periods during the 100 μs abort (see fig. 10.30), while the horizontal kicker strength would increase linearly from zero to give a maximum deflection at the dump of about 55 mm (see Fig. 10.29and Fig. 10.30). This corresponds to system kicks of 2.7 and 1.6 mrad respectively.

Parameters characterizing the kicker magnets are presented in Table 10.19.

In the present lattice the dump is placed ~30 m downstream of the kickers, corresponding to a phase advance of about 63° in the horizontal plane and 35° in the vertical plane. The minimum horizontal and vertical aperture at the dump are 26 mm and 22 mm respectively (at the dump: β_x = 37 m and β_y = 55 m, using the same beam and machine parameter

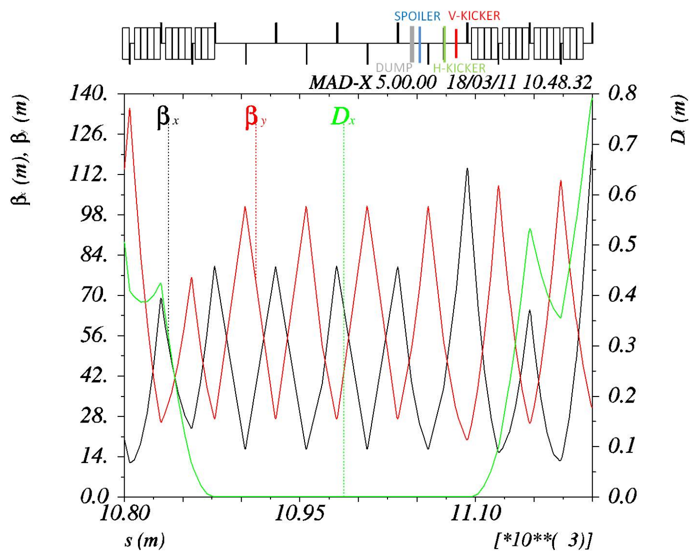

Figure 10.28: The optics in the region of the CMS bypass where the beam dump system could be installed is shown. The system consists of two kickers, one spoiler and a Carbon-composite absorber which are installed in the dispersion free region of the bypass at the right side of CMS (beam proceeds from right to left in the Figure).

assumptions, as presented in Table 10.17). The kicker system field rise time is assumed to be at most 3 μs (abort gap) and the kicker field flat-top at least 90 μs as for the LHC proton beam. Same design as for the LHC dump kicker magnets MKD can be used: a steel yoke with a one-turn HV winding. These magnets can provide a magnetic field in the gap of 0.34 T. For a magnetic length of 0.31 m (Z= 25 Ω and U = 60 kV), a total installed kicker length of 1.5 m for the horizontal system and 2.5 m for the vertical system has to be considered.

	MKDV	MKDH
Length [m]	2.5	1.5
Maximum angle [mrad]	2.7	1.6
Maximum field [T]	0.34	0.34
Rise/Fall time [ns]	800	800
Flat top length [μs]	90	90

Table 10.19: Parameters characterising vertical and horizontal kicker magnets of the extraction system.

A spoiler (one-side single graphite block: 0.3 m $\times$ 0.10 m $\times$ 0.5 m long) can be installed 5 m upstream of the dump at the extraction side to provide further dilution.

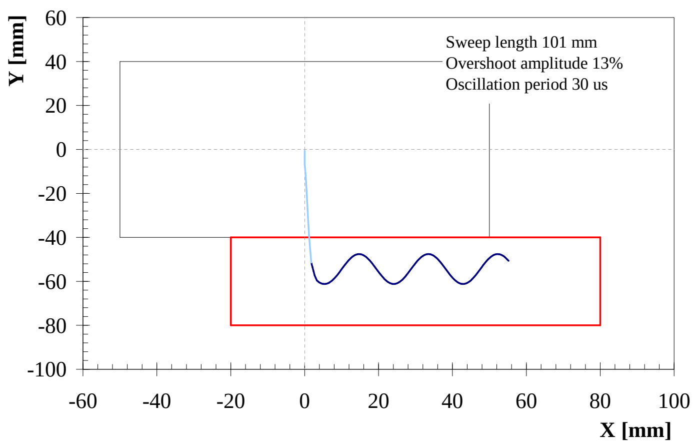

Figure 10.29: A vertical and a horizontal kicker are used to dilute the beam on the dump absorbing block.

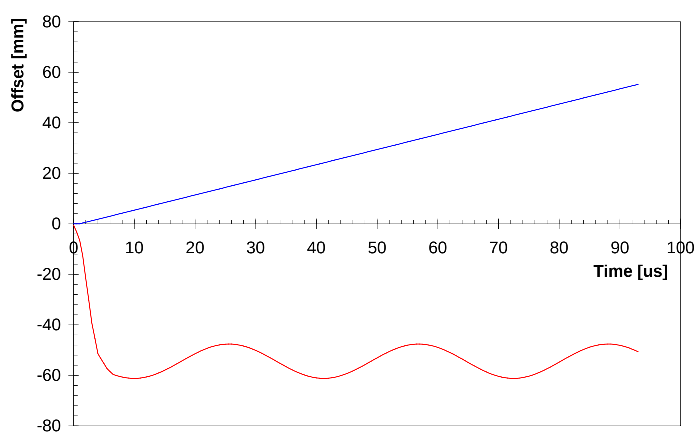

Figure 10.30: The strength of the vertical kicker oscillates in time by ± 13% around its nominal value.The deflection provided by the horizontal kicker increases almost linearly in time.

Part IV

Detector

Chapter 11

Detector Requirements

11.1 Requirements on the LHeC Detector

The new ep/A detector at the LHeC has to basically be a precision instrument of maximum acceptance. The physics programme depends on a high level of precision, as for the measurement of α_s, and in the reconstruction of complex final states, like the charged current single top production and decay or the precision measurement of the b-quark density. The acceptance has to extend as close as possible to the beam axis because of the interest in the physics at low and at large Bjorken x. The dimensions of the detector are constrained by the radial extension of the beam pipe in combination with maximum polar angle coverage [1], desirably down to about 1° and 179° for forward going final state particles and backward scattered electrons at low Q^2, respectively. A further general demand is a high modularity enabling much of the detector construction to be performed above ground for keeping the installation time at a minimum, and to be able to access inner detector parts within reasonable shut down times.

The time schedule of the project demands to have a detector ready within about ten years. This prevents any significant $R+D$ programme to be performed. The choice of components fortunately can rely on the vast experience obtained at HERA, the LHC, including its detector upgrades to come, and on ILC detector development studies. The next few sections outline the acceptance and measurement requirements on the detector in detail. Then follow more detailed technical considerations, including alternative solutions, which taken together illustrate the feasibility of experimentation at the LHeC. An overview on the detector as designed here is given in Fig. 11.1.

11.1.1 Installation and Magnets

The LHeC project represents an upgrade of the LHC. The experiment would be the fifth large experiment, and the detector the third multi-purpose 4π acceptance detector. It requires a

[1] This CDR adopts the HERA convention of the coordinate system, which has been defined with the z axis given by the proton beam direction. This implies that Rutherford "backscattering" of the electron is viewed as scattering into small angles. When the partons are essentially at rest, at very small x, the electrons are scattered "forward" as in fixed target forward spectrometers. The somewhat unfortunate HERA convention calls this backwards. The x and y coordinates are defined such that there is a right handed coordinate system formed with y pointing upwards and x to the center of the proton ring.

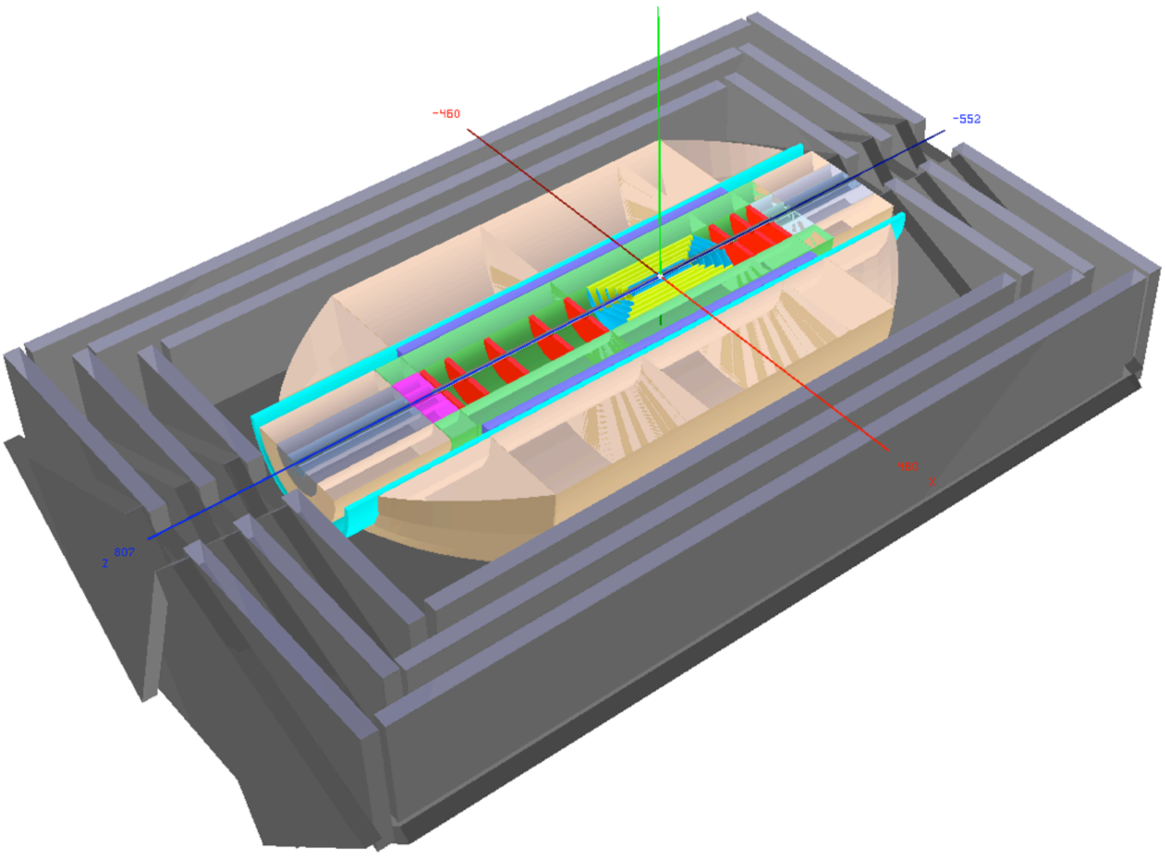

Figure 11.1: Overview of the LHeC detector design as presented in the subsequent chapter. The detector covers a polar angle acceptance down to 1° in backward and 179° in forward direction, which determines the geometry of the two (red) track telescopes. There is a central inner tracker with pixel (blue) and strip (yellow) components. The track detector is immersed in a solenoid field with the solenoid (blue) positioned around the electromagnetic calorimeter. In the LR version the solenoid is adjacent to an extended dipole magnet. For the LAr version of the eCAL both magnets and the calorimeter share a cryogenic system. A hadronic calorimeter (light ochre) surrounds the inner detector part, possibly built as an iron-scintillator (tile) calorimeter which serves as return yoke. In the very forward direction, a plug electromagnetic (pink) and hadronic (light grey) calorimeter measure the hadronic final state of very high energy O(1) TeV. The detector has a near to 4π acceptance also for the hadronic calorimeter. A muon detector (grey) surrounds the inner parts. The dimensions of the present design, in terms of its approximate length and diameter, are $15 \times 9\,\mathrm{m}^2$, to be compared with $21 \times 15\,\mathrm{m}^2$ of CMS and $45 \times 25\,\mathrm{m}^2$ of ATLAS. In backward (forward) direction the LHeC detector has taggers for electron and photon (proton, neutron and deuteron) detection, not shown.

Alice Caverne

Point 2 - Round access shaft of ~23m diameter, cavern about 50m along the beam-line

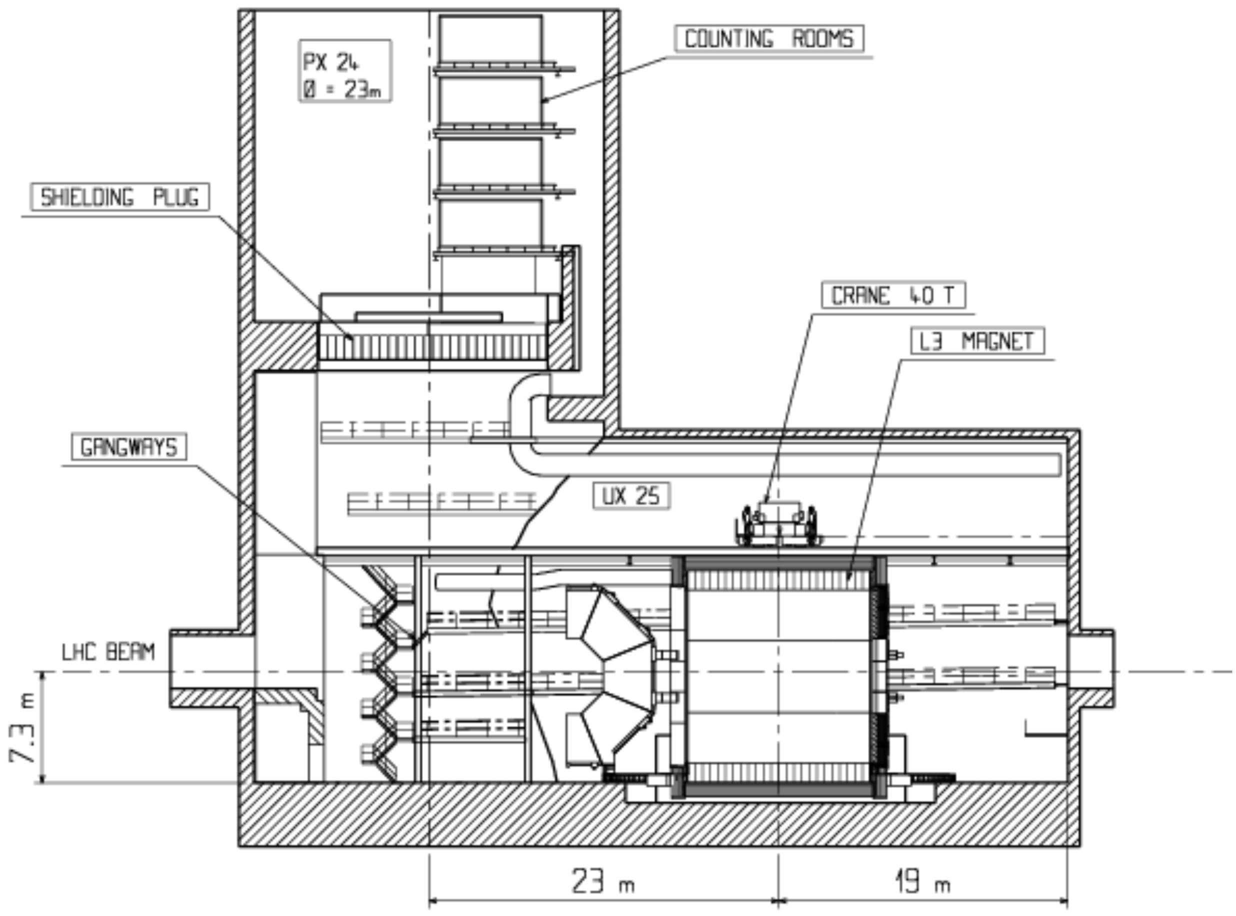

Figure 11.2: Cross section of the IP2 Caverne with the Alice detector inside the L3 magnet.

cavern, which for the purpose of the design study has been considered to be the ALICE cavern in IP2, see Fig. 11.2. The installation of the detector has to proceed as fast as possible in order to not introduce large extra delays to the LHC programme. High modularity and pre-assembly above ground are therefore inevitable demands for the design.

The cost has to be limited in order for the project to be fundable in parallel to when the large upgrade investments are presumably made for the ATLAS and CMS detectors in the high luminosity phase of the LHC. The cost is related to technology choices, the detector granularity and its size. Crucial parameters of the detector are the beam pipe dimensions, when combined with the small angle acceptance constraint, see below, and the parameters of the solenoid. The cost C of a solenoid can be represented as a function of the energy density, ρ_E, $C \simeq 0.5(\rho_E/MJ)^{0.66}$ [?], which is determined as

$$\rho_E = \frac{1}{2\mu_0} \cdot \int B^2 dV \simeq \frac{1}{2\mu_0} \cdot \pi r^2 \cdot l \cdot B^2. \tag{11.1}$$

From these relations one derives roughly that the solenoid cost scales linearly with the radius r and field strength B and with the length l to the power 0.66. The solenoid radius influences the track length in the transverse plane, which determines $\propto r^{-2}$ the transverse momentum resolution whereas field strength enters linearly $\propto B^{-1}$, see below.

In the current design the solenoid is placed in between the electromagnetic and the hadron calorimeter[2] at a radius of about 1 m. The field strength is set to 3.5 T in order to compensate the small radial extension of the tracker, the focus of which in the LHeC environment is on the forward direction.

The linac-ring version of the LHeC requires to put an extended dipole magnet of 0.3 T into the detector for ensuring head-on ep collisions and for separating the beams. The total material budget of the solenoid and the dipole, at perpendicular crossing, may be represented by about $8 + 1$ cm of Aluminium XXX– TO BE CHECKED LATER ONCE MORE, corresponding to one quarter of an interaction length but one X_0. The magnets therefore better are not placed in front of the electromagnetic calorimeter, yet placed before the hadronic calorimeter in order to limit the radial dimensions.

A detailed design study of the detector magnets is presented below.

11.1.2 Kinematic reconstruction

The inclusive ep DIS kinematics are defined by the negative four-momentum transfer squared, Q^2, and Bjorken x. Both are related to the cms energy squared s via the inelasticity y through the relation $Q^2 = sxy$, which implies $Q^2 \leq s$. The energy squared s is determined by the product of the beam energies, $s = 4E_pE_e$, for head-on collisions and large energies compared to the proton mass.

The kinematics are determined from the scattered electron with energy E'_e and polar angle θ_e and from the hadronic final state of energy E_h and scattering angle θ_h. The variables Q^2

[2] An option is also considered of placing the solenoid outside the calorimeters, at about 2.5 m radius, combined with a second, bigger solenoid for the flux return, with the muon detector in between. A two-solenoid solution was considered already in the fourth detector concept for the ILD [?].

and y can be calculated from the scattered electron kinematics as

$$\begin{aligned} Q_e^2 &= 4E_eE'_e\cos^2(\frac{\theta_e}{2}) \\ y_e &= 1-\frac{E'_e}{E_e}\sin^2(\frac{\theta_e}{2}) \end{aligned} \tag{11.2}$$

and from the hadronic final state kinematics as

$$\begin{aligned} Q_h^2 &= \frac{1}{1-y_h}\cdot E_h^2\sin^2(\theta_h) \\ y_h &= \frac{E_h}{E_e}\sin^2(\frac{\theta_h}{2}) \end{aligned} \tag{11.3}$$

and x is given as Q^2/sy. The kinematic reconstruction in neutral current scattering therefore is redundant, which is one reason why DIS experiments at ep colliders are precise. An important example is the calibration of the electromagnetic energy scale from the measurements of the electron and the hadron scattering angles. At HERA, this lead to energy calibration accuracies for E'_e at the per mil level. In a large part of the phase space, around $x = E_e/E_p$, the scattered electron energy is approximately equal to the beam energy, $E'_e \simeq E_e$, which causes a large "kinematic peak" in the scattered electron energy distribution. The hadronic energy scale can be obtained from the transverse momentum balance in neutral current scattering, $p_t^e \simeq p_t^h$. It is determined to about 1% at HERA.

Following Eq.11.3, the kinematics in charged current scattering is reconstructed from the transverse and longitudinal momenta and energy of the final state particles according to

$$\begin{aligned} Q_h^2 &= \frac{1}{1-y_h}\sum p_t^2 \\ y_h &= \frac{1}{2E_e}\sum(E-p_z). \end{aligned} \tag{11.4}$$

There have been many refinements used in the reconstruction of the kinematics, as discussed e.g. in [445], which for the principle design considerations, however, are of less importance.

11.1.3 Acceptance regions - scattered electron

The positions of isolines of constant energy and angle of the scattered electron in the (Q^2, x) plane are given by the relations:

$$\begin{aligned} Q^2(x, E'_e) &= sx\cdot\frac{E_e-E'_e}{E_e-xE_p} \\ Q^2\ (x,\theta_e) &= sx\cdot\frac{E_e}{E_e+xE_p\tan^2(\theta_e/2)}. \end{aligned} \tag{11.5}$$

Following these relations, an acceptance limitation of the scattered electron angle, as due to the beam pipe or focussing magnets, to a maximum value θ_e^{max} defines a constant minimum Q^2 which independently of E_p is given as

$$Q^2_{min}(x,\theta_e^{max}) \simeq [2E_e\cot(\theta_e^{max}/2)]^2. \tag{11.6}$$

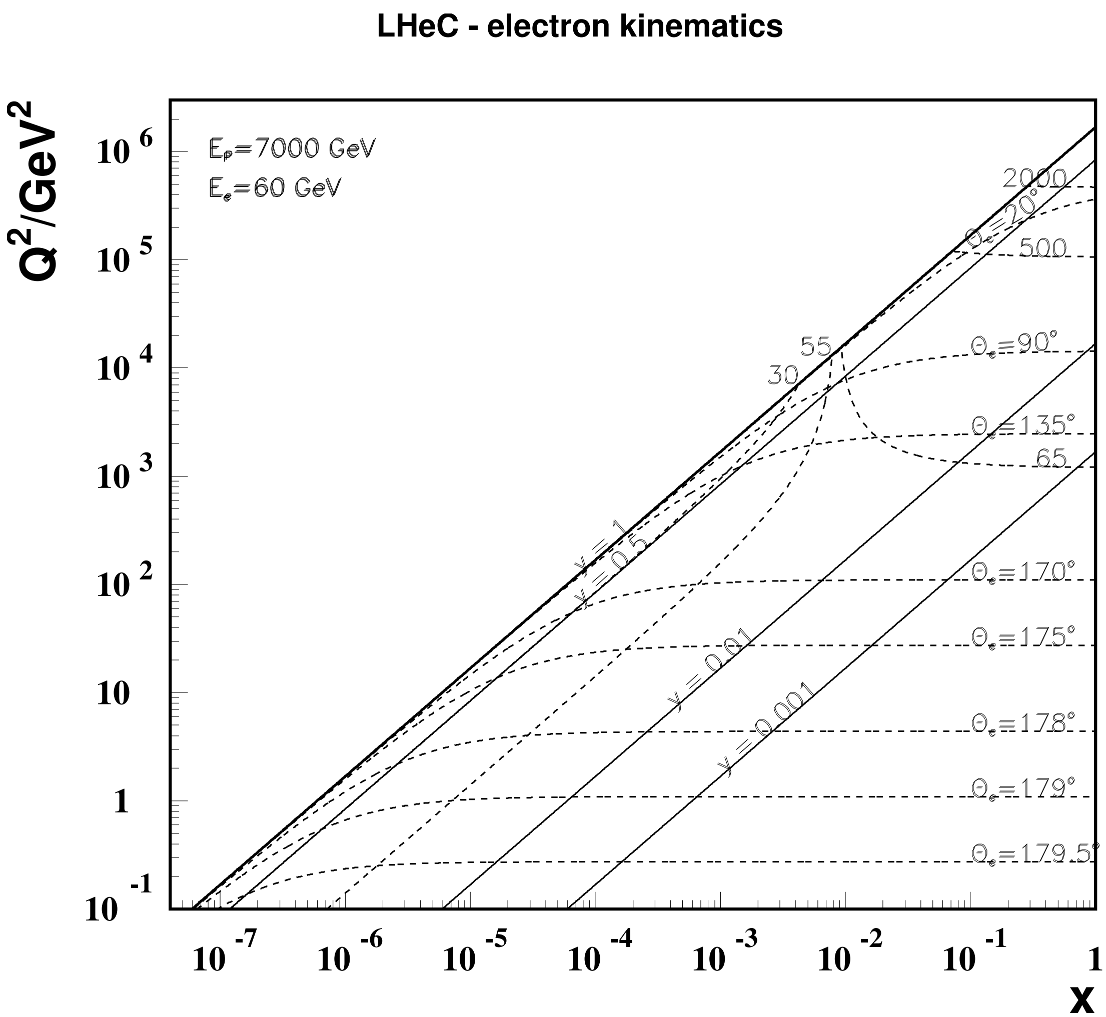

Figure 11.3: Kinematics of electron detection at the LHeC. Lines of constant scattering angle θ_e and energy, in GeV, are drawn. The region of low $Q^2 \lesssim 10^2\,\mathrm{GeV}^2$, comprising the lowest x region, requires to measure electrons scattered backwards with energies not exceeding E_e. At small energies, for $y \lesssim 0.5$ a good e/h separation is important to suppress hadronic background, as from photoprodocution. The barrel calorimeter part, of about $90 \pm 45°$, measures scattered electrons of energy not exceeding a few hundreds of GeV, while the forward calorimeter has to reconstruct electron energies of a few TeV. Both the barrel and the forward calorimeters measure the high x part, which requires very good scale calibration as the uncertainties diverge $\propto 1/(1-x)$ towards large x.

apart from the smallest x. This is illustrated in Fig. 11.3. There follows that a $179^\circ(170^\circ)$ angular cut corresponds to a minimum Q^2 of about $1\,(100)\,\mathrm{GeV}^2$ at nominal electron beam energy. One easily recognises in Fig. 11.3 that the physics at low x and Q^2 requires to measure electrons scattered backwards from about 135° up to 179°. Their energy in this θ_e region does not exceed E_e significantly. At lower x to very good approximation $y = E'_e/E_e$ (as can be seen from the lines $y = 0.5$ and $E'_e = 30\,\mathrm{GeV}$ in Fig. 11.3).

Following Eq. 11.6, Q^2_{min} varies $\propto E_e^2$. It thus is as small as $0.03\,\mathrm{GeV}^2$ for $E_e = 10\,\mathrm{GeV}$, the injection energy of the ring accelerator but increases to $6.0\,\mathrm{GeV}^2$ for $E_e = 140\,\mathrm{GeV}$, the maximum electron beam energy considered in this design report, apart from smallest x, if $\theta_e^{max} = 179^\circ$. While Q^2_{min} decreases $\propto E_e^2$, the acceptance loss towards small x is only $\propto E_e$. The measurement of the transition region from hadronic to partonic behaviour, from 0.1 to $10\,\mathrm{GeV}^2$, therefore requires to take data at lower electron beam energies[3]. These variations are illustrated in Fig. 11.4 for an electron beam energy of 10 GeV, the injection energy for the ring and a one-pass linac energy, and for the highest E_e of 140 GeV considered in this report.

Electrons scattered forward correspond to scattering at large $Q^2 \geq 10^4\,\mathrm{GeV}^2$, as is illustrated in the zoomed kinematic region plot Fig. 11.5. The energies in the very forward region, $\theta_e \lesssim 10^\circ$, exceed 1000 GeV. For large E_e and x, Eq. 11.5 simplifies to $Q^2 \simeq 4E_eE'_e$, i.e. a linear relation of Q^2 and E'_e which is independent of x and of E_p, apart from the fact that $Q^2_{max} = s$.

11.1.4 Acceptance regions - hadronic final state

The positions of isolines in the (Q^2, x) plane of constant energy and angle of the hadronic final state, approximated here by the current jet or struck quark direction, are given by the relations:

$$
\begin{aligned}
Q^2(x, E_h) &= sx \cdot \frac{xE_p - E_h}{xE_p - E_e} \\
Q^2\,(x, \theta_h) &= sx \cdot \frac{xE_p}{xE_p + E_e \cot^2(\theta_h/2)}
\end{aligned}
\tag{11.7}
$$

and are illustrated in Fig. 11.6. At low $x \lesssim 10^{-4}$, the hadronic final state is emitted backwards, $\theta_h > 135^\circ$, with energies of a few GeV to a maximum of E_e. Lines at constant y at low x are approximately at $y = 1 - E'_e/E_e$ and $E'_e + E_h = E_e$, i.e. $y = E_h/E_e$. Final state physics at lowest $x \lesssim 3 \cdot 10^{-6}$ requires access to the backward region within a few degrees of the beam pipe (Fig. 11.6). This is the high y region in which the longitudinal structure function is measured.

[3]The requirement of acceptance up to 179° determines the length of the backward detector. It could be tempting to utilise this E_e dependence in the design: if one limited the backward electron acceptance to for example 178° instead of 179° this would reduce the backward detector extension in $-z$. With data taken at reduced E_e one would come back to lower Q^2. From Eq. 11.6 one derives that $E_e = 30\,\mathrm{GeV}$ and 178° is leading to the same Q^2_{min} of about $1.1\,\mathrm{GeV}^2$, at not extremely small x, as is $E_e = 60\,\mathrm{GeV}$ and 179° However, one would loose in acceptance to the lowest x, linearly with E_e. Moreover, for the present design the (inner) beam pipe radius in vertical direction is 2.2 cm. This results in an extension of about 1.5 m for the first tracker plane to register an electron scattered at 179°. If one adds about 1 m for the tracker length, and 1 m for the backward calorimeter following the tracker, one arrives at about 3.5 m backward detector length. Obviously for 178° one could reduce the first 1.5 m to say 80 cm but one would still like to have a sizeable tracker length for achieving some sagitta to determine the charge of the scattered electron and perhaps arrive at an overall backward detector length of about 2.5 m. While this is an interesting reduction one looses the lowest x corner which opens $\propto E_e$. The access to lowest x in the DIS region is a fundamental part of the LHeC physics programme and thus the about 179° design requirement has been kept. There are reasons to take data with reduced E_e as for F_L, thus the LHeC detector will access the region below $1\,\mathrm{GeV}^2$ too.

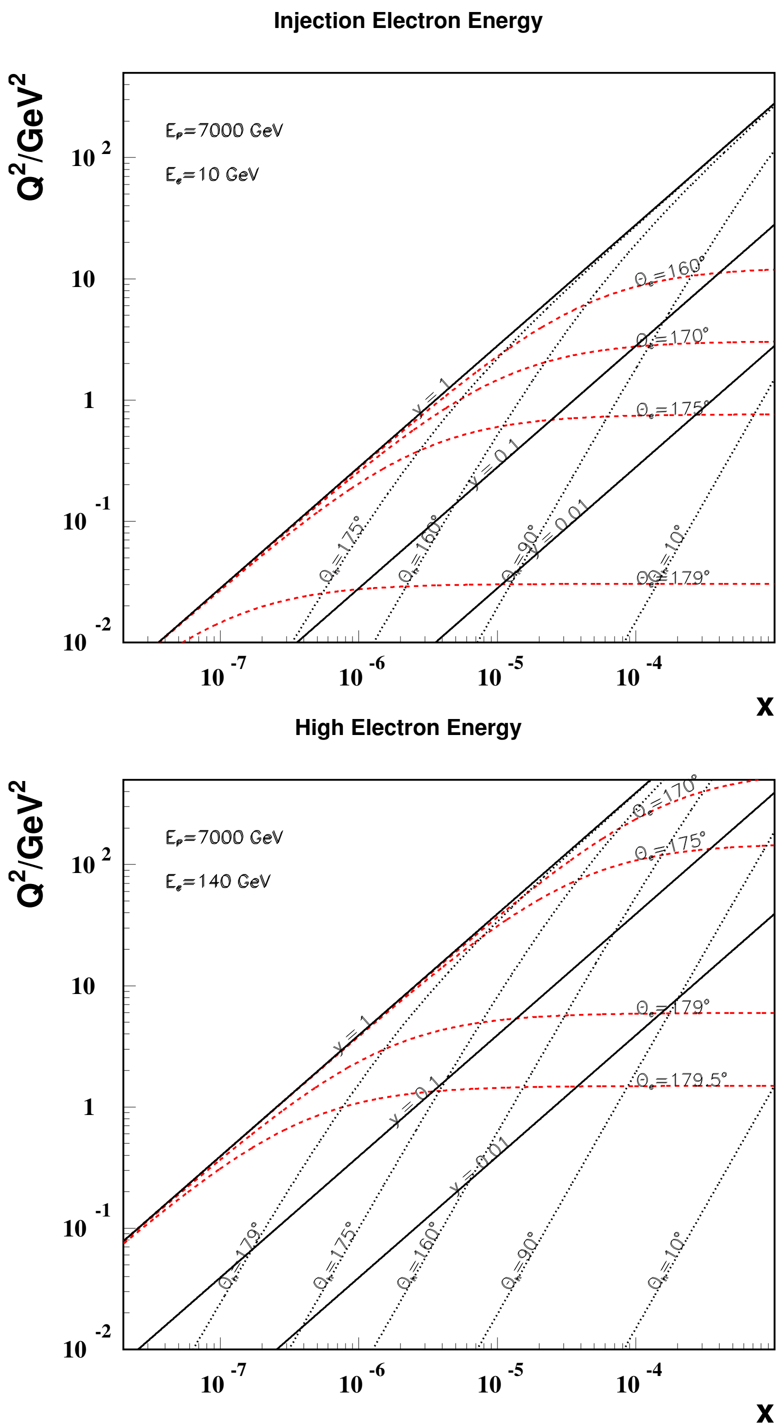

Figure 11.4: Kinematics at low x and Q^2 of electron and hadronic final state detection at the LHeC with an electron beam energy of 10 GeV (top) as compared to 140 GeV (bottom). At larger x, the iso-θ_e lines are at about constant $Q^2 \propto E_e^2$. At low x, the scattered energies, not drawn here, are approximately at $E'_e \simeq (1-y) \cdot E_e$, and at lower Q^2 and x one has $E_h \simeq E_e - E'_e \simeq y \cdot E_e$. At very high E_e part of the very low Q^2 region may be accessible with the electron tagged along the e beam direction, outside the central detector, and the kinematics measured with the hadronic final state.

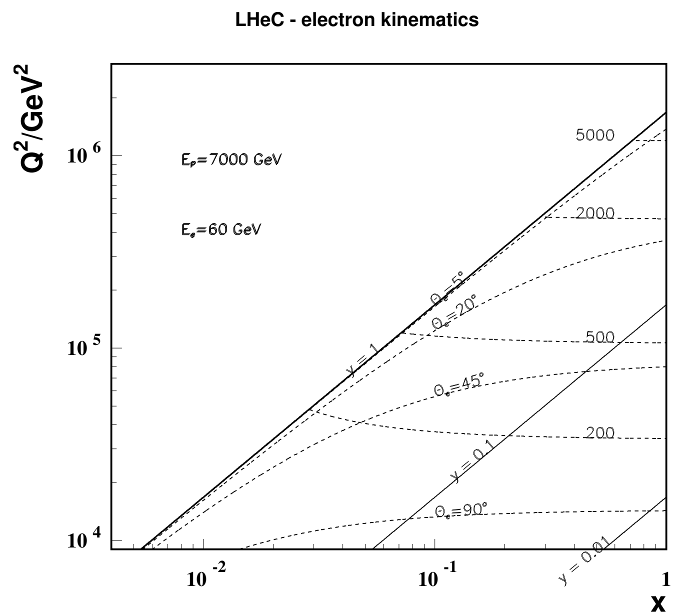

Figure 11.5: Kinematics of electron detection in the forward detector region corresponding to large $Q^2 \geq 10^4\,\mathrm{GeV}^2$. The energy values are given in GeV. At very high Q^2 the iso-E'_e lines are rather independent of x, i.e. $Q^2(x, E'_e) \simeq 4E_eE'_e$.

The x range accessed with the barrel calorimeter region, of θ_h between 135° and 45°, is typically around 10^{-4} and smaller than a decade for each Q^2, as can be seen in Fig. 11.6. The hadronic energies in this part do not exceed typically 200 GeV. The detector part which covers this region is quite large but the requirements are modest. One might even be tempted to consider a two-arm spectrometer only. However, the measurement of missing transverse energy and the importance of using the longitudinal momentum conservation for background and radiative correction reductions, with the $E - p_z$ criterion, demand the detector to be hermetic and complete.

For the measurement of the hadronic final state the forward detector is most demanding. Due to the high luminosity, the large x region will be populated and a unique physics programme at large x and high Q^2 may be pursued. In this region the relative systematic error increases like $1/(1-x)$ towards large x, see below. At high x and not extreme Q^2 the $Q^2(x, E_h)$ line degenerates to a line $x = E_h/E_p$ as can be derived from Eq. 11.7 and be seen in Fig. 11.6. High x coverage thus demands the registration of up to a few TeV of energy close to the beam pipe, i.e. a dedicated high resolution calorimeter is mandatory for the region below about $5 - 10°$ extending to as small angles as possible. A minimum angle cut $\theta_{h,min}$ in the forward region, the direction of the proton beam, would exclude the large x region from the hadronic final state acceptance (Fig. 11.6), along a line

$$Q^2\ (x, \theta_{h,min}) \simeq [2E_px\tan^2(\theta_{h,min}/2)]^2, \tag{11.8}$$

which is linear in the $\log Q^2$, $\log x$ plot and depends on E_p only. Thus at $E_p = 7\,\mathrm{TeV}$ the minimum Q^2 is roughly $(1000[100]x)^2$ at a minimum angle of $10[1]°$. Since the dependence in

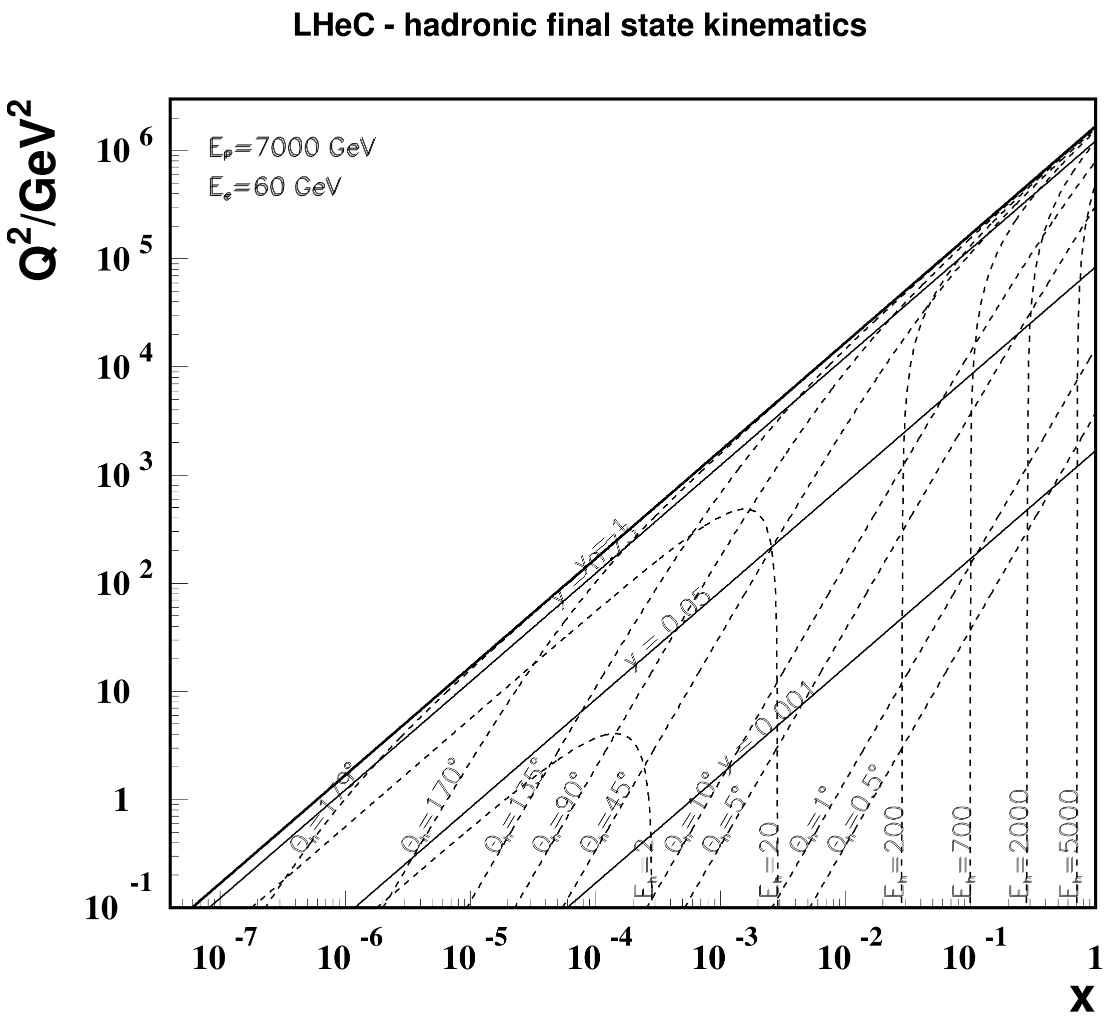

Figure 11.6: Kinematics of hadronic final state detection at the LHeC. Lines of constant energy and angle of the hadronic final state are drawn, as represented by simple kinematics of the struck quark. One easily recognises that the most demanding region is the large x domain, where very high energetic final state particles are scattered close to the (forward) direction of the proton beam. The barrel region, of about $90 \pm 45°$, is rather modest in its requirements. At low x the final state is not very energetic, $E_h + E'_e \simeq E_e$, and scattered into the backward detector region.

Eq. 11.8 is quadratic with E_p, lowering the proton beam energy is of considerable interest for reaching the highest possible x and overlapping with the large x data of previous experiments or searches for specific phenomena as intrinsic heavy flavour.

11.1.5 Acceptance at the High Energy LHC

Presently one considers to build a high energy (HE) LHC in the thirtees with proton beam energies of 16 TeV [**?**]. Such an accelerator would better be combined with an electron beam of energy exceeding the 60 GeV, considered as default here, in order to profit from the doubled proton beam energy and to limit the asymmetry of the two beam energies. Choosing the 140 GeV beam mentioned above as an example, Figure 11.7 displays the kinematics and acceptance regions for given scattering angles and energies of the electron (dashed green and red) and of the hadronic final state (black, dotted and dashed dotted). The cms energy in this case is enhanced by about a factor of five. The maximum Q^2 reaches $10\,\mathrm{TeV}^2$, which is 10^6 times higher than the typical momentum transfer squared covered by the pioneering DIS experiment at SLAC. The kinematic constraints in terms of angular acceptance would be similar to the present detector design as can be derived from the Q^2, x plot. At very high x (Q^2) the energy E_h (E'_e) to be registered would be doubled. With care in the present design, one would probably be able to use the main LHeC detector components also in the HE phase of the LHC.

11.1.6 Energy Resolution and Calibration

The LHeC detector is dedicated to most accurate measurements of the strong and electroweak interaction and to the investigation of new phenomena. The calorimetry therefore requires:

- Optimum scale calibrations, as for the measurement of the strong coupling constant. This is much helped by the redundant kinematic reconstruction and kinematic relations, as $E'_e \simeq E_e$ at low Q^2, $E'_e + E_h \simeq E_e$ at small x, the double angle reconstruction [**?**] of E'_e and the transverse momentum balance of p_T^e and p_T^h. From the experience with H1 and the much increased statistics it is assumed that E'_e may be calibrated to $0.1 - 0.5\,\%$ and E_h to $1 - 2\,\%$ accuracy. The latter precision will be most crucial in the foward, high x part of the calorimeter because the uncertainties diverge $\propto 1/(1-x)$ towards large x.

- High resolution, for the reconstruction of multi-jet final states as from the $H \to b\bar{b}$ decay. This is a particular challenge for the forward calorimeter. While detailed simulations are still ongoing one may assume that $(10-15)/\sqrt{E/GeV}\,\%$ resolutions for E'_e and $(40-50)/\sqrt{E/GeV}\,\%$ for E_h are appropriate, with small linear terms. These requirements are very similar to the ATLAS detector which quotes electromagnetic resolutions of $10/\sqrt{E/GeV} \oplus 0.007\,\%$ and hadronic energy resolutions of $50/\sqrt{E/GeV} \oplus 0.03\,\%$. The basic electromagnetic calorimeter choice for the LHeC can be for Liquid Argon [4]. The hadronic calorimeter is outside the magnets, see 11.1.1, and serving also for the magnetic flux return may be built as a tile calorimeter with the additional advantage of supporting the whole detector. The first year of operating the ATLAS combined LAr/TileCal calorimeter has been encouraging. Some special calorimeters are needed in the small angle

[4] In H1 very good experience has been collected with the longterm stability of the LAr calorimeter. A special demand is the low noise performance because the measurements at small inelasticity y are crucial for reaching large Bjorken x. In this region a small misidentified deposition of energy in the backward part of the detector can spoil the measurement at low $y \lesssim 0.01$, as can be seen from Eq. 11.4.

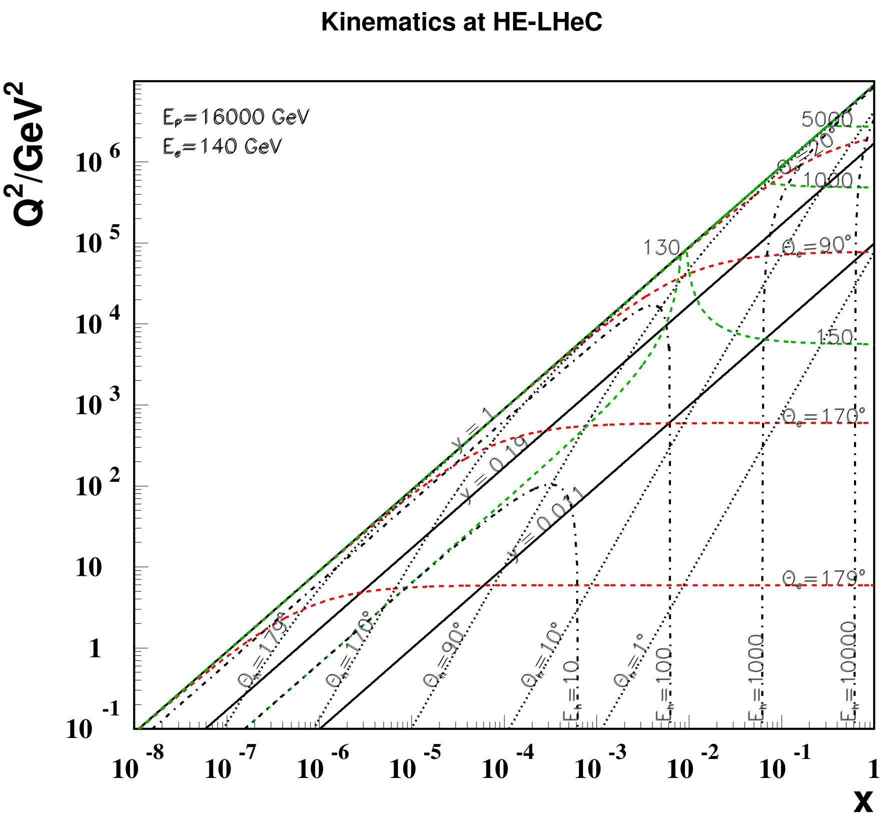

Figure 11.7: Scattered electron and hadronic final state kinematics for the HE-LHC at $E_p = 16\,\mathrm{TeV}$ coupled with a $140\,\mathrm{GeV}$ electron beam. Lines of constant scattering angles and energies are plotted. The line $y = 0.011$ defines the edge of the HERA kinematics and $y = 0.19$ defines the edge of the default machine considered in this report ($E_e = 60\,\mathrm{GeV}$ and $E_p = 7\,\mathrm{TeV}$).

forward region ($\theta \lesssim 5^\circ$) where the deposited energies are extremely large, and also in the backward region ($\theta \geq 135^\circ$) where the electron detection of modest energy is a special task.

- Good electron-hadron separation, as for the electron identification at high y and low Q^2 (backwards) or high Q^2 (in the extreme forward direction). This is a requirement on the segmentation of the calorimeters and on building trackers in front also of the forward and backward calorimeters to support the energy measurements and the electron identification in particular.

Obviously the calorimetry needs to be hermetic for the identification of the charged current process and good measurement of $E_{T,miss}$. These considerations are also summarised in Tab. 11.1.

region of detector	backward	barrel	forward
approximate angular range / degrees	179 - 135	135 -45	45-1
scattered electron energy/GeV	3-100	10-400	50-5000
x_e	$10^{-7} - 1$	$10^{-4} - 1$	$10^{-2} - 1$
elm scale calibration in %	0.1	0.2	0.5
elm energy resolution $\delta E/E$ in % $\cdot\sqrt{E/GeV}$	10	15	15
hadronic final state energy/GeV	3-100	3-200	3-5000
x_h	$10^{-7} - 10^{-3}$	$10^{-5} - 10^{-2}$	$10^{-4} - 1$
hadronic scale calibration in %	2	1	1
hadronic energy resolution in % $\cdot\sqrt{E/GeV}$	60	50	40

Table 11.1: Summary of calorimeter kinematics and requirements for the default design energies of $60 \times 7000\,\mathrm{GeV}^2$, see text. The forward (backward) calorimetry has to extend to $1^\circ(179^\circ)$.

11.1.7 Tracking Requirements

The tracking detector has to enable

- Accurate measurements of the transverse momenta and polar angles
- Secondary vertexing in a maximum polar angle acceptance range
- Resolution of complex, multiparticle and highly energetic final states in forward direction
- Charge identification of the scattered electron
- Distinction of neutral and charged particle production
- Measurement of vector mesons, as the J/ψ or Υ decay into muon pairs

The transverse momentum resolution in a solenoidal field can be approximated by

$$\frac{\delta p_T}{p_T^2} = \frac{\Delta}{0.3BL^2} \cdot \sqrt{\frac{720}{N+4}} \tag{11.9}$$

where B is the field strength, Δ is the spatial hit resolution and L the track length in the plane transverse to the beam direction, and N being the number of measurements on a track, which enters as prescribed in [**?**]. As an example, for $B = 3.5\,\mathrm{T}$, $\Delta = 10\,\mu\mathrm{m}$, $N = 4+5$ and $L = 0.6\,\mathrm{m}$ one obtains a transverse momentum measurement accuracy of about $3 \cdot 10^{-4}$. A simulation, using the LICTOY program [**?**], of the transverse momentum, transverse impact parameter and polar angle resolutions is shown in Fig. 11.8. One can see that the estimate following Eq. 11.9 is approximately correct for larger momenta where the multiple scattering becomes negligible. This momentum resolution, in terms of $\delta p_T/p_T^2$ is about ten times better than the one achieved with the H1 central drift chamber. It is similar to the ATLAS momentum resolution for central tracks and thus considered to be adequate for the enlarged momenta at LHeC as compared to HERA and the goal of high precision vertex tagging. One finds that the impact parameter resolution, for high momenta, is a factor of eight improved over the H1 or ZEUS result.

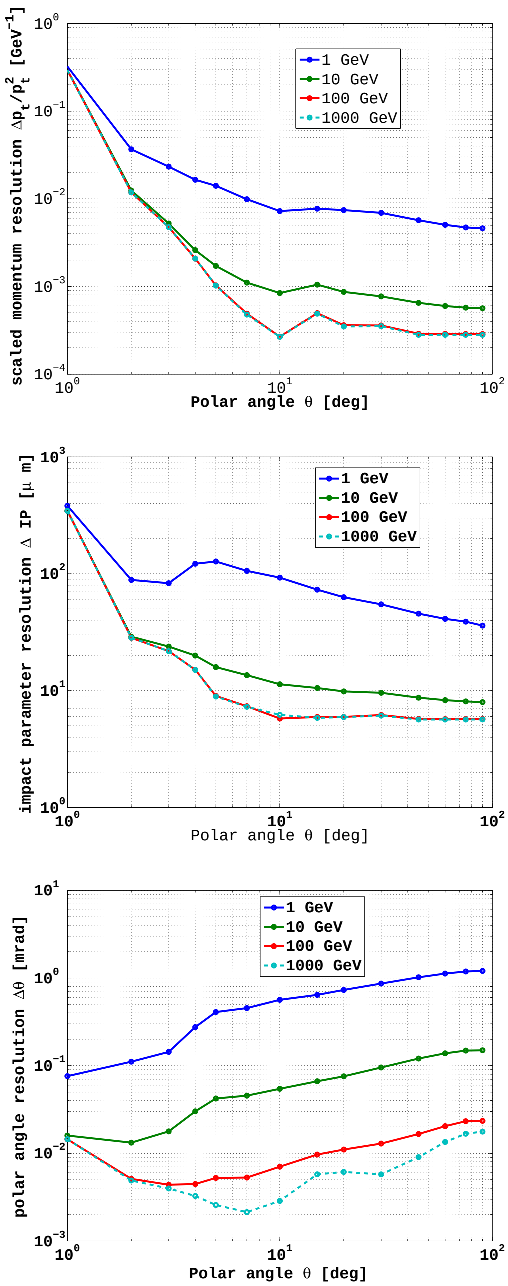

Figure 11.8: Transverse momentum (top), impact parameter (middle) and polar angle (bottom) measurement resolutions as function of the polar angle for the default detector design for four values of track transverse momentum.

In backward direction, a main tracking task is to determine the charge of the scattered electron or positron, which has momenta $E'_e \leq E_e$, down to a few GeV for DIS at high $y \simeq 1 - E'_e/E_e$. With a beam spot as accurate as about $10 \times 30\,\mu\text{m}^2$ and the beam pipe radius of a few cm only, the backward Silicon strip tracker will allow a precise E/p determination when combined with the backward calorimeter, even better than has been achieved with the H1 backward silicon detector [**?**].

In the forward region, $\theta < 5°$, as may be deduced from Figs. 11.6, 11.5, the hadronic final state, for all Q^2, and the scattered electron, when scattered "back" at high Q^2, are very energetic. This requires a dedicated calorimeter. Depending on the track path and momentum, the track sagitta becomes very small, for example about $10\,\mu$m for a 1 TeV track momentum and a 1 m track length. In such extreme cases of high momenta, the functionality of the tracker will be difficult to achieve: the sagitta becoming small means that there will be limits to the transverse momentum measurement while the ability to distinguish photons and electrons will be compromised by the high probability of showering and conversion when the pipe is passed under very small angles. A forward tracker yet is considered to be useful down to small angles for the reconstruction of the event structure, the rejection of beam induced background and the reconstruction of forward going muons. This region requires detailed simulation studies in a next phase of the project.

11.1.8 Particle Identification Requirements

The requirements on the identification of particles focus on the identification of the scattered electron, a reliable missing energy measurement and precision tracking for measuring the decay of charm and beauty particles, the latter rather on a statistical basis than individually. Classic measurements as the identification of the D meson from the $K\pi\pi$ decay with a slow pion or the identification of B production from high p_T leptons require a very precise track detector. The tracker should determine some dE/dX properties but there is no attempt to distinguish strange particles, as kaons from pions, as the measurement of the strange quark distribution is traced back to charm tagging in CC events. The identification of muons, apart from some focus on the forward and backward direction, is similar to that of pp detectors. In addition a number of taggers is foreseen to tag

- electrons scattered near the beam pipe in backward direction to access low Q^2 events and control the photoproduction background;
- photons scattered near the beam pipe in backward direction to measure the luminosity from Bethe Heitler scattering;
- protons scattered in forward direction to measure diffractive DIS in ep scattering and to tag the spectator proton in en scattering in electron-deuteron runs;
- neutrons scattered in forward direction to measure pion exchange in ep scattering and to tag the spectator neutron in ep scattering in electron-deuteron runs;
- deuterons scattered in forward direction in order to discover diffraction in lepton-nucleus scattering.

From the perspective of particle identification therefore no unusual requirements are derived. One needs a state of the art tracker with a very challenging forward part and a tagger system with the deuteron as a new component in forward direction.

Chapter 12

Central Detector

Chapter 13

Forward and Backward Detectors

13.1 Introduction

The goal of Zero Degree Calorimeter (ZDC) is to measure the energy and angles of very forward particles. At HERA experiments, H1 and ZEUS, the forward neutral particles scattered at polar angles below 0.75 mrad have been measured in the dedicated Forward Neutron Calorimeters (FNC) [**?**, 321]. The LHC experiments, CMS, ATLAS, ALICE and LHCf, have the ZDC calorimeters for detection of forward neutral particles, ALICE has also the ZDC calorimeter for the measurements of spectator protons [**?**, **?**, **?**, **?**, **?**].

The ZDC calorimeter will be an important addition to the future LHeC experiment as many physics measurements in *ep*, *ed* and *eA* collisions can be made possible with the installation of ZDC.

13.2 ZDC detector design

The position of the Zero Degree Calorimeter in the tunnel and the overall dimensions depend mainly on the space available for the installation. At the LHC the beams are deflected by two separating dipoles at about 50 m from interaction point (for IP2). These dipoles deflect the spectator protons, separating them from the neutrons, which scatter at $\sim 0^{\circ}$.

The ZDC detector will be made of two calorimeters: one for the measurement of neutral particles at 0° and another one positioned externally to the outgoing proton beam for the measurement of spectator protons from *eD* and *eA* scattering. The geometry, technical specifications and proposed design of ZDC detectors are to large extent similar to the ZDCs of the LHC experiments. Here the general considerations for the design are presented. In order to finalise the study of the geometry of detectors, a detailed simulation of the LHeC interaction region and the beamline must be performed.

13.2.1 Neutron Calorimeter

Similar to the ZDC of ALICE experiment [?, ?], the ZDC calorimeter for detection of neutral particles at the LHeC will be placed in a 90 mm narrow space between two beam pipes and have transverse size of about 7.2×7.2 cm^2. (The photo of neutron calorimeter of ALICE experiment is shown in Fig. 13.1). The design of ZDC has to satisfy various technical issues. Detector has to be capable of detecting neutrons and photons produced with scattering angles up to 0.3 mrad or more and energies between some hundreds GeV to the proton beam energy (7 TeV) with a reasonable resolution of few percents. It should be able to distinguish hadronic and electromagnetic showers (i.e. separate neutrons from photons) and to separate showers from two or more particle entering the detector (i.e. needs position resolution of $\mathcal{O}$(1mm) or better).

The condition, that at least 95% of hadronic shower of $\mathcal{O}$(TeV) is contained within the calorimeter, requires 9.5–10 nuclear interaction lengths of absorber. The neutron ZDC will be made of two sections. The front part of calorimeter (electromagnetic section) with 1.5-2 λ length and fine granularity is needed for precise determination of the position of impact point, discrimination of electromagnetic and hadronic showers and separation of showers from two or more particles entering the detector. The hadronic section of the ZDC can be built with coarser sampling, which gives an increase of average density and, consequently, the increase of effective nuclear interaction length. The ZDC will be operating in a very hard radiation environment, therefore it has to be made of radiation resistant materials. Since the different parts of calorimeter undergo different intensity of radiation (higher for front part), it is advantageous to have longitudinal segmentation of 4-5 identical sections, which will allow to control the change of energy response due to radiation damage. Comparison of the energy spectrum from the showers which start in different sections can be used for correction of changes in energy response.

A possible solution to build a compact device with good radiation resistance is to use spaghetti calorimeter with tungsten absorbers and quartz fibres. The principle of operation is based on the detection of Cherenkov light produced by the shower's charged particles in the fibres. These detectors are proven to be fast (∼few ns), radiation hard and have good energy resolution. Using tungsten as a passive material allows the construction of compact devices. One can also consider option to use thick gaseous electron multipliers (THGEM) [**?**,**?**] as active media.

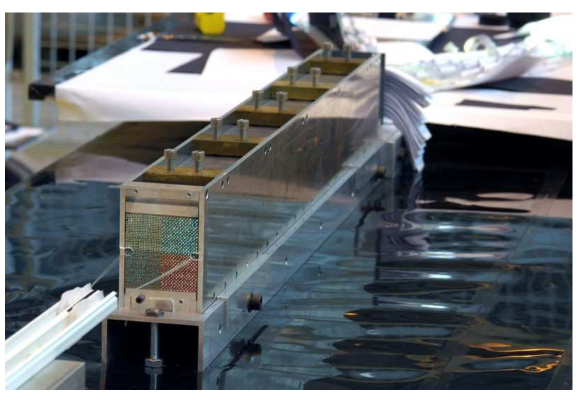

Figure 13.1: Photo of the Zero Degree Neutron Calorimeter (ZN) of ALICE experiment.

13.2.2 Proton Calorimeter

In analogy to ALICE experiment, the second ZDC for detection of spectator protons can be positioned externally to the outgoing proton beam at a same distance from IP as neutron ZDC [?, ?]. At this point the size of the spot of spectator protons is no longer gaussian. The size of proton ZDC has to be small either, due to the few cm small size of spectator proton spot. This calorimeter will be made with same technique as the neutron ZDC, with transverse size of about $23 \times 12\ cm^2$ to obtain shower containment.

13.2.3 Calibration and monitoring

After initial calibration of the ZDCs with test-beams, it is essential to have regular online and offline control of the stability of the response, in particular due to hard radiation and temperature environment. The stability of the gain of the PMTs and the radiation damage in fibres can be monitored using the laser or LED light pulses. The stability of absolute calibration can be monitored using the interactions of the proton beam and residual gas molecules in the beam-pipe and comparison with the results of Monte Carlo simulation based on pion exchange, as used at HERA [?,321]. A useful tool for absolute energy calibration will be the reconstruction of invariant masses, e.g. $\pi^0 \to 2\gamma$ or $\Lambda, \Delta \to n\pi^0$, with decay particles produced at very small opening angles and reconstructed in ZDC. This will however require the possibility to reconstruct several particles in the ZDC within one event.

Forward Proton Detection

In diffractive interactions between protons or between an electron and a proton, the proton may survive a hard collision and be scattered at a low angle θ along the beam line while loosing a small fraction ξ ($\sim 1\%$) of its energy. The ATLAS and CMS collaborations have investigated the feasibility to install detectors along the LHC beam line to measure the energy and momentum of such diffractively scattered protons [**?**]. Since the proton beam optics is primarily determined by the shape of the accelerator - which will not change for proton arm of the LHeC - the conclusions reached in this R&D study are still relevant for an LHeC detector.

In such a setup, diffractively scattered protons are separated from the nominal beam when traveling through dipole magnets with a slightly lower momentum. This spectroscopic behavior of the accelerator is described by the energy dispersion function, D_x, which, when multiplied with the actual energy loss, ξ, gives the additional offset of the trajectory followed by the off-momentum proton:

$$x_{\text{offset}} = D_x \times \xi.$$

The acceptance window in ξ is therefore determined by the closest possible approach of the proton detectors to the beam for low ξ and by the distance of the beam pipe walls from the nominal proton trajectory for high ξ. The closest possible approach is often taken to be equal to 12σ with σ equal to the beam width at a specific point. At the point of interest, 420m from the interation point, the beam width is approximatel equal to 250 μm. On the other hand, the typical LHC beam pipe radius at large distances from the interaction point is approximately 2 cm. Even protons that have lost no energy, will eventually hit the beam pipe wall if they are scattered at large angles. This therefore fixes the maximally allowed fourmomentum-transfer squared t, which is approximately equal to the square of the transverse momentum p_T of the scattered proton at the interaction point.

At 420 m from the interaction point, the dispersion function at the LHC reaches 1.5 m, which results in an optimal acceptance window for diffractively scattered protons (roughly $0.002 < \xi < 0.013$). The acceptance as function of ξ and t is shown in Fig. 13.2, using the LHC proton beam optics [**?**]. The small corrections to be applied for the LHeC proton beam optics are not considered to be relevant for the description of the acceptance.

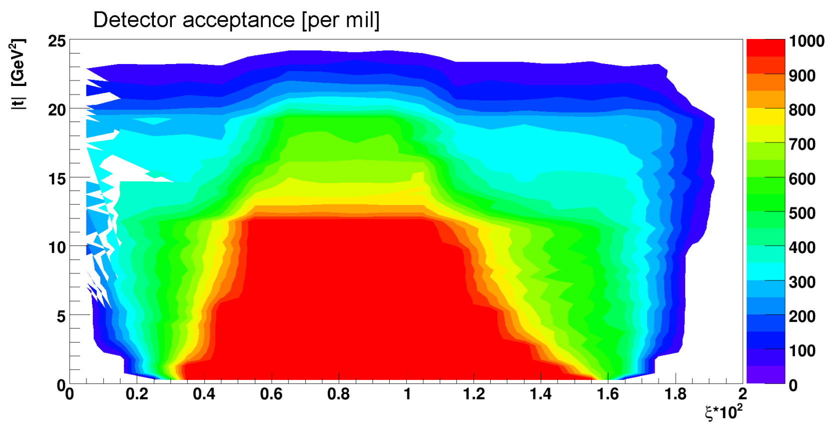

Figure 13.2: The acceptance for a proton detector placed at 420m from the interaction point is shown as function of the momentum loss ξ and the fourmomentum-transfer squared t. The color legend runs from 0‰(no acceptance) to 1000‰(full acceptance).

When the proton's position and angle w.r.t. the nominal beam can be accurately measured by the detectors, it is in principle possible to reconstructed the initial scattering angles and momentum loss of the proton at the interaction point. Even with an infinitesimally small detector resolution, the intrinsic beam width and divergence will still imply a lower limit on the resolution of the reconstructed kinematics. As the beam is typically maximally focussed at the interaction point in order to obtain a good luminosity, it will be the beam divergence that dominates the resolution on reconstructed variables.

Figure 13.3 show the relation of position and angle w.r.t. the nominal beam and the proton scattering angle and momentum loss in both the horizontal and vertical plane as obtained from the LHC proton beam optics [?]. Clearly, in order to distinguish angles and momentum losses indicated by the curves in Fig. 13.3, the detector must have a resolution better than the distance between the curves.

As stated above, protons with the same momentum loss and scattering angles will still end up at different positions and angles due to the intrinsic width and divergence of the beam. Lower limits on the resolution of reconstructed kinematics can therefore be determined. These are typically of the order of 0.5‰ for ξ and 0.2 μrad for the scattering angle θ. Figure 13.4 show the main dependences of the resolution on ξ, t and the azimuthal scattering angle ϕ.

A crucial issue in the operation of near-beam detectors is the alignment of the detectors w.r.t. the nonimal beam. Typically, such detectors are retracted when beams are injected and moved close to the beam only when the accelerator conditions are declared to be stable. Also the beam itself, may not always be reinjected at the same position. It is therefore important to realign the detectors at for each accelerator run and to monitor any drifts during the run. At

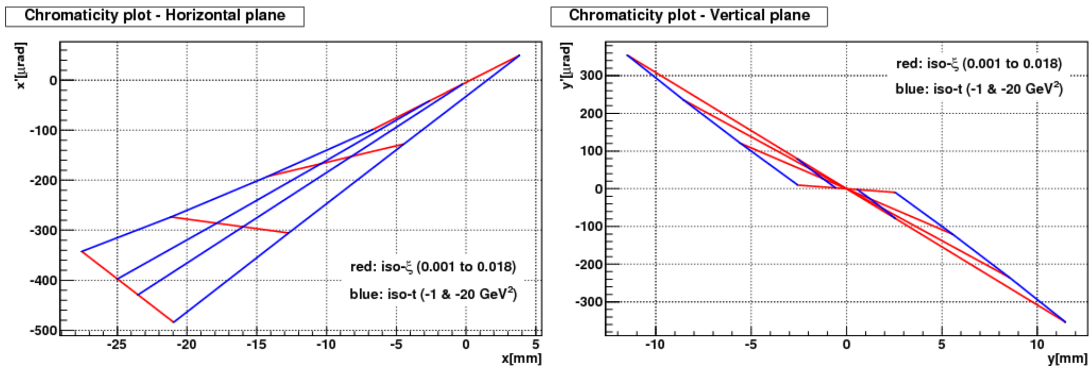

Figure 13.3: Lines of constant ξ and $t \approx (1-\xi)E_{\mathrm{beam}}\theta^2$ are shown in the plane of proton position and angle w.r.t. the nominal proton beam in the horizontal (left) and vertical (right) plane.

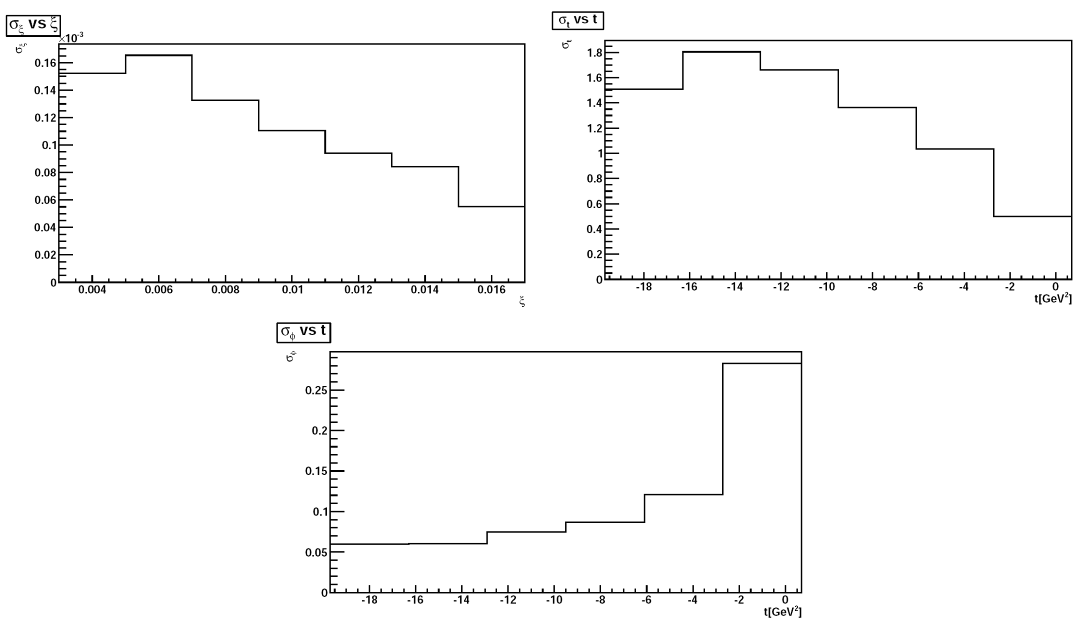

Figure 13.4: The lower limit due to the intrinsic beam width and divergence on the resolution of kinematic variables is shown for ξ as function ξ (top left), t as function t (top right) and ϕ as function of t (bottom).

HERA, a kinematic peak method section was used for alignment: as the reconstructed scattering angles depend on the misalignment, one may extract alignment constants by required that the observed cross section is maximal for forward scattering. In addition, this alignment procedure may be cross-checked by using a physics process with a exclusive system produced in the central detector such that the proton kinematics is fixed by applying energy-momentum conservation to the full set of final state particles. The feasibility of various alignment methods at the LHeC remains to be studied.

Part V

Summary

Acknowledgement

Many thanks to many

Bibliography

[1] H. Flacher, M. Goebel, J. Haller, A. Hocker, K. Monig, et al., *Gfitter - Revisiting the Global Electroweak Fit of the Standard Model and Beyond*, Eur.Phys.J. **C60** (2009, see `http://gfitter.desy.de/`) 543–583, `arXiv:0811.0009 [hep-ph]`.

[2] J. Erler, *The Mass of the Higgs Boson in the Standard Electroweak Model*, Phys.Rev. **D81** (2010) 051301, `arXiv:1002.1320 [hep-ph]`.

[3] P. Gambino, *The top priority: Precision electroweak physics from low to high energy*, Int. J. Mod. Phys. **A19** (2004) 808–820, `arXiv:hep-ph/0311257`.

[4] M. Davier, A. Hoecker, B. Malaescu, and Z. Zhang, *Reevaluation of the Hadronic Contributions to the Muon g-2 and to alpha(MZ)*, Eur.Phys.J. **C71** (2011) 1515, `arXiv:1010.4180 [hep-ph]`.

[5] S. Haywood, P. Hobson, W. Hollik, Z. Kunszt, G. Azuelos, et al., *Electroweak physics, hep-ph/0003275* , `arXiv:hep-ph/0003275 [hep-ph]`.

[6] K. Rabbertz, *QCD and Electroweak Physics at LHC*, PoS **RADCOR2009** (2010) 016, `arXiv:1002.3628 [hep-ph]`.

[7] S. `http://www.jlab.org/qweak/`, , .

[8] S. `http://hallaweb.jlab.org/12GeV/Moller/`, , .

[9] R. Cashmore, E. Elsen, B. A. Kniehl, and H. Spiesberger, *Electroweak physics at HERA: Introduction and summary*, `arXiv:hep-ph/9610251 [hep-ph]`.

[10] H1 and ZEUS Collaboration, Z. Zhang, *Electroweak and beyond the Standard Model results from HERA*, Nucl.Phys.Proc.Suppl. **191** (2009) 271–280, `arXiv:0812.4662 [hep-ex]`.

[11] H1 Collaboration, A. Aktas et al., *A Determination of electroweak parameters at HERA*, Phys.Lett. **B632** (2006) 35–42, `arXiv:hep-ex/0507080 [hep-ex]`.

[12] H1 Collaboration, Z.-Q. Zhang, *Combined electroweak and QCD fits including NC and CC data with polarised electron beam at HERA-2*, PoS **DIS2010** (2010) 056.

[13] E. Salvioni, A. Strumia, G. Villadoro, and F. Zwirner, *Non-universal minimal Z' models: present bounds and early LHC reach*, JHEP **1003** (2010) 010, `arXiv:0911.1450 [hep-ph]`.

[14] J. Erler and P. Langacker, *Indications for an extra neutral gauge boson in electroweak precision data*, Phys.Rev.Lett. **84** (2000) 212–215, `arXiv:hep-ph/9910315 [hep-ph]`.

[15] R. Barbier, C. Berat, M. Besancon, M. Chemtob, A. Deandrea, et al., *R-parity violating supersymmetry*, Phys.Rept. **420** (2005) 1–202, `arXiv:hep-ph/0406039 [hep-ph]`.

[16] M. Carpentier and S. Davidson, *Constraints on two-lepton, two quark operators*, Eur.Phys.J. **C70** (2010, and refs. therein) 1071–1090, `arXiv:1008.0280 [hep-ph]`.

[17] J. Erler, A. Kurylov, and M. J. Ramsey-Musolf, *The Weak charge of the proton and new physics*, Phys.Rev. **D68** (2003) 016006, `arXiv:hep-ph/0302149 [hep-ph]`.

[18] H. Jung, *Hard diffractive scattering in high-energy e p collisions and the Monte Carlo generator RAPGAP*, Comp. Phys. Commun. **86** (1995) 147–161.

[19] CTEQ Collaboration, H. L. Lai et al., *Global QCD analysis of parton structure of the nucleon: CTEQ5 parton distributions*, Eur. Phys. J. **C12** (2000) 375–392, `arXiv:hep-ph/9903282`.

[20] T. Sjostrand, S. Mrenna, and P. Z. Skands, *PYTHIA 6.4 Physics Manual*, JHEP **05** (2006) 026, `arXiv:hep-ph/0603175`.

[21] J. Pumplin et al., *New generation of parton distributions with uncertainties from global QCD analysis*, JHEP **07** (2002) 012, `arXiv:hep-ph/0201195`.

[22] G. Ingelman, A. Edin, and J. Rathsman, *LEPTO 6.5 - A Monte Carlo Generator for Deep Inelastic Lepton-Nucleon Scattering*, Comput. Phys. Commun. **101** (1997) 108–134, `arXiv:hep-ph/9605286`.

[23] M. Gluck, E. Reya, and A. Vogt, *Photonic parton distributions*, Phys. Rev. **D46** (1992) 1973–1979.

[24] M. Klasen and G. Kramer, *Inclusive two-jet production at HERA: Direct and resolved cross sections in next-to-leading order QCD*, Z. Phys. **C76** (1997) 67–74, `arXiv:hep-ph/9611450`.

[25] S. Catani and M. H. Seymour, *A general algorithm for calculating jet cross sections in NLO QCD*, Nucl. Phys. **B485** (1997) 291–419, `arXiv:hep-ph/9605323`.

[26] D. Stump et al., *Inclusive jet production, parton distributions, and the search for new physics*, JHEP **10** (2003) 046, `arXiv:hep-ph/0303013`.

[27] J. Pumplin, A. Belyaev, J. Huston, D. Stump, and W. K. Tung, *Parton distributions and the strong coupling: CTEQ6AB PDFs*, JHEP **02** (2006) 032, `arXiv:hep-ph/0512167`.

[28] T. Gehrmann and E. W. N. Glover, *Two-Loop QCD Helicity Amplitudes for (2+1)-Jet Production in Deep Inelastic Scattering*, Phys. Lett. **B676** (2009) 146–151, `arXiv:0904.2665 [hep-ph]`.

[29] A. Daleo, A. Gehrmann-De Ridder, T. Gehrmann, and G. Luisoni, *Antenna subtraction at NNLO with hadronic initial states: initial-final configurations*, JHEP **01** (2010) 118, `arXiv:0912.0374 [hep-ph]`.

[30] J. A. Bagger and M. E. Peskin, *EXOTIC PROCESSES IN HIGH-ENERGY e p COLLISIONS*, Phys. Rev. **D31** (1985) 2211.

[31] G. Altarelli, B. Mele, and R. Ruckl, *PHYSICS OF e p COLLISIONS IN THE TeV ENERGY RANGE*, . Presented at ECFA-CERN Workshop on Feasibility of Hadron Colliders in LEP Tunnel, Lausanne and Geneva, Switzerland, Mar 26-27, 1984.

[32] R. J. Cashmore et al., *EXOTIC PHENOMENA IN HIGH-ENERGY E P COLLISIONS*, Phys. Rept. **122** (1985) 275–386.

[33] G. Jarlskog, (Ed.) and D. Rein, (Ed.), *ECFA Large Hadron Collider Workshop, Aachen, Germany, 4-9 Oct 1990: Proceedings.1*, . CERN-90-10-V-1.

[34] G. Kopp, D. Schaile, M. Spira, and P. M. Zerwas, *Bounds on radii and magnetic dipole moments of quarks and leptons from LEP, SLC and HERA*, Z. Phys. **C65** (1995) 545–550, `arXiv:hep-ph/9409457`.

[35] A. F. Zarnecki, *Leptoquarks and Contact Interactions at LeHC*, `arXiv:0809.2917 [hep-ph]`.

[36] E. Eichten, K. D. Lane, and M. E. Peskin, *New Tests for Quark and Lepton Substructure*, Phys. Rev. Lett. **50** (1983) 811–814.

[37] R. Ruckl, *PROBING LEPTON AND QUARK SUBSTRUCTURE IN POLARIZED e-+ N SCATTERING*, Nucl. Phys. **B234** (1984) 91.

[38] P. Haberl, F. Schrempp, and H. U. Martyn, *Contact interactions and new heavy bosons at HERA: A Model independent analysis*, . In *Hamburg 1991, Proceedings, Physics at HERA, vol. 2* 1133-1148. (see HIGH ENERGY PHYSICS INDEX 30 (1992) No. 12988).

[39] A. F. Zarnecki, *Global analysis of eeqq contact interactions and future prospects for high-energy physics*, Eur. Phys. J. **C11** (1999) 539–557, `arXiv:hep-ph/9904334`.

[40] J. L. Hewett and T. G. Rizzo, *Low-Energy Phenomenology of Superstring Inspired E(6) Models*, Phys. Rept. **183** (1989) 193.

[41] E. Farhi and L. Susskind, *Technicolor*, Phys. Rept. **74** (1981) 277.

[42] C. T. Hill and E. H. Simmons, *Strong dynamics and electroweak symmetry breaking*, Phys. Rept. **381** (2003) 235–402, `arXiv:hep-ph/0203079`.

[43] J. C. Pati and A. Salam, *Lepton Number as the Fourth Color*, Phys. Rev. **D10** (1974) 275–289.

[44] W. Buchmuller, R. Ruckl, and D. Wyler, *Leptoquarks in lepton quark collisions*, Phys. Lett. **B191** (1987) 442–448.

[45] B. Schrempp, *Leptoquarks and leptogluons at HERA: Theoretical perspectives*, . In *Hamburg 1991, Proceedings, Physics at HERA, vol. 2* 1034-1042. (see HIGH ENERGY PHYSICS INDEX 30 (1992) No. 12988).

[46] S. Davidson, D. C. Bailey, and B. A. Campbell, *Model independent constraints on leptoquarks from rare processes*, Z. Phys. **C61** (1994) 613–644, `arXiv:hep-ph/9309310`.

[47] M. Leurer, *A Comprehensive study of leptoquark bounds*, Phys. Rev. **D49** (1994) 333–342, `arXiv:hep-ph/9309266`.

[48] A. Belyaev, C. Leroy, R. Mehdiyev, and A. Pukhov, *Leptoquark single and pair production at LHC with CalcHEP/CompHEP in the complete model*, JHEP **09** (2005) 005, `arXiv:hep-ph/0502067`.

[49] D0 Collaboration, V. M. Abazov et al., *Search for pair production of first-generation leptoquarks in p pbar collisions at sqrt(s)=1.96 TeV*, Phys. Lett. **B681** (2009) 224–232, `arXiv:0907.1048 [hep-ex]`.

[50] A. Belyaev and A. Pukhov.

[51] A. Pukhov, *Calchep 2.3: MSSM, structure functions, event generation, 1, and generation of matrix elements for other packages*, `arXiv:hep-ph/0412191`.

[52] S. Ovyn, X. Rouby, and V. Lemaitre, *Delphes, a framework for fast simulation of a generic collider experiment*, `arXiv:0903.2225 [hep-ph]`.

[53] H. Harari, *A Schematic Model of Quarks and Leptons*, Phys. Lett. **B86** (1979) 83.

[54] H. Fritzsch and G. Mandelbaum, *Weak Interactions as Manifestations of the Substructure of Leptons and Quarks*, Phys. Lett. **B102** (1981) 319.

[55] O. W. Greenberg and J. Sucher, *A Quantum Structure Dynamic Model of Quarks, Leptons, Weak Vector Bosons, and Higgs Mesons*, Phys. Lett. **B99** (1981) 339.

[56] R. Barbieri, R. N. Mohapatra, and A. Masiero, *Compositeness and a Left-Right Symmetric Electroweak Model Without Broken Gauge Interactions*, Phys. Lett. **B105** (1981) 369–374.

[57] U. Baur and K. H. Streng, *COLORED LEPTON MASS BOUNDS FROM p anti-p COLLIDER DATA*, Phys. Lett. **B162** (1985) 387.

[58] A. Celikel, M. Kantar, and S. Sultansoy, *A search for sextet quarks and leptogluons at the LHC*, Phys. Lett. **B443** (1998) 359–364.

[59] S. S. M. Sahin and S. Turkoz, *Resonant production color octet electron at the LHeC*, . LHeC note XXXX.

[60] H. Harari, *COMPOSITE MODELS FOR QUARKS AND LEPTONS*, Phys. Rept. **104** (1984) 159.

[61] N. T. E. Sauvan. LHeC note XXXX.

[62] O. J. P. Eboli, S. M. Lietti, and P. Mathews, *Excited leptons at the CERN Large Hadron Collider*, Phys. Rev. **D65** (2002) 075003, `arXiv:hep-ph/0111001`.

[63] E. M. Gregores, M. C. Gonzalez-Garcia, and S. F. Novaes, *Discriminating new physics scenarios at NLC: The Role of polarization*, Phys. Rev. **D56** (1997) 2920–2927, `arXiv:hep-ph/9703430`.

[64] H1 Collaboration, F. D. Aaron et al., *Search for Excited Electrons in ep Collisions at HERA*, Phys. Lett. **B666** (2008) 131–139, `arXiv:0805.4530 [hep-ex]`.

[65] H1 Collaboration, F. D. Aaron et al., *A Search for Excited Neutrinos in e-p Collisions at HERA*, Phys. Lett. **B663** (2008) 382–389, `arXiv:0802.1858 [hep-ex]`.

[66] H1 Collaboration, F. D. Aaron et al., *Search for Excited Quarks in ep Collisions at HERA*, Phys. Lett. **B678** (2009) 335–343, `arXiv:0904.3392 [hep-ex]`.

[67] OPAL Collaboration, G. Abbiendi et al., *Search for charged excited leptons in e+ e- collisions at s**(1/2) = 183-GeV - 209-GeV*, Phys. Lett. **B544** (2002) 57–72, `arXiv:hep-ex/0206061`.

[68] DELPHI Collaboration, J. Abdallah et al., *Determination of the e+ e- −¿ gamma gamma (gamma) cross- section at LEP 2*, Eur. Phys. J. **C37** (2004) 405–419, `arXiv:hep-ex/0409058`.

[69] D0 Collaboration, V. M. Abazov et al., *Search for excited electrons in $p\bar{p}$ collisions at $\sqrt{s}$ = 1.96-TeV*, Phys. Rev. **D77** (2008) 091102, `arXiv:0801.0877 [hep-ex]`.

[70] K. Hagiwara, D. Zeppenfeld, and S. Komamiya, *Excited Lepton Production at LEP and HERA*, Z. Phys. **C29** (1985) 115.

[71] F. Boudjema, A. Djouadi, and J. L. Kneur, *Excited fermions at e+ e- and e P colliders*, Z. Phys. **C57** (1993) 425–450.

[72] U. Baur, M. Spira, and P. M. Zerwas, *EXCITED QUARK AND LEPTON PRODUCTION AT HADRON COLLIDERS*, Phys. Rev. **D42** (1990) 815–824.

[73] T. Kohler, *Exotic processes at HERA: The Event generator COMPOS*, . In *Hamburg 1991, Proceedings, Physics at HERA, vol. 3* 1526-1541. (see HIGH ENERGY PHYSICS INDEX 30 (1992) No. 12988).

[74] M. Spira. provate communication.

[75] C. Berger and P. Kandel, *A new generator for wide angle bremsstrahlung*, . Prepared for Workshop on Monte Carlo Generators for HERA Physics (Plenary Starting Meeting), Hamburg, Germany, 27-30 Apr 1998.

[76] A. C. et al., *Production of the Fourth SM Family Fermions at the Large Hadron Electron Collider*, . LHeC note XXXX.

[77] J. A. Aguilar-Saavedra, *A minimal set of top anomalous couplings*, Nucl. Phys. **B812** (2009) 181–204, `arXiv:0811.3842 [hep-ph]`.

[78] H. Fritzsch and D. Holtmannspotter, *The Production of single t quarks at LEP and HERA*, Phys. Lett. **B457** (1999) 186–192, `arXiv:hep-ph/9901411`.

[79] Particle Data Group Collaboration, C. Amsler et al., *Review of particle physics*, Phys. Lett. **B667** (2008) 1.

[80] The ATLAS Collaboration, G. Aad et al., *Expected Performance of the ATLAS Experiment - Detector, Trigger and Physics*, `arXiv:0901.0512 [hep-ex]`.

[81] *ATLAS detector and physics performance. Technical design report. Vol. 2*, . CERN-LHCC-99-15.

[82] T. Han, K. Whisnant, B. L. Young, and X. Zhang, *Searching for $t \to c\ g$ at the Fermilab Tevatron*, Phys. Lett. **B385** (1996) 311–316, `arXiv:hep-ph/9606231`.

[83] E. Malkawi and T. M. P. Tait, *Top-Charm Strong Flavour-Changing Neutral Currents at the Tevatron*, Phys. Rev. **D54** (1996) 5758–5762, `arXiv:hep-ph/9511337`.

[84] T. M. P. Tait and C. P. Yuan, *Anomalous t-c-g coupling: The connection between single top production and top decay*, Phys. Rev. **D55** (1997) 7300–7301, `arXiv:hep-ph/9611244`.

[85] T. Han, M. Hosch, K. Whisnant, B.-L. Young, and X. Zhang, *Single top quark production via FCNC couplings at hadron colliders*, Phys. Rev. **D58** (1998) 073008, `arXiv:hep-ph/9806486`.

[86] T. M. P. Tait and C. P. Yuan, *Single top quark production as a window to physics beyond the standard model*, Phys. Rev. **D63** (2001) 014018, `arXiv:hep-ph/0007298`.

[87] J. J. Liu, C. S. Li, L. L. Yang, and L. G. Jin, *Single top quark production via SUSY-QCD FCNC couplings at the CERN LHC in the unconstrained MSSM*, Nucl. Phys. **B705** (2005) 3–32, `arXiv:hep-ph/0404099`.

[88] J. J. Liu, C. S. Li, L. L. Yang, and L. G. Jin, *Next-to-leading order QCD corrections to the direct top quark production via model-independent FCNC couplings at hadron colliders*, Phys. Rev. **D72** (2005) 074018, `arXiv:hep-ph/0508016`.

[89] J.-j. Cao, G.-l. Liu, J. M. Yang, and H.-j. Zhang, *Top-quark FCNC productions at LHC in topcolor-assisted technicolor model*, Phys. Rev. **D76** (2007) 014004, `arXiv:hep-ph/0703308`.

[90] J. J. Cao et al., *SUSY-induced FCNC top-quark processes at the Large Hadron Collider*, Phys. Rev. **D75** (2007) 075021, `arXiv:hep-ph/0702264`.

[91] P. M. Ferreira, R. B. Guedes, and R. Santos, *Combined effects of strong and electroweak FCNC effective operators in top quark physics at the CERN LHC*, Phys. Rev. **D77** (2008) 114008, `arXiv:0802.2075 [hep-ph]`.

[92] J. M. Yang, *Probing New Physics from Top Quark Processes at LHC: A Mini Review*, Int. J. Mod. Phys. **A23** (2008) 3343, `arXiv:0801.0210 [hep-ph]`.

[93] X.-F. Han, L. Wang, and J. M. Yang, *Top quark FCNC decays and productions at LHC in littlest Higgs model with T-parity*, `arXiv:0903.5491 [hep-ph]`.

[94] J. Cao, Z. Heng, L. Wu, and J. M. Yang, *R-parity violating effects in top quark FCNC productions at LHC*, Phys. Rev. **D79** (2009) 054003, `arXiv:0812.1698 [hep-ph]`.

[95] V. F. Obraztsov, S. R. Slabospitsky, and O. P. Yushchenko, *Search for anomalous top quark interaction at LEP-2 collider*, Phys. Lett. **B426** (1998) 393–402, `arXiv:hep-ph/9712394`.

[96] T. Han and J. L. Hewett, *Top charm associated production in high-energy e^+e^- collisions*, Phys. Rev. **D60** (1999) 074015, `arXiv:hep-ph/9811237`.

[97] J.-j. Cao, Z.-h. Xiong, and J. M. Yang, *SUSY-induced top quark FCNC processes at linear colliders*, Nucl. Phys. **B651** (2003) 87–105, `arXiv:hep-ph/0208035`.

[98] J. A. Aguilar-Saavedra, *Top flavor-changing neutral interactions: Theoretical expectations and experimental detection*, Acta Phys. Polon. **B35** (2004) 2695–2710, `arXiv:hep-ph/0409342`.

[99] A. T. Alan and A. Senol, *Single top production at HERA and THERA*, Europhys. Lett. **59** (2002) 669–673, `arXiv:hep-ph/0202119`.

[100] A. A. Ashimova and S. R. Slabospitsky, *The Constraint on FCNC Coupling of the Top Quark with a Gluon from ep Collisions*, Phys. Lett. **B668** (2008) 282–285, `arXiv:hep-ph/0604119`.

[101] H1 Collaboration, F. D. Aaron et al., *Search for Single Top Quark Production at HERA*, Phys. Lett. **B678** (2009) 450–458, `arXiv:0904.3876 [hep-ex]`.

[102] O. Cakir and S. A. Cetin, *Anomalous single top quark production at the CERN LHC*, J. Phys. **G31** (2005) N1–N8.

[103] G. A. Moortgat-Pick et al., *The role of polarized positrons and electrons in revealing fundamental interactions at the linear collider*, Phys. Rept. **460** (2008) 131–243, `arXiv:hep-ph/0507011`.

[104] S. Sultansoy, *Linac-ring type colliders: Second way to TeV scale*, Eur. Phys. J. **C33** (2004) s1064–s1066, `arXiv:hep-ex/0306034`.

[105] S. F. Sultanov, *Prospects of the future e p and gamma p colliders: Luminosity and physics*, . IC/89/409.

[106] S. I. Alekhin et al., *PHYSICS AT gamma p COLLIDERS OF TeV ENERGIES*, Int. J. Mod. Phys. **A6** (1991) 21–40.

[107] A. K. Ciftci, S. Sultansoy, S. Turkoz, and O. Yavas, *Main parameters of TeV energy gamma p colliders*, Nucl. Instrum. Meth. **A365** (1995) 317–328.

[108] A. K. Ciftci, S. Sultansoy, and O. Yavas, *TESLA*HERA based gamma p and gamma A colliders*, Nucl. Instrum. Meth. **A472** (2001) 72–78, `arXiv:hep-ex/0007009`.

[109] H. Aksakal, A. K. Ciftci, Z. Nergiz, D. Schulte, and F. Zimmermann, *Conversion efficiency and luminosity for gamma proton colliders based on the LHC-CLIC or LHC-ILC QCD Explorer scheme*, Nucl. Instrum. Meth. **A576** (2007) 287–293, `arXiv:hep-ex/0612041`.

[110] J. B. Dainton, M. Klein, P. Newman, E. Perez, and F. Willeke, *Deep inelastic electron nucleon scattering at the LHC*, JINST **1** (2006) P10001, `arXiv:hep-ex/0603016`.

[111] I. T. Cakir, O. Cakir, and S. Sultansoy, *Anomalous Single Top Production at the Large Hadron electron Collider Based gamma p Collider*, Phys. Lett. **B685** (2010) 170–173, `arXiv:0911.4194 [hep-ph]`.

[112] CMS Collaboration, G. L. Bayatian et al., *CMS technical design report, volume II: Physics performance*, J. Phys. **G34** (2007) 995–1579.

[113] O. Cakir, *Anomalous production of top quarks at CLIC + LHC based γp colliders*, J. Phys. **G29** (2003) 1181–1192, `arXiv:hep-ph/0301116`.

[114] R. Ciftci, *Production of Excited Quark at γp Collider Based on the Large Hadron Electron Collider*, . LHeC note XXXX.

[115] O. Çakır and M. Şahin, *Diquarks in γp Collisions at LHeC*, . LHeC note XXXX.

[116] CMS Collaboration, V. Khachatryan et al., *Search for Dijet Resonances in 7 TeV pp Collisions at CMS*, Phys. Rev. Lett. **105** (2010) 211801, `arXiv:1010.0203 [hep-ex]`.

[117] A. Atre, M. Carena, T. Han, and J. Santiago, *Heavy Quarks Above the Top at the Tevatron*, Phys. Rev. **D79** (2009) 054018, `arXiv:0806.3966 [hep-ph]`.

[118] O.Cakir, *Single Production of Fourth Family Quarks at LHeC*, . LHeC note XXXX.

[119] M. Duhrssen, *Measurement of Higgs boson parameters at the LHC*, Czech. J. Phys. **55** (2005) B145–B152.

[120] J. Alwall et al., *MadGraph/MadEvent v4: The New Web Generation*, JHEP **09** (2007) 028, `arXiv:0706.2334 [hep-ph]`.

[121] *PGS*. `http://www.physics.ucdavis.edu/~conway/research/software/pgs/pgs4-general.htm`.

[122] H. Fritzsch, M. Gell-Mann, and H. Leutwyler, *Advantages of the Color Octet Gluon Picture*, Phys.Lett. **B47** (1973) 365–368.

[123] T. Regge, *Introduction to complex orbital momenta*, Nuovo Cim. **14** (1959) 951.

[124] V. N. Gribov, *A REGGEON DIAGRAM TECHNIQUE*, Sov. Phys. JETP **26** (1968) 414–422.

[125] H. D. I. Abarbanel, J. B. Bronzan, R. L. Sugar, and A. R. White, *Reggeon Field Theory: Formulation and Use*, Phys. Rept. **21** (1975) 119–182.

[126] J. C. Collins, D. E. Soper, and G. F. Sterman, *Factorization of Hard Processes in QCD*, Adv. Ser. Direct. High Energy Phys. **5** (1988) 1–91, `arXiv:hep-ph/0409313`.

[127] V. N. Gribov and L. N. Lipatov, *Deep inelastic ep scattering in perturbation theory*, Sov. J. Nucl. Phys. **15** (1972) 438–450.

[128] G. Altarelli and G. Parisi, *Asymptotic Freedom in Parton Language*, Nucl. Phys. **B126** (1977) 298.

[129] Y. L. Dokshitzer, *Calculation of the Structure Functions for Deep Inelastic Scattering and e+ e- Annihilation by Perturbation Theory in Quantum Chromodynamics*, Sov. Phys. JETP **46** (1977) 641–653.

[130] L. V. Gribov, E. M. Levin, and M. G. Ryskin, *Semihard Processes in QCD*, Phys. Rept. **100** (1983) 1–150.

[131] A. H. Mueller, *Small x Behavior and Parton Saturation: A QCD Model*, Nucl. Phys. **B335** (1990) 115.

[132] J. Jalilian-Marian, A. Kovner, A. Leonidov, and H. Weigert, *The Wilson renormalization group for low x physics: Towards the high density regime*, Phys. Rev. **D59** (1999) 014014, `arXiv:hep-ph/9706377`.

[133] I. Balitsky, *Operator expansion for high-energy scattering*, Nucl. Phys. **B463** (1996) 99–160, `arXiv:hep-ph/9509348`.

[134] Y. V. Kovchegov, *Small-x F2 structure function of a nucleus including multiple pomeron exchanges*, Phys. Rev. **D60** (1999) 034008, `arXiv:hep-ph/9901281`.

[135] M. Froissart, *Asymptotic behavior and subtractions in the Mandelstam representation*, Phys. Rev. **123** (1961) 1053–1057.

[136] A. Martin, *Unitarity and high-energy behavior of scattering amplitudes*, Phys. Rev. **129** (1963) 1432–1436.

[137] E. A. Kuraev, L. N. Lipatov, and V. S. Fadin, *The Pomeranchuk Singularity in Nonabelian Gauge Theories*, Sov. Phys. JETP **45** (1977) 199–204.

[138] I. I. Balitsky and L. N. Lipatov, *The Pomeranchuk Singularity in Quantum Chromodynamics*, Sov. J. Nucl. Phys. **28** (1978) 822–829.

[139] V. N. Gribov, *Glauber corrections and the interaction between high- energy hadrons and nuclei*, Sov. Phys. JETP **29** (1969) 483–487.

[140] V. N. Gribov, *Interaction of gamma quanta and electrons with nuclei at high-energies*, Sov. Phys. JETP **30** (1970) 709–717.

[141] N. Armesto, A. B. Kaidalov, C. A. Salgado, and K. Tywoniuk, *A unitarized model of inclusive and diffractive DIS with Q2-evolution*, Phys. Rev. **D81** (2010) 074002, `arXiv:1001.3021 [hep-ph]`.

[142] N. Armesto, A. B. Kaidalov, C. A. Salgado, and K. Tywoniuk, *Nuclear shadowing in Glauber-Gribov theory with Q2- evolution*, Eur. Phys. J. **C68** (2010) 447–457, `arXiv:1003.2947 [hep-ph]`.

[143] A. H. Mueller and J.-w. Qiu, *Gluon Recombination and Shadowing at Small Values of x*, Nucl. Phys. **B268** (1986) 427.

[144] J. Bartels and M. Wusthoff, *The Triple Regge limit of diffractive dissociation in deep inelastic scattering*, Z. Phys. **C66** (1995) 157–180.

[145] L. D. McLerran and R. Venugopalan, *Computing quark and gluon distribution functions for very large nuclei*, Phys. Rev. **D49** (1994) 2233–2241, `arXiv:hep-ph/9309289`.

[146] L. D. McLerran and R. Venugopalan, *Gluon distribution functions for very large nuclei at small transverse momentum*, Phys. Rev. **D49** (1994) 3352–3355, `arXiv:hep-ph/9311205`.

[147] L. D. McLerran and R. Venugopalan, *Green's functions in the color field of a large nucleus*, Phys. Rev. **D50** (1994) 2225–2233, arXiv:hep-ph/9402335.

[148] J. Jalilian-Marian, A. Kovner, and H. Weigert, *The Wilson renormalization group for low x physics: Gluon evolution at finite parton density*, Phys. Rev. **D59** (1999) 014015, arXiv:hep-ph/9709432.

[149] A. Kovner, J. G. Milhano, and H. Weigert, *Relating different approaches to nonlinear QCD evolution at finite gluon density*, Phys. Rev. **D62** (2000) 114005, arXiv:hep-ph/0004014.

[150] H. Weigert, *Unitarity at small Bjorken x*, Nucl. Phys. **A703** (2002) 823–860, arXiv:hep-ph/0004044.

[151] E. Iancu, A. Leonidov, and L. D. McLerran, *Nonlinear gluon evolution in the color glass condensate. I*, Nucl. Phys. **A692** (2001) 583–645, arXiv:hep-ph/0011241.

[152] E. Ferreiro, E. Iancu, A. Leonidov, and L. McLerran, *Nonlinear gluon evolution in the color glass condensate. II*, Nucl. Phys. **A703** (2002) 489–538, arXiv:hep-ph/0109115.

[153] T. Altinoluk, A. Kovner, M. Lublinsky, and J. Peressutti, *QCD Reggeon Field Theory for every day: Pomeron loops included*, JHEP **03** (2009) 109, arXiv:0901.2559 [hep-ph].

[154] F. Gelis, E. Iancu, J. Jalilian-Marian, and R. Venugopalan, *The Color Glass Condensate*, arXiv:1002.0333 [hep-ph].

[155] Y. V. Kovchegov and H. Weigert, *Triumvirate of Running Couplings in Small-x Evolution*, Nucl.Phys. **A784** (2007) 188–226, arXiv:hep-ph/0609090 [hep-ph].

[156] I. Balitsky and G. A. Chirilli, *Next-to-leading order evolution of color dipoles*, Phys. Rev. **D77** (2008) 014019, arXiv:0710.4330 [hep-ph].

[157] E. Iancu, A. Mueller, and S. Munier, *Universal behavior of QCD amplitudes at high energy from general tools of statistical physics*, Phys.Lett. **B606** (2005) 342–350, arXiv:hep-ph/0410018 [hep-ph].

[158] Y. V. Kovchegov, J. Kuokkanen, K. Rummukainen, and H. Weigert, *Subleading-N(c) corrections in non-linear small-x evolution*, Nucl.Phys. **A823** (2009) 47–82, arXiv:0812.3238 [hep-ph].

[159] A. Dumitru and J. Jalilian-Marian, *Forward dijets in high-energy collisions: Evolution of QCD n-point functions beyond the dipole approximation*, Phys.Rev. **D82** (2010) 074023, arXiv:1008.0480 [hep-ph].

[160] C. Marquet and H. Weigert, *New observables to test the Color Glass Condensate beyond the large-N_c limit*, Nucl.Phys. **A843** (2010) 68–97, arXiv:1003.0813 [hep-ph].

[161] Y. Hatta, E. Iancu, C. Marquet, G. Soyez, and D. Triantafyllopoulos, *Diffusive scaling and the high-energy limit of deep inelastic scattering in QCD at large N(c)*, Nucl.Phys. **A773** (2006) 95–155, arXiv:hep-ph/0601150 [hep-ph].

[162] S. Munier, *Quantum chromodynamics at high energy and statistical physics*, Phys.Rept. **473** (2009) 1–49, `arXiv:0901.2823 [hep-ph]`. * Temporary entry *.

[163] S. Catani, M. Ciafaloni, and F. Hautmann, *High-energy factorization and small x heavy flavor production*, Nucl. Phys. **B366** (1991) 135–188.

[164] S. Catani and F. Hautmann, *High-energy factorization and small x deep inelastic scattering beyond leading order*, Nucl. Phys. **B427** (1994) 475–524, `arXiv:hep-ph/9405388`.

[165] F. Caola, S. Forte, and J. Rojo, *Deviations from NLO QCD evolution in inclusive HERA data*, Phys. Lett. **B686** (2010) 127–135, `arXiv:0910.3143 [hep-ph]`.

[166] V. S. Fadin and L. N. Lipatov, *BFKL pomeron in the next-to-leading approximation*, Phys. Lett. **B429** (1998) 127–134, `arXiv:hep-ph/9802290`.

[167] M. Ciafaloni and G. Camici, *Energy scale(s) and next-to-leading BFKL equation*, Phys. Lett. **B430** (1998) 349–354, `arXiv:hep-ph/9803389`.

[168] G. Altarelli, R. D. Ball, and S. Forte, *An anomalous dimension for small x evolution*, Nucl. Phys. **B674** (2003) 459–483, `arXiv:hep-ph/0306156`.

[169] G. Altarelli, R. D. Ball, and S. Forte, *Perturbatively stable resummed small x evolution kernels*, Nucl. Phys. **B742** (2006) 1–40, `arXiv:hep-ph/0512237`.

[170] G. Altarelli, R. D. Ball, and S. Forte, *Small x Resummation with Quarks: Deep-Inelastic Scattering*, Nucl. Phys. **B799** (2008) 199–240, `arXiv:0802.0032 [hep-ph]`.

[171] M. Ciafaloni, D. Colferai, G. P. Salam, and A. M. Stasto, *Renormalisation group improved small-x Green's function*, Phys. Rev. **D68** (2003) 114003, `arXiv:hep-ph/0307188`.

[172] M. Ciafaloni, D. Colferai, G. P. Salam, and A. M. Stasto, *The gluon splitting function at moderately small x*, Phys. Lett. **B587** (2004) 87–94, `arXiv:hep-ph/0311325`.

[173] M. Ciafaloni, D. Colferai, G. P. Salam, and A. M. Stasto, *A matrix formulation for small-x singlet evolution*, JHEP **08** (2007) 046, `arXiv:0707.1453 [hep-ph]`.

[174] J. C. Collins, *Proof of factorization for diffractive hard scattering*, Phys. Rev. **D57** (1998) 3051–3056, `arXiv:hep-ph/9709499`.

[175] K. J. Golec-Biernat and M. Wusthoff, *Saturation effects in deep inelastic scattering at low Q**2 and its implications on diffraction*, Phys. Rev. **D59** (1998) 014017, `arXiv:hep-ph/9807513`.

[176] K. J. Golec-Biernat and M. Wusthoff, *Saturation in diffractive deep inelastic scattering*, Phys. Rev. **D60** (1999) 114023, `arXiv:hep-ph/9903358`.

[177] N. Armesto, *Nuclear shadowing*, J. Phys. **G32** (2006) R367–R394, `arXiv:hep-ph/0604108`.

[178] L. Frankfurt, M. Strikman, and C. Weiss, *Small-x physics: From HERA to LHC and beyond*, Ann. Rev. Nucl. Part. Sci. **55** (2005) 403–465, `arXiv:hep-ph/0507286`.

[179] E. Iancu, K. Itakura, and S. Munier, *Saturation and BFKL dynamics in the HERA data at small x*, Phys. Lett. **B590** (2004) 199–208, `arXiv:hep-ph/0310338`.

[180] J. R. Forshaw and G. Shaw, *Gluon saturation in the colour dipole model?*, JHEP **12** (2004) 052, `arXiv:hep-ph/0411337`.

[181] A. M. Stasto, K. J. Golec-Biernat, and J. Kwiecinski, *Geometric scaling for the total gamma* p cross-section in the low x region*, Phys. Rev. Lett. **86** (2001) 596–599, `arXiv:hep-ph/0007192`.

[182] N. Armesto, C. A. Salgado, and U. A. Wiedemann, *Relating high-energy lepton hadron, proton nucleus and nucleus nucleus collisions through geometric scaling*, Phys. Rev. Lett. **94** (2005) 022002, `arXiv:hep-ph/0407018`.

[183] C. Marquet and L. Schoeffel, *Geometric scaling in diffractive deep inelastic scattering*, Phys. Lett. **B639** (2006) 471–477, `arXiv:hep-ph/0606079`.

[184] L. McLerran and M. Praszalowicz, *Saturation and Scaling of Multiplicity, Mean pT and pT Distributions from 200 GeV lt sqrt(s) lt 7 TeV*, Acta Phys.Polon. **B41** (2010) 1917–1926, `arXiv:1006.4293 [hep-ph]`.

[185] F. Caola and S. Forte, *Geometric Scaling from GLAP evolution*, Phys. Rev. Lett. **101** (2008) 022001, `arXiv:0802.1878 [hep-ph]`.

[186] N. N. Nikolaev and B. G. Zakharov, *Colour transparency and scaling properties of nuclear shadowing in deep inelastic scattering*, Z. Phys. **C49** (1991) 607–618.

[187] N. Nikolaev and B. G. Zakharov, *Pomeron structure function and diffraction dissociation of virtual photons in perturbative QCD*, Z. Phys. **C53** (1992) 331–346.

[188] A. H. Mueller and B. Patel, *Single and double BFKL pomeron exchange and a dipole picture of high-energy hard processes*, Nucl. Phys. **B425** (1994) 471–488, `arXiv:hep-ph/9403256`.

[189] A. H. Mueller, *Unitarity and the BFKL pomeron*, Nucl. Phys. **B437** (1995) 107–126, `arXiv:hep-ph/9408245`.

[190] M. L. Good and W. D. Walker, *Diffraction disssociation of beam particles*, Phys. Rev. **120** (1960) 1857–1860.

[191] A. H. Mueller, *Parton saturation: An overview*, `arXiv:hep-ph/0111244`.

[192] J. Bartels, K. J. Golec-Biernat, and H. Kowalski, *A modification of the saturation model: DGLAP evolution*, Phys. Rev. **D66** (2002) 014001, `arXiv:hep-ph/0203258`.

[193] H. Kowalski and D. Teaney, *An impact parameter dipole saturation model*, Phys. Rev. **D68** (2003) 114005, `arXiv:hep-ph/0304189`.

[194] H. Kowalski, L. Motyka, and G. Watt, *Exclusive diffractive processes at HERA within the dipole picture*, Phys. Rev. **D74** (2006) 074016, `arXiv:hep-ph/0606272`.

[195] A. D. Martin, R. G. Roberts, W. J. Stirling, and R. S. Thorne, *Uncertainties of predictions from parton distributions. I: Experimental errors. ((T))*, Eur. Phys. J. **C28** (2003) 455–473, `arXiv:hep-ph/0211080`.

[196] A. D. Martin, W. J. Stirling, R. S. Thorne, and G. Watt, *Update of Parton Distributions at NNLO*, Phys. Lett. **B652** (2007) 292–299, `arXiv:0706.0459 [hep-ph]`.

[197] P. M. Nadolsky et al., *Implications of CTEQ global analysis for collider observables*, Phys. Rev. **D78** (2008) 013004, `arXiv:0802.0007 [hep-ph]`.

[198] G. Watt, A. D. Martin, W. J. Stirling, and R. S. Thorne, *Recent Progress in Global PDF Analysis*, `arXiv:0806.4890 [hep-ph]`.

[199] A. Martin, W. Stirling, R. Thorne, and G. Watt, *Parton distributions for the LHC*, Eur.Phys.J. **C63** (2009) 189–285, `arXiv:0901.0002 [hep-ph]`.

[200] H.-L. Lai, J. Huston, Z. Li, P. Nadolsky, J. Pumplin, et al., *Uncertainty induced by QCD coupling in the CTEQ global analysis of parton distributions*, Phys.Rev. **D82** (2010) 054021, `arXiv:1004.4624 [hep-ph]`.

[201] J. R. Forshaw, R. Sandapen, and G. Shaw, *Further success of the colour dipole model*, JHEP **11** (2006) 025, `arXiv:hep-ph/0608161`.

[202] H1 Collaboration, F. D. Aaron et al., *Combined Measurement and QCD Analysis of the Inclusive ep Scattering Cross Sections at HERA*, JHEP **01** (2010) 109, `arXiv:0911.0884 [hep-ex]`.

[203] The NNPDF Collaboration, R. D. Ball et al., *Precision determination of electroweak parameters and the strange content of the proton from neutrino deep-inelastic scattering*, Nucl. Phys. **B823** (2009) 195–233, `arXiv:0906.1958 [hep-ph]`.

[204] R. D. Ball et al., *A first unbiased global NLO determination of parton distributions and their uncertainties*, Nucl. Phys. **B838** (2010) 136–206, `arXiv:1002.4407 [hep-ph]`.

[205] F. Caola, S. Forte, and J. Rojo, *HERA data and DGLAP evolution: theory and phenomenology*, `arXiv:1007.5405 [hep-ph]`.

[206] H.-L. Lai, M. Guzzi, J. Huston, Z. Li, P. M. Nadolsky, et al., *New parton distributions for collider physics*, Phys.Rev. **D82** (2010) 074024, `arXiv:1007.2241 [hep-ph]`.

[207] R. D. Ball and R. K. Ellis, *Heavy quark production at high-energy*, JHEP **05** (2001) 053, `arXiv:hep-ph/0101199`.

[208] S. Marzani, R. D. Ball, V. Del Duca, S. Forte, and A. Vicini, *Higgs production via gluon-gluon fusion with finite top mass beyond next-to-leading order*, Nucl. Phys. **B800** (2008) 127–145, `arXiv:0801.2544 [hep-ph]`.

[209] S. Marzani, R. D. Ball, V. Del Duca, S. Forte, and A. Vicini, *Finite-top-mass effects in NNLO Higgs production*, Nucl. Phys. Proc. Suppl. **186** (2009) 98–101, `arXiv:0809.4934 [hep-ph]`.

[210] S. Marzani and R. D. Ball, *High Energy Resummation of Drell-Yan Processes*, Nucl. Phys. **B814** (2009) 246–264, `arXiv:0812.3602 [hep-ph]`.

[211] S. Marzani and R. D. Ball, *Drell-Yan processes in the high-energy limit*, `arXiv:0906.4729 [hep-ph]`.

[212] G. Diana, *High-energy resummation in direct photon production*, Nucl. Phys. **B824** (2010) 154–167, `arXiv:0906.4159 [hep-ph]`.

[213] G. Diana, J. Rojo, and R. D. Ball, *High energy resummation of direct photon production at hadronic colliders*, Phys.Lett. **B693** (2010) 430–437, `arXiv:1006.4250 [hep-ph]`.

[214] S. Forte, G. Altarelli, and R. D. Ball, *Can we trust small x resummation?*, Nucl. Phys. Proc. Suppl. **191** (2009) 64–75, `arXiv:0901.1294 [hep-ph]`.

[215] M. Dittmar et al., *Parton Distributions*, `arXiv:0901.2504 [hep-ph]`.

[216] J. Rojo, G. Altarelli, R. D. Ball, and S. Forte, *Towards small x resummed DIS phenomenology*, `arXiv:0907.0443 [hep-ph]`.

[217] J. Rojo and F. Caola, *Parton distributions and small-x QCD at the Large Hadron Electron Collider*, `arXiv:0906.2079 [hep-ph]`.

[218] K. J. Eskola, H. Paukkunen, and C. A. Salgado, *EPS09 - a New Generation of NLO and LO Nuclear Parton Distribution Functions*, JHEP **04** (2009) 065, `arXiv:0902.4154 [hep-ph]`.

[219] C. A. Salgado et al., *Proton-nucleus collisions at the LHC: scientific opportunities and requirements*, . In preparation.

[220] D. G. d'Enterria, *Quarkonia photoproduction at nucleus colliders*, Nucl.Phys.Proc.Suppl. **184** (2008) 158–162, `arXiv:0711.1123 [nucl-ex]`.

[221] D. d'Enterria, *Forward jets physics in ATLAS, CMS and LHCb*, `arXiv:0911.1273 [hep-ex]`.

[222] R. Ichou and D. d'Enterria, *Sensitivity of isolated photon production at TeV hadron colliders to the gluon distribution in the proton*, Phys.Rev. **D82** (2010) 014015, `arXiv:1005.4529 [hep-ph]`.

[223] LHCb Collaboration, F. de Lorenzi et al. Proceedings of DIS2010.

[224] J. M. Jowett, *The LHC as a Nucleus-Nucleus Collider*, J.Phys.G **G35** (2008) 104028, `arXiv:0807.1397 [nucl-ex]`. * Temporary entry *.

[225] P. Quiroga-Arias, J. G. Milhano, and U. A. Wiedemann, *Testing nuclear parton distributions with pA collisions at the TeV scale*, Phys.Rev. **C82** (2010) 034903, `arXiv:1002.2537 [hep-ph]`.

[226] K. Eskola, V. Kolhinen, and R. Vogt, *Obtaining the nuclear gluon distribution from heavy quark decays to lepton pairs in pA collisions*, Nucl.Phys. **A696** (2001) 729–746, `arXiv:hep-ph/0104124 [hep-ph]`.

[227] F. Arleo and T. Gousset, *Measuring gluon shadowing with prompt photons at RHIC and LHC*, Phys.Lett. **B660** (2008) 181–187, `arXiv:0707.2944 [hep-ph]`.

[228] H. Paukkunen and C. A. Salgado, *Constraints for the nuclear parton distributions from Z and W production at the LHC*, `arXiv:1010.5392 [hep-ph]`. * Temporary entry *.

[229] A. Baltz, G. Baur, D. d'Enterria, L. Frankfurt, F. Gelis, et al., *The Physics of Ultraperipheral Collisions at the LHC*, Phys.Rept. **458** (2008) 1–171, `arXiv:0706.3356 [nucl-ex]`.

[230] BRAHMS Collaboration, I. Arsene et al., _On the evolution of the nuclear modification factors with rapidity and centrality in d + Au collisions at s(NN)**(1/2) = 200-GeV_, Phys.Rev.Lett. **93** (2004) 242303, `arXiv:nucl-ex/0403005 [nucl-ex]`.

[231] B. Kopeliovich, J. Nemchik, I. Potashnikova, M. Johnson, and I. Schmidt, *Breakdown of QCD factorization at large Feynman x*, Phys.Rev. **C72** (2005) 054606, `arXiv:hep-ph/0501260 [hep-ph]`.

[232] STAR Collaboration, E. Braidot, *Suppression of Forward Pion Correlations in d+Au Interactions at STAR*, `arXiv:1005.2378 [hep-ph]`.

[233] L. Frankfurt and M. Strikman, *Energy losses in the black disc regime and correlation effects in the STAR forward pion production in d Au collisions*, Phys.Lett. **B645** (2007) 412–421, `arXiv:nucl-th/0603049 [nucl-th]`.

[234] J. L. Albacete and C. Marquet, *Azimuthal correlations of forward di-hadrons in d+Au collisions at RHIC in the Color Glass Condensate*, Phys.Rev.Lett. **105** (2010) 162301, `arXiv:1005.4065 [hep-ph]`.

[235] STAR Collaboration, B. Abelev et al., *Three-particle coincidence of the long range pseudorapidity correlation in high energy nucleus-nucleus collisions*, Phys.Rev.Lett. **105** (2010) 022301, `arXiv:0912.3977 [hep-ex]`.

[236] CMS Collaboration, V. Khachatryan et al., *Observation of Long-Range Near-Side Angular Correlations in Proton-Proton Collisions at the LHC*, JHEP **1009** (2010) 091, `arXiv:1009.4122 [hep-ex]`.

[237] A. Dumitru, K. Dusling, F. Gelis, J. Jalilian-Marian, T. Lappi, et al., *The Ridge in proton-proton collisions at the LHC*, Phys.Lett. **B697** (2011) 21–25, `arXiv:1009.5295 [hep-ph]`.

[238] N. Armesto, *Predictions for the heavy-ion programme at the Large Hadron Collider*, `arXiv:0903.1330 [hep-ph]`.

[239] ALICE Collaboration, K. Aamodt et al., *Charged-particle multiplicity density at mid-rapidity in central Pb-Pb collisions at sqrt(sNN) = 2.76 TeV*, Phys.Rev.Lett. **105** (2010) 252301, `arXiv:1011.3916 [nucl-ex]`. * Temporary entry *.

[240] F. Arleo et al., *Photon physics in heavy ion collisions at the LHC*, `arXiv:hep-ph/0311131`.

[241] ALICE Collaboration, J. Nystrand, *Photon-Induced Physics with Heavy-Ion Beams in ALICE*, Nucl.Phys.Proc.Suppl. **179-180** (2008) 156–161, `arXiv:0807.0366 [nucl-ex]`.

[242] M. Arneodo, *Nuclear effects in structure functions*, Phys. Rept. **240** (1994) 301–393.

[243] D. F. Geesaman, K. Saito, and A. W. Thomas, *The nuclear EMC effect*, Ann. Rev. Nucl. Part. Sci. **45** (1995) 337–390.

[244] A. Accardi et al., *Hard probes in heavy ion collisions at the lhc: pdfs, shadowing and pa collisions*, arXiv:hep-ph/0308248.

[245] D. de Florian and R. Sassot, *Nuclear parton distributions at next to leading order*, Phys. Rev. **D69** (2004) 074028, arXiv:hep-ph/0311227.

[246] M. Hirai, S. Kumano, and T. H. Nagai, *Determination of nuclear parton distribution functions and their uncertainties at next-to-leading order*, Phys. Rev. **C76** (2007) 065207, arXiv:0709.3038 [hep-ph].

[247] K. Kovarik, I. Schienbein, F. Olness, J. Ju, C. Keppel, et al., *Nuclear corrections in neutrino-nucleus DIS and their compatibility with global NPDF analyses*, arXiv:1012.0286 [hep-ph]. * Temporary entry *.

[248] H. Paukkunen and C. A. Salgado, *Compatibility of neutrino DIS data and global analyses of parton distribution functions*, JHEP **07** (2010) 032, arXiv:1004.3140 [hep-ph].

[249] V. Guzey and M. Strikman, *Color fluctuation approximation for multiple interactions in leading twist theory of nuclear shadowing*, Phys. Lett. **B687** (2010) 167–173, arXiv:0908.1149 [hep-ph].

[250] K. J. Eskola, V. J. Kolhinen, and C. A. Salgado, *The scale dependent nuclear effects in parton distributions for practical applications*, Eur. Phys. J. **C9** (1999) 61–68, arXiv:hep-ph/9807297.

[251] A. Accardi et al., *Hard probes in heavy ion collisions at the LHC: Jet physics*, arXiv:hep-ph/0310274.

[252] M. Bedjidian et al., *Hard probes in heavy ion collisions at the LHC: Heavy flavor physics*, arXiv:hep-ph/0311048.

[253] M. Gyulassy and L. McLerran, *New forms of QCD matter discovered at RHIC*, Nucl. Phys. **A750** (2005) 30–63, arXiv:nucl-th/0405013.

[254] D. G. d'Enterria, *Quark-gluon matter*, J. Phys. **G34** (2007) S53–S82, arXiv:nucl-ex/0611012.

[255] T. Lappi, *Initial conditions of heavy ion collisions and high energy factorization*, Acta Phys. Polon. **B40** (2009) 1997–2012, arXiv:0904.1670 [hep-ph].

[256] A. Accardi, F. Arleo, W. K. Brooks, D. D'Enterria, and V. Muccifora, *Parton Propagation and Fragmentation in QCD Matter*, Riv. Nuovo Cim. **032** (2010) 439–553, arXiv:0907.3534 [nucl-th].

[257] ALICE Collaboration, K. Aamodt et al., *Suppression of Charged Particle Production at Large Transverse Momentum in Central Pb–Pb Collisions at* $\sqrt{s_{NN}} = 2.76\ TeV$, Phys.Lett. **B696** (2011) 30–39, arXiv:1012.1004 [nucl-ex]. * Temporary entry *.

[258] Atlas Collaboration, G. Aad et al., *Observation of a Centrality-Dependent Dijet Asymmetry in Lead-Lead Collisions at sqrt(S(NN))= 2.76 TeV with the ATLAS Detector at the LHC*, `arXiv:1011.6182 [hep-ex]`. * Temporary entry *.

[259] CMS Collaboration, S. Chatrchyan et al., *Observation and studies of jet quenching in PbPb collisions at nucleon-nucleon center-of-mass energy = 2.76 TeV*, `arXiv:1102.1957 [nucl-ex]`. * Temporary entry *.

[260] K. Golec-Biernat and A. M. Stasto, *F_L proton structure function from the unified DGLAP/BFKL approach*, Phys. Rev. **D80** (2009) 014006, `arXiv:0905.1321 [hep-ph]`.

[261] J. L. Albacete, N. Armesto, J. G. Milhano, and C. A. Salgado, *Non-linear QCD meets data: A global analysis of lepton- proton scattering with running coupling BK evolution*, Phys. Rev. **D80** (2009) 034031, `arXiv:0902.1112 [hep-ph]`.

[262] NNPDF Collaboration, R. D. Ball et al., *A determination of parton distributions with faithful uncertainty estimation*, Nucl. Phys. **B809** (2009) 1–63, `arXiv:0808.1231 [hep-ph]`.

[263] The NNPDF Collaboration, and others, *Reweighting NNPDFs: the W lepton asymmetry*, `arXiv:1012.0836 [hep-ph]`.

[264] N. Armesto, *A simple model for nuclear structure functions at small x in the dipole picture*, Eur. Phys. J. **C26** (2002) 35–43, `arXiv:hep-ph/0206017`.

[265] PHENIX Collaboration, S. S. Adler et al., *Centrality dependence of pi0 and eta production at large transverse momentum in s(NN)**(1/2) = 200-GeV d + Au collisions*, Phys. Rev. Lett. **98** (2007) 172302, `arXiv:nucl-ex/0610036`.

[266] E. R. Cazaroto, F. Carvalho, V. P. Goncalves, and F. S. Navarra, *Constraining the nuclear gluon distribution in eA processes at RHIC*, Phys. Lett. **B669** (2008) 331–336, `arXiv:0804.2507 [hep-ph]`.

[267] N. Armesto, H. Paukkunen, C. A. Salgado, and K. Tywoniuk, *Nuclear effects on the longitudinal structure function at small x*, Phys.Lett. **B694** (2010) 38–43, `arXiv:1005.2035 [hep-ph]`.

[268] A. Bruni, X. Janssen, and P. Marage, *Exclusive Vector Meson Production and Deeply Virtual Compton Scattering at HERA*, Proceedings of the HERA-LHC Workshops, 2006-8, eds. Jung, de Roeck, DESY-PROC-2009-02 (2009) 427, 2009.

[269] A. D. Martin, C. Nockles, M. G. Ryskin, and T. Teubner, *Small x gluon from exclusive J/psi production*, Phys. Lett. **B662** (2008) 252–258, `arXiv:0709.4406 [hep-ph]`.

[270] S. Munier, A. M. Stasto, and A. H. Mueller, *Impact parameter dependent S-matrix for dipole proton scattering from diffractive meson electroproduction*, Nucl. Phys. **B603** (2001) 427–445, `arXiv:hep-ph/0102291`.

[271] K. Goeke, M. V. Polyakov, and M. Vanderhaeghen, *Hard Exclusive Reactions and the Structure of Hadrons*, Prog. Part. Nucl. Phys. **47** (2001) 401–515, `arXiv:hep-ph/0106012`.

[272] M. Diehl, *Generalized parton distributions*, Phys. Rept. **388** (2003) 41–277, arXiv:hep-ph/0307382.

[273] A. V. Belitsky and A. V. Radyushkin, *Unraveling hadron structure with generalized parton distributions*, Phys. Rept. **418** (2005) 1–387, arXiv:hep-ph/0504030.

[274] S. J. Brodsky, L. Frankfurt, J. F. Gunion, A. H. Mueller, and M. Strikman, *Diffractive leptoproduction of vector mesons in QCD*, Phys. Rev. **D50** (1994) 3134–3144, arXiv:hep-ph/9402283.

[275] J. C. Collins, L. Frankfurt, and M. Strikman, *Factorization for hard exclusive electroproduction of mesons in QCD*, Phys. Rev. **D56** (1997) 2982–3006, arXiv:hep-ph/9611433.

[276] M. Burkardt, *Impact parameter dependent parton distributions and off- forward parton distributions for zeta –¿ 0*, Phys. Rev. **D62** (2000) 071503, arXiv:hep-ph/0005108.

[277] T. Rogers, V. Guzey, M. Strikman, and X. Zu, *Determining the proximity of gamma* N scattering to the black body limit using DIS and J/psi production*, Phys. Rev. **D69** (2004) 074011, arXiv:hep-ph/0309099.

[278] H. Kowalski, T. Lappi, and R. Venugopalan, *Nuclear enhancement of universal dynamics of high parton densities*, Phys. Rev. Lett. **100** (2008) 022303, arXiv:0705.3047 [hep-ph].

[279] L. Frankfurt, M. Strikman, and C. Weiss, *Dijet production as a centrality trigger for pp collisions at CERN LHC*, Phys. Rev. **D69** (2004) 114010, arXiv:hep-ph/0311231.

[280] L. Frankfurt, C. E. Hyde, M. Strikman, and C. Weiss, *Generalized parton distributions and rapidity gap survival in exclusive diffractive pp scattering*, Phys. Rev. **D75** (2007) 054009, arXiv:hep-ph/0608271.

[281] M. Deile et al., *13th International Conference on Elastic and Diffractive Scattering (Blois Workshop) - Moving Forward into the LHC Era*, arXiv:1002.3527 [hep-ph].

[282] ZEUS Collaboration, S. Chekanov et al., *Exclusive electroproduction of J/psi mesons at HERA*, Nucl. Phys. **B695** (2004) 3–37, arXiv:hep-ex/0404008.

[283] H1 Collaboration, A. Aktas et al., *Elastic J/psi production at HERA*, Eur. Phys. J. **C46** (2006) 585–603, arXiv:hep-ex/0510016.

[284] H1 Collaboration, F. D. Aaron et al., *Measurement of Deeply Virtual Compton Scattering and its t-dependence at HERA*, Phys. Lett. **B659** (2008) 796–806, arXiv:0709.4114 [hep-ex].

[285] ZEUS Collaboration, S. Chekanov et al., *A measurement of the Q^2, W and t dependences of deeply virtual Compton scattering at HERA*, JHEP **05** (2009) 108, arXiv:0812.2517 [hep-ex].

[286] C. Marquet and B. Wu, *Exclusive vs. diffractive vector meson production in DIS at small x or off nuclei*, arXiv:0908.4180 [hep-ph].

[287] A. Caldwell and H. Kowalski, *Investigating the gluonic structure of nuclei via J/psi scattering*, Phys. Rev. **C81** (2010) 025203.

[288] T. Lappi and H. Mantysaari, *How nucleons lose their identity at high energy*, `arXiv:1011.1988 [hep-ph]`. * Temporary entry *.

[289] L. Frankfurt, M. Strikman, D. Treleani, and C. Weiss, *Evidence for color fluctuations in the nucleon in high- energy scattering*, Phys. Rev. Lett. **101** (2008) 202003, `arXiv:0808.0182 [hep-ph]`.

[290] J. Bartels, K. J. Golec-Biernat, and K. Peters, *On the dipole picture in the nonforward direction*, Acta Phys. Polon. **B34** (2003) 3051–3068, `arXiv:hep-ph/0301192`.

[291] C. Marquet, R. B. Peschanski, and G. Soyez, *Exclusive vector meson production at HERA from QCD with saturation*, Phys.Rev. **D76** (2007) 034011, `arXiv:hep-ph/0702171 [HEP-PH]`.

[292] M. G. Ryskin, *Diffractive J / psi electroproduction in LLA QCD*, Z. Phys. **C57** (1993) 89–92.

[293] P. Newman, *Low x and Diffractive Physics at a Large Hadron electron Collider*, . In Proceedings of the 13th International (Blois) Conference on Elastic and Diffractive Scattering, EDS'09, CERN, 2009, p182.

[294] B. List and A. Mastroberardino, *DIFFVM: A Monte Carlo generator for diffractive processes in ep scattering*, Proceedings of the Workshop on Monte Carlo Generators for HERA Physics, DESY-PROC-1992-02 (1999) 396, 1999.

[295] J. R. Forshaw, R. Sandapen, and G. Shaw, *Colour dipoles and rho, Phi electroproduction*, Phys. Rev. **D69** (2004) 094013, `arXiv:hep-ph/0312172`.

[296] ZEUS Collaboration, S. Chekanov et al., *Exclusive photoproduction of J/psi mesons at HERA*, Eur. Phys. J. **C24** (2002) 345–360, `arXiv:hep-ex/0201043`.

[297] ZEUS Collaboration, J. Breitweg et al., *Measurement of elastic Upsilon photoproduction at HERA*, Phys. Lett. **B437** (1998) 432–444, `arXiv:hep-ex/9807020`.

[298] H1 Collaboration, C. Adloff et al., *Elastic photoproduction of J/psi and Upsilon mesons at HERA*, Phys. Lett. **B483** (2000) 23–35, `arXiv:hep-ex/0003020`.

[299] ZEUS Collaboration, S. Chekanov et al., *Exclusive photoproduction of upsilon mesons at HERA*, Phys. Lett. **B680** (2009) 4–12, `arXiv:0903.4205 [hep-ex]`.

[300] B. E. Cox, J. R. Forshaw, and R. Sandapen, *Diffractive upsilon production at the LHC*, JHEP **06** (2009) 034, `arXiv:0905.0102 [hep-ph]`.

[301] E. Perez, L. Schoeffel, and L. Favart, *MILOU: A Monte-Carlo for deeply virtual Compton scattering*, `arXiv:hep-ph/0411389 [hep-ph]`.

[302] L. Frankfurt, A. Freund, and M. Strikman, *Diffractive exclusive photoproduction in DIS at HERA*, Phys.Rev. **D58** (1998) 114001, `arXiv:hep-ph/9710356 [hep-ph]`.

[303] H1 Collaboration, F. Aaron et al., *Deeply Virtual Compton Scattering and its Beam Charge Asymmetry in e+- Collisions at HERA*, Phys.Lett. **B681** (2009) 391–399, `arXiv:arXiv:0907.5289 [hep-ex]`.

[304] L. Frankfurt, V. Guzey, and M. Strikman, *Leading twist coherent diffraction on nuclei in deep inelastic scattering at small x and nuclear shadowing*, Phys. Rep. in preparation (2011) .

[305] A. Kaidalov, *Diffractive Production Mechanisms*, Phys.Rept. **50** (1979) 157–226.

[306] K. A. Goulianos, *Diffractive Interactions of Hadrons at High-Energies*, Phys. Rept. **101** (1983) 169.

[307] G. Ingelman and P. E. Schlein, *Jet Structure in High Mass Diffractive Scattering*, Phys. Lett. **B152** (1985) 256.

[308] A. Donnachie and P. V. Landshoff, *Diffractive Deep Inelastic Lepton Scattering*, Phys. Lett. **B191** (1987) 309.

[309] G. Wolf, *Review of High Energy Diffraction in Real and Virtual Photon Proton scattering at HERA*, Rept. Prog. Phys. **73** (2010) 116202, `arXiv:0907.1217 [hep-ex]`.

[310] H1 Collaboration, A. Aktas et al., *Diffractive deep-inelastic scattering with a leading proton at HERA*, Eur. Phys. J. **C48** (2006) 749–766, `arXiv:hep-ex/0606003`.

[311] ZEUS Collaboration, S. Chekanov et al., *Deep inelastic scattering with leading protons or large rapidity gaps at HERA*, Nucl. Phys. **B816** (2009) 1–61, `arXiv:0812.2003 [hep-ex]`.

[312] F. Aaron et al., *Measurement of the Diffractive Deep-Inelastic Scattering Cross Section with a Leading Proton at HERA*, `arXiv:1010.1476 [hep-ex]`.

[313] H1 Collaboration, A. Aktas et al., *Measurement and QCD analysis of the diffractive deep- inelastic scattering cross-section at HERA*, Eur. Phys. J. **C48** (2006) 715–748, `arXiv:hep-ex/0606004`.

[314] J. Blumlein and D. Robaschik, *On the scaling violations of diffractive structure functions: Operator approach*, Phys. Lett. **B517** (2001) 222–232, `arXiv:hep-ph/0106037`.

[315] H1 Collaboration, A. Aktas et al., *Dijet Cross Sections and Parton Densities in Diffractive DIS at HERA*, JHEP **10** (2007) 042, `arXiv:0708.3217 [hep-ex]`.

[316] ZEUS Collaboration, S. Chekanov et al., *A QCD analysis of ZEUS diffractive data*, Nucl. Phys. **B831** (2010) 1–25, `arXiv:0911.4119 [hep-ex]`.

[317] A. D. Martin, M. G. Ryskin, and G. Watt, *Diffractive parton distributions from perturbative QCD*, Eur. Phys. J. **C44** (2005) 69–85, `arXiv:hep-ph/0504132`.

[318] H1 Collaboration, A. Aktas et al., *Tests of QCD factorisation in the diffractive production of dijets in deep-inelastic scattering and photoproduction at HERA*, Eur. Phys. J. **C51** (2007) 549–568, `arXiv:hep-ex/0703022`.

[319] H1 Collaboration, A. Aktas et al., *Diffractive open charm production in deep-inelastic scattering and photoproduction at HERA*, Eur. Phys. J. **C50** (2007) 1–20, `arXiv:hep-ex/0610076`.

[320] P. Newman, *Deep Inelastic Scattering at the TeV Energy Scale and the LHeC Project*, Nucl. Phys. Proc. Suppl. **191** (2009) 307–319, `arXiv:0902.2292 [hep-ex]`.

[321] H1 Collaboration, F. D. Aaron et al., *Measurement of Leading Neutron Production in Deep- Inelastic Scattering at HERA*, Eur. Phys. J. **C68** (2010) 381–399, `arXiv:1001.0532 [hep-ex]`.

[322] G. Watt and H. Kowalski, *Impact parameter dependent colour glass condensate dipole model*, Phys. Rev. **D78** (2008) 014016, `arXiv:0712.2670 [hep-ph]`.

[323] V. A. Abramovsky, V. N. Gribov, and O. V. Kancheli, *CHARACTER OF INCLUSIVE SPECTRA AND FLUCTUATIONS PRODUCED IN INELASTIC PROCESSES BY MULTI - POMERON EXCHANGE*, Yad. Fiz. **18** (1973) 595–616.

[324] L. Frankfurt and M. Strikman, *Diffraction at HERA, color opacity and nuclear shadowing*, Eur. Phys. J. **A5** (1999) 293–306, `arXiv:hep-ph/9812322`.

[325] L. Frankfurt, V. Guzey, and M. Strikman, *Leading twist nuclear shadowing: A user's guide*, Phys. Rev. **D71** (2005) 054001, `arXiv:hep-ph/0303022`.

[326] H. Abramowicz, L. Frankfurt, and M. Strikman, *Interplay of hard and soft physics in small x deep inelastic processes*, ECONF **C940808** (1994) 033, `arXiv:hep-ph/9503437`.

[327] N. Armesto, A. Capella, A. Kaidalov, J. Lopez-Albacete, and C. Salgado, *Nuclear structure functions at small x from inelastic shadowing and diffraction*, Eur.Phys.J. **C29** (2003) 531–540, `arXiv:hep-ph/0304119 [hep-ph]`.

[328] K. Tywoniuk, I. Arsene, L. Bravina, A. Kaidalov, and E. Zabrodin, *Gluon shadowing in the Glauber-Gribov model at HERA*, Phys. Lett. **B657** (2007) 170–175, `arXiv:0705.1596 [hep-ph]`.

[329] L. Frankfurt, V. Guzey, and M. Strikman, *Leading twist coherent diffraction on nuclei in deep inelastic scattering at small x and nuclear shadowing*, Phys. Lett. **B586** (2004) 41–52, `arXiv:hep-ph/0308189`.

[330] C. Marquet, *A Unified description of diffractive deep inelastic scattering with saturation*, Phys.Rev. **D76** (2007) 094017, `arXiv:0706.2682 [hep-ph]`.

[331] H. Kowalski, T. Lappi, C. Marquet, and R. Venugopalan, *Nuclear enhancement and suppression of diffractive structure functions at high energies*, Phys. Rev. **C78** (2008) 045201, `arXiv:0805.4071 [hep-ph]`.

[332] J. Collins and H. Jung, *Need for fully unintegrated parton densities*, `arXiv:hep-ph/0508280`.

[333] J. C. Collins and D. E. Soper, *Back-To-Back Jets in QCD*, Nucl. Phys. **B193** (1981) 381.

[334] J. C. Collins and D. E. Soper, *Parton Distribution and Decay Functions*, Nucl. Phys. **B194** (1982) 445.

[335] J. C. Collins, *What exactly is a parton density?*, Acta Phys. Polon. **B34** (2003) 3103, arXiv:hep-ph/0304122.

[336] J. Collins, *Rapidity divergences and valid definitions of parton densities*, PoS **LC2008** (2008) 028, arXiv:0808.2665 [hep-ph].

[337] X.-d. Ji, J.-p. Ma, and F. Yuan, *QCD factorization for semi-inclusive deep-inelastic scattering at low transverse momentum*, Phys. Rev. **D71** (2005) 034005, arXiv:hep-ph/0404183.

[338] M. Ciafaloni, *Coherence Effects in Initial Jets at Small q**2 / s*, Nucl. Phys. **B296** (1988) 49.

[339] S. Catani, F. Fiorani, and G. Marchesini, *QCD Coherence in Initial State Radiation*, Phys.Lett. **B234** (1990) 339.

[340] S. Catani, F. Fiorani, and G. Marchesini, *Small x Behavior of Initial State Radiation in Perturbative QCD*, Nucl.Phys. **B336** (1990) 18.

[341] G. Marchesini, *QCD coherence in the structure function and associated distributions at small x*, Nucl.Phys. **B445** (1995) 49–80, arXiv:hep-ph/9412327 [hep-ph].

[342] I. Balitsky, *High-energy QCD and Wilson lines*, arXiv:hep-ph/0101042.

[343] J. C. Collins, *Foundations of Perturbative QCD.* Cambridge University Press, Cambridge, 2011. To be published.

[344] S. Aybat and T. C. Rogers, *TMD Parton Distribution and Fragmentation Functions with QCD Evolution*, arXiv:1101.5057 [hep-ph]. * Temporary entry *.

[345] J. C. Collins and A. Metz, *Universality of soft and collinear factors in hard- scattering factorization*, Phys. Rev. Lett. **93** (2004) 252001, arXiv:hep-ph/0408249.

[346] F. Landry, R. Brock, P. M. Nadolsky, and C. P. Yuan, *Tevatron Run-1 Z boson data and Collins-Soper-Sterman resummation formalism*, Phys. Rev. **D67** (2003) 073016, arXiv:hep-ph/0212159.

[347] J. C. Collins, D. E. Soper, and G. F. Sterman, *Transverse Momentum Distribution in Drell-Yan Pair and W and Z Boson Production*, Nucl. Phys. **B250** (1985) 199.

[348] C. Marquet, B.-W. Xiao, and F. Yuan, *Semi-inclusive Deep Inelastic Scattering at small x*, Phys. Lett. **B682** (2009) 207–211, arXiv:0906.1454 [hep-ph].

[349] F. Dominguez, B.-W. Xiao, and F. Yuan, *kt-factorization for Hard Processes in Nuclei*, Phys. Rev. Lett. **106** (2011) 022301, arXiv:1009.2141 [hep-ph].

[350] H1 Collaboration, A. Aktas et al., *Inclusive dijet production at low Bjorken-x in deep inelastic scattering*, Eur. Phys. J. **C33** (2004) 477–493, arXiv:hep-ex/0310019.

[351] A. J. Askew, D. Graudenz, J. Kwiecinski, and A. D. Martin, *Dijet production at HERA as a probe of BFKL dynamics*, Phys. Lett. **B338** (1994) 92–97, `arXiv:hep-ph/9407337`.

[352] J. Kwiecinski, A. D. Martin, and A. M. Stasto, *Predictions for dijet production in DIS using small x dynamics*, Phys. Lett. **B459** (1999) 644–648, `arXiv:hep-ph/9904402`.

[353] A. Szczurek, N. N. Nikolaev, W. Schafer, and J. Speth, *Mapping the proton unintegrated gluon distribution in dijets correlations in real and virtual photoproduction at HERA*, Phys. Lett. **B500** (2001) 254–262, `arXiv:hep-ph/0011281`.

[354] M. Hansson and H. Jung, *Towards precision determination of uPDFs*, `arXiv:0707.4276 [hep-ph]`.

[355] F. Hautmann and H. Jung, *Angular correlations in multi-jet final states from kt-dependent parton showers*, JHEP **10** (2008) 113, `arXiv:0805.1049 [hep-ph]`.

[356] J. Bartels, C. Ewerz, H. Lotter, and M. Wusthoff, *Azimuthal distribution of quark - anti-quark jets in DIS diffractive dissociation*, Phys.Lett. **B386** (1996) 389–396, `arXiv:hep-ph/9605356 [hep-ph]`.

[357] J. Bartels, H. Jung, and M. Wusthoff, *Quark - anti-quark gluon jets in DIS diffractive dissociation*, Eur.Phys.J. **C11** (1999) 111–125, `arXiv:hep-ph/9903265 [hep-ph]`.

[358] L. Lonnblad, *ARIADNE version 4: A Program for simulation of QCD cascades implementing the color dipole model*, Comput.Phys.Commun. **71** (1992) 15–31.

[359] H. Jung and G. P. Salam, *Hadronic final state predictions from CCFM: The hadron-level Monte Carlo generator CASCADE*, Eur. Phys. J. **C19** (2001) 351–360, `arXiv:hep-ph/0012143`.

[360] A. H. Mueller, *Parton distributions at very small x values*, Nucl. Phys. Proc. Suppl. **18C** (1991) 125–132.

[361] A. H. Mueller, *Jets at LEP and HERA*, J. Phys. **G17** (1991) 1443–1454.

[362] H1 Collaboration, S. Aid et al., *Transverse energy and forward jet production in the low x regime at HERA*, Phys. Lett. **B356** (1995) 118–128, `arXiv:hep-ex/9506012`.

[363] H1 Collaboration, C. Adloff et al., *Forward jet and particle production at HERA*, Nucl. Phys. **B538** (1999) 3–22, `arXiv:hep-ex/9809028`.

[364] H1 Collaboration, A. Aktas et al., *Forward jet production in deep inelastic scattering at HERA*, Eur. Phys. J. **C46** (2006) 27–42, `arXiv:hep-ex/0508055`.

[365] ZEUS Collaboration, J. Breitweg et al., *Forward jet production in deep inelastic scattering at HERA*, Eur. Phys. J. **C6** (1999) 239–252, `arXiv:hep-ex/9805016`.

[366] ZEUS Collaboration, J. Breitweg et al., *Measurement of the E(T,jet)**2/Q**2 dependence of forward- jet production at HERA*, Phys. Lett. **B474** (2000) 223–233, `arXiv:hep-ex/9910043`.

[367] ZEUS Collaboration, S. Chekanov et al., *Forward jet production in deep inelastic e p scattering and low-x parton dynamics at HERA*, Phys. Lett. **B632** (2006) 13–26, `arXiv:hep-ex/0502029`.

[368] J. Kwiecinski, S. C. Lang, and A. D. Martin, *Single particle spectra in deep inelastic scattering as a probe of small x dynamics*, Eur. Phys. J. **C6** (1999) 671–680, `arXiv:hep-ph/9707240`.

[369] J. Kwiecinski, A. D. Martin, and J. J. Outhwaite, *Small x QCD effects in DIS with a forward jet or a forward* π^0, Eur. Phys. J. **C9** (1999) 611–622, `arXiv:hep-ph/9903439`.

[370] G. Bottazzi, G. Marchesini, G. P. Salam, and M. Scorletti, *Small-x one-particle-inclusive quantities in the CCFM approach*, JHEP **12** (1998) 011, `arXiv:hep-ph/9810546`.

[371] H. Jung, *CCFM prediction on forward jets and F2: Parton level predictions and a new hadron level Monte Carlo generator CASCADE*, `arXiv:hep-ph/9908497`.

[372] H. Jung, *CCFM prediction for F2 and forward jets at HERA*, Nucl. Phys. Proc. Suppl. **79** (1999) 429–431, `arXiv:hep-ph/9905554`.

[373] O. Kepka, C. Royon, C. Marquet, and R. B. Peschanski, *Next-leading BFKL effects in forward-jet production at HERA*, Phys. Lett. **B655** (2007) 236–240, `arXiv:hep-ph/0609299`.

[374] J. Bartels, V. Del Duca, and M. Wusthoff, *Azimuthal dependence of forward jet production in DIS in the high-energy limit*, Z.Phys. **C76** (1997) 75–79, `arXiv:hep-ph/9610450 [hep-ph]`.

[375] A. Sabio Vera and F. Schwennsen, *Azimuthal decorrelation of forward jets in Deep Inelastic Scattering*, Phys. Rev. **D77** (2008) 014001, `arXiv:0708.0549 [hep-ph]`.

[376] J. Kwiecinski, A. D. Martin, P. J. Sutton, and K. J. Golec-Biernat, *QCD predictions for the transverse energy flow in deep inelastic scattering in the HERA small x regime*, Phys. Rev. **D50** (1994) 217–225, `arXiv:hep-ph/9403292`.

[377] K. J. Golec-Biernat, J. Kwiecinski, A. D. Martin, and P. J. Sutton, *Transverse energy flow at HERA*, Phys. Lett. **B335** (1994) 220–225, `arXiv:hep-ph/9405400`.

[378] N. H. Brook et al., *A comparison of deep inelastic scattering Monte Carlo event generators to HERA data*, `arXiv:hep-ex/9912053`.

[379] G. P. Salam and G. Soyez, *A practical Seedless Infrared-Safe Cone jet algorithm*, JHEP **05** (2007) 086, `arXiv:0704.0292 [hep-ph]`.

[380] H. Jung et al., *The CCFM Monte Carlo generator CASCADE 2.2.0*, Eur. Phys. J. **C70** (2010) 1237–1249, `arXiv:1008.0152 [hep-ph]`.

[381] Y. L. Dokshitzer, V. A. Khoze, A. H. Mueller, and S. I. Troyan, *Basics of perturbative QCD*, . Editions Frontieres 1991, 274p.

[382] L. Frankfurt, V. Guzey, M. McDermott, and M. Strikman, *Revealing the black body regime of small x DIS through final state signals*, Phys. Rev. Lett. **87** (2001) 192301, `arXiv:hep-ph/0104154`.

[383] D. de Florian, R. Sassot, and M. Stratmann, *Global analysis of fragmentation functions for pions and kaons and their uncertainties*, Phys.Rev. **D75** (2007) 114010, arXiv:hep-ph/0703242 [HEP-PH].

[384] D. de Florian, R. Sassot, and M. Stratmann, *Global analysis of fragmentation functions for protons and charged hadrons*, Phys.Rev. **D76** (2007) 074033, arXiv:0707.1506 [hep-ph].

[385] V. M. Budnev, I. F. Ginzburg, G. V. Meledin, and V. G. Serbo, *The Two photon particle production mechanism. Physical problems. Applications. Equivalent photon approximation*, Phys. Rept. **15** (1975) 181–281.

[386] T. H. Bauer, R. D. Spital, D. R. Yennie, and F. M. Pipkin, *The Hadronic Properties of the Photon in High-Energy Interactions*, Rev. Mod. Phys. **50** (1978) 261.

[387] J. M. Butterworth and M. Wing, *High energy photoproduction*, Rept. Prog. Phys. **68** (2005) 2773–2828, arXiv:hep-ex/0509018.

[388] T. C. Rogers and M. I. Strikman, *Hadronic interactions of ultra-high energy photons with protons and light nuclei in the dipole picture*, J. Phys. **G32** (2006) 2041–2063, arXiv:hep-ph/0512311.

[389] ZEUS Collaboration, S. Chekanov et al., *Measurement of the photon proton total cross section at a center-of-mass energy of 209-GeV at HERA*, Nucl. Phys. **B627** (2002) 3–28, arXiv:hep-ex/0202034.

[390] H1 Collaboration, S. Aid et al., *Measurement of the total photon-proton cross-section and its decomposition at 200-GeV center-of-mass energy*, Z. Phys. **C69** (1995) 27–38, arXiv:hep-ex/9509001.

[391] G. M. Vereshkov, O. D. Lalakulich, Y. F. Novoseltsev, and R. V. Novoseltseva, *Total cross section for photon nucleon interaction in the energy range $\sqrt{s}$ = 40-GeV - 250-GeV*, Phys. Atom. Nucl. **66** (2003) 565–574.

[392] Particle Data Group Collaboration, K. Nakamura, *Review of particle physics*, J. Phys. **G37** (2010) 075021.

[393] Z. Collaboration, *Measurement of the energy dependence of the total photon-proton cross section at HERA*, Phys.Lett. **B697** (2011) 184–193, arXiv:1011.1652 [hep-ex]. * Temporary entry *.

[394] R. M. Godbole, A. Grau, G. Pancheri, and Y. N. Srivastava, *Total photoproduction cross-section at very high energy*, Eur. Phys. J. **C63** (2009) 69–85, arXiv:0812.1065 [hep-ph].

[395] M. M. Block and F. Halzen, *Evidence for the saturation of the Froissart bound*, Phys. Rev. **D70** (2004) 091901, arXiv:hep-ph/0405174.

[396] M. M. Block and F. Halzen, *New evidence for the saturation of the Froissart bound*, Phys. Rev. **D72** (2005) 036006, arXiv:hep-ph/0506031.

[397] M. M. Block, E. M. Gregores, F. Halzen, and G. Pancheri, *Photon - proton and photon-photon scattering from nucleon- nucleon forward amplitudes*, Phys. Rev. **D60** (1999) 054024, `arXiv:hep-ph/9809403`.

[398] S. Frixione, Z. Kunszt, and A. Signer, *Three jet cross-sections to next-to-leading order*, Nucl. Phys. **B467** (1996) 399–442, `arXiv:hep-ph/9512328`.

[399] S. Frixione, *A General approach to jet cross-sections in QCD*, Nucl. Phys. **B507** (1997) 295–314, `arXiv:hep-ph/9706545`.

[400] M. Gluck, E. Reya, and A. Vogt, *Parton structure of the photon beyond the leading order*, Phys. Rev. **D45** (1992) 3986–3994.

[401] S. D. Ellis and D. E. Soper, *Successive combination jet algorithm for hadron collisions*, Phys. Rev. **D48** (1993) 3160–3166, `arXiv:hep-ph/9305266`.

[402] H1 Collaboration, C. Adloff et al., *Measurement of inclusive jet cross-sections in photoproduction at HERA*, Eur. Phys. J. **C29** (2003) 497–513, `arXiv:hep-ex/0302034`.

[403] S. Frixione and G. Ridolfi, *Jet photoproduction at HERA*, Nucl. Phys. **B507** (1997) 315–333, `arXiv:hep-ph/9707345`.

[404] A. M. Stasto, *Physics of ultrahigh energy neutrinos*, Int. J. Mod. Phys. **A19** (2004) 317–340, `arXiv:astro-ph/0310636`.

[405] J. K. Becker, *High-energy neutrinos in the context of multimessenger physics*, Phys. Rept. **458** (2008) 173–246, `arXiv:0710.1557 [astro-ph]`.

[406] E. Zas, *Neutrino Detection with Inclined Air Showers*, New J. Phys. **7** (2005) 130, `arXiv:astro-ph/0504610`.

[407] N. Armesto, C. Merino, G. Parente, and E. Zas, *Charged Current Neutrino Cross Section and Tau Energy Loss at Ultra-High Energies*, Phys. Rev. **D77** (2008) 013001, `arXiv:0709.4461 [hep-ph]`.

[408] K. Hirata and E. Keil, *Barycentre motion of beams due to beam-beam interaction in asymmetric ring colliders*, Nuclear Instruments and Methods in Physics Research Section A: Accelerators, Spectrometers, Detectors and Associated Equipment **292** (1990) no. 1, 156 – 168. `http://www.sciencedirect.com/science/article/B6TJM-470F1H3-M/2/ff1b42fa7c847256a9e6c3245d3335d5`.

[409] *Private Communication with Sylvain Weisz.*, .

[410] R. Appleby, *IRSYN*, (2010) .

[411] S. Russenschuck, *Magnet Options for Q1 and Q2 (Ring-Ring and Linac-Ring*, 3^{rd} CERN-ECFA-NuPECC Workshop on the LHeC (2010) .

[412] N. Bernard, *Analytic Method to Calculate the Power Produced by Synchrotron Radiation in a Quadrupole Magnet*, CERN LHeC Note 2 (2010) .

[413] H. Wiedemann, *Synchrotron Radiation*, Springer-Verlag Berlin Heidelberg (2003) .

[414] I. B. *et al.*, *Study of beam-induced backgrounds in the ZEUS detector from 2002 HERA running*, (2002) .

[415] S. Russenschuck, *Private Communication*, (2010) .

[416] D. Barber and G. Ripken in *Handbook of Accelerator Physics and Engineering*, A. Chao and M. Tigner, eds. World Scientific, first ed., 2006. third printing.

[417] D. Barber et al., *Several articles*, in *Proc. ICFA Workshop on Quantum Aspects of Beam Physics*. World Scientific, Monterey, CA, USA, 1999.

[418] A. Sokolov and I. Ternov Sov. Phys. Dokl. **8** (1964) no. 12, 1203.

[419] J. Jackson, *Classical Electrodynamics*. Wiley & Sons, third ed., 1998.

[420] Y. Derbenev and A. Kondratenko Sov. Phys. JETP **37** (1973) 968.

[421] S. Mane Phys. Rev. **A36** (1987) 105–130.

[422] G. Hoffstätter, M. Vogt, and D. Barber Phys. Rev. ST Accel. Beams **11** (1999) no. 2, 114001.

[423] D. Barber, G. Hoffstätter, and M. Vogt in *Proc. 14th Int. Spin Physics Symp.* AIP Conf. Proc. 570 (2001), 2000.

[424] V. Baier and V. Katkov Sov. Phys. JETP **25** (1967) 944.

[425] V. Baier, V. Katkov, and V. Strakhovenko Sov. Phys. JETP **31** (1970) 908.

[426] R. Assmann et al. in *Proc. Part. Accel. Conf.*, p. 2999 and page 3002. New York, NY, USA, 1999.

[427] D. Barber et al. Phys. Lett. **343B** (1995) 436.

[428] S. Mane Nucl.Inst.Meth. **A292** (1990) 52.

[429] S. Mane Nucl.Inst.Meth. **A321** (1992) 21.

[430] D. Barber. SLICKTRACK is the extended version of SLICK [431] which includes Monte-Carlo spin-orbit tracking using the mathematical structures of SLICK.

[431] D. Barber. SLICK is a thick lens version of SLIM [416] by D.P. Barber using the formalism of [446].

[432] B. Montague Physics Reports **113** (1984) .

[433] Y. Derbenev and H. Grote Tech. Rep. SL/Note 95-37, CERN, 1995.

[434] C. Johnstone, *Local chromaticity correction of the LHC*, PAC97 (1997) .

[435] S. Fartoukh, *Optics Challenges and Solutions for the LHC Insertion Upgrade Phase I*, LHC Project Report 0038 (2010) .

[436] S. Fartoukh, *Towards the LHC Upgrade using the LHC well-characterized technology*, LHC Project Report 0049 (2010) .

[437] P. Raimondi and A. Seryi, *Novel Final Focus Design for Future Linear Colliders*, Phys. Rev. Lett. **86** (2001) .

[438] A. Gaddi, *Passive isolation*, Presented in IWLC 2010 (2010) .

[439] A. Verdier, *Alignment optics for LHC*, LHC Project Note 325 (2003) .

[440] D. Schulte, *Beam-Beam Simulations with GUINEA-PIG*, ICAP98 (1998) .

[441] R. Appleby, L. Keller, T. W. Markiewicz, A. Seryi, D. Walz, et al., *The International linear collider beam dumps*, `arXiv:physics/0601103 [physics]`.

[442] J. Amann, R. Arnold, A. Seryi, D. Walz, K. Kulkarni, et al., *Design of an 18 MW Beam Dump for 500 GeV Electron/Positron Beams at an ILC*, .

[443] M. Barnes, F. Caspers, L. Ducimetiere, N. Garrel, and T. Kroyer, *The beam screen for the LHC injection kicker magnets*, .

[444] E. Carlier, U. Jansson, R. Jung, V. Mertens, S. Peraire, et al., *The LEP beam dumping system*, .

[445] M. Klein and R. Yoshida, *Collider Physics at HERA*, `arXiv:0805.3334 [hep-ex]`.

[446] H. Mais and G. Ripken Tech. Rep. 83-62, DESY, 1983. Modern notation: replace $\mathbf{n}$ by $\mathbf{n}_0$.

Appendix 1

Tasks for a Technical Design Report

Building and Operating the LHeC

Appendix 2

Committees (SAC, Steering, Convenors)

List of Participants and Institutes